AN ANALYTICAL AND COMPUTATIONAL INVESTIGATION OF SHOCK-INDUCED VORTICAL FLOWS WITH APPLICATIONS TO SUPERSONIC COMBUSTION

Thesis by

Joseph Yang

In Partial Fulfillment of the Requirements

for the Degree of Doctor of Philosophy

California Institute of Technology

Pasadena, California

1991

(Defended April 22, 1991)

Acknowledgements

I would like to thank my research advisors, Professors Ed Zukoski and Toshi Kubota, for many stimulating hours of formal coursework and informal discussion. I am appreciative of Professor Zukoski for his courtesy and good humor, and for his many years of generous yet unfettered support throughout both my undergraduate and graduate studies. I am inspired by Professor Kubota's depth of insight, eloquence of mathematical expression, and uncommon ability to teach rather than pedantize.

I would like to thank my fellow students for their fellowship and encouragement, Mr. Tom Welmers for making my various computing needs as user-friendly as possible, and Mrs. Cecelia Lin for expert preparation of some of the figures. I would also like to thank Miss Helen Cheng for interrupting my tense moments with regular doses of exuberance, for sharing the endless hours of photocopying and cutting and pasting, and for the support and friendship she has given me over the years.

This research was supported by the Office of Naval Research through an ONR Graduate Fellowship, the National Science Foundation through a Cray supercomputer grant at the San Diego Supercomputer Center, and the Air Force Office of Scientific Research through contract number F49620-86-C-0113 and grant number AFOSR-90-0188. I would like to thank Dr. Elaine S. Oran, of the Laboratory for Computational Physics at the Naval Research Laboratory, for providing the algorithm used in the numerical simulations.

Most importantly, I would like to thank my parents, Drs. Tony T.S. and Hsiu-Ying Tsai Yang, for their stimulation, encouragement, and support. In a very real sense, they were the first and best teachers throughout all my years of study.

Abstract

The motivation for study of shock-induced vortical flows is the problem of achieving rapid and efficient mixing of fuel and oxidizer in a SCRAMJET engine. In particular, the interaction of a shock wave with a jet of light gas generates vorticity which can be used to stir and mix the fluids. This investigation consists of two parts.

The first part is a characterization of the basic fluid mechanics of the interaction. The canonical problem is a shock wave passing over a circular light gas inhomogeneity located within a finite channel. The pressure gradient from the shock wave interacts with the density gradient at the edge of the inhomogeneity to deposit vorticity around the perimeter. As time goes on, the structure rolls up into a pair of counter-rotating vortices. This flow is simulated numerically by integrating the governing equations subject to specified initial conditions. From first principles, analytical models are developed to predict the circulation, spacing, and characteristic time for development as a function of initial conditions. From perturbation analysis, another model is developed to predict the vortex pair velocity as a function of the geometrical parameters *vortex size/vortex spacing* and *vortex spacing/channel spacing*. The agreement between models and computations is generally good. These models represent the first successful and comprehensive characterization of the fluid mechanics of the canonical flow.

The second part is an investigation of mixing efficiencies for various initial configurations. In the canonical flow, stabilization of the vortex pair eventually impairs the mixing. Various initial configurations are considered with the goal of improving the mixing. The mixing is quantified by an asymptotic stretching rate of a material element. Single jet shape perturbations yield little improvement in mixing, but multiple jet arrays do, especially through the phenomenon of entrainment. Another way to improve the mixing is to hit a vortex pair with a reflected shock. Finally, a mathematical correspondence is exhibited between the unsteady 2-D flows considered here and the corresponding 3-D steady flows that may be more typical of real combustor designs.

TABLE OF CONTENTS

List of Figures

List of Tables

List of Symbols*

$\overline{(\,)}$ - A nondimensionalized variable

$(\,)^*$ - i) A quantity that is scaled locally from 0 to 1
ii) Complex conjugation

$(\,)^{in}$ - Pertaining to inside a boundary

$(\,)^{out}$ - Pertaining to outside a boundary

$(\,)_{2-D}$ - Pertaining to two-dimensional conditions

$(\,)_{3-D}$ - Pertaining to three-dimensional conditions

$(\,)_{air}$ - Pertaining to pure air

$(\,)_{avg}$ - Pertaining to the average

$(\,)_{cmf}$ - Pertaining to center of mass fraction

$(\,)_{error}$ - Pertaining to error propagation

$(\,)_{He}$ - Pertaining to pure helium

$(\,)_{max}$ - Pertaining to the maximum

$(\,)_{min}$ - Pertaining to the minimum

$(\,)_{shock\ out}$ - Pertaining to the shock wave leaving the domain

$(\,)_{wall}$ - Pertaining to the channel wall

$(\,)_0$ - Pertaining to initial conditions, before the interaction

$(\,)_1$ - Pertaining to air, ahead of the shock

$(\,)_2$ - Pertaining to air, behind the shock

$(\,)_H$ - Pertaining to heavy gas

$(\,)_I$ - Pertaining to the incident shock

$(\,)_L$ - Pertaining to light gas

$(\,)_R$ - Pertaining to the reflected shock

$(\,)_s$ - Pertaining to stoichiometric conditions

β - Oblique shock angle

δ - Oblique shock turning angle

ϵ - i) Perturbation parameter [$\equiv R/y_\infty$]
ii) Amplitude of the sinusoidal perturbation

η - i) Elliptical coordinate tangent to the ellipse

---

* In general, i) there is no difference in meaning between italicized and non-italicized versions of the same symbol, *e.g.*, v is the same as v, ii) vectors are underlined, not **boldfaced**, and iii) symbols are listed here in their dimensional forms, even though nondimensional forms predominate in the text. The convention for nondimensionalization, indicated by an overline, is defined in Chapter 2.

ii) Similarity variable in the mixing layer analysis

Γ - Circulation of the vortex pair

γ - Specific heat ratio, usually a function of mass fraction

λ - Wavelength of the sinusoidal perturbation

ν - Kinematic viscosity

$\underline{\omega}$ - Vorticity vector

ω - Vorticity

Ω - Coefficient of the linear term of a laminar jet velocity profile

ϕ - Angle between the tangent to a boundary and the tangential

ψ - i) Growth reduction factor for Richtmyer-Meshkov instability

ii) Streamfunction

$\Delta\rho$ - Density jump across the edge of the jet

ρ - Density

ρ_H - Heavy gas density

ρ_L - Light gas density

ρ_{model} - Density of the model flow

$\mathcal{D}$ - Binary diffusion coefficient

τ - Characteristic time

θ - Angle in polar coordinates

ξ - Elliptical coordinate normal to the ellipse

a - Horizontal semi-axis of the ellipse

A - i) Area

ii) Atwood number

AR - Aspect ratio of the ellipse

b - Vertical semi-axis of the ellipse

c - i) Speed of sound

ii) Hyperbolic tangent thickness parameter

iii) Ellipse shape parameter

D_0 - Initial diameter of a jet or cylinder

$\hat{e}_n$ - Unit normal vector

$\hat{e}_x$ - Unit vector in x-direction

$\hat{e}_y$ - Unit vector in y-direction

f - i) Mass fraction of the light gas

ii) A mathematical function

F - i) External force scalar potential

ii) Transformed streamfunction in the mixing layer similarity solution

g - A mathematical function

G - Mass fraction in the mixing layer similarity solution

h - i) Half height of the channel

ii) Metrical coefficient for elliptical coordinates

h_η - Metrical coefficient for the elliptical coordinate η

h_ξ - Metrical coefficient for the elliptical coordinate ξ

H - Characteristic height

$\underline{I}$ - Impulse vector

I_x - x-component of impulse

I'_x - A measure of the impulse of the flow

J - Jacobian of a transformation

L - i) Spacing of a jet pair or trio

ii) Length of a mass fraction contour level

m - Correspondence factor between 3-D steady and 2-D unsteady flows

M - Incident shock Mach number

n - Wavenumber of the sinusoidal perturbation

Δp - Pressure jump across the shock

p - Pressure

p_n^k - Coefficient for Laurent series expansion of inner self corrections

q_n^k - Coefficient for Laurent series expansion of outer self corrections

Q - i) Any quantity that is being integrated

ii) Volumetric flow rate

r - Radius in polar coordinates

r_k - Coefficient of the power series expansion for vortex boundary

R - Effective radius of the vortex core

R_0 - Initial radius of the light gas jet or cylinder

R_B - Boundary of the constant vorticity vortex model

Δt - Timestep in the computation

t - Time

u - Horizontal Cartesian velocity

$\underline{u}$ - Velocity vector

U - Velocity of the vortex pair, relative to the ambient fluid

$\underline{u}^{in'}$ - Inner velocity for an uniform density flow

u_k - Coefficient of the power series expansion for u

u_r - Radial velocity in polar coordinates

u_{r_k} - Coefficient of the power series expansion for u_r

u_θ - Tangential velocity in polar coordinates

u_{θ_k} - Coefficient of the power series expansion for u_θ

v - Vertical Cartesian velocity

v_2 - Velocity behind the shock in lab-fixed coordinates

v_k - Coefficient of the power series expansion for v

v_{r_k} - Coefficient of the power series expansion for v_r

V - Velocity of the vortex pair, relative to the ambient fluid

V_n - Coefficient of the power series expansion for vortex pair velocity

V_s - Velocity of the shock in lab-fixed coordinates

W - Characteristic width

Δx - i) Horizontal grid spacing in the computation

ii) Characteristic horizontal lengthscale

$\underline{x}$ - Position vector

x - Horizontal Cartesian coordinate

x_∞ - Half-spacing of the vortex pair at steady-state

Δy - i) Vertical grid spacing in the computation

ii) Characteristic vertical lengthscale

y - Vertical Cartesian coordinate

y_∞ - Half-spacing of the vortex pair at steady-state

y_i - i) Mass fraction of species i

ii) Howarth transformation variable

z - i) Complex position variable

ii) Cartesian coordinate in (x,y,z) triad

Chapter 1 - Introduction

The motivation for the study of shock-induced vortical flows is the combustion of fuel and oxidizer in a supersonic combustion ramjet, such as the proposed National Aerospace Plane. In such a vehicle, supersonic air flow into the combustion chamber limits the residence time to only a few milliseconds. This imposes a severe requirement for rapid and efficient mixing of fuel and oxidizer.

Marble, *et al.* (1990) proposed the mechanism of shock-induced vorticity generation as a possible means of achieving this mixing. In particular, they showed that the interaction of a shock wave with a jet of light gas surrounded by an ambient heavy gas would generate vorticity around the perimeter of the jet. This vorticity would then cause the jet to roll up at its front and rear edges, stirring and mixing the light jet gas with the ambient heavy gas (Figure 1.1). They also qualitatively argued that the three-dimensional (3-D), steady flow in an actual injector design should be analogous to a two-dimensional (2-D) unsteady flow, which is often more conveniently studied, either experimentally or computationally. In the 3-D flow, the shock wave passes vertically upward through the jet as it moves downstream. In the analogous 2-D flow, a normal shock wave propagates through a planar region of light gas as a function of time, and the gas rolls up at its upper and lower edges. This is illustrated in Figure 1.2, which shows the time evolution of the 2-D structure. The vertical direction in the 3-D flow corresponds to the downstream direction in the 2-D flow, and the downstream direction in the 3-D flow corresponds to time in the 2-D flow. That is, spatial development in the 3-D flow corresponds to temporal development in the 2-D flow.

Study of the 2-D unsteady problem predates the idea of using shock-induced vorticity for supersonic combustion. It was first investigated by Rudinger and Somers (1960), and more recently by Haas (1984, 1987), Picone and Boris (1988), Hendricks and Marble (1991), and Jacobs (1991). Unfortunately, their collective results are inconclusive. The studies all demonstrated the development of qualitatively similar vortical structures, but with unexplained quantitative discrepancies (*e.g.*, differences in the size, spacing, and velocity of vortical structures formed from similar initial conditions).

Each of these studies covered only a limited range of flow conditions, and the quantitative results were usually limited to tabulations of some fluid mechanical parameters, followed by *a posteriori* explanations of the observed measurements. In some cases, models were proposed to describe limited parts of the interaction. However, no comprehensive theory was developed. Furthermore, the proposed models were either unconfirmed by reliable data, or contradicted by other investigations. Thus, the presently available fluid mechanical description of the flow is both incomplete and unproven. Finally, with the exception of Jacobs (1991), these investigations did not address the question of mixing.

The present work is an analytical and computational investigation of the shock-induced vortical flow in the 2-D unsteady case. Two broad aims can be stated. One is to develop a comprehensive description of the canonical problem. The problem is investigated computationally, by solution of the governing differential equations with various initial conditions. This establishes a qualitative understanding of the important flow features, as well as quantifying the behavior over a range of flow parameters. Then, independently of the computations, analytical models for the flow are developed and compared against the computations. This provides, *a priori*, the ability to predict key features of the flow without having to perform expensive and time-consuming computations. Both the computations and the analytical models are also compared against the available experimental data.

The second aim is to characterize the mixing of shock-induced vortical flows, for the canonical problem and also for variations on the canonical problem that represent configurations more appropriate to a real flow. Computations are performed for a family of single jet shape variations and multiple jet geometrical variations. This gives a qualitative understanding of how the physics of each case differs from that of the canonical flow. Finally, a means of characterizing the mixing is developed and used to make quantitative comparisons.

1.1 The Canonical Problem: Interaction of a Shock Wave with a Single Circular Jet

Consider the interaction of a shock wave in air with an isolated circular inhomogeneity of lower density gas, as shown in Figure 1.2(a). This could represent, for example, a slice through a jet perpendicular to the plane of the paper.

According to the inviscid vorticity equation,

$$\frac{D}{Dt}\left(\frac{\underline{\omega}}{\rho}\right) = \frac{1}{\rho}\,(\underline{\omega}\cdot\underline{\nabla}u) + \frac{1}{\rho^3}\,(\underline{\nabla}\rho\times\underline{\nabla}p).$$

This can be rewritten as

$$\frac{D\underline{\omega}}{Dt} = \frac{1}{\rho^2}\,(\underline{\nabla}\rho\times\underline{\nabla}p) + \ldots,$$

giving a rate of generation of vorticity proportional to the cross product of the density and pressure gradients.

As the shock wave passes over the jet, vorticity is deposited around the circumference of the jet, as shown in Figure 1.2(b). The density gradient, due to the density jump at the circumference of the jet, is everywhere radially outward. The pressure gradient, due to the pressure jump across the shock, points upstream. Where the pressure gradient is perpendicular to the density gradient ($\theta = \pm\pi/2$), the vorticity is maximum. Where the two gradients are parallel ($\theta = 0, \pi$), the vorticity is zero. Elsewhere, the vorticity is intermediate.

As will be shown, the deposited vorticity will initially cause the jet to roll up into a kidney-shaped structure, as shown in Figure 1.2(c). As time goes on, the vorticity will coalesce and the structure will evolve toward a vortex pair with finite core size, as shown in Figure 1.2(d). The first part of this work, Chapters 2 to 6, is devoted to characterization of this process.

The equations that govern the flow, and the computational algorithm used in their solution, are described in Chapter 2.

A qualitative investigation of the canonical flow, using the computational technique described in Chapter 2, is presented in Chapter 3. In particular, how does the structure evolve from an initially simply connected region with circumferential vorticity to a steady-state vortex pair? Also, how is the evolution affected by changes in shock strength or light/heavy gas density ratio?

In the interpretation of computational results, there arise problems associated with uncertainties due to numerical diffusion and resolution effects. The causes of, and the corrections for, systematic errors in the quantitative description of the flows are described in Chapter 4. These error correction techniques are applied to the canonical flow computations to quantify the motion of the vortex pair.

An analytical description of the canonical flow from the point of view of fundamental fluid mechanics is presented in Chapter 5. Models are developed to characterize the behavior of the vortex pair, and the predictions of these models are compared against the computed data.

The first model describes the dependence of the circulation of either vortex, Γ, on the light/heavy gas density ratio, ρ_L/ρ_H, and the shock strength, M. This provides a measure of the total swirl in the flow as a function of the initial conditions.

The second model describes the characteristic timescale in the evolution from initial to final states. For example, suppose one wishes to compare two cases in which the processes are driven by different strength initial shocks. What will be the difference in time required for the structures to reach an equivalent stage of development, all other things being equal?

The third model describes the normalized velocity of the vortex pair, Uy_∞/Γ, where U is the absolute velocity, $2y_\infty$ is the vortex spacing, and Γ is the circulation. In the classical inviscid theory, a vortex pair is treated as a pair of point vortices in an unbounded domain. In that case, $Uy_\infty/\Gamma = constant = 1/(4\pi)$. However, in real flows, the vortices have a finite core size and the domain is bounded, and both these effects reduce the velocity below the classical limit. The model predicts the reduction in velocity due to these effects.

The fourth model describes the dependence of y_∞ on ρ_L/ρ_H *and* M. This is the last parameter needed to characterize the motion of the vortex pair, and completes the fluid mechanical description of the flow.

The computations and the models are compared to the available experimental data in Chapter 6.

1.2 Variations on the Canonical Problem

The ultimate outcome of the canonical problem is the partitioning of a single light gas structure into two smaller structures which form a vortex pair. There is a certain amount of mixing of light and heavy gases associated with this partitioning, but further breakup is inhibited by the inherent stability of the vortex pair. Geometrical variations on the canonical problem suggest the possibility of destabilizing the vortex pair, and thus enhancing the mixing beyond that achievable in the canonical case.

The basic fluid mechanics of these variations are qualitatively described in Chapter 7. Different initial cross-sectional shapes are examined in Sections 1 and 2, hitting the developing vortex pair with a reflected shock is examined in Section 3, and various multiple jet initial configurations are examined in Sections 4 to 7.

The application of these results to the problem of supersonic combustion is considered in Chapter 8. In particular, one would like to quantify the mixing that occurs in each of these cases. However, the measurement of mixing via numerical simulations is a subtle endeavor, a black art at best, and a fraud at worst. A mixing measure which sidesteps the difficulties which invalidate many computational mixing measures, while still embodying the essence of the mixing process, is proposed in Section 1. This mixing measure is then used to compare the various flows.

The aforementioned conclusions were drawn from studies of 2-D unsteady flows, while a real supersonic combustor will more closely resemble a 3-D steady flow. It was mentioned earlier that there exists an analogy between these flows, which is the basis for studying the complicated 3-D flow through the simpler 2-D flow. This analogy has been shown to be qualitatively correct (Marble, *et al.* (1990)), but to date, no quantitative comparisons have been made. However, Waitz (1991) has recently performed a computational study of a 3-D steady injector design, providing the first opportunity for direct quantitative comparison. In Section 2, the 2-D unsteady flows corresponding to Waitz's flows are computed and compared with his results. From theoretical considerations, the mathematical equivalence between the two flows is exhibited, and is used to correlate the computed values.

Chapter 2 - Description of the Computational Model

2.1 The Governing Equations

The flow is governed by the conservation equations for continuity, momentum, energy, and species. For two-dimensional unsteady flow, neglecting diffusion and viscosity, these equations are:

- Mass:

$$\frac{\partial \rho}{\partial t} + \frac{\partial}{\partial x}(\rho u) + \frac{\partial}{\partial y}(\rho v) = 0$$

- x-Momentum:

$$\frac{\partial}{\partial t}(\rho u) + \frac{\partial}{\partial x}(\rho u^2) + \frac{\partial}{\partial y}(\rho uv) = -\frac{\partial p}{\partial x}$$

- y-Momentum:

$$\frac{\partial}{\partial t}(\rho v) + \frac{\partial}{\partial x}(\rho uv) + \frac{\partial}{\partial y}(\rho v^2) = -\frac{\partial p}{\partial y}$$

- Energy:

$$\frac{\partial p}{\partial t} + \frac{\partial}{\partial x}(pu) + \frac{\partial}{\partial y}(pv) = -(\gamma - 1)p\left(\frac{\partial u}{\partial x} + \frac{\partial v}{\partial y}\right)$$

- Species:

$$\frac{\partial}{\partial t}(\rho y_i) + \frac{\partial}{\partial x}(\rho u y_i) + \frac{\partial}{\partial y}(\rho v y_i) = 0$$

As a matter of convenience, all lengthscales are normalized by the radius of the initial inhomogeneity, and all flow variables are normalized by the ambient values ahead of the shock. [1] Thus, for example,

- Scale lengths by the initial radius: $\overline{x} = x/R_0$
- Scale velocities by the speed of sound ahead of the shock: $\overline{u} = u/c_1$
- Scale times by R_0/c_1: $\overline{t} = tc_1/R_0$
- Scale densities by the density ahead of the shock: $\overline{\rho} = \rho/\rho_1$
- Scale pressures by the pressure ahead of the shock: $\overline{p} = p/p_1$

[1] This normalization renders self-normalized variables equal to unity. However, such variables are sometimes explicitly retained in expressions in which they appear, because they provide useful information. For example, the density ratio across a shock, ρ_2/ρ_1, is written in nondimensional form as $\overline{\rho}_2/\overline{\rho}_1$, instead of just $\overline{\rho}_2$, to emphasize that the physical quantity of interest is a density *ratio*.

With this normalization, the equations of motion become:

- Mass:

$$\frac{\partial \overline{\rho}}{\partial \overline{t}} + \frac{\partial}{\partial \overline{x}}(\overline{\rho u}) + \frac{\partial}{\partial \overline{y}}(\overline{\rho v}) = 0$$

- x-Momentum:

$$\frac{\partial}{\partial \overline{t}}(\overline{\rho u}) + \frac{\partial}{\partial \overline{x}}(\overline{\rho u^2}) + \frac{\partial}{\partial \overline{y}}(\overline{\rho u v}) = -\frac{1}{\gamma_1}\frac{\partial \overline{p}}{\partial \overline{x}}$$

- y-Momentum:

$$\frac{\partial}{\partial \overline{t}}(\overline{\rho v}) + \frac{\partial}{\partial \overline{x}}(\overline{\rho u v}) + \frac{\partial}{\partial \overline{y}}(\overline{\rho v^2}) = -\frac{1}{\gamma_1}\frac{\partial \overline{p}}{\partial \overline{y}}$$

- Energy:

$$\frac{\partial \overline{p}}{\partial \overline{t}} + \frac{\partial}{\partial \overline{x}}(\overline{p u}) + \frac{\partial}{\partial \overline{y}}(\overline{p v}) = -(\gamma - 1)\overline{p}\left(\frac{\partial \overline{u}}{\partial \overline{x}} + \frac{\partial \overline{v}}{\partial \overline{y}}\right)$$

- Species:

$$\frac{\partial}{\partial \overline{t}}(\overline{\rho y_i}) + \frac{\partial}{\partial \overline{x}}(\overline{\rho u y_i}) + \frac{\partial}{\partial \overline{y}}(\overline{\rho v y_i}) = 0$$

2.2 The Computational Algorithm

The computational algorithm is an explicit Eulerian finite-difference technique of the class of Flux-Corrected-Transport (FCT) solvers. This algorithm was developed by Boris (1977) at the Naval Research Laboratory (NRL), and has been extensively refined and tested by researchers there. The most recent version of the algorithm[2] was used in the present work.

The integration utilizes the technique of operator splitting, which is a means of treating a multi-dimensional system of equations with a series of one-dimensional integrations. A brief summary of the technique is excerpted below.

> *[Specializing to the nondimensional form of the equations used in this work, the conservation equations] are separated into two parts, the $\overline{y}$-direction terms and the $\overline{x}$-direction terms. This arrangement. . .separates the $\overline{y}$-derivatives and the $\overline{x}$-derivatives. . .into parts which can be treated sequentially by a general one-dimensional continuity equation solver. Each $\overline{y}$-direction row in the grid is integrated using the one-dimensional module to solve the four coupled. . .equations*

[2] LCPFCT, made available courtesy of Dr. Elaine Oran at NRL.

from time $\bar{t}$ to $\bar{t}+\Delta\bar{t}$. The $\bar{y}$-direction split-step equations are written in the form

$$\frac{\partial\overline{\rho}}{\partial\bar{t}} = -\frac{\partial}{\partial\bar{y}}(\overline{\rho v})$$

$$\frac{\partial}{\partial\bar{t}}(\overline{\rho u}) = -\frac{\partial}{\partial\bar{y}}(\overline{\rho uv})$$

$$\frac{\partial}{\partial\bar{t}}(\overline{\rho v}) = -\frac{\partial}{\partial\bar{y}}(\overline{\rho v^2}) - \frac{1}{\gamma_1}\frac{\partial\overline{p}}{\partial\bar{y}}$$

$$\frac{\partial\overline{p}}{\partial\bar{t}} = -\frac{\partial}{\partial\bar{y}}(\overline{pv}) - (\gamma-1)\overline{p}\frac{\partial\overline{v}}{\partial\bar{y}}$$

$$\frac{\partial}{\partial\bar{t}}(\overline{\rho y_i}) = -\frac{\partial}{\partial\bar{y}}(\overline{\rho v y_i})$$

[so that]. . .the one-dimensional integration connects those cells which are influencing each other through the $\bar{y}$-component of convection. The changes due to the derivatives in the $\bar{x}$-direction must now be included. This is done in a second split step of one-dimensional integrations along each $\bar{x}$-column,

$$\frac{\partial\overline{\rho}}{\partial\bar{t}} = -\frac{\partial}{\partial\bar{x}}(\overline{\rho u})$$

$$\frac{\partial}{\partial\bar{t}}(\overline{\rho u}) = -\frac{\partial}{\partial\bar{x}}(\overline{\rho u^2}) - \frac{1}{\gamma_1}\frac{\partial\overline{p}}{\partial\bar{x}}$$

$$\frac{\partial}{\partial\bar{t}}(\overline{\rho v}) = -\frac{\partial}{\partial\bar{x}}(\overline{\rho uv})$$

$$\frac{\partial\overline{p}}{\partial\bar{t}} = -\frac{\partial}{\partial\bar{x}}(\overline{pu}) - (\gamma-1)\overline{p}\frac{\partial\overline{u}}{\partial\bar{x}}$$

$$\frac{\partial}{\partial\bar{t}}(\overline{\rho y_i}) = -\frac{\partial}{\partial\bar{x}}(\overline{\rho u y_i})$$

The [$\bar{y}$- and $\bar{x}$-] integrations are alternated, each pair of sequential integrations constituting a full convection timestep. To use this split-step approach, the timestep must be small enough that the distinct components of the fluxes do not change the properties of a cell appreciably during the timestep. This approach is second-order accurate as long as the timestep is small and changed slowly enough. . .[3]

The timestep is determined by enforcing a Courant condition, which is a method of selecting the largest timestep which still meets conditions of stability. Basically, if the timestep is too large, then the integration "requires information from points more distant than the differencing scheme allows. Lack of that information gives rise to an instability. Therefore, $\Delta\bar{t}$ cannot be made too large."[4]

In the integration from time $\bar{t}$ to $\bar{t}+\Delta\bar{t}$, provided $\Delta\bar{t}$ is small enough, certain flux terms in the momentum and energy equations are assumed to be constant during the timestep. One would

[3] Oran (1989), pp. 22-23. See also Press, *et al.* (1986), p. 660, for a more general discussion.

[4] Press, *et al.* (1986), p. 627.

like to evaluate these fluxes in a time-centered fashion, *i.e.*, at $\bar{t} + \Delta\bar{t}/2$. But this information is not available when one is at $\bar{t}$. As an approximation to the time-centered quantities, one can first integrate the equations from $\bar{t}$ to $\bar{t} + \Delta\bar{t}/2$, using values at time $\bar{t}$ for the flux terms. This gives approximate time-centered values of the variables, which can be used to calculate corresponding time-centered fluxes. Then, one can go back to time $\bar{t}$ and re-integrate the equations to time $\bar{t} + \Delta\bar{t}$, using the just-calculated time-centered flux values.

These are all more-or-less standard techniques, and are common to many types of finite-difference solvers. The special feature of the LCPFCT algorithm is its treatment of numerical diffusion. All finite-difference schemes introduce some numerical diffusion as a consequence of discretization. Additional numerical diffusion is usually required to adequately capture shock waves and other steep gradients. However, even this stabilizing numerical diffusion is sometimes not enough to guarantee monotonicity of the solution. For example, consider the simple step discontinuity shown in Figure 2.1. The physical discontinuity is shown cross-hatched, while the numerical representation is shown as a solid line. In this case, ". . .note the growing nonphysical overshoot and the diffusive numerical precursor at times after $\bar{t}$=0. When the convection algorithm is stable but not positive, the numerical diffusion is not large enough to mask either numerical dispersion or the Gibbs phenomenon, so that the solution is no longer necessarily monotone. New ripples, that is, new maxima or minima, are introduced numerically."[5]

To ensure monotonicity, even more numerical diffusion beyond the stability limit must be added to the equations. The usual diffusive transport stage introduces, globally, sufficient numerical diffusion to ensure stability and monotonicity of the worst point in the domain. However, this much numerical diffusion is only needed at some points of the flow, and is excessive for others. The excessive numerical diffusion is often of greater magnitude than any physical diffusion or viscosity encountered in the real flow, and severely smears details of the solution in those areas. The LCPFCT algorithm adds a nonlinear antidiffusive stage which removes this excessive numerical diffusion where it is not needed for stability and monotonicity. The antidiffusion is computed locally, based on the constraint that antidiffusion should neither create new extrema nor accentuate already existing extrema. Thus stability and monotonicity are locally preserved with minimal amounts of numerical diffusion being used, and only where it is necessary.

As a simple example of the effects of antidiffusive correction, see Figures 2.2 (a),(b). These are density and pressure plots for a M=1.1 one-dimensional normal shock wave computed without and with antidiffusive correction. Even at this low Mach number, the numerical diffusion is evident, and at higher Mach numbers, the problem becomes worse. This simple example clearly demonstrates the beneficial effect of the antidiffusive correction in simulating a physically correct flow.

---

[5] Oran (1989), pp. 8-9.

2.3 The Computational Domain

The computational domain comprises a rectangular region containing the light gas jet, as shown in Figure 2.3. The majority of the cases have 200 × 80 cells, each cell corresponding to 0.05 of the radius of the jet, which is taken to be unity. Such a domain is 10 units wide by 4 units tall. The upper boundary condition is a perfectly reflecting wall, while the lower boundary condition is the line of symmetry through the centerline of the jet (also equivalent to a perfectly reflecting wall). Only the upper half of the channel is computed; the lower half is obtained by reflection about the axis of symmetry.

The upstream boundary condition is perfectly transmitting (zero-gradient), as is the downstream boundary condition. Other, more sophisticated boundary conditions were tried and discarded in favor of this simple scheme, because no other single boundary condition was consistently applicable to all the computations. It was desired to maintain the same boundary condition throughout the computations, so that quantitative comparisons could be made with confidence that differences in the results were due to the actual physics and not to the numerical technique.

The grid moves, in time, to keep the evolving structure centered in the field of view. In this way, only the region surrounding the structure need be computed, reducing the computational expense.

A minority of cases constitute variations on the above scheme. For example, some computational domains have 200 × 160, 200 × 40, or 400 × 80 cells, all with cells 0.05 square, or 200 × 80 with cells 0.025 and 0.1 square. Still other domains have a reflecting boundary condition at the downstream end, and the grid is not moved to track the vortical structure. When such special cases occur, this information is indicated on the actual plots or in the accompanying text.

2.4 Initialization of the Flow at $\bar{t}$=0

The finite size of cells in the grid represents an averaging of flow quantities over an area equal to the size of each cell. This presents no difficulty in representing structures with discontinuities parallel or perpendicular to the grid axes, *e.g.*, the walls or the shock wave). However, the representation of a curved boundary, *e.g.*, the circular jet, represents a potential difficulty. Suppose the actual boundary is a sharp radial discontinuity, with the value of some variable Q changing from Q_{in} to Q_{out} at the boundary. One must represent this sharp discontinuity via a finite mesh, and one possible technique is to simply assign Q_{in} to all cells completely inside the circle, and Q_{out} to all cells outside the circle. However, the resulting computational representation of the boundary will not be smooth, and may lead to development of instabilities that should not be present in the case of a smooth boundary. One can circumvent this difficulty by representing the boundary as a sharp, yet finite, gradient from

Q_{in} to Q_{out}. The computational representation will still be inexact due to averaging over a finite cell size, but this will be small if the gradient is distributed over several cell lengths. The question is, what is the appropriate distribution to use?

Suppose that the two-dimensional flow of the present study corresponds to a cross-section of a light gas jet perpendicular to the motion of the shock wave. In a real jet, diffusion at the interface will result in a mixing layer at the edge of the jet, so that the interface will be a smooth transition between pure light gas and pure heavy gas rather than an abrupt step discontinuity. A slice through this mixing layer, at a specified downstream location, can be used as a physically reasonable distribution when initializing the computations. Such a helium jet was used by Jacobs (1991) for his experiments, so it is convenient to carry out a mixing layer analysis corresponding to his experimental conditions. The details are shown in the Appendix. The resulting solution is used as the initial distribution across the jet boundary for all of the computations except for the studies involving explicit variations in initial interface thickness (Chapter 5, Section 5, Subsection 1).

Chapter 3 - Computations of the Canonical Problem

This chapter describes computations of the canonical problem for a number of shock strengths and light/heavy gas density ratios. In each case, the channel height and the initial jet interface thickness are fixed.

3.1 A Weak Shock Wave and a Low Density Ratio

Consider the interaction of a M=1.1 incident shock, in air, with an isolated single circular helium jet ($\overline{\rho}_L/\overline{\rho}_H = 0.138$), as shown in Figures 3.1 to 3.4. These are contour plots of density, pressure, vorticity, and mass fraction of the developing structure at various times throughout the interaction. The information given by the contour plots is mostly qualitative so, as a matter of convenience, the density, pressure, and vorticity contours are scaled before plotting according to the relationship

$$Q^* = \frac{\overline{Q} - \overline{Q}_{min}}{\overline{Q}_{max} - \overline{Q}_{min}},$$

where $\overline{Q}_{max}$ and $\overline{Q}_{min}$ are extremal values of the variable $\overline{Q}$ in the flow field at any particular time. Each contour plot contains 9 levels (0.1 to 0.9) of the starred quantity, representing equally spaced values from near minimum to near maximum. Since the mass fraction is constrained to take only values between 0 and 1, it is not scaled.

One visualizes development of the structure primarily in terms of the density (or mass fraction) contour plots, as these correspond most closely to the techniques of shadowgraphy or laser-induced fluorescence that other investigators have used in their experiments. The pressure and vorticity contour plots are generally less useful in interpreting the development, for the following reasons.

The pressures in the air and helium regions after the passage of the shock may be estimated from a simple 1-D analysis of a shock wave impinging on a He/air interface. This is a standard problem in many areas, for example a shock tube with different driver and driven gases, so the details are omitted here. For M=1.1, one finds $p_{2,air}/p_1 = 1.245$ and $p_{2,He}/p_1 = 1.135$. $p_{2,He}/p_1$ corresponds to the helium pressure just after the shock passes through the upstream air/He interface. At the downstream end, the shock is transmitted through the He/air interface, but part of it reflects upstream, further raising the pressure. At the air/He interface, part of the shock is again reflected, raising the pressure still further. This process continues *ad infinitum*, each reflection at an interface adding slightly to the helium pressure even as the wave grows weaker and weaker. In the air, transmitted waves also cause the pressure to decrease below the 1-D value of 1.245, but this effect is small. After all the waves have died out, the helium pressure will be slightly higher than 1.135, and the air pressure will be slightly lower than 1.245. From this point on, the flow is essentially

incompressible, and there is little additional change in pressure as the distributed vorticity coalesces into a vortex core. Because the difference in these pressures is so small, at most 10% and probably much less, it is difficult to visualize development of the structure via pressure contour plots. One does, however, expect the pressure distribution to become clearly organized as steady state is approached; that is, the contours should tend toward concentric closed curves centered on the vortex core.

The vorticity data are difficult to interpret before a well-developed vortex core has developed, because the motion within the vortex core is so complicated. This is especially true during early stages of the development when the flow field is highly non-uniform and exhibits large fluctuations. The important issues concern motion of the initially circumferential vorticity and how it coalesces into a vortex core. Rather than looking down from above at vorticity contours, it is easier to examine cuts through particular planes and study the distribution of vorticity across those cuts. As time goes on and steady-state is approached, then the velocity fields should become sufficiently smooth that the vorticity contours become useful. In that case, the vorticity contours should also tend toward concentric closed curves centered on the vortex core.

Thus, the noteworthy feature of the pressure and vorticity plots is the circularization of contours, which is an indicator of the approach toward steady state. However, it is generally more appropriate to interpret development of the vortex in terms of the density contour plots. The remainder of this section refers to the density contour plots of Figure 3.1. As a matter of convenience, only the upper half plane is considered (the lower half plane is symmetric).

At $\bar{t} = 0^+$, the shock wave passes over the jet and vorticity is deposited around the circumference. It is the self-induced motion from the vorticity distribution that drives the development of the structure. The induced motion at any point could be predicted by integrating the Biot-Savart law for a continuous vorticity distribution around the perimeter; however, for qualitative purposes, it is easier to replace the continuous distribution with an equivalent discrete distribution and look at the induced motion of each point due to the others. This is shown schematically in Figure 3.5. The motion of each point is governed primarily by the two nearest-neighbor vortices, *e.g.*, the induced motion of C is due primarily to B and D. The labeled single arrows show the induced motion due to each nearest neighbor, and a broad arrow shows the net contribution from both neighbors. It can be seen that the net motions are: E downstream, D radially inward, C upstream, B outward, and A downstream.

Thus, at a later time the circular section should deform to a kidney shaped structure, as shown in the $\bar{t} = 10$ density contours of Figure 3.1 and schematically in Figure 3.6. Again, the arrows on the schematic indicate the expected induced motions of points A through E.

Figure 3.7 shows a horizontal cut through the approximate center of the lobe ($\bar{y}$=0.75). The density and mass fraction show a pure helium core where the pressure is essentially constant and

the vorticity is primarily counterclockwise (although there are some local fluctuations). The $\overline{u}$- and $\overline{v}$-velocity plots show a distribution of positive and negative velocities due to the influences of the vorticity at the edge of the structure. Refer again to the Figure 3.6, which shows the motions of three points along a horizontal cut in the interior of the structure. The upstream-most point moves, under the influence of C and D, both downward and slightly downstream. This appears as a slightly positive $\overline{u}$-velocity and a large negative $\overline{v}$-velocity at $\overline{x} = 4$ in Figure 3.7. The central point moves, primarily under the influence of C and D, upward and upstream. This appears as a large negative $\overline{u}$-velocity and a large positive $\overline{v}$-velocity at $\overline{x} = 5$ in Figure 3.7. The downstream-most point moves, under the influence of B and C, upward and rightward. This appears as small positive $\overline{u}$- and $\overline{v}$-velocities at $\overline{x} = 7$ in Figure 3.7.

Figure 3.8 shows density, $\overline{u}$-velocity, $\overline{v}$-velocity, pressure, mass fraction, and vorticity data across a vertical cut through the approximate center of the structure ($\overline{x}$=5). The density and mass fraction plots show pure helium in the cores, with some intermediate fluid in the region in between. The pressure is essentially constant, and the vorticity is almost entirely counterclockwise. The $\overline{u}$-velocity plot shows the strong downstream motion of point E, along with a slight upstream motion in the center of the lobe. The $\overline{v}$-velocity plot shows a strong upward velocity in the center of the lobe. This motion is due to the dominant effect of the vorticity at D on the central point, as indicated in Figure 3.6.

As development progresses, one expects point E to continue moving downstream, separating the structure into two lobes connected by only a thin filament, as shown in the $\overline{t} = 20$ density contour plots, and schematically in Figure 3.9. Again, arrows in the schematic indicate the expected induced motions of points A through E.

Figure 3.10 shows a horizontal cut through the approximate center of the lobe ($\overline{y}$=0.75). Again, the $\overline{u}$- and $\overline{v}$-velocity plots show a distribution of positive and negative velocities due to the influence of the vorticity at the edge of the structure. Refer again to Figure 3.9, which shows the motions of three points along a horizontal cut in the interior of the structure. The upstream-most point moves, under the influence of B and C, both downward and slightly downstream. This appears as a slightly positive $\overline{u}$-velocity and a large negative $\overline{v}$-velocity at $\overline{x} = 4$ in Figure 3.10. The central point moves, primarily under the influence of D, downward and upstream. This appears as negative $\overline{u}$- and $\overline{v}$-velocities at $\overline{x} = 5$ in Figure 3.10. The downstream-most point moves, under the influence of B and D, upward and rightward. This appears as positive $\overline{u}$- and $\overline{v}$-velocities at $\overline{x} = 7$ in Figure 3.10.

Figure 3.11 shows $\overline{\rho}, \overline{u}, \overline{v}, \overline{p}, f$, and $\overline{w}$ data across a vertical cut through the approximate center of the structure ($\overline{x}$=5). The primary change from the vertical cut data of the previous time is that the $\overline{v}$-velocity inside the structure is negative, whereas before it was positive. Figure 3.9 shows that

this is just the induced motion of the central point due to the vorticity at D.

Returning to Figure 3.1, at $\bar{t} = 30$ the contours start to coalesce into the characteristic closed shape of a vortex core, and this process pinches off a region of lower vorticity fluid as an upstream tail. At the downstream end, a well-defined thin filament connects the vortex with its lower half plane image. This filament stretches and thins in the vertical direction as the high-vorticity fluid in the core rotates in a counterclockwise direction. Figures 3.12 and 3.13 show horizontal and vertical cuts through the approximate center of the structure ($\bar{y}$=0.75 and $\bar{x}$=5). Because the structure is part vortex core and part tail, a vertical cut through the center of the structure passes somewhat to the left of the center of the vortex core. Also, the horizontal cut through the center of the structure passes below the center of the vortex core. As time approaches infinity, one expects the vorticity within the structure to tend toward some well-defined steady distribution, which can be approximates as an "ideal" region of uniform vorticity. Within such a region the vorticity and the induced velocity at any point are (to lowest order) essentially due to solid body rotation. Figure 3.14 is a schematic of such a region, along with cuts through planes somewhat to the left of and below its center (corresponding to the location of the cuts in the actual case). Even at this early stage, the developing structure is beginning to qualitatively approach the ideal case (compare Figures 3.12 and 3.13 to Figure 3.14). There is a significant amount of fluctuation, but the general trends are well represented.

Returning again to Figure 3.1, note the emergence of an almost circular closed contour in the center of the vortex at $\bar{t} = 40$, indicating stabilization of the core. As the vorticity in the core continues to coalesce and organize, the lowest vorticity fluid is spun off at the upstream and downstream ends. Note the appearance of an inward-pointing finger of fluid at the downstream end. Also note the appearance of additional low vorticity fluid at the upstream end, filling the region between the upstream tail and the vortex core. This is fluid that was spun off as a downstream finger between the last frame ($\bar{t} = 30$) and this one, and which was then swirled counterclockwise around the periphery of the vortex core by the concentrated vorticity there.

At $\bar{t} = 50$, the downstream finger formed in the previous frame swirls around to the upstream end. The tail rotates counterclockwise relative to the core, due to the strong induced velocity it experiences. The core experiences a strong horizontal induced velocity from its lower half plane image. The net result is that the core moves downstream much more rapidly than the tail, which stretches upstream as it trails behind.

The remainder of the time history shows continued organization of the vortex core, thinning and stretching of the tails, and the occasional shedding of new tail material as the vortex stabilizes. Even though the vorticity distribution is non-uniform throughout a finite-sized core and the core is attached to trailing tails, the core behaves very much like an equivalent uniform vorticity region

after about $\bar{t}$=60. This is shown in Figures 3.15 to 3.18, which show the usual cuts through the approximate center of the structure at $\bar{t}$ = 60 and at $\bar{t}$ = 90. Compare these figures with the idealized case of Figure 3.14. Figures 3.19 to 3.22 show expanded density, pressure, vorticity, and mass fraction contour plots for $\bar{t}$ = 90. In both the cuts and the contour plots, note the extent to which the fluctuations in all variables have smoothed out since earlier times. Even the pressure and vorticity are indicative of the approach toward a steady-state condition: notice the cores' essentially radially monotonic pressure and vorticity contours.

3.2 The Effect of Variations in Shock Strength

The basic features of the interaction were described in the case of an M=1.1 incident shock wave. In this section, the density ratio is held fixed (at $\bar{\rho}_L/\bar{\rho}_H$ = 0.138), and effects of variation in shock strength are studied.

• Case M=1.2

Consider a M=1.2 incident shock, as shown in Figure 3.23. As can be seen by comparing the contour plots with the M=1.1 case, the basic mechanics of the interaction are identical. Vorticity is deposited around the circumference, the jet rolls up into a kidney shape, the vorticity coalesces into a vortex pair connected by a thin downstream filament, the low-vorticity fluid is pinched off as a low vorticity tail, the tail moves inward due to the induced velocity of the vortices, and it stretches and thins as it is left behind by the faster moving vortex pair.

The principal quantitative differences between this case and the M=1.1 case are twofold. First, the aspect ratio (height/width) of the structure is increased, because of the greater streamwise compression due to the shock. Second, the increased shock strength increases the strength of the vortex pair. Thus the resulting structure is more nearly an ideal vortex pair: the vortices are more compact and uniform in shape, and the tails are less prominent.

Notice also that the relative rate of development of the vortical structure in the two Mach number cases appears to be constant. For example, arbitrarily choose two times from the M=1.1 contour plots: $\bar{t}$=10, corresponding to deformation into a kidney-shaped structure and $\bar{t}$=30, corresponding to pinching off of the tails. Now look for comparable stages of development from the M=1.2 contour plots. They occur at $\bar{t}$ = 5 and 15, respectively. The ratios of times for corresponding development are 10/5 = 2 and 30/15 = 2, *i.e.*, a constant. This is an important point, and is discussed in detail in Chapter 5, Section 2.

• Case M=1.5

Figure 3.24 shows density contour plots for this case. The trends seen in the M=1.2 case continue as the Mach number is increased to M=1.5, so no further discussion is necessary.

• Case M=2.0

Figure 3.25 shows density contour plots for this case.

• Case M=1.05

Finally, consider M=1.05, a slightly weaker shock than the M=1.1 case described previously. The density contour plots are shown in Figure 3.26. This time, the trends are opposite those seen for increasing Mach number. The flow develops more slowly, the size of the tails increases, and the overall structure is less like an ideal vortex pair than in the stronger shock cases.

3.3 The Effect of Variations in Density Ratio

The previous section considered the effects of varying the shock strength in the case of a fixed light/heavy gas density ratio. This section discusses the complementary problem of varying the light/heavy density ratios at fixed shock strength. Two sets, consisting of four cases each, are studied. The first set, for M=1.1, has density ratios of $\overline{\rho}_L/\overline{\rho}_H$ = 0.785, 0.569, 0.354, and 0.138. The second set has the same density ratios at M=2.0. Note that the density ratio 0.138 cases are just those described in Sections 1 and 2 of this chapter.

• Case M=1.1, $\overline{\rho}_L/\overline{\rho}_H$ = 0.785

In this case, the density ratio is so close to unity that one expects very little development of the vortex pair, unless the computation is carried out to very long times. The density contour plots are shown in Figure 3.27.

• Case M=1.1, $\overline{\rho}_L/\overline{\rho}_H$ = 0.569

The density contour plots are shown in Figure 3.28. A decrease in the density ratio leads to faster development of the structure, and this is evident in the plots shown. Times $\overline{t}$ = 0 to 60 are similar to the previous case, showing the initial deformation of the structure. Times $\overline{t}$ = 70 to 100 show details of the beginning of the coalescence of the high-vorticity fluid into a vortex pair. Notice the very high swirling in the inner portions of the two lobes, resulting in very high gradients in that area.

• Case M=1.1, $\overline{\rho}_L/\overline{\rho}_H$ = 0.354

The density contour plots are shown in Figure 3.29. The density ratio is now sufficiently low that the times of the computation are sufficient to exhibit stabilization of the structure into a vortex pair. Times $\overline{t}$ = 0 to 40 are similar to the previous case, showing stretching of the fluid in the lobes. Note the loss of resolution in the filament as it is stretched so thin that it can no longer be resolved by the grid size. Times $\overline{t}$ = 50 and 60 show a noticeable stretching of high density contours, as the tail begins to be pinched off by the extremely high swirling motions. Finally, times $\overline{t}$ = 70 to 100 show clearly the flow within the developing vortex core. A high spatial density of regions of very

high gradients leads to loss of resolution, and the apparent coalescence of previously distinct fluid striations. This leads to the appearance of concentric closed contours within the lobes.

- Case M=1.1, $\overline{\rho}_L/\overline{\rho}_H = 0.138$

  This case was discussed in detail in Section 1.

Now consider the same light/heavy gas density ratios at M=2.0. The principal quantitative difference between these cases and the M=1.1 cases is that the strength of the interaction is increased. However, the qualitative trends throughout this series are similar to those discussed above. Therefore, the contour plots are presented without discussion.

- Case M=2.0, $\overline{\rho}_L/\overline{\rho}_H = 0.785$

  Density contours are shown in Figure 3.30.

- Case M=2.0, $\overline{\rho}_L/\overline{\rho}_H = 0.569$

  Density contours are shown in Figure 3.31.

- Case M=2.0, $\overline{\rho}_L/\overline{\rho}_H = 0.354$

  Density contours are shown in Figure 3.32.

- Case M=2.0, $\overline{\rho}_L/\overline{\rho}_H = 0.138$

  This case was discussed in detail in Section 2.

Chapter 4 - Assessment of the Computational Results

4.1 Qualitative Description of the Flow

In the previous chapter, the evolution and development of the structure was described in terms of the contour plots. Besides these large-scale motions, one would also like to obtain information about small-scale phenomena such as mixing of the light and heavy gases.

Numerical simulations often accurately represent large scale features of a real flow, but poorly represent fine details such as molecular mixing. This is a common difficulty in using computations for mixing studies, and reflects the near impossibility of simultaneously including real diffusive effects, excluding numerical diffusive effects, and guaranteeing stability of the steep gradients necessary to drive the mixing.

With regard to mixing, how faithful are the contour plots to a real flow? In assessing the reliability of numerical simulations, it is necessary to consider two effects. One is grid resolution, and the other is numerical diffusion.

4.1.1 Gridding and Resolution

In any numerical simulation, it necessary to check if the flow is adequately resolved with the chosen grid. This is done by halving and doubling the grid size and comparing the results.

Consider a M=2.0, $\overline{\rho}_L/\overline{\rho}_H$=0.138 flow. The flow in this strong shock case develops very quickly, which minimizes the consumption of valuable supercomputer time. This is particularly important because doubling the resolution leads to a eight-fold increase in computational costs.

In Chapter 3, the computation was performed for a 200 × 80 grid, with cells 0.05 square (Figure 3.25). Figure 4.1 shows the same computation using a 400 × 160 grid with cells 0.025 square. Figure 4.2 shows the same computation using a 100 × 40 grid with cells 0.10 square. As expected, the 400 × 160 grid resolves the finest details, followed by the 200 × 80 grid, then the 100 × 40 grid. The general flow features are adequately captured by any of these grids, although the 100 × 40 grid is marginal.

Two guidelines for selecting the 'correct' grid to use are as follows. The first is to compare the computations with experimental results, such as those of Jacobs (1991), paying particular attention to the smoothness of the contours at corresponding times. This suggests that the 200 × 80 grid is the most appropriate. The second is to estimate a characteristic diffusion lengthscale based on the diffusion coefficient, and to make the grid that size. In the case of Jacobs' experiments, the duration of the flow was about $\tau = 10^{-3}$ sec., and for Helium or air, the diffusion coefficient is about $\mathcal{D} =$

10^{-4} m^2/s, giving a characteristic diffusion lengthscale of $\sqrt{\tau\mathcal{D}} = 3.2 \times 10^{-4}$ m. Jacobs' actual jet radius was 0.004 m, so this length corresponds to 0.08 of the jet radius. Thus, in the computations, when the jet radius is unity, an appropriate grid spacing would be 0.08. The 200 × 80 grid has a just slightly smaller spacing of 0.05, the 400 × 160 grid has a much smaller spacing of 0.025, and the 100 × 40 grid has a just slightly larger spacing of 0.10. A grid spacing much smaller than the diffusion lengthscale of the real flow is superfluous, because the computation will be asked to resolve details finer than can be resolved in the actual flow. On the other hand, a larger grid spacing will be insufficient to capture details of the flow, especially at early times before diffusion becomes important. Thus, of the three computational grids, one again concludes that 200 × 80 is the most appropriate.

4.1.2 Numerical Diffusion

Recall from Chapter 2 that the governing equations are assumed to be inviscid and diffusionless. This is a reasonable approximation when the principal features are not smeared out by diffusion during the timescales of interest. On the other hand, no finite-difference computation can be truly diffusionless, because numerical diffusion arises as a direct consequence of the discretization process. This results in a paradoxical situation in which the diffusion is first approximated out of the governing equations, and then the numerical solution reintroduces diffusion back into the flow! This problem is further complicated in the presence of steep gradients, whose stability requirements demand a numerical diffusion far in excess of the minimal diffusion that would be present in a real flow.

In the present algorithm, excessive numerical diffusion is eliminated by an antidiffusive stage. In regions of high gradients, only the minimum numerical diffusion necessary for stability is retained. In all other regions, the numerical diffusion is removed almost entirely. Only a very small residual diffusion is left in the flow, an amount of the same order of magnitude as the real diffusion.

The discretized form of the diffusionless species equation has a term that mathematically corresponds to the actual diffusion in the complete species equation. In the LCPFCT code, this can be expressed as a numerical diffusion coefficient given by

$$\frac{1}{6}\frac{(\Delta\bar{x})^2}{\Delta\bar{t}} \leq \bar{\mathcal{D}} \leq \frac{1}{4}\frac{(\Delta\bar{x})^2}{\Delta\bar{t}}$$

where the exact value depends on the local character of the flow. In most of the field, this numerical diffusion is in excess of that required for stability, and is therefore removed by LCPFCT's antidiffusive stage. A very small residual amount, 0.1%, is retained to match the diffusion which would be present in a real flow. Thus, the residual numerical diffusion is, at most, $(0.001)(0.25)(\Delta\bar{x})^2/\Delta\bar{t}$, in regions where stability is not a problem. For a typical computation $\Delta\bar{x} = 0.05$ and $\Delta\bar{t} = 0.008$, giving a residual diffusion coefficient of 8×10^{-5}. This is to be compared to the nondimensional real diffusion

coefficient, given by $\overline{\mathcal{D}} = \mathcal{D}/(R_0 c_1)$, which, using values roughly corresponding to the experiments of Jacobs gives

$$\overline{\mathcal{D}} \equiv \frac{(10^{-4}\ \frac{m^2}{s})}{(0.004m)(340\frac{m}{s})} = 7 \times 10^{-5}.$$

The agreement in magnitude is quite good. Unfortunately, there is no guarantee that its distribution in space and time is identical to the real flow. However, since the real diffusion is assumed to be insignificant, and since the numerical diffusion is almost exactly equal to the real diffusion, the numerical diffusion is still consistent with the original assumption. The good agreement in magnitude means that the numerical diffusion will not affect the flow in the computation until the real diffusion would affect the flow in an actual experiment. Thus, the computation should be quantitatively correct up to a certain point. But beyond that point, what qualitative information can be extracted from the computations? In particular, can the contour plots be used to qualitatively describe the mixing that occurs between the light and heavy gases? The following subsection describes how to interpret the contour plots in that regard.

4.1.3 Interpretation of the Contour Plots

Consider again the contour plots from the computations of the previous chapter. In particular, what does the evolution of the contours over time indicate about mixing in the flow? In a two-dimensional flow, mixing depends critically on an increase of (interfacial) length of a contour separating the two fluids (or mass fraction levels) of interest. Thus, it is appropriate to study the evolution of the lengths of constant mass fraction contours as a function of time. In the ideal case of a diffusionless computation with infinite resolution, a fluid element may be swirled and stretched, but never torn apart. Thus all (density or mass fraction) contours must monotonically increase in length, as a function of time. In practice, however, these contours do eventually shorten with time. Two reasons for this shortening are discussed below.

The first, which can be called 'diffusion-shortening,' is due to the residual numerical diffusion. The diffusion may be small enough that diffusive effects are negligible over short timescales, but even weak effects accumulate over time. For example, consider a smoothed top hat profile, as shown in Figure 4.3(a). A high mass fraction contour is shown as a dashed line. Suppose further that this is the dominant feature of a flow, and is stable, while the flow around it shows fast period disturbances. Then, over short timescales when the surrounding disturbances undergo dramatic changes, the top hat profile changes negligibly. However, on a very long timescale, its profile will diffuse as shown in Figure 4.3(b), and the high mass fraction contour will shorten accordingly. Thus 'diffusion shortening' has a weak, but cumulative, long-time effect on the flow.

The second reason is the finite resolution of the grid. For example, Figure 4.4(a) shows a strip

of light fluid (mass fraction 1) being uniaxially strained at both ends. The light fluid is surrounded by heavy (mass fraction 0) fluid. As the strip is stretched, a contour representing the high mass fraction fluid will coincide with the perimeter of the strip, provided that the strip width is greater than the cell size (Figure 4.4(b)). When the strip becomes thinner than the cell size, it can no longer be resolved (Figure 4.4(c)). Cells straddling the thin strip then take on weighted values intermediate between the magnitude of the light and heavy fluids, and the pure heavy fluid is 'lost.' This is a rapidly occurring phenomena, in contrast to the long-time diffusive effects mentioned above. Thus 'resolution shortening' has a strong, but immediate effect on the flow.

Although these are purely computational phenomena, they are not indiscriminate events. They are specific responses to high gradients, high swirl, or other large-scale phenomena that would drive molecular mixing in an actual flow. Thus their appearance, as well as their location in space and time, indicate the expectation of corresponding phenomena in an actual flow.

Figure 4.5 is a histogram of mass fraction contour lengths versus mass fraction and time. The plot corresponds to the series of contour plots shown in Figure 3.1(d), for the M=1.1, $\overline{\rho}_L/\overline{\rho}_H$ = 0.138 canonical flow.

At $\bar{t} = 0$, there is a monotonic distribution of contour lengths, shortest at the center of the jet (pure He, f=1) and longest at the outside edge (pure air, f=0).

At $\bar{t} = 10$, the shock has passed over the jet, depositing vorticity which deforms the circular cross-section into a kidney shape. There are two competing effects here. First is the compression of the fluid due to the shock passage, which tends to decrease the contour lengths. This is particularly true for the low mass-fraction levels at the outside of the structure. A much stronger effect is the stretching of all the contours as they deform from their initial circular shape (recall that the minimum-length closed contour, for a given area, is a circle). This is particularly true for the higher mass-fraction levels at the inside of the structure. The net result is a slight decrease in the lengths of the 3 lowest contour lengths, and an increase in the remaining ones.

At $\bar{t} = 20$, development of the lobes leads to an increase in the lengths of the low to intermediate contours. These contours reflect stretching of fluid between the lobes, at the upstream end, and also in the thin filament connecting the lobes, at the downstream end. Note the abrupt transition at f=0.6, beyond which the high contours increase in length only slightly. Were the grid infinitely fine, there would be a very thin strip of high mass fraction fluid connecting the centers of the two lobes. The contours would not be closed in the upper lobe, as they are now, but would extend through the thin filament into the lower half plane lobe. The closing of the contours reflects the inability of the finite grid to track the thinning of the filament. This is an example of resolution-shortening.

At $\bar{t} = 30$, the continued stretching of the fluid between the vortices leads to an increase in length of the $0.05 < f < 0.35$ contours. At the point where the filament joins the developing vortex,

the $0.4 < f < 0.6$ contours disappear from the filament, again due to resolution-shortening. The contours close inside the lobe, just as the highest contours did at the previous time, and the contour plots reflects their corresponding decrease in length. Near the centerline of the flow, between the upper and lower lobes, there is an increase in length of the lowest contours due to stretching. Where the tails are pinched off, between the vortex and the tail, there is a significant amount of stretching of the $0.65 < f < 0.9$ levels. Finally, there is a slight decrease in the length of the innermost f=0.95 contour as it separates into two closed regions, one in the tail and one in the vortex. This is again a resolution-shortening effect.

At $\bar{t} = 40$, the $0.05 < f < 0.25$ contours continue to increase in length due to stretching between the lobes. There is also a slight contribution due to stretching of the tails. The abrupt drop off in the $0.3 < f < 0.35$ contours is again due to resolution-shortening in the filament joining the lobes. The $0.40 < f < 0.70$ contours lengthen slightly due to stretching of the tails as they move inward and trail behind the faster moving cores. The $0.75 < f < 0.90$ contours show a significant decrease in length, due to resolution-shortening in the pinched region between the tail and vortex. Finally, the very abrupt drop in the length of the f=0.95 contour is due to stabilization of the core of the vortex, leading to the circularization, and hence length-minimization, of the innermost contour there.

At $\bar{t} = 50$ and beyond, the lengthening of lowest mass fraction contours occurs primarily due to stretching of the tails, rather than stretching of fluid between the lobes. At slightly higher values, there is again an abrupt drop-off due to resolution-shortening in the filament. There is also a drop-off in $f > 0.5$ contours levels due to resolution-shortening within the tail. Again note the trend toward successively smaller mass fraction values at which the abrupt drop-offs occur: as the highest values disappear due to resolution-shortening, the highest resolvable values become successively lower.

This time marks the beginning of the late-time regime where diffusion-shortening effects play a role. This corresponds to the spreading of the top hat profile in the core of the vortex mentioned earlier. As time goes on, this is most apparent in the slow, weak decrease in length of the f=0.95 contour. It is also directly visible in the contour plots, as an increase over time of the width of the interface at the core boundary.

In summary, the contour lengths generally increase due to stretching at three principal sites: between the lobes, at the filament connecting the lobes, and in the tails. These regions are indicated on the histogram by the letters L, F, and T, respectively. As the filament thins beyond the cell size, the highest resolvable mass fraction decreases monotonically as a function of time. This is seen in the histogram as the locus of the right-most portion of the F-labelled regions. In addition, there is a late-time diffusive shortening of contours within the lobes, as indicated by the letter D. In the early stages of the interaction, mixing occurs primarily at the region between the vortices. Later, mixing occurs at the filament/vortex junction. At very late times, mixing occurs at the tails. The

vortex pair, once stabilized, is itself the site of relatively little mixing. Its principal effect, as far as the mixing is concerned, is to thin the tails, increasing their gradients and promoting mixing there as a result.

4.2 Quantitative Description of the Flow

4.2.1 Strength and Motion

Besides the detailed qualitative descriptions of the flow, one is also interested in the overall fluid mechanical behavior, *i.e.*, the strength and motion of the vortex pair. These data may be obtained from the computations as follows.

Consider again the M=1.1, $\overline{\rho}_L/\overline{\rho}_H = 0.138$ flow of Chapter 3, Section 1 (*c.f.* Figure 3.1). The circulation about one of the vortical structures is shown in Figure 4.6(a). It is calculated by evaluating the integral

$$\overline{\Gamma} = \oint \underline{\overline{u}} \cdot d\underline{\overline{x}}$$

around a rectangular contour coincident with the upper-half-plane of the flow field. The circulation rises rapidly as the shock passes through the jet, the peak (at $\overline{t} = 4$) corresponding to the point where the transmitted shock is just exiting the downstream end of the jet. Thereafter, there are some very small oscillations due to various reflected and transmitted waves, but the changes due to these waves are small and may be neglected. The $\overline{x}_{cmf}$-trajectory is shown in Figure 4.6(b). This trajectory is defined as the location of the center of mass fraction, computed relative to the moving fluid behind the shock, *i.e.*,

$$\overline{x}_{cmf} \equiv \frac{\int \overline{x} f \, d\overline{A}}{\int f \, d\overline{A}} .$$

There is a small early time dip just after the shock passes over the jet, when the still stationary jet appears to move backwards relative to the ambient fluid. This occurs because the jet initially behaves like a solid cylinder, whose inertia prevents it from instantaneously acquiring the velocity behind the shock. However, the deposited vorticity soon accelerates the structure to a velocity faster than the ambient fluid. At this point, the fluid inside the structure is somewhat irregular, and the center of mass is noncoincident with the center of rotation. Minor oscillations occur in the trajectory until the structure stabilizes around $\overline{t} = 60$ to form a core of high vorticity, high mass fraction fluid with trailing low vorticity tails. After the core stabilizes, the trajectory is very steady, the velocity of translation being essentially constant.

The $\overline{y}_{cmf}$-trajectory is shown in Figure 4.6(c). This trajectory is defined as the location of the

center of mass fraction, in the $\overline{y}$-direction, of the upper half plane portion of the structure, *i.e.*,

$$\overline{y}_{cmf} \equiv \frac{\int \overline{y} f \, d\overline{A}}{\int f \, d\overline{A}} .$$

The trajectory shows a rapid initial increase as the lobes first develop ($\overline{t} = 10$), then increases less rapidly as the fluid begins to organize itself into a high-vorticity core and a low-vorticity trailing tail ($\overline{t}$=20 to 30). After the core develops, there are small fluctuations as the vortex continues to stabilize, but $\overline{y}_{cmf}$ is essentially constant as a function of time.

$\overline{\Gamma}$(t), $\overline{x}_{cmf}$(t), and $\overline{y}_{cmf}$(t) may similarly be plotted for the other canonical flows. For example, consider the $\overline{\rho}_L/\overline{\rho}_H = 0.138$ family of cases with M=1.2, 1.5, 2.0, and 1.05. Data for these cases are plotted in Figures 4.7 to 4.10, respectively.[6] Two phenomena are of special interest. The first is an increase in the height of the early-time circulation peak as the Mach number is increased. For example, in the M=2 case, the steady state circulation is about 1.2, but the peak value is 1.9. One might guess that this peak corresponds to vorticity generated by the primary transmitted shock, and that the decrease to 1.2 is a consequence of the various wave interactions that occur thereafter. This is incorrect. Careful consideration of the contour length histogram shows that the circulation drops to its steady value as soon as the shock leaves the domain. This suggests that the peak is actually caused by the curvature of the shock. Figure 4.11 illustrates this point. Consider a rectangular contour A-B-C-D-E-F-G-A, representing the circulation due to the curved shock. In lab-fixed coordinates,[7] the velocity behind the shock is approximately uniform and very closely equal to the value $\overline{v}_2$ from one-dimensional normal shock theory. The velocity ahead of the shock is everywhere zero. Segments A-B, B-C, C-D and E-F give no contribution, and segments D-E and F-G cancel. The net contribution, due to G-A, is just $\overline{v}_2$ |GA|. For the M=2.0 flow, $\overline{v}_2 =$ 1.25 and |GA| $\approx$ 0.6, so that the circulation due to the shock is approximately 0.7, which is just the difference between peak and steady-state values in the circulation plot. Thus the circulation associated with only the developing vortex structure is essentially constant.

The second phenomenon of interest is the kink in the $\overline{x}_{cmf}$-trajectory plot at $\overline{t} = 12$. This is an error associated with the downstream boundary condition, and is discussed in the next section.

4.2.2 Horizontal Boundary Conditions and Error Correction

There are two errors associated with the horizontal boundary condition. One is directly caused by the numerical representation of the boundary, and the other is a diffusive error associated with

[6] In Figure 4.8 and 4.9, the data were saved at the times indicated by the hollow squares, in contrast to Figures 4.7 and 4.10, where data were saved at each timestep.

[7] This is a matter of convenience. The circulation is obviously independent of the choice of coordinates.

the horizontal size of the domain. This section describes these boundary condition-related errors, and methods by which they can be corrected.

Consider first the boundary representation error. In Chapter 2, Section 3, it was mentioned that a simple transmitting boundary condition was chosen for the horizontal direction because it was found to be applicable to a wide variety of cases, whereas other, more sophisticated conditions had to be applied on an *ad hoc* basis, working well in some situations and poorly in others. However, such a boundary condition introduces quantitative errors into the flow field, particularly in the $\overline{u}$-velocities and in the $\overline{x}_{cmf}$-trajectory.

Suppose a region of constant negative slope, such as the gradient across a shock wave, is propagating from left to right, as shown in Figure 4.12. The region is discretized across the computational grid, and the value of each cell is updated in time according to the particular finite-difference algorithm being used. In general, a quantity Q is updated according to

$$Q(\overline{x}_i, \overline{t} + \Delta\overline{t}) = Q(\overline{x}_i, \overline{t}) + f[Q(\overline{x}_{i-1}, \overline{t}), Q(\overline{x}_i, \overline{t}), Q(\overline{x}_{i+1}, \overline{t})]\Delta\overline{t},$$

where the function f represents the derivative terms of a truncated Taylor series expansion of Q with time $\overline{t}$ as variable. Therefore, the value of Q, at a certain point in space and a future point in time, depends on its value at the present time, and also on the values of its neighbors at the present time.

Now consider the boundary of the domain, as shown in Figure 4.13. To advance cell N from $\overline{t}$ to $\overline{t} + \Delta\overline{t}$, it is necessary to know the values of cells N-1, N, and N+1 at time $\overline{t}$. But cell N+1 is outside the domain, and its value is unknown. Cell N+1 is called a guard cell. Its present value, needed for the computation of the future value at cell N, is prescribed by an extrapolation of present-time values of cells N-1 and N, rather than by the finite-difference algorithm.

The extrapolation scheme may be zeroth order, first order, spline, or even more complicated, depending on the local properties of the differential equation under consideration. However, when using any but the simplest schemes, it is often necessary to modify or adjust the scheme on an *ad hoc* basis, to achieve an acceptable degree of accuracy.

This was the problem encountered throughout preliminary testing of the algorithm. It was desired to use the same boundary condition for the various cases under study, and the only one which performed consistently for all the cases[8] was the simple zero-gradient boundary condition.

In that case, the value at the guard cell is simply taken to be the value of the last cell in the domain. Obviously, this works perfectly when the gradient is negligible but introduces an error when the gradient is large. Thus, shock waves are expected to lead to errors, and the stronger the shock, the greater the errors. Such errors will propagate backwards into the domain and eventually cause quantitative errors in the trajectory of the vortex pair.

[8] Except, of course, for the "exact" reflected shock computation in Chapter 7, Section 3, Subsection 1.

The second type of error, due to numerical diffusion, is related to the horizontal size of the domain. Recall that the FCT algorithm corrects the numerical diffusion errors everywhere except in the vicinity of a steep gradient. At those points, some correction is possible, but a certain minimum diffusion is necessary for stability of the solution. The accumulated error due to the numerical diffusion is related to the amount of time that steep gradients remain in the domain before they are swept out the downstream boundary.

As a specific example, consider the strongest shock/highest density gradient case studied previously, the M=2, $\overline{\rho}_L/\overline{\rho}_H = 0.138$ case, shown in Figure 3.25. This computation was carried out on a grid with streamwise length equal to 10 jet radii. The time after which boundary representation-induced errors may become significant is $\overline{t} = 8$, when the shock is just exiting the domain.

The same computation, on a grid with twice the streamwise length (*i.e.*, 20 jet radii) is shown in Figure 4.14. The time when the shock is just exiting the domain now occurs much later, at $\overline{t} = 16$, and the propagation of errors back into the domain should also occur at a correspondingly later time. At a time when the short domain computation may exhibit errors, the long domain computation should still be error free. Therefore, the long domain computation can be used to test the accuracy of the short domain computation.

Comparison of the contour plots shows little qualitative difference in the results. No matter what the boundary condition may do quantitatively, the qualitative features of the flow remain unchanged. This is especially important for interpretations of time development, swirling, and mixing that are based on the contour plots.

Quantitatively, one may compare circulation and trajectory. Circulation plots for both cases are shown in Figure 4.15(a). Note the higher circulation of the long domain case, at times $\overline{t}$=8 to 16. Because the circulation is computed as a line integral around the entire computational domain, and its value is affected by the presence of a shock wave inside the domain. Until $\overline{t} = 8$, the shock wave remains inside both domains, and the circulations are identical. The incident shock exits the short domain at $\overline{t} = 8$, but it remains in the long domain until $\overline{t} = 16$. Thus, the circulations differ during this interval. Note that the short domain circulation just after the shock exits, the long domain circulation just after the shock exits, and the late-time circulation in either domain are all virtually identical. Thus, when the flow is interpreted correctly, the boundary condition has no effect on the steady-state circulation. One expects this to be the case, because the circulation is directly related to the time scaling, and the time development of the flow appeared unchanged by the boundary condition errors.

$\overline{x}_{cmf}$-trajectory plots for both cases are shown in Figure 4.15(b). As mentioned above, the boundary condition can introduce an error at some time after the shock exits the domain. The magnitude of this error, as well as when it will become important, can be estimated as follows.

The flow is approximately one-dimensional, and the velocities are measured with respect to the flow behind the shock. From one-dimensional theory, the velocity of propagation along the upstream-moving characteristic is just the speed of sound behind the shock. This is closely approximated by the speed of sound in air, neglecting the presence of the Helium in the region. Dividing the speed of sound behind the shock, $\bar{c}_2$, into the distance the signal has to travel before reaching the vortex pair, $\Delta\bar{x}_{error}$, gives the time it takes for the error to propagate upstream to the vortex pair: $\Delta\bar{t}_{error} = \Delta\bar{x}_{error}/\bar{c}_2$. The last time at which the trajectory is quantitatively correct is then $\bar{t}_{error} = \bar{t}_{shock\ out} + \Delta\bar{t}_{error}$. The slope of the $\bar{x}$-trajectory at this time is then taken to be the velocity of the vortex pair. For the short domain case, $\bar{c}_2 = 1.299$, $\Delta\bar{x}_{error} = 5$, and therefore, $\Delta\bar{t}_{error} = 5/1.299 = 4.1$. The shock exits the domain at $\bar{t}_{shock\ out} = 8$, so its disturbance is expected to affect the vortex pair at $\bar{t}_{error} = 8 + 4.1 = 12.1$. This is confirmed by the short domain $\bar{x}$-trajectory plot, which shows an abrupt kink at $\bar{t}$=12.

Also notice the very slight curvature of the long domain trajectory after about $\bar{t} = 14$. Though noticeable, the error is not very large, suggesting that the algorithm's antidiffusion stage is still able to minimize the effects of antidiffusion. There is no corresponding curvature in the short domain trajectory. The longer the shock remains in a domain, the greater the diffusive errors. Hence, diffusive errors are perceptible in the long domain but in the short domain.

$\bar{y}_{cmf}$-trajectory plots for both cases are shown in Figure 4.15(c). Again, the boundary condition error becomes significant in the short domain case after $\bar{t} = 12$. At that time, the development has essentially reached a steady state, so the $\bar{y}_{cmf}$-trajectory should be flat. Beyond $\bar{t} = 12$, both short and long domains exhibit errors that deviate from the expected solution. The late-time (half-) spacing of the vortex pair, $\bar{y}_\infty$, is therefore taken as the value of the $\bar{y}_{cmf}$-trajectory at this time.

This method works well for high Mach number cases, where $\bar{t}_{error}$ occurs after the vortex pair has stabilized, and where it is easy to determine a velocity prior to $\bar{t}_{error}$. But for low Mach number cases, it is not possible to accurately measure the velocity prior to the time of error, because the vortex pair has not yet stabilized.

A second method of determining the translational velocity of the vortex pair is as follows. In the absence of the light gas vortex pair, upstream conditions at the beginning of the computational domain should exactly equal those behind the shock. This is still essentially true near the walls, where there is little influence of the light gas or of the curvature of the shock wave. Therefore, in the coordinate system employed here, one should find $\bar{u}_{wall} = 0$. But vertical cuts through the domain indicate that, at late times, $\bar{u}_{wall}$ is not identically zero, because of errors due to passage of the shock out of the domain. Assuming that the shock is approximately a normal shock when it leaves the domain, any (erroneous) increase in $\bar{u}$-velocity it induces will be everywhere uniform. Therefore, any non-zero value of $\bar{u}_{wall}$ should be everywhere and uniformly subtracted from $\bar{u}$ as an

error correction. The corrected late-time vortex pair velocity, $\overline{U}$, is likewise found by subtracting the late-time wall velocity, $\overline{u}$, from the late-time slope of the $\overline{x}$-trajectory.

Consider again the short domain M=2 flow. A late-time cut through the beginning of the computational domain is shown in Figure 4.16. The late-time slope of the $\overline{x}$-trajectory is 0.27, and the late-time wall velocity is 0.20, giving a corrected vortex pair velocity of 0.07. This is in close agreement with the value of 0.064 as determined by the first method. The difference is about 10%, which is not significant considering the uncertainties in each of these methods of error correction.

In summary, the qualitative features of the flow, the circulation, and the time history are all adequately captured using a short domain. The trajectory shows some errors, but it is possible to predict when they will become significant. Two independent methods of error estimation yield consistent results, providing a means of estimating the true velocity of the vortex pair. The benefits of being able to adequately describe the flow without having to adjust boundary conditions on an *ad hoc* basis, or to compute long computationally expensive domains, more than offset the small losses of accuracy in using error estimates of this type.

Furthermore, it is important to note that neither the short nor the long domain is completely error-free. In the long domain, diffusive error is the primary error, in contrast to the short domain, where boundary representation error is dominant. Of the two errors, boundary representation error is clearly more significant. But this error can be quantified, and the trajectory can be corrected accordingly. The diffusive error, while so small as to be almost insignificant, is not easily estimated. This is an important point. In trying to perform as many computations as possible with a limited amount of computer resources, a relatively quick short domain computation with a predictable and correctable error is clearly preferable to a time-consuming, long domain computation with a smaller but unpredictable error.

At this point, a complete quantitative description of the vortex pair is possible, using the techniques described above where necessary to correct systematic errors in the computations.

Table 4.1 summarizes steady-state values of circulation, $\overline{\Gamma}$, late-time (half) spacing, $\overline{y}_\infty$, and (corrected) velocity, $\overline{U}$, for all the single jet cases of Chapter 3. In cases where the computation was not carried out long enough for certain parameters to achieve steady state conditions those parameters are not reported. In these cases, there was no physical reason why the computation should not have eventually reached steady-state; rather, in the interest of conserving limited computer resources, the computations were simply stopped after most of the interesting features had been exhibited.

M	$\overline{\rho}_L/\overline{\rho}_H$	$\overline{\Gamma}$	$\overline{y}_\infty$	$\overline{U}$
1.05	0.138	0.24	0.72	0.018
1.1	0.138	0.45	0.75	0.033
1.2	0.138	0.72	0.82	0.054
1.5	0.138	0.97	1.00	0.063
2.0	0.138	1.20	1.00	0.070
1.1	0.354	0.272	0.82	0.0195
1.1	0.569	0.162	Not steady state	
1.1	0.785	0.075	Not steady state	
2.0	0.354	0.765	1.20	0.0300
2.0	0.569	0.448	1.20	0.0193
2.0	0.785	0.205	Not steady state	

Table 4.1 - Steady-state $\overline{\Gamma}$, $\overline{y}_\infty$, and $\overline{U}$ for the canonical flows

Chapter 5 - Analytical Models for the Canonical Problem

In Chapter 2, it was mentioned that the use of a moving domain reduced the computer time consumed in a calculation by computing only that portion of the domain containing the developing vortex pair. In Chapter 4, it was mentioned that the use of a short domain further reduced the necessary computer time. But no matter how much a code is optimized or how fast it is run, it gives only a specific output corresponding to a specific set of initial conditions. Furthermore, large numbers of computations necessary to develop a useful database. Computations are useful for understanding details about a specific flow, but less so for understanding the fundamental physics of a class of flows. This chapter describes analytical models to characterize the late-time vortex pair flows exhibited in the computations.

5.1 A Model for the Strength of the Vortex Pair

The analytical results of this section are derived for lab-fixed coordinates. This is in contrast to the computations, which were performed in coordinates moving with the fluid behind the shock. However, the circulation is obviously independent of the choice of coordinate system.

Consider the time rate of change of the circulation following a material element. From the definition of circulation and the momentum equation, one can show that

$$\begin{aligned}
\frac{D\Gamma}{Dt} &= \frac{D}{Dt}\oint \underline{u}\cdot d\underline{x} \\
&= \oint \left[\frac{D\underline{u}}{Dt}\cdot d\underline{x} + \underline{u}\cdot\frac{D}{Dt}(d\underline{x})\right] \\
&= \oint \left[\frac{D\underline{u}}{Dt}\cdot d\underline{x} + \underline{u}\cdot d(\frac{D\underline{x}}{Dt})\right] \\
&= \oint \left[-(\frac{\nabla p}{\rho} + \nabla F)\cdot d\underline{x} + \underline{u}\cdot d(\frac{\partial \underline{x}}{\partial t} + \underline{u}\cdot\nabla\underline{x})\right] \\
&= \oint \left[-(\frac{\nabla p}{\rho} + \nabla F)\cdot d\underline{x} + \underline{u}\cdot d(0+\underline{u})\right] \\
&= \oint \left[-\frac{dp}{\rho} + dF + d(\frac{\underline{u}^2}{2})\right].
\end{aligned}$$

The last two terms vanish over a closed contour, leaving

$$\frac{D\Gamma}{Dt} = -\oint \frac{dp}{\rho}$$

or, equivalently,

$$\frac{D\overline{\Gamma}}{D\overline{t}} = -\frac{1}{\gamma_1}\oint \frac{d\overline{p}}{\overline{\rho}},$$

a term which represents the effects of baroclinic vorticity generation.

The passage of the shock wave is clearly the dominant interaction between density and pressure gradients, so the flow is approximately barotropic after the shock has passed, at least in an integrated sense. Then, $D\overline{\Gamma}/D\bar{t} \approx 0$ and the circulation remains constant after passage of the shock through the light gas region (*c.f.* Chapter 4, Section 2, Subsection 1).

Therefore, the strength of the vortex pair, throughout the development from post-shock roll-up to late-time steady-state, is completely characterized by a single value of $\overline{\Gamma}$. Since this circulation is determined only by the initial interaction, it should be a function of only the shock strength and the density ratio. Various authors have attempted to develop models to describe this relationship.

Rudinger and Somers (1960) considered the interaction to consist of two steps. In the initial step, the jet is given an impulse by the passing shock which accelerates it to the velocity which a solid body of the same density would attain. There is no distortion of the jet during this step. In the second step, the jet is actually transformed into a vortex. This process is modeled as the impulsive motion of an infinite lamina accelerated from rest. Rudinger and Somers explicitly derived a formula only for the velocity of the vortex pair relative to the velocity behind the shock. That is, their principal interests were not in developing a scaling law for the circulation of the vortex pair. However, it is possible to manipulate their results to give the following expression for the steady-state circulation of the vortex pair:

$$\overline{\Gamma} = \frac{8}{\pi}\,\overline{y}_{\infty}\,\overline{v}_2\left(\frac{1-\overline{\rho}_L/\overline{\rho}_H}{1+\overline{\rho}_L/\overline{\rho}_H}\right).$$

Notice that this predicted circulation depends on the vortex separation, $\overline{y}_{\infty}$, which is not predicted *a priori*, and must be measured experimentally. Rudinger and Somers did not measure circulation or vortex core spacing, a direct comparison between their model and their results can not be made.

Picone, *et al.* (1985, 1988) analytically integrated the vorticity equation for the case of a shock passing through a circular cross-section. They derived the following expression for the circulation:

$$\overline{\Gamma} = 2\,\overline{v}_2\left(\frac{\overline{v}_2}{2M}-1\right) ln\left(\frac{\overline{\rho}_L}{\overline{\rho}_H}\right).$$

An obvious improvement of this model over that of Rudinger and Somers is that the circulation is predicted in terms of readily available parameters; there is no dependence on vortex core spacing. The derivation of this result is very intricate and sensitive to the order of various manipulations. Also, the physical meaning of the various terms is not clear. Furthermore, their own computations, for the case of a helium cylinder in air, show that their model overpredicts the computed circulation by at least a factor of two.

Most recently, using simple one-dimensional gasdynamics, Hendricks and Marble (1991) derived a set of coupled, nonlinear equations that could be solved numerically for the circulation as a function of Mach number and density ratio. The disadvantages of this method are that the physical

dependences on the shock strength and density ratio can not be easily visualized, and that the equations are tedious, although straightforward, to solve numerically. Hendricks and Marble also presented computational data for two low Mach number He/air cases, and showed good agreement between their model and their computations. In summary, each of the currently available scaling laws suffers from one or more of following defects: 1) dependence on data that is not available *a priori*, 2) inability to accurately predict the circulation (to, say, within 15 or 20%, a reasonable criterion for a scaling law), and 3) difficulty of interpretation due to lack of a simple analytical expression.

One would like to have a circulation model which overcomes the deficiencies listed above. The derivation is as follows. Consider a cross section through an axisymmetric circular jet, as shown in Figure 5.1. The radius of the jet is R, and the interface is idealized as a sharp step discontinuity in density. The light jet gas has density ρ_L and the heavy gas has density ρ_H $(=\rho_1)$. A shock wave of strength M approaches from left to right. The density and pressure ratios across the shock wave are ρ_2/ρ_1 and p_2/p_1. The vorticity production term of the vorticity equation is

$$\frac{D\underline{\omega}}{Dt} = \frac{1}{\rho^2}(\underline{\nabla}\rho \times \underline{\nabla}p) + \cdots .$$

The vorticity is perpendicular to the plane of the jet, $\underline{\omega} = \omega \hat{e}_z$. Integrating the vorticity equation for ω gives

$$\begin{aligned}
\omega &= \int_0^\infty \frac{1}{\rho^2} |\underline{\nabla}\rho \times \underline{\nabla}p| \; dt \\
&= \frac{1}{\rho^2} \int_0^\infty |\underline{\nabla}\rho||\underline{\nabla}p| \; sin\theta \; dt \\
&= \frac{1}{\rho^2} \int_0^\infty |\underline{\nabla}\rho| \; \Delta p \; \delta(x - V_s t) \; sin\theta \; dt \\
&= \frac{|\underline{\nabla}\rho|}{\rho} \frac{\Delta p}{\rho} \; sin\theta \int_\infty^\infty \delta(x - V_s t) \; dt \\
&= \frac{1}{V_s} \frac{\Delta\rho}{\rho} \frac{\Delta p}{\rho} \; sin\theta .
\end{aligned}$$

Having this expression for the vorticity, integrating over the area of the jet gives the circulation:

$$\begin{aligned}
\Gamma &= \int\int \omega dA \\
&= \int_{r=0}^\infty \int_{\theta=0}^\pi \frac{1}{V_s} \frac{\Delta p}{\rho} \frac{\Delta\rho}{\rho} \; sin\theta \; r \; dr \; d\theta \\
&= \frac{1}{V_s} \frac{\Delta p}{\rho} \frac{\Delta\rho}{\rho} \int_0^\pi \int_0^\infty \delta(r - R_0) \; sin\theta \; r \; dr \; d\theta \\
&= \frac{2}{V_s} \frac{\Delta p}{\rho} \frac{\Delta\rho}{\rho} \int_0^\infty \delta(r - R_0) \; r \; dr \\
&= \frac{2R_0}{V_s} \frac{\Delta p}{\rho} \frac{\Delta\rho}{\rho} .
\end{aligned}$$

In this expression, it is necessary to choose suitable values of ρ, one for the pressure term, and one for the density term. Since the pressure gradient is due to the shock, choose ρ_2 for the pressure term,

and since the density gradient is across the interface, choose the average density at the interface, $(\rho_L + \rho_H)/2$, for the density term. The circulation then becomes

$$\Gamma = \frac{4R_0}{V_s} \frac{\Delta p}{\rho_2} \left(\frac{\Delta \rho}{\rho_L + \rho_H} \right) .$$

Finally, nondimensionalize all lengths by R_0, all densities by ρ_1, all pressures by p_1, all velocities by c_1, and the circulation by $R_0 c_1$. The circulation then becomes

$$\overline{\Gamma} = \frac{4}{\gamma_1 M} \left(\frac{\overline{\rho}_1}{\overline{\rho}_2} \right) \left(\frac{\overline{p}_2}{\overline{p}_1} - 1 \right) \left(\frac{1 - \overline{\rho}_L/\overline{\rho}_H}{1 + \overline{\rho}_L/\overline{\rho}_H} \right) .$$

Notice that the density ratio across the shock and the pressure jump across the shock are well-known functions of only the shock Mach number and the air specific heat ratio:

$$\frac{\overline{\rho}_2}{\overline{\rho}_1} = \frac{(\gamma_1 + 1)M^2}{(\gamma_1 - 1)M^2 + 2} ,$$

and

$$\frac{\overline{p}_2}{\overline{p}_1} = 1 + \left(\frac{2\gamma_1}{\gamma_1 + 1} \right) (M^2 - 1).$$

One can test this model against those described earlier, in predicting the computed circulation data of Table 4.1. The results are tabulated in Table 5.1, for the cases which were computed to steady state.

		Computed	Predicted			
M	$\overline{\rho}_L/\overline{\rho}_H$	$\overline{\Gamma}$	$\overline{\Gamma}$(R-S)	$\overline{\Gamma}$(P-B)	$\overline{\Gamma}$(H-M)	$\overline{\Gamma}$(Yang)
1.05	0.138	0.240	0.113	0.310	0.196	0.228
1.1	0.138	0.450	0.230	0.584	0.376	0.412
1.2	0.138	0.720	0.483	1.056	0.699	0.690
1.5	0.138	0.970	1.339	2.113	1.455	1.130
2.0	0.138	1.200	2.410	3.402	2.338	1.420
1.1	0.354	0.272	0.159	0.318	0.239	0.260
1.1	0.569	0.162	0.098	0.172	0.144	0.150
1.1	0.785	0.075	0.038	0.074	0.069	0.066
2.0	0.354	0.765	1.824	1.787	1.415	0.896
2.0	0.569	0.448	1.049	0.969	0.863	0.515
2.0	0.785	0.205	0.461	0.417	0.453	0.226

Table 5.1 - Computed and predicted $\overline{\Gamma}$ for the canonical flows

Page 33, Top of Table 5.1
"Hend." should read "H-M"

These data are also plotted in Figures 5.2, 5.3, and 5.4 (as a matter of convenience, these are actually plots of the ratio of predicted to computed circulation, which should be unity, in the case of a 'perfect' scaling law.)

Figure 5.2 shows the case of a fixed density ratio ($\overline{\rho}_L/\overline{\rho}_H = 0.138$) and varying shock strengths. The present ('Yang') model appears to give the best result, with about 15% maximum deviation between predicted and computed values. The Hendricks and Marble ('H-M') model works reasonably well, but the Rudinger and Somers ('R-S') and Picone and Boris ('P-B') models are as much as a factor of 2 in error.

Figure 5.3 shows the case of a fixed weak shock (M=1.1) and varying density ratios. The Picone and Boris, Hendricks and Marble, and present models all work reasonably well, with the present model giving the best result. The Rudinger and Somers ('R-S') model underpredicts the circulation by a factor of almost two.

Figure 5.4 shows the case of a fixed strong shock (M=2) and varying density ratios. The Rudinger and Somers, Picone and Boris, and Hendricks and Marble models all group closely together, but they overpredict the circulation by a factor of about two. The present model does considerably better, with about 15% maximum deviation between predicted and measured values.

Overall, the present model performs as well as, or better than, the existing models at predicting the strength of the vortex pair. It works for a wide range of shock strengths and density ratios, and is easy to interpret and use.

5.2 A Model for the Characteristic Time for Development

One would also like to have a model to describe the characteristic time for development of a flow. This would provide the ability to make temporal comparisons between different flows within the same family. For example, given a full description of the time-dependent flow for specific values of M and $\overline{\rho}_L/\overline{\rho}_H$, one could predict the times for corresponding development if either of these initial conditions were changed. The question may arise, why should flows with different initial conditions be comparable at all? The effects of the incident shock strength and light/heavy gas density ratio can be folded into an equivalent configuration without any shocks or density differences, but with an initial spatial distribution of vorticity equal to that created by the passage of the shock over the region. This is the basis of the so-called 'vortex dynamics' method of computation. Because the initial distribution of vorticity is the same[9] regardless of what combination of shock strength and density difference is used to create it, this defines a family of flows which must develop in a

[9] Recall from the previous section that the initial vorticity distribution is given by $\overline{\omega}(R_0,\theta) = (1/V_s)\ (\Delta p/\rho)\ (\Delta p/\rho)\ sin\theta$. This can be expressed as $\overline{\omega}(R_0,\theta) = \overline{\omega}_{max}\ sin\theta$, which clearly shows the independence of the spatial distribution from its associated amplitude.

quantifiably similar manner.

Of course, the flows must evolve in a manner consistent with their creation, and this will cause fine differences in the details. For example, at $\bar{t} = 0^+$, the passage of the shock deforms the circular jet to an elliptical jet whose aspect ratio is a function of the shock strength and light/heavy gas density ratio. At the other extreme, as $\bar{t} \rightarrow \infty$, the flow reaches steady state and the shape and aspect ratio of the vortex pair are a function of the vortex spacing (this is discussed in detail in Section 3), and the spacing is a function of the shock strength and light/heavy gas density ratio (discussed in Section 4). Thus the following model relates only corresponding stages of development, and overlooks differences in specific details of the flows.

A characteristic time for the interaction can be formulated as

$$\tau = \frac{(H/W)}{\Gamma} ,$$

where H is a characteristic height, W is a characteristic width, and Γ is the circulation. For H, one takes R_0, the vertical dimension, and for L, one takes $(\rho_1/\rho_2)R_0$, the horizontal dimension just after the shock has passed (the factor (ρ_1/ρ_2) accounts for the streamwise compression due to the shock). Therefore,

$$\tau = \frac{\rho_1}{\rho_2} \frac{R_0^2}{\Gamma} .$$

Nondimensionalizing and substituting the previous expressions for $\overline{\Gamma}$ and ρ_2/ρ_1 gives

$$\overline{\tau} = \left(\frac{\gamma_1 + 1}{8}\right)\left(\frac{M}{M^2 - 1}\right)\left(\frac{1 + \overline{\rho}_L/\overline{\rho}_H}{1 - \overline{\rho}_L/\overline{\rho}_H}\right) .$$

This model can be tested against the data from the computations of Chapter 3. For the case $\overline{\rho}_L/\overline{\rho}_H = 0.138$, the model predicts the following characteristic times:

$\overline{\tau}(M = 1.05) = 4.057$,

$\overline{\tau}(M = 1.1) = 2.075$,

$\overline{\tau}(M = 1.2) = 1.083$,

$\overline{\tau}(M = 1.5) = 0.475$, and

$\overline{\tau}(M = 2.0) = 0.264$.

These numbers are most useful for comparing the results of one case against another, as the ratio of any two numbers gives the ratio of times needed for the two cases to reach the same stage of development. For example, the above cases may be taken a pair at a time, to give

$\overline{\tau}(M = 1.05) \; / \; \overline{\tau}(M = 1.1) = 1.955$,

$\overline{\tau}(M = 1.1) \; / \; \overline{\tau}(M = 1.2) = 1.92$,

$\overline{\tau}(M = 1.2) \; / \; \overline{\tau}(M = 1.5) = 2.27$, and

$\overline{\tau}(M = 1.5) \; / \; \overline{\tau}(M = 2.0) = 1.80$.

So, for example, the following pairs should represent similar stages of development:

M=1.05 at $\bar{t}$=195.5 and M=1.1 at $\bar{t}$=100 ($\bar{t}$ = 200 and 100 are shown in Figure 5.5),

M=1.1 at $\bar{t}$=38.4 and M=1.2 at $\bar{t}$=20 ($\bar{t}$ = 40 and 20 are shown in Figure 5.6),

M=1.2 at $\bar{t}$=45.4 and M=1.5 at $\bar{t}$=20 ($\bar{t}$ = 45 and 20 are shown in Figure 5.7), and

M=1.5 at $\bar{t}$=10.8 and M=2.0 at $\bar{t}$=6 ($\bar{t}$ = 10 and 6 are shown in Figure 5.8).

The comparisons are quite good.

Besides the contour plots, Figures 5.9 and 5.10 show density, momentum, pressure, mass fraction, and vorticity data along vertical cuts through the centers of the structures of Figure 5.5. Again, the comparisons are quite good.

In addition to the dependence on Mach number, one can also test the accuracy of the model for dependence on density ratio. Consider the two sets of constant shock strength data mentioned previously, M=1.1 and M=2.0.

For the case of M=1.1, the model predicts the following characteristic times:

$\bar{\tau}(\bar{\rho}_L/\bar{\rho}_H = 0.785) = 13.05$,

$\bar{\tau}(\bar{\rho}_L/\bar{\rho}_H = 0.569) = 5.72$,

$\bar{\tau}(\bar{\rho}_L/\bar{\rho}_H = 0.354) = 3.29$, and

$\bar{\tau}(\bar{\rho}_L/\bar{\rho}_H = 0.138) = 2.07$.

Again, the cases may be taken a pair at a time, to give $\bar{\tau}(\bar{\rho}_L/\bar{\rho}_H = 0.785) \,/\, \bar{\tau}(\bar{\rho}_L/\bar{\rho}_H = 0.569) = 2.29$,

$\bar{\tau}(\bar{\rho}_L/\bar{\rho}_H = 0.569) \,/\, \bar{\tau}(\bar{\rho}_L/\bar{\rho}_H = 0.354) = 1.74$, and

$\bar{\tau}(\bar{\rho}_L/\bar{\rho}_H = 0.354) \,/\, \bar{\tau}(\bar{\rho}_L/\bar{\rho}_H = 0.138) = 1.59$.

So, for example, the following pairs should represent similar stages of development:

$\bar{\rho}_L/\bar{\rho}_H = 0.785$ at $\bar{t}$=91.6 and $\bar{\rho}_L/\bar{\rho}_H = 0.569$ at $\bar{t}$=40 ($\bar{t}$ = 90 and 40 are shown in Figure 5.11),

$\bar{\rho}_L/\bar{\rho}_H = 0.569$ at $\bar{t}$=69.2 and $\bar{\rho}_L/\bar{\rho}_H = 0.354$ at $\bar{t}$=40 ($\bar{t}$= 70 and 40 are shown in Figure 5.12), and

$\bar{\rho}_L/\bar{\rho}_H = 0.354$ at $\bar{t}$=63.6 and $\bar{\rho}_L/\bar{\rho}_H = 0.138$ at $\bar{t}$=40 ($\bar{t}$= 60 and 40 are shown in Figure 5.13).

The comparisons are quite good.

Figures 5.14 and 5.15 show density, momentum, pressure, mass fraction, and vorticity data along vertical cuts through the centers of the structures ($\bar{x}$ = 5) of Figure 5.11. Again, the comparisons are quite good.

The same time ratios hold for the M=2 case. So, for example, the following pairs should represent similar stages of development:

$\bar{\rho}_L/\bar{\rho}_H = 0.785$ at $\bar{t}$=18.32 and $\bar{\rho}_L/\bar{\rho}_H = 0.569$ at $\bar{t}$=8 ($\bar{t}$ = 18 and 8 are shown in Figure 5.16),

$\bar{\rho}_L/\bar{\rho}_H = 0.569$ at $\bar{t}$=13.84 and $\bar{\rho}_L/\bar{\rho}_H = 0.354$ at $\bar{t}$=8 ($\bar{t}$ = 14 and 8 are shown in Figure 5.17), and

$\bar{\rho}_L/\bar{\rho}_H = 0.354$ at $\bar{t}$=6.36 and $\bar{\rho}_L/\bar{\rho}_H = 0.138$ at $\bar{t}$=4 ($\bar{t}$ = 6 and 4 are shown in Figure 5.18).

Once again, the comparisons are quite good.

These comparisons verify the ability of the model to predict time scaling relationships as a function of the initial conditions.

5.3 A Model for the Motion of the Vortex Pair

The late-time structure resulting from the interaction of a shock wave and a single jet is essentially a vortex pair with finite core size, in a channel of finite height (Figure 5.19). Relative to the ambient fluid, the structure moves downstream with a velocity due to the induced motion of each vortex by the other.

The simplest model for the motion of a vortex pair is the potential flow of a point vortex pair in an unbounded domain, which predicts the normalized velocity to be $\overline{U}\overline{y}_\infty/\overline{\Gamma} = 1/(4\pi)$. This model would be an accurate representation of the velocity in the simultaneous limits of core size tending toward zero and channel spacing tending toward infinity. Qualitatively, it is clear that this model represents an upper limit for the velocity that can be realized in an actual flow. As either the core size or channel spacing becomes finite, the velocity must decrease below $\overline{U}\overline{y}_\infty/\overline{\Gamma} = 1/(4\pi)$. The ultimate goal of this section is to derive and demonstrate a closed-form analytical model which can adequately describe the effects of both these phenomena on the motion of the vortex pair. In the analysis that follows, these effects are first treated separately, and then in combination. The coordinate system used in this section is the same as in the computations: the coordinate system moves with the fluid behind the shock. That is, the vortex pair is imbedded in ambient fluid that is at rest.

5.3.1 The Effect of Finite Channel Spacing

First, consider the effect of channel spacing alone. This problem consists of a pair of point vortices in a bounded domain. Mathematically, one formulates a solution by superposition of the point vortex solution, treating each wall or horizontal line of symmetry as a line of reflection. As shown in Figure 5.20, the flow is equivalent to an infinite array of vortex pairs of strength $\pm\overline{\Gamma}$, each of spacing $2\overline{y}_\infty$, in a channel of height $2\overline{h}$. The actual vortex pair divides the domain into "upper" and "lower" halves, and the image vortex pairs are referred to as "first upper," "second upper," . . .and "first lower," "second lower,". . .respectively.

The upper actual vortex experiences induced velocity contributions from each of the other vortices, as follows. The lower actual vortex induces velocity

$$\frac{\overline{\Gamma}}{2\pi}\,\frac{1}{2\overline{y}_\infty},$$

the n-th upper image pair induces velocity

$$\frac{\overline{\Gamma}}{2\pi}\left[\frac{1}{2n\overline{h}}-\frac{1}{2n\overline{h}-2\overline{y}_\infty}\right],$$

and the n-th lower image pair induces velocity

$$\frac{\overline{\Gamma}}{2\pi}\left[\frac{1}{2n\overline{h}+2\overline{y}_\infty}-\frac{1}{2n\overline{h}}\right].$$

The total induced velocity is

$$\begin{aligned}\overline{U} &= \frac{\overline{\Gamma}}{2\pi}\left[\frac{1}{2\overline{y}_\infty}+\sum_{n=1}^{\infty}\left\{\frac{1}{2n\overline{h}}-\frac{1}{2n\overline{h}-2n\overline{y}_\infty}\right\}+\sum_{n=1}^{\infty}\left\{\frac{1}{2n\overline{h}+2\overline{y}_\infty}-\frac{1}{2n\overline{h}}\right\}\right]\\ &= \frac{\overline{\Gamma}}{4\pi\overline{h}}\left[\frac{\overline{h}}{\overline{y}_\infty}+\sum_{n=1}^{\infty}\left\{\frac{1}{n+\overline{y}_\infty/\overline{h}}-\frac{1}{n-\overline{y}_\infty/\overline{h}}\right\}\right]\\ &= \frac{\overline{\Gamma}}{4\pi\overline{h}}\left[\frac{\overline{h}}{\overline{y}_\infty}-2\,\frac{\overline{y}_\infty}{\overline{h}}\sum_{n=1}^{\infty}\frac{1}{(n+\overline{y}_\infty/\overline{h})(n-\overline{y}_\infty/\overline{h})}\right].\end{aligned}$$

The sum may be evaluated by use of the relations[10]

$$\sum_{n=1}^{\infty}\frac{1}{(n+a)(n-a)}=-\frac{1}{2a}\int_0^1\frac{x^a-x^{-a}}{1-x}dx$$

and

$$\int_0^1\frac{x^a-x^{-a}}{1-x}dx=-\frac{1}{a}+\pi\ ctg(a\pi).$$

The final result is

$$\overline{U}=\frac{\overline{\Gamma}}{4\overline{h}}\ ctg\left(\pi\frac{\overline{y}_\infty}{\overline{h}}\right),$$

or

$$\frac{\overline{U}\overline{y}_\infty}{\overline{\Gamma}}=\frac{1}{4}\,\frac{\overline{y}_\infty}{\overline{h}}\ ctg\left(\pi\frac{\overline{y}_\infty}{\overline{h}}\right).$$

This function is shown in Figure 5.21. As $\overline{y}_\infty/\overline{h}$ increases, *i.e.*, as the channel spacing decreases, the velocity decreases. As $\overline{y}_\infty/\overline{h}$ tends toward zero, the unbounded point vortex result, $\overline{U}\overline{y}_\infty/\overline{\Gamma} = 1/(4\pi)$, is recovered.

5.3.2 The Effect of Finite Core Size

Now consider the effect of finite core size alone. The model for this flow is a vortex pair with constant vorticity inside a finite core, in an unbounded domain. The simplifying assumption of constant vorticity, although not realizable in an actual flow, should be a reasonable approximation when the vortex core is large compared to the vorticity gradient at the edge of the region.

[10] Gradshteyn and Ryzhik (1980), Formulas 0.244.1 and 3.231.3.

This problem was first investigated by Deem and Zabusky (1978). They used the Poisson equation for the streamfunction and vorticity, together with the appropriate boundary conditions for steady translational motion without change of boundary shape, to derive a nonlinear integro-differential equation for the boundary shape. They solved this equation numerically with a Newton-Raphson method, and discovered one vortex pair of fixed size, shape, and spacing that satisfied the governing equation.

Using a closely related formulation, Pierrehumbert (1980) generalized Deem and Zabusky's work to exhibit a family of solutions characterized by a single parameter $\overline{R}/\overline{y}_\infty$, the ratio of effective core size, $\overline{R} = (\overline{A}/\pi)^{1/2}$, to centroid-to-centerline spacing, $\overline{y}_\infty$. This family of solutions is shown in Figure 5.22.[11] Only half of each vortex pair is plotted, the configuration being symmetric about the straight line corresponding to the flattened lower face of the outermost vortex core. As a matter of convenience, each member of the family has been scaled such that its outermost edge is at the same fixed distance from the line of symmetry. The corresponding normalized velocity is shown in Figure 5.23. As $\overline{R}/\overline{y}_\infty$ increases, the convective velocity decreases monotonically. "The decrease. . .may be traced to the elongation of the vortices as they approach each other. Essentially, when all the vorticity is concentrated in a small region, the velocity induced at a given point on a vortex by its image receives nearly the same contribution from each point on the image. When the vortices are elongated, however, the contribution from the distant portions of the image vortex are significantly less than those from the near portions, and the total induced velocity is correspondingly less than if the same circulation were concentrated in a smaller region."[12] Unfortunately, since this is a numerical solution, the results exist only as plots of boundary contours and tabulated values of $\overline{U}\overline{y}_\infty/\overline{\Gamma}$ for certain values of $\overline{R}/\overline{y}_\infty$. In the event one is interested in a value of $\overline{R}/\overline{y}_\infty$ which has not been computed, one is forced to interpolate or extrapolate from the tabulated regions, an inconvenient procedure at best. Furthermore, a table of numbers provides no insight into the physics of the solution. Finally, it is difficult to extend the solution to the case with walls.

One would like to have a closed-form analytical model that overcomes the above deficiencies. This suggests a perturbation analysis, expressed through the perturbation parameter $\epsilon \equiv \overline{R}/\overline{y}_\infty$. The perturbation is shown in Figure 5.24. As a matter of convenience, *for the present derivation only*, the flow is rotated counterclockwise by 90 degrees. The vortices become a horizontal pair moving upward at velocity $\overline{V}$, all previous $(\overline{x}, \overline{y})$ coordinates become $(\overline{y}, \overline{x})$, and all $(\overline{u}, \overline{v})$ velocities become $(\overline{v}, \overline{u})$. Thus, the vortex spacing becomes $2\overline{x}_\infty$, and the perturbation parameter becomes $\epsilon \equiv \overline{R}/\overline{x}_\infty$. The unperturbed flow is assumed to be a pair of circular vortices with initial radii

[11] Wu, *et al.* (1984) confirmed the inner members of this family of solutions, but found that the outermost contour intersects the line of symmetry between the two vortices as a corner, rather than as a cusp. This is a limiting case which is seldom encountered in actual flows, and is of little concern to the present investigation.

[12] Pierrehumbert (1980), p. 140.

$\overline{R}_0$. The flow is assumed to be incompressible with uniform density throughout. The vortices are characterized by $\overline{\omega}$ = constant, $\overline{\Gamma}$ = constant, $\overline{A}$ = constant, and therefore, $\overline{R} \equiv (\overline{A}/\pi)^{1/2}$ = constant = $\overline{R}_0$. The boundary is allowed to deform to $\overline{r} = \overline{R}_B(\theta, \epsilon)$, subject to the kinematical conditions that the vortex pair moves, without change of spacing (centroid), upward at velocity $\overline{V}(\epsilon)$. This centroid condition is expressed as

$$\int\int \overline{x} dA = 2\int_0^{\pi} d\theta \int_0^{\overline{R}_B(\theta,\epsilon)} (\overline{r}cos\theta)\overline{r}d\overline{r} = \frac{2}{3}\int_0^{\pi} \overline{R}_B^3(\theta,\epsilon) \;=\; 0.$$

The velocity is expressed as

$$\frac{\overline{V}\overline{x}_\infty}{\overline{\Gamma}} = \frac{1}{4\pi} + \sum_{n=1}^{\infty} \epsilon^n \overline{V}_n$$

or, since $\overline{\Gamma} = \overline{\omega}\pi\overline{R}_0^2$,

$$\overline{V} = \epsilon\pi\overline{\omega}\overline{R}_0\Big(\frac{1}{4\pi} + \sum_{n=1}^{\infty} \epsilon^n \overline{V}_n\Big) .$$

The boundary conditions at $\overline{r} = \overline{R}_B(\theta, \epsilon)$ require continuity of velocity

$$(\overline{u} - i\overline{v})^{in}|_{\overline{r}=\overline{R}_B} = (\overline{u} - i\overline{v})^{out}|_{\overline{r}=\overline{R}_B}$$

and specification of normal velocity

$$(\overline{u}\hat{e}_x + \overline{v}\hat{e}_y)|_{\overline{r}=\overline{R}_B} \cdot \hat{e}_n = \overline{V}\hat{e}_y \cdot \hat{e}_n .$$

From the boundary shape schematic, Figure 5.25, it may be shown that

$$\begin{aligned} \overline{V}\hat{e}_y \cdot \hat{e}_n &= \overline{V}cos\Big(\frac{\pi}{2} - \theta - \phi\Big) \\ &= \overline{V}sin(\theta + \phi) \\ &= \overline{V}(sin\theta\ cos\phi + cos\theta\ sin\phi) \end{aligned}$$

and

$$\begin{aligned} (\overline{u}\hat{e}_x + \overline{v}\hat{e}_y)|_{\overline{r}=\overline{R}_B} \cdot \hat{e}_n &= (\overline{u}_r\hat{e}_r + \overline{u}_\theta\hat{e}_\theta) \cdot \hat{e}_n \\ &= \overline{u}_r\ cos\phi + \overline{u}_\theta cos\Big(\frac{\pi}{2} - \phi\Big) \\ &= \overline{u}_r cos\phi + \overline{u}_\theta sin\phi \end{aligned}$$

where

$$tan\phi = -\frac{1}{\overline{R}_B}\frac{d\overline{R}_B}{d\theta} .$$

The normal velocity boundary condition can then be expressed as

$$\overline{u}_r - \overline{V}sin\theta = (\overline{u}_\theta - \overline{V}cos\theta)\frac{1}{\overline{R}_B}\frac{d\overline{R}_B}{d\theta} .$$

The boundary itself is expressed as a power series in perturbation parameter ϵ as

$$\overline{r} = \overline{R}_B(\theta, \epsilon) = \sum_{k=0}^{\infty} \overline{r}_k(\theta)\epsilon^k ,$$

with shape factors $\overline{r}_k(\theta)$ to be determined from the matching process.

The velocities must also be expanded in the perturbation parameter ϵ. The flow is symmetric about $\overline{x} = -\overline{x}_\infty$, so only the velocity field about one vortex (*e.g.* , the right one) need be considered. Superscripts "in" and "out" refer to the velocity fields inside and outside the vortex, respectively. Each velocity field is a superposition of self-induced velocities and velocities induced by the other vortex. First consider the "inner" velocity. The lowest order "self" contribution is due to a solid body rotation. Higher order "self" contributions, which are corrections for deformation of boundary shape, are expressed as a power series in ϵ. The lowest order "other" contribution is due to a point vortex. Higher order "other" contributions are again expressed as a power series in ϵ. Therefore, at any point $\overline{z}$,

$$(\overline{u} - i\overline{v})^{in} = (\overline{u} - i\overline{v})^{in,\ self}_{solid\ body} + \sum_{k=1}^{\infty} \epsilon^k (\overline{u}_k - i\overline{v}_k)^{in,\ self}_{corrections}$$
$$+ (\overline{u} - i\overline{v})^{in,\ other}_{point\ vortex} + \sum_{k=1}^{\infty} \epsilon^k (\overline{u}_k - i\overline{v}_k)^{in,\ other}_{corrections} .$$

In a similar manner,

$$(\overline{u} - i\overline{v})^{out} = (\overline{u} - i\overline{v})^{out,\ self}_{point\ vortex} + \sum_{k=1}^{\infty} \epsilon^k (\overline{u}_k - i\overline{v}_k)^{out,\ self}_{corrections}$$
$$+ (\overline{u} - i\overline{v})^{out,\ other}_{point\ vortex} + \sum_{k=1}^{\infty} \epsilon^k (\overline{u}_k - i\overline{v}_k)^{out,\ other}_{corrections} .$$

It will be convenient to work with polar velocities, defined as

$$(\overline{u}_r - i\overline{u}_\theta) = e^{i\theta}(\overline{u} - i\overline{v}).$$

Under this transformation, the above expressions become

$$(\overline{u}_r - i\overline{u}_\theta)^{in} = (\overline{u}_r - i\overline{u}_\theta)^{in,\ self}_{solid\ body} + \sum_{k=1}^{\infty} \epsilon^k (\overline{u}_{r_k} - i\overline{u}_{\theta_k})^{in,\ self}_{corrections}$$
$$+ (\overline{u}_r - i\overline{u}_\theta)^{in,\ other}_{point\ vortex} + \sum_{k=1}^{\infty} \epsilon^k (\overline{u}_{r_k} - i\overline{u}_{\theta_k})^{in,\ other}_{corrections}$$

and

$$(\overline{u}_r - i\overline{u}_\theta)^{out} = (\overline{u}_r - i\overline{u}_\theta)^{out,\ self}_{point\ vortex} + \sum_{k=1}^{\infty} \epsilon^k (\overline{u}_{r_k} - i\overline{u}_{\theta_k})^{out,\ self}_{corrections}$$
$$+ (\overline{u}_r - i\overline{u}_\theta)^{out,\ other}_{point\ vortex} + \sum_{k=1}^{\infty} \epsilon^k (\overline{u}_{r_k} - i\overline{u}_{\theta_k})^{out,\ other}_{corrections} .$$

From analytic function theory, the complex velocity $\overline{u} - i\overline{v}$ is a function of the complex variable $\overline{z} = \overline{x} + i\overline{y}$. General expressions for the solid body and point vortex motions are, of course, well known. Figure 5.26(a) shows a clockwise solid body rotation about point $\overline{z}_0$. The velocity at $\overline{z}$ given by

$$(\overline{u} - i\overline{v})_{solid\ body} = \frac{i\overline{\omega}}{2}(\overline{z} - \overline{z}_0)^*$$

or

$$(\overline{u}_r - i\overline{u}_\theta)_{solid\ body} = \frac{i\overline{\omega}}{2}(\overline{z} - \overline{z}_0)^* e^{i\theta}.$$

Therefore, for $\overline{z}_0 = 0$,

$$(\overline{u}_r - i\overline{u}_\theta)^{in,\ self}_{solid\ body} = \frac{i\overline{\omega r}}{2}.$$

Figure 5.26(b) shows a clockwise point vortex at point $\overline{z}_0$. The velocity at $\overline{z}$ is given by

$$(\overline{u} - i\overline{v})_{point\ vortex} = \frac{i\overline{\Gamma}}{2\pi}\frac{1}{\overline{z} - \overline{z}_0}$$

or

$$(\overline{u}_r - i\overline{u}_\theta)_{point\ vortex} = \frac{i\overline{\Gamma}}{2\pi}\frac{e^{i\theta}}{\overline{z} - \overline{z}_0}$$

Therefore, for $\overline{z}_0 = 0$,

$$(\overline{u}_r - i\overline{u}_\theta)^{out,\ self}_{point\ vortex} = \frac{i\overline{\Gamma}}{2\pi}\frac{e^{i\theta}}{\overline{z}}$$

and for $\overline{z}_0 = -2\overline{x}_\infty$,

$$(\overline{u}_r - i\overline{u}_\theta)^{in\ or\ out,\ other}_{point\ vortex} = -\frac{i\overline{\Gamma}}{2\pi}\frac{e^{i\theta}}{\overline{z} + 2\overline{x}_\infty}.$$

Figure 5.26(c) is a schematic of a distributed vorticity $\overline{\omega}(\overline{z})$ representing the "correction" velocities due to deformation of boundary shape. These can be expressed as appropriate Laurent series in $\overline{z}$. The "inner" velocity must have only positive powers of $\overline{z}$, so that

$$(\overline{u}_{r_k} - i\overline{u}_{\theta_k})^{in,\ self}_{corrections} = i\sum_{n=0}^{\infty}\overline{p}_n^k\left(\frac{\overline{z}}{\overline{R}_0}\right)^n.$$

The "outer" velocity must have only negative powers of z, so that

$$(\overline{u}_{r_k} - i\overline{u}_{\theta_k})^{out,\ self}_{corrections} = i\sum_{n=2}^{\infty}\overline{q}_n^k\left(\frac{\overline{R}_0}{\overline{z}}\right)^n.$$

The last velocity components needed are

$$(\overline{u}_{r_k} - i\overline{u}_{\theta_k})^{in,\ other}_{corrections}$$

and

$$(\overline{u}_{r_k} - i\overline{u}_{\theta_k})^{out,\ other}_{corrections}.$$

These represent corrections to the velocity field near the first (say the right) vortex, due to the second vortex (say the left one), so the distinction between "in" and "out," which refer to the first vortex, does not matter. That is, the velocity induced by the second vortex only depends on the distance from the other vortex to the point of interest, and not on whether this point is inside or outside the boundary of the first vortex. Therefore,

$$(\overline{u}_{r_k} - i\overline{u}_{\theta_k})^{in,\ other}_{corrections} = (\overline{u}_{r_k} - i\overline{u}_{\theta_k})^{out,\ other}_{corrections}.$$

Figure 5.27 illustrates the symmetry by which the "in or out, other" velocity is expressed as the negative of a shifted and conjugated "self, other" velocity. That is,

$$(\overline{u}_{r_k} - i\overline{u}_{\theta_k})^{\text{in or out, other}}_{\text{corrections}}\Big|_{\overline{z}} = \left[-(\overline{u}_{r_k} - i\overline{u}_{\theta_k})^{\text{out, self}}_{\text{corrections}}\Big|_{(-2\overline{x}_\infty - \overline{z}^*)}\right]^* .$$

At this point, the mathematics are in place for determination of the unknown coefficients in $\overline{R}_B$, $\overline{V}$, and the correction velocities. All the velocity terms are evaluated at $\overline{R}_B$, using expansions such as

$$\frac{1}{1+x} = \sum_{n=0}^{\infty} (-x)^n$$

and

$$(x+y)^n = \sum_{k=0}^{n} \frac{n!}{(n-k)!k!} x^k y^{n-k}$$

to express everything as power series expansions in ϵ. For each order of ϵ, the order of analysis is as follows. First, the inner and outer radial velocities $\overline{u}_r$ are matched at the boundary. This relates one set of unknown coefficients $\overline{q}_n^k$ to another set $\overline{p}_n^k$. Second, the inner and outer tangential velocities $\overline{u}_\theta$ are matched at the boundary. This defines the boundary shape coefficients $\overline{r}_k$ as a Fourier cosine series with coefficients related to $\overline{p}_n^k$. Third, the constancy of the $\overline{x}$-centroid determines some of the unknown coefficients $\overline{p}_n^k$. Fourth, the normal velocity boundary condition determines the remainder of the unknown coefficients $\overline{p}_n^k$. At this point, the solution is completely known to the specified order. The algebraic manipulations in this process are tremendous, especially at higher orders. For this reason, the results are presented in summary form only.[13]

[13] With appropriate forethought, it is possible to avoid doing some of the algebra, but only some of it. For example, in the radial and tangential velocity matching, each velocity is composed of two single terms and two infinite sums. However, some of the terms cancel, because velocities induced at the boundary of one vortex, by the other vortex, must be continuous across the boundary. That is,

$$(\overline{u} - i\overline{v})^{\text{in, other}}_{\text{point vortex}}\Big|_{\overline{r}=\overline{R}_B} = (\overline{u} - i\overline{v})^{\text{out, other}}_{\text{point vortex}}\Big|_{\overline{r}=\overline{R}_B}$$

and

$$(\overline{u} - i\overline{v})^{\text{in, other}}_{\text{corrections}}\Big|_{\overline{r}=\overline{R}_B} = (\overline{u} - i\overline{v})^{\text{out, other}}_{\text{corrections}}\Big|_{\overline{r}=\overline{R}_B} .$$

Therefore, these terms need not be included when velocity-matching at the boundary; one knows *a priori* that they must cancel. However, these terms must be included in the normal velocity boundary condition, which has no such fortuitous cancellation of terms. The algebra involved in these calculations comprised some 30-odd pages of handwritten algebra, and took weeks to complete, even after the method of solution had been defined. It is characteristic of these types of analyses that a single mistake early in the solution can invalidate the remainder of the solution, necessitating many iterations of checking and rechecking. It was chosen to omit the details here only because of good confidence that the results are correct. Shortly after the solution was executed by hand, the symbolic manipulation program Mathematica was obtained, and used to verify the results. In using Mathematica, the time required for solution was reduced by at least an order of magnitude, requiring only tens of hours of keyboard manipulations. In view of the widespread distribution of such programs, it seems pointless to fill valuable space with endless pages of algebra. The problem has been described in sufficient detail that anyone wishing to check (or extend) the solution can do so straightforwardly via a computer.

• To order ϵ^0:

All conditions are identically satisfied.

• To order ϵ^1:

$\overline{u}_r$-matching gives

$$\overline{q}^1_{n+1} = -\overline{p}^1_{n-1},\ (n \geq 1),$$

$\overline{u}_\theta$-matching gives

$$\overline{r}_1 = -\frac{2}{\overline{\omega}} \sum_{n=1}^{\infty} \overline{p}^1_{n-1} cosn\theta,$$

the centroid condition gives

$$\overline{p}^1_0 = 0,$$

and the normal velocity condition gives

$$\overline{p}^1_n = 0,\ (n \geq 1).$$

After substitution, one finds that

$$\overline{r}_1 = 0.$$

• To order ϵ^2:

$\overline{u}_r$-matching gives

$$\overline{q}^2_{n+1} = -\overline{p}^2_{n-1},\ (n \geq 1),$$

$\overline{u}_\theta$-matching gives

$$\overline{r}_2 = -\frac{2}{\overline{\omega}} \sum_{n=1}^{\infty} \overline{p}^2_{n-1} cosn\theta,$$

the centroid condition gives

$$\overline{p}^2_0 = 0,$$

and the normal velocity condition gives

$$\overline{V}_1 = 0,$$

$$\overline{p}^2_1 = \frac{1}{8}\overline{\omega r}_0,$$

and

$$\overline{p}^2_n = 0,\ (n \geq 2).$$

After substitution, one finds that

$$\overline{r}_2 = -\frac{1}{4}\overline{R}_0 cos2\theta.$$

• To order ϵ^3:

$\overline{u}_r$-matching gives

$$\overline{q}^3_{n+1} = -\overline{p}^3_{n-1},\ (n \geq 1),$$

$\overline{u}_\theta$-matching gives

$$\overline{r}_3 = -\frac{2}{\overline{\omega}} \sum_{n=1}^{\infty} \overline{p}_{n-1}^3 cosn\theta,$$

the centroid condition gives

$$\overline{p}_0^3 = 0,$$

and the normal velocity condition gives

$$\overline{V}_2 = 0,$$

$$\overline{p}_2^3 = -\frac{1}{32}\overline{\omega}\overline{r}_0,$$

and

$$\overline{p}_n^3 = 0, \ (n \neq 2).$$

After substitution, one finds that

$$\overline{r}_3 = \frac{1}{16}\overline{R}_0 cos3\theta.$$

- To order ϵ^4:

  $\overline{u}_r$-matching gives

$$\overline{q}_5^4 = -\overline{p}_3^4 + \frac{1}{16}\overline{\omega}\overline{R}_0$$

and

$$\overline{q}_{n+1}^4 = -\overline{p}_{n-1}^4, \ (n \neq 4),$$

$\overline{u}_\theta$-matching gives

$$\overline{r}_4 = -\frac{1}{64}\overline{R}_0 + \frac{3}{64}\overline{R}_0 cos4\theta - \frac{2}{\overline{\omega}} \sum_{n=1}^{\infty} \overline{p}_{n-1}^4 cosn\theta,$$

the centroid condition gives

$$\overline{p}_0^4 = 0,$$

and the normal velocity condition gives

$$\overline{V}_3 = 0,$$

$$\overline{p}_3^4 = \frac{1}{96}\omega\overline{r}_0,$$

and

$$\overline{p}_n^4 = 0, \ (n \neq 3).$$

After substitution, one finds that

$$\overline{r}_4 = -\frac{1}{64}\overline{R}_0 + \frac{5}{192}\overline{R}_0 cos4\theta.$$

- To order ϵ^5:

$\overline{u}_r$-matching gives

$$\overline{q}_2^5 = -\overline{p}_0^5 - \frac{1}{128}\overline{\omega}\overline{R}_0,$$

$$\overline{q}_6^5 = -\overline{p}_4^5 - \frac{5}{128}\overline{\omega}\overline{R}_0,$$

and

$$\overline{q}_{n+1}^5 = -\overline{p}_{n-1}^5, \ (n \neq 1, 5),$$

$\overline{u}_\theta$-matching gives

$$\overline{r}_5 = -\frac{1}{32}\overline{R}_0 cos5\theta - \frac{2}{\overline{\omega}}\sum_{n=1}^{\infty}\overline{p}_{n-1}^5 cosn\theta,$$

the centroid condition gives

$$\overline{p}_0^5 = -\frac{1}{128}\overline{\omega}\overline{R}_0,$$

and the normal velocity condition gives

$$\overline{V}_4 = -\frac{1}{32\pi},$$

$$\overline{p}_4^5 = -\frac{1}{256}\overline{\omega}\overline{r}_0,$$

and

$$\overline{p}_n^5 = 0, \ (n \neq 0, 4).$$

After substitution, one finds that

$$\overline{r}_5 = -\frac{1}{64}\overline{R}_0 cos\theta - \frac{3}{128}\overline{R}_0 cos5\theta.$$

• To order ϵ^6:

$\overline{u}_r$-matching gives

$$\overline{q}_3^6 = -p_1^6 - \frac{1}{384}\overline{\omega}\overline{R}_0,$$

$$\overline{q}_7^6 = -p_5^6 - \frac{9}{512}\overline{\omega}\overline{R}_0,$$

and

$$\overline{q}_{n+1}^6 = -\overline{p}_{n-1}^6, \ (n \neq 2, 6),$$

$\overline{u}_\theta$-matching gives

$$\overline{r}_6 = -\frac{1}{1024}\overline{R}_0 + \frac{7}{1536}\overline{R}_0 cos2\theta + \frac{25}{3072}\overline{R}_0 cos6\theta - \frac{2}{\overline{\omega}}\sum_{n=1}^{\infty}\overline{p}_{n-1}^6 cosn\theta,$$

the centroid condition gives

$$\overline{p}_0^6 = 0,$$

and the normal velocity condition gives

$$\overline{V}_5 = 0,$$

$$\overline{p}_1^6 = -\frac{7}{384}\overline{\omega r}_0,$$

$$\overline{p}_5^6 = \frac{1}{640}\overline{\omega r}_0,$$

and

$$\overline{p}_n^6 = 0, \ (n \neq 1, 5).$$

After substitution, one finds that

$$\overline{r}_6 = -\frac{1}{1024}\overline{R}_0 + \frac{21}{512}\overline{R}_0 cos2\theta + \frac{77}{15360}\overline{R}_0 cos6\theta.$$

It is interesting to note that, even though the shape of the vortex pair begins to deform at order ϵ^2, there is no change in velocity until order ϵ^5. Carrying out the solution to 6-th order shows no additional change in velocity, and the additional time and effort necessary to continue to even higher orders is unjustifiable. The reason for this is that a perturbation solution is an asymptotic series, and can therefore be convergent or divergent. In either case, there is an optimal number of terms for which the error is a minimum. This is illustrated in Figure 5.28. There is no way, *a priori*, to determine where a certain order solution falls on the error curve. It may be that adding just a few more terms will minimize the error, if the solution is rapidly convergent; it may be that many more terms have to be added, if the solution is slowly convergent; or it may be that adding more terms will only increase the error, if the solution is divergent.

Summarizing the solution to 6-th order, one finds that the shape is given by

$$\frac{\overline{R}_B}{\overline{R}_0} = \left(-\frac{1}{4}cos2\theta\right)\epsilon^2 + \left(\frac{1}{16}cos3\theta\right)\epsilon^3 + \left(-\frac{1}{64} + \frac{5}{192}cos4\theta\right)\epsilon^4 + \left(-\frac{1}{64}cos\theta - \frac{3}{128}cos5\theta\right)\epsilon^5$$
$$+ \left(-\frac{1}{1024} + \frac{21}{512}cos2\theta + \frac{77}{15360}cos6\theta\right)\epsilon^6 + O(\epsilon^7)$$

and that the normalized velocity is given by

$$\frac{\overline{V}\overline{x}_\infty}{\overline{\Gamma}} = \frac{1}{4\pi} - \left(\frac{1}{32\pi}\right)\epsilon^4 + O(\epsilon^6).$$

Returning to the notation used everywhere except in this particular derivation, the normalized velocity is expressed as

$$\frac{\overline{U}\overline{y}_\infty}{\overline{\Gamma}} = \frac{1}{4\pi} - \frac{1}{32\pi}\left(\frac{\overline{R}}{\overline{y}_\infty}\right)^4 + O\left(\frac{\overline{R}}{\overline{y}_\infty}\right)^6.$$

For convenience in the derivation of this solution, the density was assumed to be uniform everywhere. This is not the case in the actual flow. For consistency with the assumption of piecewise constant vorticity, one should at least model the density as piecewise constant: low inside the

vortex core and high outside the vortex core. However, the uniform density solution can easily be transformed into the solution for the case of piecewise constant density.

Consider the governing equations for steady flow in the case of piecewise constant inner and outer densities:

$$\underline{\nabla} \cdot (\underline{u}^{in}) = 0$$

$$\underline{\nabla} \cdot (\underline{u}^{out}) = 0$$

and

$$\underline{\nabla} \cdot (\overline{\rho}^{in} \overline{\underline{u}}^{in} \overline{\underline{u}}^{in}) + \underline{\nabla} \overline{p}^{in} = 0$$

$$\underline{\nabla} \cdot (\overline{\rho}^{out} \overline{\underline{u}}^{out} \overline{\underline{u}}^{out}) + \underline{\nabla} \overline{p}^{out} = 0.$$

Define a modified inner velocity as

$$\overline{\underline{u}}^{in'} \equiv \sqrt{\frac{\overline{\rho}^{in}}{\overline{\rho}^{out}}}\, \overline{\underline{u}}^{in}.$$

The inner continuity equation is transformed to

$$\underline{\nabla} \cdot (\overline{\underline{u}}^{in'}) = 0,$$

and the inner momentum equation is transformed to

$$\underline{\nabla} \cdot (\overline{\rho}^{out} \overline{\underline{u}}^{in'} \overline{\underline{u}}^{in'}) + \underline{\nabla} \overline{p}^{in} = 0.$$

The velocity and pressure terms in the continuity and momentum equations still refer to separate inner and outer flows, but all the density terms now refer to the same outer flow. Thus, these equations exactly describe an equivalent uniform density flow, where inner velocities for the uniform density flow are interpreted as $\overline{\underline{u}}^{in'} \equiv \sqrt{\overline{\rho}^{in}/\overline{\rho}^{out}}\, \overline{\underline{u}}^{in}$.

The specification of a problem entails differential equations plus boundary conditions, and it is necessary to check the boundary conditions for the piecewise constant density flow to see if the uniform density flow and the piecewise constant density flow, connected by the above transformation, represent the same physical problem. The first boundary condition, continuity of velocity in the uniform density flow, is replaced by continuity of pressure in the piecewise constant density flow. These appear to be different boundary conditions. However, velocity matching implies pressure matching in a uniform density flow, and pressures are not changed by the proposed transformation of velocity. Thus, velocity matching in the uniform density flow satisfies pressure matching in the piecewise constant density flow. The second boundary condition, that the surface velocity be tangential to the boundary, is the same in either case.

Thus it is clear that the perturbation analysis, which was carried out for a uniform density flow, is directly applicable to a piecewise constant density flow. The outer velocities, boundary shapes,

and normalized velocities are the same in either case. The inner velocities for the piecewise constant density flow are simply constant multiples of the inner velocities found for the uniform density case.

The above analysis assumes the flow to be incompressible. For the higher Mach number cases discussed in Chapter 3, although the flow behind the shock is certainly subsonic, the assumption of incompressibility is no longer guaranteed. Moore and Pullin (1987) demonstrated numerically and analytically that the effect of compressibility is to reduce the velocity of a finite core size vortex pair in an unbounded domain. They found that the normalized velocity depends on two parameters: 1) the ratio of boundary velocity to vortex pair velocity, $\overline{U}_{boundary}/\overline{U}$, and 2) the ratio of vortex pair velocity to the sound speed far behind the shock, $\overline{U}/\overline{c}_2$. The worst (limiting) case is the so-called 'evacuated vortex,' corresponding to zero pressure inside the vortex. In that case, the normalized velocity is only a function of $\overline{U}/\overline{c}_2$.

This result can be used as an (upper bound) estimate of compressibility effects in the flows of the present investigation. The velocity $\overline{U}$ is available from Tables 5.2 to 5.4 and the speed of sound far behind the shock is given by one-dimensional normal shock theory as

$$\frac{\overline{c}_2}{\overline{c}_1} = 1 + 2\frac{(\gamma-1)}{(\gamma+1)^2}\left(\frac{\gamma M^2+1}{M^2}\right)(M^2-1).$$

Consider the highest compressibility case of the present investigation, M=2 and $\overline{\rho}_L/\overline{\rho}_H = 0.138$. In that case, $\overline{U} = 0.070$ and $\overline{c}_2 = 1.30$, so that $\overline{U}/\overline{c}_2 = 0.070/1.30 = 0.054$. An upper bound for the compressibility effects is given by an 'evacuated vortex' with $\overline{U}/\overline{c}_2 = 0.06$, which Moore and Pullin found to have a normalized velocity 1.6% below the classical $1/(4\pi)$ value. Therefore, the assumption of incompressibility in the present study is quantitatively justified.

This completes the perturbation solution for the effect of vortex size. It is appropriate to compare the analytical results against Pierrehumbert's numerical result as a check on the accuracy of the solution. As a matter of convenience, the present results are plotted according to the convention used by Pierrehumbert, *i.e.*, the extreme points of the boundary, normal to the direction of motion, are taken to be ± 1. Figure 5.29(a) shows the family of boundary shapes from the perturbation analysis for $\epsilon = 0.048, 0.100, 0.159, 0.225, 0.390, 0.500, 0.639$, and 0.844. These agree quite well with Pierrehumbert's shapes (Figure 5.22). Figure 5.29(b) is a comparison of normalized velocity, $\overline{U}\overline{y}_\infty/\overline{\Gamma}$, Figure 5.29(c) is a comparison of Pierrehumbert's so-called 'intervortex gap ratio,' and Figure 5.29(d) is a comparison of aspect ratio. In all cases, for values of $\overline{R}/\overline{y}_\infty$ less than about 1.1, the results agree quite well. This agreement both verifies the perturbation analysis and provides an independent check of Pierrehumbert's numerical analysis.

5.3.3 The Combined Effects of Channel Spacing and Core Size

The last step is to modify the solution to account for the effect of channel spacing. Mathemati-

cally, this introduces a second perturbation parameter, $\overline{y}_\infty/\overline{h}$, making the problem a two parameter perturbation analysis. This complicates the already intricate mathematics in the one-parameter solution. To carry out a two parameter perturbation analysis to more than just lowest order involves truly intractable mathematics, and one would be well advised to consider parametric studies using numerical solutions, instead of perturbation theory, in those cases. For this reason, the present analysis will deal with only the lowest order solution to the two-parameter perturbation, which should be expressible as a superposition of the effects of channel spacing and core size taken separately.

Considering the effect of channel spacing alone, the normalized velocity may be represented as

$$\frac{\overline{U}\overline{y}_\infty}{\overline{\Gamma}} = \frac{\overline{U}\overline{y}_\infty}{\overline{\Gamma}}\bigg|_{\overline{y}_\infty/\overline{h}=0} f\Big(\frac{\overline{y}_\infty}{\overline{h}}\Big) ,$$

where

$$\frac{\overline{U}\overline{y}_\infty}{\overline{\Gamma}}\bigg|_{\overline{y}_\infty/\overline{h}=0} = \frac{1}{4\pi}$$

represents the unperturbed velocity (in the limit of infinite channel spacing), and

$$f\Big(\frac{\overline{y}_\infty}{\overline{h}}\Big)$$

represents the effects of finite channel spacing (*c.f.* Subsection 1).

Considering the effect of core size alone, the normalized velocity may be represented as

$$\frac{\overline{U}\overline{y}_\infty}{\overline{\Gamma}} = \frac{\overline{U}\overline{y}_\infty}{\overline{\Gamma}}\bigg|_{\overline{R}/\overline{y}_\infty=0} g\Big(\frac{\overline{R}}{\overline{y}_\infty}\Big) ,$$

where

$$\frac{\overline{U}\overline{y}_\infty}{\overline{\Gamma}}\bigg|_{\overline{R}/\overline{y}_\infty=0} = \frac{1}{4\pi}$$

represents the unperturbed velocity (in the limit of infinitesimal core size), and

$$g\Big(\frac{\overline{R}}{\overline{y}_\infty}\Big)$$

represents the effect of finite core size (from the perturbation solution above).

One expects to obtain the lowest order solution in both effects by simply substituting either of the above solutions for the 'unperturbed velocity' term of the other solution, *i.e.*,

$$\frac{\overline{U}\overline{y}_\infty}{\overline{\Gamma}}\bigg|_{\overline{R}/\overline{y}_\infty=0} \leftarrow \frac{\overline{U}\overline{y}_\infty}{\overline{\Gamma}}\bigg|_{\overline{y}_\infty/\overline{h}=0} f\Big(\frac{\overline{y}_\infty}{\overline{h}}\Big) .$$

The result is

$$\frac{\overline{U}\overline{y}_\infty}{\overline{\Gamma}} = \frac{1}{4\pi} f\Big(\frac{\overline{y}_\infty}{\overline{h}}\Big)\, g\Big(\frac{\overline{R}}{\overline{y}_\infty}\Big)$$

or

$$\frac{\overline{U}\overline{y}_\infty}{\overline{\Gamma}} \approx \frac{1}{4\pi}\,\frac{\pi\overline{y}_\infty}{\overline{h}}\,\Big[ctg\Big(\frac{\pi\overline{y}_\infty}{\overline{h}}\Big)\Big]\Big[1-\frac{1}{8}\Big(\frac{\overline{R}}{\overline{y}_\infty}\Big)^4\Big] .$$

This represents a lowest-order, but completely analytical, model for the effects of both channel spacing and core size. One can test this model using data from the computations of Chapter 3. Besides the circulation, spacing, and velocity, it is also necessary to know size and location parameters. These are computed as follows. The effective vortex core radius,

$$\overline{R} \equiv \sqrt{\frac{\overline{A}}{\pi}},$$

is based on the mass fraction-weighted area,

$$\overline{A} \equiv \int f \, d\overline{A}.$$

From these one can calculate the parameters necessary for use in the model, the ratio of core size to vortex spacing, $\overline{R}/\overline{y}_\infty$, and the ratio of vortex spacing to channel spacing, $\overline{y}_\infty/\overline{h}$. The first set of data consists of fixed $\overline{\rho}_L/\overline{\rho}_H = 0.138$ and $1.05 \leq M \leq 2.0$. As the Mach number is increased, the ratio of effective core size to vertical spacing decreases, and the qualitative dependence of $\overline{U}\overline{y}_\infty/\overline{\Gamma}$ vs. M should look like Figure 5.30(a) (the vortices move faster as they become more compact). Also, as the Mach number is increased, the ratio of vortex spacing to channel spacing increases, and the qualitative dependence of $\overline{U}\overline{y}_\infty/\overline{\Gamma}$ *vs.* M should look like Figure 5.30(b) (the vortices slow down as they get closer to the walls). Considering both effects together, one expects the qualitative trend to look like Figure 5.30(c). The initial rise in velocity due to the vortex size effects should be offset by a decrease due to channel spacing effects. The net effect should be approximately constant or perhaps have a slight concave downward curvature, depending on the exact values of vortex size, vortex spacing, and channel spacing.

Table 5.2 lists the computed and predicted normalized velocities as a function of the incident shock strength, so that the dependencies of core size and channel spacing are implicit in the single parameter M.

M	$\overline{R}/\overline{y}_\infty$	$\overline{y}_\infty/\overline{h}$	Computed $\overline{U}\overline{y}_\infty/\overline{\Gamma}$	Predicted $\overline{U}\overline{y}_\infty/\overline{\Gamma}$
1.05	1.0540	0.1800	0.0540	0.0600
1.1	0.9866	0.1875	0.0550	0.0618
1.2	0.8808	0.2000	0.0600	0.0636
1.5	0.6693	0.2375	0.0617	0.0626
2.0	0.5470	0.2500	0.0583	0.0618

Table 5.2 - Computed and predicted $\overline{U}\overline{y}_\infty/\overline{\Gamma}$ for canonical flows with $\overline{\rho}_L/\overline{\rho}_H = 0.138$

These data are also plotted in Figure 5.31. The computed data are indicated by □, and the predicted values are indicated by ×. The second set of data is for M=1.1 and $\overline{\rho}_L/\overline{\rho}_H$ = 0.138 and 0.354 (two higher density ratio cases are not included because those cases were not carried out to late enough times to give a steady state vortex pair). Table 5.3 lists the computed and predicted normalized velocities as a function of the density ratio.

$\overline{\rho}_L/\overline{\rho}_H$	$\overline{R}/\overline{y}_\infty$	$\overline{y}_\infty/\overline{h}$	Computed $\overline{U}\overline{y}_\infty/\overline{\Gamma}$	Predicted $\overline{U}\overline{y}_\infty/\overline{\Gamma}$
0.138	0.9866	0.1875	0.0550	0.0618
0.354	0.8982	0.2050	0.0588	0.0627

Table 5.3 - Computed and predicted $\overline{U}\overline{y}_\infty/\overline{\Gamma}$ for canonical flows with M=1.1

These data are also plotted in Figure 5.32.

The last set of data is for M=2 and $\overline{\rho}_L/\overline{\rho}_H$ = 0.138, 0.354, and 0.569 (again, omitting one higher density ratio case which lacks a steady-state vortex pair). Table 5.4 lists the computed and predicted normalized velocities as a function of the density ratio.

$\overline{\rho}_L/\overline{\rho}_H$	$\overline{R}/\overline{y}_\infty$	$\overline{y}_\infty/\overline{h}$	Computed $\overline{U}\overline{y}_\infty/\overline{\Gamma}$	Predicted $\overline{U}\overline{y}_\infty/\overline{\Gamma}$
0.138	0.5470	0.2500	0.0583	0.0618
0.354	0.4558	0.3000	0.0471	0.0542
0.569	0.4443	0.3000	0.0517	0.0542

Table 5.4 - Computed and predicted $\overline{U}\overline{y}_\infty/\overline{\Gamma}$ for canonical flows with M=2.0

These data are also plotted in Figure 5.33. The agreement is quite good throughout the range of Mach numbers and density ratios, verifying the ability of even this lowest order model to accurately capture the physics of the flow.

5.4 A Model for the Spacing of the Vortex Pair

The previous sections described analytical models for the circulation and normalized velocity of the vortex pair. The last quantity necessary for a complete description of the overall fluid mechanical

behavior is the vortex half-spacing, $\overline{y}_\infty$. Then the actual velocity $\overline{U}$ may be predicted from $\overline{U}\overline{y}_\infty/\overline{\Gamma}$, and the size of the vortex pair may be predicted from the known dependence of $\overline{U}\overline{y}_\infty/\overline{\Gamma}$ on the ratio of vortex spacing to channel spacing, $\overline{y}_\infty/\overline{h}$, and the ratio of core size to vortex spacing, $\overline{R}/\overline{y}_\infty$. The two classical measures of a vortical flow are its circulation and impulse. The circulation has already been considered, but not the impulse. This is the additional consideration necessary for characterizing the spacing of the vortex pair.

In the previous section, the vortex pair was modelled as an equivalent constant-vorticity region. Representation of the computed flow by the model flow requires the correspondence of both circulation and spacing: the model's circulation must match that of the computed flow, and the model's centroid must be coincident with the mass-fraction-weighted centroid of the computed flow (*i.e.*, the vorticity is assumed to follow the light gas in the cores).

Dimensionally, the product of these quantities suggests a measure of the impulse of the flow:

$$\overline{I}_x{}' = \overline{\rho}_{model}\ \overline{y}_\infty\ \overline{\Gamma},$$

where $\overline{\rho}_{model}$ is an appropriate density for the model flow. The prime notation is used to emphasize that $\overline{I}_x{}'$ is not exactly a true impulse, which is properly defined as an integral, but is a closely related quantity.

Recall from the previous section that the density of the core fluid in the model has no effect on the normalized velocity. Thus, there appears to be some ambiguity in what density to choose as the reference value, $\overline{\rho}_{model}$. However, this is not so. The steady-state quantity $\overline{I}_x{}' = \overline{\rho}_{model}\ \overline{y}_\infty\ \overline{\Gamma}$ must be directly related to the applied impulse, so one may write:

$$\overline{I}_x{}' \approx \overline{I}_x(\overline{t} = 0^+).$$

The unspecified density gives one the freedom to match $\overline{I}_x{}'$ for the constant vorticity model to the initial impulse $\overline{I}_x(\overline{t} = 0^+)$ caused by the passage of a shock over a circular jet. If this freedom did not exist, there would be no way to correlate the two quantities. The reason is that an uniform vorticity vortex pair cannot have exactly the same circulation and impulse as the shock-generated flow, which has a nonuniform distribution of core vorticity. These quantities represent zeroth and first moments of the vorticity distribution, which cannot simultaneously be matched when a nonuniform distribution is approximated as an uniform one.

Consider now the impulse of the shock-generated flow. The derivation very closely follows that for the circulation model (Section 1). Again, refer to Figure 5.1 for a schematic of the flow. The impulse in a two-dimensional flow is defined as

$$\underline{I} \equiv \int \rho\omega\ \underline{x} \times d\underline{A},$$

Page 54, Line 6

The expression should read

$$\omega = \frac{1}{V_s} \frac{\Delta\rho}{\rho} \frac{\Delta p}{\rho} \, sin\theta \, \delta(R - R_0)$$

Page 54, Line 8

The expression should read

$$I_x(\bar{t} = 0^+) = \int_{r=0}^{\infty} \int_{\theta=0}^{\pi} \Big(\frac{1}{V_s} \frac{\Delta\rho}{\rho} \frac{\Delta p}{\rho} \, sin\theta \, \delta(R - R_0) \Big) (\rho r sin\theta)(r dr d\theta)$$

Page 54, Line 11

so that

$$I_x(\bar{t}=0^+) = \hat{e}_x \cdot \underline{I}(\bar{t}=0^+)$$
$$= \int \rho\omega r sin\theta \; dA.$$

This is similar to the expression for circulation derived in Section 1, except for the additional term $\rho r sin\theta$. The vorticity is again given by

$$\omega = \frac{1}{V_s} \frac{\Delta\rho}{\rho} \frac{\Delta p}{\rho} \, sin\theta,$$

so that the x-component of impulse becomes

$$I_x(\bar{t}=0^+) = \int_{r=0}^{\infty} \int_{\theta=0}^{\pi} \left(\frac{1}{V_s} \frac{\Delta\rho}{\rho} \frac{\Delta p}{\rho} \, sin\theta \right) (\rho r sin\theta)(r dr d\theta)$$
$$= \frac{1}{V_s} \frac{\Delta p}{\rho} \frac{\Delta\rho}{\rho} \rho \int_0^{\pi} \int_0^{\infty} \delta(r - R_0) \, sin^2\theta \, r^2 \, dr \, d\theta$$
$$= \frac{\pi}{2} \frac{1}{V_s} \frac{\Delta p}{\rho} \frac{\Delta\rho}{\rho} \rho \int_{\infty}^{\infty} \delta(r - R_0) \, r^2 \, dr$$
$$= \frac{\pi}{2} \frac{1}{V_s} \frac{\Delta p}{\rho} \frac{\Delta\rho}{\rho} \rho R_0^2$$

Taking $\rho = \rho_2$ as the reference density, and nondimensionalizing, the final result is

$$\bar{I}_x(\bar{t}=0^+) = \frac{\pi}{2\gamma_1} \left(\frac{1}{M} \right) \left(\frac{\bar{p}_2}{\bar{p}_1} - 1 \right) \left(\frac{\bar{\rho}_1}{\bar{\rho}_2} \right) \left(1 - \frac{\bar{\rho}_L}{\bar{\rho}_H} \right)$$

or

$$\bar{I}_x(\bar{t}=0^+) \approx \left(\frac{1}{M} \right) \left(\frac{\bar{p}_2}{\bar{p}_1} - 1 \right) \left(\frac{\bar{\rho}_1}{\bar{\rho}_2} \right) \left(1 - \frac{\bar{\rho}_L}{\bar{\rho}_H} \right).$$

Again, note that $\bar{p}_2/\bar{p}_1$ and $\bar{\rho}_2/\bar{p}_1$ are known functions of M.

Tables 5.5, 5.6, and 5.7 show a comparison of the quantities $\bar{I}_x'$ and $\bar{I}_x(\bar{t}=0^+)$. Note that a value of 1/2 has been assigned to $\bar{\rho}_{model}$, in order to collapse the data, and therefore, from this point on, $\bar{I}_x' \equiv 0.5 \, \bar{y}_\infty \bar{\Gamma}$). Values of $\bar{y}_\infty$ and $\bar{\Gamma}$, for use in computing $\bar{I}_x'$, are for the computations of Chapter 3.

Table 5.5 is the case $\bar{\rho}_L/\bar{\rho}_H = 0.138$.

M	$\bar{I}_x'$	$\bar{I}_x(\bar{t}=0^+)$
1.05	0.086	0.091
1.1	0.169	0.164
1.2	0.295	0.275
1.5	0.485	0.450
2.0	0.600	0.566

Table 5.5 - Computed $\bar{I}_x'$ and predicted $\bar{I}_x(\bar{t}=0^+)$ for canonical flows with $\bar{\rho}_L/\bar{\rho}_H = 0.138$

These data are also plotted in Figure 5.34. The agreement is very good.

Table 5.6 is the case M=1.1.

M	$\overline{I}_x'$	$\overline{I}_x(\overline{t}=0^+)$
0.138	0.169	0.164
0.354	0.112	0.123

Table 5.6 - Computed $\overline{I}_x'$ and predicted $\overline{I}_x(\overline{t}=0^+)$ for canonical flows with M=1.1

These data are also plotted in Figure 5.35. The agreement is very good. Table 5.7 is the case M=2.0.

M	$\overline{I}_x'$	$\overline{I}_x(\overline{t}=0^+)$
0.138	0.600	0.566
0.354	0.459	0.424
0.569	0.269	0.283

Table 5.7 - Computed $\overline{I}_x$ ' and predicted $\overline{I}_x(\overline{t}=0^+)$ for canonical flows with M=2.0

These data are also plotted in Figure 5.36. The agreement is very good. At this point, both $\overline{\Gamma}$ and $\overline{I}_x'$ ($= 0.5\,\overline{y}_\infty\overline{\Gamma}$) have been successfully modelled as a function of M and $\overline{\rho}_L/\overline{\rho}_H$. These results may be combined to give the following expression for $\overline{y}_\infty$:

$$\overline{y}_\infty = \frac{\gamma_1}{2}\left(1+\frac{\overline{\rho}_L}{\overline{\rho}_H}\right).$$

This result states that the spacing of the vortices (vorticity centroid of the model flow or mass-fraction centroid of the actual flow) is a function only of the light/heavy gas density ratio, and independent of the strength of the shock.

The data from the computations are collected together, along with the corresponding predicted values, in Table 5.8.

M	$\overline{\rho}_L/\overline{\rho}_H$	Computed $\overline{y}_\infty$	Predicted $\overline{y}_\infty$
1.05	0.138	0.72	0.797
1.1	0.138	0.75	0.797
1.2	0.138	0.82	0.797
1.5	0.138	1.00	0.797
2.0	0.138	1.00	0.797
1.1	0.354	0.82	0.948
2.0	0.354	1.20	0.948
2.0	0.569	1.20	1.098

Table 5.8 - Computed and predicted $\overline{y}_\infty$ for the canonical flows

The agreement between the computed and predicted values of $\overline{y}_\infty$ is not as good as one might hope. In cases where the shock strength spans a range, the predicted value closely matches the median computed value (corresponding to an intermediate strength shock). The model for $\overline{y}_\infty$ was derived by combining the circulation and impulse models, and therefore suffers from the cumulative errors of both. For example, when the light/heavy gas density ratio is fixed and the Mach number is varied, the circulation model gives an error between computed and predicted values of about 15%. That is, it doesn't completely capture the dependence of $\overline{\Gamma}$ on M. Similarly, the impulse model gives about 10% error. It, too, fails to completely capture the dependence of $\overline{I}_x$ on M. Unfortunately, when taken together, the M dependencies in the two models combine in such a way as to completely cancel, when they should only partially cancel. Thus the computed $\overline{y}_\infty$ data exhibit a dependence on M that is not predicted by the model.

The expression for $\overline{y}_\infty$ completes the analytical scaling laws for the vortex pair. The models for circulation, characteristic time, normalized velocity, and impulse quite accurately predict the corresponding computed values. Combining the strength and impulse models gives a model for spacing. This spacing model acceptably predicts the dependence on density ratio, but fails to predict the dependence on shock strength.

5.5 Additional Tests of the Vortex Pair Models

This section describes two additional sets of computations which, in addition to constituting interesting flow variations, can also be used as further tests of the vortex pair models.

5.5.1 The Effect of Variations in Initial Interface Thickness

The analytical model for circulation assumed a step-function distribution of density at the interface, which is the limiting case of no mixing layer at the edge of a jet. But an actual jet will certainly have a mixing layer; thus the deliberate use of a mixing layer in initializing the computations.

One might wonder what effect the thickness of the initial interface has on the behavior of the vortex pair. For example, the same density jump spread over a broader interface would lessen the density gradient at the edge of the jet, reducing the amplitude of the circumferential vorticity. But this effect must be at least partially offset by deposition of this vorticity over a larger area. Thus, the effect on the integrated vorticity, or circulation, might be minimal. Or, how does the change in interface thickness change the details of the vortex pair development? The previously computed mixing layer solution does not lend itself to generation of a family of profiles with varying interface thicknesses. For this purpose, it is more convenient to use a hyperbolic-tangent distribution:

$$\frac{\overline{\rho}}{\overline{\rho}_H} = \frac{\overline{\rho}_L}{\overline{\rho}_H} + 0.5\left(1 - \frac{\overline{\rho}_L}{\overline{\rho}_H}\right)\left(1 + tanh\frac{c(\overline{r}-1)}{\Delta\overline{x}}\right),$$

where $\Delta\overline{x}$ is the length of the side of each cell. Note that $\overline{r}$=1 is the density contour halfway between the light and heavy gases. This profile provides a smooth distribution of density from pure light gas at $\overline{r} = -\infty$ to pure heavy gas at $\overline{r} = +\infty$. The thickness of the distribution is controlled by the single parameter c. Four values of c (2, 0.5, 0.25, and 0.125) are computed, corresponding to progressively thicker interfaces. The corresponding interface thicknesses, arbitrarily defined as the distance from the 10% level to the 90% level, are 0.055, 0.11, 0.22, and 0.88, *i.e.*, approximately 1, 2, 4, and 17 cell thickness. In all cases, the Mach number is 1.1, and the light/heavy gas density ratio is $\overline{\rho}_L/\overline{\rho}_H = 0.138$. These computations (the 'tanh' cases) may be compared to the previous M=1.1, $\overline{\rho}_L/\overline{\rho}_H = 0.138$ case (the 'mixing layer' case).

5.5.1.1 Qualitative Description

• Sharpest Interface

The density contour plots for this case are shown in Figure 5.37. The general features are somewhat similar to the 'mixing layer' case, but there is a very significant difference. The initial profile, being only one cell thick, is not smoothly resolved. This results in the appearance of a numerically-induced Richtmyer-Meshkov instability at the unstable light-heavy downstream interface. Note the small perturbations that are just visible at $\theta = 0$ and $\theta = \pm\pi/4$, as early as $\overline{t}$=10. Exactly as in the well-known case of a plane interface, the instability at first grows slowly and without change of shape, remaining roughly sinusoidal in character. This is followed by nonlinear growth of the

perturbation into a series of broad fingers of light fluid pushing into the heavy fluid (see $\bar{t}$=20). This is of especial interest, because it is possible that the growth of the $\theta = \pm\pi/4$ perturbations may lead to enhanced mixing of the light and heavy gases. As the instabilities move upstream, they are shed and become part of the tail, increasing its size. The sizes of the tail and the core are more nearly equal, resulting in better partitioning of the structure into two distinct pieces. Again, this may favor mixing.

Thus, it appears that the development of instability is a possible method of enhancing mixing in the flow. However, this instability is most likely an artifact of the computation. It occurs due to a lack of resolution of the initial profile, and would not be expected in a real flow. These results are spurious, and must be discounted.[14]

• Slightly Diffuse Interface

The density contour plots for this 'tanh' case are shown in Figure 5.38. Comparison of these plots with the 'mixing layer' case shows very good agreement, except for the outermost contour, which has a much smaller radius. Since this contour is nearer to the deposited vorticity, it is experiences a greater induced motion. Thus, as time goes on, it is stretched more than the corresponding contour in the 'mixing layer' case. This is the only real difference between the two cases.

• Moderately Diffuse Interface

The density contour plots for this case are shown in Figure 5.39. Compared to the previous case, the slight increase in diffusion thickness means that the vorticity is deposited over an annulus of increased thickness, decreasing the spatial vorticity concentration. At $\bar{t}$=10, as the initially circular cross section begins to roll up into a kidney shape, the outer contours are less influenced by the vorticity, and consequently are stretched less than in the previous case. Similarly, the decrease in vorticity concentration increases the time required for coalescence of the vorticity into a strong core and for pinching off a tail of low-vorticity fluid. Thus at $\bar{t}$=30, a comparison of the contour plots shows that this case has a less well-defined and smaller vortex core, and a slightly more pronounced tail with higher residual vorticity, as compared to the previous case. Lower vorticity in the cores means lower induced motions in the remainder of the structure, and hence less stretching and mixing throughout. Compare the contour plots at $\bar{t}$=60, for example. The present case shows less stretching of the upstream tails and slower disappearance of the thin filament connecting the vortex cores.

• Broadly Diffuse Interface

The density contour plots for this case are shown in Figure 5.40. The trends described above, for an increase in diffusion layer thickness, continue here. The vorticity is deposited in a still larger

[14] Why, then, is this case mentioned at all? First, it illustrates the caution one must exercise in interpreting numerical results. But more importantly, it provides the motivation for the sinusoidally perturbed jets of Chapter 7, Section 1, which do indeed exhibit a *bona fide* Richtmyer-Meshkov instability.

annulus, leading to a decrease in stretching of the outer contours, a weaker vortex core, a more pronounced tail, and reduced stretching of the tail and filament due to smaller induced motions from the core.

5.5.1.2 Quantitative Description

The vortices may be characterized quantitatively by circulation, vortex spacing, and velocity. Because the vorticity generation is proportional to density gradient, one expects that a tighter initial distribution will lead to a higher overall circulation and faster velocity. These, in turn, will affect the normalized velocity, $\overline{U}\overline{y}_\infty/\overline{\Gamma}$.

The circulation model assumes a sharp interface between the light and heavy gases. Variations in the computed values of $\overline{\Gamma}$ will provide a check on the applicability of this approximation. The velocity model also assumes a sharp interface between the light and heavy gases. It describes the dependence of the normalized velocity on the size and spacing parameters, $\overline{R}/\overline{y}_\infty$ and $\overline{y}_\infty/\overline{h}$. Variations in the size and spacing of the vortices in the computations will provide a check on the ability of the the normalized velocity model to predict the effects of these changes. Table 5.9 shows steady-state computational data and the corresponding predictions from the analytical models.

Interface	$\overline{\Gamma}$	$\overline{U}$	$\overline{y}_\infty$	$\overline{R}$	Computed $\overline{U}\overline{y}_\infty/\overline{\Gamma}$	Predicted $\overline{U}\overline{y}_\infty/\overline{\Gamma}$
Sharp	0.450	0.034	0.686	0.740	0.0524	0.060
Slightly Diffuse	0.449	0.037	0.696	0.714	0.0568	0.062
Moderately Diffuse	0.427	0.032	0.757	0.717	0.0564	0.063
Broadly Diffuse	0.401	0.028	0.798	0.731	0.0556	0.063

Table 5.9 - Computed and predicted $\overline{U}\overline{y}_\infty/\overline{\Gamma}$ for variations in initial interface thickness

The expected trends in circulation and velocity are borne out by the data. In addition, there is an associated change in vortex core spacing. The circulation values show a drop of about 12%, a relatively minor change considering the changes in the thicknesses of the density profiles. The values are close to the constant value of 0.41 predicted by the circulation model, indicating that neglecting the details of the initial density distribution still yields acceptable values of predicted circulation. Figure 5.41 is a plot of the computed and predicted normalized velocities. The model overpredicts the actual data by a small amount, but it does reproduce the qualitative trend of a slight increase and then a decrease in velocity as the density gradient is increased. In any event, the normalized

velocities are essentially constant, exhibiting almost negligible change over a wide variation in initial interface thickness. One concludes that both the strength of the vortex pair and its normalized velocity are only weak functions of the initial interface thickness, and that the models' assumption of a sharp interface is indeed satisfactory.

5.5.2 The Effect of Variations in Channel Spacing

This section examines the effect of channel spacing on the motion of the vortex pair. The Mach number is M=1.1, and the density ratio is $\overline{\rho}_L/\overline{\rho}_H = 0.138$. Three cases are computed: Channel spacing = 16, 8, and 4 (the spacing = 8 data are those of Chapter 3, Section 1). The explicit variation of channel spacing provides additional checks of the circulation, impulse, and velocity models. The circulation and impulse models assume an unbounded domain, and it is interesting to see if and how $\overline{\Gamma}$ and $\overline{I}_x'$ are affected by variations in channel spacing. The velocity model predicts an explicit dependence of the normalized velocity on the ratio of vortex spacing to channel spacing. Previously, this effect was tested only through variations in vortex spacing as either the shock strength or the density ratio was changed. The present computations provide an opportunity to test the model through variations in channel spacing.

5.5.2.1 Qualitative Description

The primary contribution to the velocity of the upper-half-plane vortex is the induced motion from the vortex in the lower-half-plane (and *vice versa*). This contribution is in the sense of a downstream velocity. However, there are also contributions from the infinite array of image vortices that constitute the mathematical equivalent to the perfectly reflecting channel walls. The net contribution from these vortices is a much smaller upstream velocity. Therefore, changes in channel spacing can have a slight influence on the behavior of the system, but no major changes are expected. Contour plots for the three cases are shown in Figures 5.42, 3.1, and 5.43. Qualitatively, they look very similar. The details of the structures are essentially the same in all three cases. However, there are minor differences in the tails. As the channel spacing is decreased and the strength of the vortex pair decreases, these is less induced motion of the tails. This means there is less inward and upstream stretching of the tails, relative to the cores, and consequently one expects less straining of the fluid within the tails relative to the ambient fluid. This may have implications for mixing enhancement. The case of narrow channel spacing shows more high mass fraction fluid in a more well-defined structure than does the case of wide channel spacing.

5.5.2.2 Quantitative Description

Table 5.10 shows steady-state computational data and corresponding predictions from the analytical models.

Ch. Spac.	$\overline{\Gamma}$	$\overline{U}$	$\overline{y}_\infty$	$\overline{R}$	Computed $\overline{U}\overline{y}_\infty/\overline{\Gamma}$	Predicted $\overline{U}\overline{y}_\infty/\overline{\Gamma}$	Computed $\overline{I}_x{}'$	Predicted $\overline{I}_x(\bar{t}=0^+)$
16	0.46	0.041	0.725	0.736	0.065	0.067	0.167	0.165
8	0.45	0.033	0.753	0.740	0.055	0.062	0.169	0.165
4	0.39	0.016	0.727	0.734	0.031	0.036	0.140	0.165

Table 5.10 - Computed and predicted $\overline{U}\overline{y}_\infty/\overline{\Gamma}$ and $\overline{I}_x{}'$ and $\overline{I}_x(\bar{t}=0^+)$ for variations in channel spacing

The retarding influence of the image vortices on the motion of the actual vortex pair is a strong function of the wall spacing. As the channel walls are brought closer together, one expects a monotonic decrease in the velocity of the vortex pair. In Section 3, the velocity model was only tested against computed data spanning a relatively small range of vortex spacing/channel spacing (less than 30% variation). The present four-fold variation in channel spacing provides a more rigorous and explicit test of the model. From the table above, note the reasonable agreement between the computed and predicted values of normalized velocity (see also Figure 5.44). The model again slightly overpredicts the measured values, but the difference is slight.

Now, since the motion of the vortex is related to its strength, the circulation may change as well. Note, however, that Kelvin's Theorem, $D\overline{\Gamma}/D\bar{t} = 0$, must still be valid, because this result was derived independently of any boundary conditions. The decrease in channel spacing affects the interaction between the shock and the circular jet, and hence the value of the circulation at $\bar{t} = 0^+$, but then this circulation remains essentially invariant thereafter. The table shows only a negligible change in circulation in reducing the channel spacing from 16 to 8, but the value drops about 11% if the spacing is again halved. Also note that there are essentially no variations in the size or spacing of the vortices, the maximum difference in these quantities being less than 4%. These differences are too small to be meaningful. The size of the vortex pair, $\overline{R}$, is primarily a function of the initial shock strength, which does not change. Similarly, the spacing, $\overline{y}_\infty$, is primarily a function of the light/heavy gas density ratio, which, too, does not change.

Finally, recall that a measure of the impulse is $\overline{I}_x{}' \equiv 0.5\,\overline{y}_\infty\,\overline{\Gamma}$, which is to be compared with the predicted initial impulse, $\overline{I}_x(\bar{t}=0^+)$. $\overline{I}_x{}'$ is essentially unchanged as the spacing is halved from

16 to 8, but shows a large drop as the spacing is further halved to 4. Since $\overline{y}_{\infty}$ is essentially constant, the decrease in impulse appears to be manifested primarily through a decrease in circulation. The findings may be summarized as follows. The computed circulation and impulse values are essentially the same for the two wide channel spacings but drop about 13% and 17% respectively for the narrow channel spacing. The circulation and impulse models do not capture this dependence on channel spacing, but they are still satisfactory as these are relatively small differences relative to a factor of four variation in channel spacing. The computed normalized velocities decrease monotonically with decreasing channel spacing, and this decrease is quite well represented by the velocity model.

Chapter 6 - Comparison with Available Experimental Data

In any numerical simulation, it is useful to compare the results with corresponding experimental results. Unfortunately, at the present time, there do not exist sufficiently reliable experimental data for making a definitive comparison. The available data, briefly described below, are few in number and have significant measurement uncertainties. It is difficult to construct a two-dimensional jet or cylinder of helium to initialize the flow prior to shock passage, and it is also difficult to non-intrusively measure the development of the vortical structure during and after shock passage. Nevertheless, given the existence of any experimental data, one is compelled to make whatever comparisons are possible.

6.1 Microfilm Cylinder (Haas)

Haas (1984, 1987) used a thin microfilm cylinder to contain the helium gas, forming an approximately two-dimensional structure, at least in the regions away from the ends of the cylinder. This cylinder was inserted in a shock tube, normal to the direction of flow, and data were acquired using spark shadowgraphy. Experiments were performed for shock strengths of M=1.085 and 1.22, and density ratio $\overline{\rho}_L/\overline{\rho}_H$= 0.138. The cylinder was two inches in diameter, and the test section was 3.5 inches square, giving a nondimensional channel spacing of $2\overline{h}$ = 3.5.

Figures 6.1 and 6.2 are Haas' shadowgraph pictures for his M=1.085 and M=1.22 experiments. The time indicated on each picture is the actual time (in μs) measured from when the shock was at the upstream edge of the cylinder. It may be converted to an equivalent nondimensional time, $\overline{t}$ = tc_1/R_0, where for Haas' data, R_0 = 1 inch and c_1 = 1115 ft/s, *i.e.*, $\overline{t}$ = 0.0134 t(μs).

First consider the lower Mach number. Haas' M=1.085 data corresponds most closely with the M=1.1, $2\overline{h}$ = 4 case of the present investigation (Figure 5.43). Comparison of the shadowgraphs with the computed contour plots shows quite good agreement in the qualitative features of the structure, the spacing of the vortex cores, and in the evolution of the structure in time.

Quantitatively, one may compare the measured and computed vortex pair velocities. Relative to the velocity behind the shock, and normalized by the speed of sound ahead of the shock, Haas measured a value of $\overline{U}$= 0.039, more than twice the present (computed) value of $\overline{U}$= 0.016. This remains an unexplained discrepancy.

Next consider the higher Mach number. Haas' M=1.22 data also should be compared to a $2\overline{h}$ = 4 case from the present investigation, but such a case was not computed. The closest computation is M=1.2 and $2\overline{h}$ = 8. Recall from Chapter 5, Section 5, Subsection 2 that variations in channel spacing were found to have little effect on the qualitative features of the flow. Thus, it is still reasonable to

compare Haas' flow with the computed $2\overline{h} = 8$ flow (Figure 3.23). Again, the qualitative agreement is quite good.

Quantitatively, the flows are not directly comparable, since the experimental and computational cases have different channel spacings. However, one may extrapolate the computed $2\overline{h} = 8$ flow to a $2\overline{h} = 4$ flow. Again recall from Chapter 5, Section 5, Subsection 2, that the circulation and vortex size and spacing remained essentially constant as the channel spacing was varied, but that the velocity changed. Also recall from the model for the motion of motion of the vortex pair that

$$\frac{\overline{U}\overline{y}_\infty}{\overline{\Gamma}} = fctn\Big(\frac{\overline{R}}{\overline{y}_\infty}, \frac{\overline{y}_\infty}{\overline{h}}\Big) .$$

For two flows in which $\overline{y}$, $\overline{\Gamma}$, and $\overline{\mathrm{R}}$ are constant, the ratio of their velocities can be determined as a function of their channel spacings. In particular,

$$\frac{\overline{U}_2}{\overline{U}_1} = \frac{\overline{h}_1}{\overline{h}_2} \frac{tan(\pi\overline{y}_\infty/\overline{h}_1)}{tan(\pi\overline{y}_\infty/\overline{h}_2)} .$$

Substituting specific values

$$((\ )_1 \Leftrightarrow 2\overline{h} = 4,\ (\ )_2 \Leftrightarrow 2\overline{h} = 8,\ \overline{y}_\infty = 0.82,\ \overline{h}_1 = 2,\ \text{and}\ \overline{h}_1 = 4),$$

one finds that

$$\overline{U}_{2\overline{h}=4} = 0.44\, \overline{U}_{2\overline{h}=8} = (0.44)(0.054) = 0.024,$$

about 33% less than Haas' measured value of $\overline{U} = 0.039$.

Haas measured the same velocities for both the M=1.085 and M=1.22 cases, *i.e.*, he found no variation with shock strength. This is a surprising result, and suggests a lack of consistency within his experiments. One may speculate as to the causes of these errors: 1) dynamical or mechanical effects due to the finite thickness of the microfilm (the weight of the microfilm was about 25% of the weight of the helium contained by the microfilm), 2) lack of two-dimensionality due to nonuniformities in microfilm thickness or variations in radius along the length of the cylinder, 3) effects of an initial non-zero flow rate through the cylinder, and 4) contamination of the helium gas through leakage.

6.2 Buoyant Jet (Jacobs)

Jacobs (1991) used a buoyant helium jet, again giving an approximately two-dimensional structure at least in regions sufficiently far from the nozzle. This jet was inserted in a shock tube, normal to the direction of flow, and data were acquired using laser-induced-fluorescence (LIF) of a biacetyl tracer. Experiments were performed for shock strengths of M=1.093 and 1.15, at a density ratio of $\overline{\rho}_L/\overline{\rho}_H = 0.152$ (Jacobs used a ratio of 10 parts helium to 1 part biacetyl, giving an effective density

ratio higher than the pure He/air value of 0.138). The jet was 5/16 inches in diameter, and the test section was 10.5 inches square, giving a nondimensional channel spacing of $2\overline{h} = 67$.

First consider the lower Mach number. Figure 6.3 shows density contour plots made from Jacobs' M=1.093 LIF pictures,[15] the images being cuts through a plane 4.8 diameters downstream of the nozzle. As usual, $\bar{t} = tc_1/R_0$, where for Jacobs' data, $R_0 = 5/32$ inch and $c_1 = 1115$ ft/s.

Jacobs' experiments were conducted for $2\overline{h} = 67$, which does not correspond to any of the present computations. The closest available computation is a M=1.1, $2\overline{h} = 16$ case. The channel spacing is different by a factor of 4, but this effect is believed to have a negligible effect on the shape and development of the vortex pair. Thus the qualitative features of Jacobs' experiments and the present computations should be similar. However, Jacobs' measured vortex spacing is significantly larger than the computed spacing.

Given the good agreement between Haas' measured spacing and the corresponding computed spacing, and given the computational finding that variation in channel spacing has little effect on vortex spacing, one would expect the vortex spacing to be the same for all flows of the same Mach number and density ratio, regardless of the initial channel spacing. More fundamentally, one could argue that the vortex spacing is determined from the circulation and impulse of a flow, which are uniquely determined from the initial distribution of vorticity, *i.e.*, independent of the channel spacing. Jacobs' large spacing is inconsistent with both Haas' experiments and the present computations, and indicates the presence of some unknown additional phenomena peculiar to his experiment.

Jacobs measured a velocity of $\overline{U} = 0.018$. The $2\overline{h} = 16$ computation has $\overline{U} = 0.041$. A direct comparison with the computation is not possible, because of differing channel spacings. Exactly as before, one can extrapolate the computed $2\overline{h} = 16$ velocity to the case $2\overline{h} = 67$. One finds the velocity corresponding to $2\overline{h} = 67$ to be $\overline{U} = 0.042$, more than twice Jacobs' measured value (this trend is opposite that shown by Haas' data).

One may speculate as to possible reasons for disagreement in the measured and computed values of spacing and velocity. One possible error is buoyancy effects. Jacobs used a vertical jet of the helium, which was then cut off by the passage of the shock wave, forming a rising column of helium as time went on. Consequently, a sequence of images taken at fixed height above the orifice may actually correspond to different cuts through the original jet. A second possibility is that the fluorescent tracer used for visualization may not follow the same kinematical trajectory as the helium (biacetyl is about 22 times as heavy as helium). A third possibility is that viscous effects are significant: a moderate jet velocity and small jet diameter leads to very high Reynolds number.

In spite of differences in velocity and spacing between Jacobs' experiments and the present

[15] These pictures were not shown in Jacobs (1991). They are plotted from unpublished data made available courtesy of Dr. Jacobs.

computations, one expects the dynamical motions to be similar; they are still basically the same flow, a pair of finite-core-size vortices in a walled domain. Therefore, they should be governed by the same two important parameters for this class of flows: vortex spacing/channel spacing and vortex size/vortex spacing. In this sense, the analytical model for normalized vortex velocity $\overline{U}\overline{y}_\infty/\overline{\Gamma}$ should still model Jacobs' flow, even though individual values of $\overline{U}$ and $\overline{y}_\infty$ may vary.

The model requires specification of values for channel spacing/vortex spacing, and vortex size/vortex spacing. Jacobs reported both core size and spacing data, as well as an estimated value of circulation. For the M=1.093 flow at late times, Jacobs reported a core size of half the initial area and a vortex spacing of 1.26 times the initial diameter. In the usual nondimensional notation, one finds $\overline{h} = 33.6$, $\overline{y}_\infty = 1.26$, $\overline{y}_\infty/\overline{h} = 0.038$, and $\overline{R}/\overline{y}_\infty = 0.56$ so that the model predicts $\overline{U}\overline{y}_\infty/\overline{\Gamma} = 0.078$. This can be compared to the value obtained by direct substitution of Jacobs' data. He estimated $\Gamma = fv_2D_0$, or equivalently, $\overline{\Gamma} = 2f\overline{v}_2$. f is an empirically determined factor (= 1 in this case), v_2 is the velocity behind the shock, and D_0 is the initial diameter of the jet. In this case, $\overline{v}_2 = 0.15$, so that $\overline{\Gamma} = 0.30$ and $\overline{U}\overline{y}_\infty/\overline{\Gamma} = 0.076$. The predicted value is within 3% of the measured value.

Finally, besides spacing, velocity, and normalized velocity, one may also compare values of circulation. The circulation model of Chapter 4, Section 1, with $\overline{\rho}_L/\overline{\rho}_H = 0.152$ and M = 1.093, gives a predicted circulation $\overline{\Gamma} = 0.38$, which is 27% higher than Jacobs' value.

Next consider the higher Mach number, M=1.15. Late-time data for Jacobs' experiment can be read from the appropriate graphs and text of Jacobs (1991). In the present notation, these are $\overline{U} = 0.024$, $\overline{y}_\infty = 1.45$, and $\overline{\Gamma} = 0.48$. Then $\overline{U}\overline{y}_\infty/\overline{\Gamma} = 0.072$. No computation was performed for M=1.15, but it is possible to compare the predictions from the analytical models for circulation and normalized velocity to Jacobs' data. The predicted circulation is $\overline{\Gamma} = 0.55$, a difference of 12% from Jacobs' value. Using late-time values of $\overline{R}/\overline{y}_\infty = 0.69$ and $\overline{y}_\infty/\overline{h} = 0.043$, read from the graphs of Jacobs (1991), the predicted normalized velocity is $\overline{U}\overline{y}_\infty/\overline{\Gamma} = 0.077$. This is within 7% of Jacobs' measured value. The ability of the velocity model to represent both the present computations and Jacobs' data confirms that they are vortical flows of the same general family.

In summary, comparison between Haas' and Jacobs' experiments and the present computations shows good agreement in the shape and development of the vortical structure, but poor agreement in terms of directly measurable quantities (*e.g.*, spacing or velocity). These differences remain unresolved. Neither experiment is conclusive, because of inherent difficulties in constructing a reasonable approximation to the ideal flow. Haas' experiments are not self-consistent, and Haas' and Jacobs' experiments are neither consistent with each other nor with the computations. Thus, in an absolute sense, the experiments can neither be used to confirm nor to deny the accuracy of the computations. In a general sense, both the experiments and the computations represent *bona fide* vortical flows,

and should obey the same model for normalized vortex velocity. This was demonstrated by Jacobs' data. Haas' data did not include circulation values, so it was impossible to test the model in that case.

Chapter 7 - Variations on the Canonical Problem

The remainder of this work investigates a number of geometrical variations on the canonical problem. Up to this point, only the case of a single shock wave interacting with a single, isolated, circular jet has been considered. Although this canonical problem is convenient for studying the basic physics of the interaction, it is probably not representative of flows that would occur in real devices. For example, real jets may be noncircular in shape. Also, there may be multiple shock waves in the domain. Finally, technological applications usually involve arrays of multiple jets as opposed to a single jet.

7.1 Sinusoidal Perturbation to Cross-Sectional Shape

In the canonical problem, the jets are circumferentially smooth; however, this is not necessarily always the case. For example, the cross section of a jet near its source, when the mixing layer is small, may not exhibit the stabilizing diffusive effects which damp out minor instabilities. Similarly, a turbulent jet may show noticeable deviations from a smooth circumference. The interaction of a shock wave with such initial perturbations leads to the possibility of instabilities, which may contribute additional mixing across the interface.

The development of instabilities due to nonimpulsive acceleration of a sinusoidally perturbed one-dimensional plane interface was first studied by Taylor (1950), and is referred to as Rayleigh-Taylor instability. Extension of this work to the case of impulsive acceleration (*e.g.*, a shock wave) was treated by Richtmyer (1960) and Meshkov (1970), and is referred to as Richtmyer-Meshkov instability. The development of the instability can again be described by the baroclinic generation of vorticity. The behavior depends critically on whether the shock propagates from a light to heavy fluid, or *vice versa*. The case of a heavy/light interface is shown schematically in Figure 7.1. At early times, the perturbations exhibit negative amplitude growth, that is, they are stable. As time goes on, the negative growth continues unchecked, and there occurs a phase reversal followed by an unstable continued increase in amplitude. The case of a light/heavy interface is shown schematically in Figure 7.2. In that case, the perturbations exhibit positive amplitude growth for all times, *i.e.*, the growth is always unstable. This is also illustrated in Figure 7.3.

Consider the interaction of a shock wave with a jet having small sinusoidal perturbations around its circumference. The initial configuration is shown in Figure 7.4, where the jet radius is perturbed to

$$\bar{r}(\theta) - 1 = \epsilon_0 \, cos(n\theta),$$

where 1 is the nominal radius of the jet, and $\epsilon_0 \ll 1$ and n are the amplitude and wavenumber of the

perturbation. The wavelength of the perturbation is $\bar{\lambda} = 2\pi/n$. The Richtmyer-Meshkov instability will be important where the mean density gradient is more or less parallel to the direction of the shock, that is, at the upstream and downstream interfaces. The upstream interface is of heavy-light type, and therefore, the initial result will be damping of the perturbations. The downstream interface is of light-heavy type, and the result will be growth of the perturbations. However, because of the radius of curvature, the overall behavior of the instabilities will be different from that of the plane case.

The gross features of the flow should be similar to that of the unperturbed circular jet, because the mean shape is still circular. However, Richtmyer-Meshkov instabilities superimposed on the mean flow may promote mixing beyond that of the circular jet case.

Three pairs of runs are computed, each pair consisting of two amplitudes at fixed wavenumber:

n=8, ϵ_0=0.05 (Figure 7.6) and n=8, ϵ_0=0.1 (Figure 7.7)

n=16, ϵ_0=0.05 (Figure 7.8) and n=16, ϵ_0=0.1 (Figure 7.9)

n=32, ϵ_0=0.1 (Figure 7.10) and n=32, ϵ_0=0.2 (Figure 7.11)

A detailed discussion of one of these cases illustrates the qualitative changes from the canonical flow. As a matter of convenience, consider the case n=16, ϵ_0=0.1 (Figure 7.9), which is intermediate in wavenumber and amplitude, and should be representative of this family of flows.

Consider the upstream interface, and for convenience, restrict the discussion to the upper half plane. The fluid initially near $\theta = \pi/2$ is rotated counterclockwise to form a kidney-shaped structure which evolves into a well-defined lobe as time goes on. The fluid initially near $\theta = \pi$ is rapidly pushed between the lobes, on a timescale smaller than that required for the phase reversal of the instabilities alluded to above. Damping of the instabilities is coincident with development of the vortex pair, and the instabilities cease to exist as distinct phenomena before unstable growth can occur. This can be seen at times $\bar{t}$ =10 and 20, which show the damping of the perturbations, in all contour levels, at the upstream interface.

At the downstream interface, the perturbations are unstable from the outset. Again, consider the upper half plane only. The overall motion, like the circular jet case, is a stretching of the fluid as it rotates counterclockwise toward the upstream end. A portion of the perimeter of the perturbed jet is shown schematically in Figure 7.5(a). The density gradients are shown as vectors. "A" labels the portions of the perimeter that are turned toward the horizontal, and "B" the portions that are turned toward the vertical. Since vorticity is generated by the component of density gradient in the vertical direction (normal to the pressure gradient from the shock), it is clear that the vorticity concentration will be increased in regions "A" and decreased in regions "B", as compared to the circular jet case. The effect of such a distribution of vorticity is to distort the original sinusoid into a N-shaped perturbation, as shown in Figure 7.5(b). This is clear from the $\bar{t}$=10 contour

plot, particularly at $\theta = \pi/8$ instability[16], counting in a counterclockwise manner starting at the downstream-most point.

Examination of the $\bar{t}$=20 contour plot shows substantial growth of this first ($\theta = \pi/8$) instability, which is the primary instability of importance in development of the tail. By $\bar{t}$=30, this instability has swirled around to the top of the lobe and has attained a length on the order of the initial radius of the jet. The long, finger-like protrusion traps and isolates the vorticity in the instability, preventing it from coalescing with the remainder of the high-vorticity fluid in developing a vortex core. Because the instability is formed from such a small portion (1/16 th) of the circumference of the original jet, only limited vorticity is thus isolated. Though practically negligible compared with the remainder of the flow, it nevertheless represents a change in character of the tail development, as compared to the single jet case.

In the case of a unperturbed circular jet, there was a clean 'pinching off' of a relatively compact region of low-vorticity fluid as a upstream tail. In the present case, the tail is formed from a long finger of fluid that protrudes far beyond the original lobe (see $\bar{t}$=30 and 40). Tail development is accompanied by a 'folding over' of this fluid, as seen at $\bar{t}$=40 to 60. This folding contributes to the mixing of the fluid within the tail. However, it contributes little toward destabilizing the vortex core, which is still dominant.

Secondary tail growth is fed by fluid from the much smaller $\theta = 0$ instability, which swirls around the outer perimeter of the upper lobe in a counterclockwise fashion in the same manner as the $\theta = \pi/8$ instability. This motion may be seen at times $\bar{t}$=20 to 70.

Overall, compared to the unperturbed circular vortex, the tail development is more complicated and the tail contains greater vorticity. This greater vorticity is evident in the greater circularization of the local density contours in the tail at times $\bar{t}$=60 to 100. This vorticity stabilizes the tail, which shows much less late-time stretching and thinning than in the unperturbed circular jet case. However, this effect is offset by more of the original light gas being contained in the tail. That is, the original jet is more effectively partitioned into two distinct structures.

Now consider the other member of the first pair, case n=16, ϵ_0=0.05 (Figure 7.8), which is the same initial wavelength, but only half the initial amplitude. Exactly the same deviations from the circular jet case are observed, the only difference being that the perturbations are somewhat smaller (see $\bar{t}$=20 to 40). Again, the primary contribution to the tail is from the first ($\theta = \pi/8$) instability. The smaller initial amplitude leads to a smaller instability, reducing the amount of light gas that is trapped in the instability. Compared to the ϵ_0=0.1 case, the instability forms a significantly shorter finger of fluid. This finger is too short to fold over on itself (compare the two runs at $\bar{t}$ =50 and 60), and represents less of a disturbance to the structure of the tail a a whole. Thus the contours in the

[16] making reference to an instability by its location at t=0

tail becomes monotonically distributed at an earlier time (compare the runs at $\bar{t}$=50), and the tail itself is longer and thinner.

The smaller initial amplitude means that other instabilities besides $\theta = \pi/8$ are also weaker, and their role in augmenting the tail growth is also reduced. For example, note the weaker secondary tail growth due to the $\theta = 0$ instability at times $\bar{t} = 40$ to 70. However, these are minor changes in the qualitative behavior.

Now consider the remaining (first and last) pairs of the series of runs.

The first pair is n=8, ϵ_0=0.05 (Figure 7.6) and n=8, ϵ_0=0.1 (Figure 7.7). These have twice the wavelength as the previous pair ($\bar{\lambda} = \pi/4$ compared to $\bar{\lambda} = \pi/8$). This is the largest allowable wavelength such that the structure can still be considered a perturbation about a circle. The tail formation is still primarily due to the first (in this case, at $\theta = \pi/4$) instability, whose dominant role is clear from the contour plots at times $\bar{t}$ =0 to 20.

Because a single wavelength of the initial perturbation spans most of the perimeter of the first quadrant, the width of the instability is considerably larger than in the shorter wavelength (n=16) case. In this case, the entire perturbation is pinched off as a tail, very early on (see $\bar{t} = 20$ and 30), and the area of the tail is larger than in the corresponding n=16 case.

Finally, consider the last pair, n=32, ϵ_0=0.1 (Figure 7.10) and n=32, ϵ_0=0.2 (Figure 7.11). This is the shortest-wavelength case. Notice the remarkable similarity to the unperturbed circular jet, even for amplitudes as large as 0.2. With such a small wavelength, the circumferential distortion of the vorticity distribution is minimal, and several wavelengths of perturbations from the first quadrant are pinched off to form a tail. There is no preferential pinching off of part of the first quadrant to affect the shape of the tail, as was the case for n=8. The behavior is essentially indistinguishable from the unperturbed circular jet.

Comparing the three pairs as a whole, one sees substantial differences among jets with different wavelengths, but only little differences among jets with the same wavelength, regardless of amplitude. The qualitative behavior is determined primarily by the angular location of instability peaks and troughs, *i.e.*, the wavelength, and not by the initial amplitude of the perturbation.

Quantitatively, one may compare strengths and trajectories of the vortex pairs. For consistency, the discussion is restricted to the ϵ_0=0.1 case of each of the three pairs of perturbed flows and to the unperturbed circular jet case. In the mean, one expects the perturbed jets to behave like the circular jet. But the correspondence should be poorer at larger wavelengths, because the cancellation between crest and neighboring trough is less complete, due to distribution over a larger portion of circumference. Figure 7.12 shows slight differences in $\bar{\Gamma}(\bar{t})$ among the cases. The circulation appears to be a monotonically increasing function of wavelength, but the dependence is weak–less than 10% change in circulation for a factor of 4 change in wavelength. This is not a significant change,

considering that the worst case corresponds to a perturbation wavelength of the same order as the radius!

In summary, Richtmyer-Meshkov instability affects the qualitative details of the tail development, but not the stability of the vortex core. The instability traps high mass fraction fluid within the tail, resulting in a more efficient partitioning of the initial jet into discrete sub-structures. This phenomenon becomes more pronounced as wavelength or amplitude is increased. Wavelength is the primary factor which affects tail development. The amplitude affects the size of the instability, and particularly its length, but not its character.

7.2 Elliptical Jets

7.2.1 Qualitative Description

The simplest perturbation of the circular cross-section is to an elliptical cross-section, characterized by an aspect ratio $AR \equiv b/a$, where b is the vertical semi-axis and a is the horizontal semi-axis. The height, b, replaces the radius of the circular jet, R_0, in nondimensionalizing all lengths and times. In other words, the nondimensional height of the ellipse is 1.

The passage of the shock deposits vorticity around the perimeter much as in the circular case, but the distribution is slightly different. The pressure gradient still points upstream, but the density gradient is no longer radially outward. Maximum vorticity generation is still at $\theta = \pm\pi/2$, where $\nabla\rho$ and ∇p are perpendicular, and minimum vorticity generation is still at $\theta = 0, \pi$. Consider an AR $>$ 1 ellipse: near $\theta = \pm\pi/2$, there is less perimeter over which to integrate the distributed vorticity and so the circulation is correspondingly lower than in a circular jet of the same height. Conversely, an AR $<$ 1 ellipse has greater circulation than a circular jet of the same height.

Computations were performed for two Mach numbers (M=1.1 and M=2) at two aspect ratios (AR=0.5 and AR=2.0) each. In all cases, the light/heavy gas density ratio is $\overline{\rho}_L/\overline{\rho}_H = 0.138$. First consider the low Mach number pair.

• M=1.1, AR=0.5

Density contour plots of this case are shown in Figure 7.13. These can be compared with the corresponding plots for the circular jet case (Figure 3.1). The qualitative details of the vortex development are similar. Again, the high vorticity fluid swirls around to the downstream end of the structure, and organizes to form a core with a monotonic distribution of vorticity. Note the detailed swirling within in the lobes as they develop, particularly at $\bar{t}$=20. The swirling is resolvable in this case because of the large initial horizontal dimension, but like the circular case, the gradients eventually become too high, and the distinct layers of fluid coalesce. The remainder of the fluid is

again spun off as an upstream tail, which stretches vertically inward and trails behind the faster vortex core. Because of the longer streamwise dimension of the original structure, the tails are longer than in the circular case.

• M=1.1, AR=2.0

Density contour plots of this case are shown in Figure 7.14. Again, the basic interaction is similar to the circular jet case. In this case, because of the reduced initial horizontal dimension, less swirling is resolvable within the developing vortex, and the tail development is reduced.

Next consider a strong shock, with the same aspect ratios as above.

• M=2.0, AR=0.5

In the circular jet case, increasing the Mach number from 1.1 to 2.0 resulted in suppression of the tails, because the increased shock strength greatly compressed the jet in the streamwise direction. The same phenomenon occurs with the elliptical jet: compare the contour plots of this M=2.0, AR=0.5 case (Figure 7.15) with those of the M=1.1, AR=0.5 case (Figure 7.13). Another consequence of the compression is that swirling within the lobes, clearly visible in the M=1.1 case, can no longer be resolved; there are simply not enough cells in the streamwise direction.

• M=2.0, AR=2.0

Density contour plots of this case are shown in Figure 7.16. There is now almost no tail, because of the combination of high Mach number and small initial horizontal dimension. Likewise, no swirling within the lobes can be resolved.

7.2.2 Quantitative Description

This section quantitatively describes the elliptical jet interactions. In particular, the analytical models for circulation, timescaling, velocity, and spacing of the steady-state vortex pairs are extended to the elliptical jet case.

Table 7.1 summarizes the computed data for the elliptical jet runs. For completeness, the circular jet data are included, treating the circular jets as ellipses of unit aspect ratio. In the usual manner, the velocities of the vortex pairs have been error-corrected according to the prescription of Chapter 4, Section 2, Subsection 2.

M	AR	$\overline{y}_\infty$	$\overline{U}$	$\overline{\Gamma}$	$\overline{U}\overline{y}_\infty/\overline{\Gamma}$
1.1	0.5	0.72	0.067	1.06	0.046
1.1	1.0	0.75	0.033	0.45	0.055
1.1	2.0	0.80	0.015	0.20	0.060
2.0	0.5	1.15	0.100	2.80	0.041
2.0	1.0	1.00	0.070	1.20	0.058
2.0	2.0	1.10	0.025	0.53	0.052

Table 7.1 - Steady-state $\overline{\Gamma}$, $\overline{U}\overline{y}_\infty/\overline{\Gamma}$, and $\overline{U}$ for the elliptical jet flows

First, consider the circulation. The derivation of the model proceeds in an analogous manner to the circular jet scaling law of Chapter 5, Section 1. The essential difference is that an additional parameter, the aspect ratio of the ellipse, now appears.

Consider a cross section through an elliptical jet, as shown in Figure 7.17. The horizontal and vertical semi-axes are a and b, respectively, and the interface is idealized as a sharp step discontinuity in density. The light jet gas has density ρ_L and the ambient gas has density ρ_H. A shock wave of strength M approaches from left to right. The density and pressure ratios across the shock wave are ρ_2/ρ_1 and p_2/p_1.

The vorticity production term of the vorticity equation is

$$\frac{D\underline{\omega}}{Dt} = \frac{1}{\rho^2}(\underline{\nabla}\rho \times \underline{\nabla}p).$$

The vorticity is perpendicular to the plane of the jet, $\underline{\omega} = \omega\hat{e}_z$. Integrating the vorticity equation for ω gives

$$\omega = \int_0^\infty \frac{1}{\rho^2} |\underline{\nabla}\rho \times \underline{\nabla}p| \; dt.$$

To evaluate the integrand, one works in elliptical coordinates, where ξ and η denote coordinates normal and tangent to the ellipse, respectively. The ellipse is given by

$$f(x,y) = \left(\frac{x}{a}\right)^2 + \left(\frac{y}{b}\right)^2 - 1 = 0,$$

so that the gradient is

$$\underline{\nabla}f = \frac{2x}{a^2}\,\hat{e}_x + \frac{2y}{b^2}\,\hat{e}_y$$

and the unit vector normal to the surface is

$$\hat{e}_\xi = \frac{\underline{\nabla}f}{|\underline{\nabla}f|} = \frac{(x/a^2)\,\hat{e}_x + (y/b^2)\,\hat{e}_y}{\sqrt{(x/a^2)^2 + (y/b^2)^2}}$$

The (ξ, η) coordinates are related to (x,y) under the transformation

$$x = c\ cosh\xi\ cos\eta,\ \ y = c\ sinh\xi\ sin\eta.$$

This defines a family of ellipses for which

$$\left(\frac{x}{c\ cosh\xi}\right)^2 + \left(\frac{y}{c\ sinh\xi}\right)^2 = 1,$$

with the particular ellipse of interest being given by $\xi = \xi_0$.

Equivalently,

$$a = c\ cosh\xi_0,\ \ b = c\ sinh\xi_0,\ \ and\ c^2 = a^2 - b^2,$$

so that

$$cosh\xi_0 = \frac{a}{\sqrt{a^2 - b^2}} \text{ and } sinh\xi_0 = \frac{b}{\sqrt{a^2 - b^2}}.$$

The density is given by

$$\rho = \rho_L + \Delta\rho\ H(\xi - \xi_0),$$

and the density gradient is given by

$$\underline{\nabla}\rho = \frac{1}{h_\xi}\frac{\partial\rho}{\partial\xi}\ \hat{e}_\xi + \frac{1}{h_\eta}\frac{\partial\rho}{\partial\eta}\ \hat{e}_\eta,$$

where

$$h = h_\xi = h_\eta = c\sqrt{sinh^2\xi + sin^2\eta}.$$

Therefore,

$$\underline{\nabla}\rho = \Delta\rho\ \frac{\delta(\xi - \xi_0)}{c\sqrt{sinh^2\xi + sin^2\eta}}\ \hat{e}_\xi\ .$$

The pressure gradient is simply

$$\underline{\nabla}p = -\Delta p\ \delta(x - V_s t)\ \hat{e}_x,$$

so that

$$\begin{aligned}\underline{\nabla}\rho \times \underline{\nabla}p &= -\Delta\rho\ \Delta p\ \frac{\delta(x - V_s t)\ \delta(\xi - \xi_0)}{c\sqrt{sinh^2\xi + sin^2\eta}}\ (\hat{e}_\xi \times \hat{e}_x) \\ &= \Delta\rho\ \Delta p\ \frac{\delta(x - V_s t)\ \delta(\xi - \xi_0)}{c\sqrt{sinh^2\xi + sin^2\eta}}\ \frac{sin\eta}{\sqrt{(b/a)^2 cos^2\eta + sin^2\eta}}\hat{e}_z\ .\end{aligned}$$

The integral thus becomes

$$\begin{aligned}\omega &= \frac{\Delta\rho\ \Delta p}{\rho^2 c}\ \frac{\delta(\xi - \xi_0)}{\sqrt{sinh^2\xi + sin^2\eta}}\ \frac{sin\eta}{\sqrt{(b/a)^2 cos^2\eta + sin^2\eta}}\int_0^\infty \delta(x - V_s t)\ dt \\ &= \frac{\Delta\rho\ \Delta p}{\rho^2 V_s c}\ \frac{\delta(\xi - \xi_0)}{\sqrt{sinh^2\xi + sin^2\eta}}\ \frac{sin\eta}{\sqrt{(b/a)^2 cos^2\eta + sin^2\eta}}\ .\end{aligned}$$

Having this expression for the vorticity, one integrates over the area of the jet to obtain the circulation:

$$\Gamma = \int\int \omega \, dA$$
$$= \frac{\Delta\rho \, \Delta p}{\rho^2 V_s c} \int\int \frac{\delta(\xi - \xi_0)}{\sqrt{sinh^2\xi + sin^2\eta}} \frac{sin\eta}{\sqrt{(b/a)^2 cos^2\eta + sin^2\eta}} \, dA \, .$$

The transformation of dA from Cartesian to elliptical coordinates is as follows:

$$dA = dxdy = |J| d\xi d\eta,$$

where

$$|J| = \frac{\partial x}{\partial \xi}\frac{\partial y}{\partial \eta} - \frac{\partial x}{\partial \eta}\frac{\partial y}{\partial \xi}$$
$$= c^2 sinh^2\xi \; cos^2\eta + c^2 cosh^2\xi \; sin^2\eta$$
$$= c^2 sinh^2\xi \; (1 - sin^2\eta) + c^2(1 + sinh^2\xi) \; sin^2\eta$$
$$= c^2(sinh^2\xi + sin^2\eta).$$

Therefore,

$$dA = c^2(sinh^2\xi + sin^2\eta) d\xi d\eta,$$

and

$$\Gamma = \frac{\Delta\rho \, \Delta p}{\rho^2 V_s} \, c \int\int \frac{sin\eta \;\; \delta(\xi - \xi_0)}{\sqrt{sinh^2\xi + sin^2\eta}\sqrt{(b/a)^2 cos^2\eta + sin^2\eta}} \, (sinh^2\xi + sin^2\eta) \; d\xi d\eta.$$

Evaluating the delta-function in the usual manner and inserting the appropriate limits for $0 \leq \eta \leq \pi$ in the upper half plane gives

$$\Gamma = \frac{\Delta\rho\Delta p}{\rho^2 V_s} \, c \int_0^\pi sin\eta \frac{\sqrt{sinh^2\xi_0 + sin^2\eta}}{\sqrt{(b/a)^2 cos^2\eta + sin^2\eta}} d\xi$$
$$= \frac{\Delta\rho\Delta p}{\rho^2 V_s} \, c \int_0^\pi sin\eta \frac{\sqrt{b^2/(a^2 - b^2) + sin^2\eta}}{\sqrt{(b/a)^2(1 - sin^2\eta) + sin^2\eta}} d\xi$$
$$= \frac{\Delta\rho\Delta p}{\rho^2 V_s} \, c \int_0^\pi sin\eta \frac{\sqrt{b^2/(a^2 - b^2) + sin^2\eta}}{\sqrt{(1 - (b/a)^2) sin^2\eta + (b/a)^2}} d\xi$$
$$= \frac{\Delta\rho\Delta p}{\rho^2 V_s} \, \frac{c}{\sqrt{1 - (b/a)^2}} \int_0^\pi sin\eta \; d\xi$$
$$= 2a \, \frac{\Delta\rho\Delta p}{\rho^2 V_s} \, .$$

In this expression, it is necessary to choose suitable values of ρ, one for the pressure term, and one for the density term. Since the pressure gradient is due to the shock, choose ρ_2 for the pressure term, and since the density gradient is across the interface, choose the average density at the interface, $(\rho_L + \rho_H)/2$, for the density term. The circulation then becomes

$$\Gamma = \frac{4a}{V_s} \, \frac{\Delta p}{\rho_2} \left(\frac{\Delta\rho}{\rho_L + \rho_1}\right) \, .$$

Finally, nondimensionalize all lengths by b, all densities by ρ_1, all pressures by p_1, all velocities by c_1, and the circulation by bc_1. The circulation then becomes

$$\overline{\Gamma} = \frac{4}{\gamma_1 M} \frac{\overline{\rho}_1}{\overline{\rho}_2} \left(\frac{\overline{p}_2}{\overline{p}_1} - 1 \right) \left(\frac{1 - \overline{\rho}_L/\overline{\rho}_H}{1 + \overline{\rho}_L/\overline{\rho}_H} \right) \frac{1}{AR}.$$

This formula is exactly that for the circular jet case divided by the aspect ratio of the ellipse!

Summarized below are the computed and predicted circulation values for the elliptical jet runs. The computed values are simply copied from Table 7.1 above.

M	AR	Computed $\overline{\Gamma}$	Predicted $\overline{\Gamma}$
1.1	0.5	1.06	0.83
1.1	1.0	0.45	0.41
1.1	2.0	0.20	0.21
2.0	0.5	2.80	2.84
2.0	1.0	1.20	1.42
2.0	2.0	0.51	0.71

Table 7.2 - Computed and predicted $\overline{\Gamma}$ for the elliptical jet flows

These data are also plotted in Figure 7.18 (as a matter of convenience, these are actually plots of the ratio of predicted to computed circulation, which should be unity in the case of a perfect scaling law). The model underpredicts the M=1.1 circulation at low aspect ratios, and overpredicts the M=2.0 circulation at high aspect ratios. The overall results are within ±30%, considerably worse than the circular jet case.

Besides the circulation, one is interested in the time scaling; Exactly as before, one defines a characteristic timescale as

$$\tau = \frac{(H/W)}{\Gamma},$$

where H is a characteristic height, W is a characteristic width, and Γ is the circulation. For H, one takes b, the vertical dimension, and for L, one takes $(\rho_1/\rho_2)a$, the horizontal dimension just after the shock has passed (the factor ρ_1/ρ_2 accounts for the streamwise compression due to the shock). Therefore,

$$\tau = \frac{\rho_1}{\rho_2} \frac{a\,b}{\Gamma}.$$

Substituting and nondimensionalizing gives

$$\overline{\tau} = \left(\frac{\gamma_1 + 1}{8} \right) \left(\frac{M}{M^2 - 1} \right) \left(\frac{1 + \overline{\rho}_L/\overline{\rho}_H}{1 - \overline{\rho}_L/\overline{\rho}_H} \right),$$

which is exactly the same result as in the circular jet case. This means that aspect ratio does not affect the time scaling. Thus, at fixed Mach number, the AR = 0.5, 1, and 2 flows should all be at the same stage of development at the same time. This is indeed shown by the computations: see Figure 7.19 for a comparison at M=1.1 and Figure 7.20 for a comparison at M=2.0.

Now consider the model for the motion of the vortex pair derived in Chapter 5, Section 3. This model needs no modification for the case of initially elliptical jets, because it is independent of the initial configuration.

Summarized below are the computed and predicted normalized velocity values for the elliptical jet runs. The computed values are simply copied from Table 7.1 above. The predicted values follow from a straightforward determination of the size and spacing parameters, $\overline{R}/\overline{y}_\infty$, and $\overline{y}_\infty/\overline{h}$.

M	AR	Computed $\overline{R}/\overline{y}_0$	Computed $\overline{y}_\infty/\overline{h}$	Computed $\overline{U}\overline{y}_\infty/\overline{\Gamma}$	Predicted $\overline{U}\overline{y}_\infty/\overline{\Gamma}$
1.1	0.5	1.417	0.1800	0.046	0.035
1.1	1.0	1.056	0.1875	0.055	0.059
1.1	2.0	0.887	0.2000	0.060	0.067
2.0	0.5	0.662	0.2875	0.041	0.055
2.0	1.0	0.547	0.2500	0.058	0.062
2.0	2.0	0.392	0.2750	0.052	0.059

Table 7.3 - Computed and predicted $\overline{U}\overline{y}_\infty/\overline{\Gamma}$ for the elliptical jet flows

These data are also plotted in Figures 7.21 and 7.22. As in the circular jet case, the model faithfully reproduces the qualitative trends. The quantitative agreement, while reasonable, is not as good as before.

Next consider the model for impulse of the vortex pair. Exactly as in the circular jet case,

$$I_x(\bar{t} = 0^+) = \int \rho\omega r sin\theta \; dA.$$

Substituting for the vorticity distribution, carrying out the integral, picking appropriate reference values, and nondimensionalizing gives

$$\overline{I}_x(\bar{t} = 0^+) \approx \left(\frac{1}{M}\right)\left(\frac{\overline{p}_2}{\overline{p}_1} - 1\right)\left(\frac{\overline{\rho}_1}{\overline{\rho}_2}\right)\left(1 - \frac{\overline{\rho}_L}{\overline{\rho}_H}\right)\frac{1}{AR}.$$

One correlates the steady-state product of spacing and circulation with the initial impulse deposited by the passing shock,

$$\overline{I}_x' \approx \overline{I}_x(\bar{t} = 0^+),$$

where again, $\overline{I}_x' \equiv 0.5\,\overline{y}_\infty\,\overline{\Gamma}$. Table 7.4 shows a comparison of the quantities $\overline{I}_x'$ and $\overline{I}_x(\overline{t}=0^+)$.

M	AR	$\overline{I}_x'$	$\overline{I}_x(\overline{t}=0^+)$
1.1	0.5	0.382	0.329
1.1	1.0	0.169	0.165
1.1	2.0	0.080	0.082
2.0	0.5	1.11	1.13
2.0	1.0	0.60	0.57
2.0	2.0	0.29	0.29

Table 7.4 - Computed $\overline{I}_x'$ and predicted $\overline{I}_x(\overline{t}=0^+)$ for the elliptical jet flows

These data are also plotted in Figures 7.23 and 7.24. The qualitative agreement is good throughout. The quantitative agreement is very good at moderate and high aspect ratios, but not for low aspect ratios.

Finally, the circulation and impulse models may be combined to give an expression for the half-spacing, $\overline{y}_\infty$. The result is exactly the same as in the circular jet case,

$$\overline{y}_\infty = \frac{\gamma_1}{2}\left(1+\frac{\overline{\rho}_L}{\overline{\rho}_H}\right).$$

i.e., there is no dependence on aspect ratio. The computed data in Table 7.1, which show very little variation in $\overline{y}_\infty$ for varying aspect ratio at fixed Mach number, verifies this prediction. However, just as before, the model fails to predict the dependence of $\overline{y}_\infty$ on the Mach number.

7.3 Reflected Shock Interactions with a Vortex Pair

7.3.1 Late-Time Interactions

In Chapter 3, the canonical problem of an incident shock wave interacting with a single jet of light gas was discussed. It was found that at large times, the resulting structure was very nearly an ideal vortex pair, with a thin filament connecting the vortex cores and with upstream tails of trailing low-vorticity material. If the interaction occurs in a closed domain, the incident shock will eventually hit the end wall, and propagate upstream as a reflected shock. The interaction between the reflected shock and the late-time vortex pair created by the incident shock is investigated in this section.

Five cases are considered. In each case, the light/heavy density ratio is $\overline{\rho}_L/\overline{\rho}_H = 0.138$. First, is the exact computation of a M=2.0 shock interacting with a single jet in a closed domain. The entire interaction is studied, from the formation of a vortex pair by the incident shock, to the subsequent interaction of this vortex pair with the reflected shock.

Second, the same flow is computed using an approximate technique, which gives almost identical results to the exact computation, while consuming only a fraction of the computer time needed for the exact solution. The approximation consists of taking a late-time vortex pair resulting from the interaction of a shock wave and a single jet, overwriting part of the domain with appropriate pressures and densities to simulate a reflected shock, and computing the truncated region containing only the reflected shock and the vortex pair. Not only does one avoid computing a long domain, but one also avoids recomputing the initial interaction, which is available from the computations of Chapter 3. Such approximations are necessary because the computer time required to computing the whole domain and the whole interaction is enormous. Even for this fast M=2 flow, where the end wall is relatively close to the initial jet, the exact computation requires about 20 minutes of Cray Y-MP time. To perform the same exact calculation on a slower M=1.1 case, where the end wall must be sufficiently far downstream for the vortex pair to develop and stabilize before the reflected shock hits, would consume about 12 hours! The last three runs use the same approximation to examine the reflected shock interactions that would arise from incident shocks of strength M=1.5, 1.2, and 1.1. The need to justify the approximation leads to the unusual order of presentation (*i.e.*, decreasing Mach number) in this case.

In all that follows, the discussion is for the upper half plane only. The flow is always symmetric about the horizontal centerline, so the results apply equally well to the lower half plane.

• M=2 Reflected Shock Exact Computation

The case of a M=2 shock impinging on a single jet is carried out in lab-frame coordinates, using a reflecting boundary condition for the downstream end and a transmitting boundary condition for the upstream end. The length of the domain is such that the reflected shock hits the vortex pair after it has stabilized, and is approximately in steady-state motion (about $\overline{t}$=12).

Density contour plots for this computation are shown in Figure 7.25. The early-time interaction, times $\overline{t}$=0 to 8, is identical to the results shown in Figure 3.25. Just before $\overline{t}$=10, the shock hits the end wall and reflects back toward the vortex pair. At this point, the velocity behind the reflected shock is zero, and the velocity ahead of the reflected shock is still that behind the incident shock. The interaction of the reflected shock with the vortex core results in baroclinic generation of vorticity similar, but opposite in sense, to that produced by the interaction of an incident shock with a single jet. However, the subsequent motion shows significant differences.

As a matter of convenience, consider the upper half plane in the remainder of the discussion.

The most important feature is the strong vorticity initially present in the vortex core. In the absence of this vorticity, the approximately circular core would behave like the single circular jet considered previously. Clockwise vorticity deposited in the outer half of the cross-section would develop into a clockwise vortex, and counterclockwise vorticity deposited in the inner half would develop into a counterclockwise vortex. These vortices would convect upstream relative to the ambient velocity because of their mutually induced velocities. In this case, however, the strong counterclockwise initial vorticity suppresses the outer half's development and enhances the inner half's development. The result is the formation of a non-symmetrical vortex pair, consisting of a small, clockwise outer vortex and a large, counterclockwise inner vortex. The strong inner vortex induces a counterclockwise downward and inward motion of the weak outer vortex. The weak outer vortex induces negligible motion of the inner vortex. Thus the overall motion is a counterclockwise rotation of the weak outer vortex about the strong inner vortex. Notice that there is no tail associated with either of these vortices.

• M=2 Reflected Shock Approximate Computation

In the case described above, one is interested primarily in the $\bar{x}$=10 to 20 portion of the $\bar{t} \geq 10$ exact computation. It would be convenient to be able to compute only this part of the flow, skipping over the interaction of the incident shock wave with the initial circular jet, which is well known from Figure 3.25. One method is as follows. The $\bar{t}$=10 data from the canonical flow computation are converted to lab-fixed coordinates and are used to represent the portion of the exact computation ahead of the reflected shock. A reflected shock is then overwritten on the right side of the domain. It is assumed, in calculating the pressure and density behind this shock, that the amount of helium in the field is so small that it may be neglected. Thus the reflected shock is calculated from one-dimensional shock theory assuming only air is present. In selecting the portion of the domain to be overwritten with the reflected shock, the shock is placed nearer to the vortex pair than in the actual computation. This is a convenience to keep the interaction closer to the center of the domain. It should have little effect on the results, provided the flow behind the reflected shock is uniform.

The density contour plots are shown in Figure 7.26. The approximate computation may be compared to the previous exact computation to check the accuracy of the approximation. To make a quantitative comparison, it is convenient to shift the approximate computation's trajectory to the same origin as the exact computation. The offsets are calculated as follows. The start of the approximate computation, labelled $\bar{t}$=0, is equivalent to a time $10 < \bar{t} < 11$ in the exact computation when the vortex pair and reflected shock have the same separation as in the approximate computation. This means that the location of the end wall will be slightly different in the two cases, but this is of little consequence as long as the flow behind the reflected shock is uniform. The distances between the vortex pair and the shock are 2.00 (at $\bar{t}$=0 in the approximate computation)

and 4.60 (at $\bar{t}$=10 in the exact computation). The vortex pair moves at velocity 1.31 in the lab frame, and the reflected shock moves at velocity -1.00. Therefore, the approach velocity is 1.31 - (-1.000) = 2.31, corresponding to a time shift is 10 + (4.60-2.00)/2.31 = 11.12, so that $\bar{t}$=0 in the approximate computation corresponds to $\bar{t}$=11.12 in the exact computation. At that time, the vortex pair in the exact computation is at $\bar{x}$=6.18 and the vortex pair in the approximate computation is at $\bar{x}$=0. Thus the $\bar{x}$-trajectory shift is 6.18. Circulation and trajectory data for the exact and approximate computations are plotted in Figure 7.27(a),(b),(c), where the times correspond to the exact computation. The results are quite similar, indicating that the approximation is indeed acceptable.

Qualitative comparisons are made by comparing the contour plots of the two computations, keeping in mind that 11.12 should be added to the times shown in the approximate computation to obtain equivalent times for the exact computation. The comparisons look quite good, except for at $\bar{t}$=4 ($\bar{t}$=15.12 in the exact computation), when the weak outer vortex is somewhat different. This is a minor difference. Overall, this approximation models the exact computation sufficiently well that its use in this and the following cases is justified.

• M=1.5 Reflected Shock Approximate Computation

The interaction of the reflected shock and the vortex pair is very similar to the M=2 case described above. The density contour plots are shown in Figure 7.28. A noticeable feature of the M=1.5 case not seen in the M=2 case is the pronounced late-time ($\bar{t}$=8 to 10) shedding of a tail at the outer vortex. This may be explained as follows. The strengths of these vortices may be crudely modelled by superposition: let $\overline{\Gamma}_I$ be the circulation initially present in the vortex pair, and let $\overline{\Gamma}_R$ be the additional circulation that is deposited by the reflected shock (clockwise in the outer vortex, counterclockwise in the inner vortex). Then the approximate circulation in the two vortices will be $\overline{\Gamma}_R$ - $\overline{\Gamma}_I/2$ and $\overline{\Gamma}_R$ + $\overline{\Gamma}_I/2$. The circulation of the outer vortex, normalized by the initial circulation, is $(\overline{\Gamma}_R - \overline{\Gamma}_I/2)/(\overline{\Gamma}_I/2)$ or 2 $\overline{\Gamma}_R/\overline{\Gamma}_I$ - 1. But what is $\overline{\Gamma}_R/\overline{\Gamma}_I$? The interaction of a reflected shock hitting a vortex core (which is approximated as a circular jet) can be approximated using the circulation model developed in Chapter 5, Section 1, computing the additional circulation deposited by the reflected shock as if there were no initial vorticity in the core. After some manipulations[17] one finds that $\overline{\Gamma}_R/\overline{\Gamma}_I$ is a monotonic function of the incident Mach number. As the incident Mach number decreases, $\overline{\Gamma}_R/\overline{\Gamma}_I$ decreases, the relative strength of the outer vortex decreases, there is relatively less circulation available to organize the fluid, stabilization of the structure into a vortex core is less vigorous, and more low-vorticity fluid is shed in the form of a tail.

Interestingly, one observes no corresponding change in the structure of the inner vortex. Why is this so? The circulation of the inner vortex, normalized by the initial circulation, is approximately

[17] The details are omitted, since this is a crude approximation, at best.

$2\overline{\Gamma}_R/\overline{\Gamma}_I + 1$. This, too, can be shown to decrease as incident Mach number decreases, but the effect is less than for the outer vortex. That is, the proportional decrease in $2\overline{\Gamma}_R/\overline{\Gamma}_I + 1$ is less than that in $2\overline{\Gamma}_R/\overline{\Gamma}_I - 1$ for the same decrease in Mach number. In addition, whereas the outer vortex results from the coalescence of vorticity of opposite sign, the inner vortex results from the coalescence of vorticity of the same sign. Thus the effect of decreased Mach number is much less evident in the inner vortex than in the outer vortex.

Overall, compared to the M=2 case, there is increased induced motion of the weak outer vortex by the strong inner one. In particular, the outer vortex is swirled farther counterclockwise, and trails farther upstream. Again, simple approximate mathematics reveals why this is so. The ratio of the circulation in the inner vortex to that in the outer vortex is $(\overline{\Gamma}_R + \overline{\Gamma}_I/2)$ / $(\overline{\Gamma}_R - \overline{\Gamma}_I/2)$ or $(2\overline{\Gamma}_R/\overline{\Gamma}_I + 1)$ / $(2\overline{\Gamma}_R/\overline{\Gamma}_I - 1)$, which measures the extent to which the weak outer vortex will be swirled around counterclockwise by the strong inner vortex. As the Mach number decreases, $\overline{\Gamma}_R/\overline{\Gamma}_I$ decreases, so both numerator and denominator decrease as well. However, the denominator decreases more rapidly than does the numerator, so that $(2\overline{\Gamma}_R/\overline{\Gamma}_I + 1)$ / $(2\overline{\Gamma}_R/\overline{\Gamma}_I - 1)$ increases.

• M=1.2 Reflected Shock Approximate Computation

This interaction of the reflected shock and the vortex pair is similar to the higher Mach number cases described above. The density contour plots are shown in Figure 7.29.

One difference between the M=1.2 case and the higher Mach number cases is in the original structure. Because of the relatively weak incident shock, the initial structure is not purely a vortex pair, but also exhibits upstream-pointing tails of low-vorticity fluid. These tails have a very slight density gradient perpendicular to the pressure gradient from the reflected shock, so some vorticity is generated there. However, this is quite small, and is of little overall importance.

Another difference is that the vortices formed by the reflected shock are noticeably less compact than in the M=2 and M=1.5 cases. As mentioned earlier, the ratio of the circulation due to the reflected shock to the circulation due to the incident shock decreases with decreasing Mach number. This ratio is a measure of the ability of the additional distributed vorticity to coalesce with the original concentrated vorticity in forming the new vortices. Hence the increased size of vortices, as evident at time $\bar{t}$=20. Also as mentioned earlier, the effect of decreasing Mach number is greater for the weak outer vortex than for the strong inner vortex. Thus the deviation from a tight, compact vortex core is greater for the outer vortex than for the inner vortex. The last frames of Figures 7.26, 7.28, and 7.29 show a marked increase in size of the outer structure relative to the inner structure. The weaker the shock, the more equitable the partitioning of the original vortex core into two new vortices.

• M=1.1 Reflected Shock Approximate Computation

The density contour plots for this case are shown in Figure 7.30. The trends mentioned above

continue as the Mach number is further decreased to 1.1.

• Summary of Late-Time Interaction

The initial flow is a left-moving reflected shock which is just entering a domain containing the late-time structure produced by the incident shock. This structure consists of a counter-rotating vortex pair, counterclockwise in the UHP, and clockwise in the LHP, connected by a thin filament at the downstream end and with trailing tails at the upstream end.

Consider the flow in the upper half plane. The reflected shock first passes over the thin filament, whose density gradient is parallel to the pressure gradient from the shock and thus contributes negligible vorticity. As the shock passes over the approximately circular vortex, vorticity is deposited around its circumference. Just as in the case of the single jet, this vorticity has a distribution in both space and intensity. Equal-magnitude vorticity of opposite sense is distributed over the outer and inner halves: clockwise above and counterclockwise below. The magnitude of this vorticity, expressed as a circulation, is greater than the initial circulation in the vortex. This vorticity coalesces with the initial vorticity to form two distinct counter-rotating vortices connected by a thin filament.

A small, weak, clockwise outer vortex results from coalescence of the counterclockwise initial vorticity with a stronger clockwise distributed vorticity. Because of the mixed-sign vorticity, the rate at which the structure develops into a dominant vortex core is rather slow. The overall circulation equals a clockwise circulation from the reflected shock less a counterclockwise circulation from the incident shock.

A large, strong, counterclockwise inner vortex results from coalescence of the counterclockwise initial vorticity with a stronger counterclockwise distributed vorticity. Because the vorticity of the fluid is all of the same sense, the development of a dominant vortex core is rapid, and the shedding of tails is much less pronounced.

As the incident shock Mach number is decreased, the ratio of circulation due to the reflected shock to the circulation due to the incident shock decreases. This quantity drives the organization of the fluid, so the development of the two vortices is slower and less organized. This is especially noticeable in the outer vortex, whose size approaches that of the inner vortex. The circulation of the strong inner vortex increases relative to the weak outer vortex. Thus the outer vortex experiences greater induced motion, is swirled farther counterclockwise, and trails farther upstream. Finally, the importance of the initial tail relative to the initial vortex pair, and the vorticity due to the interaction of this tail with the reflected shock, increase as well.

7.3.2 Intermediate- and Early-Time Interactions

The previous subsection considered the late-time interaction of a reflected shock and a vortex

pair. In that case, the vortex pair created by the incident shock was stable and well-developed by the time it was hit by a reflected shock. Now consider what happens as the reflected shock is allowed to interact with an initial structure at successively earlier times. How does the interaction change if the initial structure has not yet stabilized into a vortex pair before the reflected shock hits?

Again, an approximate technique is used to compute the flow. The single circular jet flows from Chapter 3 are overwritten with reflected shocks to initialize the reflected shock computations. For each Mach number, both intermediate- and early-time interactions are studied:

$$M = 1.1, \bar{t} = 40 \text{ (Figure 7.31)}$$
$$M = 1.1, \bar{t} = 20 \text{ (Figure 7.32)}$$
$$M = 1.2, \bar{t} = 20 \text{ (Figure 7.33)}$$
$$M = 1.2, \bar{t} = 10 \text{ (Figure 7.34)}$$
$$M = 1.5, \bar{t} = 10 \text{ (Figure 7.35)}$$
$$M = 1.5, \bar{t} = 5 \text{ (Figure 7.36}$$
$$M = 2.0, \bar{t} = 4 \text{ (Figure 7.37)}$$
$$M = 2.0, \bar{t} = 2 \text{ (Figure 7.38)}$$

These contour plots may be compared with the corresponding late-time cases from the previous subsection. For a fixed Mach number and varying time of shock reflection, the qualitative results look similar. In each case, each half of the original vortex pair is split into a strong inner vortex and a weak outer vortex. These vortices become more nearly equal in size as the time of shock reflection is reduced.

The reason for this phenomenon is clear. Consider either core of the original vortex pair. A reflected shock generates additional vorticity of both positive and negative sense, and it is the preferential coalescence of same-sense vorticity that determines the relative sizes of the strong inner vortex and the weak outer vortex that are formed. The earlier the reflected shock hits, the less time the original vortex pair has had to stabilize, and the weaker is its ability to append the additional vorticity due to the reflected shock. Therefore, the original vortex core will be fissioned into two new vortices that are nearly equal in size.

7.4 Horizontal Jet Pair

7.4.1 Qualitative Description

The flows considered to this point have involved only a single jet, but actual technological applications will probably involve multiple jets. The simplest configuration is a horizontal pair of jets. A family of such cases is computed, using superposition of single jet profiles to initialize the

domain. The Mach number is varied from $1.1 \leq M \leq 2.0$, and the center-to-center spacing is varied from $2.5 \leq \overline{L}_0 \leq 6$. In all cases, the light/heavy gas density ratio is $\overline{\rho}_L/\overline{\rho}_H = 0.138$. These runs are summarized below:

$M = 1.1, \overline{L}_0 = 6$, (Figure 7.39)
$M = 1.1, \overline{L}_0 = 4$, (Figure 7.40)
$M = 1.1, \overline{L}_0 = 3$, (Figure 7.41)
$M = 1.1, \overline{L}_0 = 2.5$, (Figure 7.42)
$M = 1.2, \overline{L}_0 = 6$, (Figure 7.43)
$M = 1.2, \overline{L}_0 = 4$, (Figure 7.44)
$M = 1.2, \overline{L}_0 = 3$, (Figure 7.45)
$M = 1.2, \overline{L}_0 = 2.5$, (Figure 7.46)
$M = 1.5, \overline{L}_0 = 6$, (Figure 7.47)
$M = 1.5, \overline{L}_0 = 4$, (Figure 7.48)
$M = 1.5, \overline{L}_0 = 3$, (Figure 7.49)
$M = 1.5, \overline{L}_0 = 2.5$, (Figure 7.50)
$M = 2.0, \overline{L}_0 = 6$, (Figure 7.51)
$M = 2.0, \overline{L}_0 = 4$, (Figure 7.52)
$M = 2.0, \overline{L}_0 = 3$, (Figure 7.53)
$M = 2.0, \overline{L}_0 = 2.5$, (Figure 7.54)

Consider the M=1.1 family. The first case is $\overline{L}_0 = 6$ (Figure 7.39). In this case, the jets are initially far apart, and their time evolution is essentially non-interacting. Each behaves like the canonical isolated single jet, as if it were the only one in the field. The only difference is that the development of the downstream structure is slightly delayed relative to the upstream one. This is due to the time it takes the incident shock to propagate through the upstream jet and travel the distance between the two jets, before initializing development of the downstream jet.

If the initial spacing is decreased or the shock strength is increased, vorticity will still be distributed around the perimeter of the two jets, and each will still stabilize into a vortex pair, just as in the case of an isolated jet. But as time goes on, the two vortex pairs will interact, in a manner that can be predicted from simple induced motion considerations. The single arrows on Figure 7.55(a) illustrate the induced motion of each vortex core due to all the others. For example, consider the UHP downstream core. It experiences a rightward velocity due to its LHP neighbor, an upward velocity due to its upstream UHP neighbor, and a rightward and downward velocity due to its upstream LHP neighbor. The net velocity, shown as a double arrow, is upward and to the right. Similarly, the net velocity of the UHP upstream core is downward and rightward. As the downstream cores move apart, they induce in each other smaller downstream velocities, and the

pair decelerates. Similarly, as the the upstream cores move closer together, they induce in each other larger downstream velocities, and the pair accelerates. Thus, the upstream vortex pair will be entrained into the downstream one. Figure 7.55(b) shows the induced motion of the tail of the downstream UHP structure, due to the two UHP vortex cores. Its net motion is upward and to the left. Thus, the tail will be pulled up and around the outer edge of the upstream UHP vortex core.

These phenomena are illustrated in the case $\overline{L}_0 = 4$ (Figure 7.40). At $\bar{t} \leq 30$, the developing structures look like identical but time-shifted canonical flow structures. However, they soon begin to interact. At times $\bar{t} = 40$ to 70, notice the decrease in spacing of the upstream vortex pair as it accelerates toward the downstream pair. Also, the tails of the downstream structure are pulled upstream, around the outer edges of the upstream vortex cores. At $\bar{t} = 80$ to 100, the entrainment becomes so strong that the upstream vortex pair merges into the downstream pair, and the overall structure reorganizes to form a single stable vortex pair.

As the initial spacing is further decreased, neither jet has time to develop into a stable vortex pair before interaction occurs. This is illustrated in the case $\overline{L}_0 = 3$ (Figure 7.41). As early as $\bar{t}$ = 10 and 20, the upstream structure is starting to be entrained into the downstream structure. At $\bar{t} = 30$ to 60, the two vortical structures merge and reorganize to form a single vortex pair. Note the convolutions in the developing structure, due to the fact that almost all of the fluid in both upstream and downstream structures participates in the merger. In the previous case, the upstream and downstream structures first self-organized into high vorticity cores with trailing tails, and then just the cores merged to form a new vortex pair. In the present case, the upstream and downstream structures intermingle before they have had time to self-organize, and then a single vortex pair develops from the whole.

These general trends are even more pronounced in the last case of the M=1.1 family, $\overline{L}_0 = 2.5$ (Figure 7.42).

What happens as the shock strength is increased (Figures 7.43 to 7.54)? A stronger shock reduces the effective distance between the two jets, and drives the flow on a faster timescale due to the increased vorticity, so that the merger occurs more rapidly. But the general behavior is the same as for the M=1.1 family, so further qualitative discussion is unnecessary.

7.4.2 A Criterion for Vortex Merging

In some of the cases, the two vortices merge and coalesce into a single vortex, while in others, they remain separate. In general, the stronger the shock wave or the smaller the initial separation, the higher the likelihood of merger. One would like to classify the merging behavior in terms of a simple parameter that is easily obtained even without detailed knowledge of the features of the flow.

The canonical problem of merging of an isolated pair of identical circular or nearly-circular vortices has been studied by numerous investigators. These investigations have been carried out for a variety of initial spacings, vortex strengths and vorticity distributions.

Roberts and Christiansen (1972), Rossow (1977), and Zabusky, *et al.* (1979), numerically modelled the unsteady flow of a pair of identical, initially circular vortices and found that the critical value for merger to be L/D = 1.7, where L and D are the initial spacing and vortex diameter. That is, when L/D < 1.7, merger occurred, but when L/D > 1.7, the vortices remained separated. Saffman and Szeto (1980) analytically solved the related problem of a steady, non-circular equilibrium vortex pair, and found the critical value for existence of steady motions to be 1.58.

These results indicate that the merging of two single vortices is characterized by a single number, namely the ratio of initial spacing to vortex diameter, L/D, and that the critical value for merger is about 1.6 or 1.7.

The present flows concern the merger of noncircular, developing vortex pairs, rather than the simpler case of circular or nearly-circular, organized single vortices. Yet one might expect the merger still to be characterizable in terms of a critical value of L/D, where L represents the spacing of the vortex pairs, D the size of a vortex core.

It is the passage of the shock that deposits the vorticity, so one must use an appropriate post-shock state for the "initial" specification of L/D. After the shock has passed, the developing vortical structure may be approximated as a pair of vortices each of which has an area equal to half the area of the circular jet, less some compression due to the passage of the shock. To lowest order, this gives

$$\frac{A}{A_0} = \frac{1}{2}\,\frac{\rho_1}{\rho_2}\,,$$

or

$$\frac{D}{D_0} = \sqrt{\frac{1}{2}\,\frac{\rho_1}{\rho_2}}\,,$$

where subscript 0 denotes the pre-shock condition, no subscript denotes the post-shock condition, and ρ_2/ρ_1 is the jump in density across the shock.

One must also determine the post-shock separation of the two jets, to account for the fact that the shock passes over the upstream jet and sets it into motion while the downstream jet is still stationary. Assume that the time delay is given by the pre-shock jet separation divided by the shock speed, L_0/V_s, and that the upstream structure initially moves with the velocity behind the shock, v_2. Then the upstream structure moves a distance $L_0 v_2/V_s$ before the shock hits the downstream jet, giving a post-shock separation of

$$L = \left(1 - \frac{v_2}{V_s}\right) L_0.$$

Thus, the "initial" ratio of spacing to diameter is properly taken to be

$$\frac{L}{D} = \frac{L_0}{D_0}\left(1 - \frac{v_2}{V_s}\right)\sqrt{\frac{1}{2}\,\frac{\rho_2}{\rho_1}}$$

or, in nondimensional form,

$$\frac{\overline{L}}{\overline{D}} = \frac{\overline{L}_0}{\overline{D}_0}(1 - \frac{\overline{v}_2}{M})\sqrt{\frac{1}{2}\frac{\overline{\rho}_2}{\overline{\rho}_1}}$$

These values are tabulated in Table 7.5, along with the observed outcome of the merger process.

M	$\overline{v}_2$	$\overline{\rho}_2$	$\overline{D}/\overline{D}_0$	$\overline{L}_0/\overline{D}_0$	$\overline{L}/\overline{L}_0$	$\overline{L}/\overline{D}$	MERGER
2.0	1.250	2.667	0.433	1.25	0.375	1.08	YES
1.5	0.694	1.862	0.518	1.25	0.537	1.30	YES
2.0	1.250	2.667	0.433	1.50	0.375	1.30	YES
1.2	0.306	1.342	0.611	1.25	0.745	1.53	YES
1.5	0.694	1.862	0.518	1.50	0.537	1.55	YES
1.1	0.159	1.169	0.654	1.25	0.855	1.63	YES
2.0	1.250	2.667	0.433	2.00	0.375	1.73	YES
1.2	0.306	1.342	0.611	1.50	0.745	1.83	YES
1.1	0.159	1.169	0.654	1.50	0.855	1.96	YES
1.5	0.694	1.862	0.518	2.00	0.537	2.07	YES
1.2	0.306	1.342	0.611	2.00	0.745	2.44	YES
2.0	1.250	2.667	0.433	3.00	0.375	2.60	YES
1.1	0.159	1.169	0.654	2.00	0.855	2.62	YES
1.5	0.694	1.862	0.518	3.00	0.537	3.11	YES
1.2	0.306	1.342	0.611	3.00	0.745	3.66	NO
1.1	0.159	1.169	0.654	3.00	0.855	3.92	NO

Table 7.5 - Horizontal jet pair merging characteristics

Of particular interest is the transition from merger to non-merger at $\overline{L}/\overline{D}$ = 3.1 to 3.7. This is about twice as high as the corresponding value for circular vortices, about 1.6 or 1.7. That is, this system is more critical than the single vortex case and merger will occur at greater initial spacings. This is to be expected, because entrainment of the upstream pair into the downstream pair accelerates the merging process.

7.5 Horizontal Jet Trio

Another case of interest is that of a trio of horizontal jets. Here there exists the possibility of a similar but more complicated merger than that observed in the horizontal jet pair cases. Four cases

are computed, all at M=1.1 and $\overline{\rho}_L/\overline{\rho}_H$ = 0.138, for center-to-center spacings of 6, 4, 3, and 2.5 radii. Contour plots for these runs are shown in Figures 7.56, 7.57, 7.58, and 7.59, respectively.

Since the case of horizontal jet trios is an extension of the case of horizontal jet pairs, one expects that much of the same phenomena will be observed.

A developing trio initially consists of three separate structures, which can be referred to as 'upstream,' 'central,' and 'downstream' vortex pairs. The motion of each of these structures may be understood in terms of the induced motions due to all the other vortices, exactly as was done for the horizontal jet pairs.

Consider first the downstream UHP vortex. Its primary motion is a rightward induced velocity induced by its LHP image. It experiences a small secondary motion from the central vortex pair: an upward velocity from the UHP vortex, and a rightward and downward velocity from the LHP vortex. The net contribution from the central vortex pair is upward and to the right. The upstream vortex pair contributes an even smaller tertiary motion that is also upward and to the right. The motion of the downstream LHP vortex is symmetrical about the line of symmetry. Thus, the net motion of the horizontal jet trio's downstream vortex pair is just that of the horizontal jet pair's downstream vortex pair, but slightly more exaggerated. The vortices move apart vertically, and also decelerate slightly as a consequence of the spacing increase.

Next, consider the central UHP vortex. Its primary motion is a rightward induced velocity from its LHP image. It also experiences secondary motions from the upstream and downstream vortex pairs. These are approximately equal in magnitude and opposite in sense, and so their net effect is to cancel. The motion of the central LHP vortex is symmetric about the line of symmetry. Thus the net motion of the central vortex pair is rightward and somewhat faster than that of the downstream vortex pair.

Finally, consider the upstream UHP vortex. Its primary motion is a rightward induced velocity from its LHP image. It also experiences small secondary and tertiary motions from the central and downstream vortex pairs. These are directed downward and rightward. The motion of the LHP upstream vortex is symmetrical about the line of symmetry. Thus, the net motion of the horizontal jet trio's upstream vortex pair is just that of the horizontal jet pair's upstream vortex pair, but slightly more exaggerated. The vortices move together vertically, and also speed up slightly as a consequence of the spacing decrease.

Overall, the upstream and downstream vortex pairs of the horizontal jet trio are analogous to the upstream and downstream vortex pairs of the horizontal jet pair. Comparison of the trio contour plots with the corresponding pair contour plots demonstrates this similarity, especially at early times.

However, at late times, entrainment becomes important and the presence of the central vortex

pair plays a critical role. Since the shock wave first hits the upstream jet, then the central jet, and finally the downstream one, the development of vortex pairs from the jets follows in the same order. At any given time, the upstream vortex pair is the most developed, and the central and downstream vortex pairs are successively less developed. Since development of a vortex pair implies stability to external disturbances, the two most unstable vortex pairs are the central and downstream ones. Hence, if the spacing is small enough that merger will occur, it is these two that will merge first, to form a single larger vortex pair. Finally, the upstream vortex pair may or may not merge into this larger vortex pair, depending on how much the upstream vortex pair has stabilized during the formation of the larger vortex pair. In terms of merger, then, it is the trio's central and downstream vortex pairs that correspond to the pair's upstream and downstream vortex pairs. This is especially clear from comparison of corresponding late-time contour plots.

One may summarize as follows: at early times, the upstream and downstream vortex pairs of the trio correspond to the upstream and downstream vortex pairs of its corresponding pair. At late times, this correspondence transitions to the central and downstream vortex pairs of the trio. With this transitional behavior in mind, the qualitative behaviors of the pairs and the trios are very similar at corresponding times. Specific comments about tail stretching and entrainment as a function of initial jet separation, from the discussion of the pairs, carry over directly to the trios. At very late times, the upstream vortex pair may eventually be entrained and merged into the larger vortex formed from merger of the central and downstream vortices.

7.6 Vertical Jet Pair

7.6.1 Symmetric Pair

In this section, the interaction of an incident shock wave with a vertical pair of identical circular jets is studied. The jets are symmetric about the centerline of the channel, which extends from -8 to 8 vertically and 0 to 10 horizontally.

Recall that the upper and lower walls are equivalent to lines of symmetry, so that the channel can be viewed as a portion of an infinite array of jets obtained by reflection, *ad infinitum*, about the upper and lower walls.[18] This is shown schematically in Figure 7.60. Note that a pair spacing of 8 radii is exactly the canonical case, because then the array is perfectly periodic.

Four cases are computed, with center-to-center jet spacings of 6, 4, 3, and 2.5 radii. In all cases,

[18] Alternatively, one could regard the centerline of the channel as a hard wall, since it, too, is a line of symmetry. The flow can then be regarded as an off-center single jet located in a new channel whose walls are the centerline, plus either channel wall. It is purely a matter of convenience how the flow is interpreted. The present work will refer to a vertical pair of jets, but the existence of equivalent configurations should be noted.

the shock strength is M=1.1 and the light/heavy gas density ratio is $\overline{\rho}_L/\overline{\rho}_H = 0.138$.

In the spacing=6 case (Figure 7.61), the spacing is so close to the canonical case (Figure 3.1) that very little change in the flow is noticeable.

The next case is spacing = 4 (Figure 7.62). As usual, the shock passes over the jets, deposits vorticity around their perimeters, and the jets roll up into kidney-shaped structures. However, the inner portions of the structures, because of their closeness, induce motions in each other that lead to an asymmetry between the inner and outer lobes of each kidney. This is illustrated schematically in Figure 7.65. Since the flow is symmetric and periodic, it is only necessary to consider one of the structures, say the actual upper-half-plane vortex pair. The two halves of this vortex pair are labelled "UHP, inner" and "UHP, outer," as appropriate. Their motion can be predicted with the aid of the usual induced motion diagrams. Mathematically, one must consider an infinite array of vortices, but since the induced velocity from a vortex decays like 1/r, and since the vertical wall spacing is so large (16 times the jet radius), it is qualitatively sufficient to describe the motion of any one vortex in terms of only its two nearest neighbors. The UHP outer vortex experiences a strong downstream velocity due to the UHP inner vortex, and a very weak upstream velocity from its image vortex across the upper wall. Its net velocity is downstream. The UHP inner vortex experiences a strong downstream velocity from the UHP outer vortex, and a weaker upstream velocity from the LHP inner vortex. Its net velocity is downstream, but less than that of the UHP outer vortex. Relative to the outer vortex, the inner vortex experiences a stretching in the upstream direction. This is apparent in the contour plots, for example, at $\overline{t} = 20$ of Figure 7.62.

This upstream stretching causes the inner vortical structure to pinch off a larger tail than the corresponding canonical flow. Since more of the fluid is in the tail, the vortex core must be correspondingly smaller. Similarly, the outer tail is smaller, and the outer vortex core is larger, than in the canonical flow. This very large discrepancy between the inner and outer structures is visible at $\overline{t} > 40$. The difference in vortex core sizes results in the small UHP inner vortex core being rotated counterclockwise around the larger UHP outer vortex core, and *vice versa* for the LHP flow. This is evident at $\overline{t} > 50$.

The remaining two computations (Figures 7.63 and 7.64) show a continued decrease in initial jet spacing, exhibit these asymmetries to an even greater degree. The contour plots are self-explanatory, so no further discussion is necessary.

7.6.2 Asymmetric Pair

The multiple jet arrays considered to this point have all involved identical jets located symmetrically about the centerline. However, in a real flow, it is likely that different jets may be slightly

different in size, due to small differences in flow rates, nozzles, or other factors.

Therefore, it is of interest to investigate a vertical jet pair, similar to those investigated previously, but where there is a small asymmetry in the jet pair. Two cases are computed: a weak shock with a very slight asymmetry (M=1.1, upper jet radius = 0.95, lower jet radius = 1.05) and a strong shock with a moderate asymmetry (M=2.0, upper jet radius = 0.9, lower jet radius = 1.1). In each case, the light/heavy gas density ratio is $\overline{\rho}_L/\overline{\rho}_H = 0.138$. Density contour plots for these cases are shown in Figures 7.66 and 7.67. The jet spacing, fixed at 8 radii, is the same as the distance to the image jet across the nearest wall (recall that the wall is mathematically equivalent to a line of symmetry). Each jet forms a vortex pair. The upper vortex pair, formed from a smaller jet, will be weaker that the lower vortex pair, formed from a larger jet. Each vortex pair will have two nearest-neighbor vortex pairs: one of the same size and strength, and one that is slightly different in size and strength. The flow is equivalent to an infinite series of vortex pairs, but one in which the basic pattern is 2 weaker vortex pairs followed by 2 stronger vortex pairs. From the contour plots of the M=1.1 case, it is just barely possible to detect these asymmetries, but the flow is negligibly different from the canonical case (Figure 3.1). In the M=2.0 flow, even with twice the initial asymmetry, the effect is even less noticeable. This might have been expected from consideration of the strong kinematical stability of a developing vortex pair.

7.7 Equilateral Jet Trio

Consider three jets in an equilateral jet formation, with center-to-center spacing of 3 radii and upstream-facing vertex. Four incident shock strengths, M=1.1, 1.2, 1.5, and 2.0, are computed. These are shown in Figures 7.68, 7.69, 7.70, and 7.71, respectively. In each case, the light/heavy gas density ratio is $\overline{\rho}_L/\overline{\rho}_H = 0.138$.

At early times, as the shock passes over each jet, vorticity is deposited around its perimeter, and it begins to roll up in a manner similar to the canonical problem. At later times, interactions among the developing vortex structures cause deviations from the canonical flow.

As a matter of convenience, the discussion is restricted to the upper half plane. In that case, the three developing vortices may be identified as 'UHP upstream,' 'UHP inner upper,' and 'UHP outer upper,' counting from the one closest to the centerline and moving upward.

Consider first the UHP upstream vortex. In addition to the usual downstream induced motion from its LHP image, it experiences an upward and upstream induced motion from the UHP inner vortex. Its net motion is downstream and upward. As this vortex moves upward, notice the stretching of the thin filament connecting it to its LHP neighbor. A second significant feature is the entrainment of the tail material from the UHP upstream vortex between the lobes of the UHP inner

and outer vortices. This is similar to the entrainment in the horizontal jet cases.

The third distinguishing feature is the swirling of tail material, from either the UHP inner or the UHP outer vortex, upstream and around the outer edge of the UHP upstream vortex. This, too, is similar to the tail stretching observed in the horizontal jet cases.

Chapter 8 - Applications to Supersonic Combustion

8.1 Characterization of the Mixing

The previous chapter presented qualitative discussions of the fluid mechanics of a number of variations on the canonical flow. These flows are of interest insofar as they may be used to enhance the mixing of fuel and oxidizer in an application such as supersonic combustion. Thus it is necessary to have a quantitative basis for comparing their mixing efficiencies.

Characterization of mixing via numerical simulations is a delicate process, and one should be careful to avoid the common problem of overexaggerating the facilities of numerical simulations and overstepping the bounds of their applicability.

One may think of mixing as a two-step process, as shown in Figure 8.1. The first step, stretching, is a necessary precursor to the second step, diffusion, because it is through gradient intensification that diffusive effects become important.

Of these phenomena, the measuring of stretching via numerical simulation is the least difficult, because it is primarily a problem of ensuring 1) accurate representation of regions of high gradients in the flow and 2) adequate gridding to resolve the smallest scales of interest. These ensure that the forces driving the stretching are accurately captured and that the resulting stretching is resolvable to a level consistent with that of the real flow.

However, satisfaction of the above constraints is often inconsistent with an accurate representation of the diffusion. The reason is that the numerical diffusion required for stability, or even that associated with the finite-difference discretization, is often far greater than the actual physical diffusion. As mentioned earlier, a significant feature of the flux-corrected transport algorithm used here is its ability to resolve these issues in a not unsatisfactory manner. This is not to say that the numerical diffusion is correct. As argued in Chapter 4, Section 1, Subsection 2, the numerical diffusion approximates the physically correct diffusion, but there is no reason to believe that its spatial distribution is correct. Nevertheless, it represents an significant improvement over the far greater errors encountered in many other, *i.e.*, non-FCT types of finite-difference schemes.

With these *caveats* in mind, one has quantitative confidence in the numerical solution up to the time that diffusion begins to play a role, but only qualitative confidence thereafter. Thus, the most reliable measure of mixing one can obtain from the simulations is that of stretching. How can this phenomenon be quantified?

Batchelor (1952) investigated the effect of homogeneous turbulence on material elements of fluid, and found that the best achievable stretching rate was exponential. More recently, other investigators have found that exponential stretching is also possible, at least locally, in two-dimensional unsteady

flows or in three-dimensional steady flows.[19] In expectation of this possibility, one can define a specific stretching rate as

$$\frac{1}{\overline{L}}\frac{D\overline{L}}{D\bar{t}} = \frac{D}{D\bar{t}}\,[ln(\overline{L})],$$

and study the approach to exponential stretching as evidenced by the asymptotic behavior of this quantity as a function of time. $\overline{L}$ is the length of a material element following the fluid, and is taken to be a particular mass-fraction level of interest.

This choice of mass-fraction level is guided by flows of technological interest. Since the application of mixing is combustion, imagine a flow where the light gas is hydrogen, and the heavy gas is air, so that the balanced chemical equation is

$$2H_2 + (3.76N_2 + O_2) \rightarrow 3.76N_2 + 2H_2O$$

The stoichiometric fuel mass fraction is then found to be

$$f_s = \frac{2(2)}{2(2) + 3.76(28) + 2(16)} = 0.028.$$

The anticipated technological application for shock-induced mixing is, of course, the National Aerospace Plane, which will carry an excess of hydrogen, beyond stoichiometric conditions, for cooling the structure in flight. Assuming a surplus on the order of 50%, this suggests that the actual fuel mass fraction will be

$$f \approx 1.5 f_s = 1.5(0.028) = 0.042.$$

Therefore, it is appropriate to pick f=0.05 as the contour whose stretching rate is of interest.

Two typical plots of D[ln $\overline{L}$(f=0.05)]/D$\bar{t}$ are shown schematically in Figures 8.2(a),(b). The first plot shows a gradual drop in D[ln $\overline{L}$]/D$\bar{t}$ as diffusion effects become important This is the so-called "diffusion-shortening" effect mentioned in Chapter 4, Section 1, Subsection 3. The second plot shows a sharp drop in D[ln $\overline{L}$] /D$\bar{t}$ as the limit of resolution is reached, *i.e.*, when some of the fluid enclosed by the contour of interest is stretched thinner than the cell size and can no longer be resolved. This is the so-called "resolution-shortening" effect mentioned in Chapter 4, Section 1, Subsection 3. In either case, the point of drop-off should correspond to the analogous point of transition in a real flow, but the quantitative reliability of the data beyond that point is not guaranteed.

Thus, for a mixing measure, one can define an critical stretching rate as that rate which is achieved at the drop-off point. This represents the best level of stretching that is achieved in the flow, before resolution or diffusion losses become important. In almost all the cases, the plots of D[ln $\overline{L}$]/D$\bar{t}$ show a nearly straight-line approach to this point, indicating that the global stretching

[19] A. Leonard, personal communication.

can indeed be well represented by an exponential expectation.[20] Listed below are critical stretching rates for the various cases considered in Chapter 7.

- Single Circular Jets

  i) Variation in Shock Strength or Density Ratio

  Table 8.1 shows stretching rates for the canonical flows.

M	$\overline{\rho}_L/\overline{\rho}_H$	D[ln $\overline{L}$]/D$\overline{t}$
1.05	0.138	0.007
1.1	0.138	0.014
1.2	0.138	0.024
1.5	0.138	0.050
2.0	0.138	0.085
1.1	0.354	0.010
1.1	0.569	0.006
1.1	0.785	0.002
2.0	0.354	0.061
2.0	0.569	0.048
2.0	0.785	0.035

Table 8.1 - Stretching rates for the canonical flows

The stretching rate increases as either the density ratio is decreased or the shock strength is increased. This is a consequence of the previously observed increases in strength and compactness of the vortex pair, as both factors lead to increased induced motions and thus higher stretching rates. Note that the rate of increase of stretching rate is greatest in cases of low Mach number or high density ratio. For example, at M=1.1, decreasing the density ratio from 0.785 to 0.138 increases the stretching rate by a factor of 7, while at M=2, the increase is only 2.5. Similarly, at $\overline{\rho}_L/\overline{\rho}_H = 0.785$,

[20] The exponential measure is a global characterization of stretching. Recently, Beigie, Leonard, & Wiggins (1991) examined the spatial dependence of stretching for some vortical flows, and found that stretching varies dramatically as a function of arc-length along a material element. In that case, it has been proposed that notions of chaotic flow from the theory of dynamical systems theory can be used to characterize the stretching. Such is beyond the scope and ambition of the present work. To quote Ottino (1989), ". . .under these conditions the [exact] calculation of the length and location of lines and areas in hopelessly complicated. As we shall see. . .even extremely simplified flows might be inherently chaotic and a complete characterization is not possible. The problem here is how to best characterize the mixing, knowing beforehand that a complete characterization is impossible." Clearly, a global measure of stretching such as D[ln $\overline{L}$]/D$\overline{t}$ defined above is far from a complete description of the mixing process; however, for the present purposes, it is adequate. One is interested in the overall mixing of one flow compared to another, as opposed to the detailed spatial distribution of mixing of any particular flow.

increasing M from 1.1 to 2.0 increases the stretching rate by a factor of 17, while at $\overline{\rho}_L/\overline{\rho}_H$= 0.138, the increase is only a factor of 6.

These are baseline stretching rates for an idealized, canonical flow against which the remaining flows should be compared. It is hoped that stretching rates for those flows will exceed these values, demonstrating mixing enhancement through configurations that are also more characteristic of actual technological applications.

ii) Effect of Channel Spacing

Table 8.2 shows the computed stretching rates for the three channel spacing variations. The Mach number is M=1.1 and the light/heavy gas density ratio is $\overline{\rho}_L/\overline{\rho}_H$ = 0.138.

$2\overline{h}$	D[ln $\overline{L}$]/D$\overline{t}$
4	0.015
8	0.014
16	0.016

Table 8.2 - Stretching rates for the channel spacing variations

There is no observed trend as the channel spacing is increased, and the stretching rates are all essentially the same. Note that the spacing = 8 case is exactly the canonical single jet.

iii) Effect of Initial Interface Thickness

Table 8.3 shows the computed stretching rates for the variations in initial interface thickness. The Mach number is M=1.1 and the light/heavy gas density ratio is $\overline{\rho}_L/\overline{\rho}_H$ = 0.138.

Interface	D[ln $\overline{L}$]/D$\overline{t}$
Sharp	0.044
Slightly Diffuse	0.038
Moderately Diffuse	0.028
Broadly Diffuse	0.014

Table 8.3 - Stretching rates for the interface thickness variations

As the thickness of the interface increases, the radius of the f=0.05 contour level (the outermost contour) increases. Thus the distance to the distributed vorticity increases, the induced motion decreases, and the stretching rate decreases. The profiles used here are 'tanh' profiles, so the stretching

rates should not be compared with the canonical 'mixing layer' case, because the initial distributions are different. It is only valid to compare variations of interface thickness from within a single family of profiles. The 'mixing layer' case has a much larger low-mass-fraction tail than any of these cases, and yet its rate of stretching is about the same as the most diffuse case here.

• Sinusoidally Perturbed Circular Jets

Table 8.4 shows stretching rates for only wavenumbers n = 8 and 16, because losses of resolution prevented an accurate measure in the n = 32 case. The Mach number is M = 1.1, and the light/heavy gas density ratio is $\overline{\rho}_L/\overline{\rho}_H = 0.138$.

n	ϵ_0	$D[\ln \overline{L}]/D\overline{t}$
8	0.05	0.013
8	0.10	0.012
16	0.05	0.013
16	0.10	0.014

Table 8.4 - Stretching rates for the sinusoidal jets

From the contour plots (Figures 7.6 to 7.9) one might expect growth of the instabilities to cause a dramatic increase in stretching rate compared to the corresponding canonical circular jet case ($D[\ln \overline{L}]/D\overline{t}$= 0.014). However, this is not so. In fact, the stretching rates are essentially unchanged from the circular jet case, to within the uncertainties in their determination.

As a first approximation, one may describe the instabilities at the upstream and downstream edges by the equations for Richtmyer-Meshkov instability at a sinusoidally perturbed plane interface. At early times, the differential equation for amplitude growth (Brouillette (1989)) is

$$\frac{1}{\epsilon_0}\frac{d\epsilon}{d\overline{t}} = \frac{n\,\overline{v}_2\,A}{\psi}.$$

ϵ_0 is the initial amplitude, n is the wavenumber, $\overline{v}_2$ is the velocity behind the shock, A is the Atwood number $[(\overline{\rho}_H - \overline{\rho}_L)/(\overline{\rho}_H + \overline{\rho}_L)$ at the upstream interface and $(\overline{\rho}_L - \overline{\rho}_H)/(\overline{\rho}_L + \overline{\rho}_H)$ at the downstream interface] and ψ is a growth reduction factor ($\psi > 1$) that depends on $|A|$ and interface thickness.

For the cases considered here, $\overline{v}_2$, $|A|$, and ψ are constant, so the growth rate is proportional to n and ϵ_0. However, because the upstream Atwood number is $-|A|$ and the downstream Atwood number is $+|A|$, the growth rates at the upstream and downstream interfaces are equal and opposite. The stretching at the downstream interface may increase due to increases in n or ϵ_0, but this is balanced by an equal decrease at the upstream interface. Thus, the overall stretching rate, $D[\ln \overline{L}]/D\overline{t}$, remains

essentially constant, independent of the initial amplitude or wavenumber of the perturbation.

• Elliptical Jets

Table 8.5 shows the computed stretching rates for the elliptical jet flows.

M	AR	$D[\ln \bar{L}]/D\bar{t}$
1.1	0.5	0.008
1.1	1.0	0.014
1.1	2.0	0.015
2.0	0.5	0.080
2.0	1.0	0.085
2.0	2.0	0.092

Table 8.5 - Stretching rates for the elliptical jets

At high Mach number, as the aspect ratio is increased, the streamwise dimension of the vortical structures is decreased, and the induced motions are increased. This is reflected in a slightly growing trend in the stretching rate. The same trend is observed at low Mach number, but there is an abrupt drop in the AR=0.5 case. The contour plots for this case (Figure 7.13) show that the outermost contour level has a small upstream protrusion, in contrast to the purely downstream stretching of higher levels[21] Even though this is a real phenomenon, it is due to the special combination of low aspect ratio, outlying contour level, and low Mach number. A comparison of stretching rates of higher mass fraction levels, say f=0.5, probably would not show such an abrupt drop in stretching rate, but rather the expected slow and gradual decrease.

Overall, the elliptical jet stretching rates show a very slight monotonic dependence on aspect ratio, and this dependence is greater at higher Mach number.

• Reflected Shock Interactions with a Vortex Pair

Table 8.6 shows the computed stretching rates for the reflected shock interactions. These data are also shown in Figure 8.3.

[21] These are actually density contour plots, and the outermost contour corresponds roughly to f=0.1, but the f=0.05 mass fraction contour shows the same behavior.

Interaction	M	$D[\ln \bar{L}]/D\bar{t}$	% Increase over Corresponding Single Jet Case
LATE	2	0.165	94
LATE	2	0.157	88
LATE	1.5	0.067	34
LATE	1.2	0.027	13
LATE	1.1	0.014	0
INT.	2	0.285	235
INT.	1.5	0.132	164
INT.	1.2	0.057	138
INT.	1.1	0.026	86
EARLY	2	0.290*	—
EARLY	1.5	0.222	344
EARLY	1.2	0.085	254
EARLY	1.1	0.035	150

* These data are discounted because of probable resolution losses. See text below.

Table 8.6 - Stretching rates for the reflected shock flows

Recall from Chapter 7, Section 3 that these computations were performed using an approximation to the reflected shock, and that one comparison was made to the exact computation to verify the accuracy of the approximation. Similarly, the first line of the above table is for the "exact" case, and is to be compared with the second line, for the "approximate" case. The close agreement between the two stretching rates again confirms the validity of the approximation.

The remaining lines of the table are for the approximate computations. One case, indicated by an asterisk, is discounted because careful examination of the appropriate contour plot shows a probable very-early-time loss of resolution of the f=0.05 contour level. In general, the earlier the reflected shock hits, the better the stretching. This is a consequence of the limited amount of time the vortex pair has had to form a stable core before the reflected shock hits. Likewise, the stronger the reflected shock, the better the stretching. However, the effect of earlier interaction is greater than the effect of increased shock strength.

- Horizontal Jet Pairs

Table 8.7 shows the computed stretching rates for the reflected shock interactions.

M	Spacing	D[ln $\overline{L}$]/D$\bar{t}$	% Increase over Corresponding Single Jet Case
1.1	6.0	0.014	0
1.1	4.0	0.018	29
1.1	3.0	0.010*	—
1.1	2.5	0.009*	—
1.2	6.0	0.032	33
1.2	4.0	0.040	67
1.2	3.0	0.028*	—
1.2	2.5	0.011*	—
1.5	6.0	0.061	22
1.5	4.0	0.046*	—
1.5	3.0	0.055*	—
1.5	2.5	0.069*	—
2.0	6.0	0.127	49
2.0	4.0	0.105*	—
2.0	3.0	0.112*	—
2.0	2.5	0.139*	—

* These data are discounted because of probable resolution losses. See text below.

Table 8.7 - Stretching rates for the horizontal jet pairs

At low Mach numbers (1.1 and 1.2), as the center-to-center spacing is decreased from infinity (the isolated single jet case) to 6 and then 4, the stretching rate increases. This is obviously due to entrainment of the upstream vortical structure by the downstream vortical structure. As the spacing is further decreased, the stretching then appears to decrease, but this is misleading. First, the initial character of the f=0.05 contour changes from being two closed contours, one around each jet, to being a single closed contour around both jets, with slight indentations between the two jets. Thus, the behavior of the f=0.05 contour is more like a single elongated jet than a pair of single jets. Second, the contour is not well-resolved between the two developing vortex pairs as the interaction progresses. That is, thin filaments that should be sucked into the region between the jets are unresolved by the finite size of the grid. For these regions, the computed stretching rates become unreliable as the separation is decreased below 4. However, there is little doubt that the real stretching rate continues to increase, due to the increased entrainment. As usual in numerical simulations of mixing, one must exercise appropriate caution in interpretation of the results!

At high Mach numbers (1.5 and 2), the decrease in spacing from infinity to 6 and then to 4 again shows a initial increase in stretching followed by a decrease. This is exactly the same phenomenon as described above. Again, the apparent decrease should be discounted! Note that as the spacing is further decreased to 3 and then to 2.5, entrainment becomes so strong that the stretching unavoidably shows a steep increase, notwithstanding the previous resolution losses which tend to (artificially) decrease the stretching rate.

In general, two trends may be noted. First, the incremental increase in stretching is greater for higher Mach numbers. Second, the point at which the artificial stretching loss first appears moves to progressively higher values of spacing as the Mach number decreases.

• Horizontal Jet Trios

Table 8.8 shows the computed stretching rates for the horizontal jet trios. The Mach number is M=1.1 and the light/heavy gas density ratio is $\overline{\rho}_L/\overline{\rho}_H = 0.138$.

Spacing	D[ln $\overline{L}$]/D$\overline{t}$	% Increase over Corresponding Single Jet Case
4.0	0.015	7
3.0	0.010*	—
2.5	0.012*	—

* These data are discounted because of probable resolution losses. See text below.

Table 8.8 - Stretching rates for the horizontal jet trios

The results for this case follow the pattern established for the horizontal jet pair case. As the spacing is decreased from infinity, the stretching rate first increases slightly, then (artificially) decreases due to resolution losses, then again increases as entrainment becomes so strong that it overwhelms the resolution losses.

At spacing=4, note that the increase in stretching for the trio is considerably less than that for the pair of jets. This is due to the presence of a second upstream vortical structure, which offsets the entrainment of the middle structure by the downstream one (*c.f.* Chapter 7, Section 4).

• Symmetric Vertical Jet Pairs

Table 8.9 shows the computed stretching rates for the symmetric vertical jet pairs. The Mach number is M=1.1 and the light/heavy gas density ratio is $\overline{\rho}_L/\overline{\rho}_H = 0.138$.

Spacing	D[ln $\overline{L}$]/D$\overline{t}$	% Increase over Corresponding Single Jet Case
8.0	0.014	0
6.0	0.015	7
4.0	0.015	7
3.0	0.018	29
2.5	0.018	29

Table 8.9 - Stretching rates for the symmetric vertical jet pairs

As the vortex spacing is decreased, mixing rates increase in a slow, steady trend (the apparent piecewise constant character of the stretching rates is a consequence of the uncertainties in their determination). The increase in stretching occurs primarily in the inner tails, which experience greater induced motion because of their close proximity to the image vortex pair just across the centerline. These stretching rate increases are comparable to those of the horizontal jet pairs at the same Mach number (Table 8.7)

• Asymmetric Vertical Jet Pairs

Table 8.10 shows the computed stretching rates for the asymmetric jet pairs. The light/heavy gas density ratio is $\overline{\rho}_L/\overline{\rho}_H = 0.138$.

M	Jet Radii	D[ln $\overline{L}$]/D$\overline{t}$	% Increase over Corresponding Single Jet Case
1.1	(0.95, 1.05)	0.014	0
2.0	(0.90, 1.10)	0.087	2

Table 8.10 - Stretching rates for the asymmetric vertical jet pairs

In the case of low Mach number and weak asymmetry (M=1.1 and $\Delta\overline{R} = \pm 5\%$), the stretching rate is the same as the canonical single jet. Even with a strong Mach number and moderate asymmetry (M=2 and $\Delta\overline{R} = \pm 10\%$), the stretching rate is negligibly higher than the canonical single jet case.

• Equilateral Jet Trios

Table 8.11 shows the computed stretching rates for the equilateral jet trios. The light/heavy gas density ratio is $\overline{\rho}_L/\overline{\rho}_H = 0.138$.

M	D[ln $\overline{L}$]/D$\tilde{t}$	% Increase over Corresponding Single Jet Case
1.1	0.015	7
1.2	0.025	4
1.5	0.056	12
2.0	0.136	60

Table 8.11 - Stretching rates for the equilateral jet trios

Just as in the horizontal jet cases, the stretching rate is increased due to entrainment. Each of the three jets forms a vortex pair, the upper vortex from the centerline jet is entrained into the vortex pair from the upper jet, and the lower vortex from the centerline jet is entrained into the vortex pair from the lower jet. The stretching is increased significantly from that of a single jet, and the greater the Mach number, the greater the increase in stretching.

• Experimental Data

As a check on the accuracy of these stretching measures, one may compare against data from the experiments of Haas and Jacobs.

i) Haas

Haas (1984, 1987) did not explicitly tabulate mass fraction contour lengths, so a direct comparison of f=0.05 levels is not possible. However, it is possible to digitize the perimeters of his published shadowgraph pictures, and thus to determine their contour lengths as a function of time. Because the shadowgraphs represent information that is integrated along the optical path, one can not differentiate among different contour levels. One can only assume that the shadowgraph perimeter corresponds to some averaged value of f, say f_{avg}, and that this value remains the same for all the shadowgraphs. Without knowing the exact value of f_{avg}, the best recourse is to assume it represents the median value, *i.e.*, f=0.5. Therefore, the stretching rates determined from Haas' shadowgraphs are compared to stretching rates of the f=0.5 contours of the present computations.

Furthermore, the determination of D/Dt[ln ($\overline{L}$)] is a line-fitting process and the accuracy of this process depends on having many points. Thus it is necessary to use Haas' entire time sequence of data, even though diffusive processes are unavoidably involved at intermediate and late times. Therefore, the comparable stretching rate from the computations is no longer the critical value as defined in Section 1, but rather the best straight-line value past the critical point (see Figure 8.4). As mentioned earlier, this value depends on matching the numerical diffusion of the computation to the real flow, and one expects, at best, only qualitative agreement. Haas' stretching rates were found to be:

M=1.085, $D[\ln \overline{L}]/D\bar{t} = 0.026$

M=1.22, $D[\ln \overline{L}]/D\bar{t} = 0.080$

The f=0.5 stretching rates for the comparable single jet computations are:

M=1.1, $D[\ln \overline{L}]/D\bar{t} = 0.033$

M=1.2, $D[\ln \overline{L}]/D\bar{t} = 0.073$

The agreement is surprisingly good, reinforcing the argument that the numerical diffusion, though inexact, is nevertheless a reasonable approximation to that in the real flow.

ii) Jacobs

Jacobs' data were taken with a laser-induced-fluorescence technique, and there were considerable uncertainties in calibrating the light variation across the laser sheet in any single run (a single time in a sequence), as well as the variation at different times. Furthermore, the CID camera used for data acquisition had a relatively poor signal-to-noise ratio at the lower intensity levels (corresponding to low mass fraction levels). For these reasons, the highest confidence is associated with the median intensity level, again corresponding to f=0.5. Jacobs experiments consisted of two M=1.093 runs, one near the jet exit and one farther away, and also a 'far' run at M=1.22. Unknown (and hence uncorrectable) variations in the camera angle in the M=1.093 'near' run precludes the use of those data, and an insufficient number of data points (time values) in the M=1.22 run preclude the use of those data.

For the remaining case, the M=1.093 'far' run (Figure 6.3), the stretching rate is found to be 0.034, which agrees surprisingly well with the corresponding Haas and Yang values (0.026 and 0.033).

• Summary

In summary, the stretching rate can be increased by variation of the fluid mechanical parameters and/or by variation of geometry. The stronger the incident shock or the initial density difference, the larger the stretching rate. A sharper initial interface also results in an increase in stretching rate. Sinusoidal perturbations at the boundary do not increase the stretching, because the effects at the upstream and downstream edges cancel. Elliptical elongation normal to the flow increases the stretching, while elongation parallel to the flow decreases the stretching. However, these are both very minor effects. The stretching is also increased when a reflected shock hits the vortex pair formed by the incident shock. The sooner the reflected shock hits, the better. Horizontal jet pairs, horizontal jet trios, and equilateral triangle configurations all show a pronounced increase in stretching rate, due to the effects of entrainment. To a lesser extent, symmetric vertical jet pairs also show an increase in stretching rate. The effect of an asymmetry in a vertical pair of jets is negligible. Finally, the computed stretching rates, after diffusive processes become important, agree surprisingly well with measured values for comparable experimental flows.

8.2 Comparison with a Three-Dimensional Steady Flow

8.2.1 Qualitative

This section investigates the correspondence between the idealized studies of the present investigation and a more practical, design-oriented application which incorporates the same phenomenon of shock-induced vortical flow. These are current parallel research efforts here at Caltech, aimed at understanding the principles behind, and applications of, shock-induced mixing.

Waitz (1991) has performed experimental and computational investigations of a contoured wall injector for a scramjet combustion chamber. His general injector configuration is shown in Figure 8.5. "The injector consists of alternate compression ramps and expansion troughs, of 5 degrees each, for the. . .Mach 6 air stream. The end of each ramp houses a nozzle discharging helium (hydrogen) at an appropriate pressure level. At the same streamwise location the flow in each trough is turned back to the free stream direction, forming a weak oblique shock. This shock moves away from the combustor wall and under the helium jet, thus providing a shock impingement on the light gas stream. . .and lifting the helium flow away from the combustor wall and into the air stream."[22]

In general, Waitz's injector has two mechanisms of vorticity generation. The first is shock-generated vorticity generated by passage of the columns of helium between the oblique shocks formed as the flow between the ramps was compressed in the exit plane. The second mechanism is ramp-generated vorticity associated with the migration of fluid from the high pressure regions above the ramps to the lower pressure regions in the troughs.[23] One goal of Waitz's work was to examine the effects of these two vorticity generation mechanisms separately. To that end, he performed computations for two generic injector designs that are subcases of the general injector design. The first which he called the 'all-shock geometry,' consisted of an injector with ramps parallel to the combustor wall, all the way to minus infinity. This geometry produced only shock-generated vorticity. The second, which he called the 'no-shock' geometry, consisted of an injector with the combustor wall everywhere coplanar to the trough. This geometry produced only ramp-generated vorticity. Waitz concluded that these two mechanisms generated vorticity of comparable magnitude, but that the all-shock geometry ". . .[is] more desirable from a [wall] heating standpoint. . .[and also that] greater mixing was afforded for lower losses."[24]

Figure 8.6 shows one of Waitz's computed all-shock flows. The front and rear edges of the graph are planes of symmetry that separate this flow from identical flows due to identical injectors on either side. The vortical structure results as a consequence of the same type of baroclinic vorticity

[22] Marble(1990), p. 4.
[23] Waitz (1991), Chapter 6.
[24] *ibid.*

generation as in the present study, with the spatial development of the vortices in the steady, 3-D flow being analogous to the temporal development in the time-dependent, 2-D flow.

Note the general similarities between Waitz's flow and the canonical case of a single circular jet in the present study. The similarities become even more apparent when the initial circular jet of the present study is replaced by a rectangular jet. Figure 8.7 shows a 2-D computation corresponding to Figure 8.6.

The geometries are matched in the following sense: the upper and lower walls of the 2-D flow correspond to the planes of symmetry in the 3-D flow, the left end of the 2-D flow is a wall corresponding to the combustor wall downstream of the injector, and the open right end of the 2-D flow corresponds to the open top of the injector. The height of the rectangular jet in the 2-D flow corresponds to the width of the injector in the 3-D flow.

In addition to geometry, fluid mechanical parameters are also matched: the light/heavy gas density ratio, and pressure and density jumps across the shocks are exactly the same: $\overline{\rho}_L/\overline{\rho}_H = 0.082$, $\overline{p}_2/\overline{p}_1 = 1.949$, and $\overline{\rho}_2/\overline{\rho}_1 = 1.597$.

Comparison of these plots shows good agreement between the flows, especially up to times $\overline{t}$=12 in the 2-D case. This is evidence that the present studies, although more idealized than the flow in an actual injector, do indeed capture the main phenomena of interest. Beyond $\overline{t}$=12, small differences appear in the details of the flows, most notably at the downstream end of the 2-D structure and at the uppermost portion of the 3-D structure. This is most likely a consequence of the different amounts of dissipation in the two flows. The 3-D flow has higher viscous and diffusive terms, so its flow is much more smeared out, at late times, than the 2-D flow. Nevertheless, the general features are still fairly well correlated.

The evolution of the flow is qualitatively different from the canonical circular jet, so some discussion of the details is warranted. A schematic of the interaction is shown in Figure 8.8. Along the top edge, the density gradient and pressure gradients are perpendicular, and counterclockwise vorticity is generated as shown in Figure 8.8(a). As usual, the flow is symmetric about the horizontal centerline. The single arrows indicate induced motions due to both the upper and lower half plane vorticities. The broad double arrows indicate the net effect. Upstream (U), there is a downward induced velocity from the upper half plane vorticity and a rightward and slightly upward induced velocity from the lower half plane vorticity. The net velocity is rightward and downward. Downstream (D), there is an upward induced velocity from the upper half plane vorticity and a rightward and slightly downward induced velocity from the lower half plane vorticity. The net velocity is rightward and upward. As time goes on, the rectangular jet is deformed into a trapezoidal shape (Fig. 8.8(b)). In addition, at the centerline, the upstream face of the jet experiences a net downstream motion which which tends to separate the upper and lower halves into a distinct pair of lobes (Fig. 8.8(c)).

The late-time history (refer to the contour plots of Fig. 8.7) shows consolidation of the vorticity into the two lobes into an organized vortex pair, with pinching off of tails of low-vorticity fluid in a similar manner as the circular jet case. The rectangular jet has a larger streamwise extent, and different initial streamwise distribution of vorticity, than does the circular jet. Thus the detailed features of the developing structure are different. However, the clear dominance of the developing vortex core is still apparent.

8.2.2 Quantitative

The 2-D and 3-D shock waves are shown schematically in Figures 8.9(a),(b). The corresponding equations for pressure and density jumps across the shock are given below.

2-D:

$$\frac{p_2}{p_1} = 1 + \frac{2\gamma_1}{\gamma_1 + 1}(M_{2-D}^2 - 1)$$

$$\frac{\rho_2}{\rho_1} = \frac{(\gamma_1 + 1)M_{2-D}^2}{(\gamma_1 - 1)M_{2-D}^2 + 2}$$

3-D:

$$M_{3-D}^2 = \frac{2cos(\beta - \delta)}{(sin\beta)[sin(2\beta - \delta) - \gamma_1 sin\delta]}$$

$$\frac{p_2}{p_1} = 1 + \frac{2\gamma_1}{\gamma_1 + 1}(M_{3-D}^2 sin^2\beta - 1)$$

$$\frac{\rho_2}{\rho_1} = \frac{(\gamma_1 + 1)M_{3-D}^2 sin^2\beta}{(\gamma_1 - 1)M_{3-D}^2 sin^2\beta + 2}$$

Correspondence of the pressure and density jumps requires that $M_{2-D} = M_{3-D}\ \sin\beta$, where β is determined from M_{3-D} and the turning angle δ. Quantitative comparison between the 2-D and 3-D flows requires the association of time in the 2-D unsteady flow with downstream distance in the 3-D steady flow. In that case, a velocity $(d\bar{x}/d\bar{t})_{2-D}$ may be related to a corresponding slope $(d\bar{z}/d\bar{x})_{3-D}$ by the simple relation

$$(d\bar{x}/d\bar{t})_{2-D} = m(d\bar{z}/d\bar{x})_{3-D},$$

where m is a conversion factor that is completely determined from the matching process: since the pressure and density jumps have been matched across the shock, consistency dictates that the motion of the shock be matched as well. Therefore, m must satisfy the relation

$$M_{2-D} = m\ tan(\beta - \delta)$$

or

$$m = \frac{M_{2-D}}{tan(\beta - \delta)}$$

In the 2-D/3-D comparison shown earlier, $M_{3-D} = 6$ and $\delta = tan^{-1}(1/12)$, so that $\beta = 0.2263$ rad, $M_{2-D} = 1.346$, and m = 9.34.

With m thus determined, one can compare the 2-D trajectory of the center of mass fraction and the 3-D jet lift-off:

$$(d\bar{x}/d\bar{t})_{2-D} = 0.18$$

and

$$m(d\bar{z}/d\bar{x})_{3-D} = (9.34)(0.017) = 0.16$$

The agreement is very good, indicating a trajectory correspondence that is in agreement with the matching of geometry, light/heavy gas density ratio, shock pressure jump, and shock density jump. Together with the observed qualitative agreement between the developing 2-D and 3-D structures, this reinforces the belief that the 2-D unsteady flow can be directly associated with a corresponding 3-D steady flow.

Chapter 9 - Conclusions

The motivation for shock-induced vortical flow is the problem of achieving rapid and efficient mixing of fuel and oxidizer in a supersonic combustion ramjet engine. This is a complicated three dimensional problem, but its primary features can be abstracted to a two-dimensional flow. As a first step, the flow was reduced to a canonical form which illustrated the fundamental features of the interaction. This understanding then allowed consideration of more sophisticated flows likely to be encountered in real applications.

The canonical shock-induced vortical flow was the two-dimensional unsteady passage of a shock wave over a single circular inhomogeneity ('jet') of light gas. The shock wave provided an upstream pointing pressure gradient, and the light/heavy interface provided a radially outward density gradient. The interaction of these gradients generated vorticity in accordance with the vorticity production term of the vorticity equation

$$\frac{D\underline{\omega}}{Dt} = \frac{1}{\rho^2}(\underline{\nabla}\rho \times \underline{\nabla}p) + \cdots$$

This vorticity caused the jet to roll up into a kidney shape, counterclockwise in the upper half plane and clockwise in the lower half plane. As time went on, the structure evolved toward a vortex pair of finite core size. This vortex pair moved downstream relative to the ambient fluid due to the motion each vortex induced in the other. The velocity and circulation of this vortex pair were essentially constant throughout the evolution of the flow. Together with the late-time core spacing, these variables constituted a complete fluid mechanical description of the flow.

The governing equations were integrated for various initial conditions, and the above flow variables were tabulated from these computations. Independently of the computations, invariance principles for vortical flows were invoked to derive closed-form analytical models for the circulation and spacing. A model was also derived for the characteristic time of development. These models all agreed quite well with the computational results, except for the spacing model, which failed to capture the dependence on Mach number. In addition, a perturbation analysis was performed to describe the normalized velocity of the vortex pair on its two geometrical parameters: the ratio of vortex size to vortex spacing, and the ratio of vortex spacing to channel spacing. This model gave good agreement with the computations for a wide range of different initial conditions.

Besides the canonical flow, a number of geometrical variations were considered. These cases included sinusoidally perturbed jets, elliptical jets, and arrays of horizontal, vertical, and equilateral trio jets. The aim here was to examine the mixing characteristics of configurations that would be more representative of actual injectors. In quantifying mixing via these numerical simulations, the most reliable measure was just the asymptotic stretching rate at the point where either resolution

losses or diffusion losses first became important. This is consistent with the expectation that the best possible stretching of material lines is exponential.

The single jet shape perturbations did not significantly alter the mixing from the canonical single circular jet case. The only ways to significantly enhance mixing in the single jet case were to decrease the light/heavy gas density ratio, increase the shock strength, or reduce the initial interface thickness. Interestingly, the latter had little effect on the overall strength and motion of the vortex pair.

If a developing vortex pair was hit by a reflected shock, the mixing increased dramatically. Furthermore, the earlier the reflected shock hit, the better.

All the multiple jet configurations showed large increases in mixing, especially as the phenomenon of entrainment became important. In the case of a horizontal jet pair, the merger of the upstream vortex pair into the downstream vortex pair could be simply characterized by a critical ratio of spacing to diameter. Furthermore, this merging was about twice as critical as merging of a pair of like-signed isolated circular vortices.

All of the above results were for studies of two-dimensional unsteady flows, while real technological applications are more likely to be three dimensional and steady. It was argued that there exists a analogy between spatial development in the three-dimensional steady flow and temporal development in the two-dimensional unsteady flow that can be used to relate the two flows. This analogy was described mathematically, and used to construct an equivalent two-dimensional unsteady flow corresponding to another investigator's computation of a particular three-dimensional steady flow. The resulting flows agreed very well, both qualitatively as characterized by comparable stages of development, and quantitatively as characterized by comparable trajectories.

Appendix - A Similarity Solution for the Jet Mixing Layer

• Theoretical Formulation

Consider an axisymmetric jet, as shown in Figure A.1. The jet fluid is Helium and the ambient fluid is air. One seeks a solution for the concentration profile across the mixing layer at the edge of the jet, at a specified downstream distance from the orifice.

The flow is assumed to be laminar and at constant pressure. Furthermore, the mixing layer is assumed to be much smaller than the jet radius, so that a two-dimensional approximation may be used. A local (x,y) coordinate system is affixed to the jet as shown.

The governing equations conserve continuity, x-momentum, and species:

$$\frac{\partial}{\partial x}(\rho u) + \frac{\partial}{\partial y}(\rho v) = 0 \tag{1}$$

$$\rho\Big(u\frac{\partial u}{\partial x} + v\frac{\partial u}{\partial y}\Big) = \frac{\partial}{\partial y}\Big(\rho\nu\frac{\partial u}{\partial y}\Big) \tag{2}$$

$$\rho\Big(u\frac{\partial f}{\partial x} + v\frac{\partial f}{\partial y}\Big) = \frac{\partial}{\partial y}\Big(\rho\mathcal{D}\frac{\partial f}{\partial y}\Big) \tag{3}$$

where the density, ρ, is related to the mass fraction, f, by

$$\rho = f\ \rho_{He} + (1-f)\ \rho_{Air}. \tag{4}$$

The initial conditions are

$$eqalignu(x,y) \rightarrow \begin{cases} \Omega y, & y > 0 \\ 0, & y < 0 \end{cases} \quad \text{and} \quad f(x,y) = \begin{cases} 1, & y > 0 \\ 0, & y < 0 \end{cases}. \tag{5}$$

Note that the velocity is approximated by its linear portion, which is valid near the edge of the jet. The flow at the base of the jet is assumed to be fully developed and laminar, for which

$$u(y) = -\frac{2Q}{\pi R_0^4}(y^2 - 2yR_0),$$

where Q is the volumetric flow rate and R_0 is the radius. Under these conditions,

$$\Omega = \frac{4Q}{\pi R_0^3}.$$

The boundary conditions are

$$u(x,y) \rightarrow \begin{cases} \Omega y, & y \rightarrow +\infty \\ 0, & y \rightarrow -\infty \end{cases} \quad \text{and} \quad f(x,y) = \begin{cases} 1, & y \rightarrow +\infty \\ 0, & y \rightarrow -\infty \end{cases}. \tag{6}$$

Introduce the Howarth Transformation

$$y_i = \int_0^y \frac{\rho}{\rho_{He}} dy \tag{7}$$

and change coordinates from (x,y) to (x,y_i). The derivatives are transformed as

$$\frac{\partial}{\partial x} \rightarrow \frac{\partial}{\partial x} + \frac{\partial y_i}{\partial x}\frac{\partial}{\partial y_i} \quad \text{and} \quad \frac{\partial}{\partial y} \rightarrow \frac{\rho}{\rho_{He}}\frac{\partial}{\partial y_i} . \tag{8}$$

Also introduce a streamfunction ψ such that

$$\rho u = \rho_{He}\frac{\partial \psi}{\partial y} \quad \text{and} \quad \rho v = -\rho_{He}\frac{\partial \psi}{\partial x} . \tag{9}$$

In (x,y_i) coordinates, the streamfunction becomes

$$\rho u = \rho\frac{\partial \psi}{\partial y_i} \quad \text{and} \quad \rho v = -\rho_{He}\left(\frac{\partial \psi}{\partial x} + \frac{\partial y_i}{\partial x}\frac{\partial \psi}{\partial y_i}\right) . \tag{10}$$

The streamfunction identically satisfies the continuity equation (1), the momentum equation (2) is transformed to

$$\left(\frac{\partial \psi}{\partial y_i}\frac{\partial}{\partial x} - \frac{\partial \psi}{\partial x}\frac{\partial}{\partial y_i}\right)\frac{\partial \psi}{\partial y_i} = \nu_{He}\frac{\partial}{\partial y_i}\left(\frac{\rho^2 \nu}{\rho_{He}^2 \nu_{He}}\frac{\partial^2 \psi}{\partial y_i^2}\right) , \tag{11}$$

and the species equation (3) is transformed to

$$\left(\frac{\partial \psi}{\partial y_i}\frac{\partial}{\partial x} - \frac{\partial \psi}{\partial x}\frac{\partial}{\partial y_i}\right) f = \mathcal{D}_{He}\frac{\partial}{\partial y_i}\left(\frac{\rho^2 \mathcal{D}}{\rho_{He}^2 \mathcal{D}_{He}}\frac{\partial f}{\partial y_i}\right) . \tag{12}$$

The initial conditions are transformed to

$$\frac{\partial \psi}{\partial y_i}(0,y) = \begin{cases} \Omega y_i, & y_i > 0 \\ 0, & y_i < 0 \end{cases} \quad \text{and} \quad f(0,y) = \begin{cases} 1, & y_i > 0 \\ 0, & y_i < 0 \end{cases} . \tag{13}$$

A similarity variable, η, is defined by

$$\eta = y_i\left(\frac{\Omega}{3\nu_{He}x}\right)^{1/3} . \tag{14}$$

The streamfunction is transformed to a new function $F(\eta)$ such that

$$\psi = \Omega\left(\frac{3\nu_{He}x}{\Omega}\right)^{2/3} F(\eta) \tag{15}$$

and the mass fraction is transformed to a new function $G(\eta)$ such that

$$f = G(\eta). \tag{16}$$

Change coordinates from (x, y_i) to (x, η) and transform the derivatives as

$$\frac{\partial}{\partial x} \rightarrow \frac{\partial}{\partial x} - \frac{\eta}{3x}\frac{\partial}{\partial \eta} \quad \text{and} \quad \frac{\partial}{y_i} \rightarrow \left(\frac{\Omega}{3\nu_{He}x}\right)^{1/3}\frac{\partial}{\partial \eta} . \tag{17}$$

Then the momentum equation (11) becomes

$$\frac{d}{d\eta}\left(\frac{\rho^2 \nu}{\rho_{He}^2 \nu_{He}}F''\right) + 2FF'' - (F')^2 = 0 , \tag{18}$$

the species equation (12) becomes

$$\frac{\mathcal{D}_{He}}{\nu_{He}}\frac{d}{d\eta}\left(\frac{\rho^2\mathcal{D}}{\rho_{He}^2\mathcal{D}_{He}}G'\right)+2FG'=0, \tag{19}$$

and the boundary conditions become

$$F'(\eta)\rightarrow\begin{cases}\eta, & \eta\rightarrow+\infty\\ 0, & \eta\rightarrow-\infty\end{cases}\quad\text{and}\quad G(\eta)\rightarrow\begin{cases}1, & \eta\rightarrow+\infty\\ 0, & \eta\rightarrow-\infty\end{cases}. \tag{20}$$

Values for $\nu(G)$ and D(G), to be used in equations (18) and (19), are found in Baron (1959). Note that the density, ρ, is itself a function of G according to equation (4). Finally, one recovers the original variable y as a derivative of the twice-transformed variable η:

$$y'(\eta)=\left(\frac{3\nu_{He}x}{\Omega}\right)^{1/3}\left(\frac{\rho_{He}}{\rho_{Air}+(\rho_{He}-\rho_{Air})G}\right) \tag{21}$$

with boundary condition

$$y=0\quad at\quad \eta=0. \tag{22}$$

Equations (18), (19), and (21), along with the boundary conditions, can be solved for the variables F and G in terms of η. These may then be expressed as ψ and f in terms of y. The downstream distance, x, is an independent variable that specifies at the position of interest.

• Numerical Solution

The principal coupling is between F and G in equations (18) and (19). These equations constitute a pair of two-point boundary value problems which can be solved by a variety of numerical methods. One is the well-known method of relaxation.

This technique relies on successive iterations of an initial guess to solve the equations. The F- and G-equations are integrated as follows. One first computes initial approximations to the F- and G-profiles. Then one fixes the approximate G-profile, and relaxes the F-profile until it converges. Similarly, one fixes the approximate F-profile and relaxes the G-profile until it converges. These solutions are used as updated approximate solutions for F and G. The process is then continued until complete convergence in both variables is obtained.

The initial guesses are obtained using an integral method in which polynomial fits are made to the profiles. The procedure for the F-equation is briefly described below. Equation (18) can be written as

$$\frac{d}{d\eta}\left(\frac{\rho^2\nu}{\rho_{He}^2\nu_{He}}F''\right)+2FF''-(F')^2=0, \tag{23}$$

where $\rho^2\nu/\rho_{He}^2\nu_{He}(\eta)$ contains the terms that would normally depend on G. In the numerical solution of this equation, finite limits η_{min} and η_{max} are used to approximate -∞ and +∞, respectively. The appropriate boundary conditions are

$$F'(\eta_{min})\sim 0 \tag{24}$$

and

$$F'(\eta_{max}) \sim \eta \quad (and\ F''(\eta_{max}) \sim 1). \tag{25}$$

Also, since the absolute value of the streamfunction is arbitrary, one can set

$$F(0) = 0. \tag{26}$$

Equation (23) is integrated from $\eta = \eta_{min}$ to $\eta = 0$ and from $\eta = 0$ to η_{max}, where $F'(\eta)$ in each region is represented by a polynomial of the form $F'(\eta) = a\eta^2 + b\eta + c$. The coefficients are determined by the above boundary conditions and the additional constraint are that F'(η) and F''(η) must match at η=0. In performing the integration, it is necessary to know values of $\rho^2\nu/\rho_{He}^2\nu_{He}$ at the endpoints of the intervals. Clearly,

$$\frac{\rho^2\nu}{\rho_{He}^2\nu_{He}}(\eta_{min}) = \frac{\rho_{air}^2\nu_{air}}{\rho_{He}^2\nu_{He}}$$

and

$$\frac{\rho^2\nu}{\rho_{He}^2\nu_{He}}(\eta_{max}) = 1.$$

Then

$$\frac{\rho^2\nu}{\rho_{He}^2\nu_{He}}(0)$$

may be approximated as the mean of these two quantities.

The G-equation is fitted in exactly the same way. Once the initial guesses are made, the actual relaxation can proceed. There are many good standard relaxation algorithms available; the one used here is the SOLVDE subroutine of Press, *et al.* (1986).

The resulting solutions for F(η) and G(η) are shown in Figures A.2(a),(b). After these solutions are obtained, equation (21) is integrated for the original variable, y. Finally, the solutions for G(η) and y(η) are combined to give a solution for G(y), and this is substituted in equation (4) to give ρ(y). The resulting profile, for conditions corresponding to Jacobs' (1991) experiments* is shown in Figure A.3.

* R_0 = 5/16 " = 0.004 m, Q = 6.6 $\times 10^{-5}$ m^2/s, and T = 20 °C

References

Baron, J. and Scott, P. (1959), "The Laminar Diffusion Boundary Layer with External Flow Field Pressure Gradients," MIT Naval Supersonic Lab Technical Report 419.

Batchelor, G. K. (1952), "The Effect of Homogeneous Turbulence on Material Lines and Surfaces," Proc. Roy. Soc. London 213A, pp. 349-366.

Beigie, D., Leonard, A., and Wiggins, S. (1991) "A Global Study of Enhanced Stretching and Diffusion in Chaotic Tangles," Preliminary draft of a manuscript in preparation.

Boris, J. P. (1977), "SHAS2D - A Fully Compressible Hydrodynamics Code in Two Dimensions," Naval Research Laboratory Memorandum NRL-MR-2542.

Brouillette, M. (1989), "On the Interaction of Shock Waves with Contact Surfaces Between Gases of Different Densities," Ph.D. Thesis, California Institute of Technology.

Deem, G. S. and Zabusky, N. J. (1978), "Vortex Waves: Stationary 'V States,' Interactions, Recurrence, and Breaking," Phys. Rev. Lett. 40(13), pp. 859-862.

Haas, J.-F. (1984), "Interaction of Weak Shock Waves and Discrete Gas Inhomogeneities," Ph.D. Thesis, California Institute of Technology.

Haas, J.-F. and Sturtevant, B. (1987), "Interaction of Weak Shock Waves with Cylindrical and Spherical Gas Inhomogeneities," J. Fluid Mech. 181, pp. 41-76.

Hendricks, G. J. and Marble, F. E. (1991), "Shock Enhancement of Supersonic Combustion Processes," Preliminary draft of a manuscript in preparation.

Jacobs, J. W. (1991), "Shock Induced Mixing of a Light Gas Cylinder," Preliminary draft of a manuscript in preparation.

Marble, F. E., Hendricks, G. J., and Zukoski, E. E. (1987) "Progress toward Shock Enhancement of Supersonic Combustion Processes," AIAA Paper 87-1880.

Marble, F. E., Zukoski, E. E., Jacobs, J. W., Hendricks, G. J., and Waitz, I. A. (1990), "Shock Enhancement and Control of Hypersonic Mixing and Combustion," AIAA Paper 90-1981.

Meshkov, Y. Y. (1970), "Instability of a Shock Wave Accelerated Interface Between Two Gases," NASA TT F-13074.

Moore, D. W. and Pullin, D. I. (1987), "The Compressible Vortex Pair," J. Fluid Mech. 185, pp. 171-204.

Oran, E. S. and Boris, J. P. (1987), Numerical Simulation of Reactive Flow, Elsevier.

Oran, E. S. (1991), "LCPFCT - A Monotone Algorithm for Solving Continuity Equations," Preliminary draft of a manuscript in preparation.

Ottino, J. M. (1989), The Kinematics of Mixing: Stretching, Chaos, and Transport, Cambridge University Press.

Picone, J. M. and Boris, J. P. (1988), "Vorticity Generation by Shock Propagation Through Bubbles in a Gas," J. Fluid Mech. 189, pp. 23-51.

Picone, J. M., Oran, E.S., Boris, J. P. and Young, T. R. (1985), "Theory of Vorticity Generation by Shock Wave and Flame Interactions," in Dynamics of Shock Waves, Explosions, and Detonations, AIAA, pp. 429-448.

Pierrehumbert, R. T. (1980), "A Family of Steady, Translating Vortex Pairs with Distributed Vorticity," J. Fluid Mech. 99, pp. 129-144.

Press, W. H., Flannery, B. P., Teukolsky, S. A., and Vetterling, W. T. (1986), Numerical Recipes, Cambridge University Press.

Richtmyer, R. D. (1960), "Taylor Instability in Shock Acceleration of Compressible Fluids," Comm. Pure Appl. Math. XIII, pp. 291-319.

Roberts, K. V. and Christiansen, J. P. (1972), "Topics in Computational Fluid Mechanics," Comp. Phys. Comm. 3(Suppl.), pp. 14-32.

Rossow, V. J. (1977), "Convective Merging of Vortex Cores in Lift-Generated Wakes," J. Aircraft 14(3), pp. 283-290.

Rudinger, G. and Somers, L. M. (1960), "Behaviour of Small Regions of Different Gases Carried in Accelerated Gas Flows," J. Fluid Mech. 7, pp. 161-176.

Saffman, P. G. and Szeto, R. (1980), "Equilibrium Shapes of a Pair of Equal Uniform Vortices," Phys. Fluids 23(12), pp. 2339-2342.

Taylor, G. I. (1950), "The Instability of Liquid Surfaces when Accelerated in a Direction Perpendicular to their Planes (I)," Proc. Roy. Soc. London A 201, pp. 192-196.

Van Dyke, M. (1975), Perturbation Methods in Fluid Mechanics, Parabolic Press.

Waitz, I. A. (1991) "A Contoured Wall Injector for Hypervelocity Mixing Augmentation," Ph.D. Thesis, California Institute of Technology.

Wu, H. M., Overman, E. A., and Zabusky, N. J. (1984), "Steady-State Solutions of the Euler Equations in Two Dimensions: Rotating and Translating V-States with Limiting Cases. I. Numerical Algorithms and Results," J. Comp. Phys. 53, pp. 42-71.

Zabusky, N. J., Hughes, M. H., and Roberts, K. V. (1979), "Contour Dynamics for the Euler Equations in Two Dimensions," J. Comp. Phys. 30, pp. 96-106.

Figures

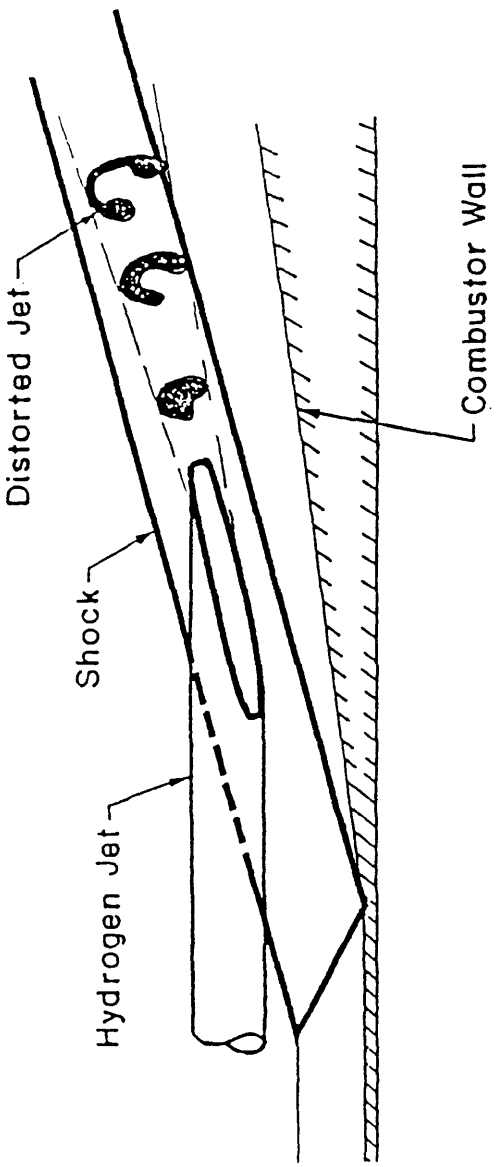

Figure 1.1 - Schematic of shock-induced mixing in a 3-D steady flow [Reproduced from Marble (1990), p.7].

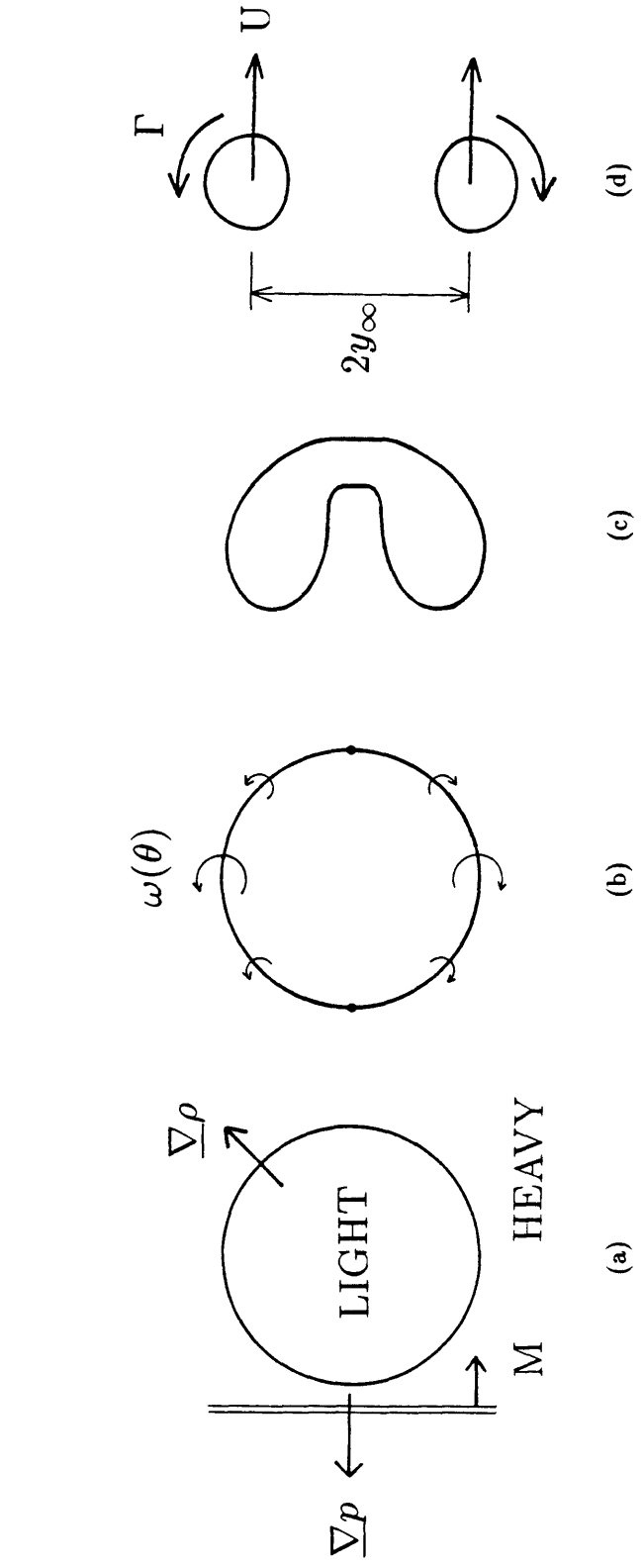

Figure 1.2 - 2-D unsteady flow of a shock wave over a single circular jet (a) $t = 0^-$, (b) Vorticity distribution at $t=0^+$, (c) Initial roll up, (d) Steady state vortex pair.

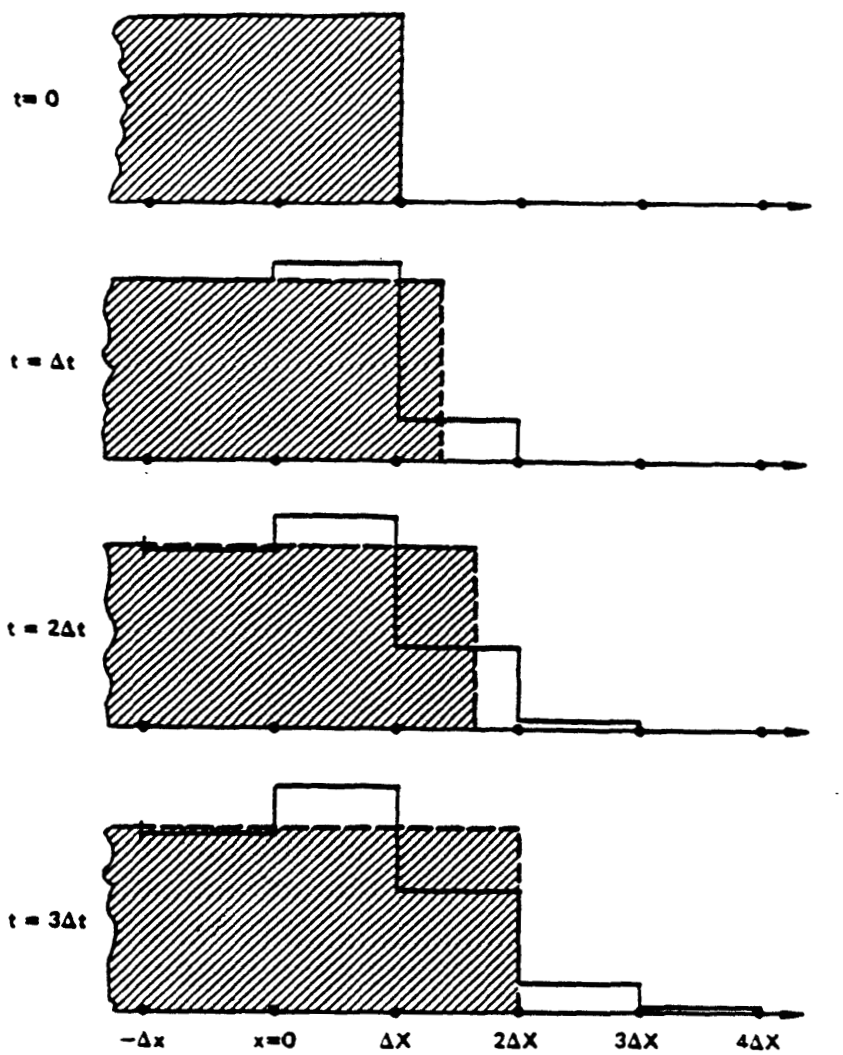

Figure 2.1 - Numerical representation of the propagation of a steep discontinuity.

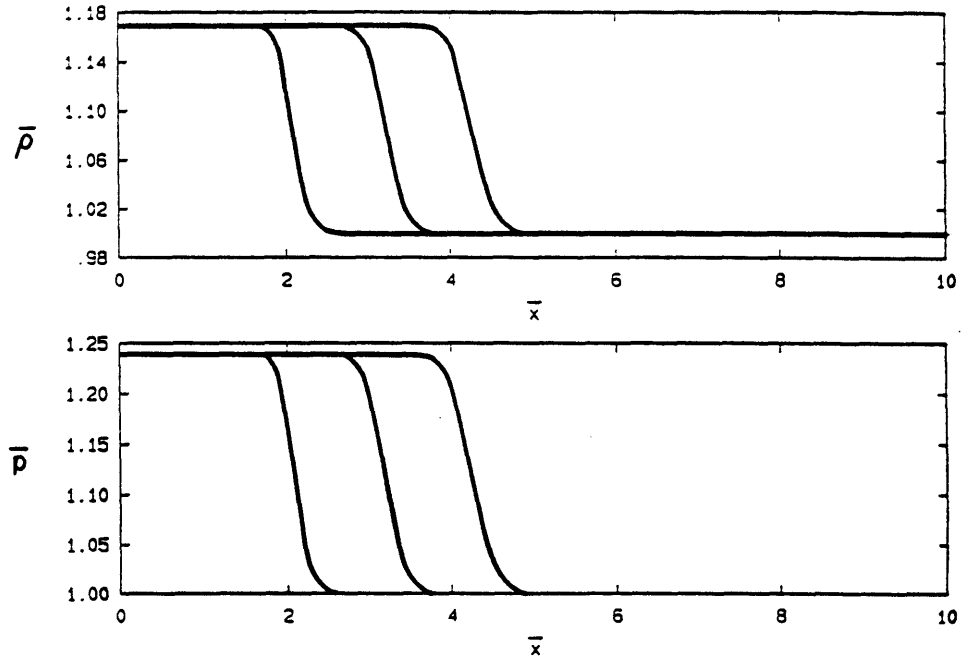

(a)

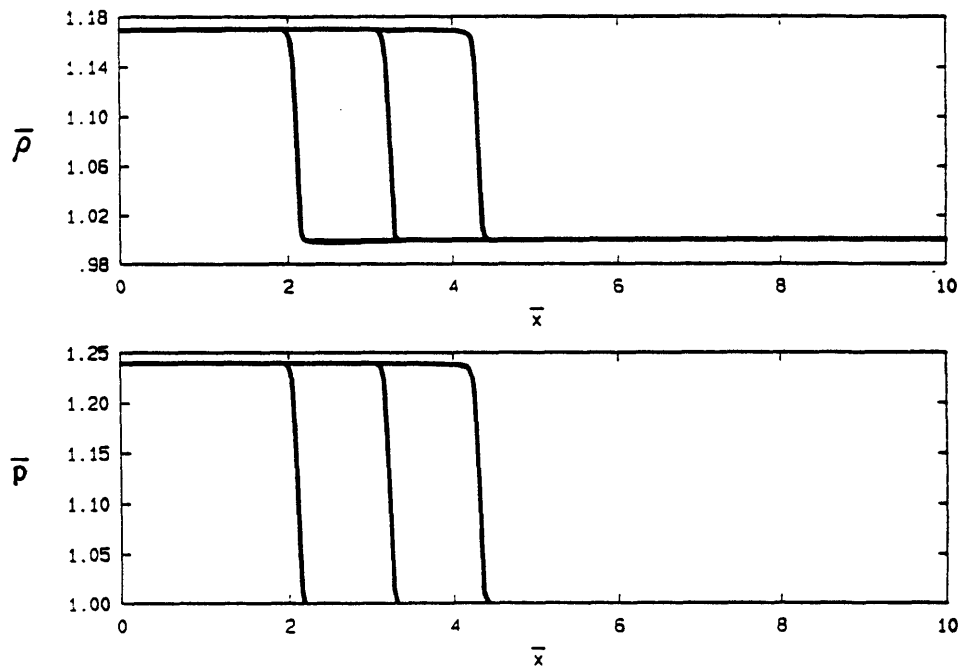

(b)

Figure 2.2 - Computation of a M=1.1 normal shock: (a) no antidiffusion, (b) full antidiffusion.

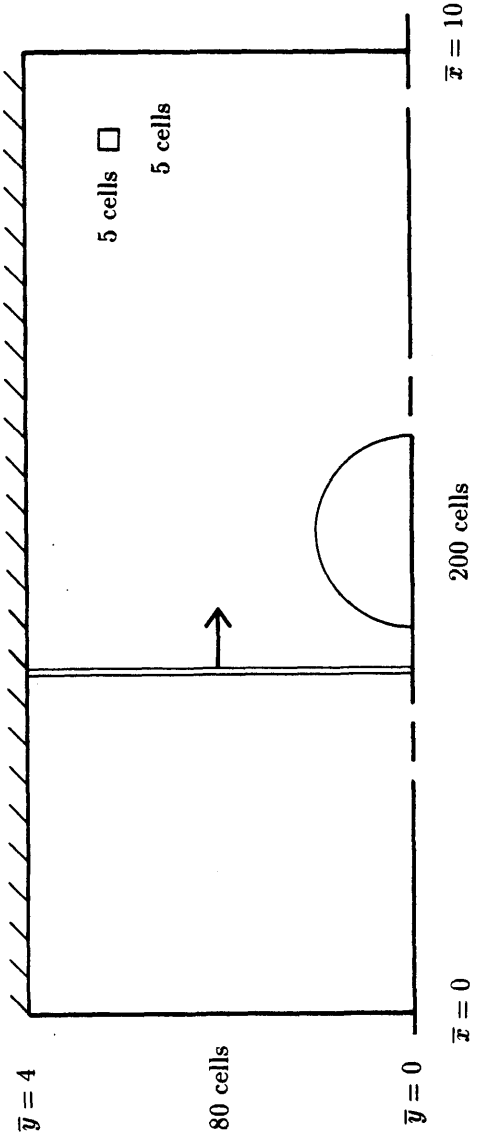

Figure 2.3 - A typical computational domain.

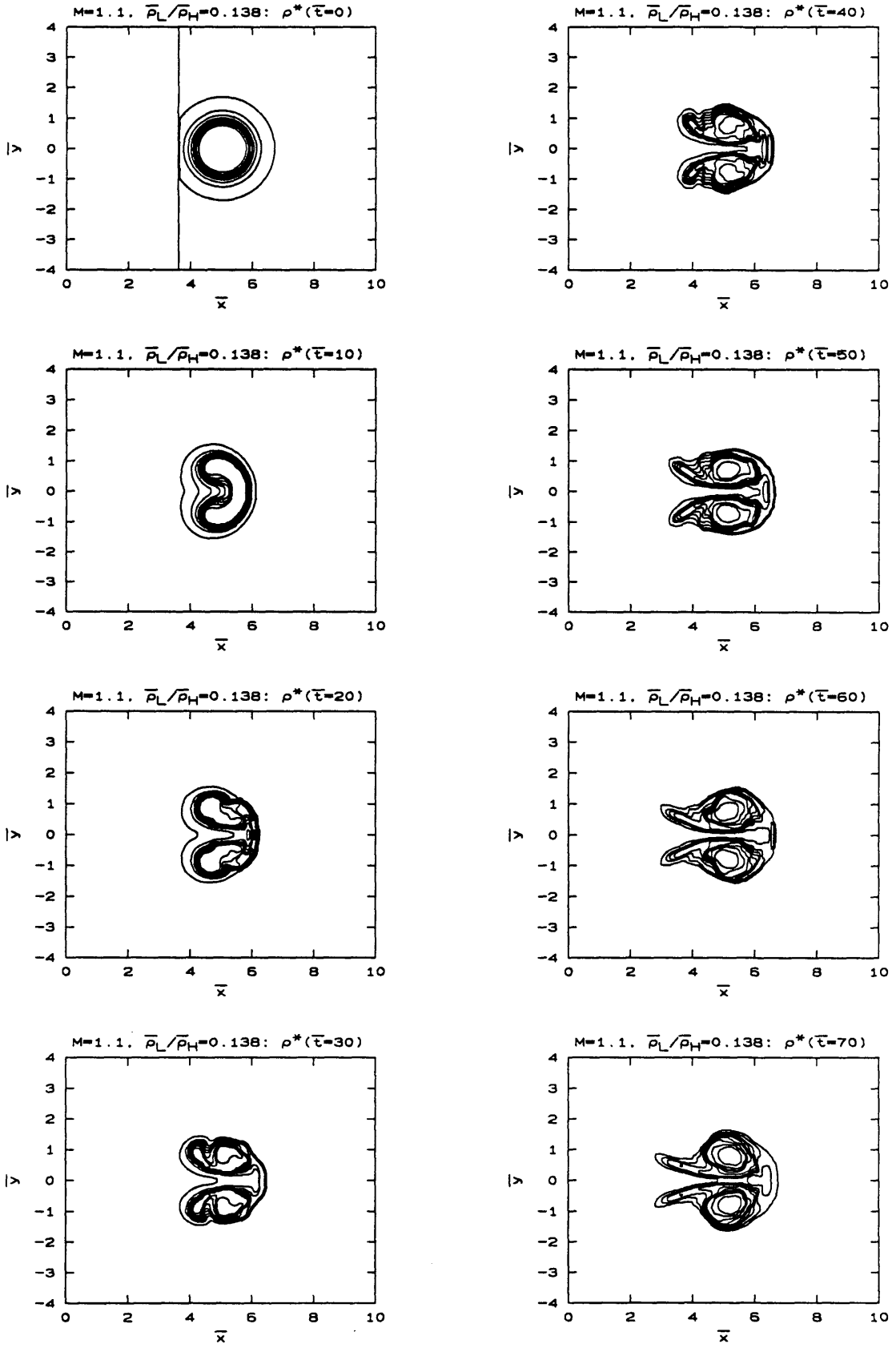

Figure 3.1 - Circular jet with M=1.1 and $\overline{\rho}_L/\overline{\rho}_H = 0.138$. Density contours.

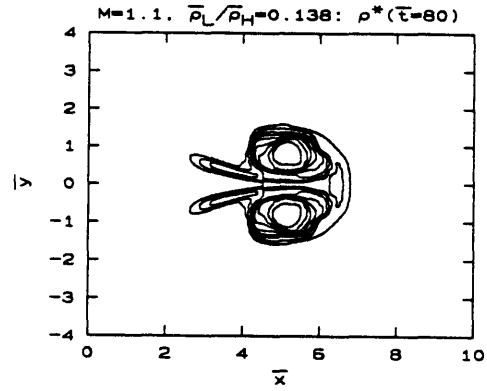
M=1.1. $\overline{\rho}_L/\overline{\rho}_H$=0.138: $\rho^*(\overline{t}$=80)
$\overline{y}$
$\overline{x}$

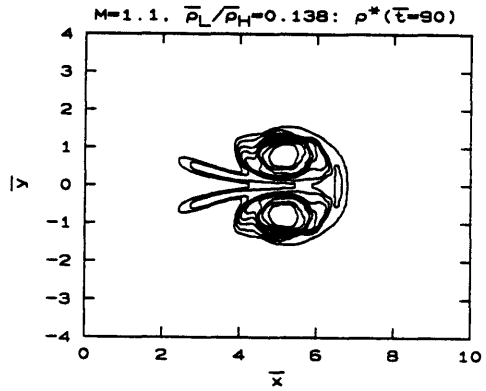
M=1.1. $\overline{\rho}_L/\overline{\rho}_H$=0.138: $\rho^*(\overline{t}$=90)
$\overline{y}$
$\overline{x}$

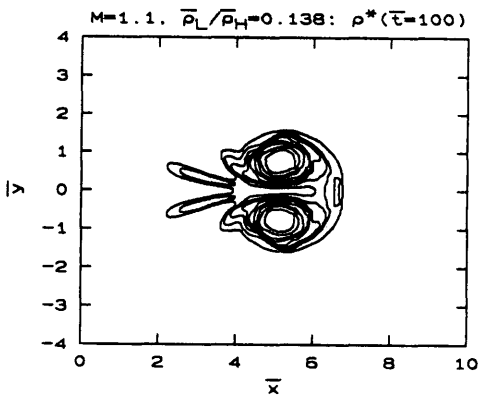
M=1.1. $\overline{\rho}_L/\overline{\rho}_H$=0.138: $\rho^*(\overline{t}$=100)
$\overline{y}$
$\overline{x}$

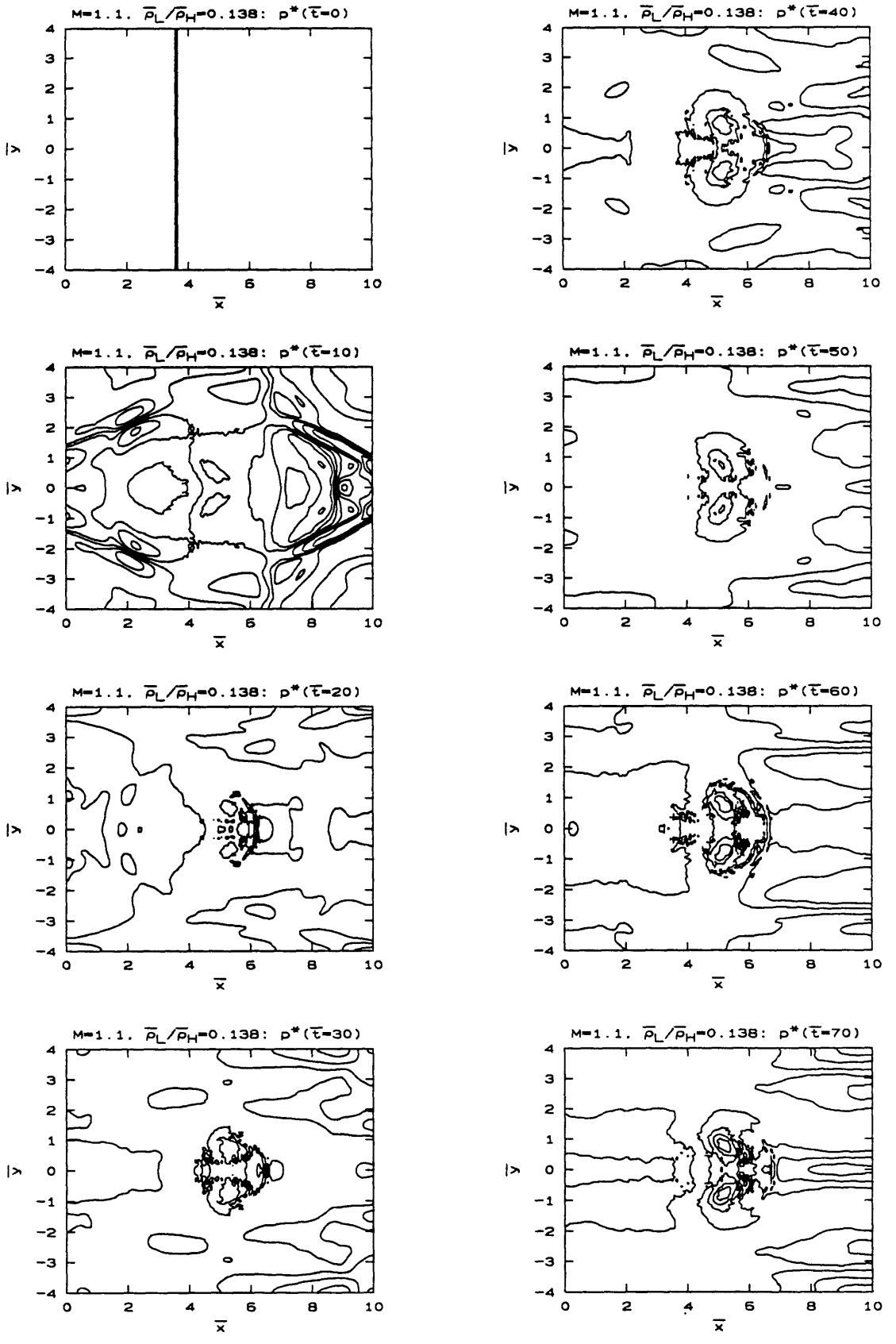

Figure 3.2 - Circular jet with M=1.1 and $\overline{\rho}_L/\overline{\rho}_H = 0.138$. Pressure contours.

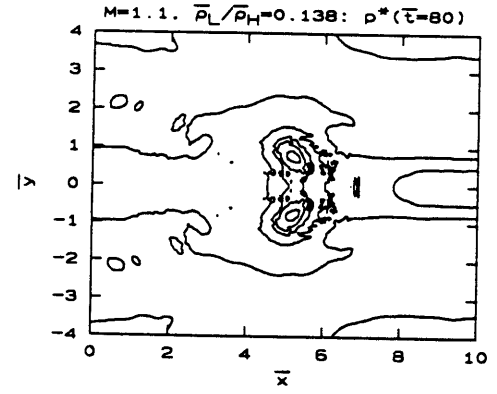
M=1.1. $\bar{\rho}_L/\bar{\rho}_H$=0.138: p*($\bar{t}$=80)
$\bar{y}$
$\bar{x}$

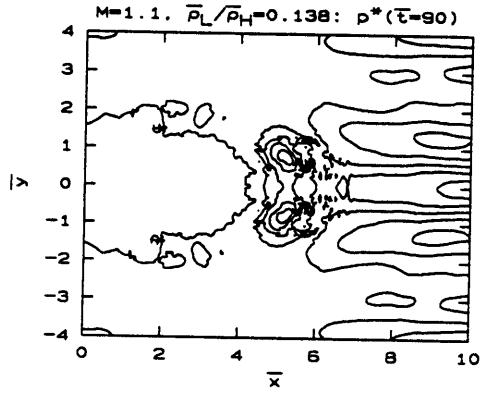
M=1.1. $\bar{\rho}_L/\bar{\rho}_H$=0.138: p*($\bar{t}$=90)
$\bar{y}$
$\bar{x}$

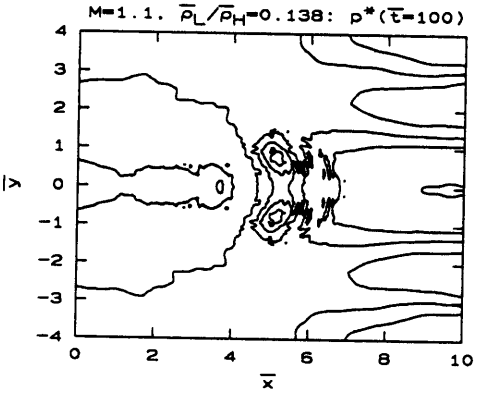
M=1.1. $\bar{\rho}_L/\bar{\rho}_H$=0.138: p*($\bar{t}$=100)
$\bar{y}$
$\bar{x}$

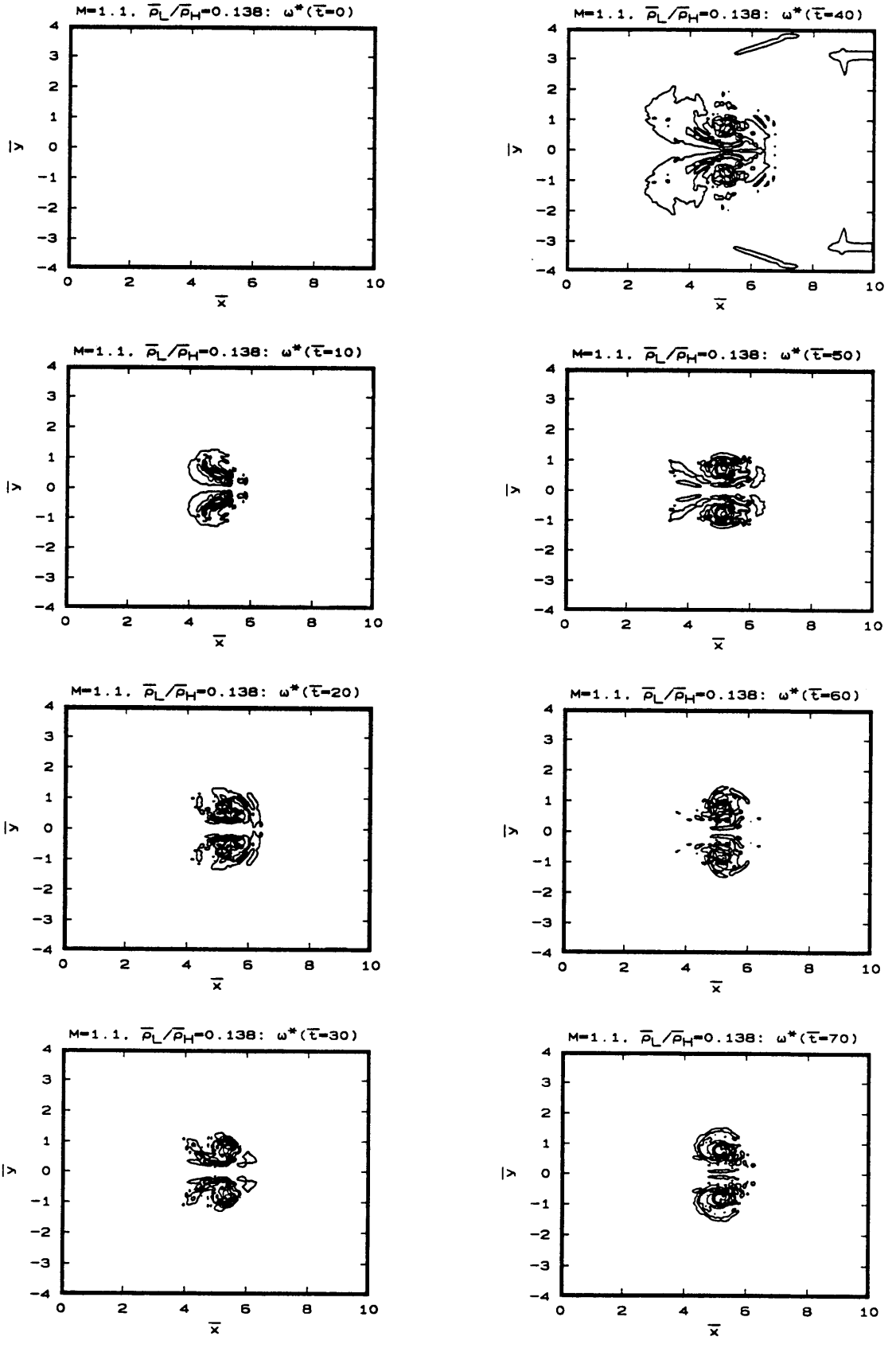

Figure 3.3 - Circular jet with M=1.1 and $\overline{\rho}_L/\overline{\rho}_H = 0.138$. Vorticity contours.

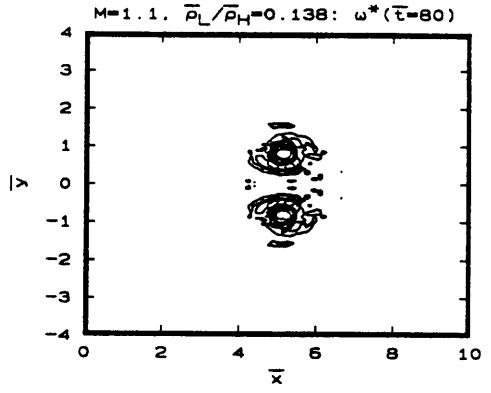
M=1.1. $\bar{\rho}_L/\bar{\rho}_H$=0.138: $\omega^*(\bar{t}$=80)
$\bar{y}$
$\bar{x}$

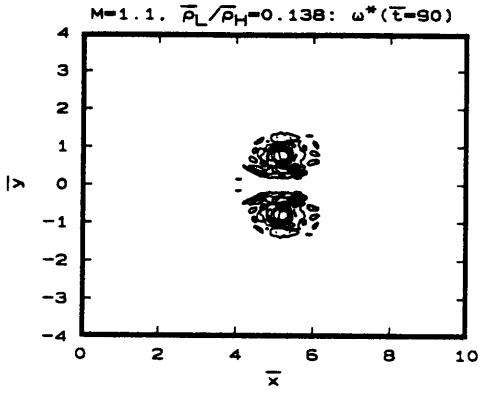
M=1.1. $\bar{\rho}_L/\bar{\rho}_H$=0.138: $\omega^*(\bar{t}$=90)
$\bar{y}$
$\bar{x}$

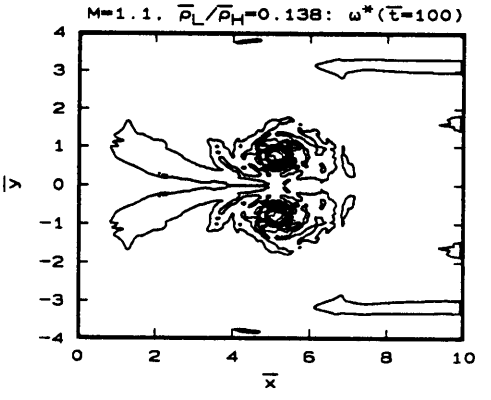
M=1.1. $\bar{\rho}_L/\bar{\rho}_H$=0.138: $\omega^*(\bar{t}$=100)
$\bar{y}$
$\bar{x}$

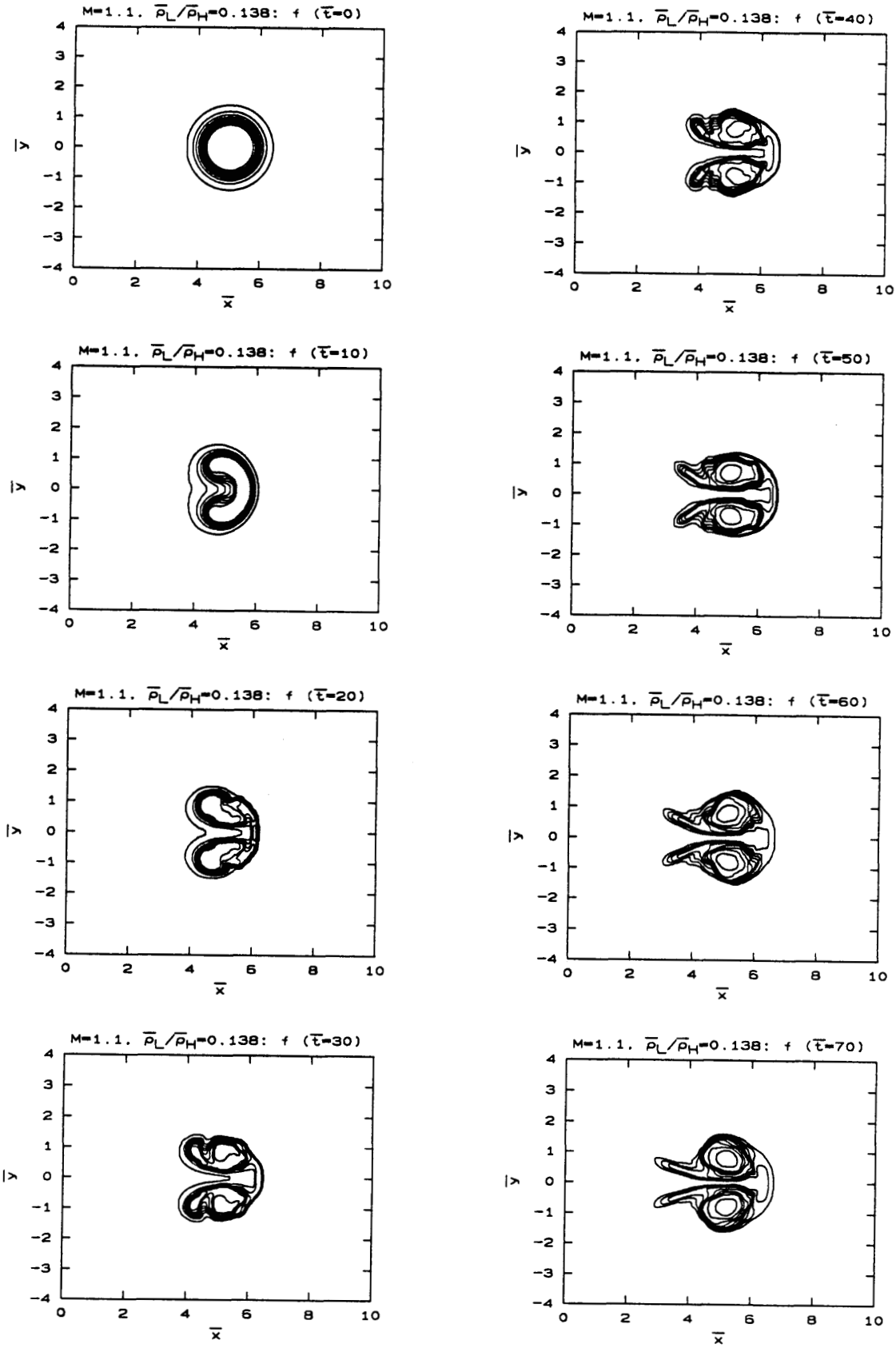

Figure 3.4 - Circular jet with M=1.1 and $\overline{\rho}_L/\overline{\rho}_H = 0.138$. Mass fraction contours.

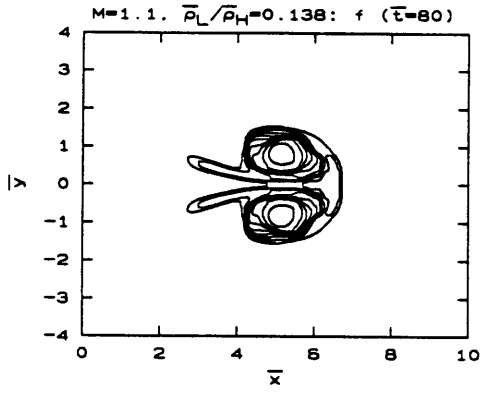
M=1.1. $\bar{\rho}_L/\bar{\rho}_H$=0.138: f ($\bar{t}$=80)
$\bar{y}$
$\bar{x}$

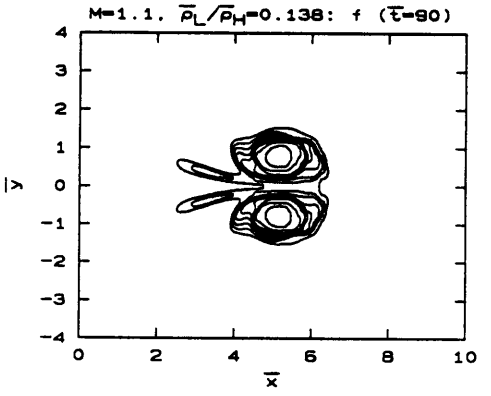
M=1.1. $\bar{\rho}_L/\bar{\rho}_H$=0.138: f ($\bar{t}$=90)
$\bar{y}$
$\bar{x}$

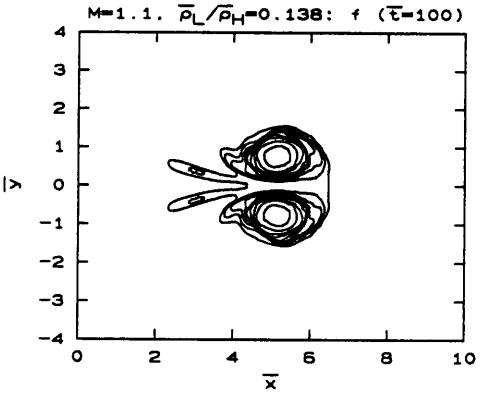
M=1.1. $\bar{\rho}_L/\bar{\rho}_H$=0.138: f ($\bar{t}$=100)
$\bar{y}$
$\bar{x}$

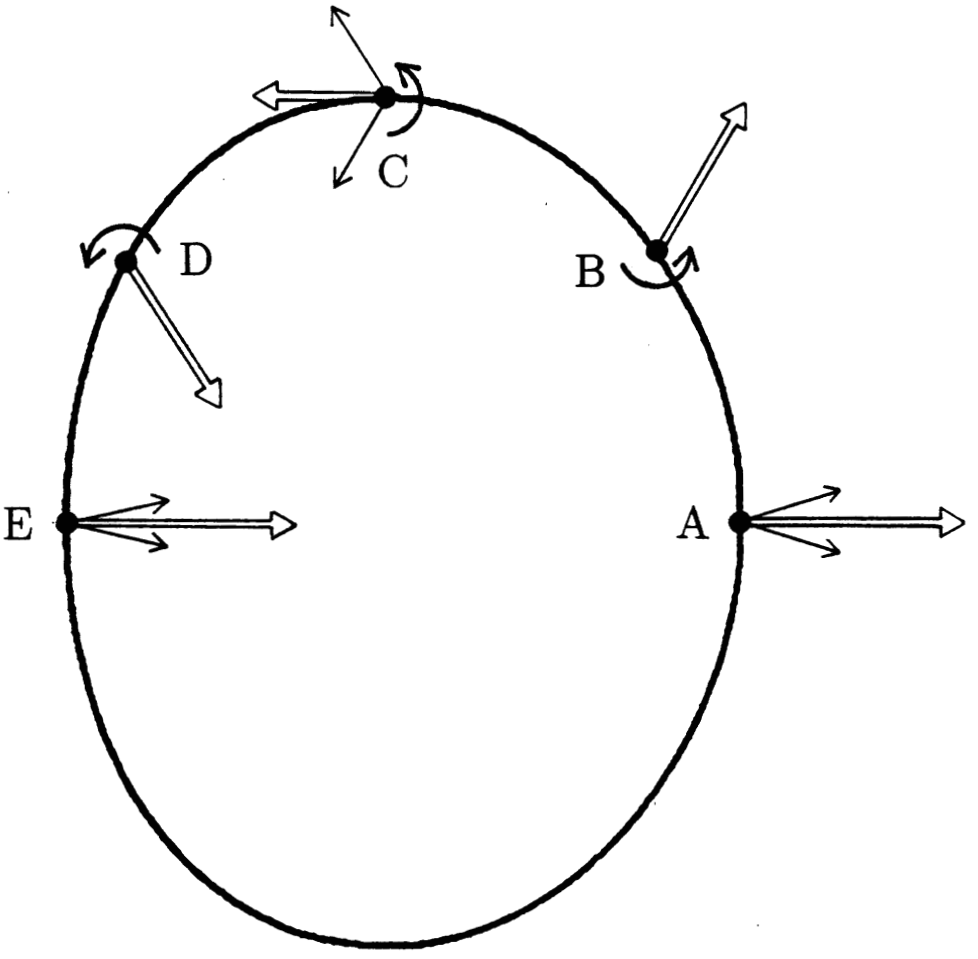

Figure 3.5 - Circular jet with M=1.1 and $\overline{\rho}_L/\overline{\rho}_H = 0.138$. Induced velocities at $\overline{t} = 0^+$.

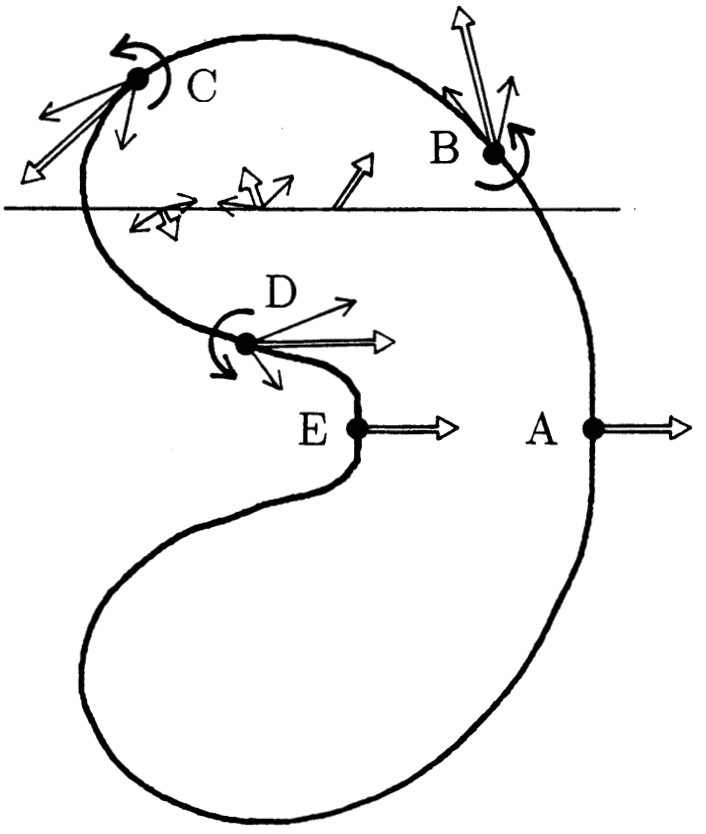

Figure 3.6 - Circular jet with M=1.1 and $\overline{\rho}_L/\overline{\rho}_H = 0.138$. Induced velocities at $\bar{t} = 10$.

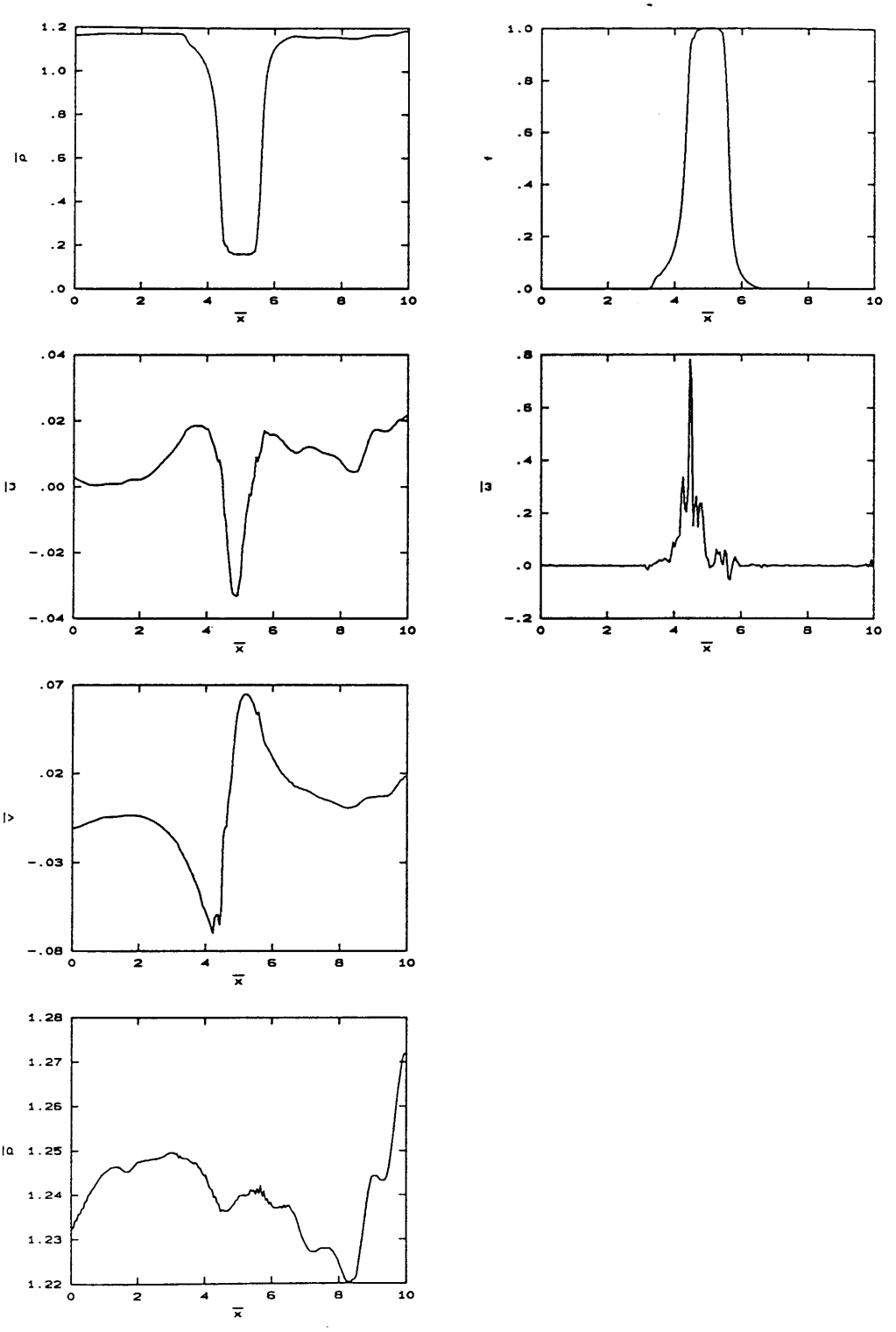

Figure 3.7 - Circular jet with M=1.1 and $\overline{\rho}_L/\overline{\rho}_H = 0.138$. Horizontal cuts through the approximate center of the structure at $\overline{t} = 10$.

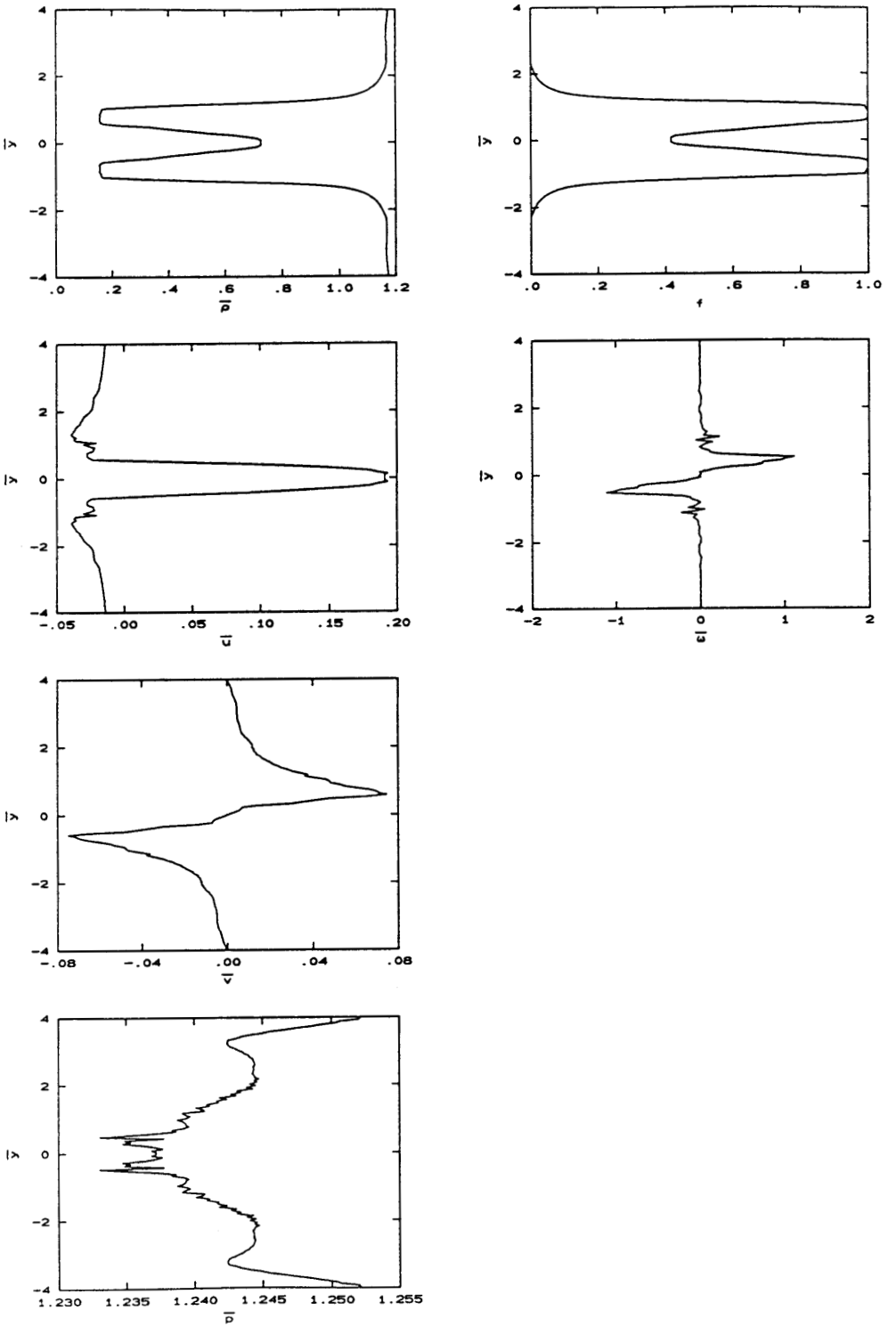

Figure 3.8 - Circular jet with M=1.1 and $\bar{\rho}_L/\bar{\rho}_H = 0.138$. Vertical cuts through the approximate center of the structure at $\bar{t} = 10$.

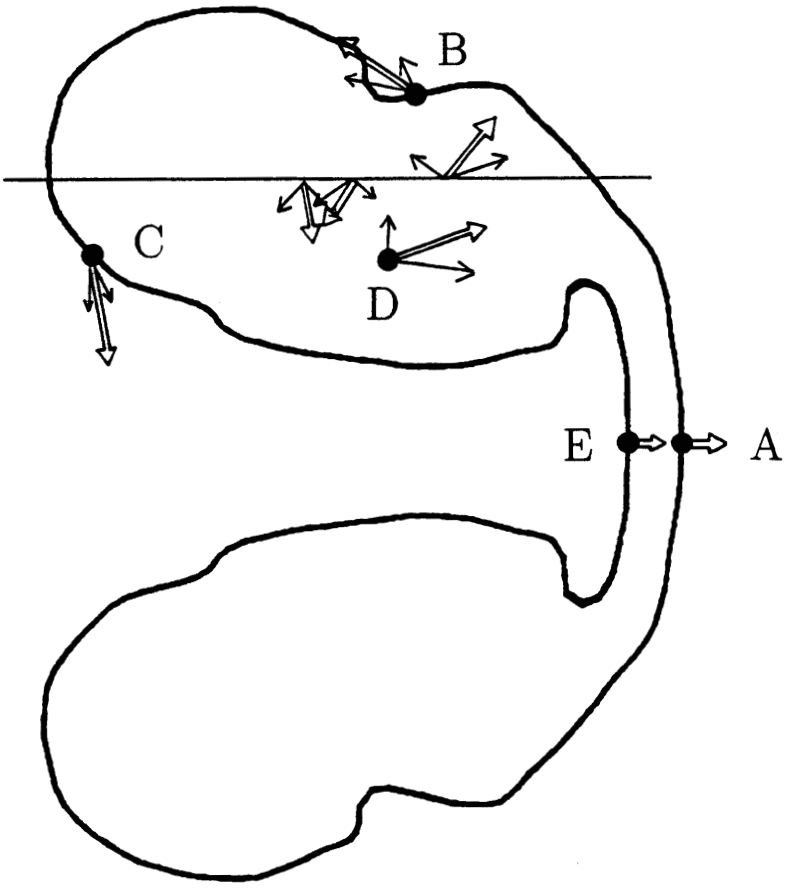

Figure 3.9 - Circular jet with M=1.1 and $\overline{\rho}_L/\overline{\rho}_H = 0.138$. Induced velocities at $\overline{t} = 20$.

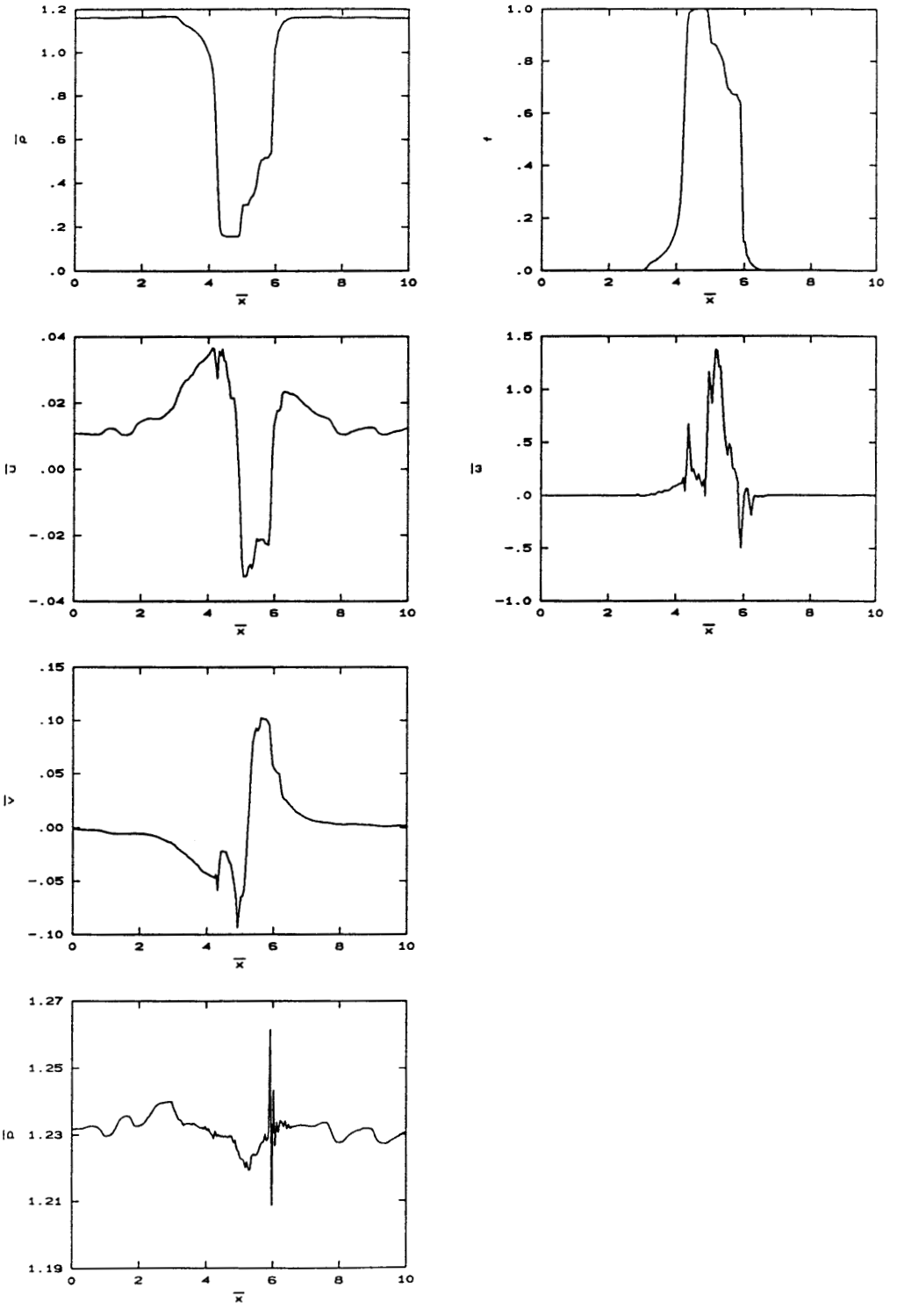

Figure 3.10 - Circular jet with M=1.1 and $\overline{\rho}_L/\overline{\rho}_H = 0.138$. Horizontal cuts through the approximate center of the structure at $\bar{t} = 20$.

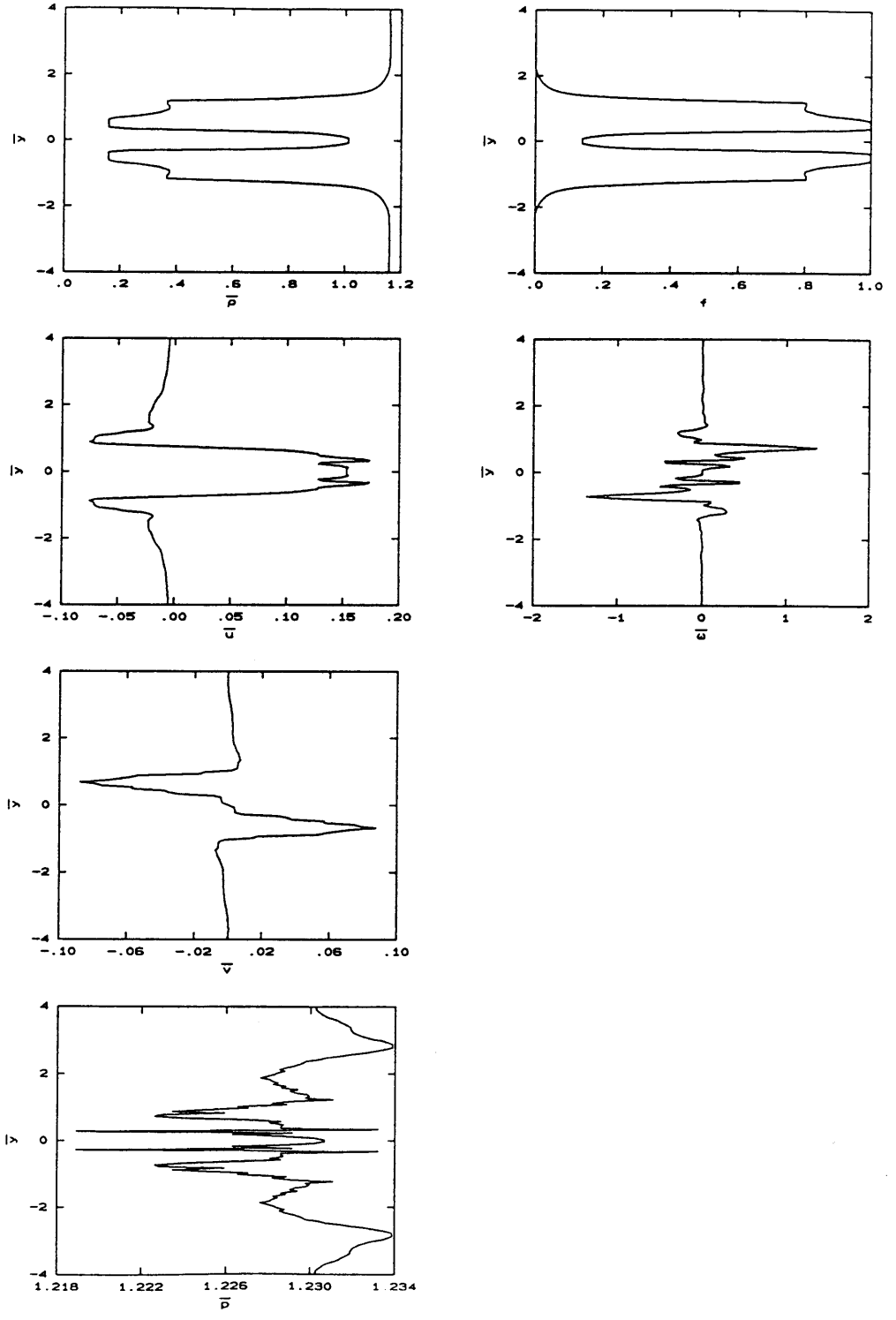

Figure 3.11 - Circular jet with M=1.1 and $\overline{\rho}_L/\overline{\rho}_H = 0.138$. Vertical cuts through the approximate center of the structure at $\overline{t} = 20$.

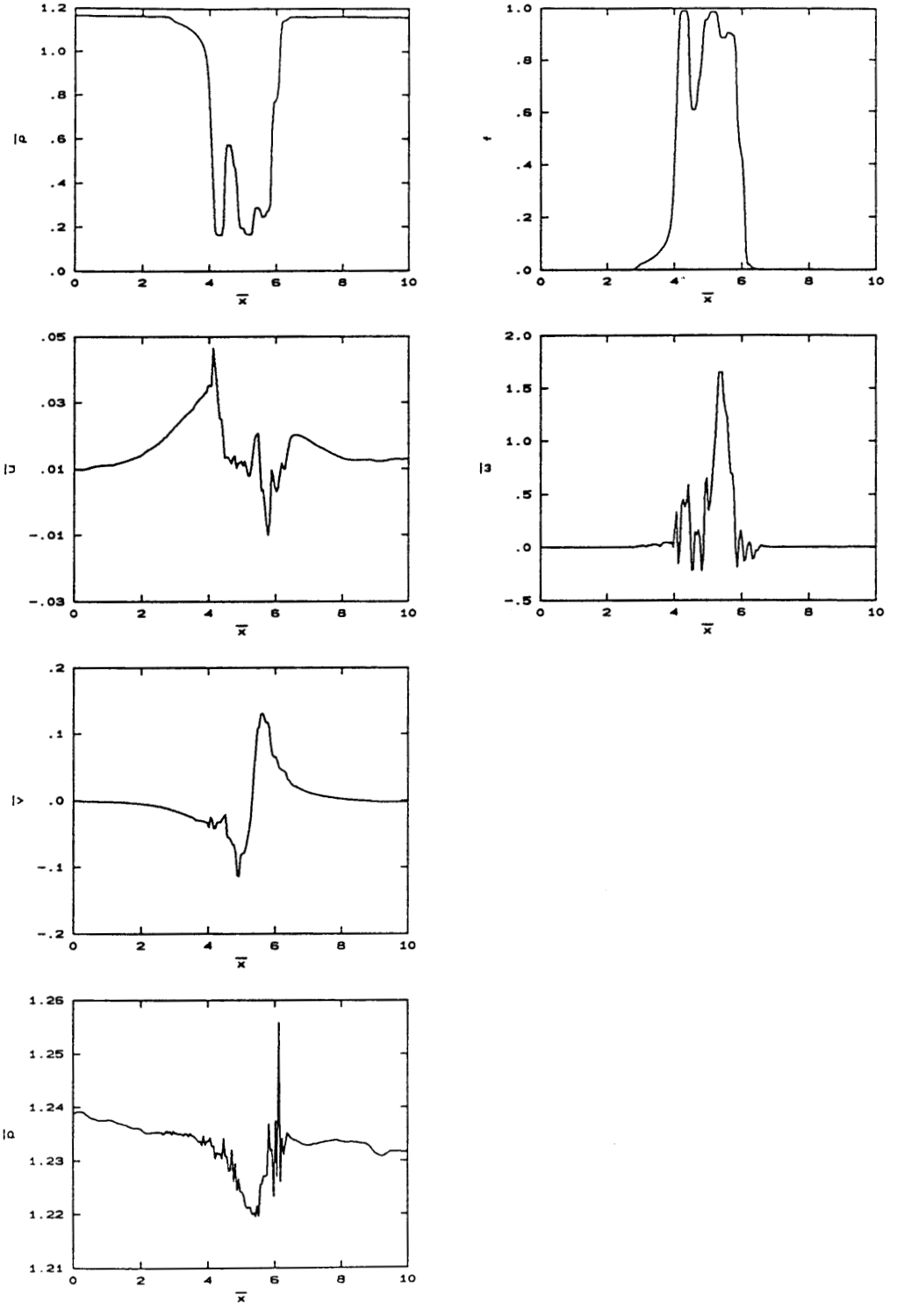

Figure 3.12 - Circular jet with M=1.1 and $\overline{\rho}_L/\overline{\rho}_H = 0.138$. Horizontal cuts through the approximate center of the structure at $\overline{t} = 30$.

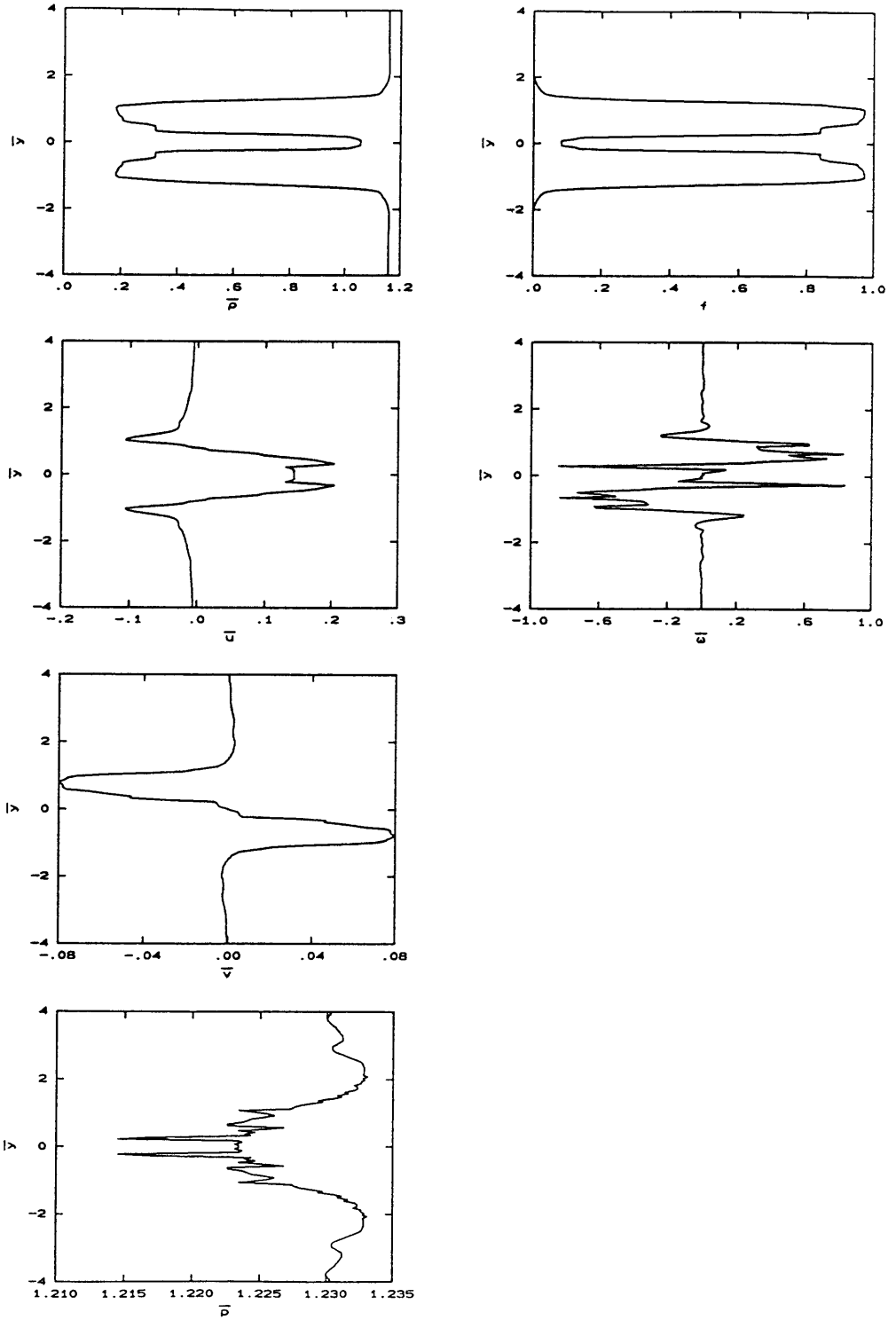

Figure 3.13 - Circular jet with M=1.1 and $\overline{\rho}_L/\overline{\rho}_H = 0.138$. Vertical cuts through the approximate center of the structure at $\overline{t} = 30$.

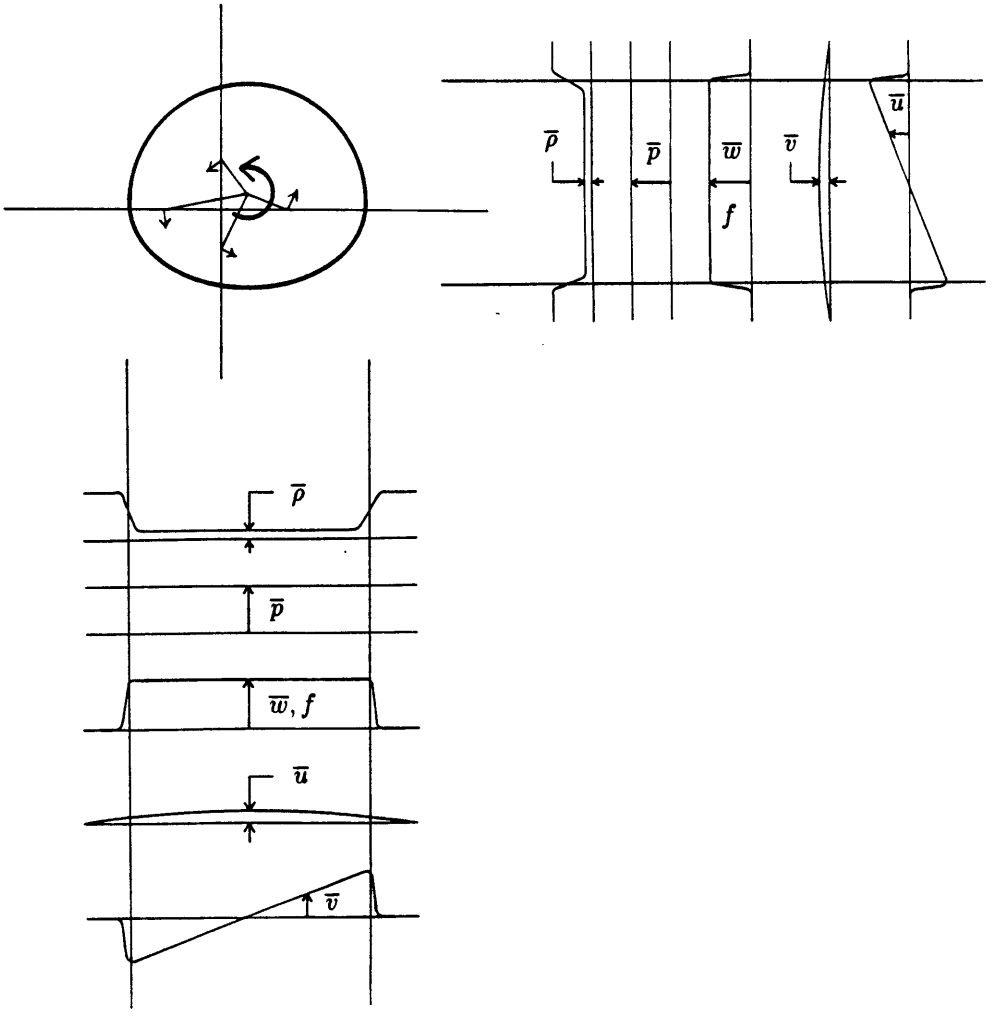

Figure 3.14 - Schematic of an uniform vorticity region.

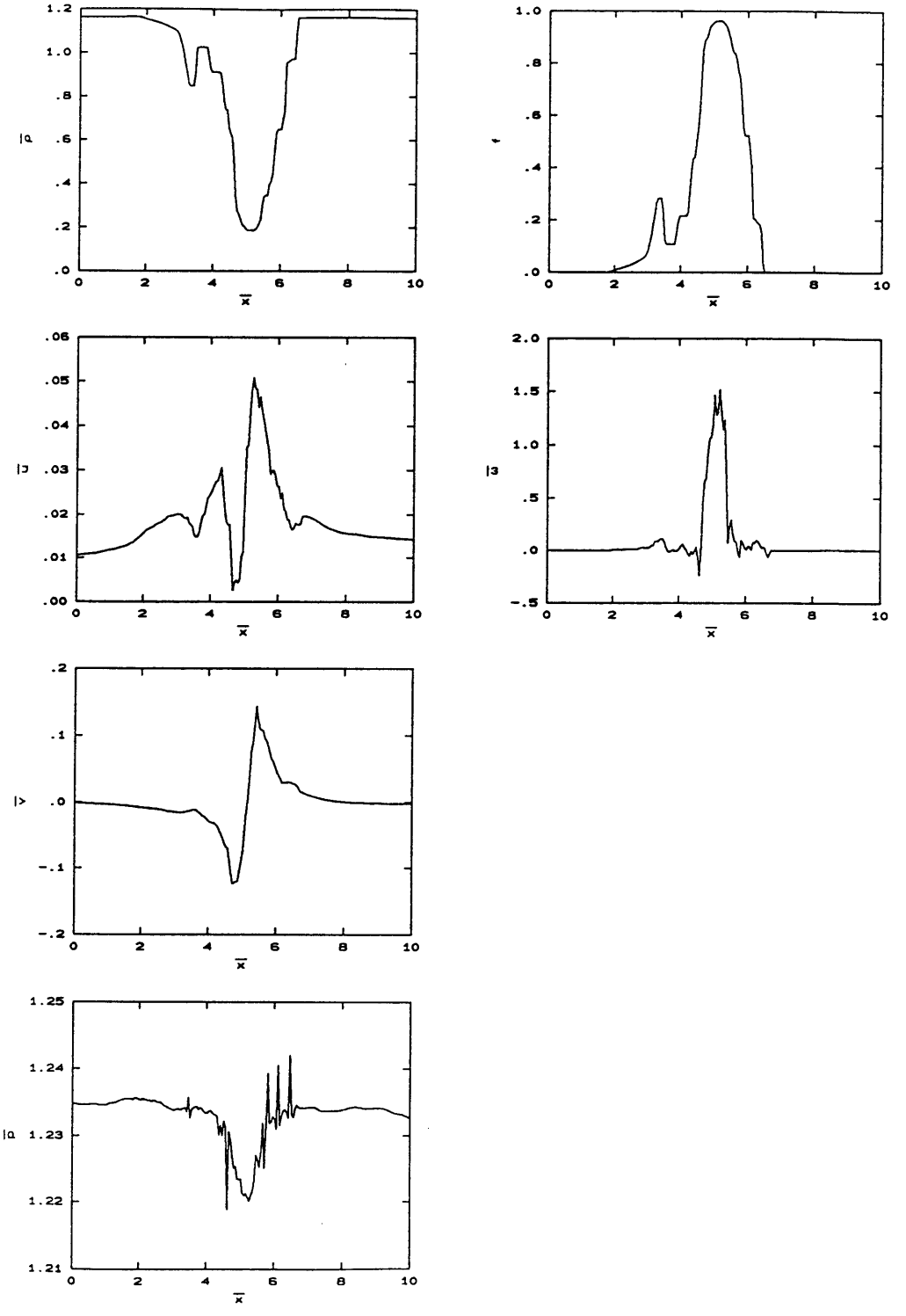

Figure 3.15 - Circular jet with M=1.1 and $\overline{\rho}_L/\overline{\rho}_H = 0.138$. Horizontal cuts through the approximate center of the structure at $\bar{t} = 60$.

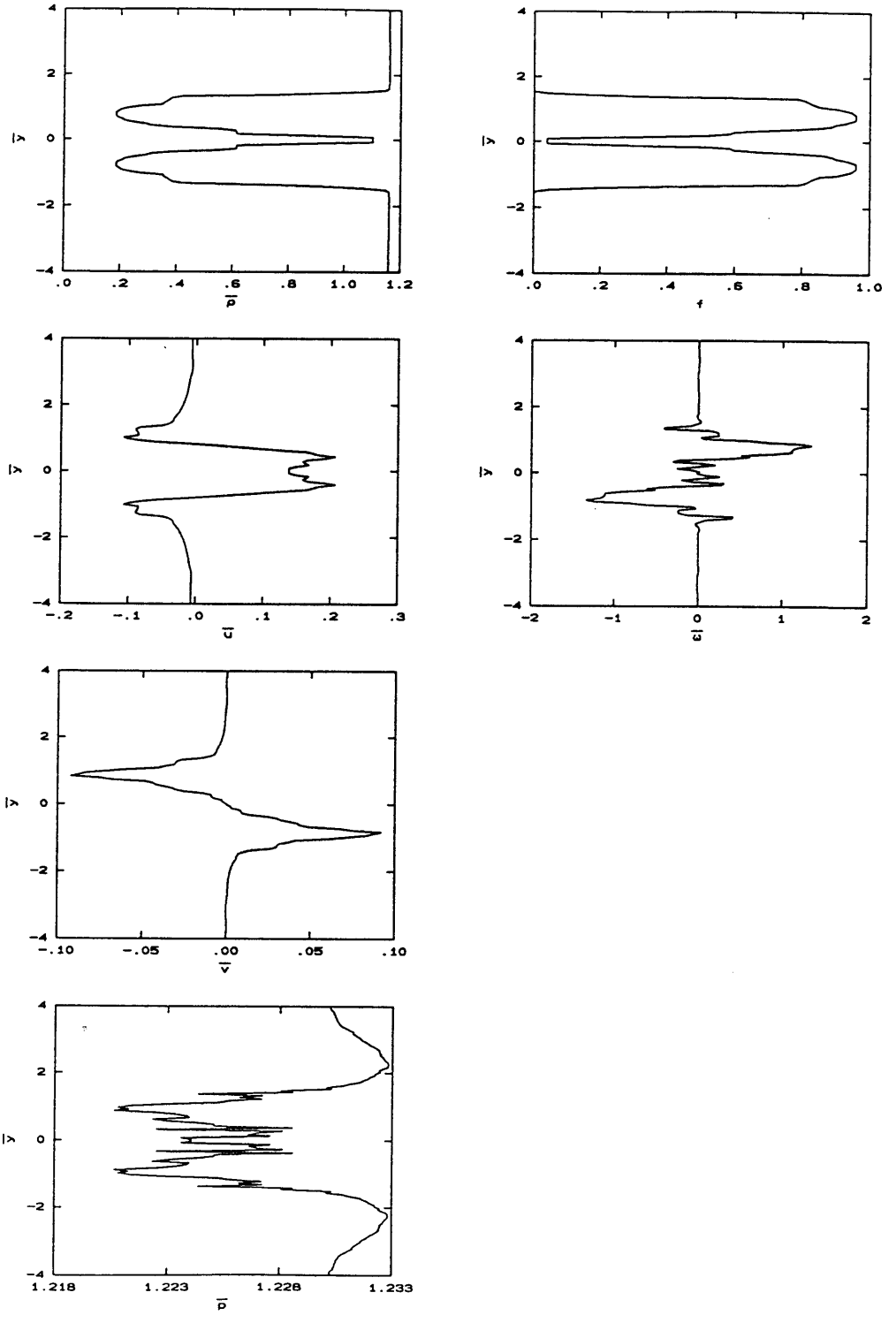

Figure 3.16 - Circular jet with M=1.1 and $\overline{\rho}_L/\overline{\rho}_H = 0.138$. Vertical cuts through the approximate center of the structure at $\bar{t} = 60$.

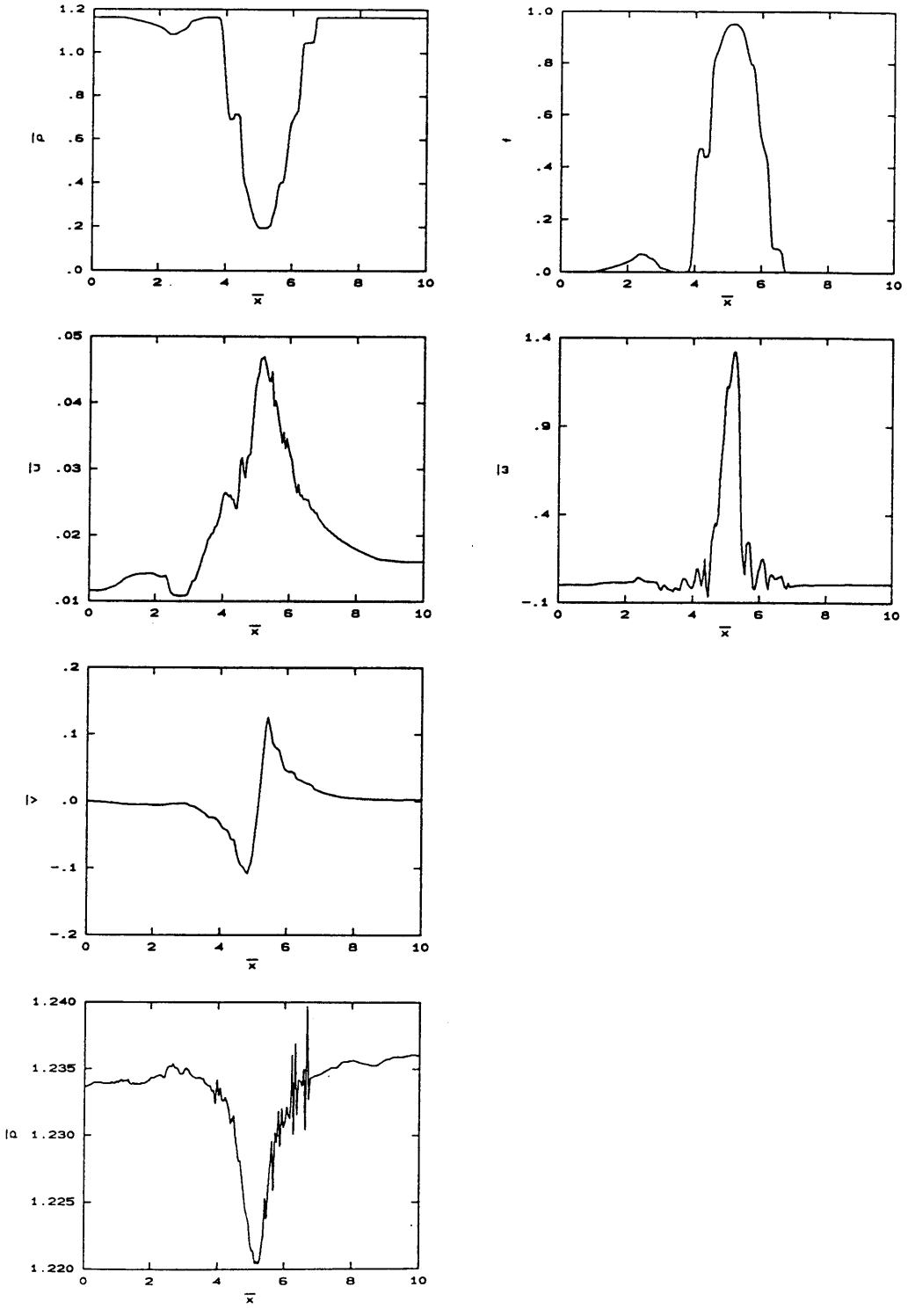

Figure 3.17 - Circular jet with M=1.1 and $\bar{\rho}_L/\bar{\rho}_H = 0.138$. Horizontal cuts through the approximate center of the structure at $\bar{t} = 90$.

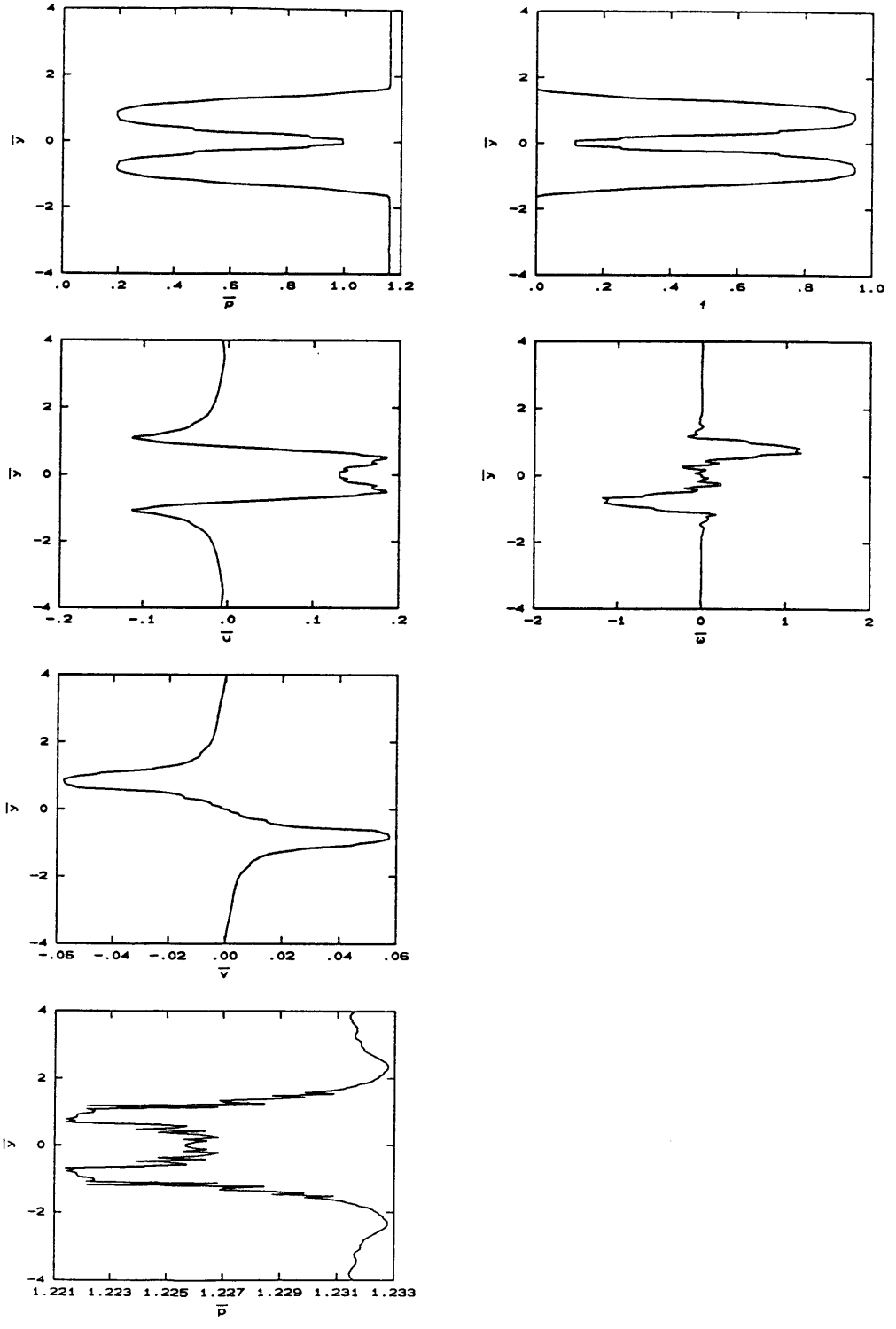

Figure 3.18 - Circular jet with M=1.1 and $\bar{\rho}_L/\bar{\rho}_H = 0.138$. Vertical cuts through the approximate center of the structure at $\bar{t} = 90$.

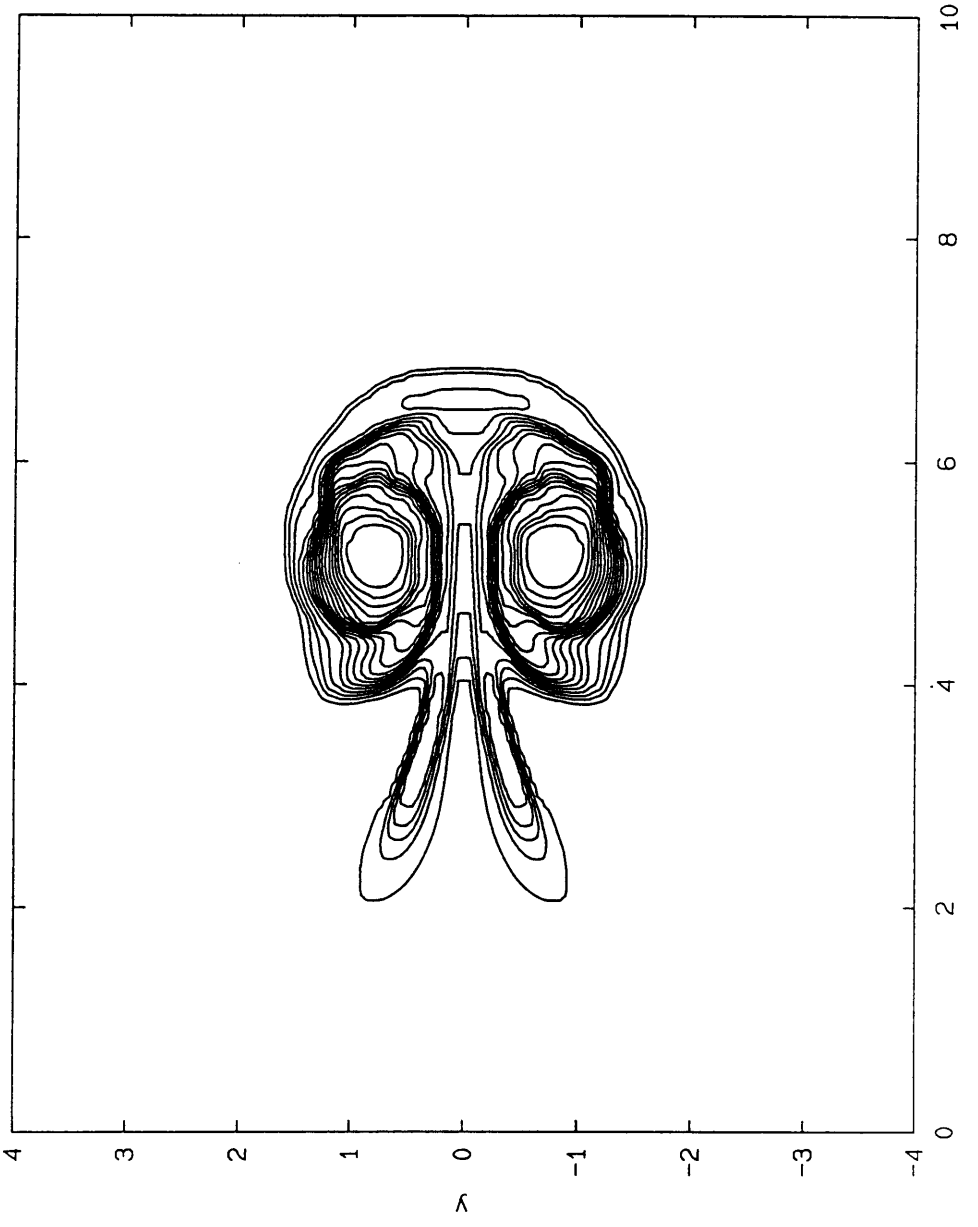

Figure 3.19 - Circular jet with M=1.1 and $\bar{\rho}_L/\bar{\rho}_H = 0.138$. Expanded density contours of $\bar{t} = 90$.

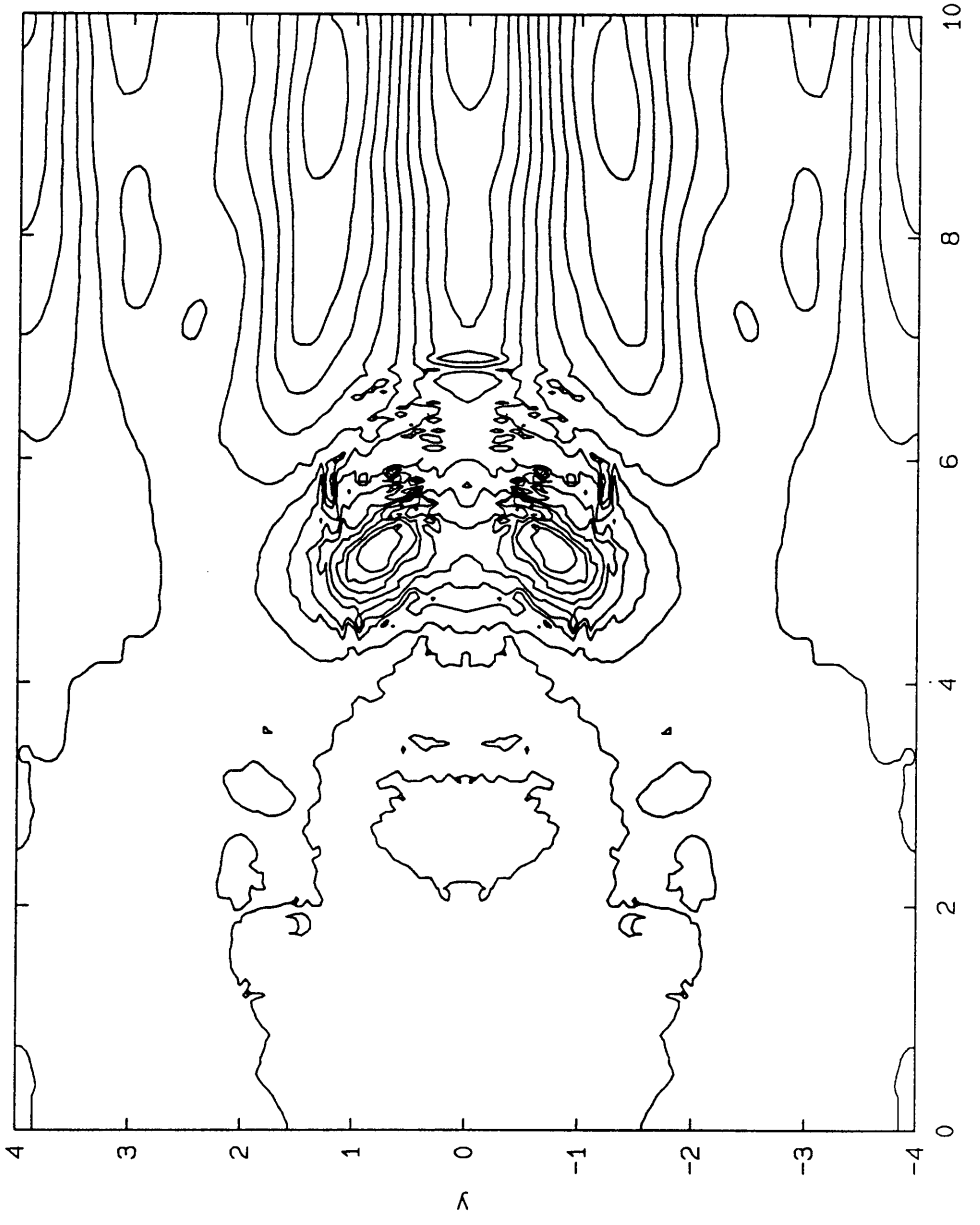

Figure 3.20 - Circular jet with M=1.1 and $\bar{\rho}_L/\bar{\rho}_H = 0.138$. Expanded pressure contours of $\bar{t} = 90$.

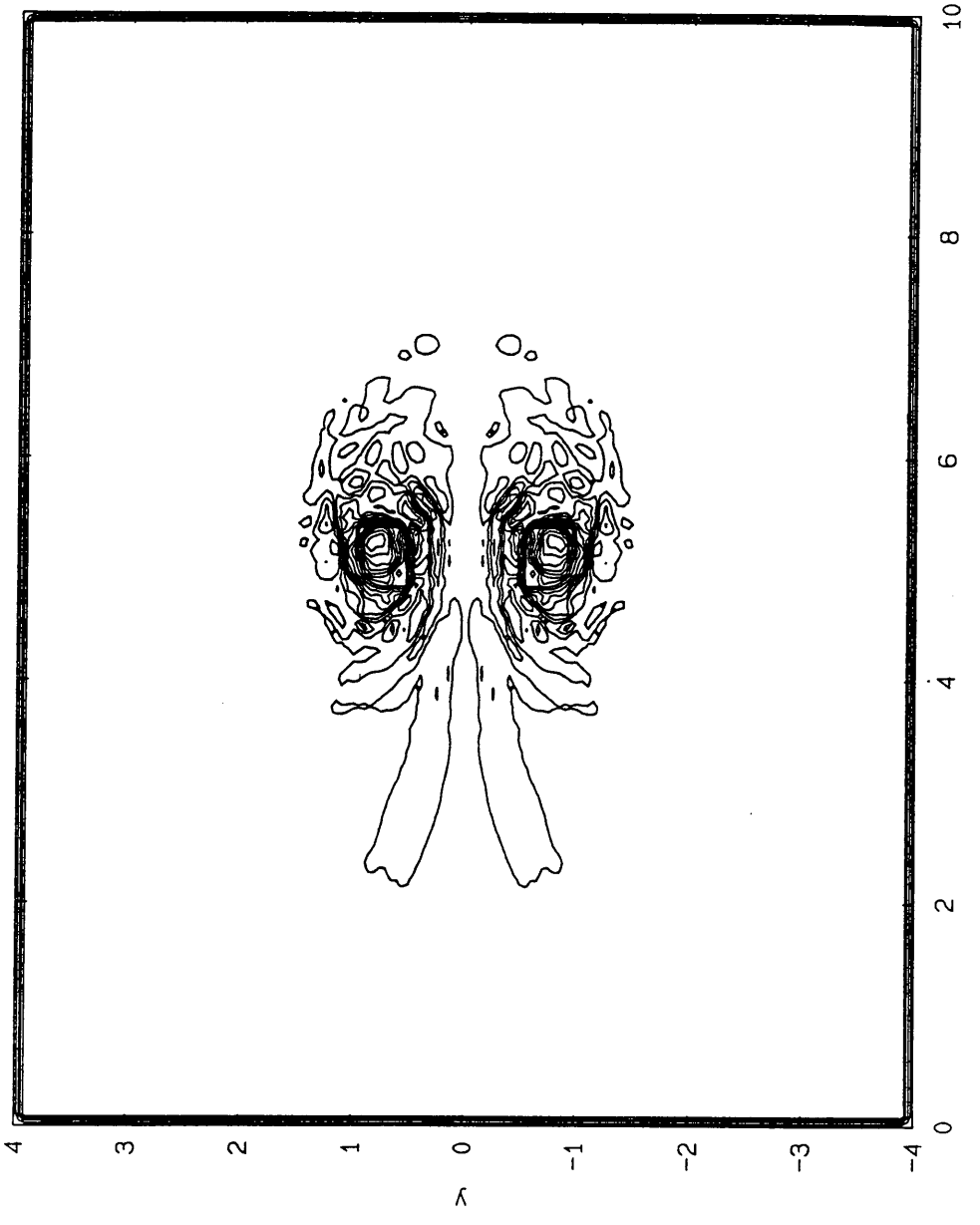

Figure 3.21 - Circular jet with M=1.1 and $\bar{\rho}_L/\bar{\rho}_H = 0.138$. Expanded vorticity contours of $\bar{t} = 90$.

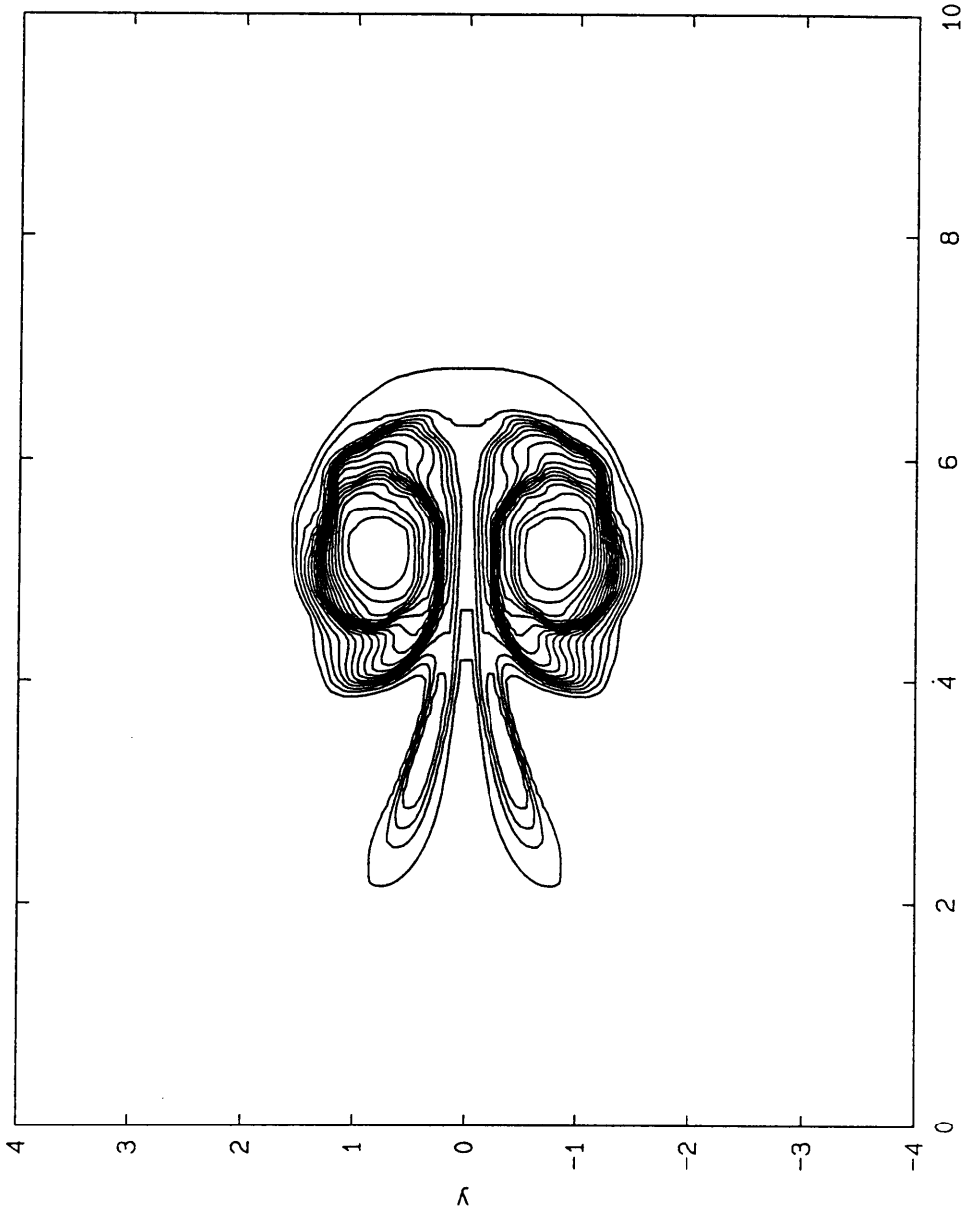

Figure 3.22 - Circular jet with M=1.1 and $\overline{\rho}_L/\overline{\rho}_H = 0.138$. Expanded mass fraction contours of $\bar{t} = 90$.

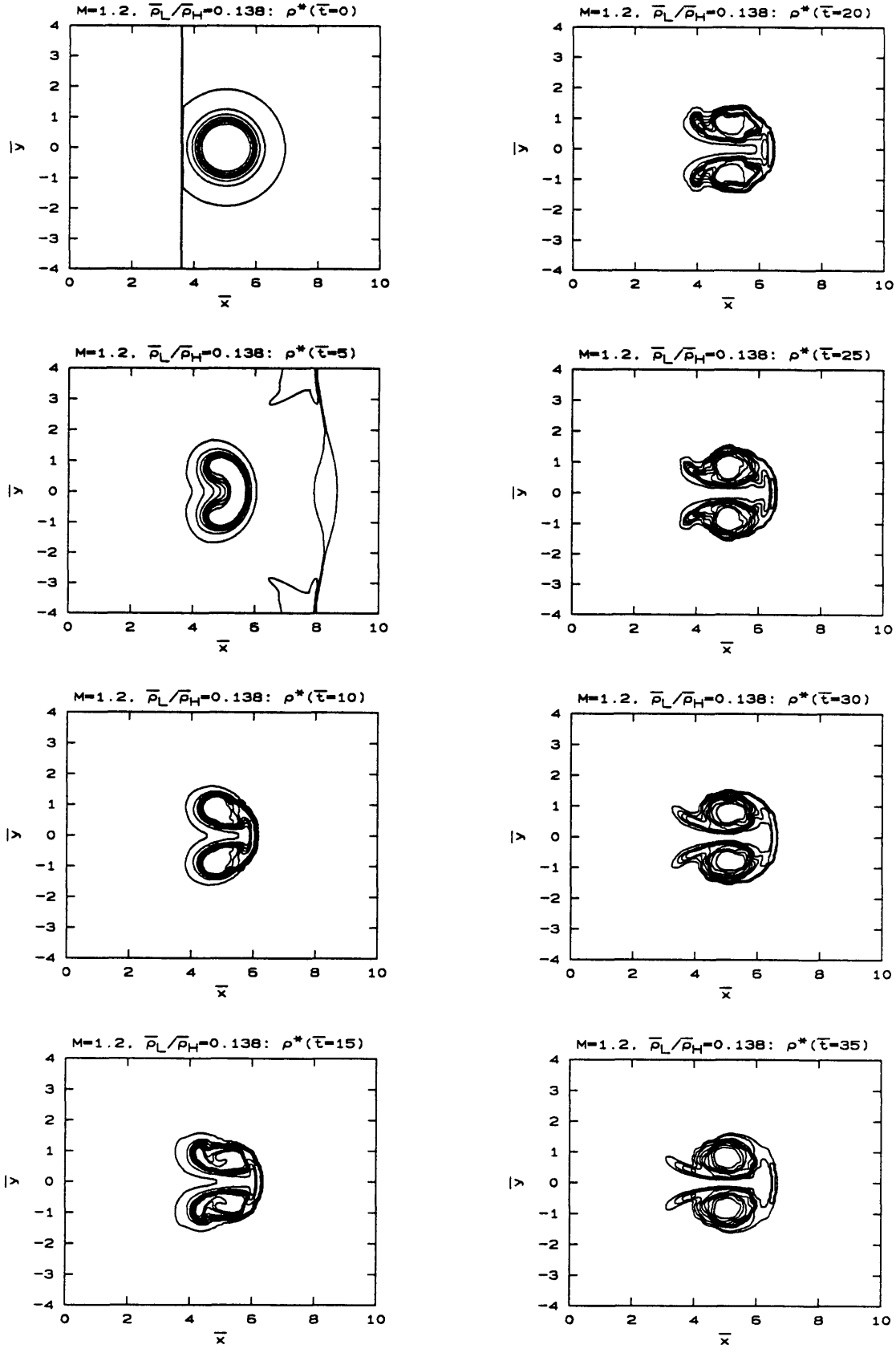

Figure 3.23 - Circular jet with M=1.2 and $\overline{\rho}_L/\overline{\rho}_H = 0.138$. Density contours.

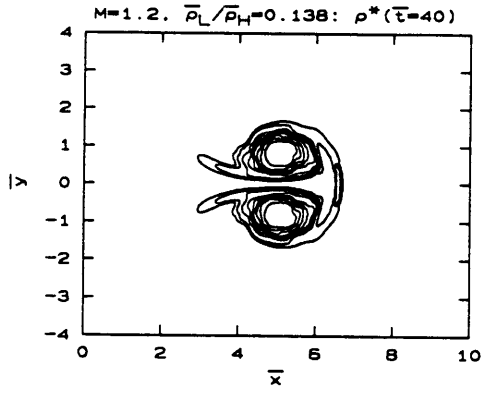
M=1.2. $\overline{\rho}_L/\overline{\rho}_H$=0.138: $\rho^*(\overline{t}$=40)
$\overline{y}$
$\overline{x}$

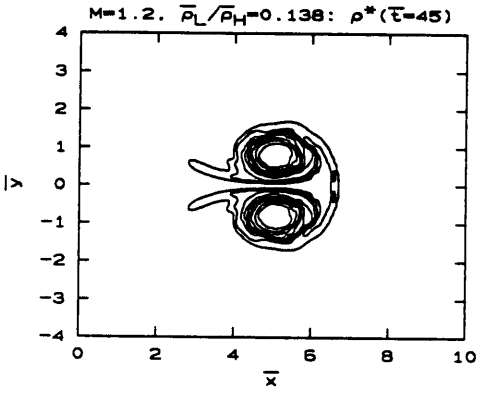
M=1.2. $\overline{\rho}_L/\overline{\rho}_H$=0.138: $\rho^*(\overline{t}$=45)
$\overline{y}$
$\overline{x}$

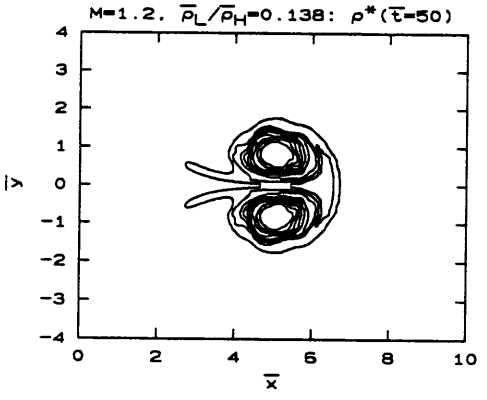
M=1.2. $\overline{\rho}_L/\overline{\rho}_H$=0.138: $\rho^*(\overline{t}$=50)
$\overline{y}$
$\overline{x}$

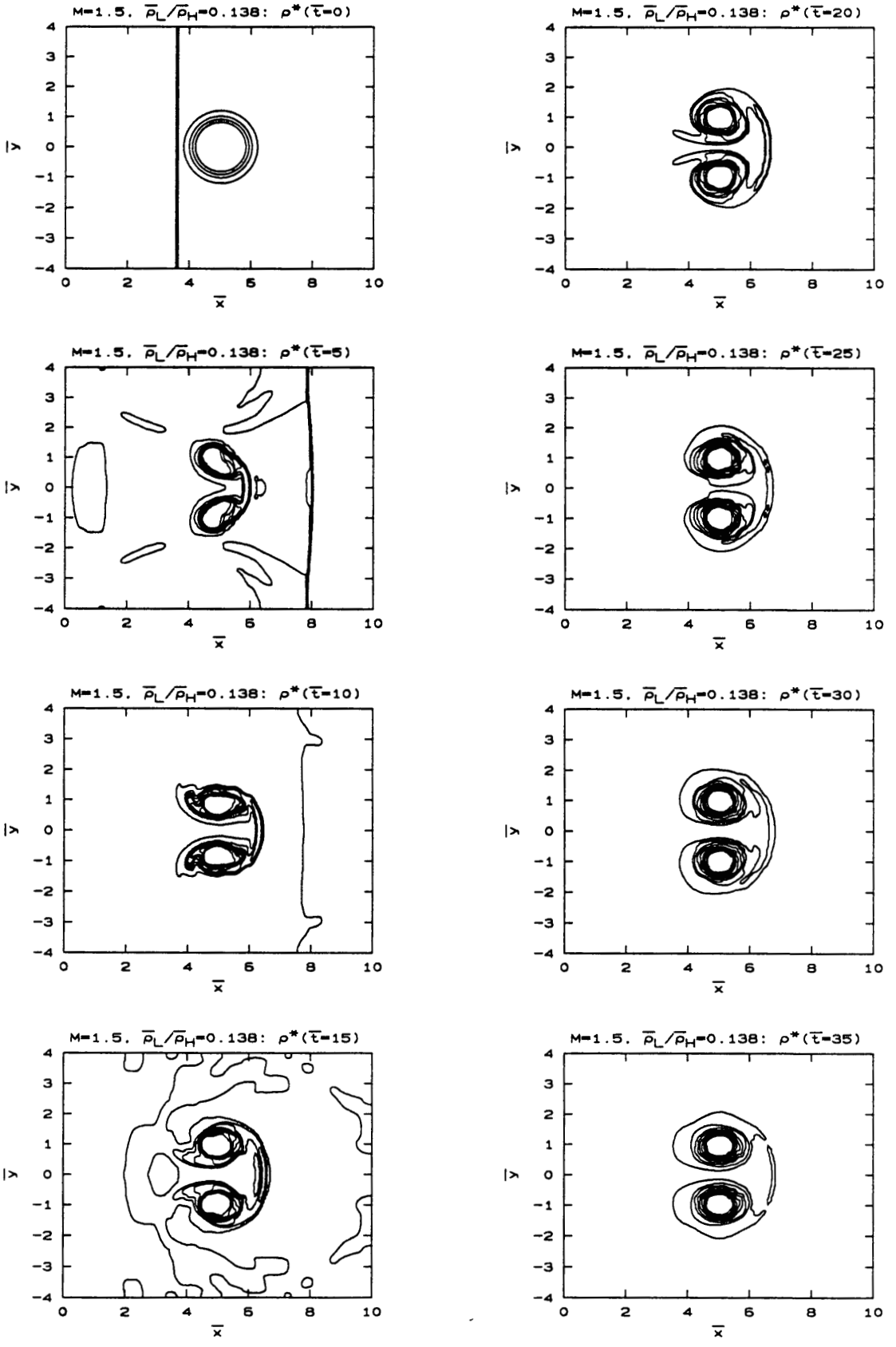

Figure 3.24 - Circular jet with M=1.5 and $\overline{\rho}_L/\overline{\rho}_H = 0.138$. Density contours.

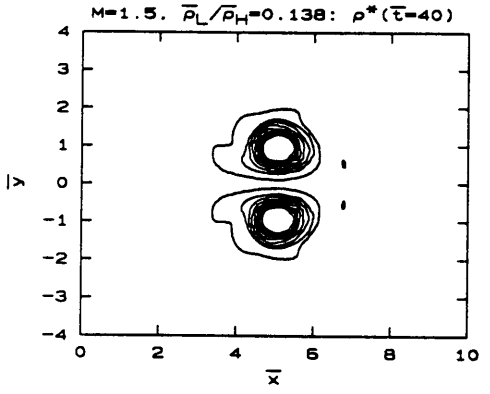
M=1.5. $\overline{\rho}_L/\overline{\rho}_H$=0.138: $\rho^*(\overline{t}$=40)
$\overline{y}$
$\overline{x}$

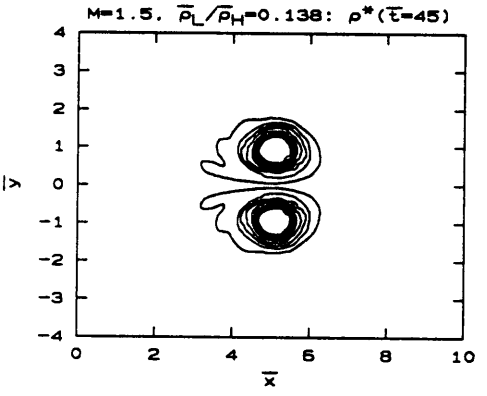
M=1.5. $\overline{\rho}_L/\overline{\rho}_H$=0.138: $\rho^*(\overline{t}$=45)
$\overline{y}$
$\overline{x}$

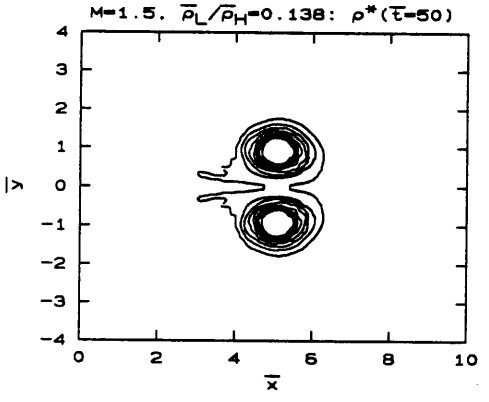
M=1.5. $\overline{\rho}_L/\overline{\rho}_H$=0.138: $\rho^*(\overline{t}$=50)
$\overline{y}$
$\overline{x}$

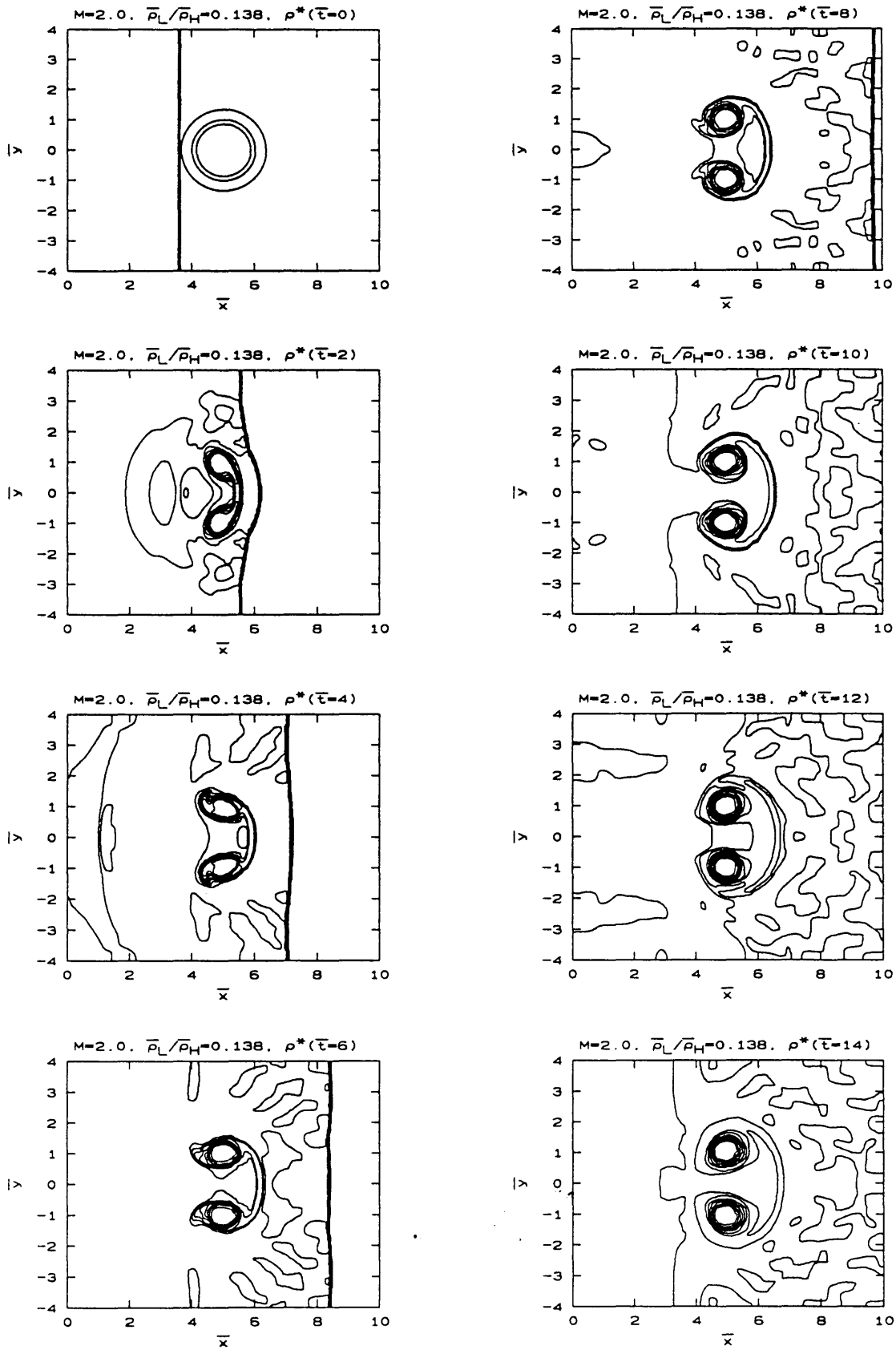

Figure 3.25 - Circular jet with M=2.0 and $\overline{\rho}_L/\overline{\rho}_H = 0.138$. Density contours.

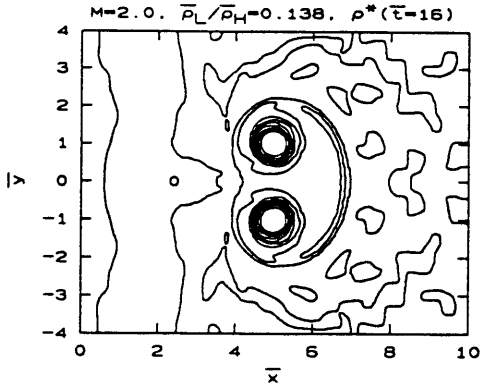
M=2.0. $\overline{\rho}_L/\overline{\rho}_H$=0.138. $\rho^*(\overline{t}$=16)
$\overline{y}$
$\overline{x}$

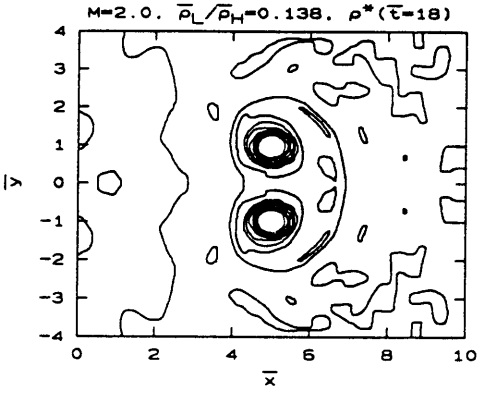
M=2.0. $\overline{\rho}_L/\overline{\rho}_H$=0.138. $\rho^*(\overline{t}$=18)
$\overline{y}$
$\overline{x}$

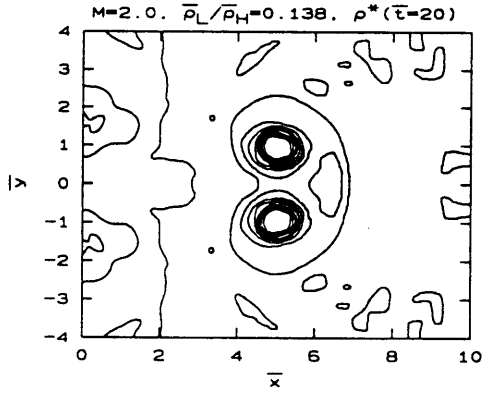
M=2.0. $\overline{\rho}_L/\overline{\rho}_H$=0.138. $\rho^*(\overline{t}$=20)
$\overline{y}$
$\overline{x}$

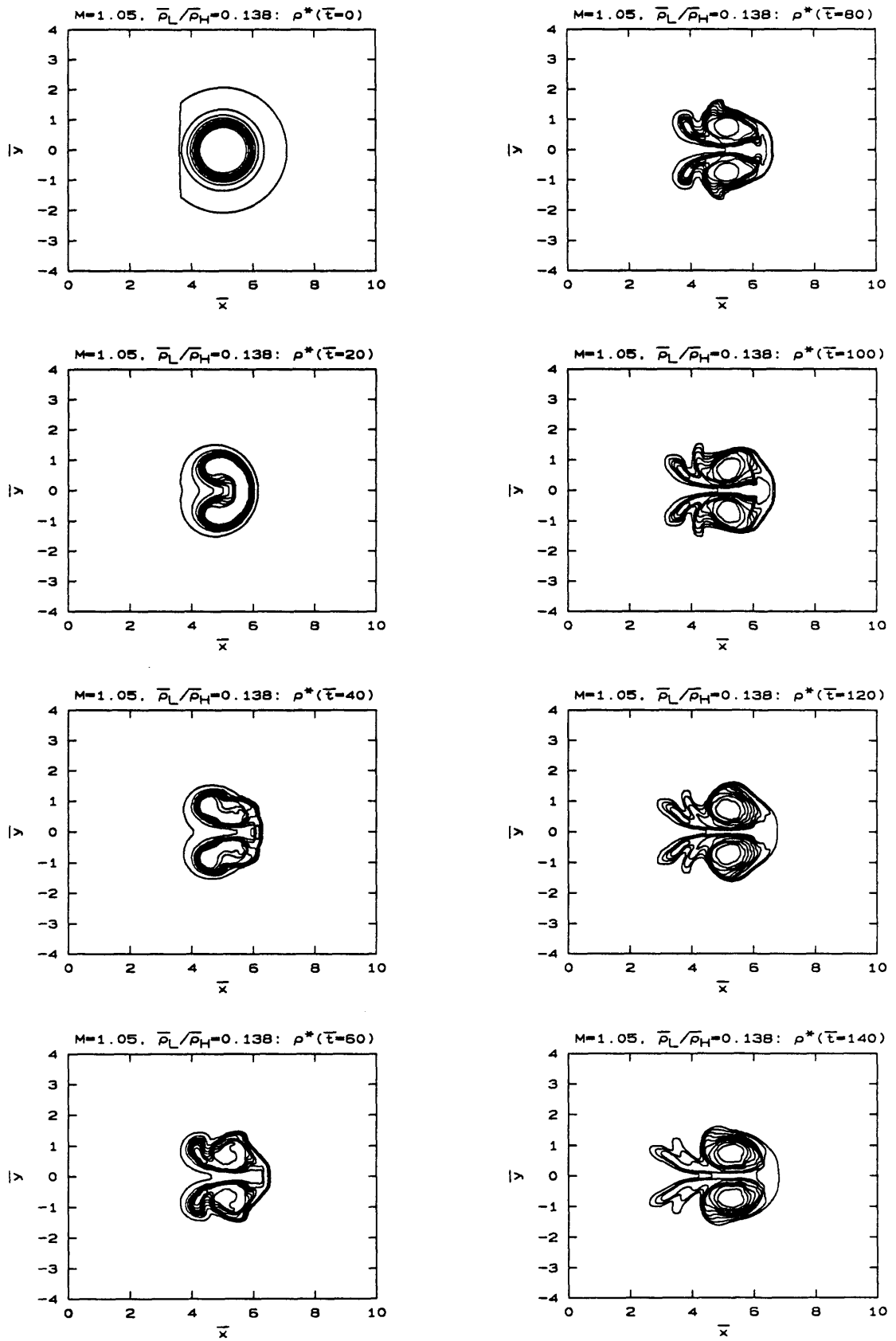

Figure 3.26 - Circular jet with M=1.05 and $\overline{\rho}_L/\overline{\rho}_H = 0.138$. Density contours.

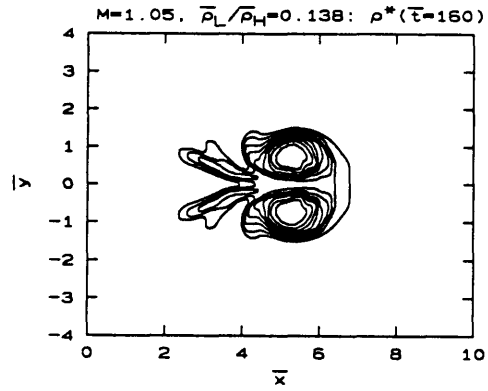
M=1.05, $\overline{\rho}_L/\overline{\rho}_H$=0.138: $\rho^*(\overline{t}$=160)
$\overline{y}$
$\overline{x}$

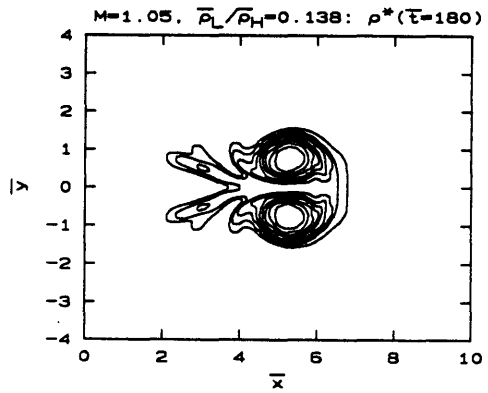
M=1.05, $\overline{\rho}_L/\overline{\rho}_H$=0.138: $\rho^*(\overline{t}$=180)
$\overline{y}$
$\overline{x}$

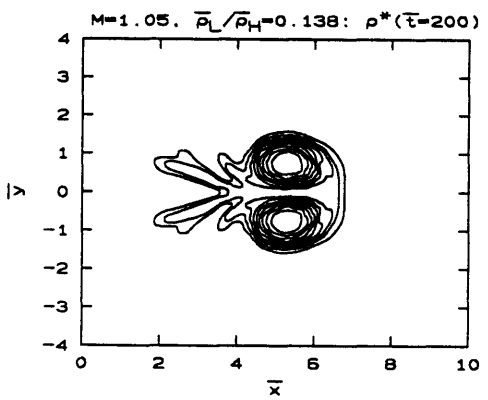
M=1.05, $\overline{\rho}_L/\overline{\rho}_H$=0.138: $\rho^*(\overline{t}$=200)
$\overline{y}$
$\overline{x}$

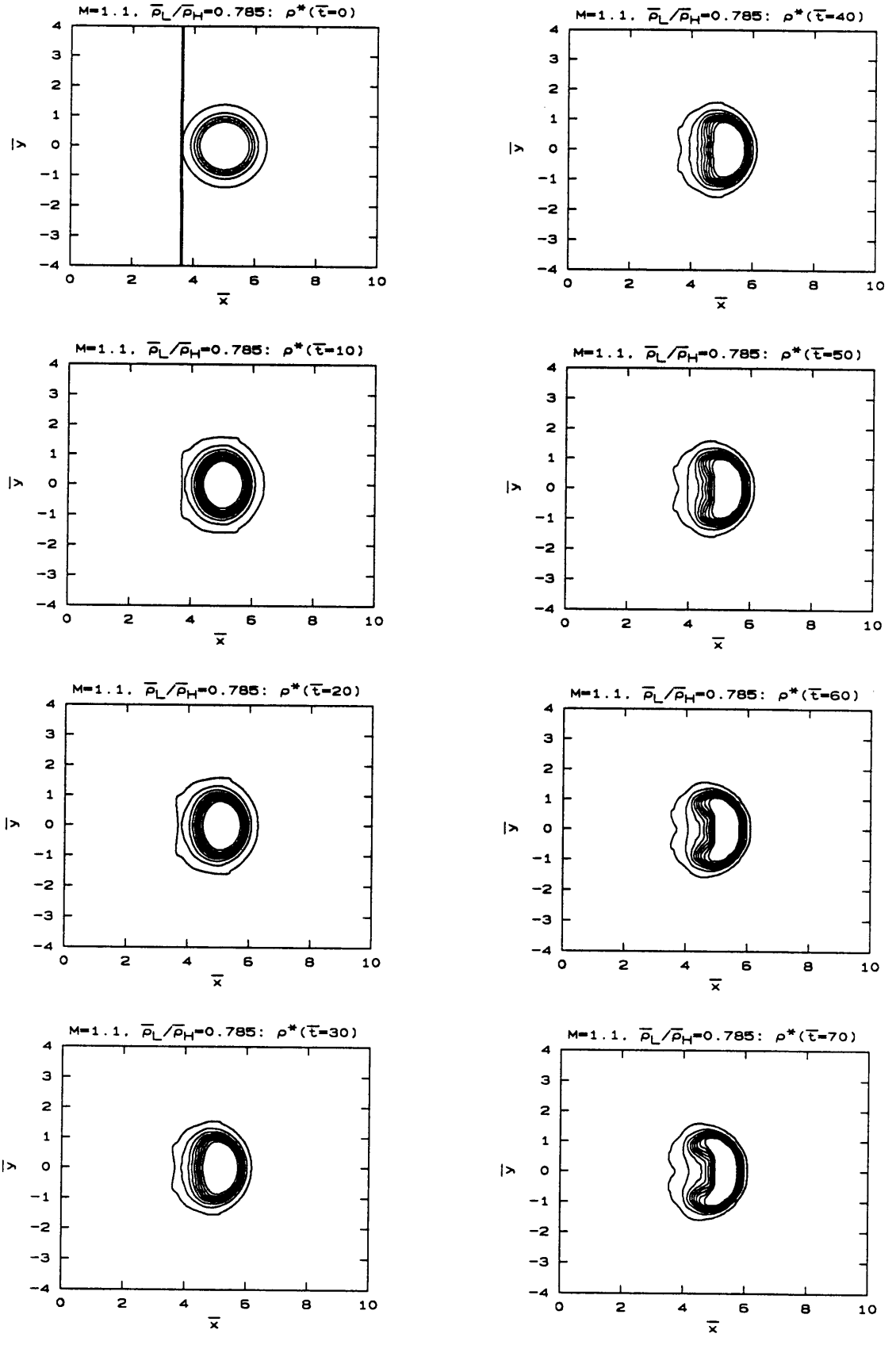

Figure 3.27 - Circular jet with M=1.1 and $\overline{\rho}_L/\overline{\rho}_H = 0.785$. Density contours.

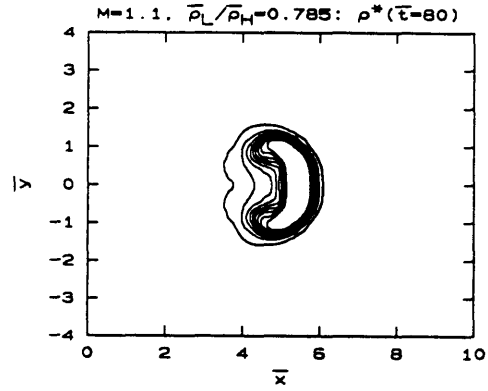
M=1.1, $\bar{\rho}_L/\bar{\rho}_H$=0.785: $\rho^*(\bar{t}$=80)
$\bar{y}$
$\bar{x}$

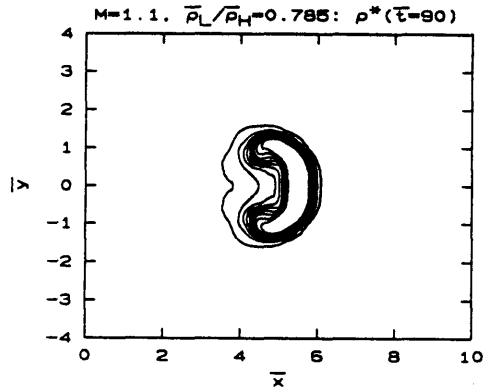
M=1.1, $\bar{\rho}_L/\bar{\rho}_H$=0.785: $\rho^*(\bar{t}$=90)
$\bar{y}$
$\bar{x}$

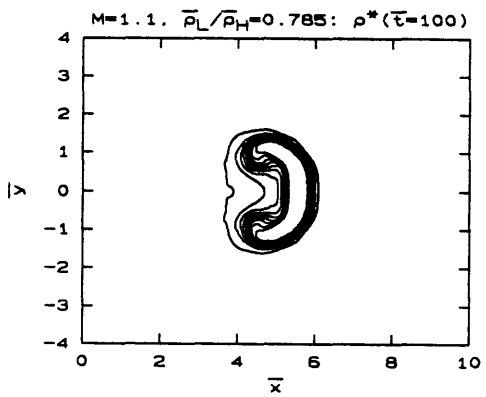
M=1.1, $\bar{\rho}_L/\bar{\rho}_H$=0.785: $\rho^*(\bar{t}$=100)
$\bar{y}$
$\bar{x}$

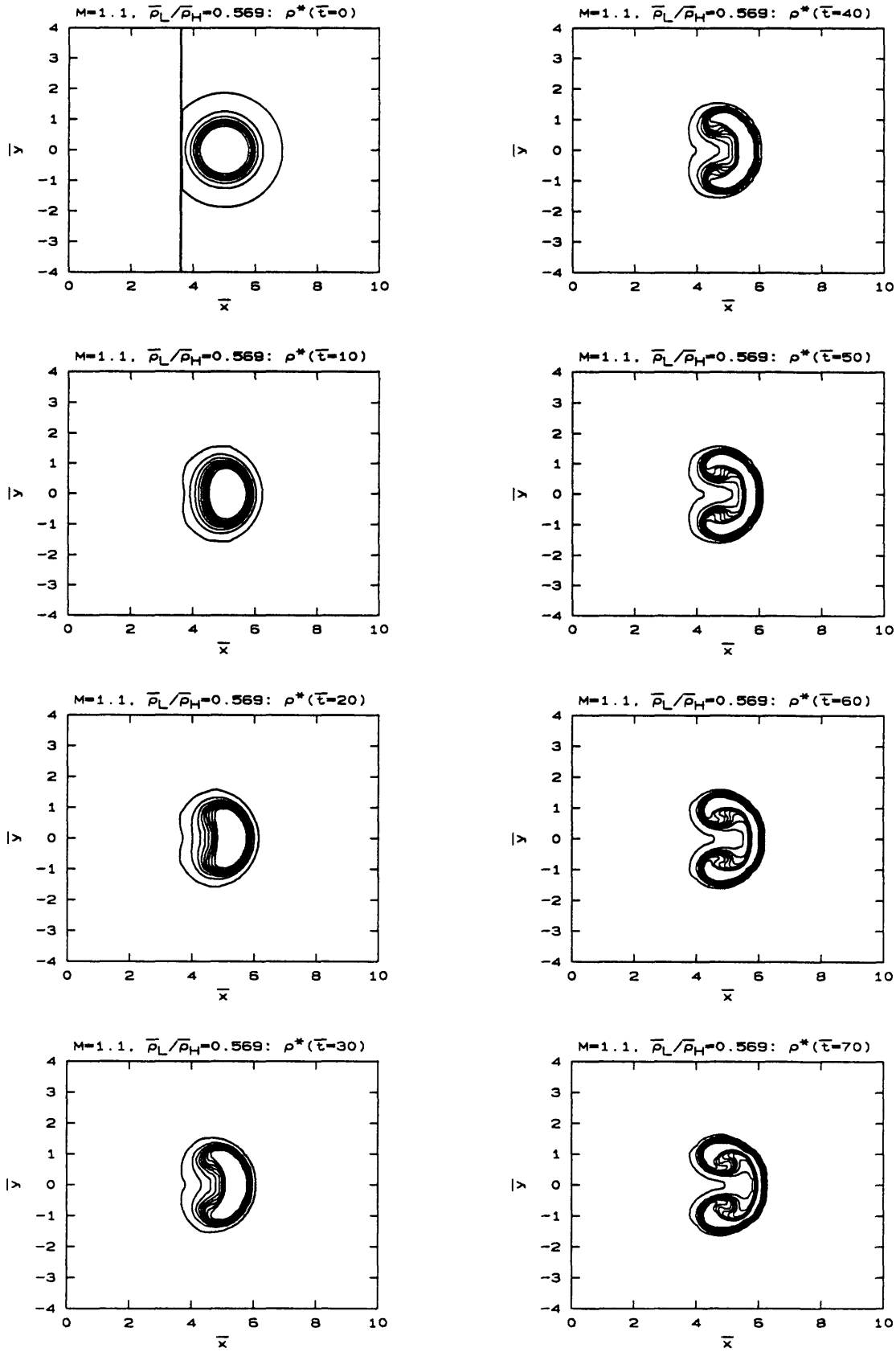

Figure 3.28 - Circular jet with M=1.1 and $\overline{\rho}_L/\overline{\rho}_H = 0.569$. Density contours.

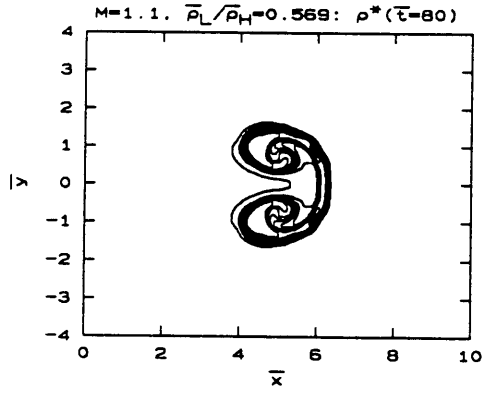
M=1.1, $\overline{\rho}_L/\overline{\rho}_H$=0.569: $\rho^*(\overline{t}$=80)
$\overline{y}$
$\overline{x}$

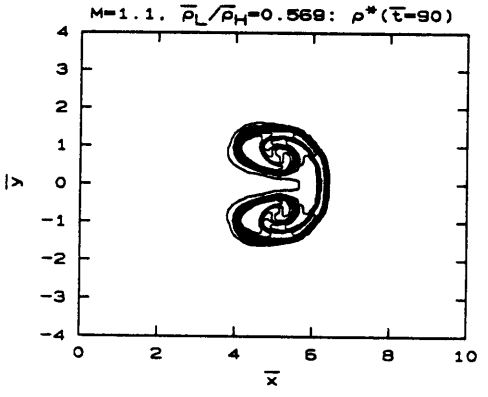
M=1.1, $\overline{\rho}_L/\overline{\rho}_H$=0.569: $\rho^*(\overline{t}$=90)
$\overline{y}$
$\overline{x}$

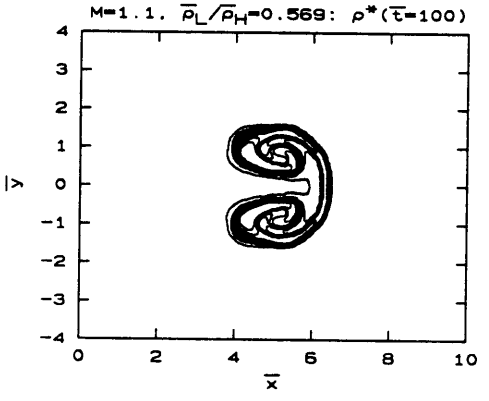
M=1.1, $\overline{\rho}_L/\overline{\rho}_H$=0.569: $\rho^*(\overline{t}$=100)
$\overline{y}$
$\overline{x}$

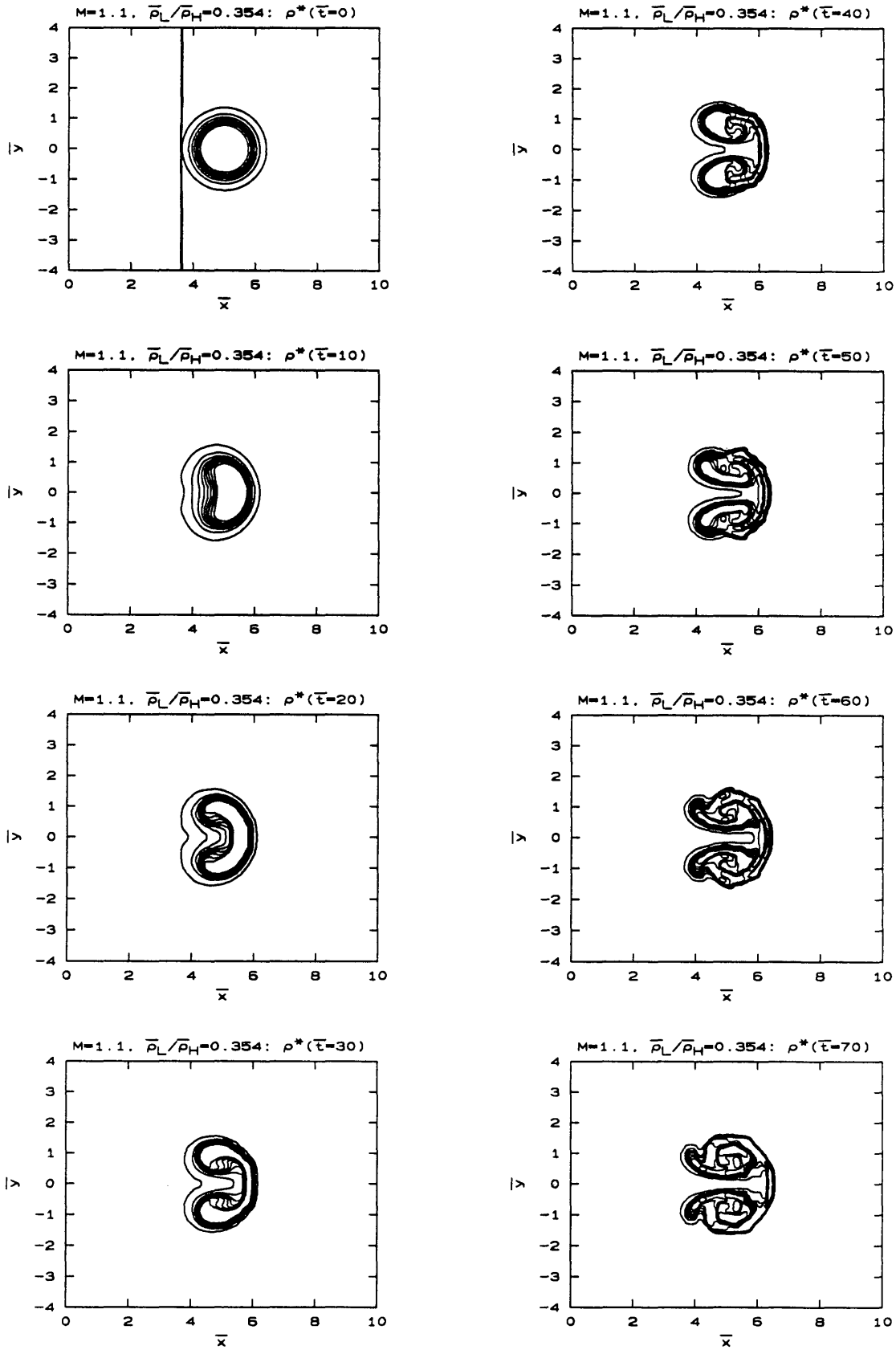

Figure 3.29 - Circular jet with M=1.1 and $\overline{\rho}_L/\overline{\rho}_H = 0.354$. Density contours.

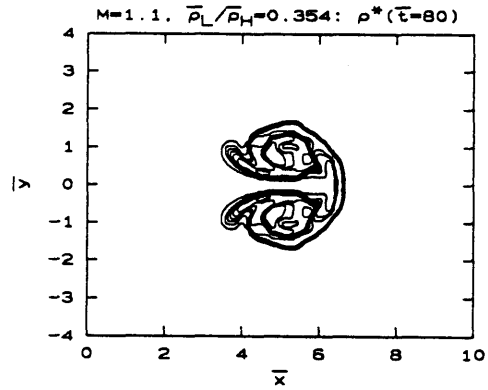
M=1.1. $\overline{\rho}_L/\overline{\rho}_H$=0.354: $\rho^*(\overline{t}$=80)
$\overline{y}$
$\overline{x}$

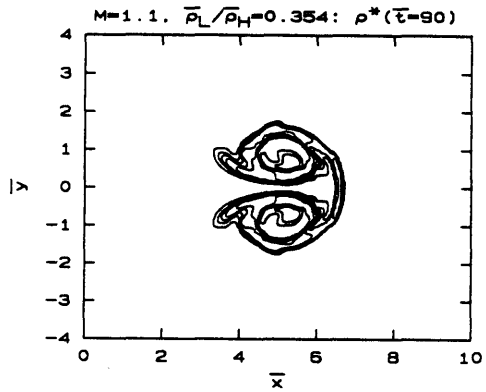
M=1.1. $\overline{\rho}_L/\overline{\rho}_H$=0.354: $\rho^*(\overline{t}$=90)
$\overline{y}$
$\overline{x}$

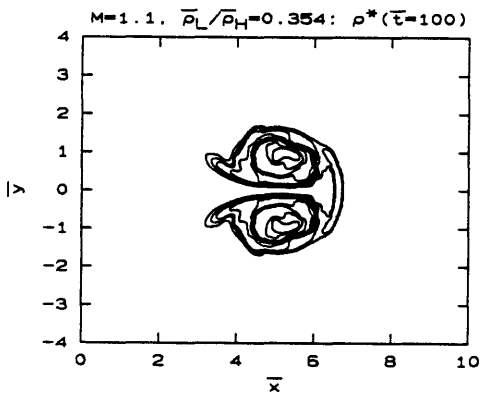
M=1.1. $\overline{\rho}_L/\overline{\rho}_H$=0.354: $\rho^*(\overline{t}$=100)
$\overline{y}$
$\overline{x}$

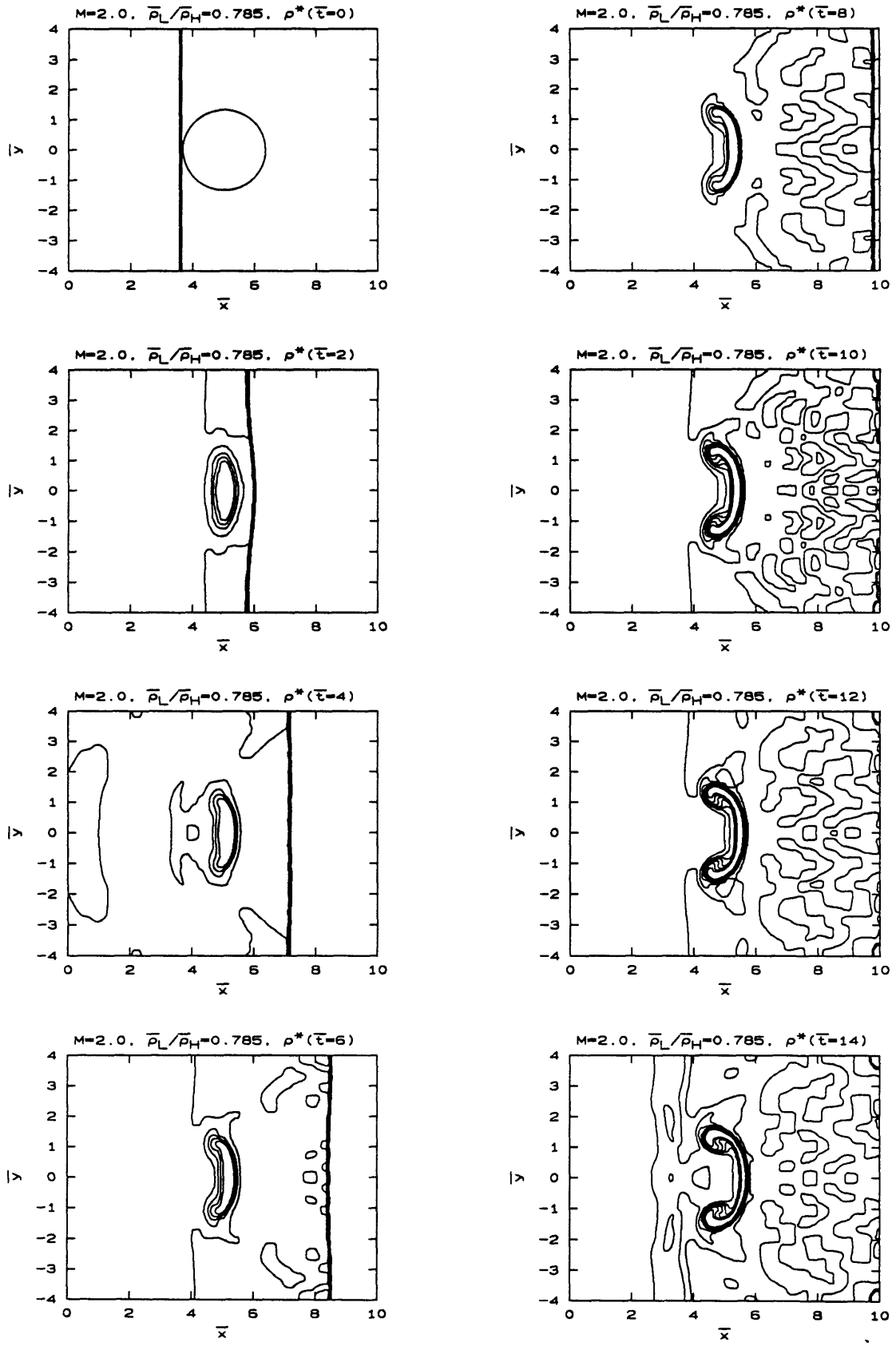

Figure 3.30 - Circular jet with M=2.0 and $\overline{\rho}_L/\overline{\rho}_H = 0.785$. Density contours.

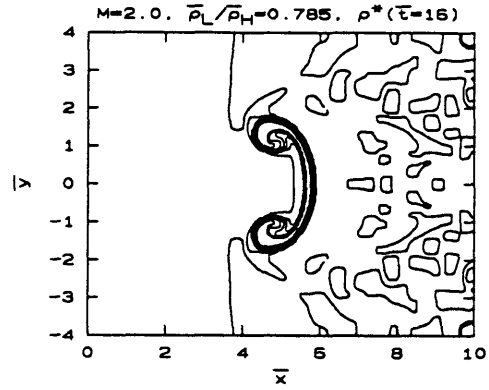
M=2.0. $\bar{\rho}_L/\bar{\rho}_H$=0.785. $\rho^*(\bar{t}$=16)
$\bar{y}$
$\bar{x}$

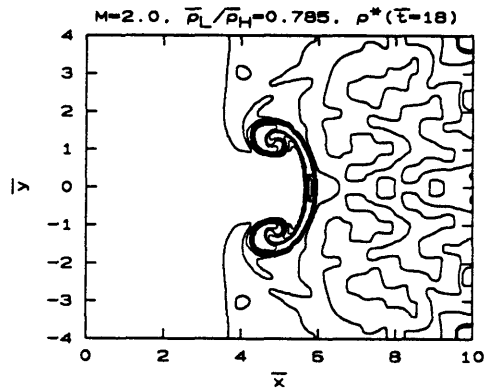
M=2.0. $\bar{\rho}_L/\bar{\rho}_H$=0.785. $\rho^*(\bar{t}$=18)
$\bar{y}$
$\bar{x}$

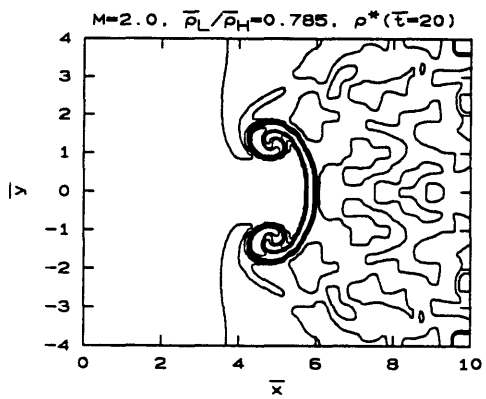
M=2.0. $\bar{\rho}_L/\bar{\rho}_H$=0.785. $\rho^*(\bar{t}$=20)
$\bar{y}$
$\bar{x}$

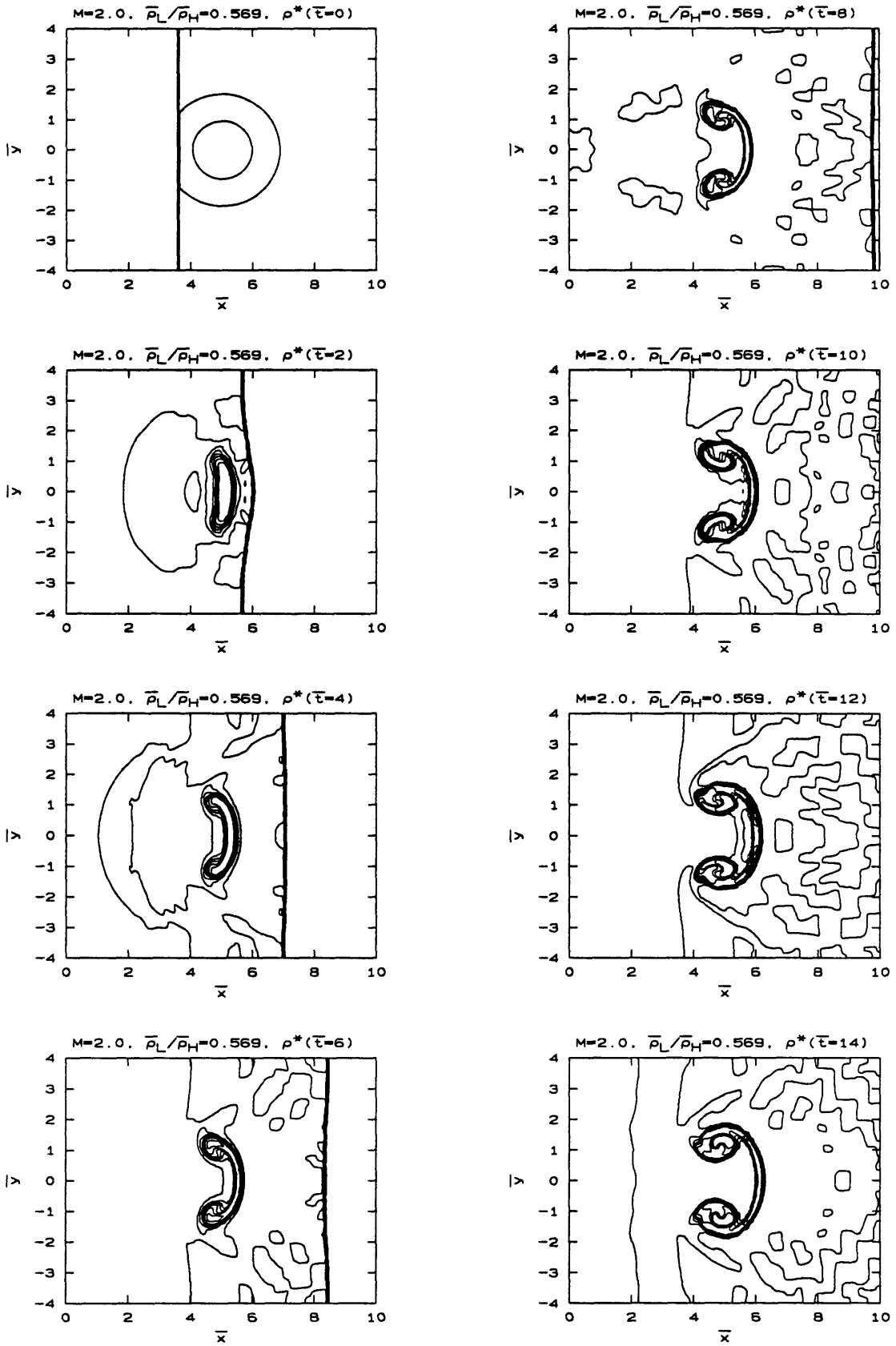

Figure 3.31 - Circular jet with M=2.0 and $\overline{\rho}_L/\overline{\rho}_H = 0.569$. Density contours.

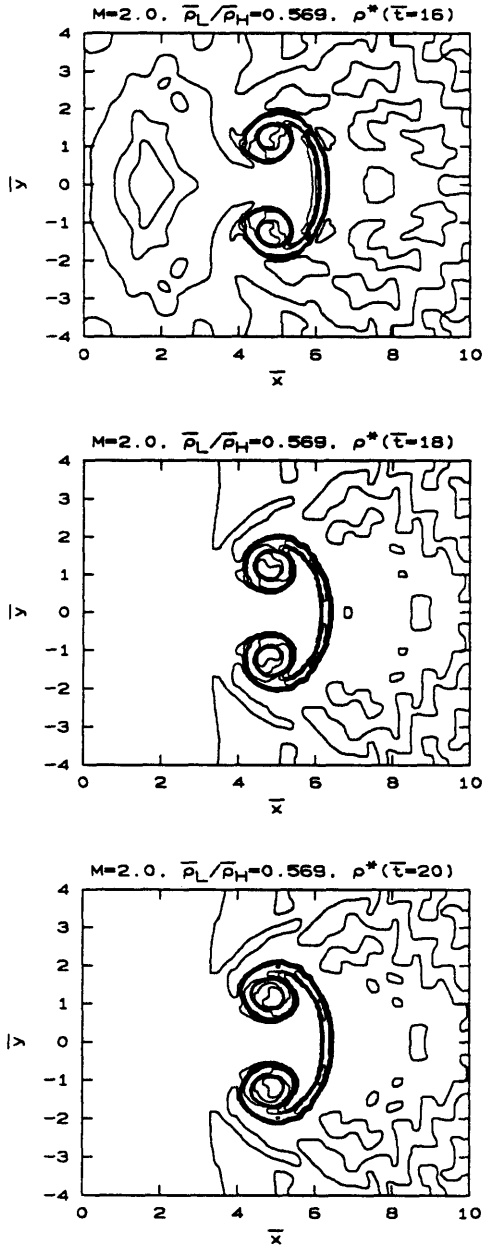
M=2.0. $\bar{\rho}_L/\bar{\rho}_H$=0.569. $\rho^*(\bar{t}$=16)
M=2.0. $\bar{\rho}_L/\bar{\rho}_H$=0.569. $\rho^*(\bar{t}$=18)
M=2.0. $\bar{\rho}_L/\bar{\rho}_H$=0.569. $\rho^*(\bar{t}$=20)
$\bar{y}$
$\bar{x}$
4
3
2
1
0
-1
-2
-3
-4
0
2
4
6
8
10

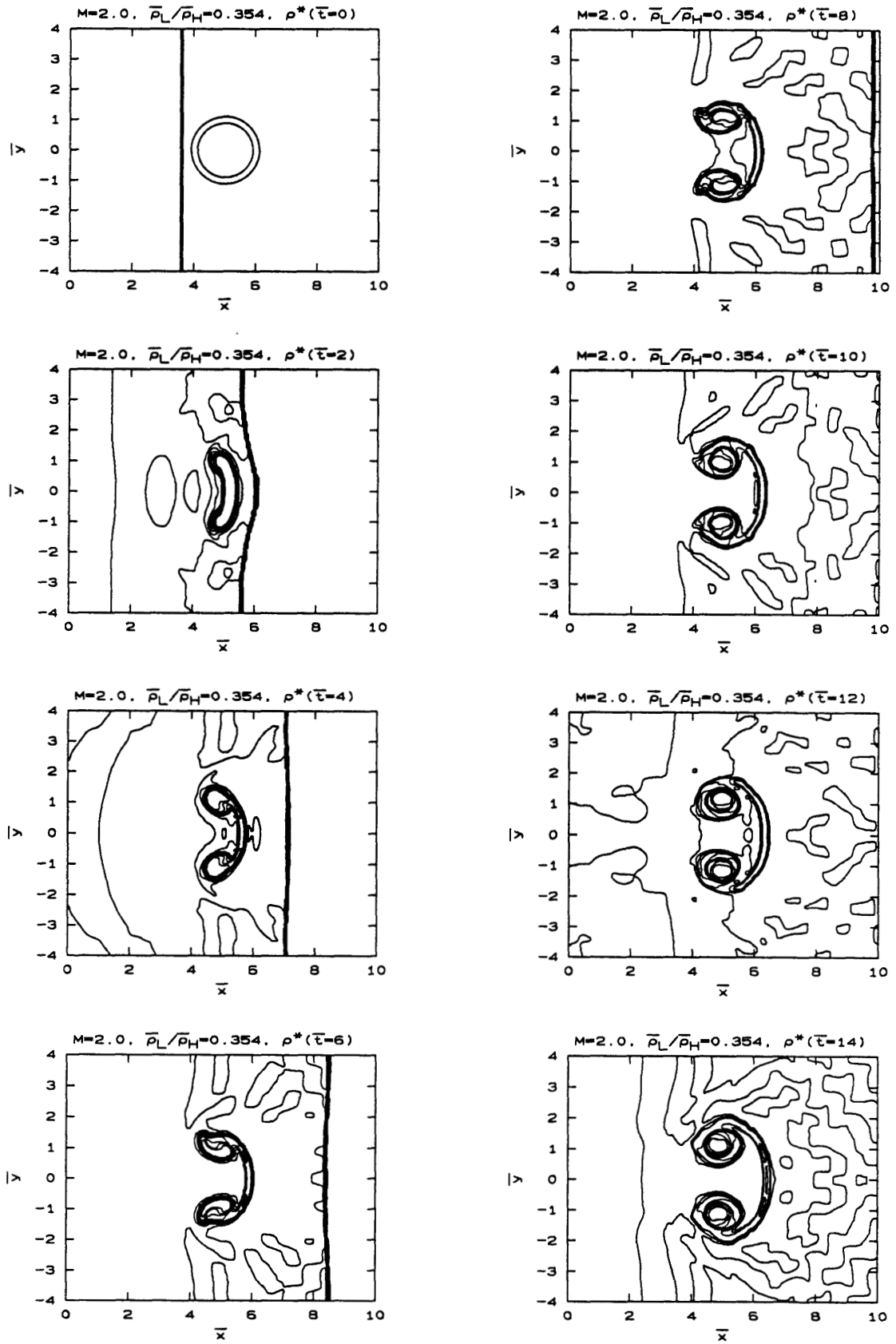

Figure 3.32 - Circular jet with M=2.0 and $\overline{\rho}_L/\overline{\rho}_H = 0.354$. Density contours.

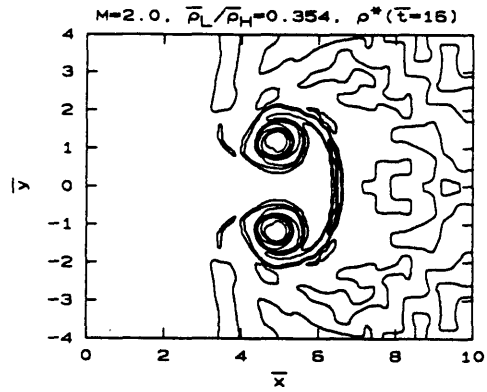
M=2.0. $\bar{\rho}_L/\bar{\rho}_H$=0.354. $\rho^*(\bar{t}$=16)
$\bar{y}$
$\bar{x}$

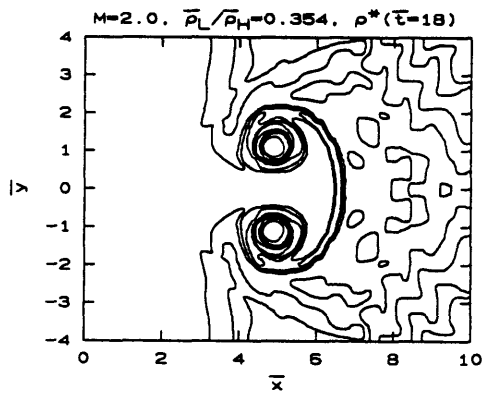
M=2.0. $\bar{\rho}_L/\bar{\rho}_H$=0.354. $\rho^*(\bar{t}$=18)
$\bar{y}$
$\bar{x}$

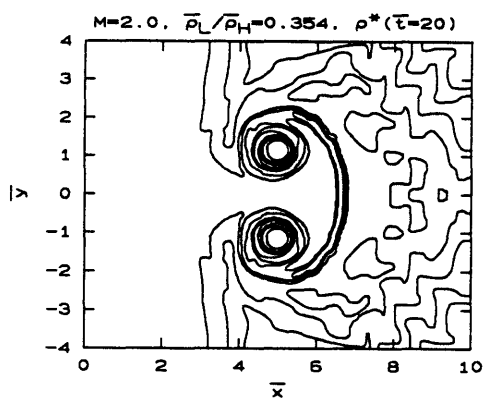
M=2.0. $\bar{\rho}_L/\bar{\rho}_H$=0.354. $\rho^*(\bar{t}$=20)
$\bar{y}$
$\bar{x}$

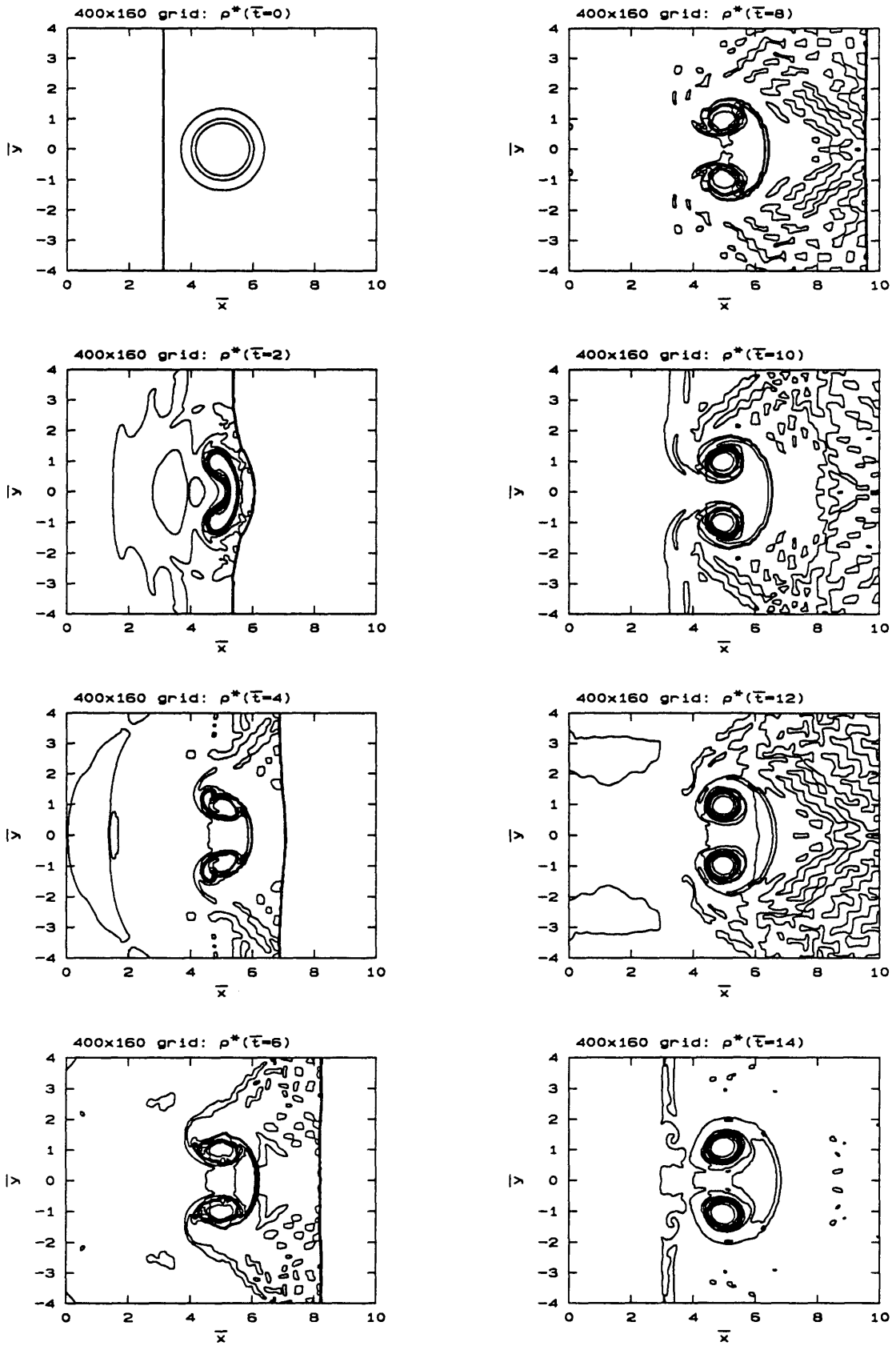

Figure 4.1 - Circular jet with M=2.0 and $\overline{\rho}_L/\overline{\rho}_H = 0.138$. 400x160 grid. Density contours.

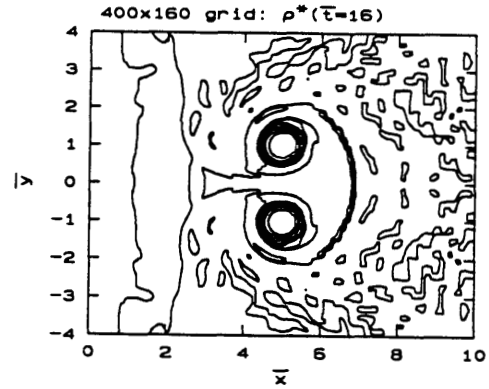
400x160 grid: ρ*(t̄=16)
ȳ
x̄

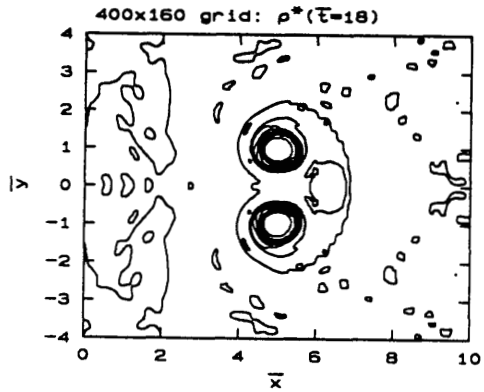
400x160 grid: ρ*(t̄=18)
ȳ
x̄

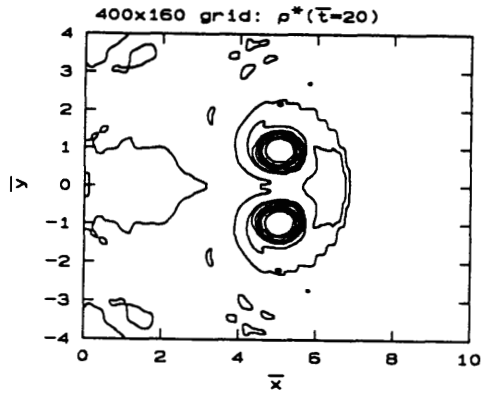
400x160 grid: ρ*(t̄=20)
ȳ
x̄

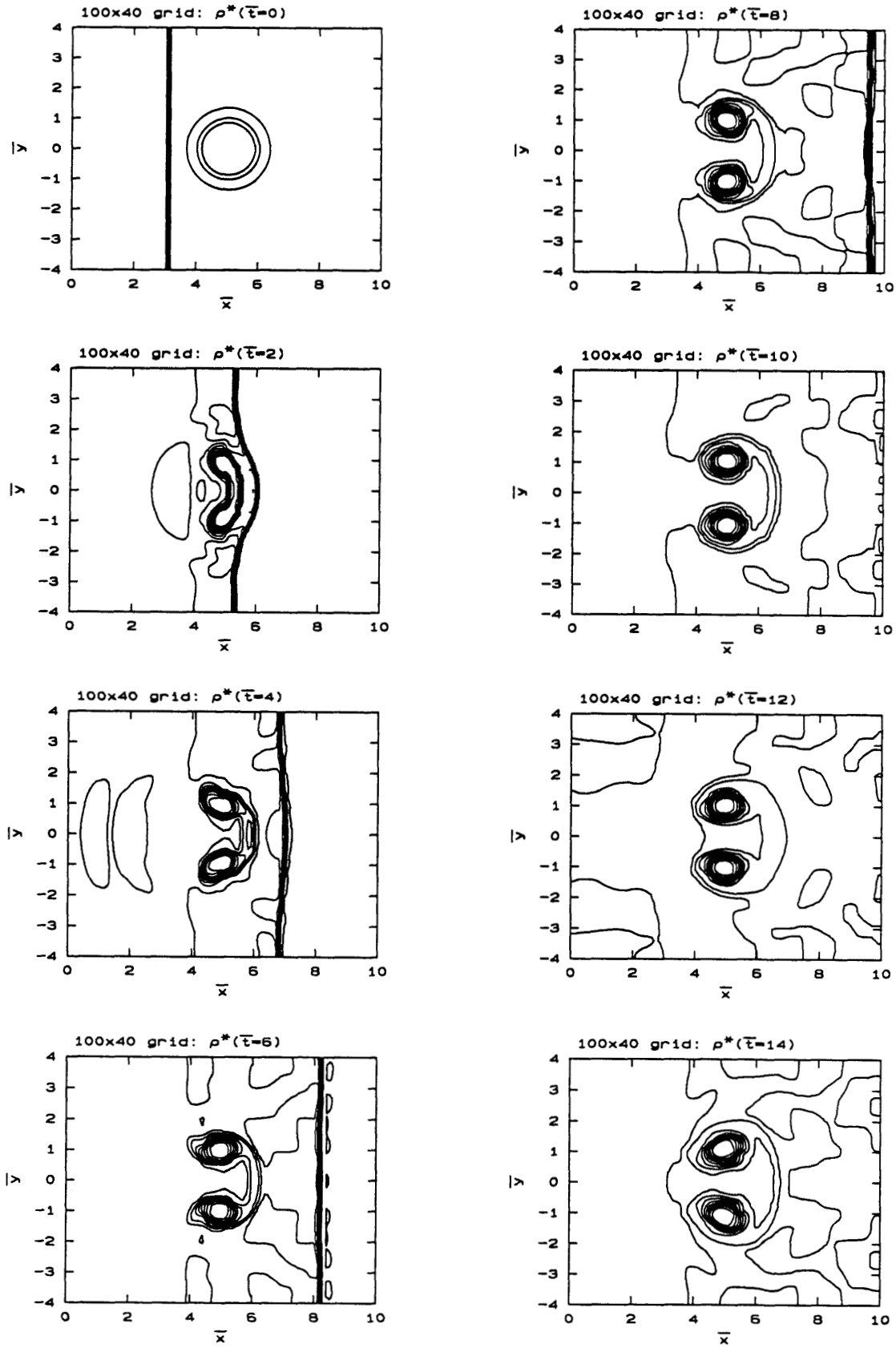

Figure 4.2 - Circular jet with M=2.0 and $\overline{\rho}_L/\overline{\rho}_H = 0.138$. 100x40 grid. Density contours.

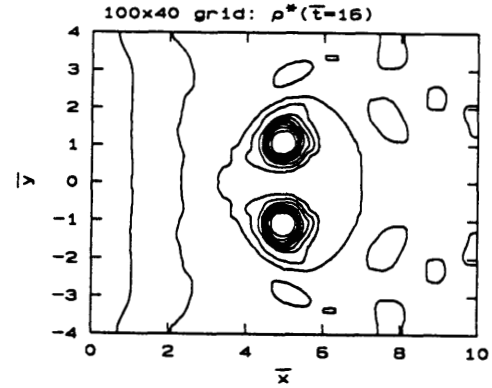
100x40 grid: ρ*(t̄=16)
ȳ
x̄
4
3
2
1
0
-1
-2
-3
-4
0
2
4
6
8
10

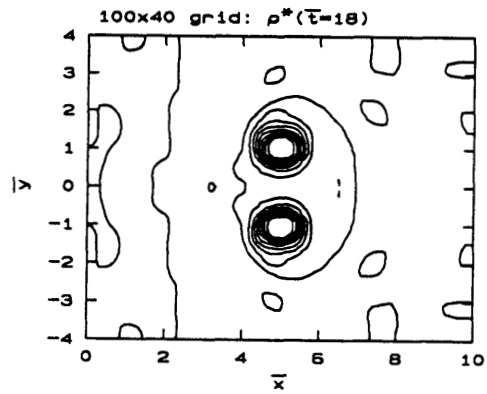
100x40 grid: ρ*(t̄=18)
ȳ
x̄
4
3
2
1
0
-1
-2
-3
-4
0
2
4
6
8
10

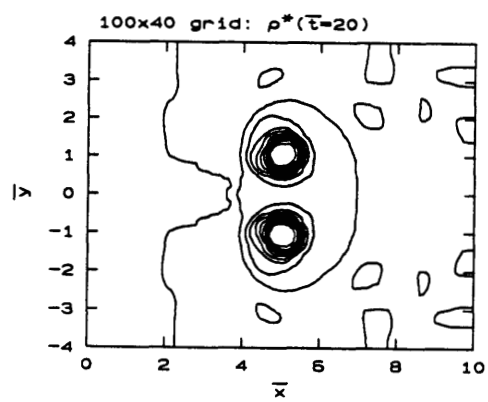
100x40 grid: ρ*(t̄=20)
ȳ
x̄
4
3
2
1
0
-1
-2
-3
-4
0
2
4
6
8
10

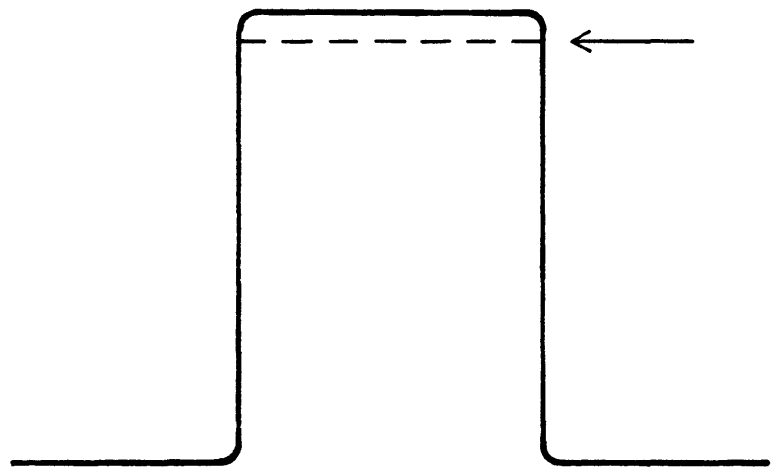

(a)

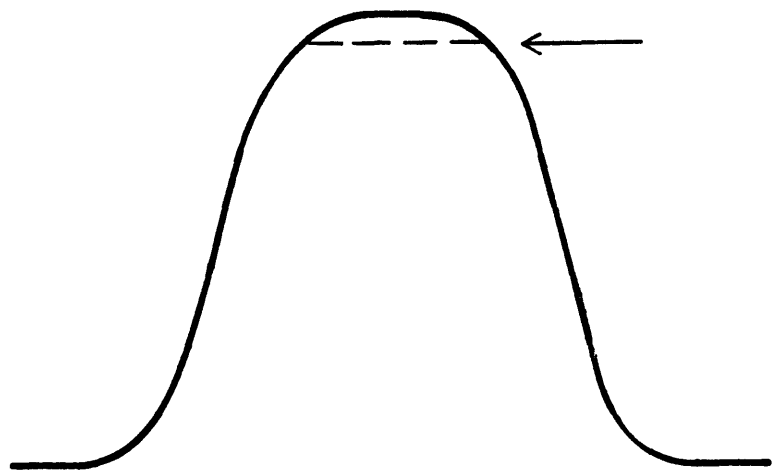

(b)

Figure 4.3 - Effect of residual diffusion on a smoothed top hat profile (a) $\bar{t}=0^{+}$, (b) $\bar{t} \gg 0$.

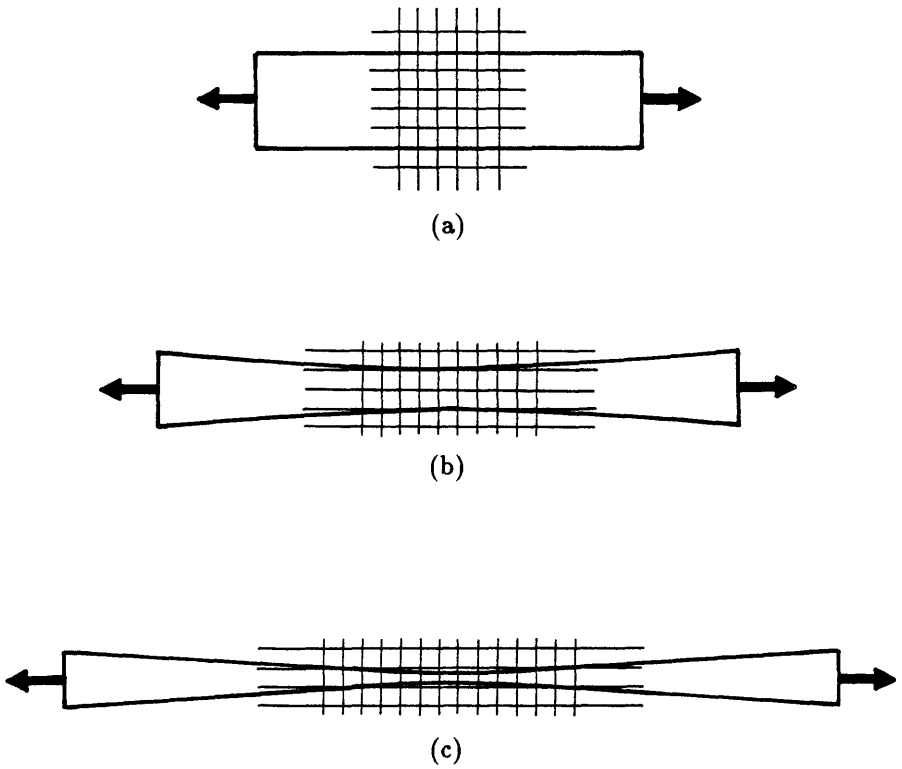

Figure 4.4 - Strained thin strip (a) early-time (resolvable), (b) intermediate time (about to lose resolution), (c) late time (too thin to resolve).

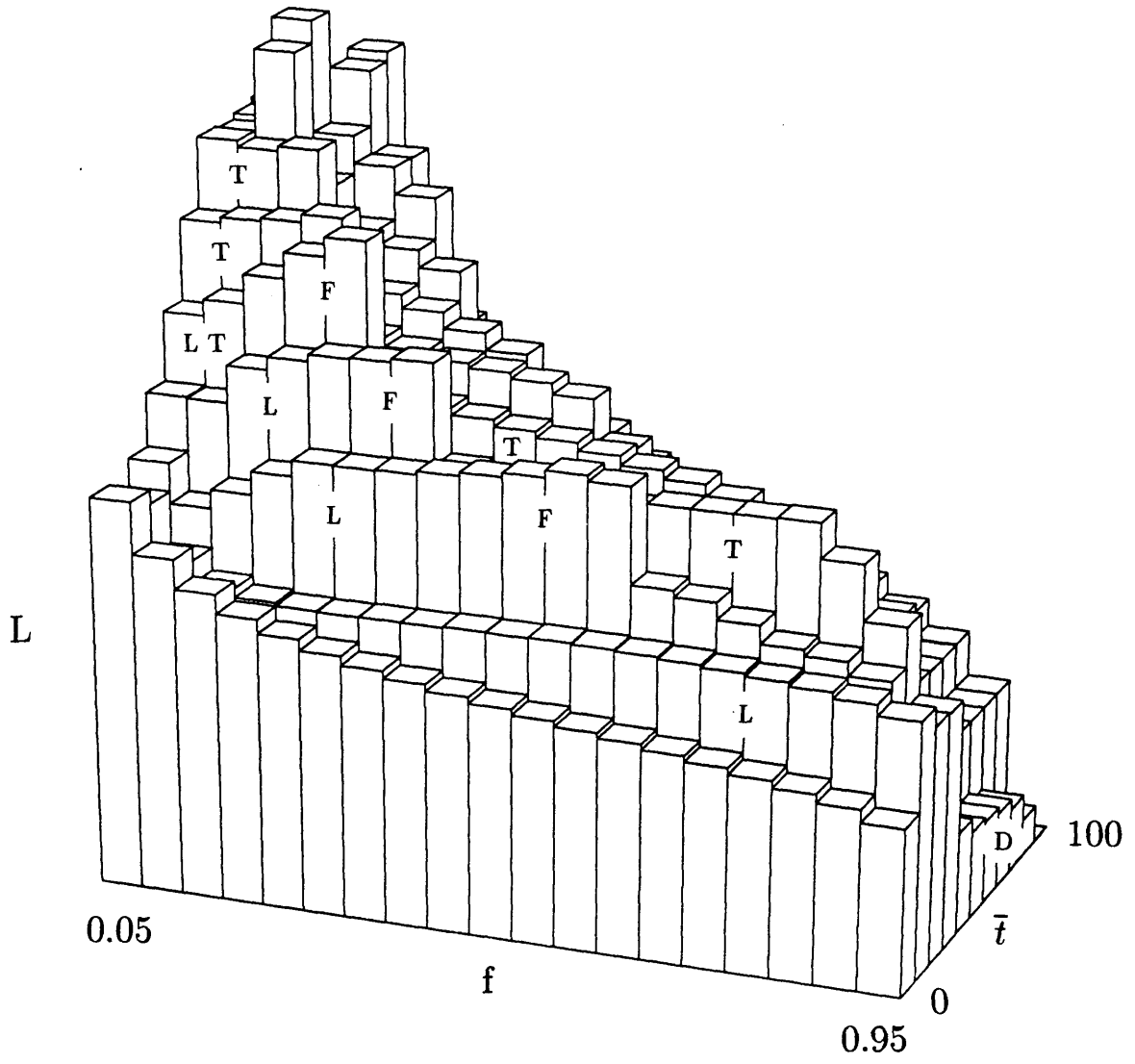

Figure 4.5 - Contour length histogram for M=1.1 and $\overline{\rho}_L/\overline{\rho}_H = 0.138$.

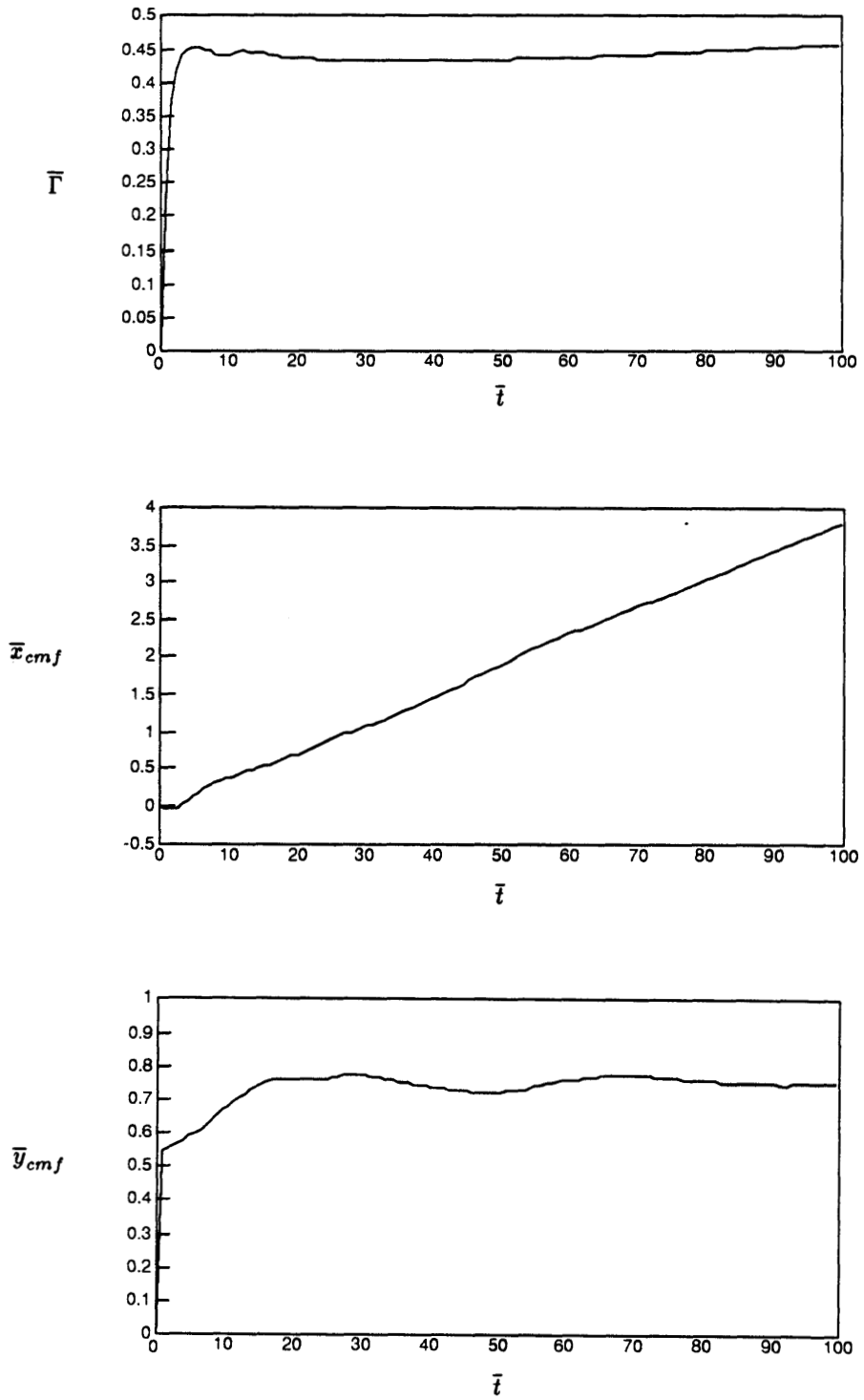

Figure 4.6 - Circular jet with M=1.1 and $\overline{\rho}_L/\overline{\rho}_H = 0.138$: (a) $\overline{\Gamma}(\overline{t})$, (b) $\overline{x}_{cmf}(\overline{t})$, (c) $\overline{y}_{cmf}(\overline{t})$.

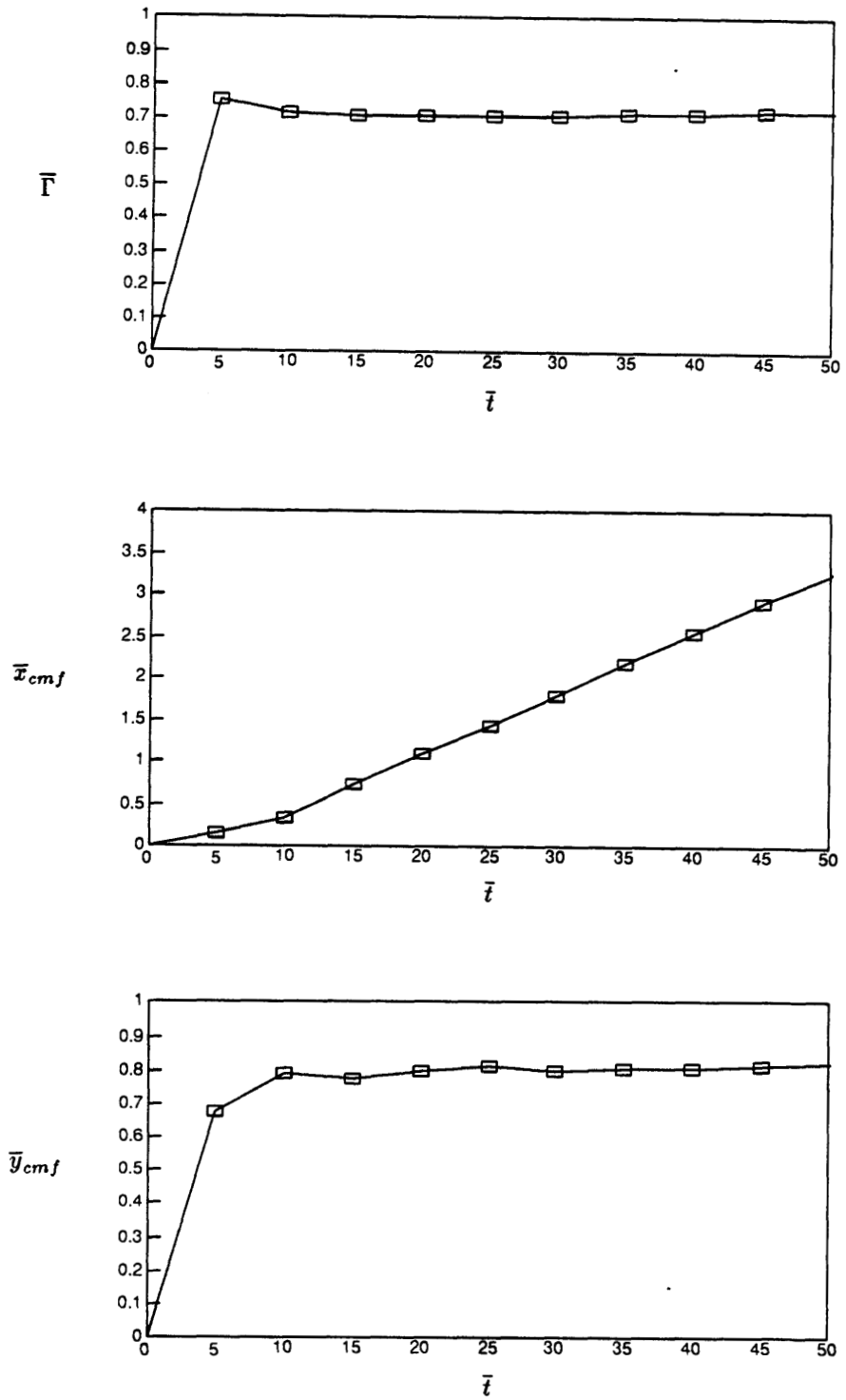

Figure 4.7 - Circular jet with M=1.2 and $\overline{\rho}_L/\overline{\rho}_H = 0.138$: (a) $\overline{\Gamma}(\overline{t})$, (b) $\overline{x}_{cmf}(\overline{t})$, (c) $\overline{y}_{cmf}(\overline{t})$.

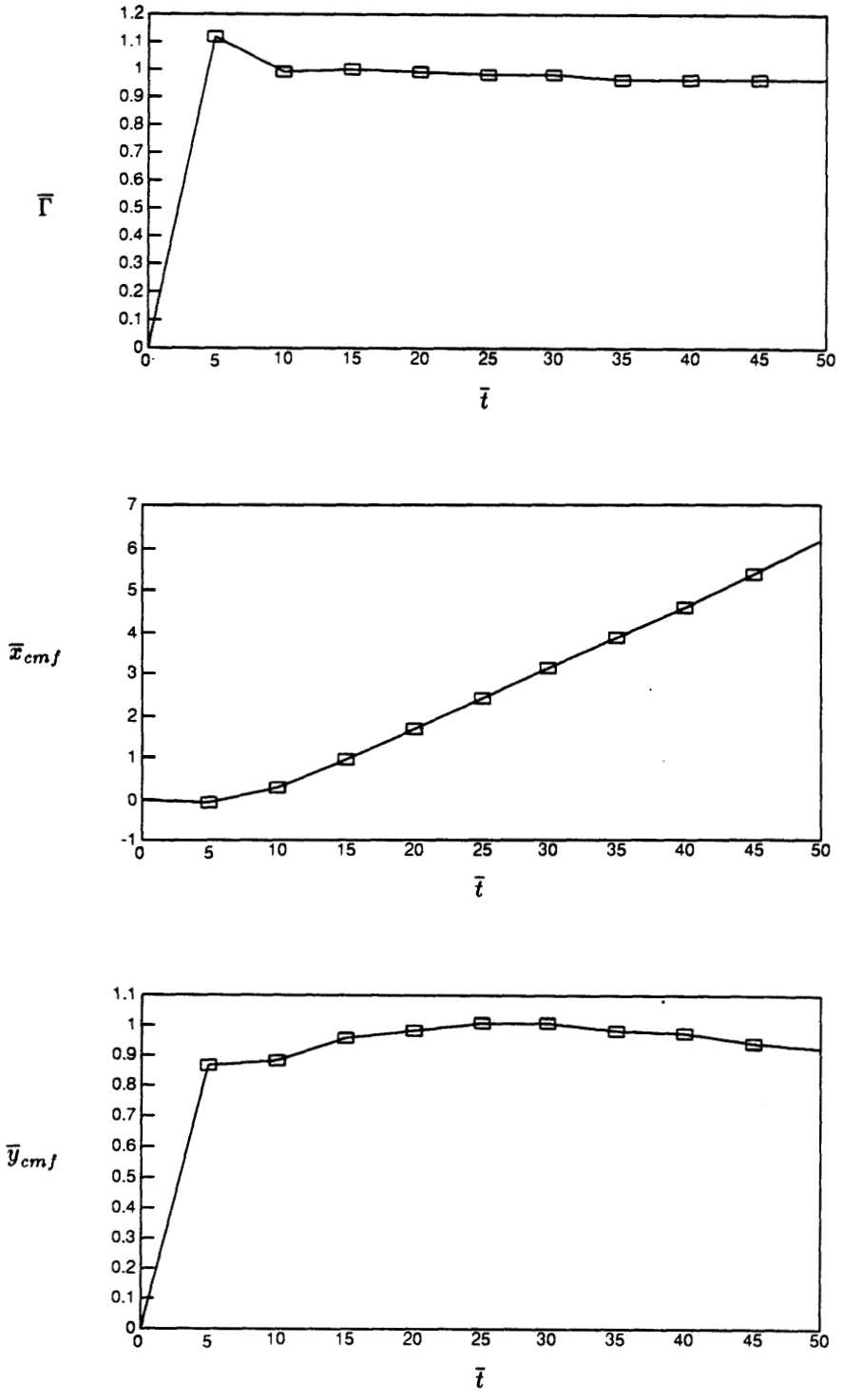

Figure 4.8 - Circular jet with M=1.5 and $\overline{\rho}_L/\overline{\rho}_H = 0.138$: (a) $\overline{\Gamma}(\overline{t})$, (b) $\overline{x}_{cmf}(\overline{t})$, (c) $\overline{y}_{cmf}(\overline{t})$.

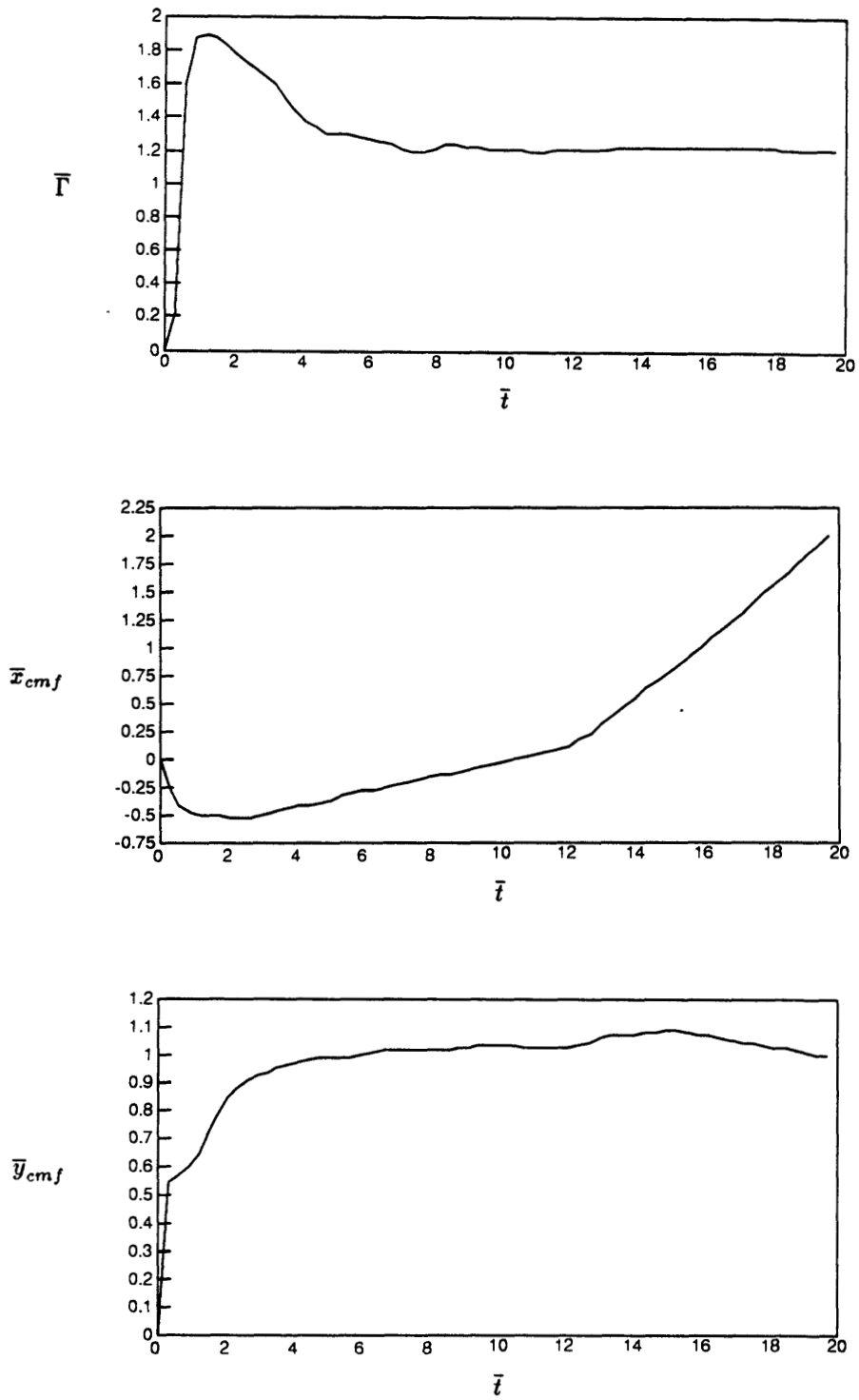

Figure 4.9 - Circular jet with M=2.0 and $\overline{\rho}_L/\overline{\rho}_H = 0.138$: (a) $\overline{\Gamma}(\overline{t})$, (b) $\overline{x}_{cmf}(\overline{t})$, (c) $\overline{y}_{cmf}(\overline{t})$.

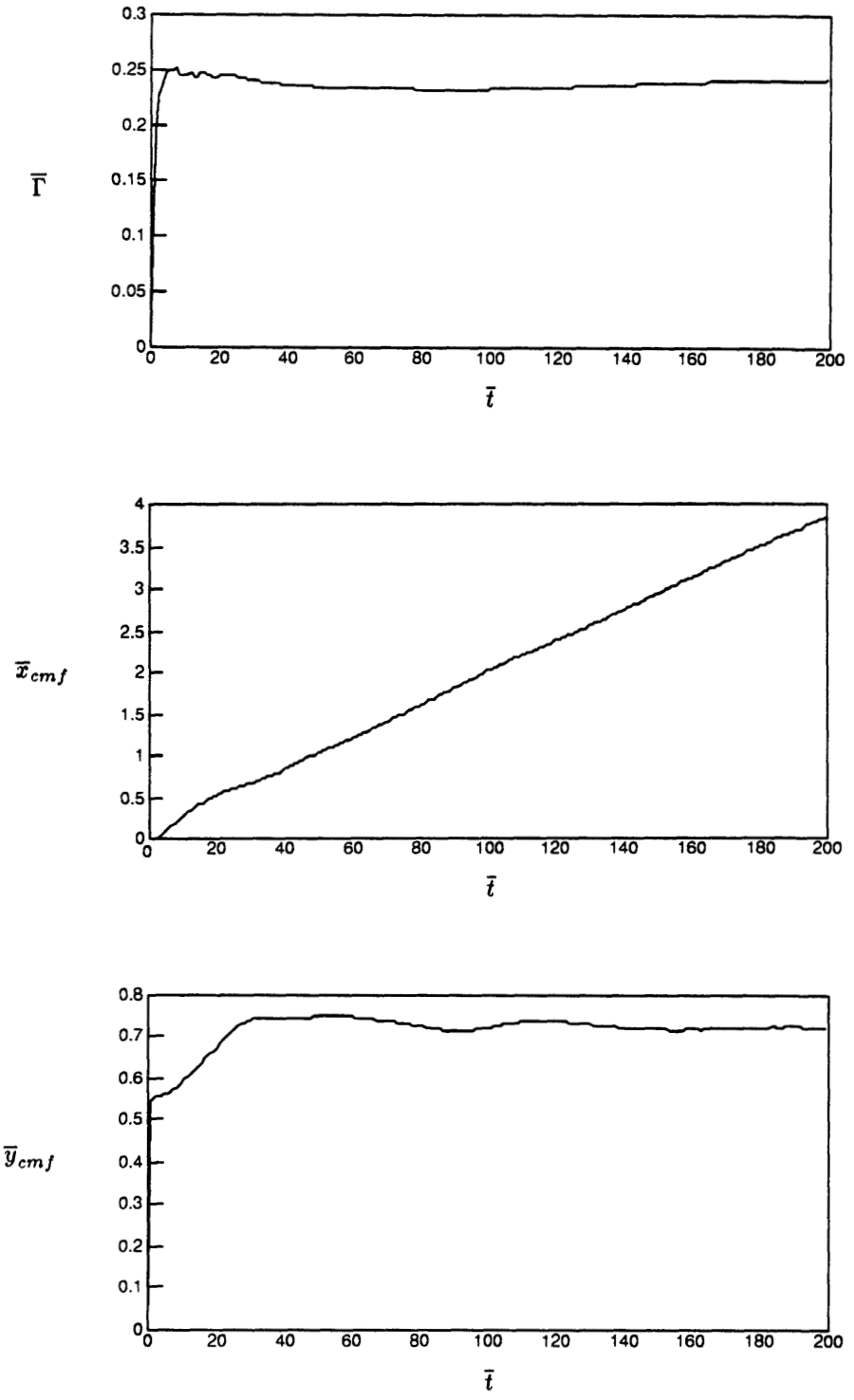

Figure 4.10 - Circular jet with M=1.05 and $\overline{\rho}_L/\overline{\rho}_H = 0.138$: (a) $\overline{\Gamma}(\overline{t})$, (b) $\overline{x}_{cmf}(\overline{t})$, (c) $\overline{y}_{cmf}(\overline{t})$.

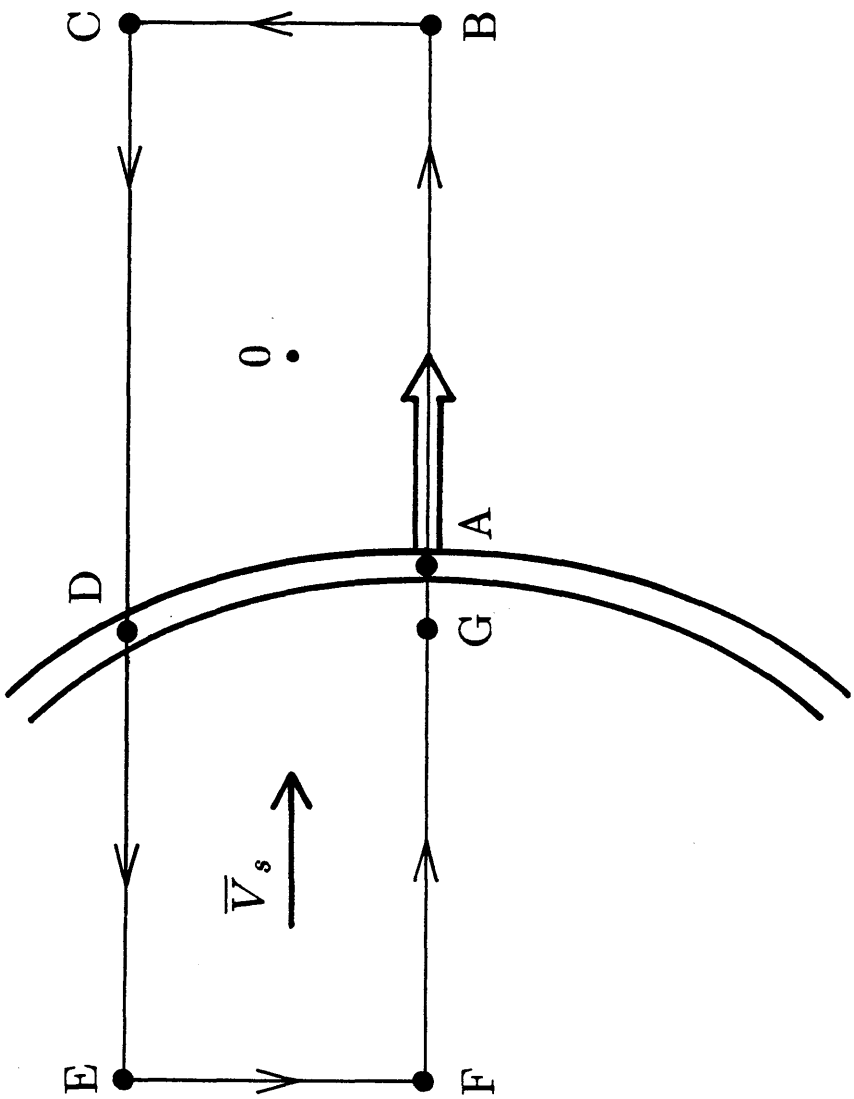

Figure 4.11 - Fictitious circulation due to a curved shock wave.

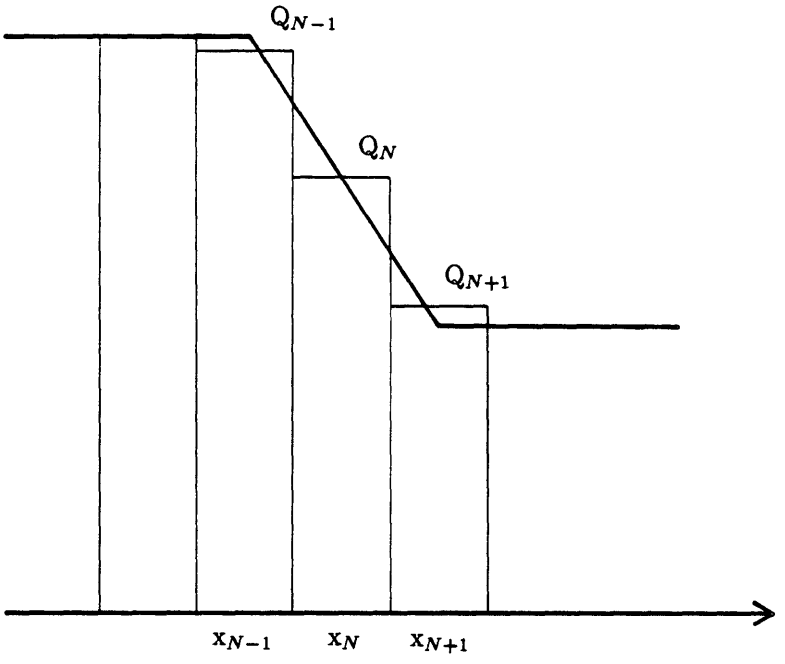

Figure 4.12 - Propagation of a gradient.

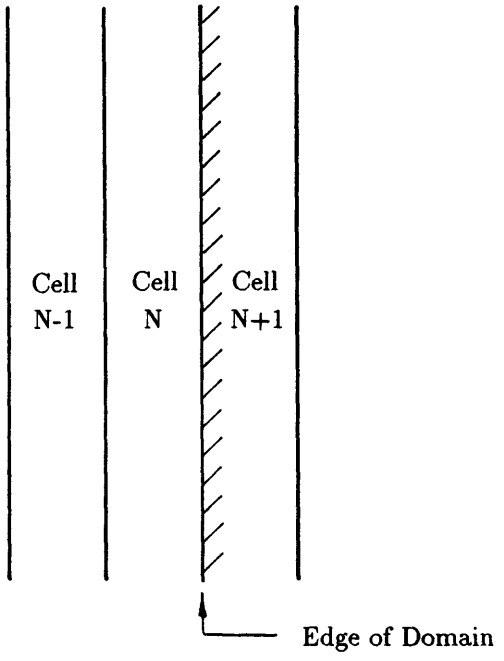

Figure 4.13 - A guard cell at the edge of the domain.

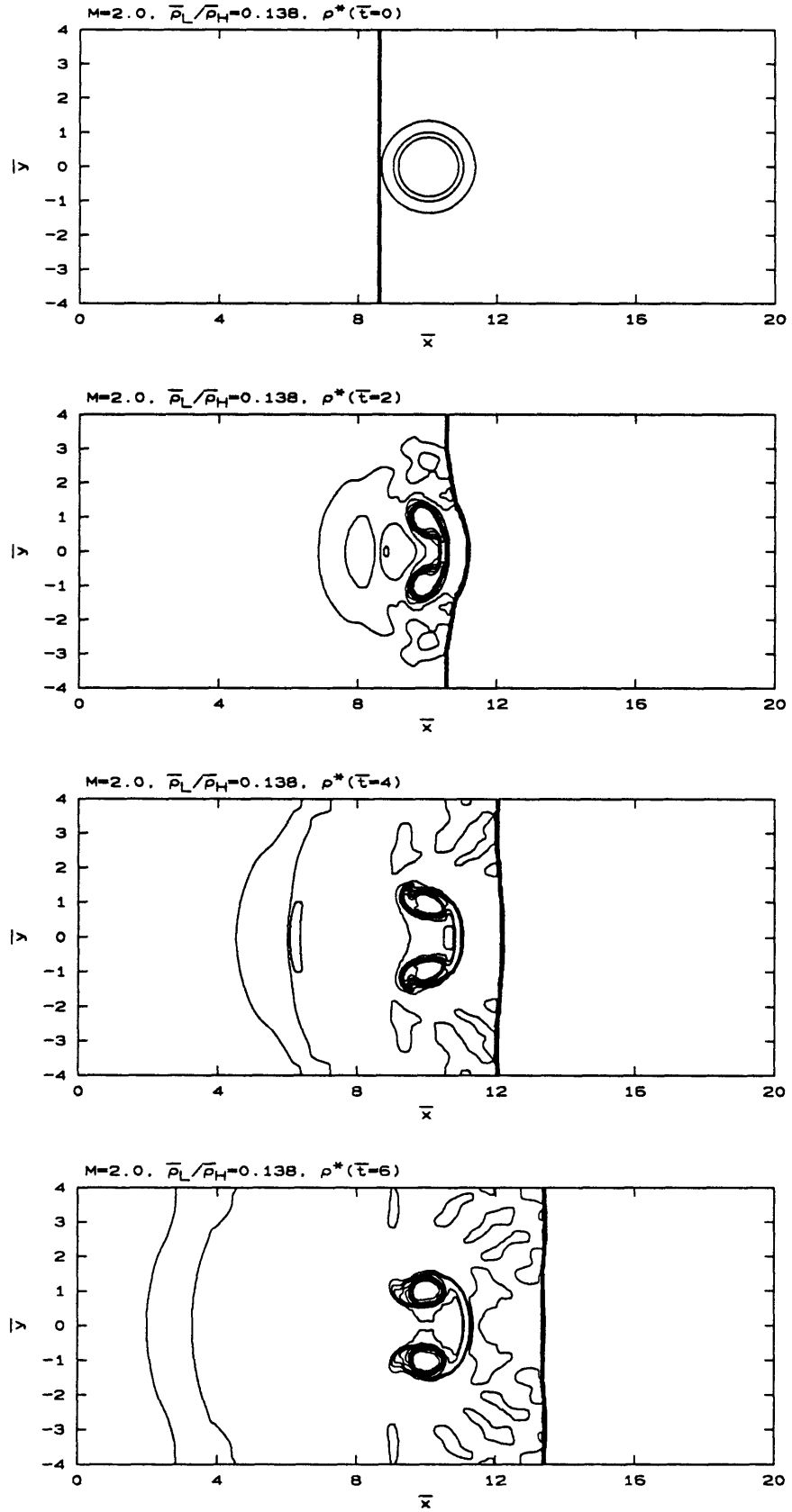

Figure 4.14 - Circular jet with M=2.0 and $\overline{\rho}_L/\overline{\rho}_H = 0.138$. Long domain. Density contours.

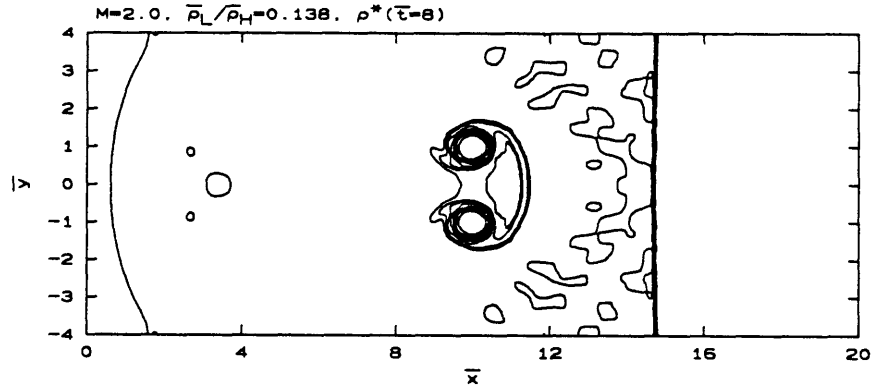
M=2.0. $\bar{\rho}_L/\bar{\rho}_H$=0.138. $\rho^*(\bar{t}$=8)
$\bar{y}$
$\bar{x}$

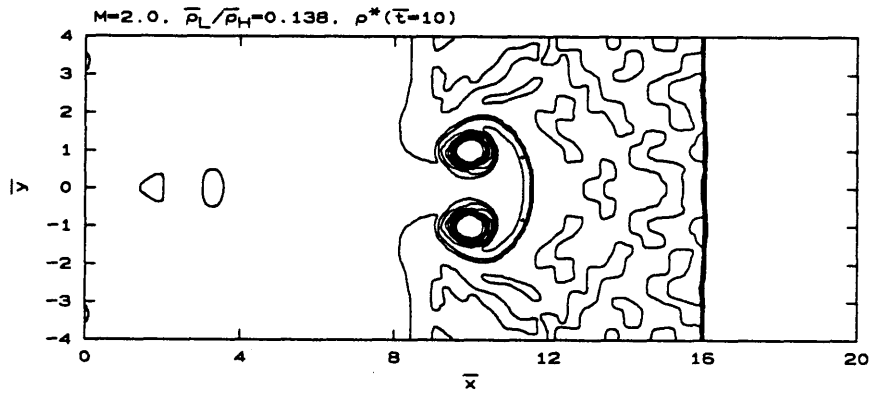
M=2.0. $\bar{\rho}_L/\bar{\rho}_H$=0.138. $\rho^*(\bar{t}$=10)
$\bar{y}$
$\bar{x}$

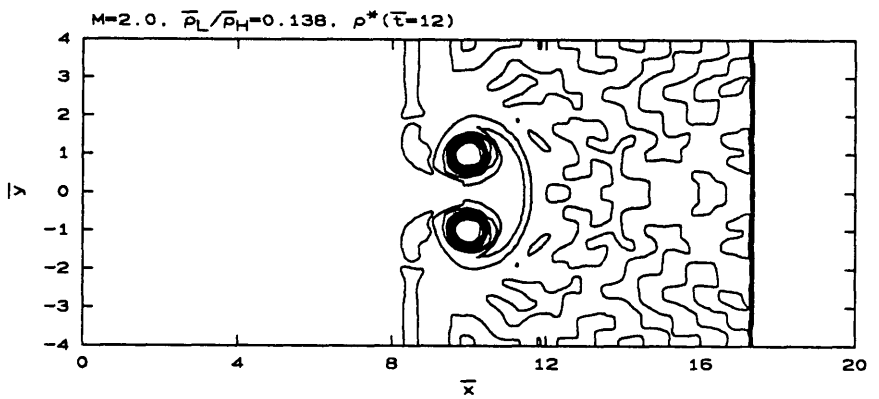
M=2.0. $\bar{\rho}_L/\bar{\rho}_H$=0.138. $\rho^*(\bar{t}$=12)
$\bar{y}$
$\bar{x}$

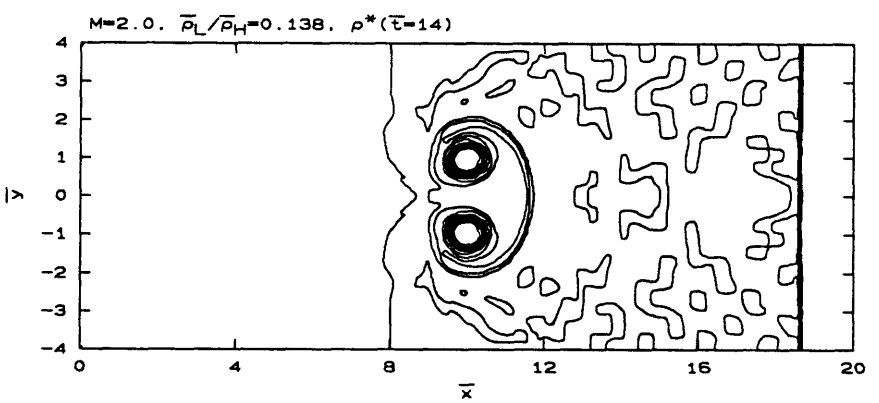
M=2.0. $\bar{\rho}_L/\bar{\rho}_H$=0.138. $\rho^*(\bar{t}$=14)
$\bar{y}$
$\bar{x}$

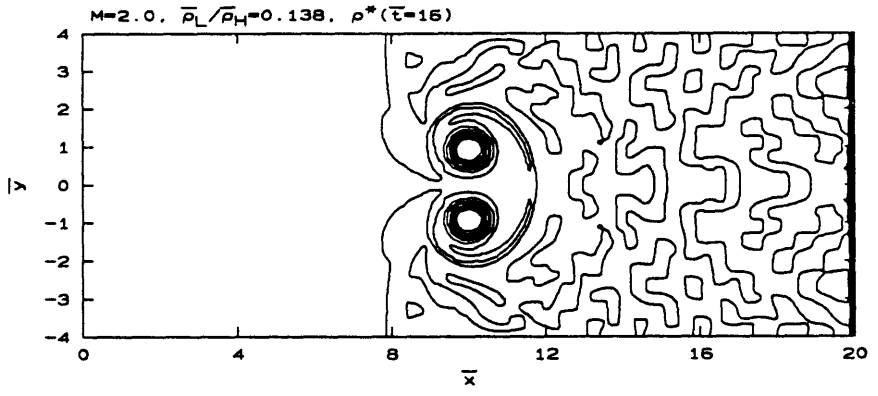
M=2.0, $\overline{\rho}_L/\overline{\rho}_H$=0.138, $\rho^*(\overline{t}$=16)
$\overline{y}$
$\overline{x}$

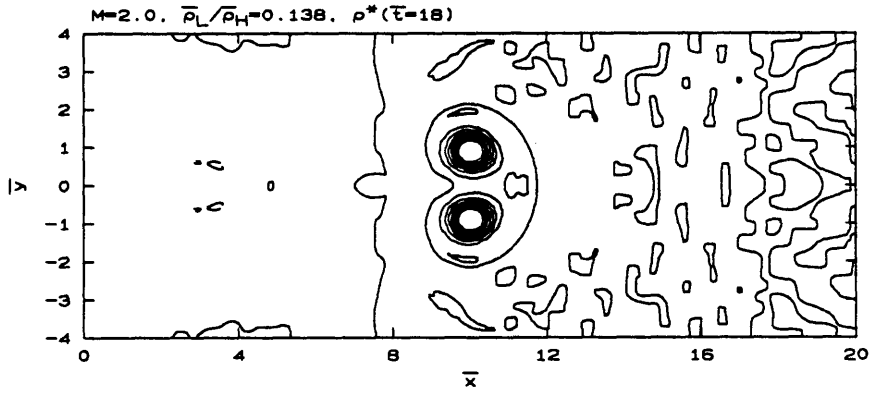
M=2.0, $\overline{\rho}_L/\overline{\rho}_H$=0.138, $\rho^*(\overline{t}$=18)
$\overline{y}$
$\overline{x}$

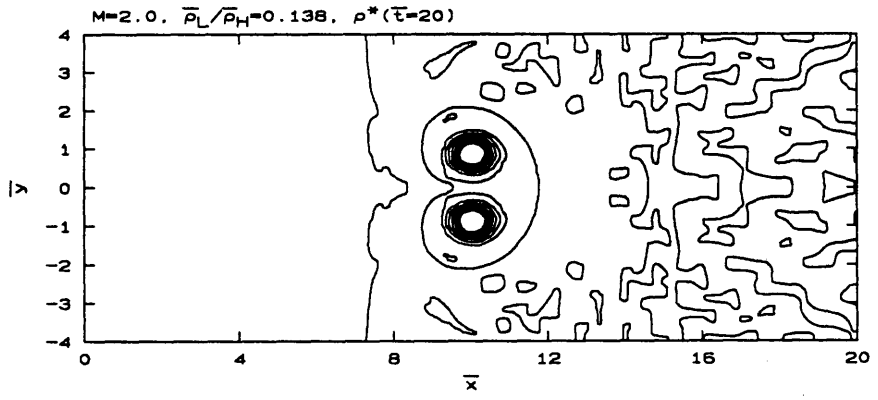
M=2.0, $\overline{\rho}_L/\overline{\rho}_H$=0.138, $\rho^*(\overline{t}$=20)
$\overline{y}$
$\overline{x}$

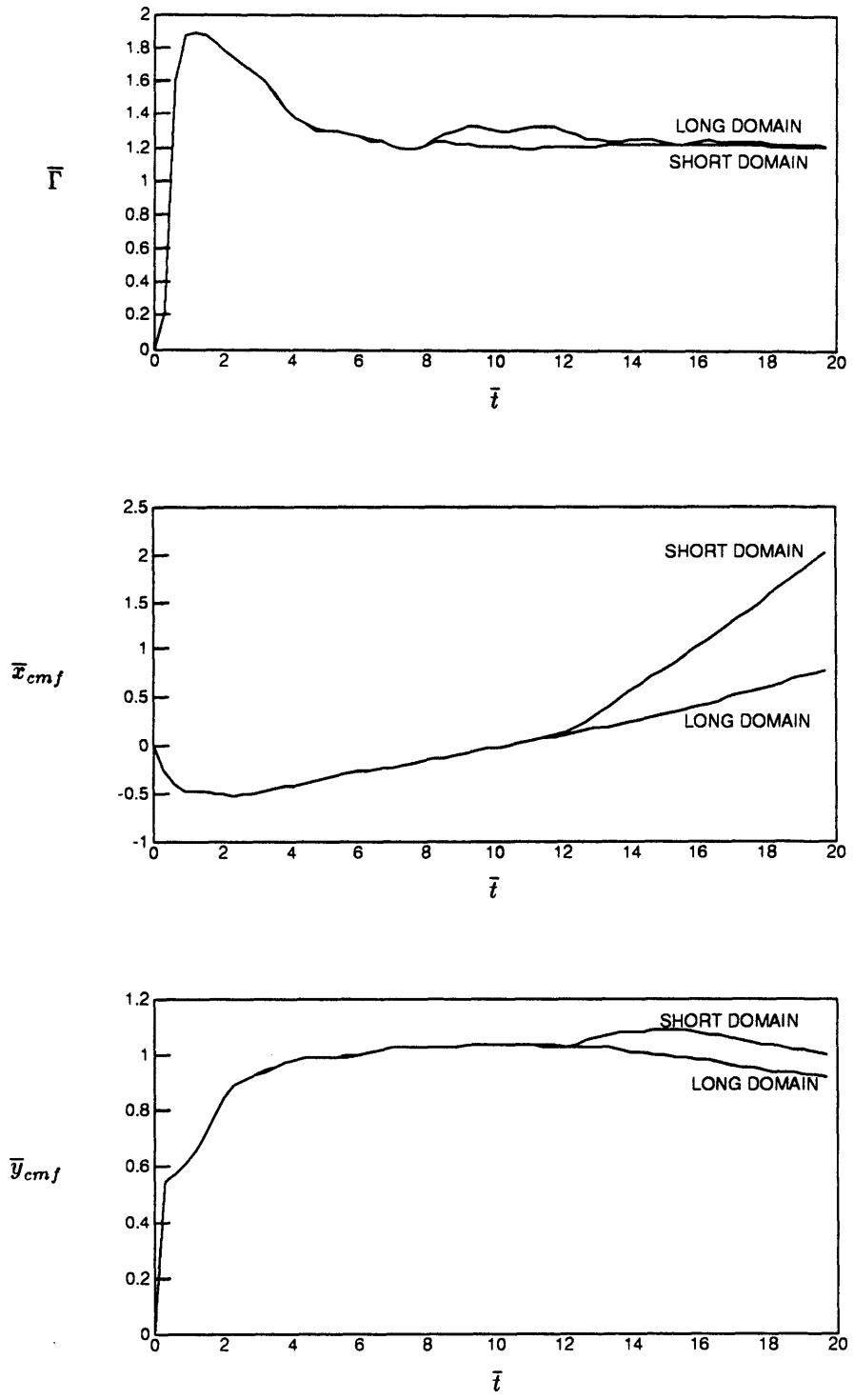

Figure 4.15 - Circular jet with M=2.0 and $\overline{\rho}_L/\overline{\rho}_H = 0.138$. Comparison of short- and long-domain: (a) $\overline{\Gamma}(\bar{t})$, (b) $\overline{x}_{cmf}(\bar{t})$, (c) $\overline{y}_{cmf}(\bar{t})$.

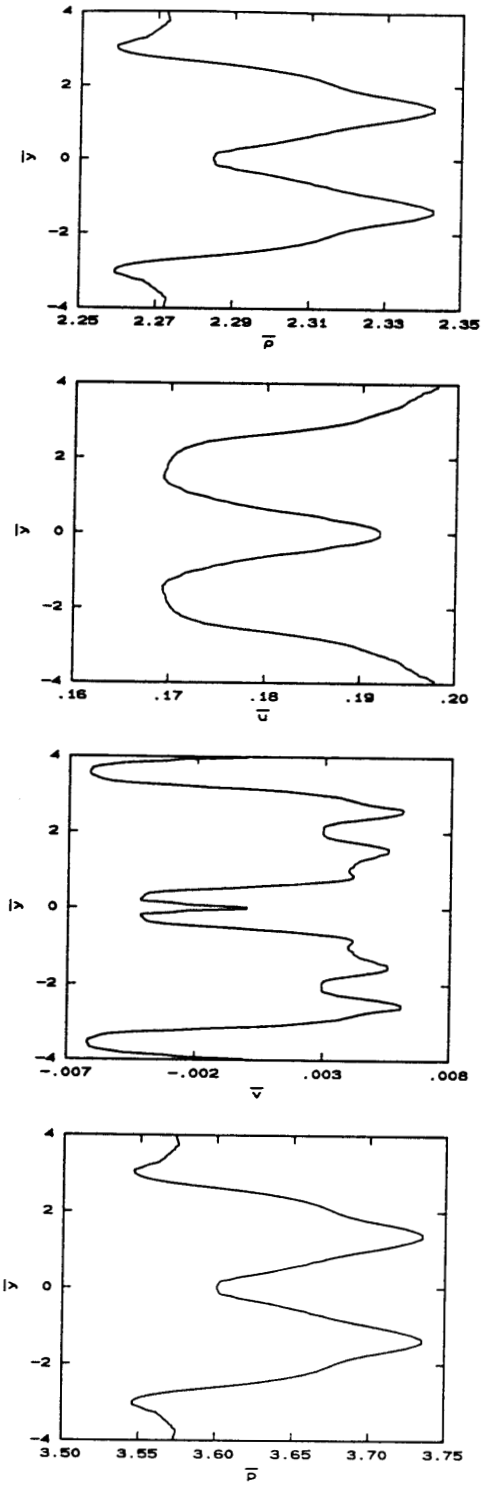

Figure 4.16 - Circular jet with M=2.0 and $\overline{\rho}_L/\overline{\rho}_H = 0.138$. Vertical cut through $\overline{x}$=0 at $\overline{t} = 18$.

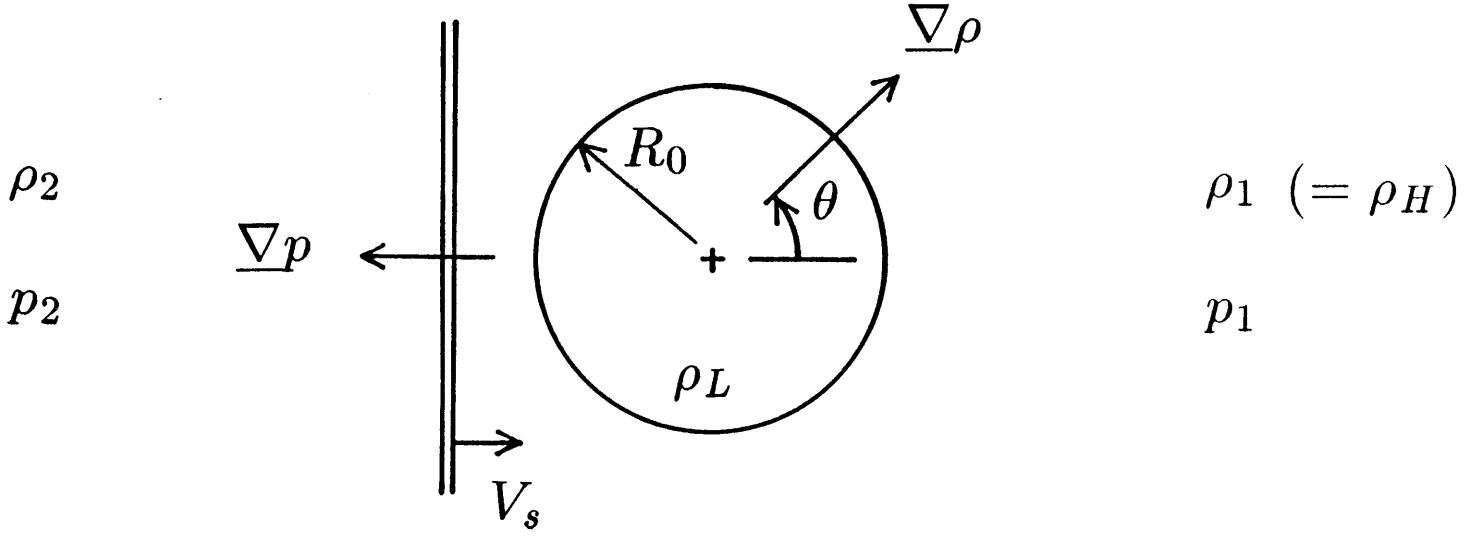

Figure 5.1 - Schematic for circular jet circulation and impulse models.

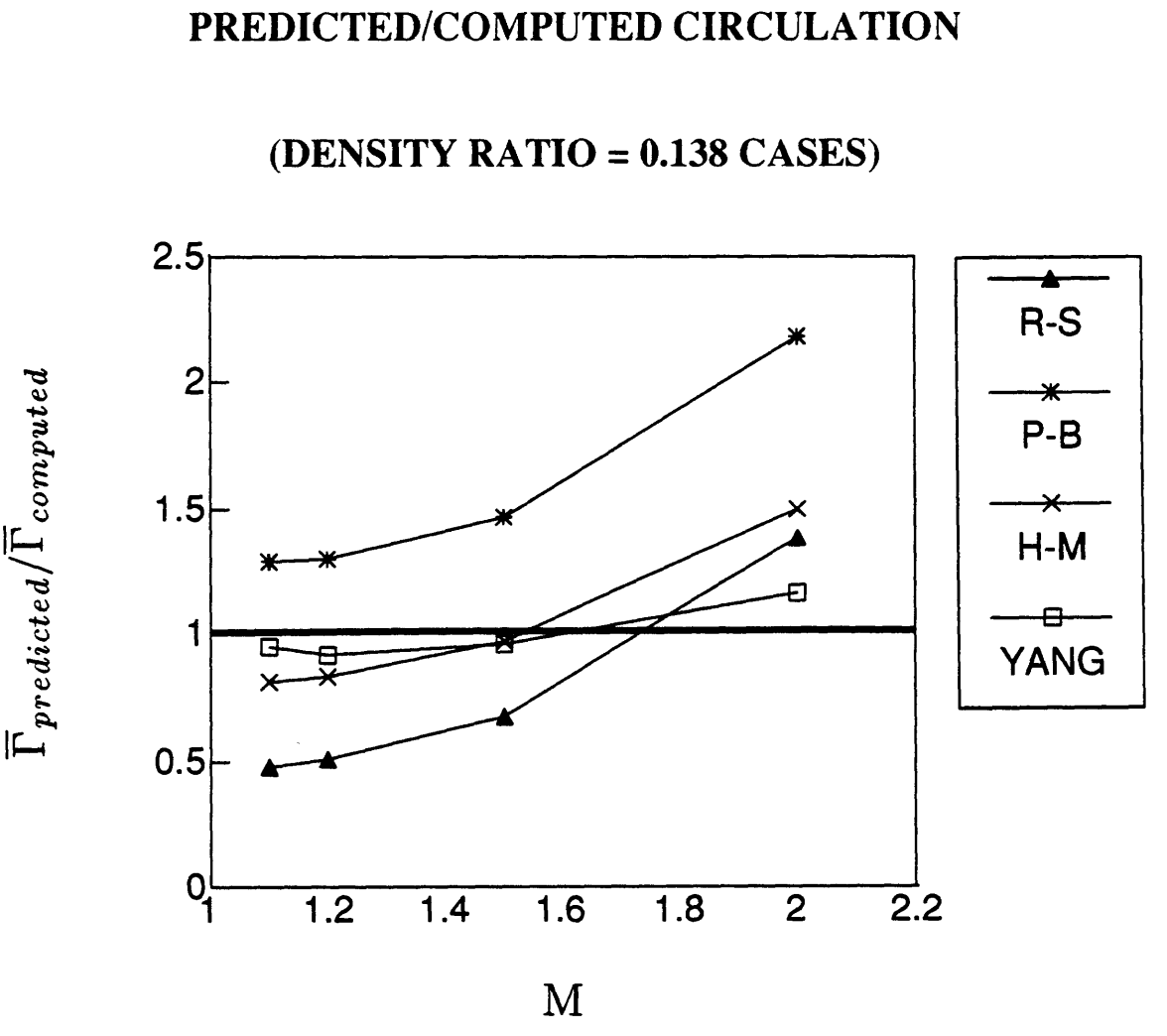

Figure 5.2 - Computed and predicted $\overline{\Gamma}$ for the $\overline{\rho}_L/\overline{\rho}_H = 0.138$ canonical flows.

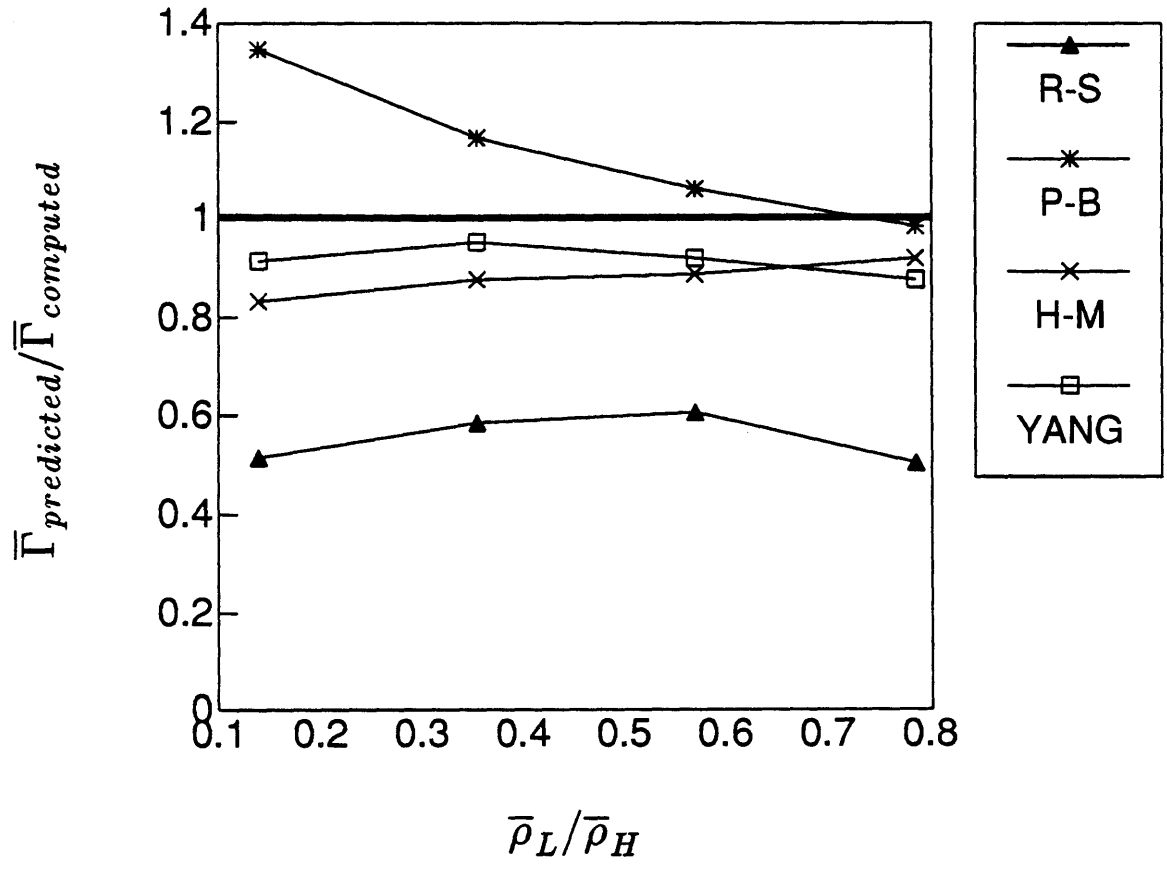

Figure 5.3 - Computed and predicted $\overline{\Gamma}$ for the M=1.1 canonical flows.

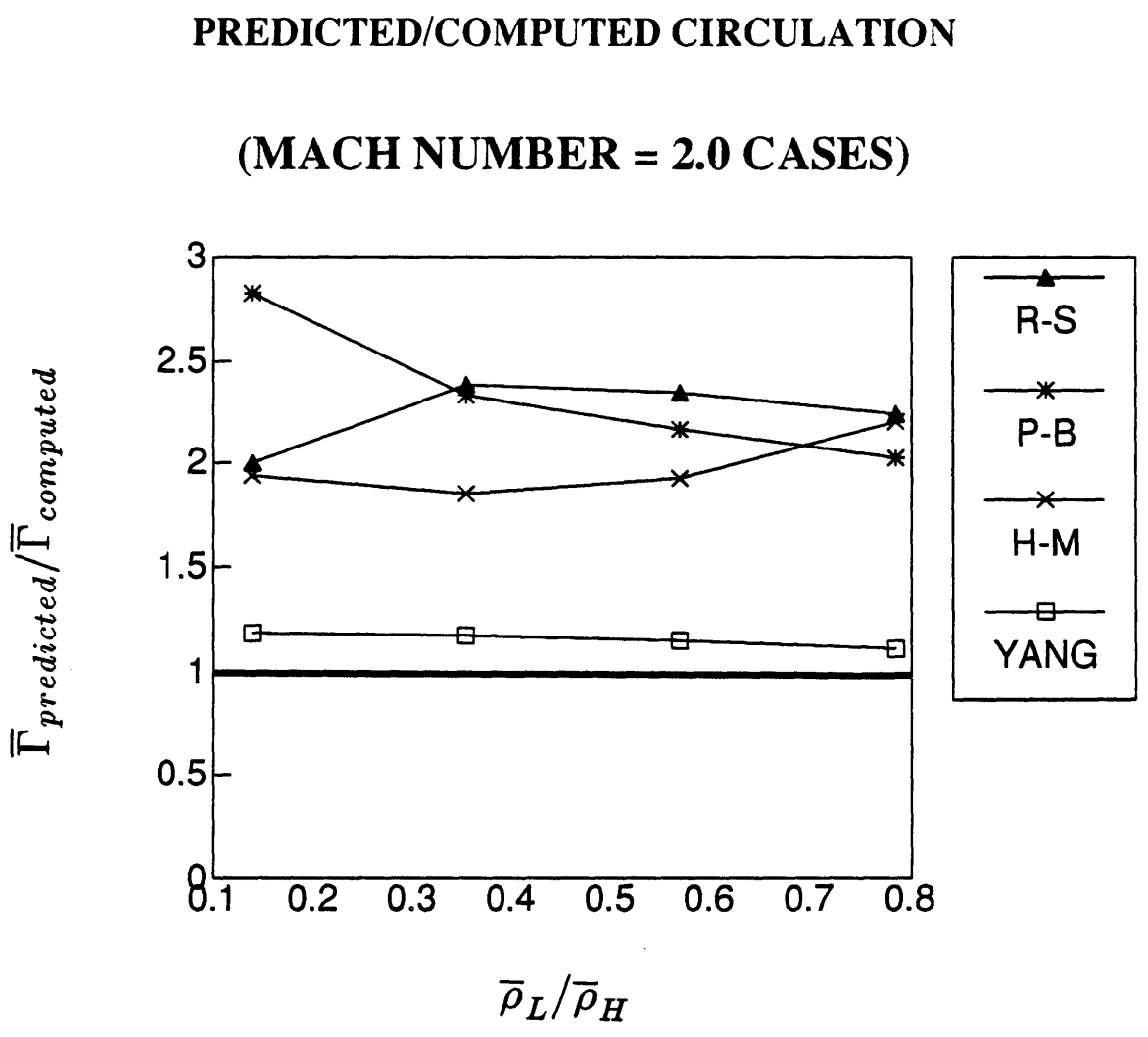

Figure 5.4 - Computed and predicted $\overline{\Gamma}$ for the M=2.0 canonical flows.

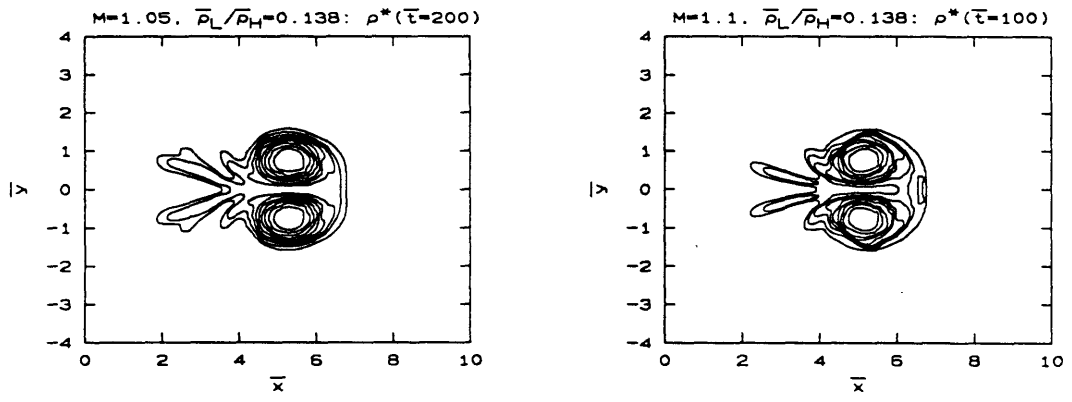

Figure 5.5 - Circular jet density contours for $\overline{\rho}_L/\overline{\rho}_H = 0.138$: (a) M=1.05 at $\overline{t} = 200$, (b) M=1.1 at $\overline{t} = 100$.

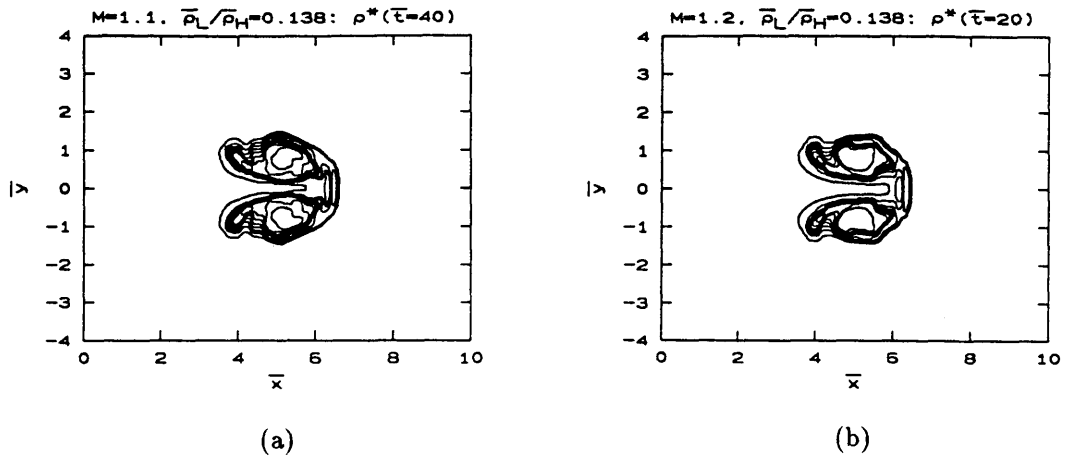

Figure 5.6 - Circular jet density contours for $\overline{\rho}_L/\overline{\rho}_H = 0.138$: (a) M=1.1 at $\overline{t} = 40$, (b) M=1.2 at $\overline{t} = 20$.

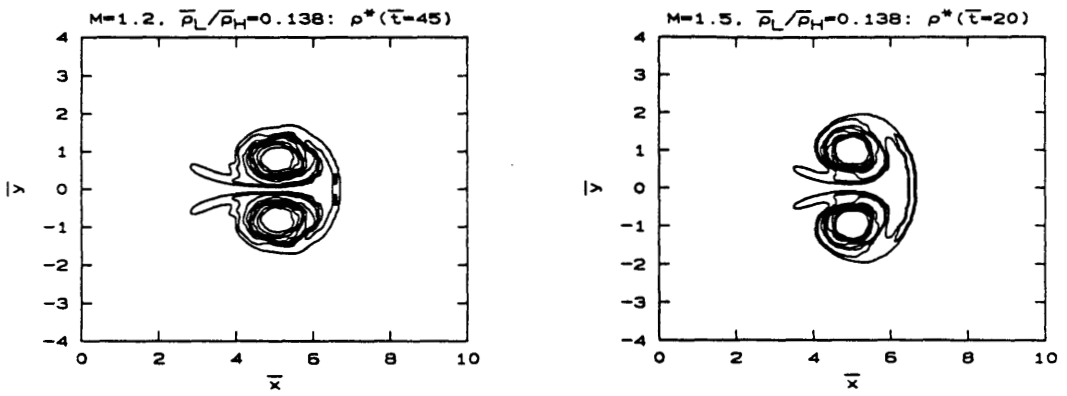

Figure 5.7 - Circular jet density contours for $\overline{\rho}_L/\overline{\rho}_H = 0.138$: (a) M=1.2 at $\overline{t} = 45$, (b) M=1.5 at $\overline{t} = 20$.

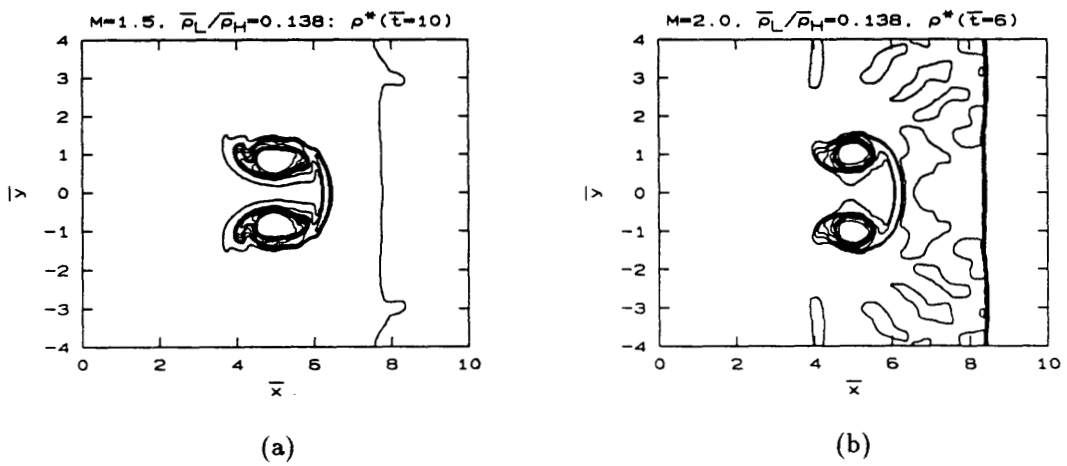

Figure 5.8 - Circular jet density contours for two $\overline{\rho}_L/\overline{\rho}_H = 0.138$: (a) M=1.5 at $\overline{t} = 10$, (b) M=2.0 at $\overline{t} = 6$.

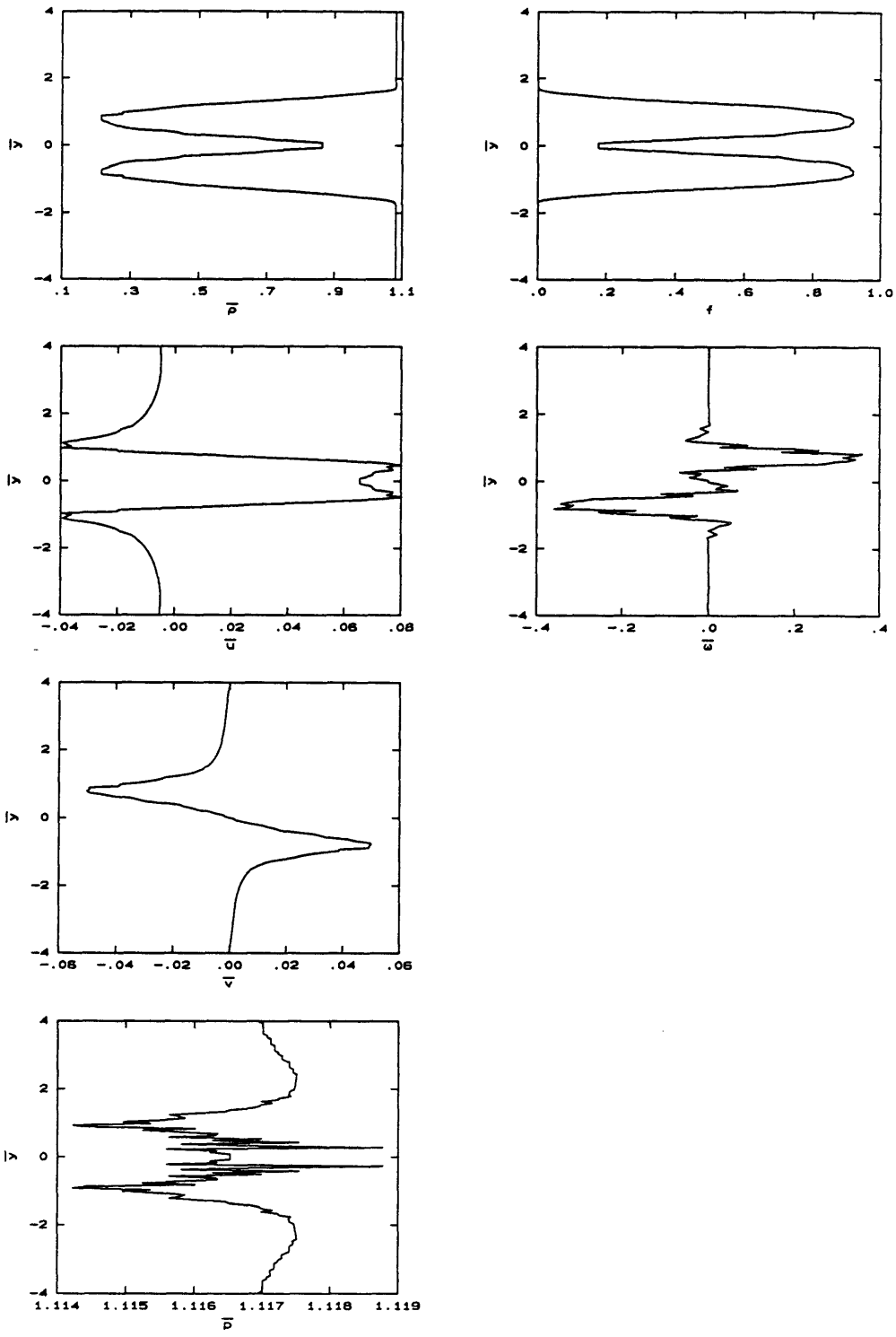

Figure 5.9 - Circular jet with M=1.05 and $\bar{\rho}_L/\bar{\rho}_H = 0.138$. Vertical cuts through the approximate center of the structure at $\bar{t} = 200$.

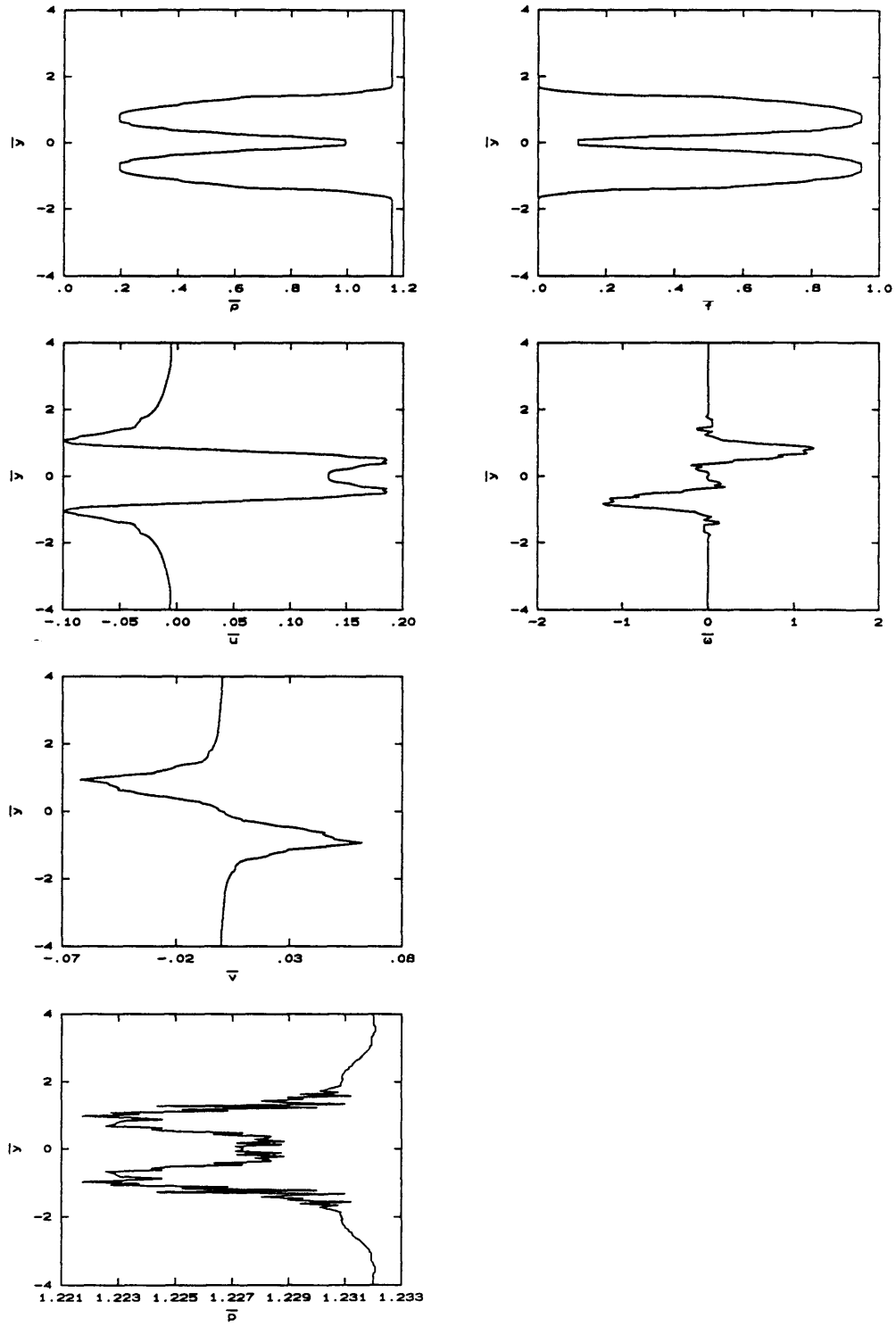

Figure 5.10 - Circular jet with M=1.1 and $\bar{\rho}_L/\bar{\rho}_H = 0.138$. Vertical cuts through the approximate center of the structure at $\bar{t} = 100$.

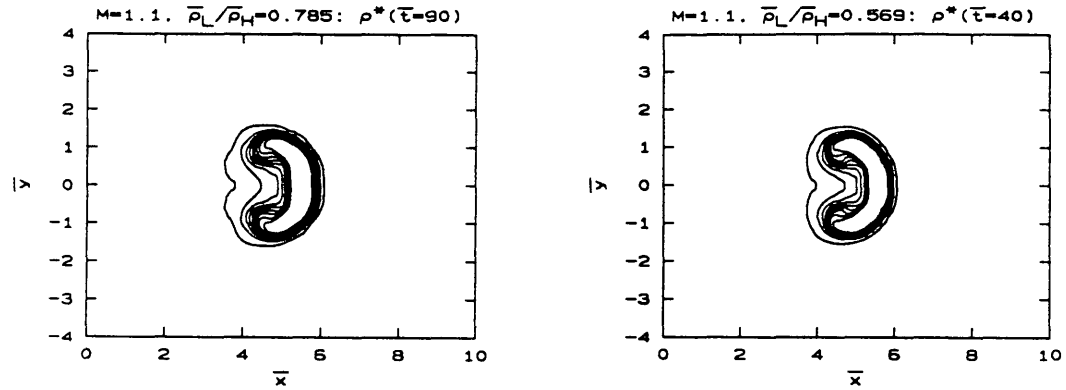

(a) (b)

Figure 5.11 - Circular jet density contours for M=1.1: (a) $\overline{\rho}_L/\overline{\rho}_H = 0.785$ at $\overline{t} = 90$, (b) $\overline{\rho}_L/\overline{\rho}_H = 0.569$ at $\overline{t} = 40$.

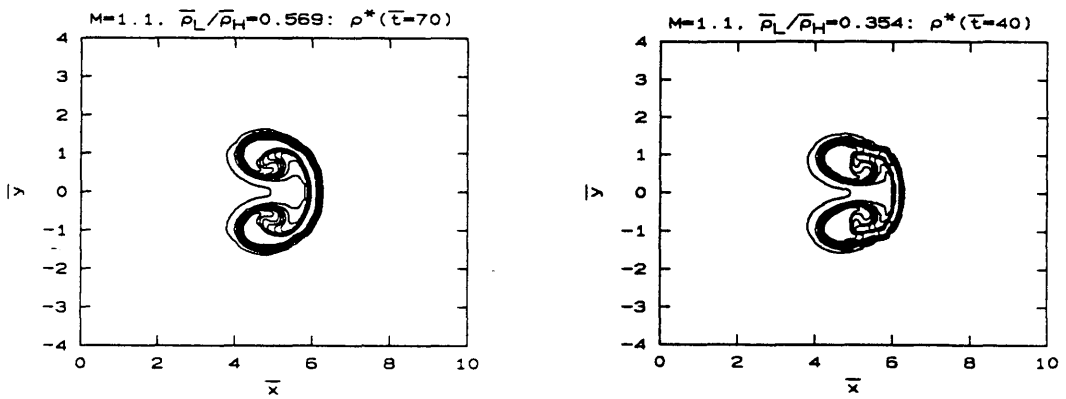

(a) (b)

Figure 5.12 - Circular jet density contours for M=1.1: (a) $\overline{\rho}_L/\overline{\rho}_H = 0.569$ at $\overline{t} = 70$, (b) $\overline{\rho}_L/\overline{\rho}_H = 0.354$ at $\overline{t} = 40$.

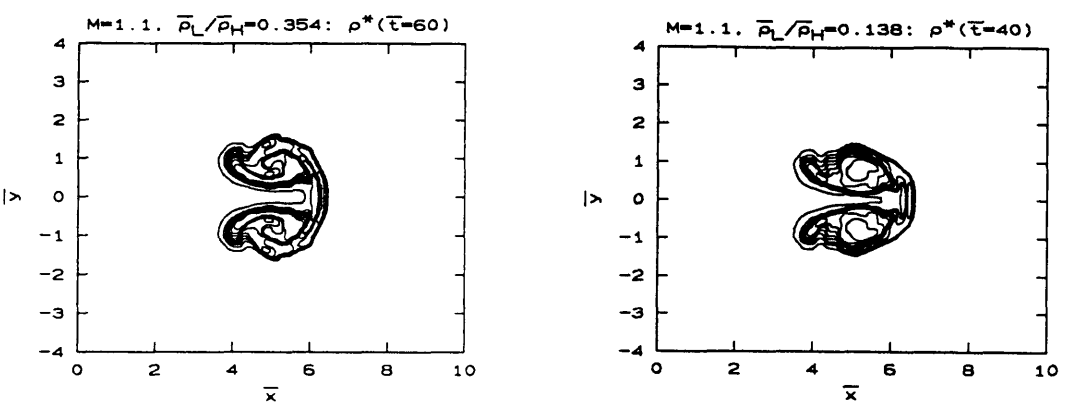

(a) (b)

Figure 5.13 - Circular jet density contours for M=1.1: (a) $\overline{\rho}_L/\overline{\rho}_H = 0.354$ at $\overline{t} = 60$, (b) $\overline{\rho}_L/\overline{\rho}_H = 0.138$ at $\overline{t} = 40$.

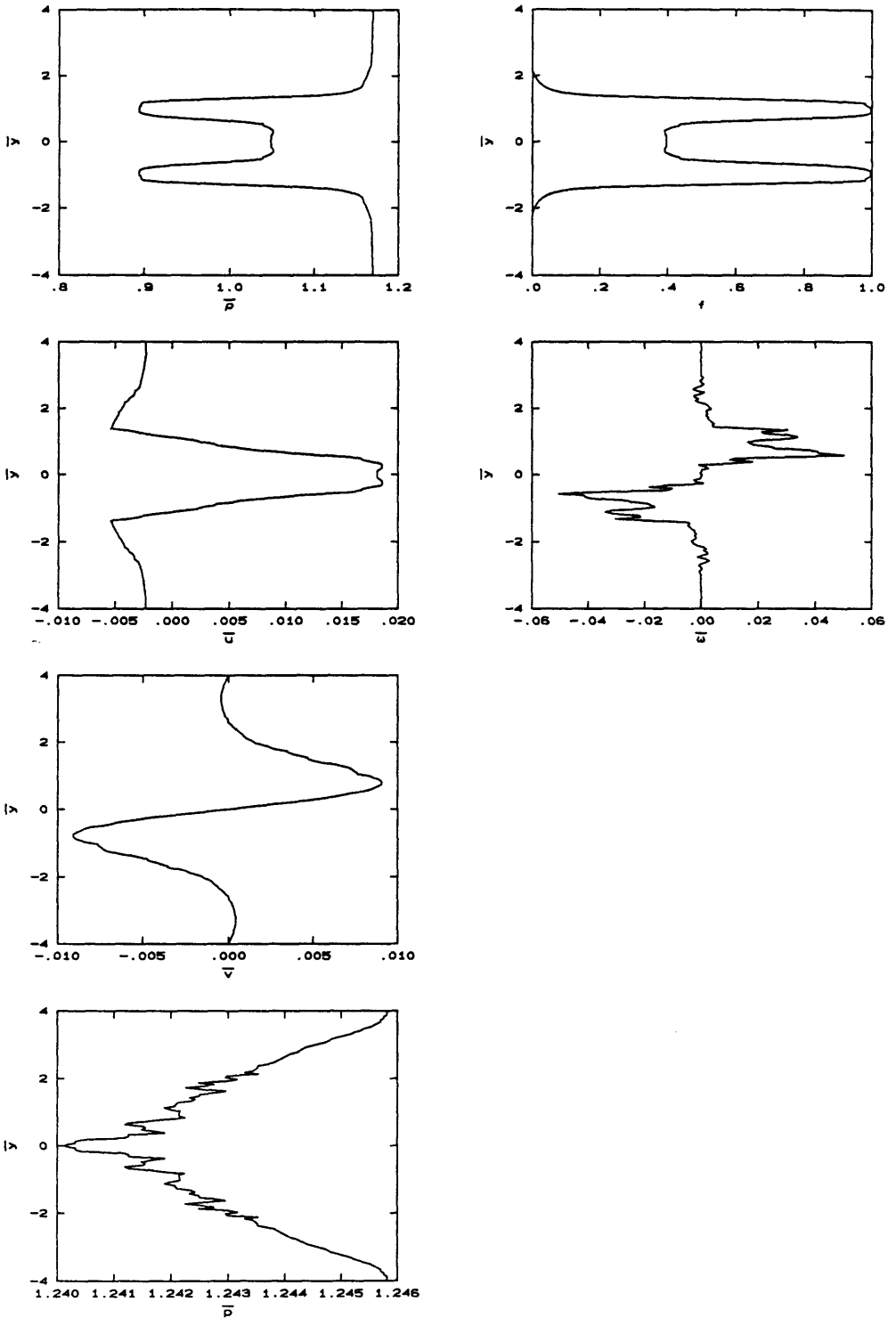

Figure 5.14 - Circular jet with M=1.1 and $\bar{\rho}_L/\bar{\rho}_H = 0.569$. Vertical cuts through the approximate center of the structure at $\bar{t} = 40$.

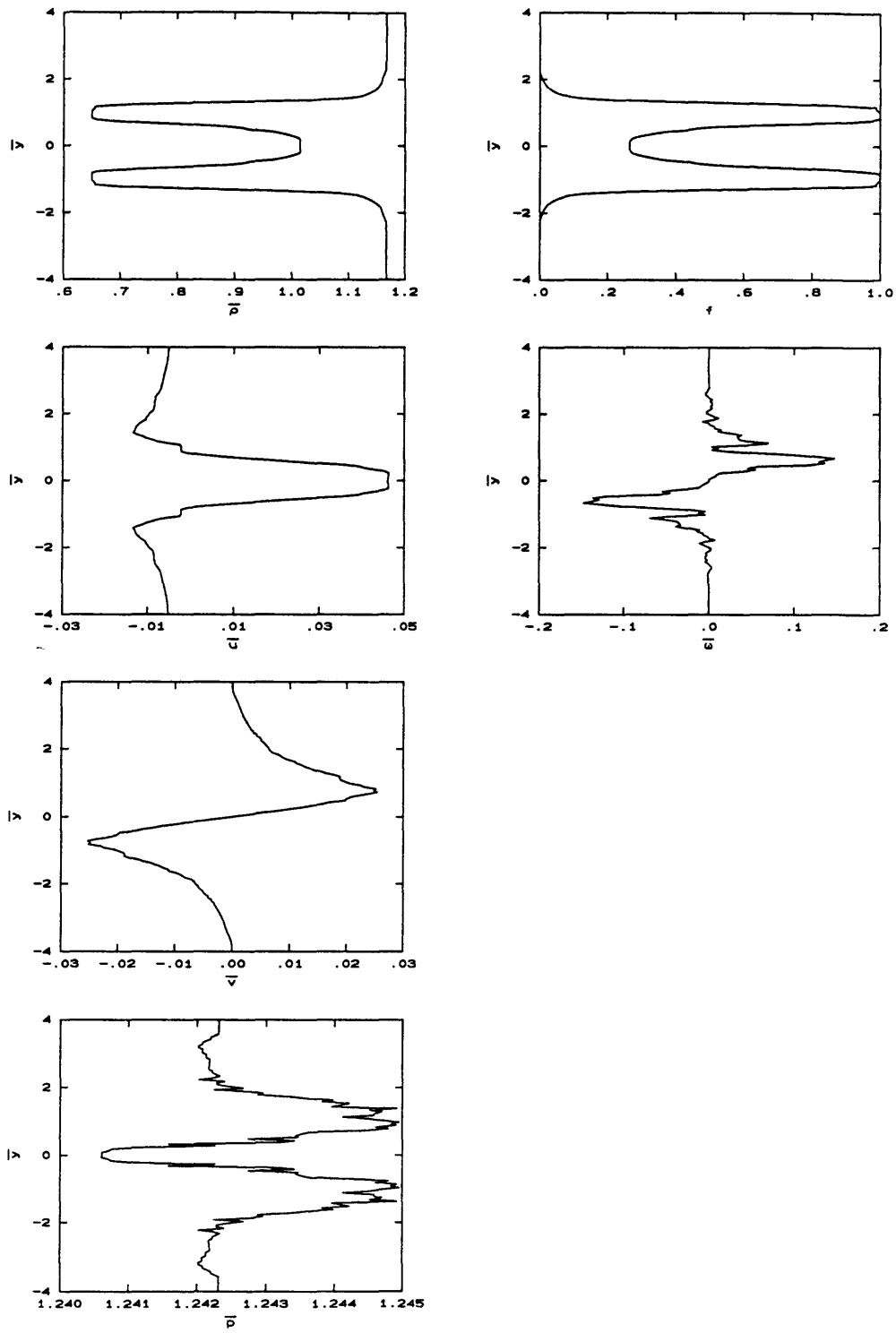

Figure 5.15 - Circular jet with M=1.1 and $\overline{\rho}_L/\overline{\rho}_H = 0.785$. Vertical cuts through the approximate center of the structure at $\bar{t} = 90$.

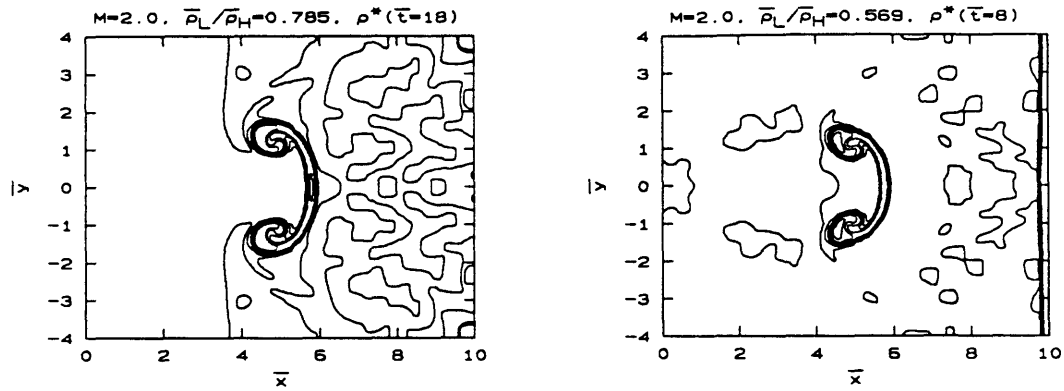

(a) (b)

Figure 5.16 - Circular jet density contours for M=2.0: (a) $\overline{\rho}_L/\overline{\rho}_H = 0.569$ at $\overline{t} = 14$, (b) $\overline{\rho}_L/\overline{\rho}_H = 0.354$ at $\overline{t} = 8$.

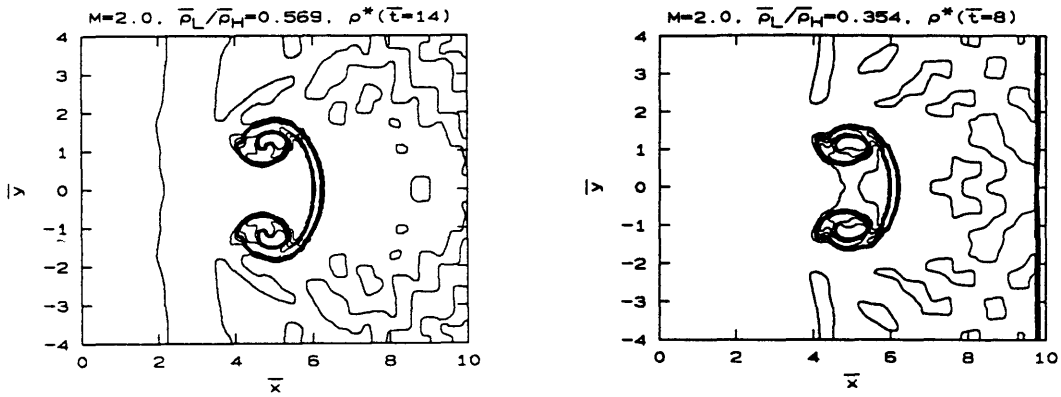

(a) (b)

Figure 5.17 - Circular jet density contours for M=2.0: (a) $\overline{\rho}_L/\overline{\rho}_H = 0.785$ at $\overline{t} = 18$, (b) $\overline{\rho}_L/\overline{\rho}_H = 0.569$ at $\overline{t} = 8$.

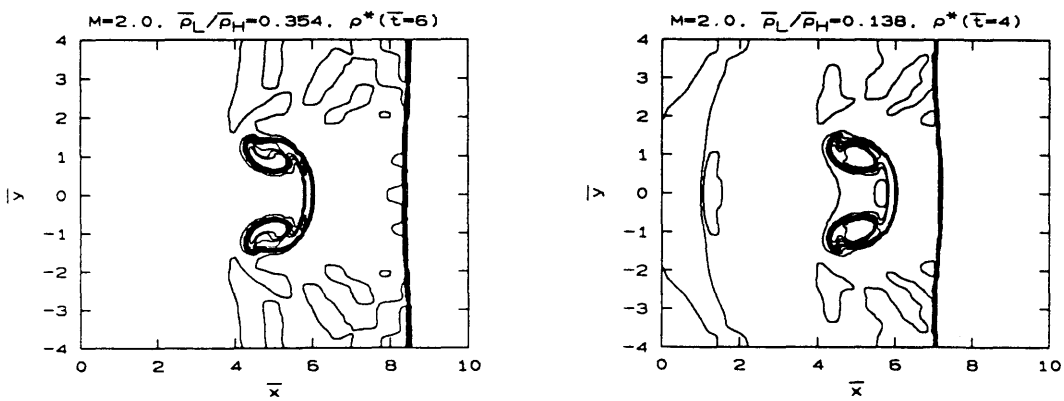

(a) (b)

Figure 5.18 - Circular jet density contours for M=2.0: (a) $\overline{\rho}_L/\overline{\rho}_H = 0.354$ at $\overline{t} = 6$, (b) $\overline{\rho}_L/\overline{\rho}_H = 0.138$ at $\overline{t} = 4$.

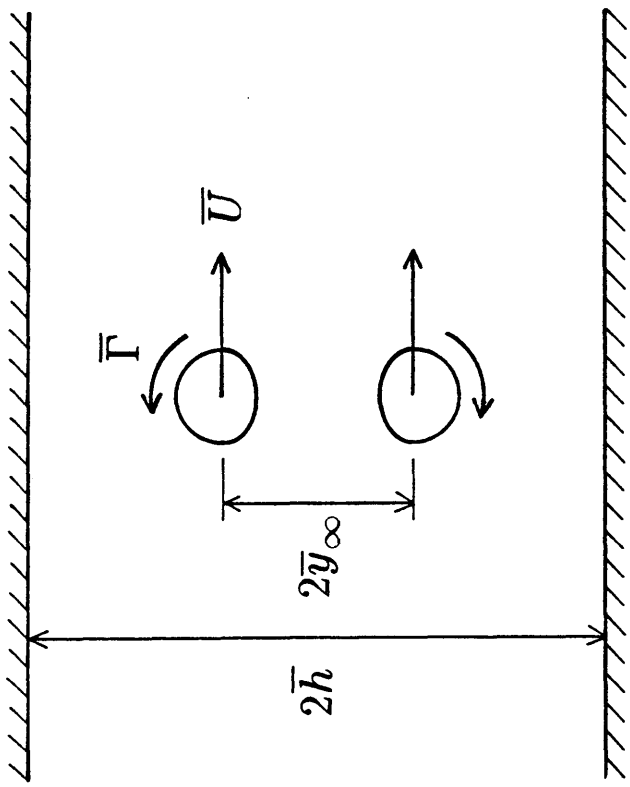

Figure 5.19 - Finite core size vortex pair in a channel.

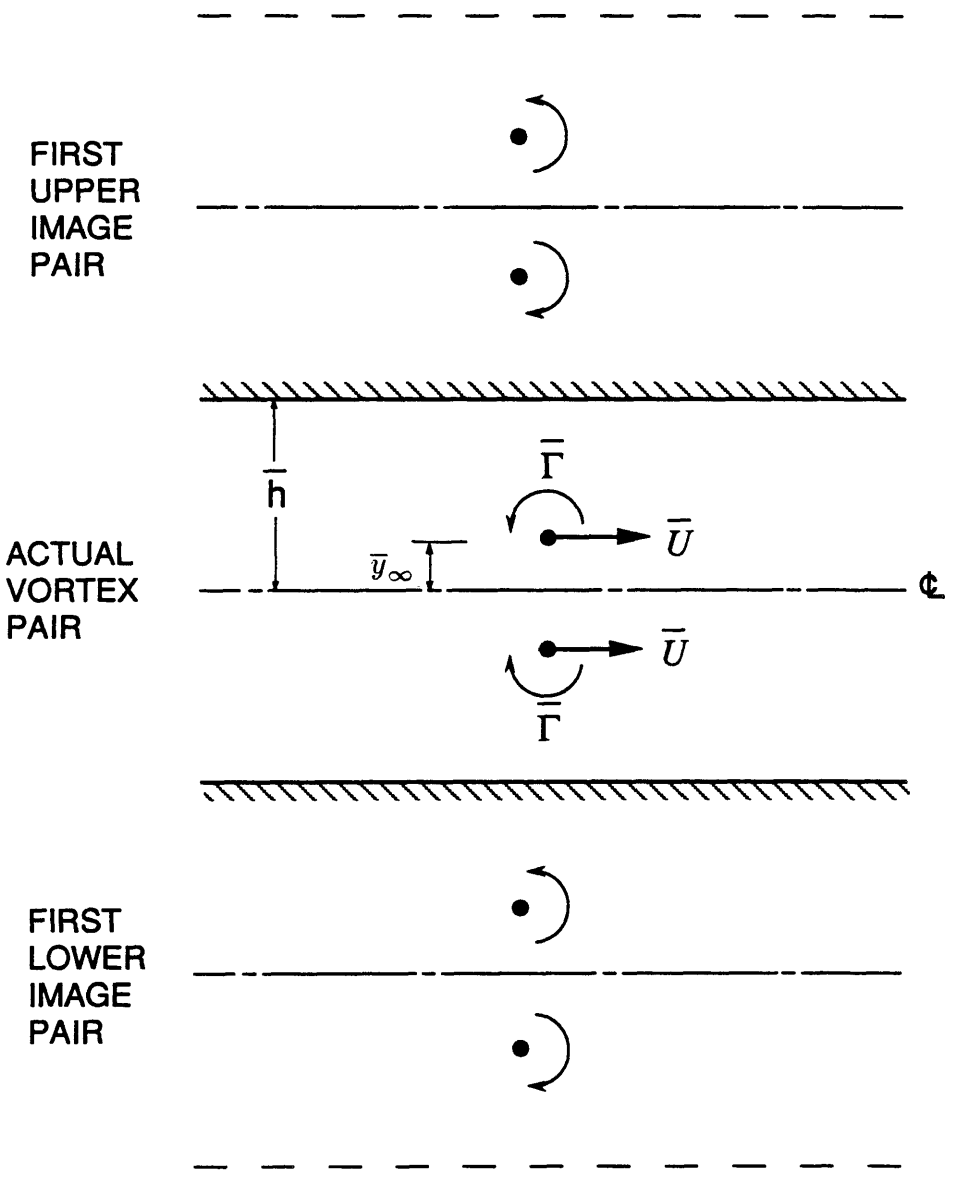

Figure 5.20 - Point vortex in a channel.

NORMALIZED VELOCITY FOR A

POINT VORTEX PAIR IN A CHANNEL

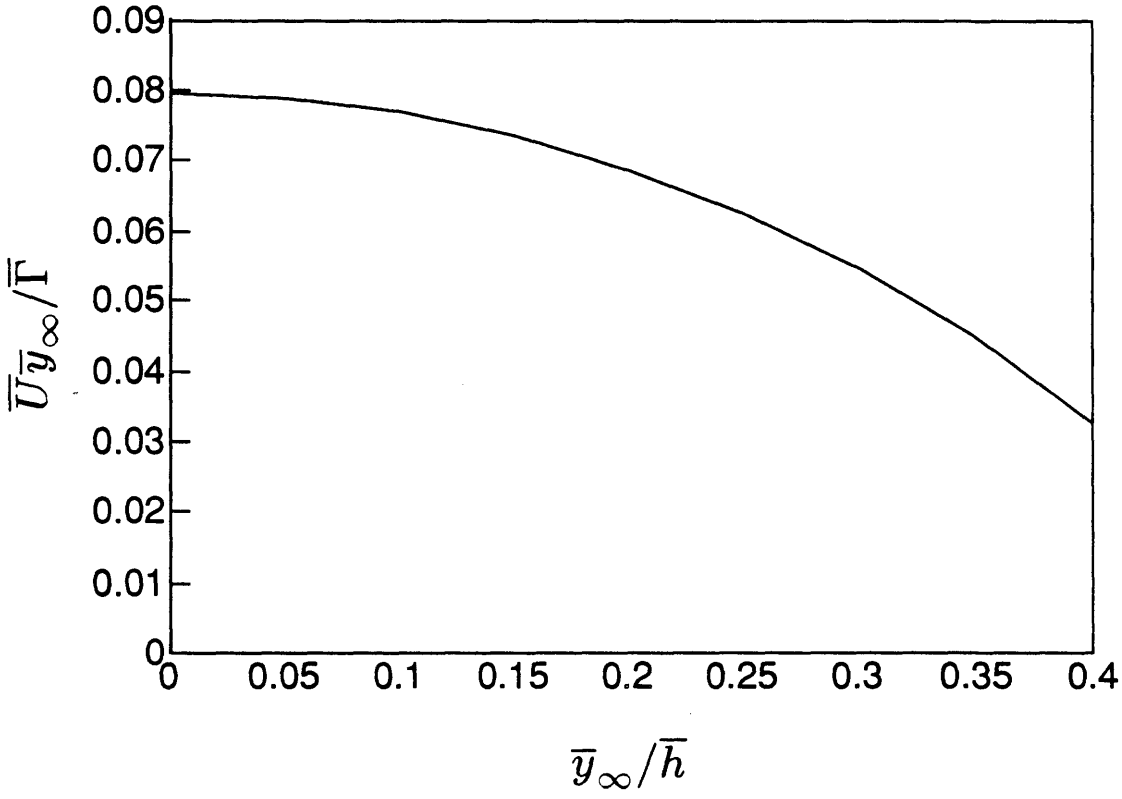

Figure 5.21 - Normalized velocity for a point vortex pair in a channel.

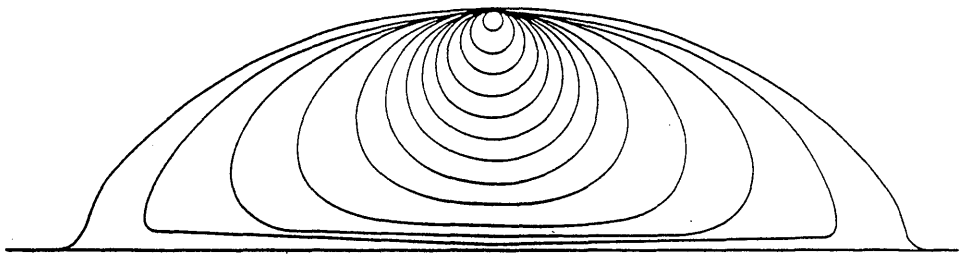

Figure 5.22 - Family of finite core size vortex pairs in an unbounded domain [reproduced from Pierrehumbert (1980), p. 136]. Starting from the inside and moving outward, the contours correspond to $\overline{R}/\overline{y}_\infty$ = 0.048, 0.100, 0.159, 0.225, 0.390, 0.500, 0.639, 0.844, 1.22, 1.55, 1.97, and 2.16. The outermost contour, which is the limit of touching vortices, was shown by Wu, *et al.* (1984) to be incorrect.

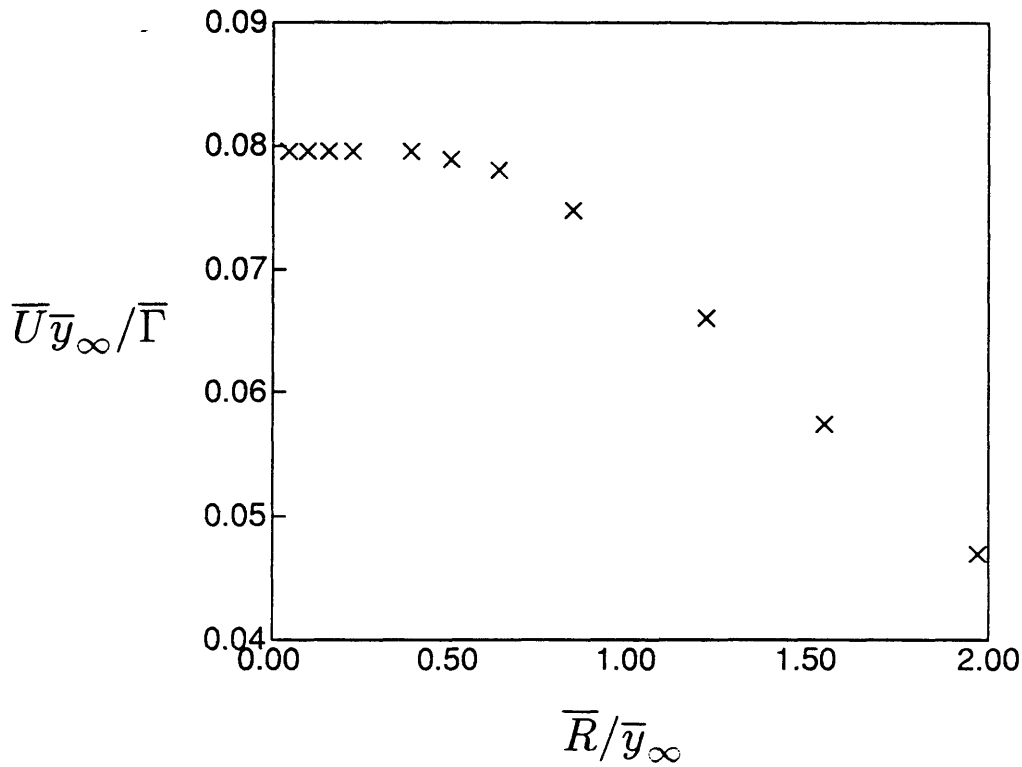

Figure 5.23 - Normalized velocity of a finite core size vortex pair.

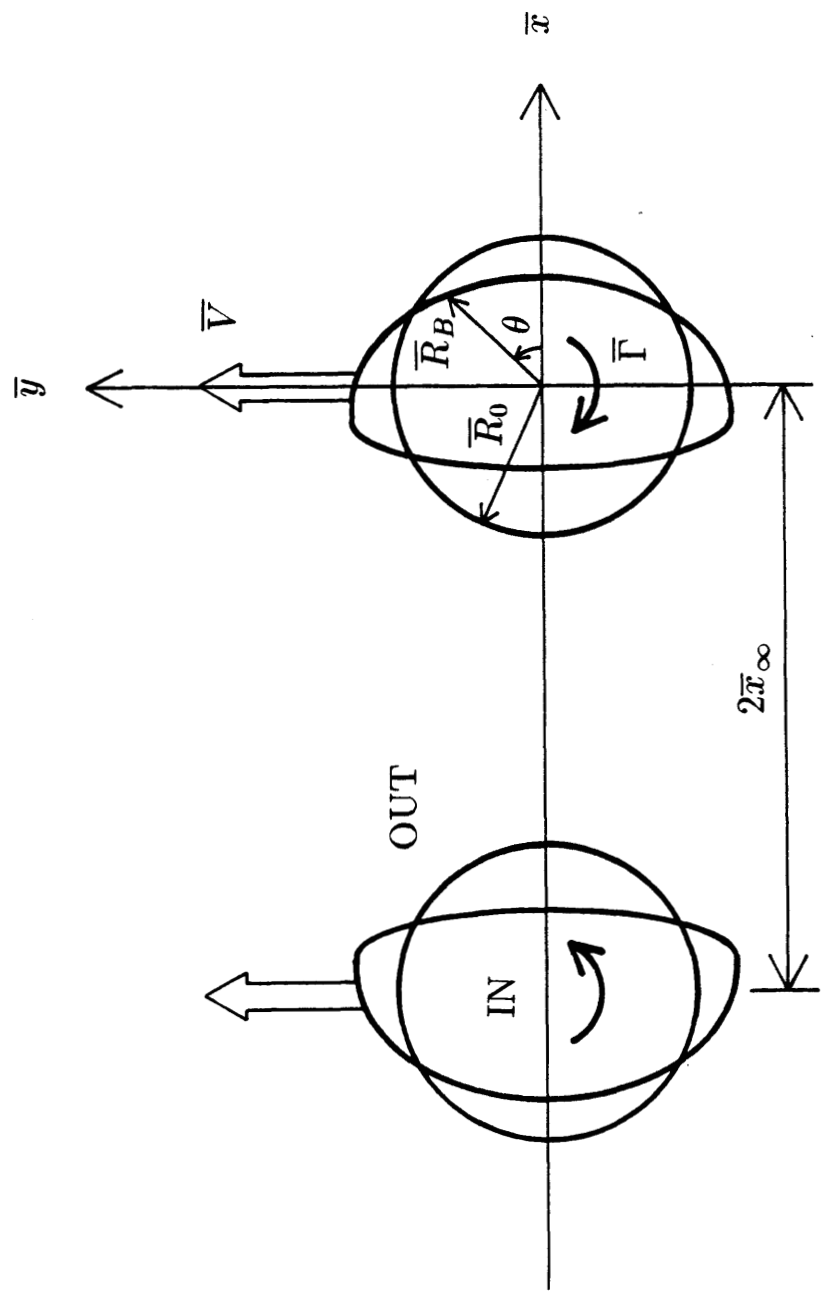

Figure 5.24 - Perturbation analysis in an unbounded domain.

Page 207
$\tilde{e}_n$ should read $\hat{e}_n$

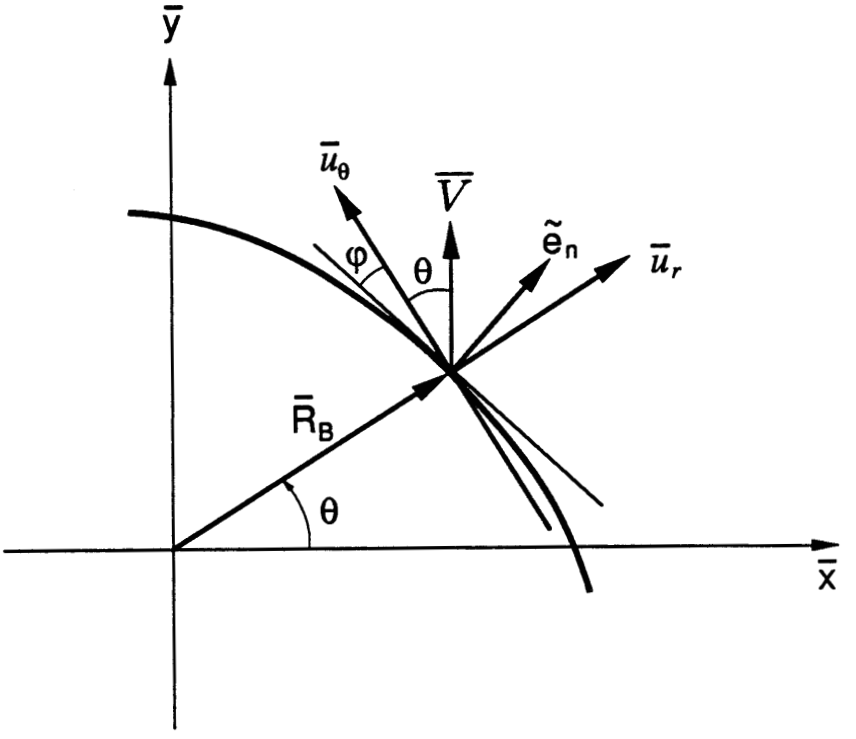

Figure 5.25 - Boundary shape schematic.

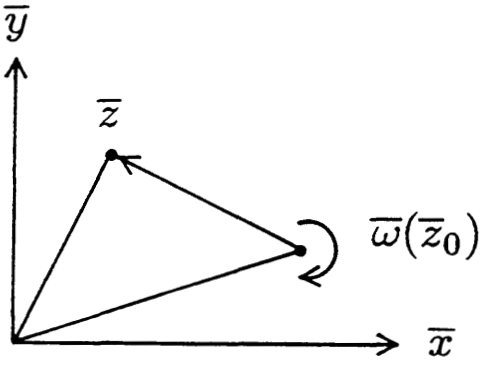

(a)

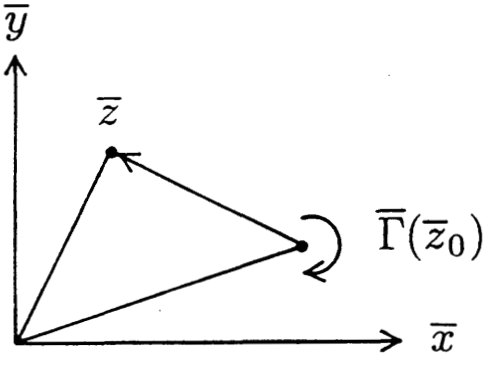

(b)

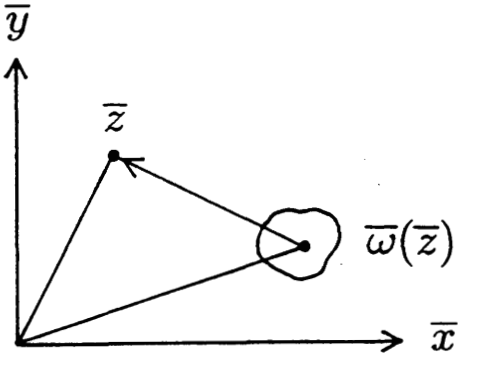

(c)

Figure 5.26 - Potential theory results: (a) solid body rotation, (b) point vortex, (c) distributed vorticity.

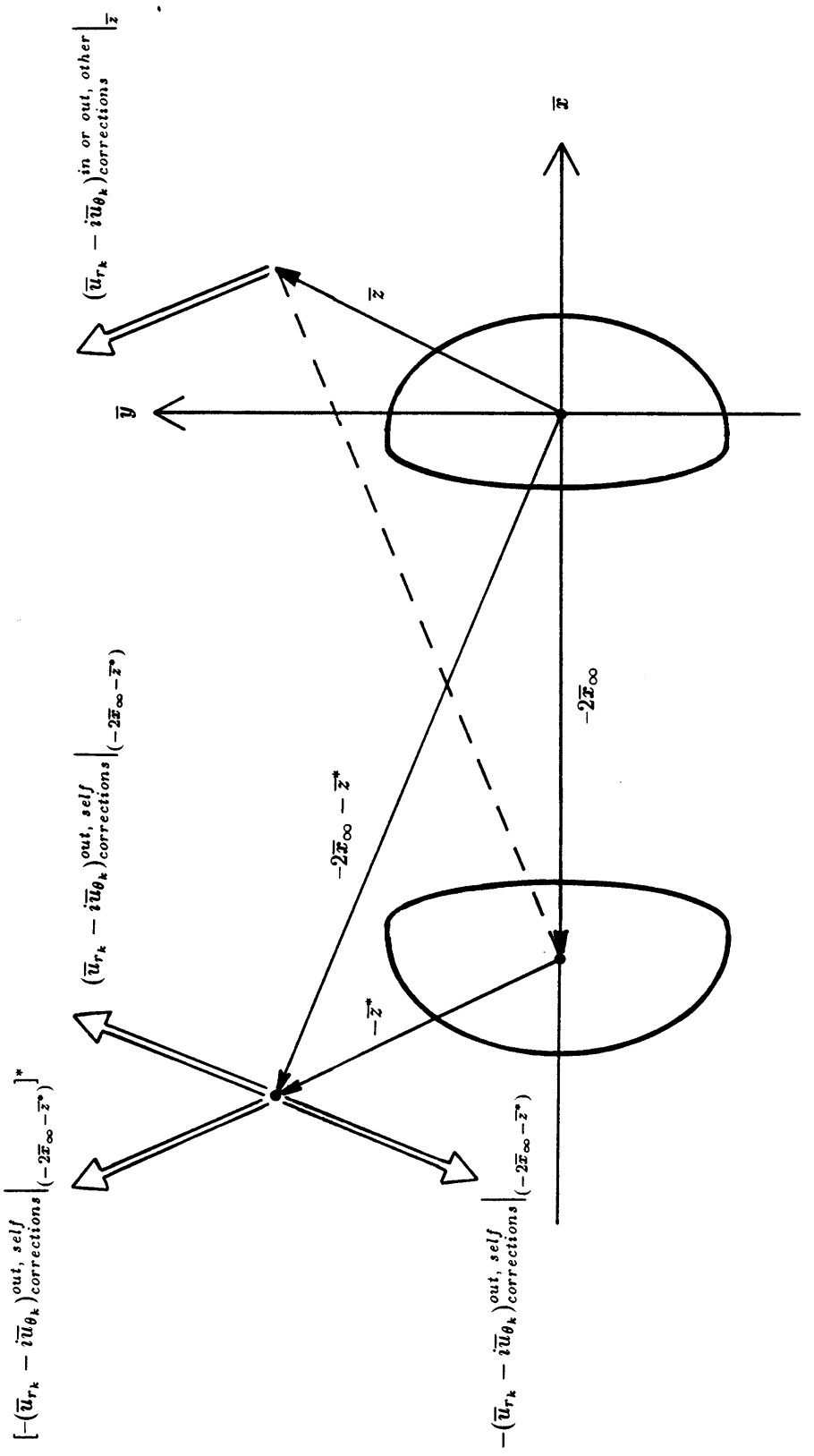

Figure 5.27 - Symmetry considerations for "other" velocity determination.

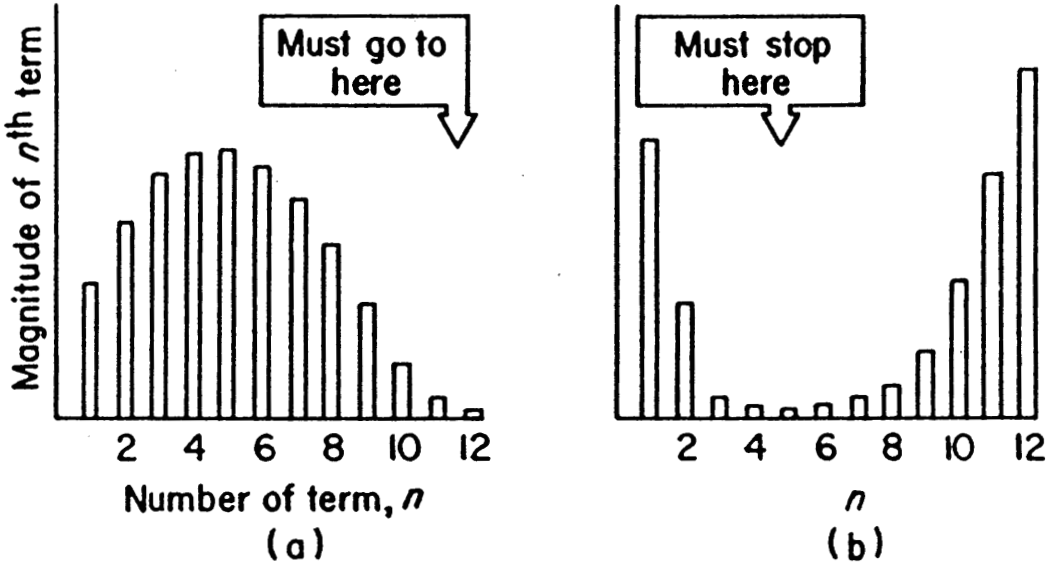

Figure 5.28 - Asymptotic series: (a) slowly convergent, (b) divergent [reproduced from Van Dyke (1975), p.31].

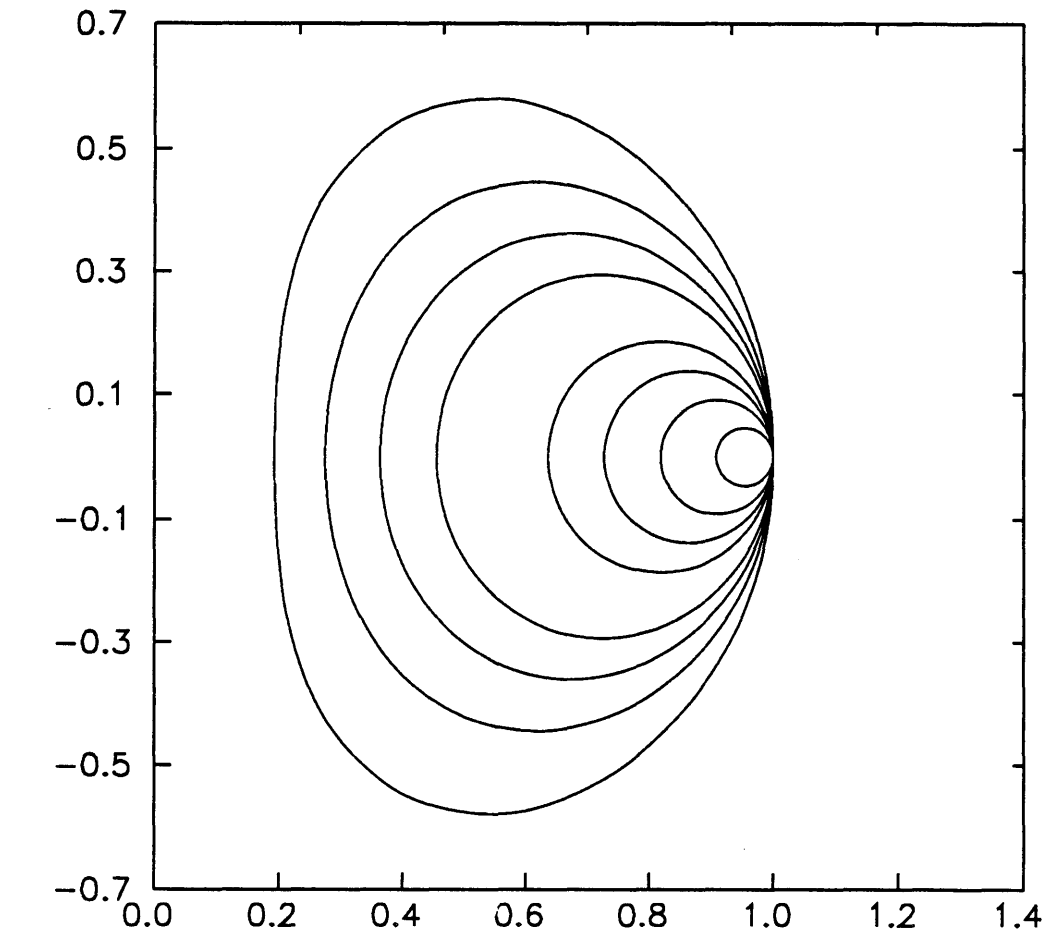

(a)

Figure 5.29 - Comparison of Pierrehumbert's and Yang's finite core size vortex pairs: (a) boundary shapes, (b) normalized velocities, (c) intervortex gap ratios, (d) aspect ratios.

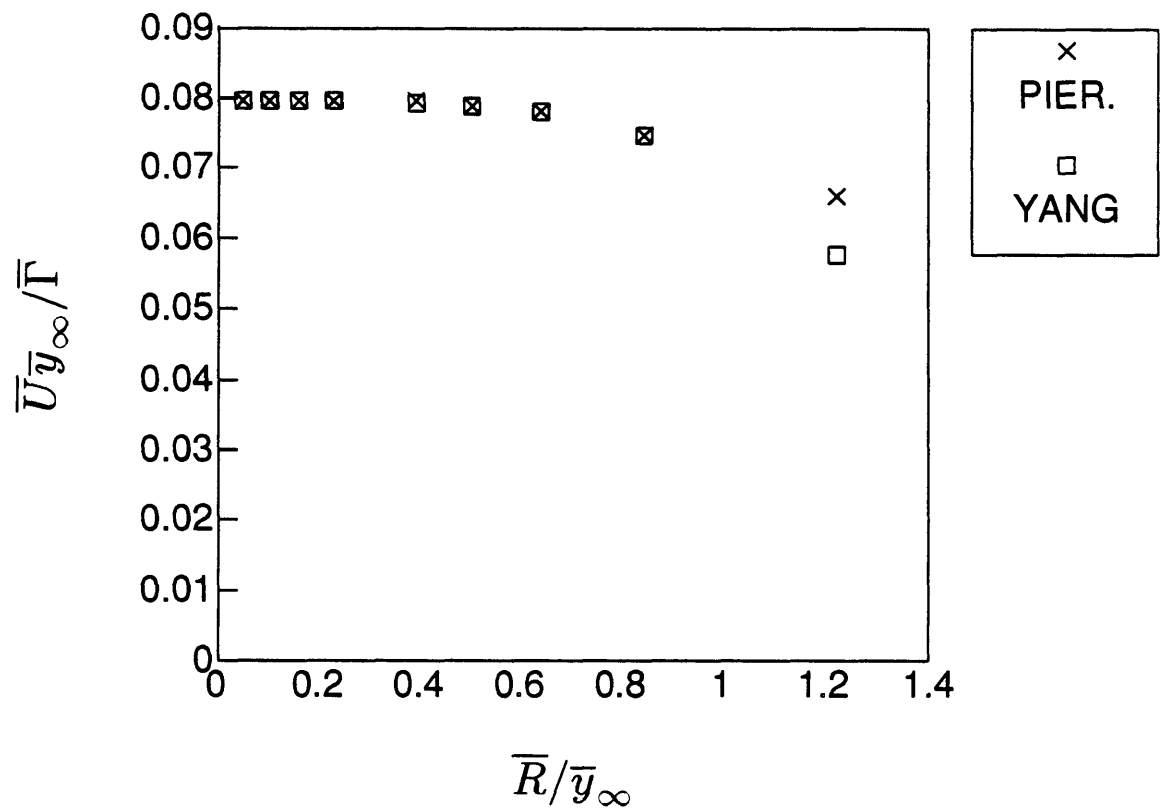

(b)

Figure 5.29 - Comparison of Pierrehumbert's and Yang's finite core size vortex pairs: (a) boundary shapes, (b) normalized velocities, (c) intervortex gap ratios, (d) aspect ratios.

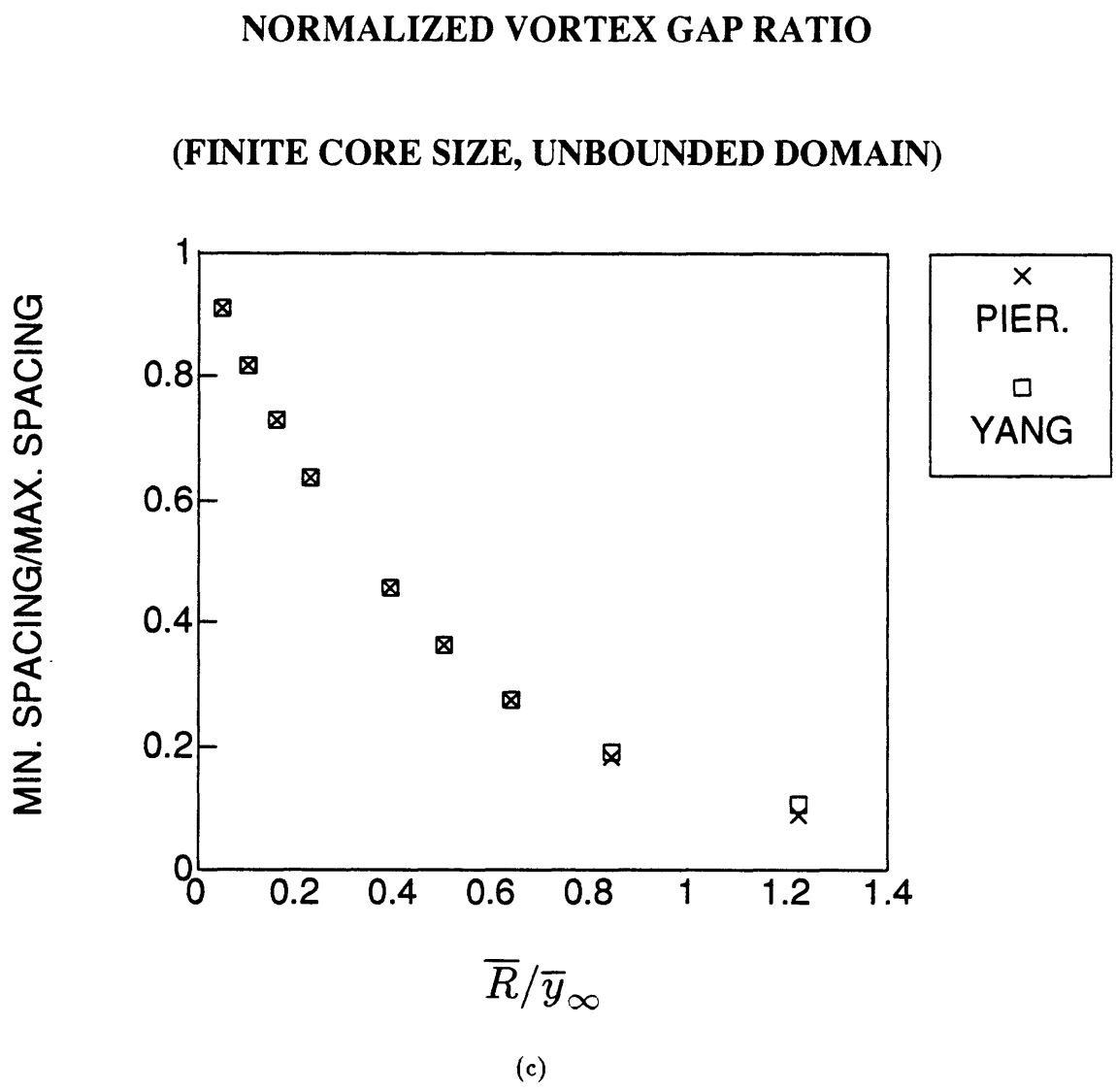

(c)

Figure 5.29 - Comparison of Pierrehumbert's and Yang's finite core size vortex pairs: (a) boundary shapes, (b) normalized velocities, (c) intervortex gap ratios, (d) aspect ratios.

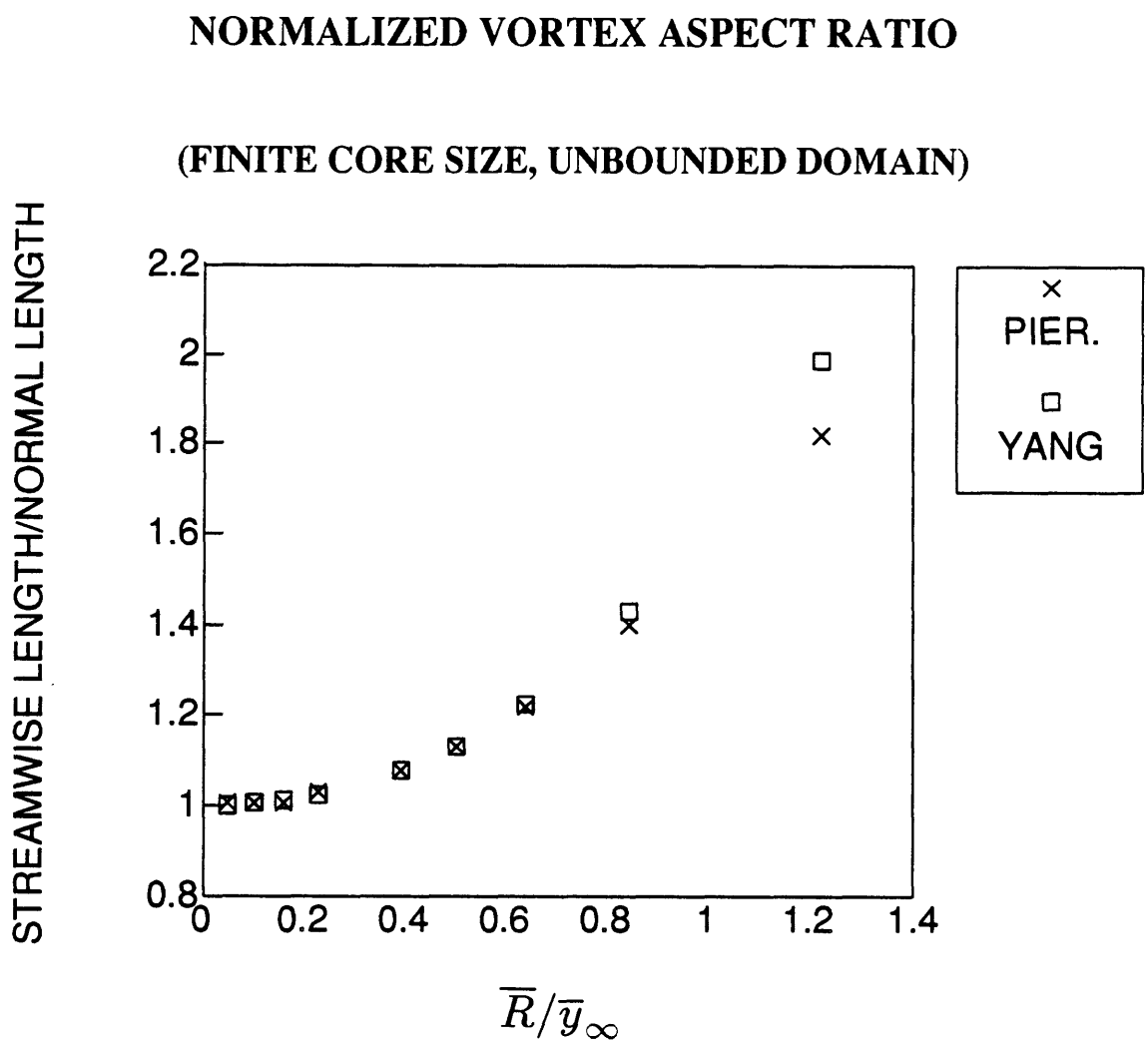

(d)

Figure 5.29 - Comparison of Pierrehumbert's and Yang's finite core size vortex pairs: (a) boundary shapes, (b) normalized velocities, (c) intervortex gap ratios, (d) aspect ratios.

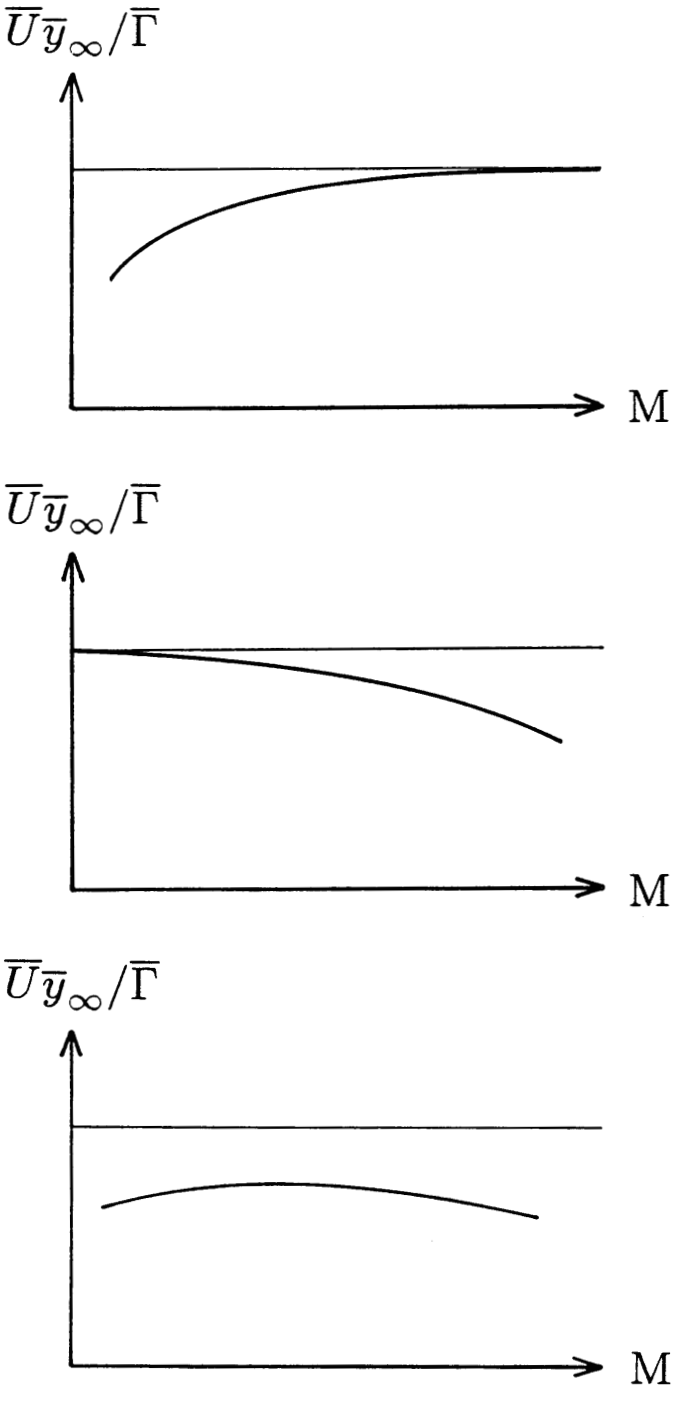

Figure 5.30 - Qualitative dependence of $\overline{U}\overline{y}_\infty/\overline{\Gamma}$ on M: (a) core size effects as function of M, (b) channel spacing effects as function of M, (c) both spacing effects together.

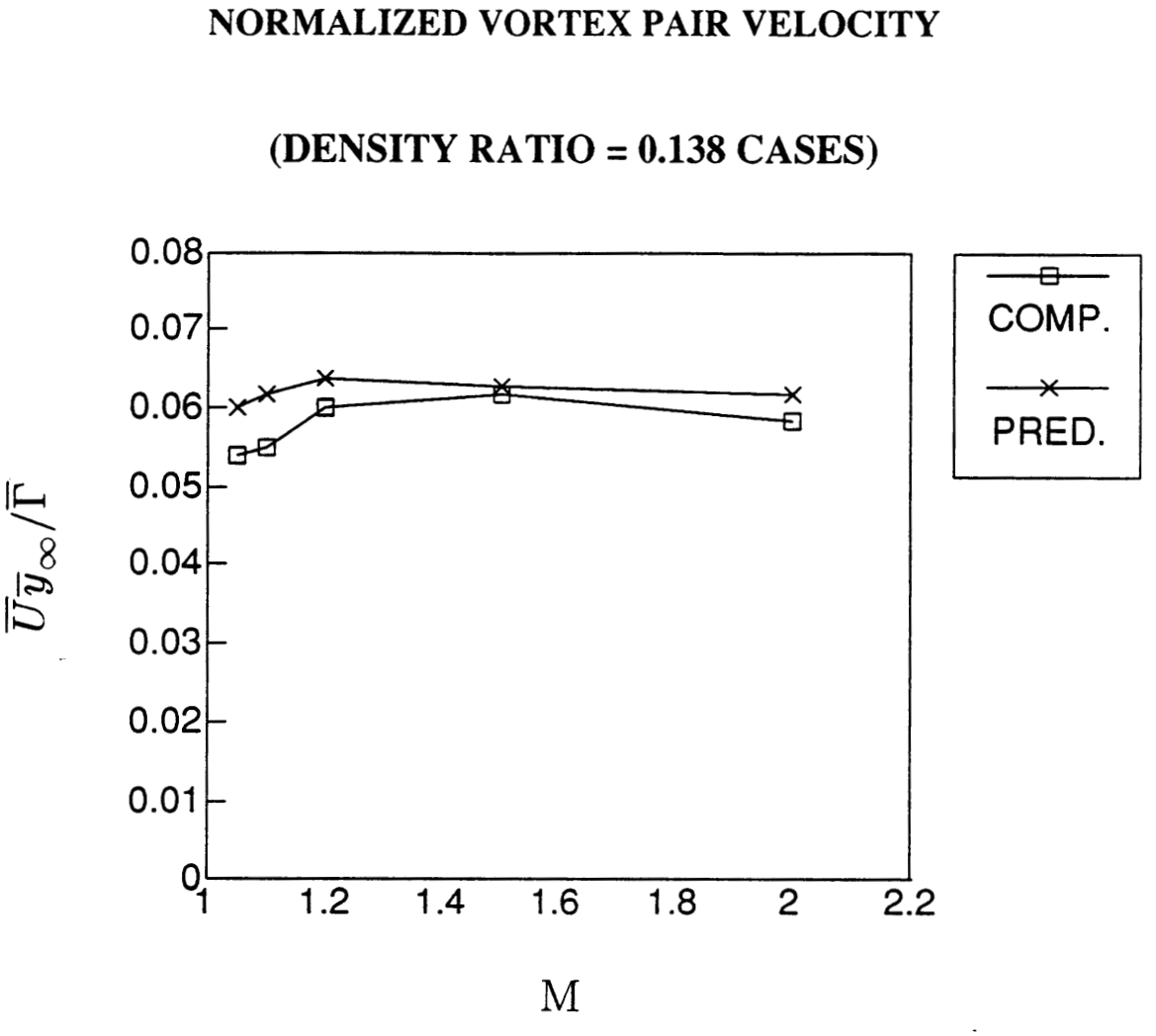

Figure 5.31 - Computed and predicted $\overline{U}\overline{y}_\infty/\overline{\Gamma}$ for the $\overline{\rho}_L/\overline{\rho}_H = 0.138$ canonical flows.

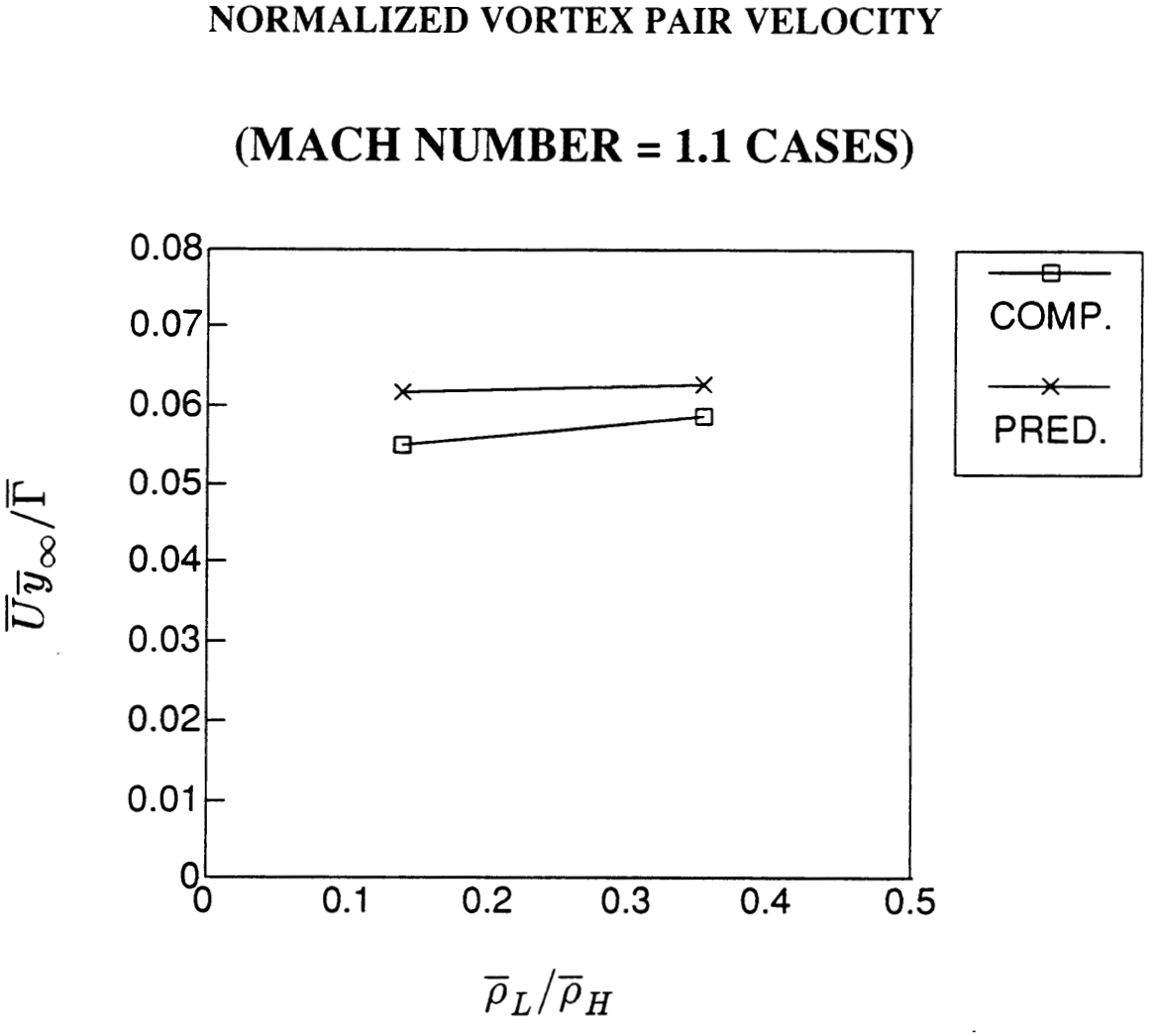

Figure 5.32 - Computed and predicted $\overline{U}\overline{y}_\infty/\overline{\Gamma}$ for the M=1.1 canonical flows.

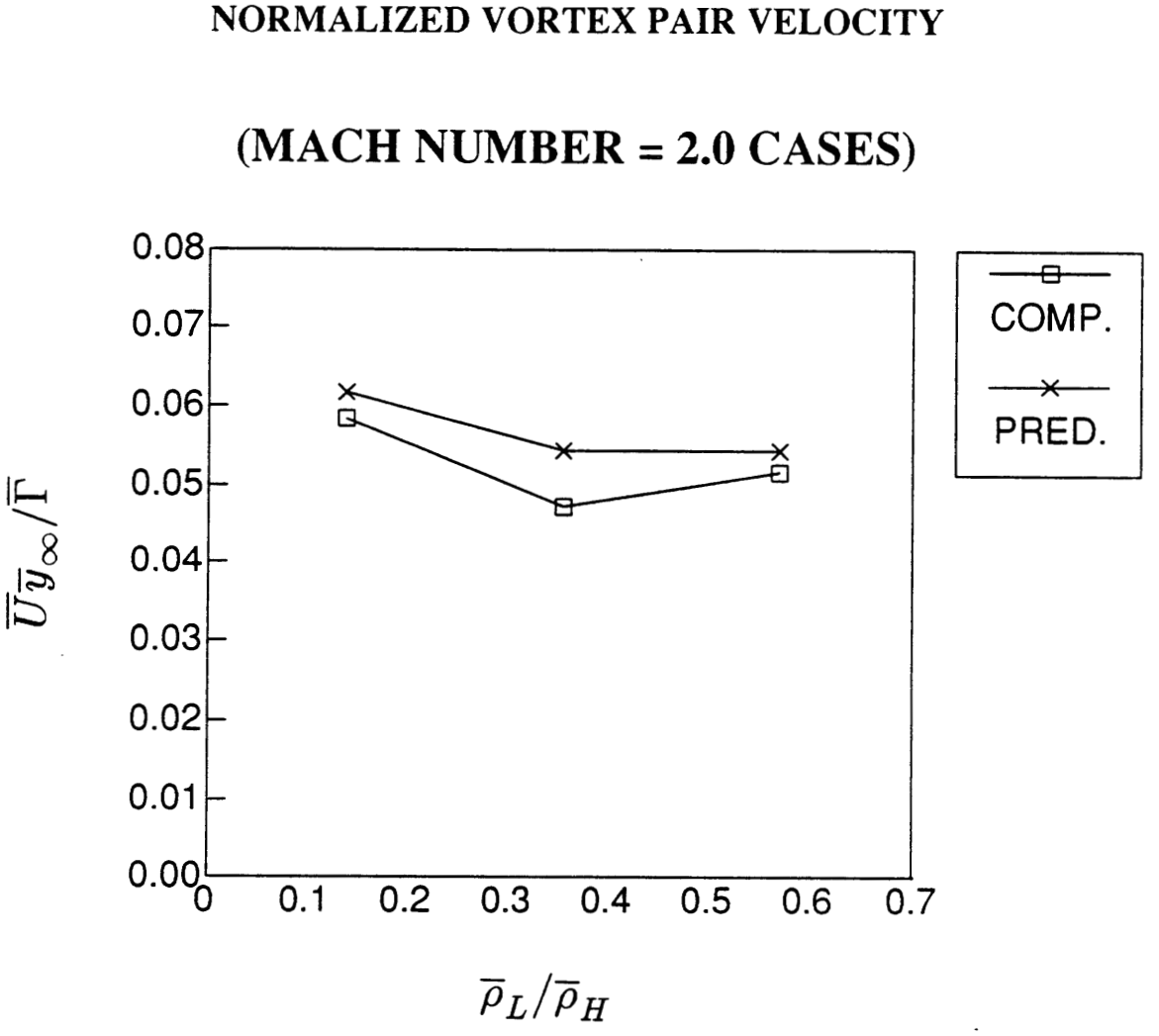

Figure 5.33 - Computed and predicted $\overline{U}\overline{y}_\infty/\overline{\Gamma}$ for the M=2.0 canonical flows.

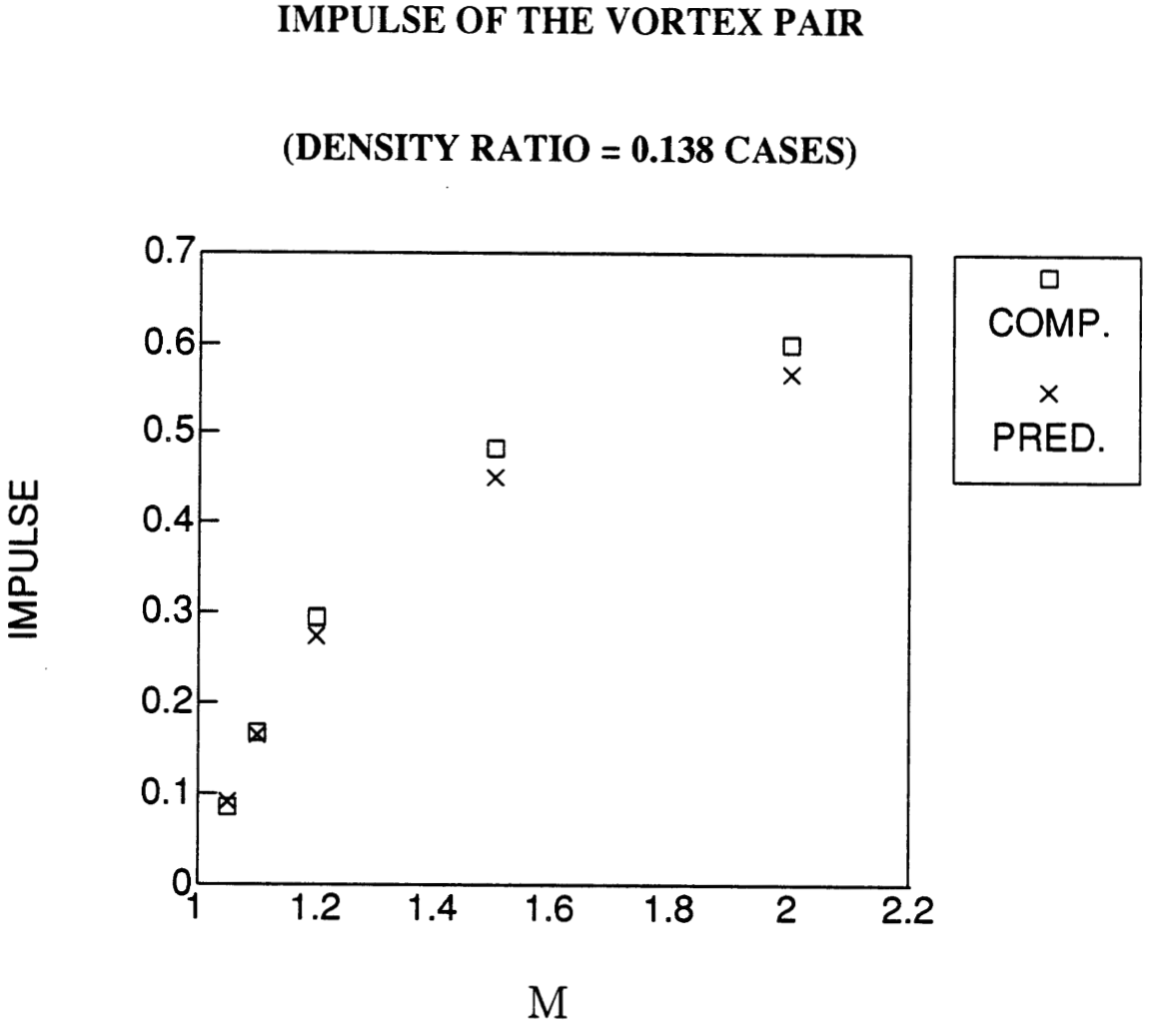

Figure 5.34 - Computed $\overline{I}_x'$ and predicted $\overline{I}_x(\overline{t} = 0^+)$ for the $\overline{\rho}_L/\overline{\rho}_H = 0.138$ canonical flows.

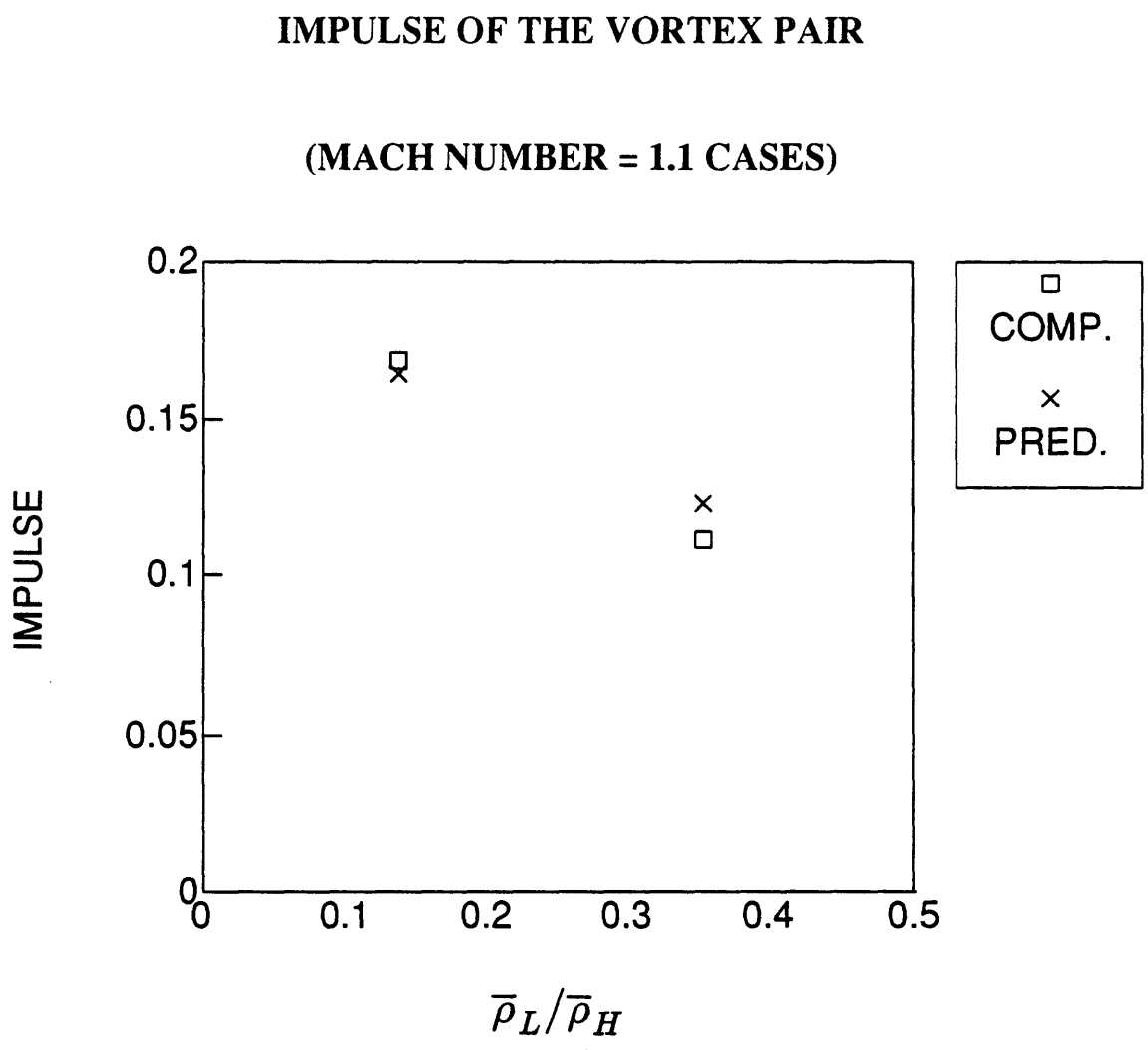

Figure 5.35 - Computed $\overline{I}_x'$ and predicted $\overline{I}_x(\overline{t}=0^+)$ for the M=1.1 canonical flows.

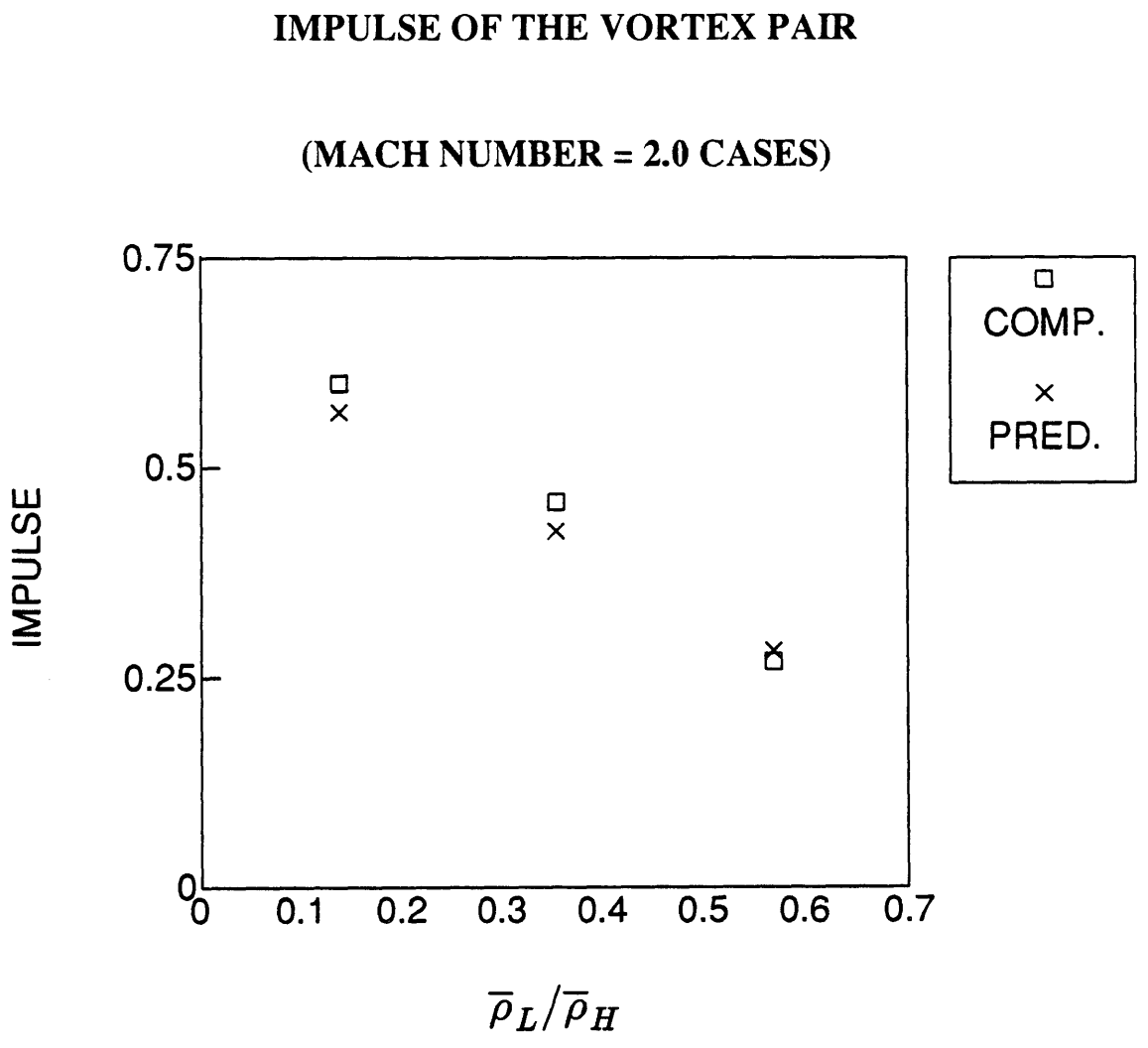

Figure 5.36 - Computed $\overline{I}_x'$ and predicted $\overline{I}_x(\bar{t} = 0^+)$ for the M=2.0 canonical flows.

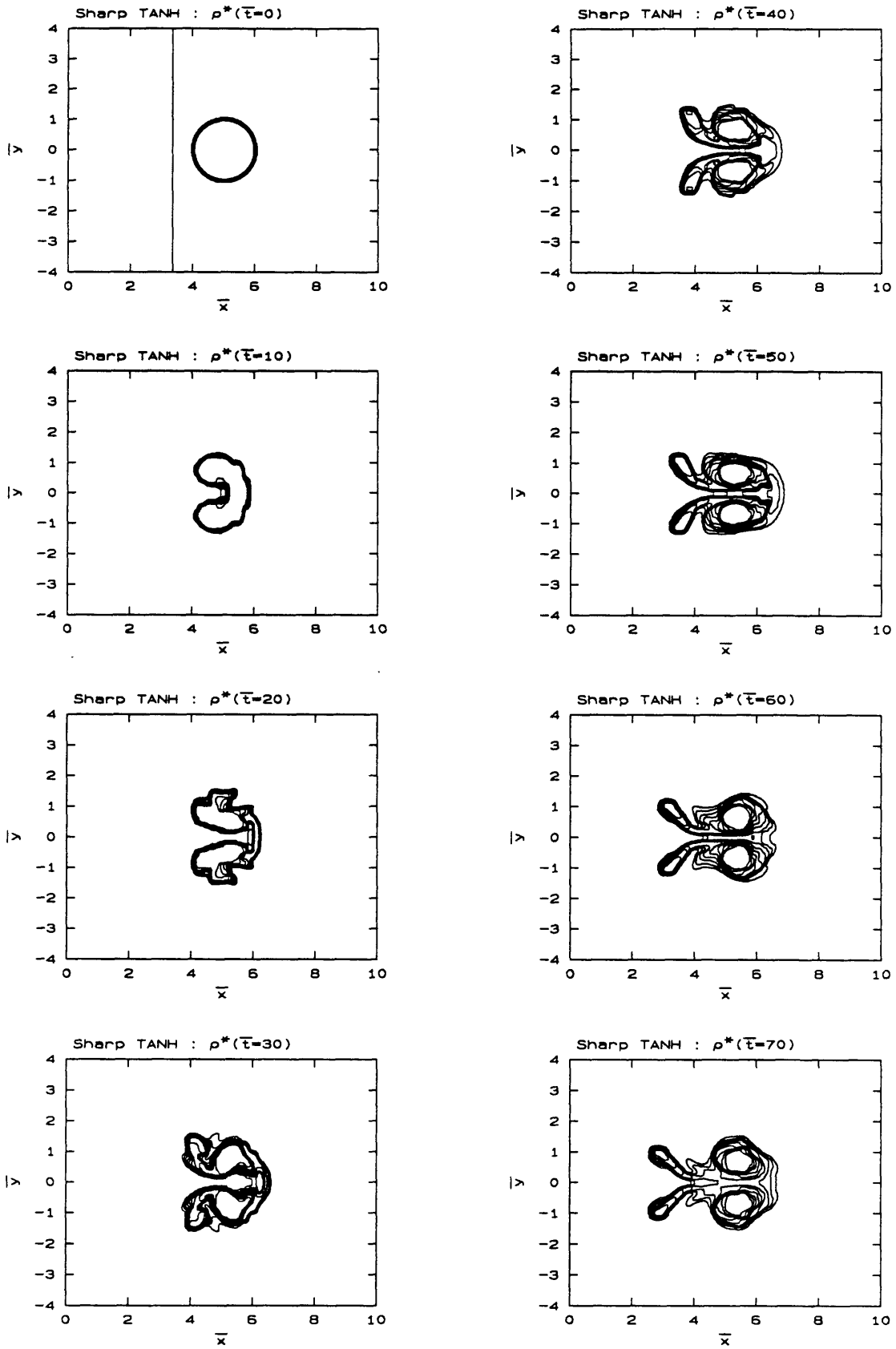

Figure 5.37 - Sharpest 'tanh' circular jet with M=1.1 and $\overline{\rho}_L/\overline{\rho}_H = 0.138$.

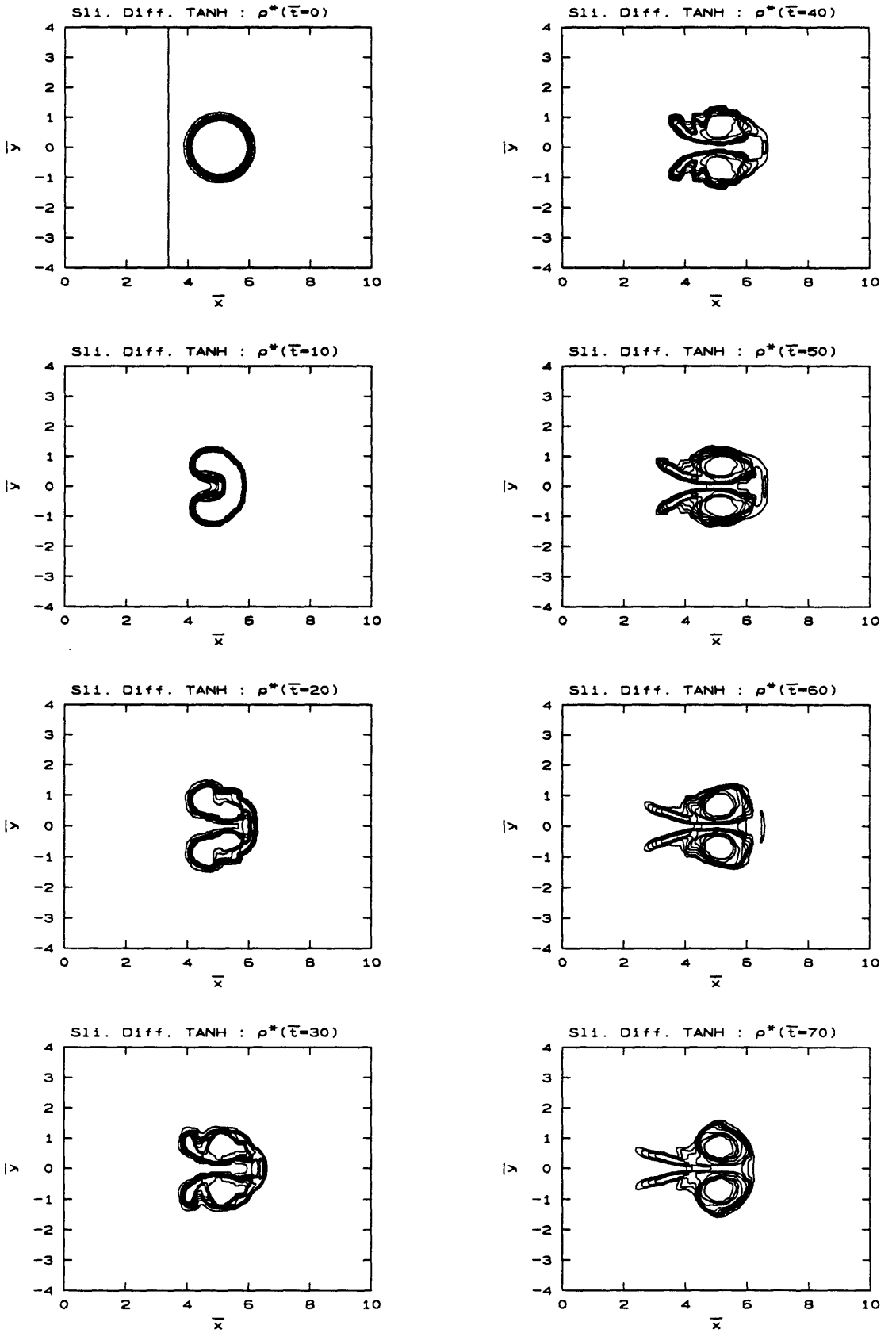

Figure 5.38 - Slightly diffuse 'tanh' circular jet with M=1.1 and $\overline{\rho}_L/\overline{\rho}_H = 0.138$.

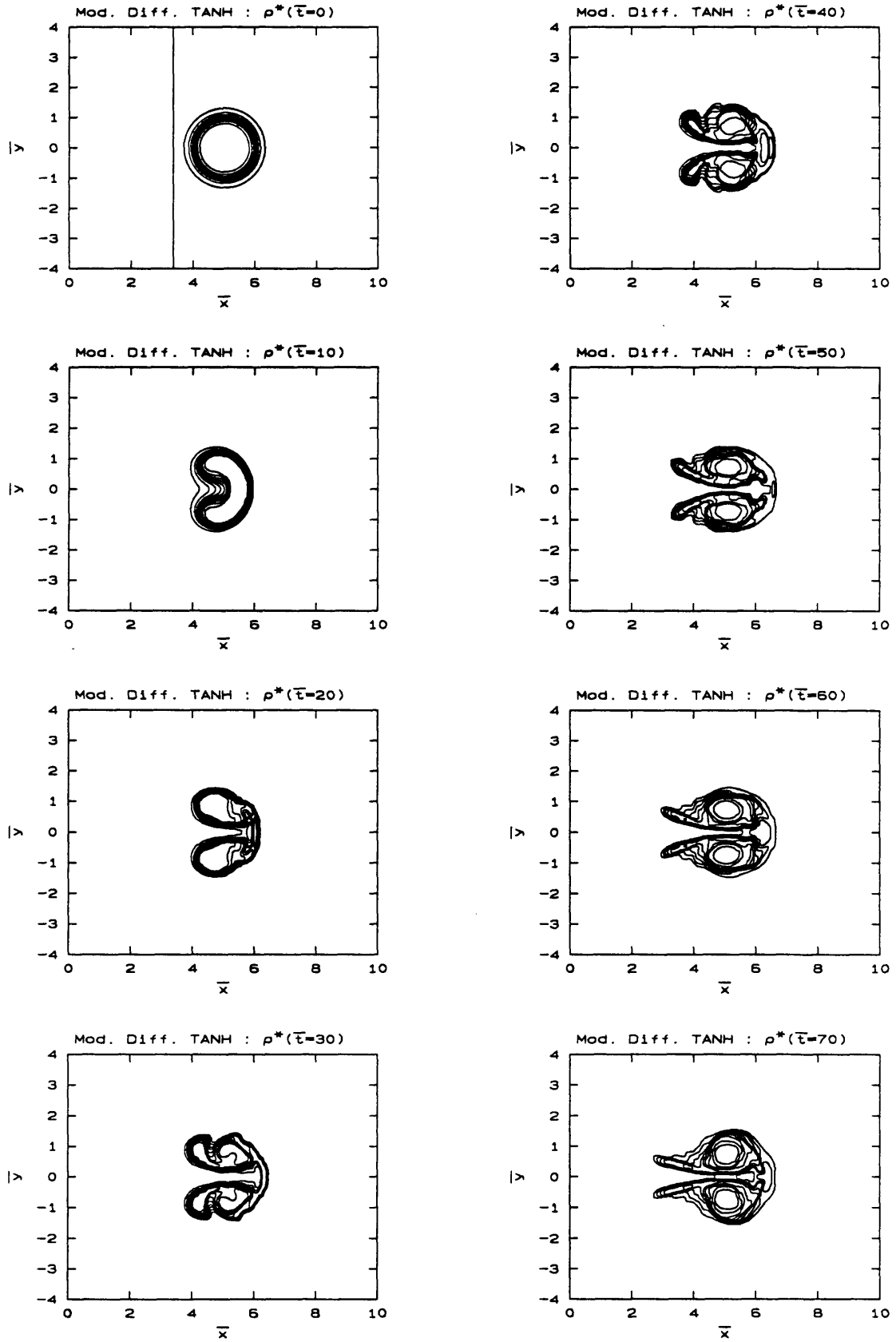

Figure 5.39 - Moderately diffuse 'tanh' circular jet with M=1.1 and $\overline{\rho}_L/\overline{\rho}_H = 0.138$.

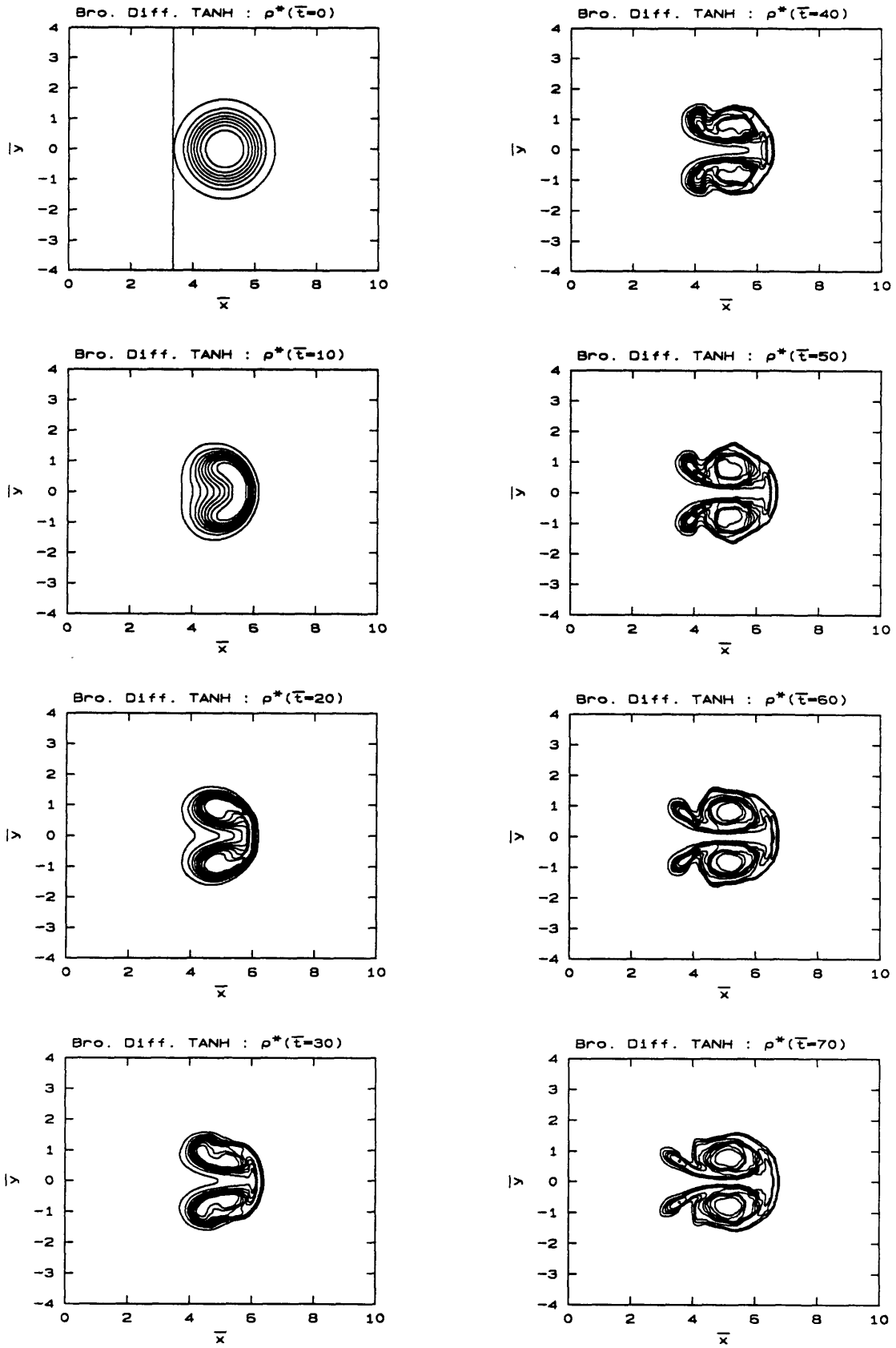

Figure 5.40 - Broadly diffuse 'tanh' circular jet with M=1.1 and $\overline{\rho}_L/\overline{\rho}_H = 0.138$.

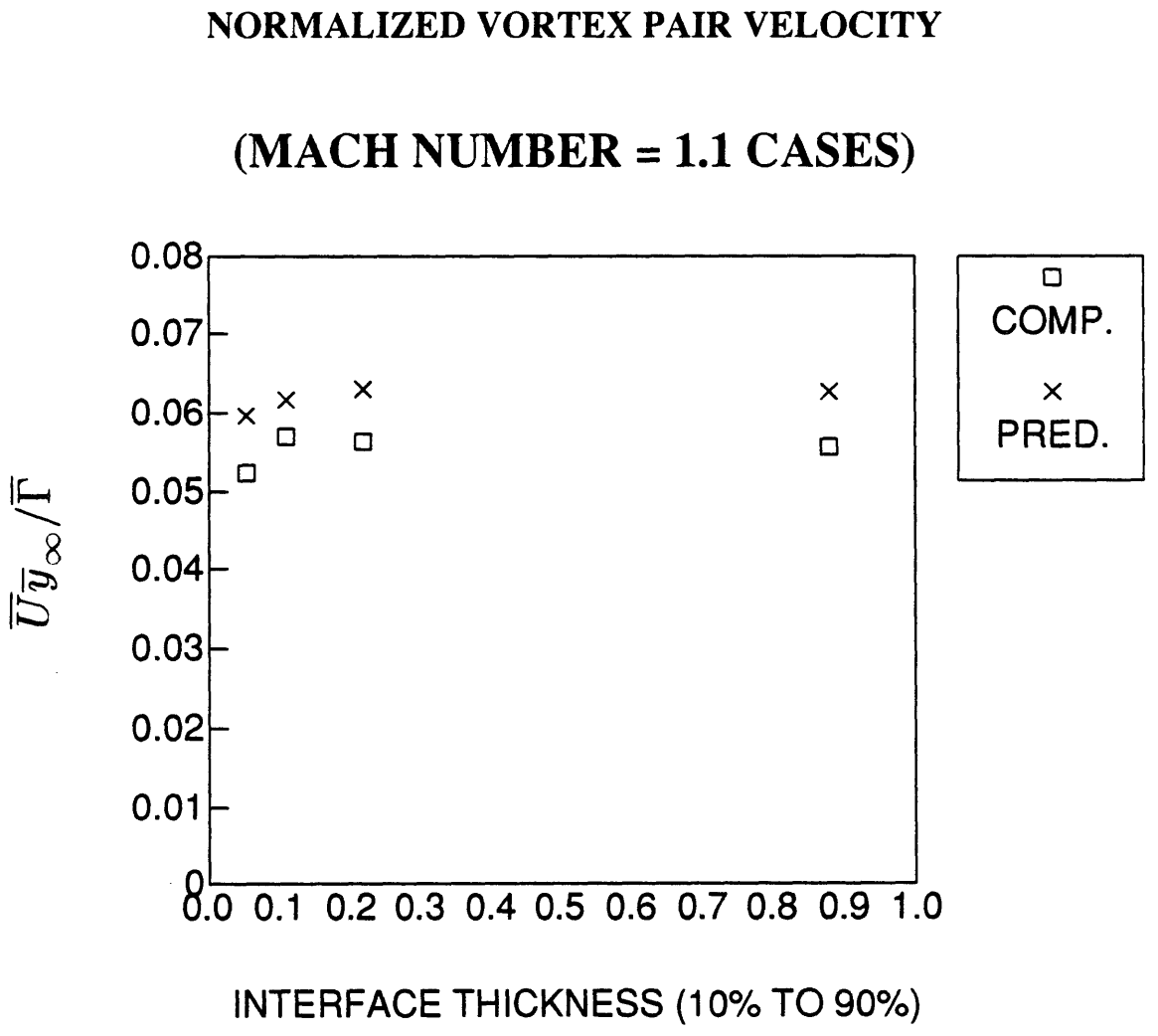

Figure 5.41 - Computed and predicted $\overline{U}\overline{y}_\infty/\overline{\Gamma}$ for variations in initial interface thickness.

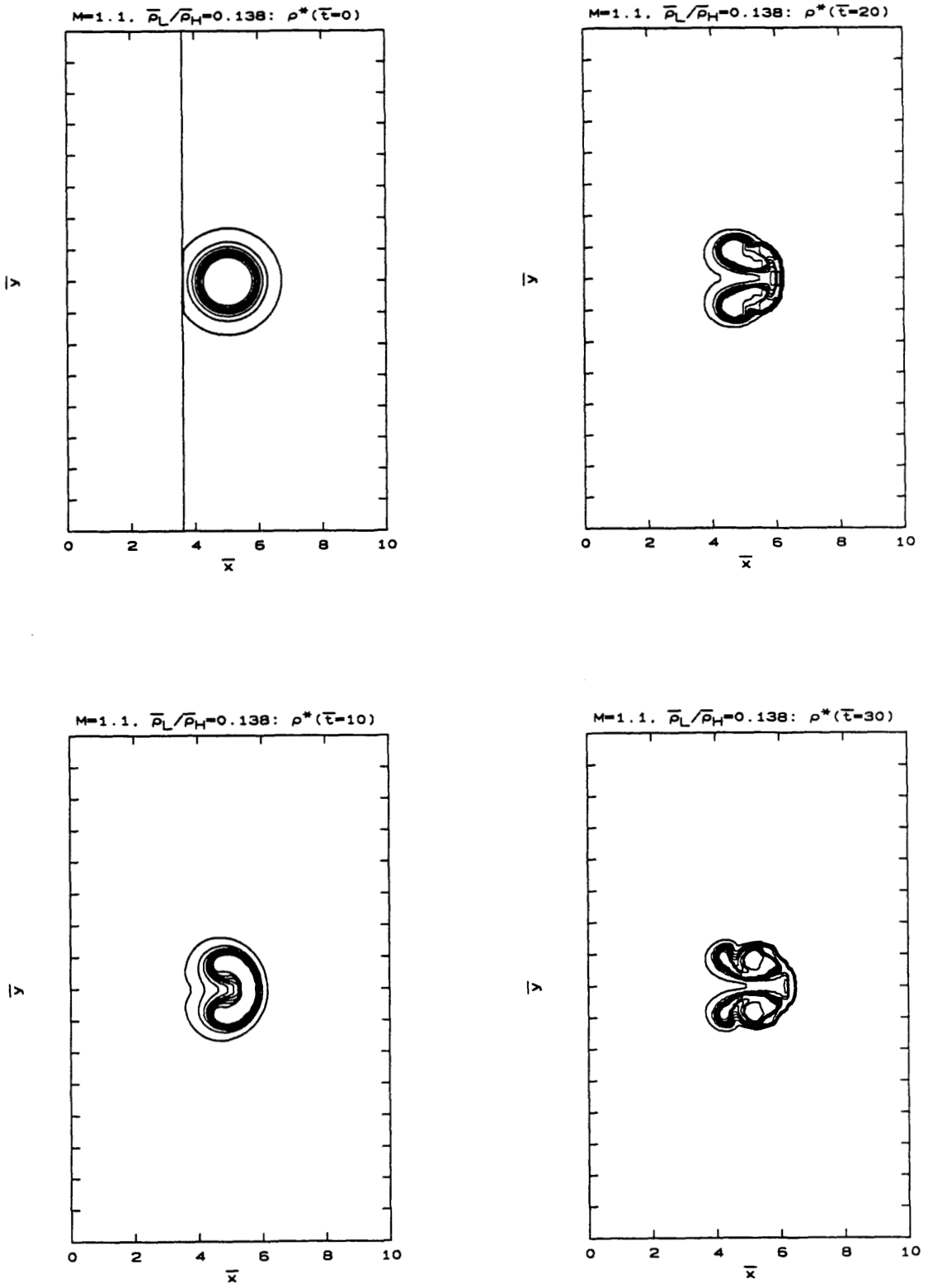

Figure 5.42 - Circular jet with M=1.1 and $\overline{\rho}_L/\overline{\rho}_H = 0.138$. Channel spacing = 16.

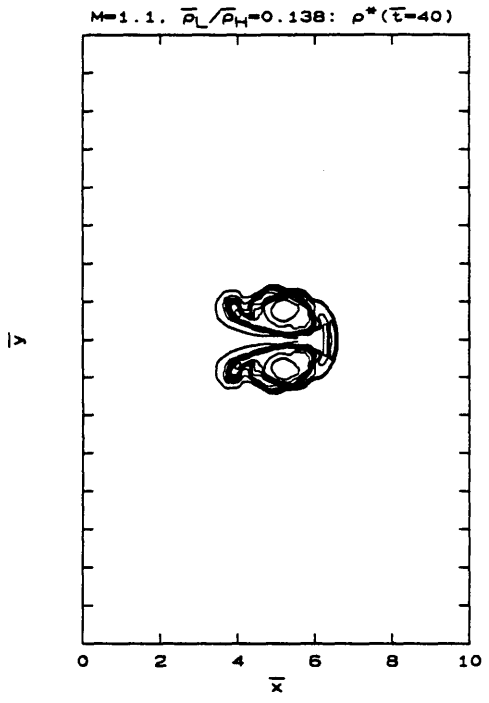
M=1.1. $\overline{\rho}_L/\overline{\rho}_H$=0.138: $\rho^*(\overline{t}$=40)
$\overline{y}$
0
2
4
6
8
10
$\overline{x}$

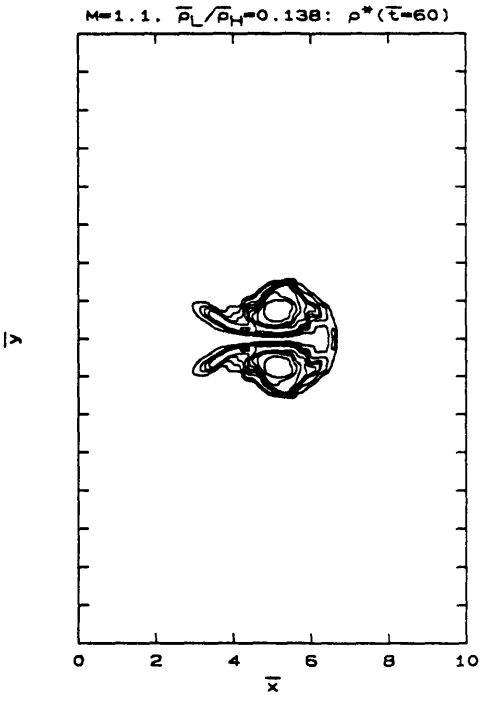
M=1.1. $\overline{\rho}_L/\overline{\rho}_H$=0.138: $\rho^*(\overline{t}$=60)
$\overline{y}$
0
2
4
6
8
10
$\overline{x}$

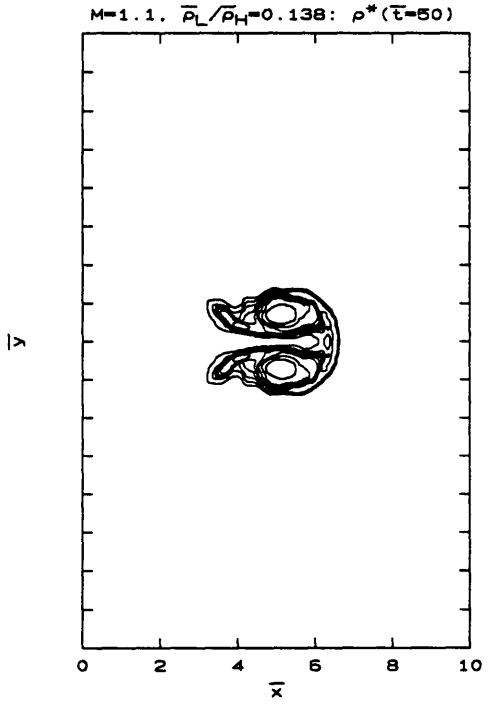
M=1.1. $\overline{\rho}_L/\overline{\rho}_H$=0.138: $\rho^*(\overline{t}$=50)
$\overline{y}$
0
2
4
6
8
10
$\overline{x}$

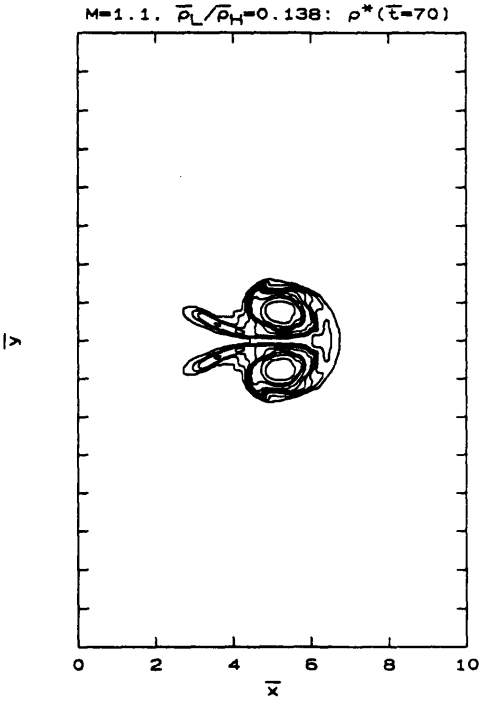
M=1.1. $\overline{\rho}_L/\overline{\rho}_H$=0.138: $\rho^*(\overline{t}$=70)
$\overline{y}$
0
2
4
6
8
10
$\overline{x}$

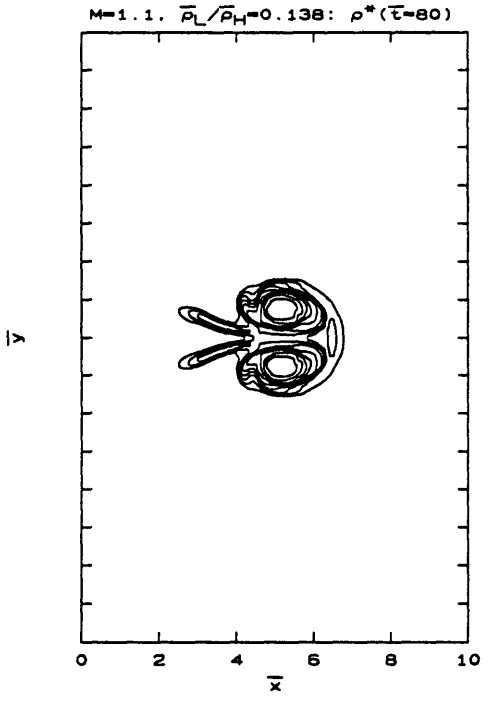
M=1.1. $\overline{\rho}_L/\overline{\rho}_H$=0.138: $\rho^*(\overline{t}$=80)
$\overline{y}$
0
2
4
6
8
10
$\overline{x}$

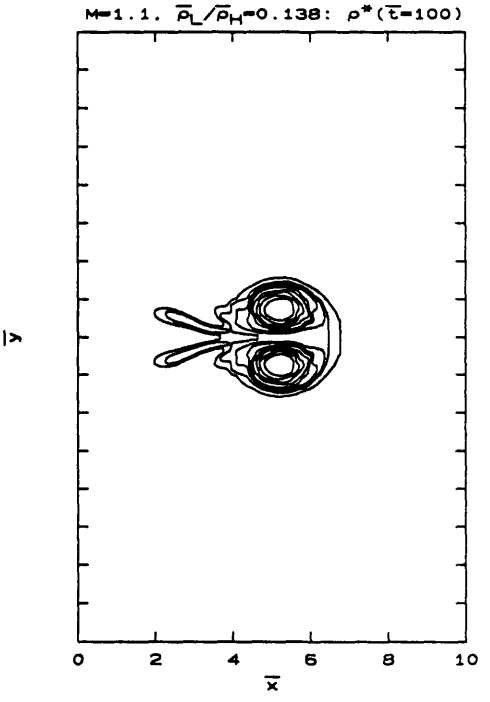
M=1.1. $\overline{\rho}_L/\overline{\rho}_H$=0.138: $\rho^*(\overline{t}$=100)
$\overline{y}$
0
2
4
6
8
10
$\overline{x}$

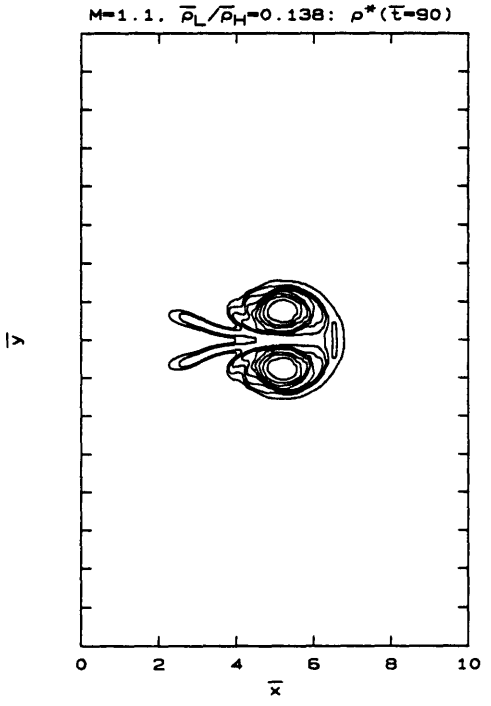
M=1.1. $\overline{\rho}_L/\overline{\rho}_H$=0.138: $\rho^*(\overline{t}$=90)
$\overline{y}$
0
2
4
6
8
10
$\overline{x}$

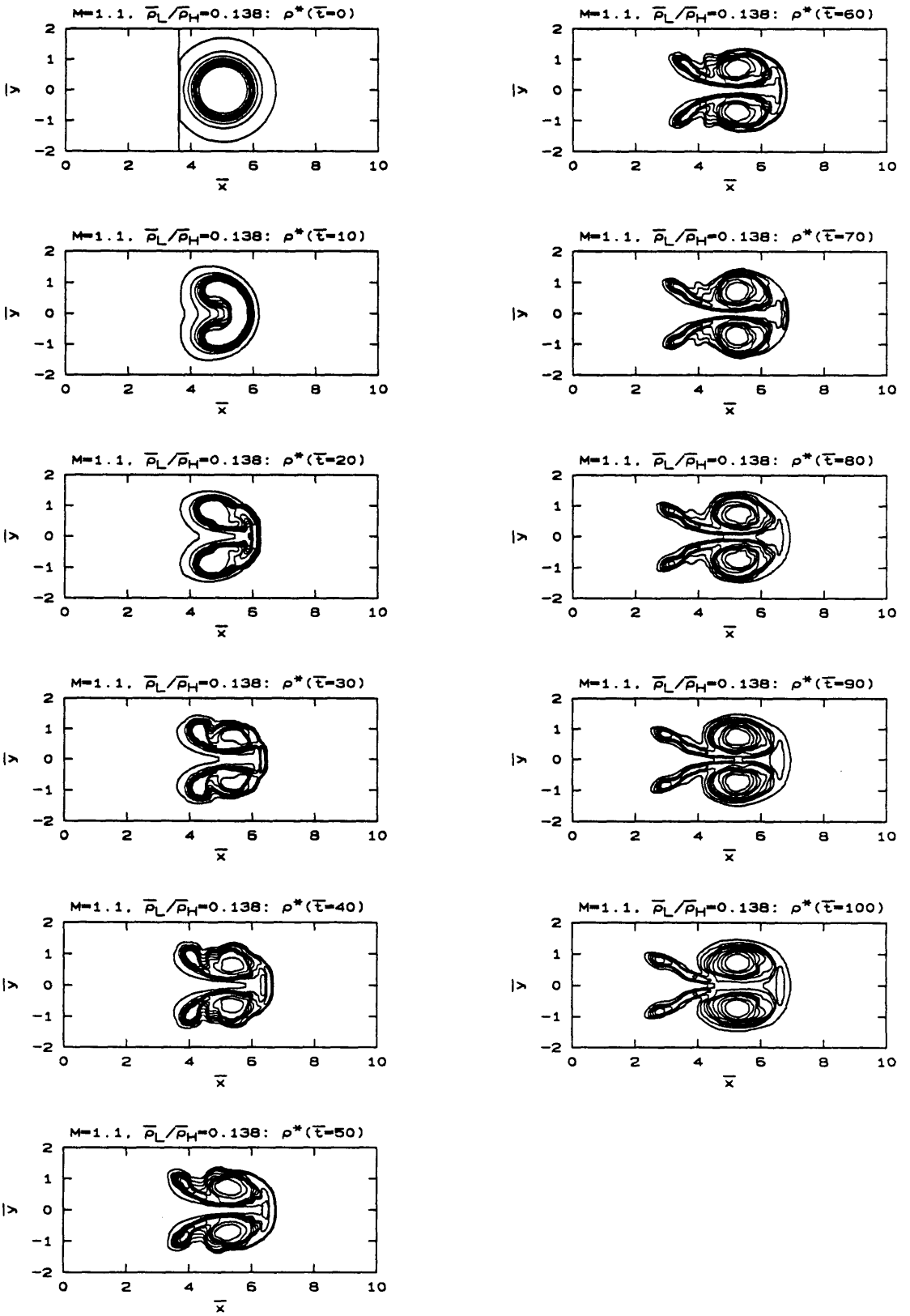

Figure 5.43 - Circular jet with M=1.1 and $\overline{\rho}_L/\overline{\rho}_H = 0.138$. Channel spacing = 4.

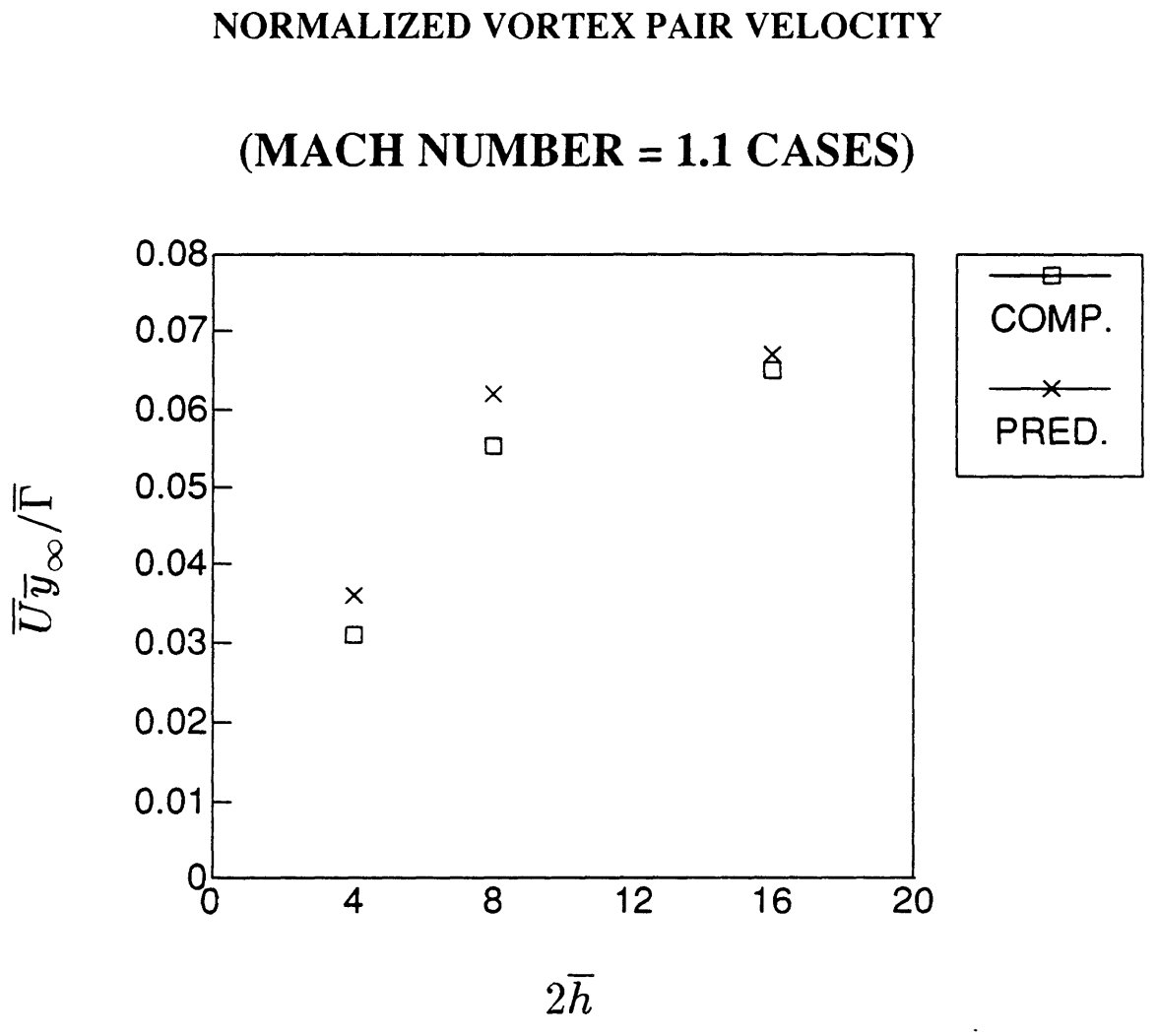

Figure 5.44 - Computed and predicted $\overline{U}\overline{y}_\infty/\overline{\Gamma}$ for variations in channel spacing.

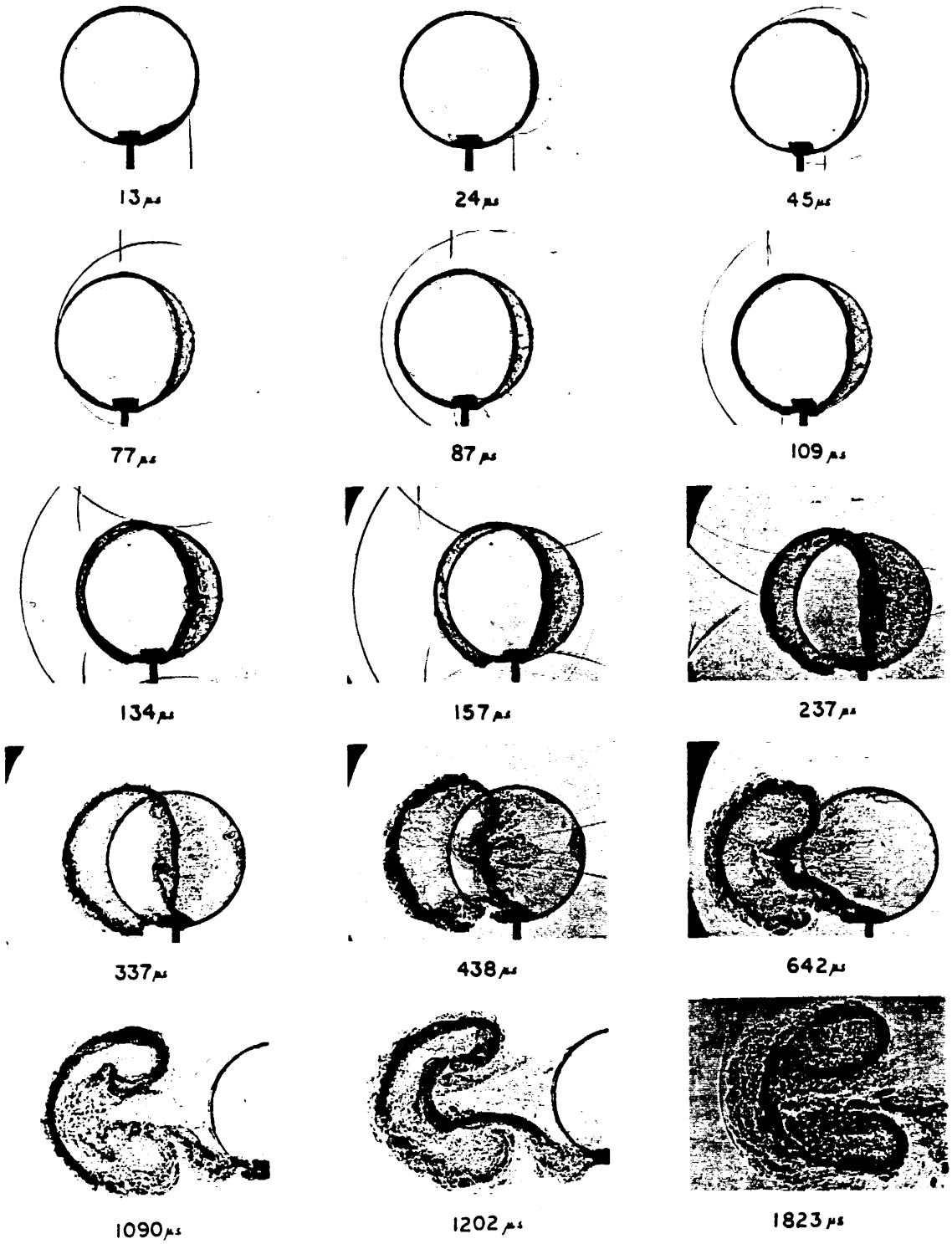

Figure 6.1 - Shadowgraphs of Haas' microfilm cylinder experiment: M=1.085, $\overline{\rho}_L/\overline{\rho}_H = 0.138$.

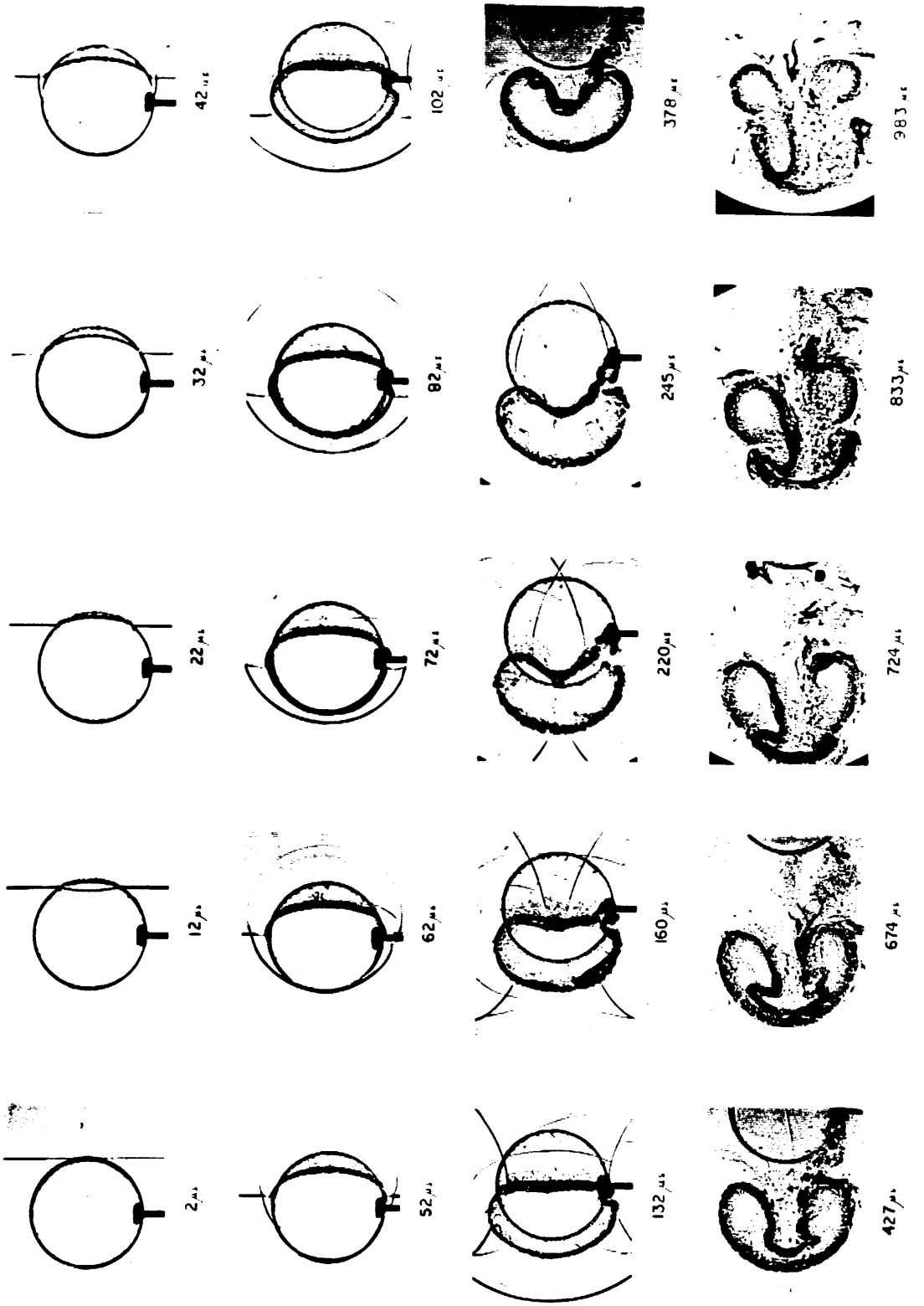

Figure 6.2 - Shadowgraphs of Haas' microfilm cylinder experiment: M=1.22, $\bar{\rho}_L/\bar{\rho}_H = 0.138$.

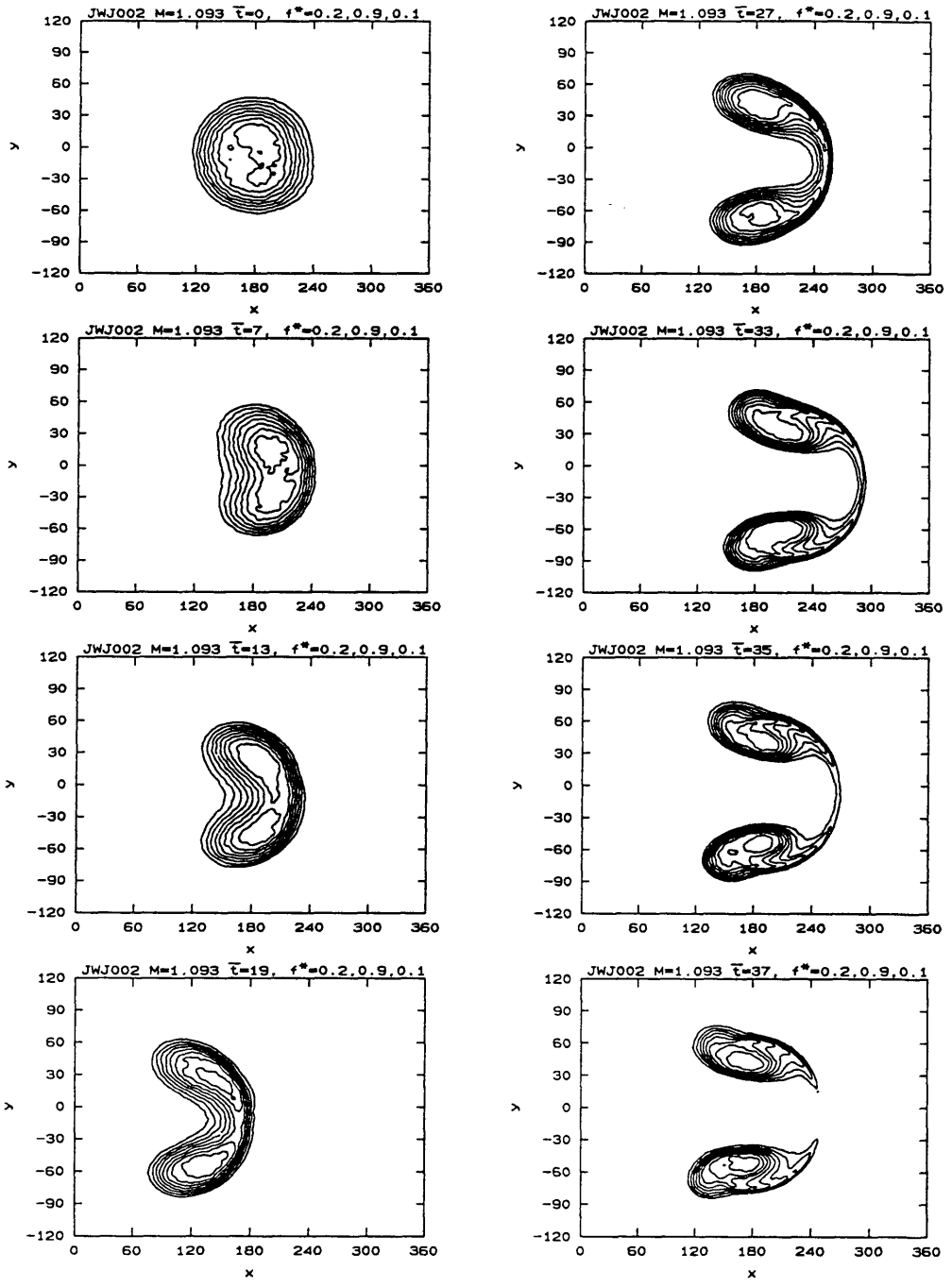

Figure 6.3 - Density contours of Jacobs' buoyant jet experiment: M=1.093, $\overline{\rho}_L/\overline{\rho}_H = 0.152$.

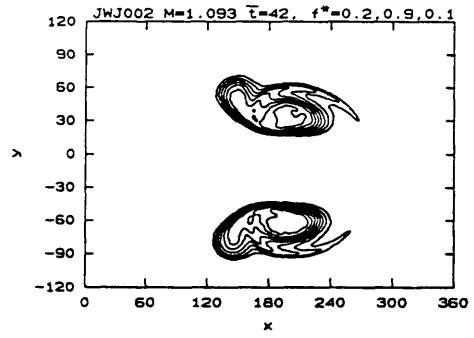
JWJ002 M=1.093 t̄=42, f*=0.2,0.9,0.1
120
90
60
30
0
-30
-60
-90
-120
y
0
60
120
180
240
300
360
x

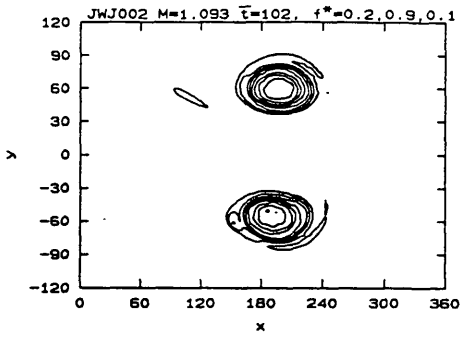
JWJ002 M=1.093 t̄=102, f*=0.2,0.9,0.1
120
90
60
30
0
-30
-60
-90
-120
y
0
60
120
180
240
300
360
x

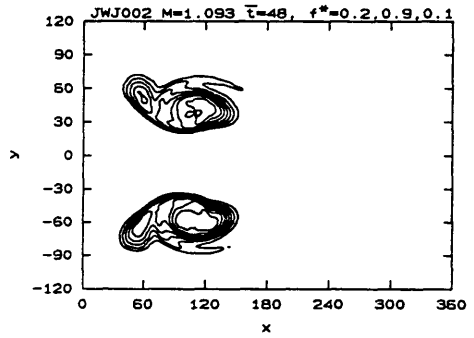
JWJ002 M=1.093 t̄=48, f*=0.2,0.9,0.1
120
90
60
30
0
-30
-60
-90
-120
y
0
60
120
180
240
300
360
x

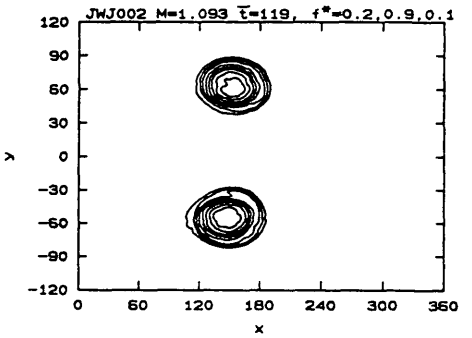
JWJ002 M=1.093 t̄=119, f*=0.2,0.9,0.1
120
90
60
30
0
-30
-60
-90
-120
y
0
60
120
180
240
300
360
x

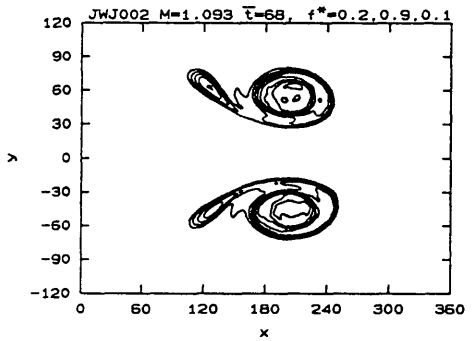
JWJ002 M=1.093 t̄=68, f*=0.2,0.9,0.1
120
90
60
30
0
-30
-60
-90
-120
y
0
60
120
180
240
300
360
x

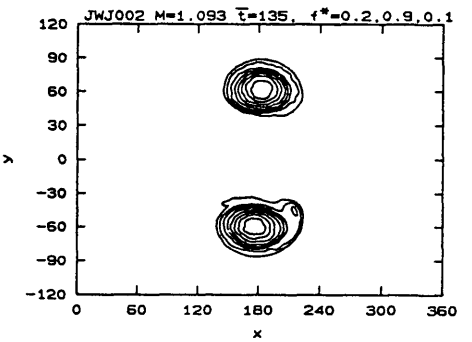
JWJ002 M=1.093 t̄=135, f*=0.2,0.9,0.1
120
90
60
30
0
-30
-60
-90
-120
y
0
60
120
180
240
300
360
x

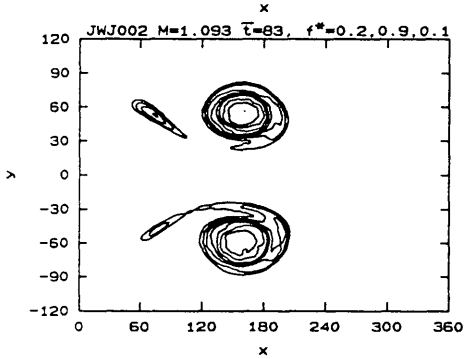
JWJ002 M=1.093 t̄=83, f*=0.2,0.9,0.1
120
90
60
30
0
-30
-60
-90
-120
y
0
60
120
180
240
300
360
x

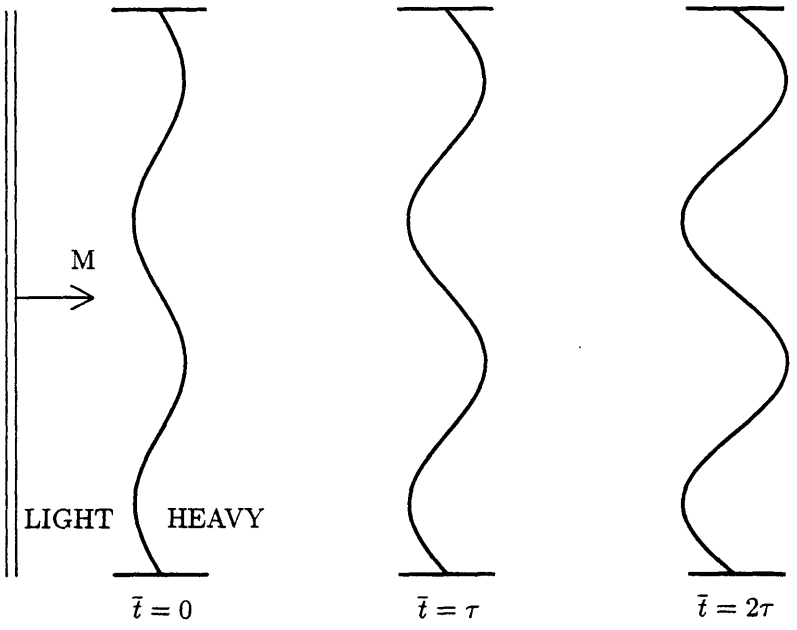

Figure 7.1 - Richtmyer-Meshkov instability at a heavy-light interface.

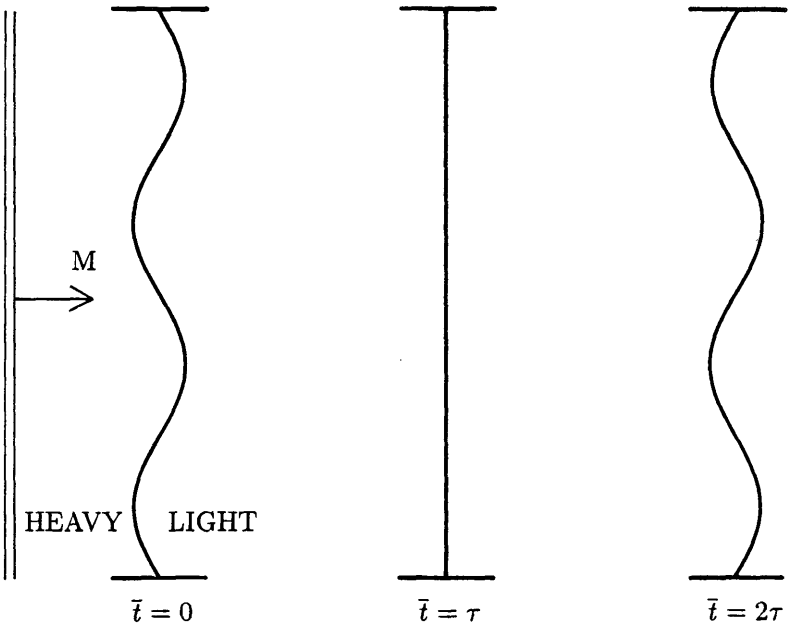

Figure 7.2 - Richtmyer-Meshkov instability at a light-heavy interface.

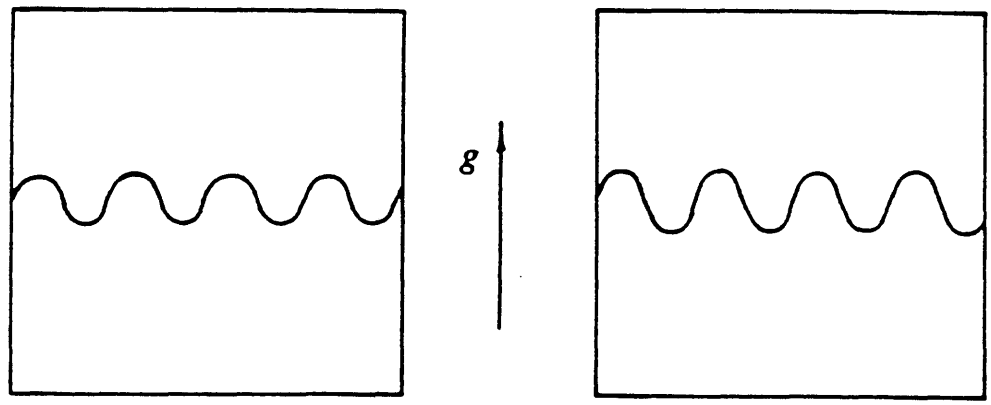

a. Initial configuration.

b. Linear growth.

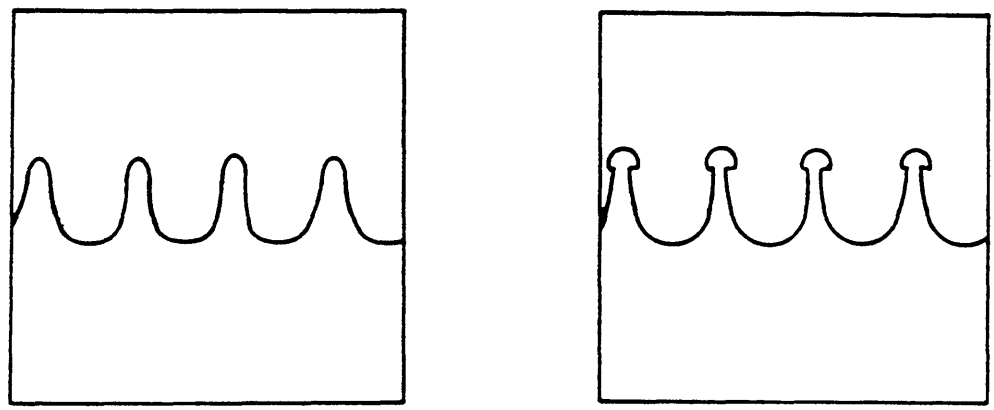

c. Asymmetric development

d. Appearance of secondary instabilities.

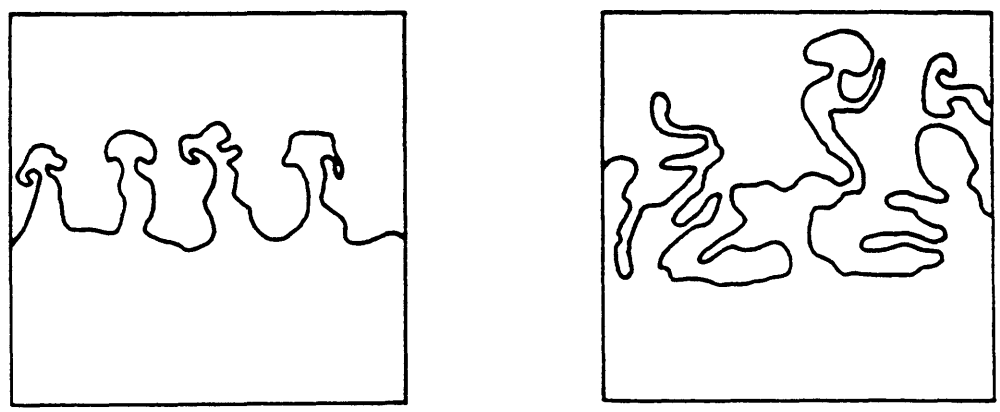

e. Appearance of turbulence.

f. Fully developed turbulent mixing layer.

Figure 7.3 - Late-time instability at a light-heavy interface [Reproduced from Brouillette (1989), p.111].

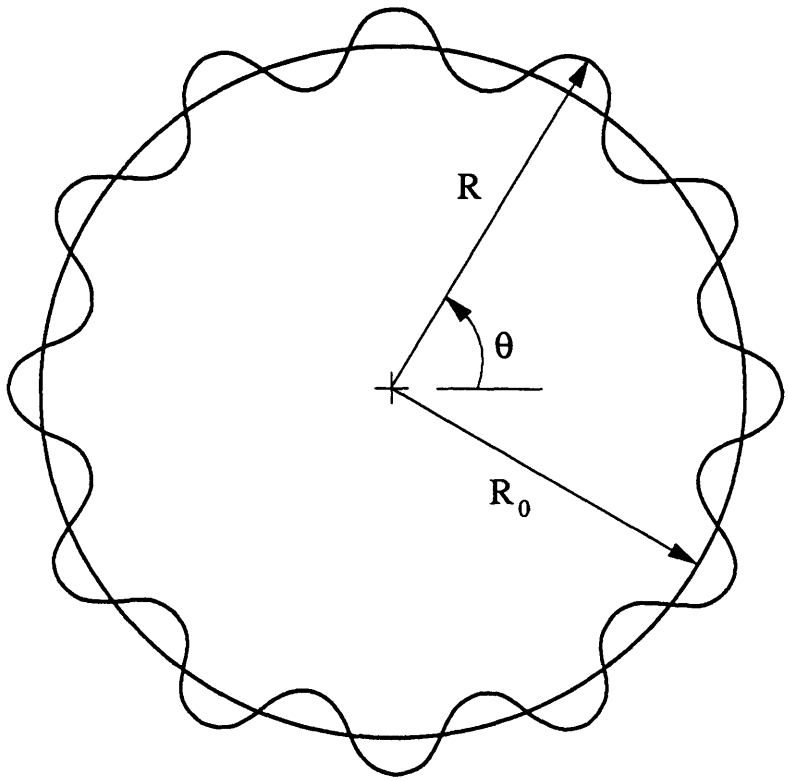

Figure 7.4 - Sinusoidal perturbation of a circular jet.

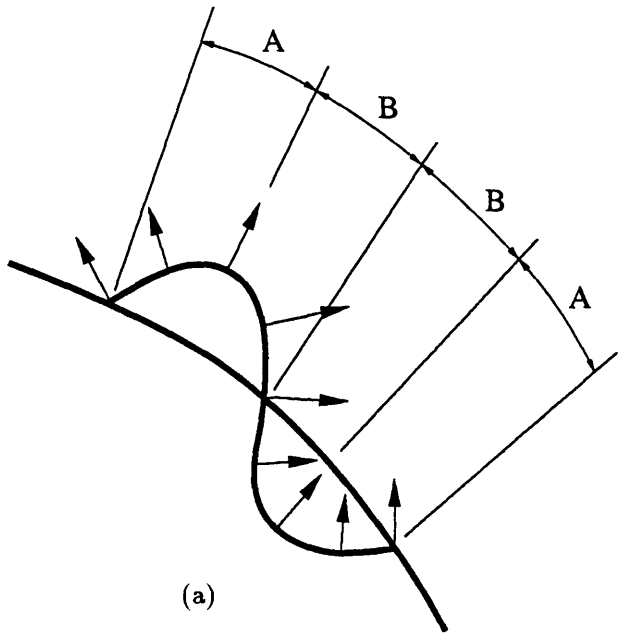

(a)

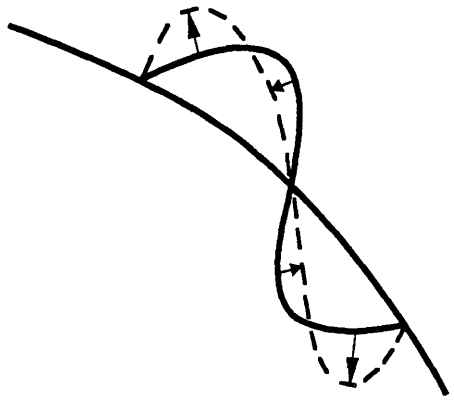

(b)

Figure 7.5 - Details of the light-heavy instability: (a) regions of increased/decreased vorticity, (b) initial, N-shaped distortion.

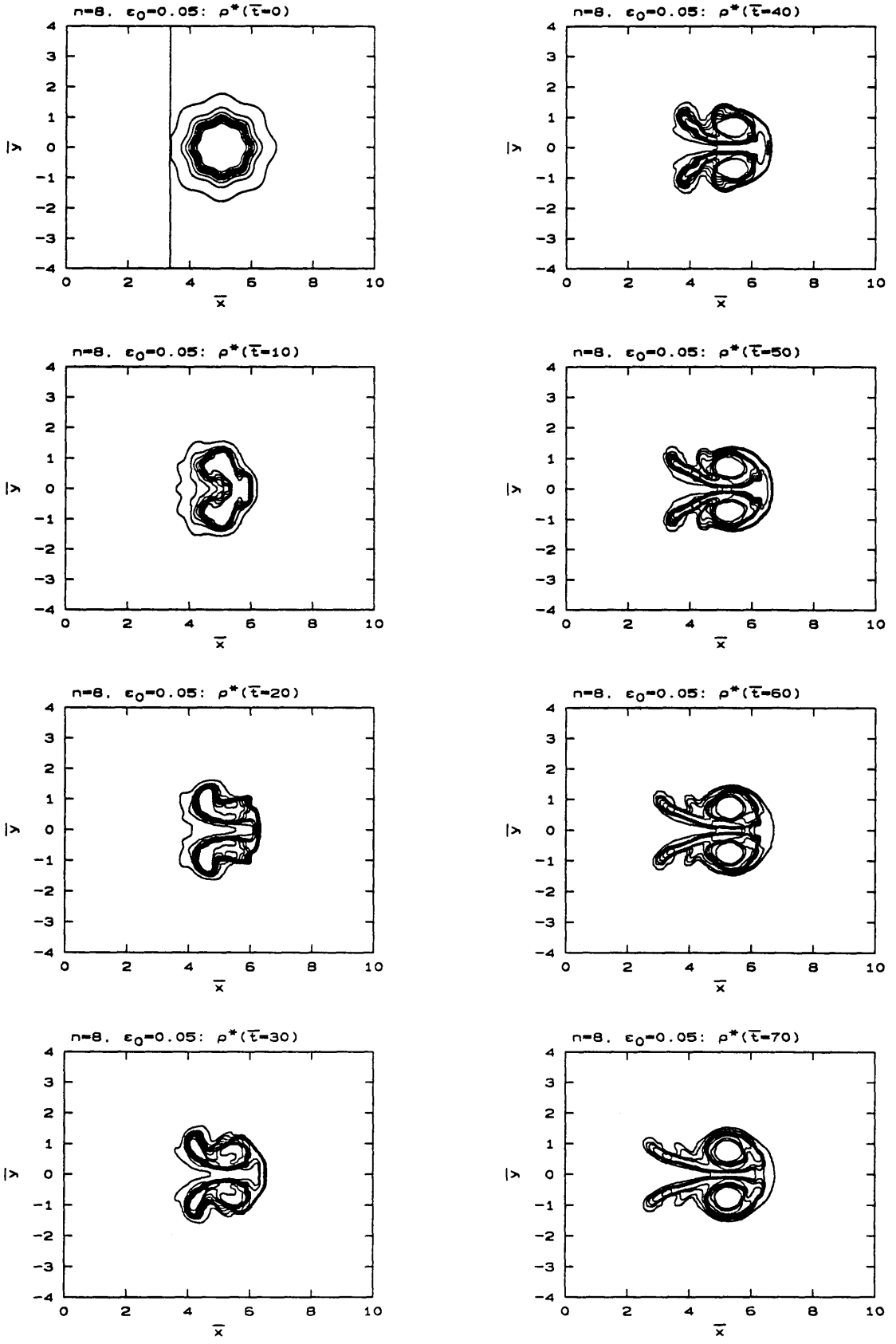

Figure 7.6 - Sinusoidal jets with M=1.1 and $\overline{\rho}_L/\overline{\rho}_H = 0.138$, n=8, ϵ_0=0.05.

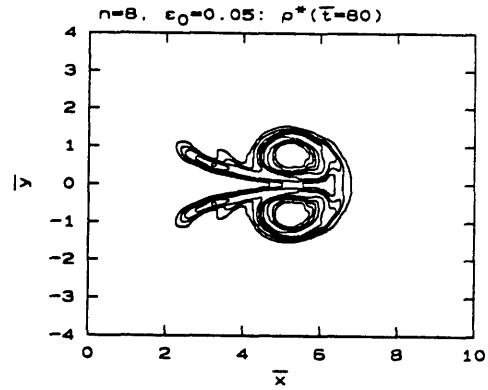
n=8, ε_0=0.05: $\rho^*(\bar{t}$=80)
$\bar{y}$
$\bar{x}$

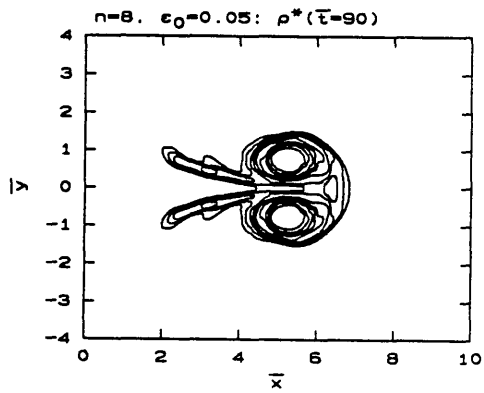
n=8, ε_0=0.05: $\rho^*(\bar{t}$=90)
$\bar{y}$
$\bar{x}$

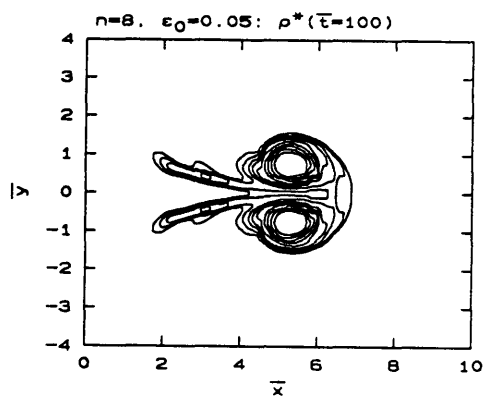
n=8, ε_0=0.05: $\rho^*(\bar{t}$=100)
$\bar{y}$
$\bar{x}$

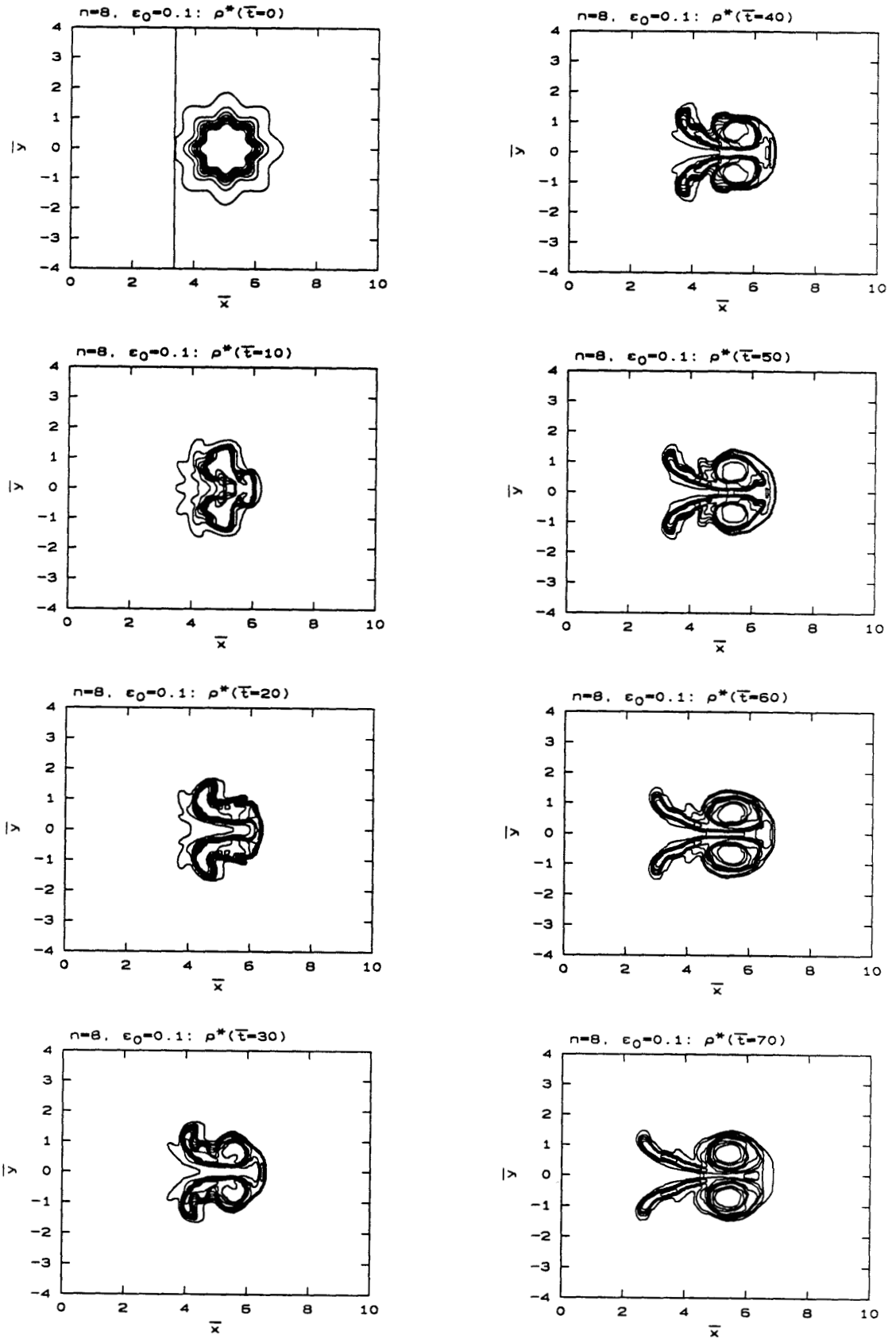

Figure 7.7 - Sinusoidal jets with M=1.1 and $\overline{\rho}_L/\overline{\rho}_H = 0.138$, n=8, ϵ_0=0.1.

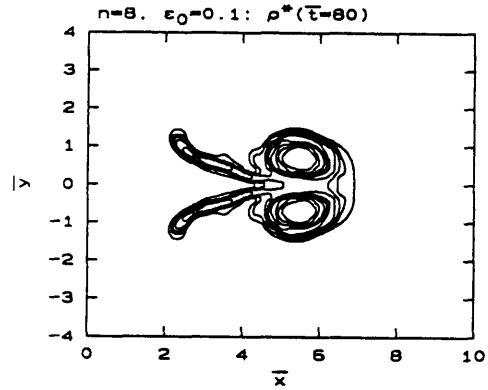
n=8, ε0=0.1: ρ*(t̄=80)
ȳ
x̄

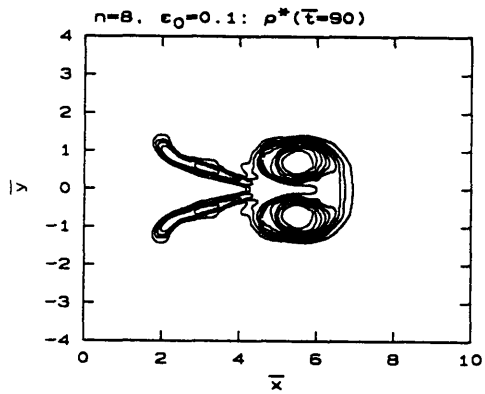
n=8, ε0=0.1: ρ*(t̄=90)
ȳ
x̄

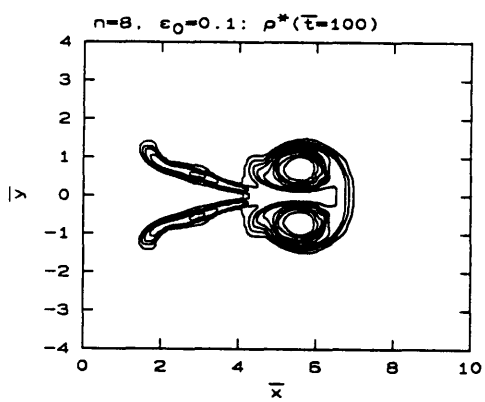
n=8, ε0=0.1: ρ*(t̄=100)
ȳ
x̄

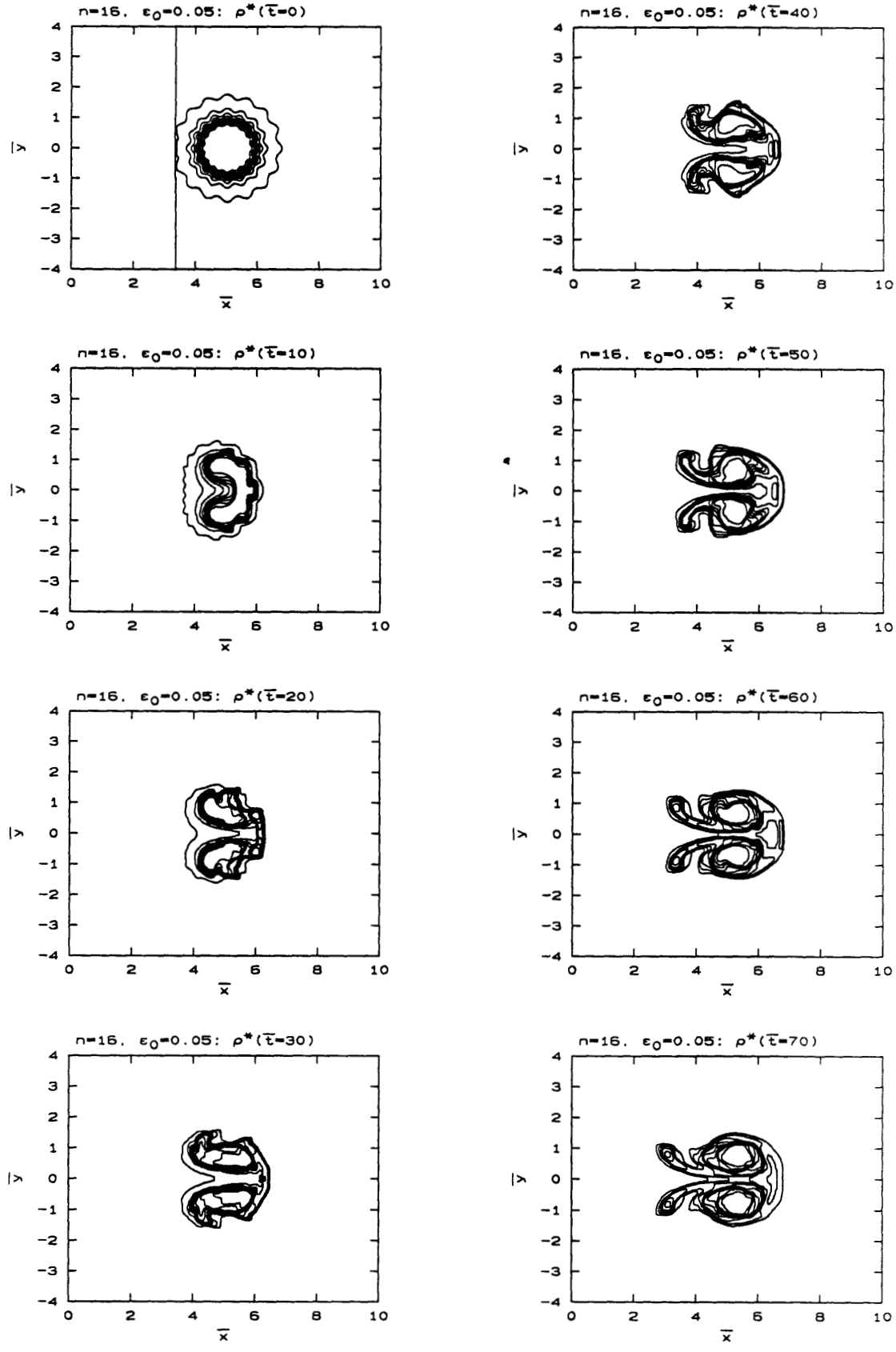

Figure 7.8 - Sinusoidal jets with M=1.1 and $\overline{\rho}_L/\overline{\rho}_H = 0.138$, n=16, ϵ_0=0.05.

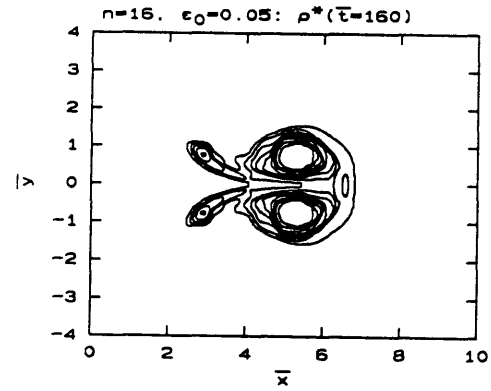
n=16, ε0=0.05: ρ*(t̄=160)
ȳ
x̄

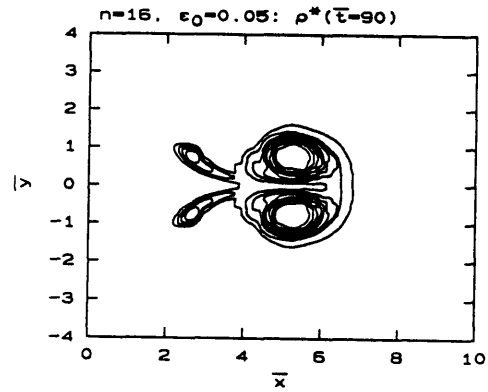
n=16, ε0=0.05: ρ*(t̄=90)
ȳ
x̄

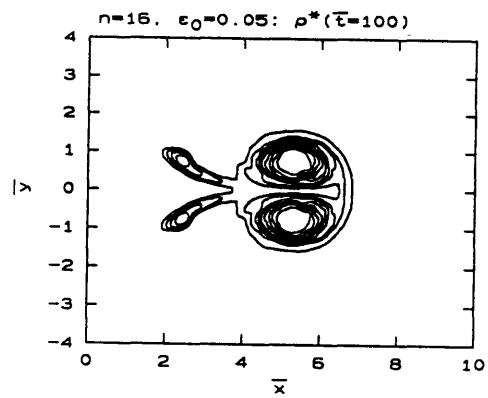
n=16, ε0=0.05: ρ*(t̄=100)
ȳ
x̄

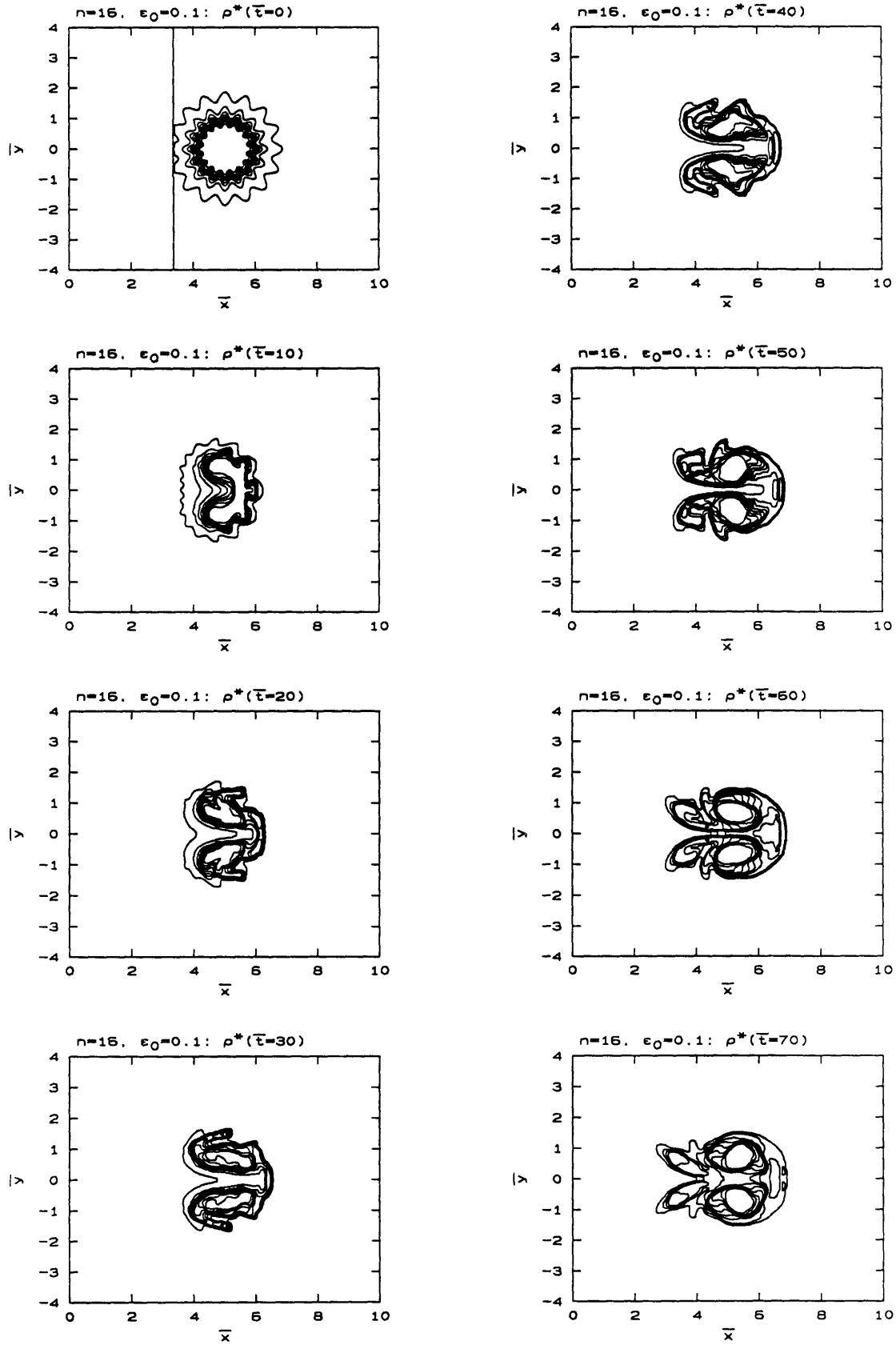

Figure 7.9 - Sinusoidal jets with M=1.1 and $\bar{\rho}_L/\bar{\rho}_H = 0.138$, n=16, ϵ_0=0.1.

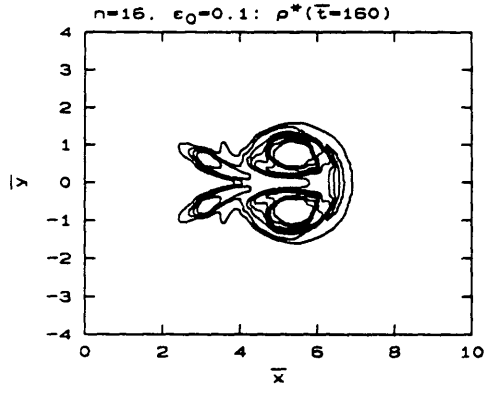
n=16, ε_0=0.1: $\rho^*(\bar{t}$=160)
$\bar{y}$
$\bar{x}$

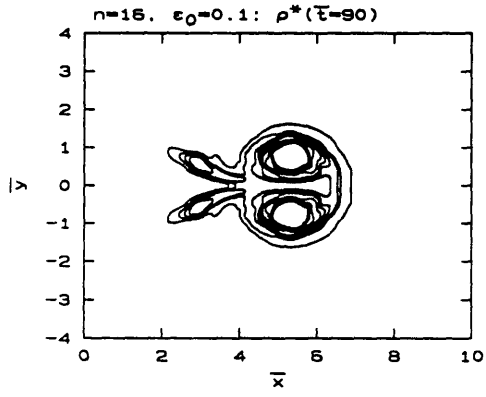
n=16, ε_0=0.1: $\rho^*(\bar{t}$=90)
$\bar{y}$
$\bar{x}$

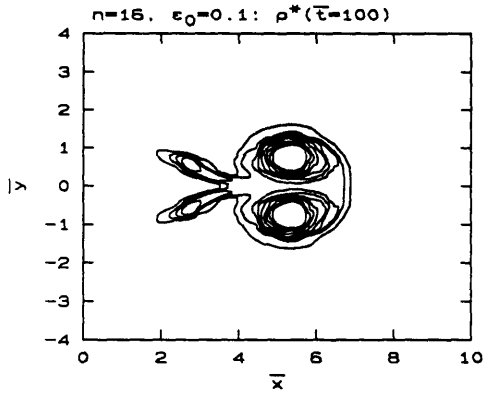
n=16, ε_0=0.1: $\rho^*(\bar{t}$=100)
$\bar{y}$
$\bar{x}$

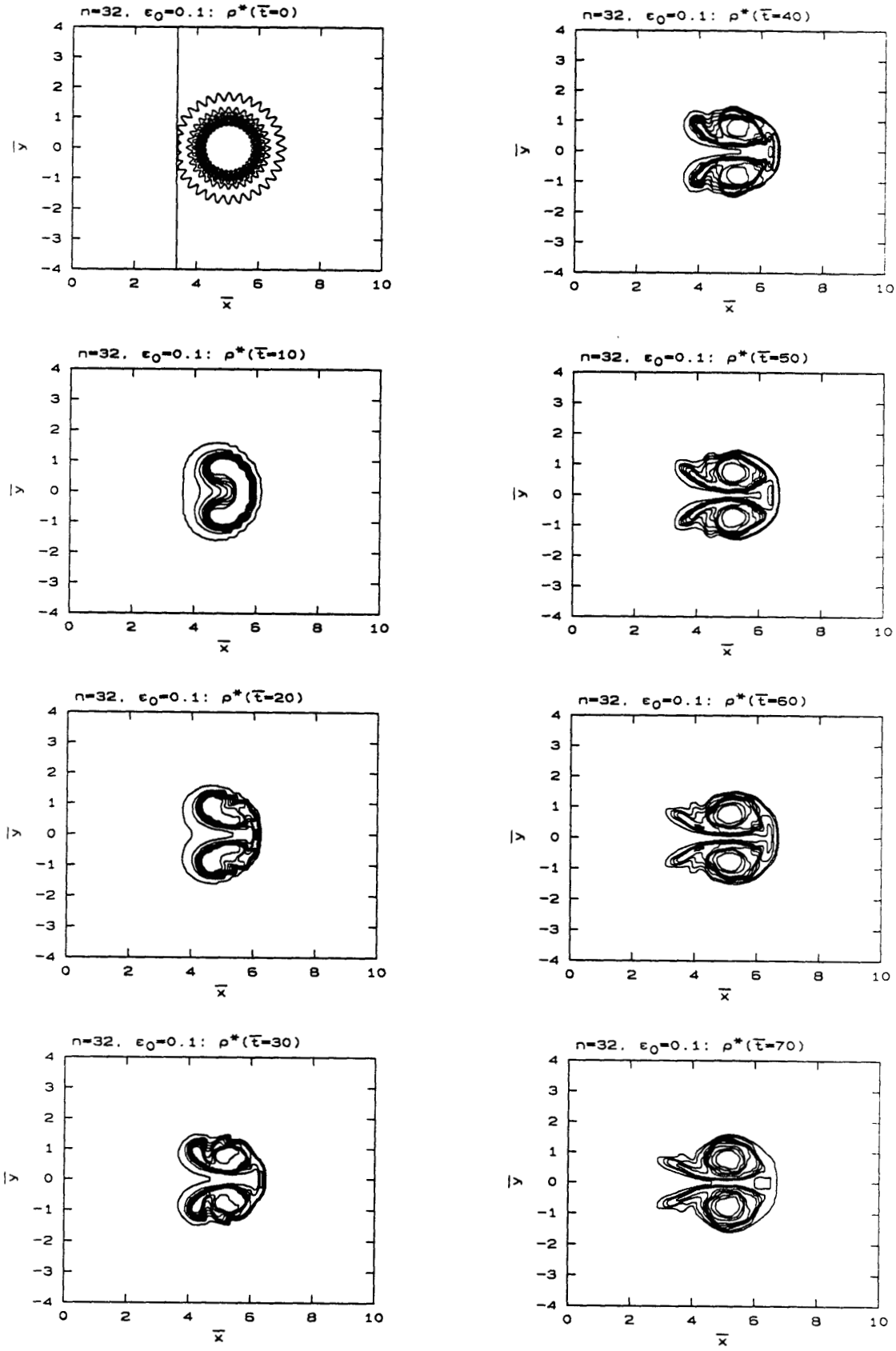

Figure 7.10 - Sinusoidal jets with M=1.1 and $\overline{\rho}_L/\overline{\rho}_H = 0.138$, n=32, ϵ_0=0.1.

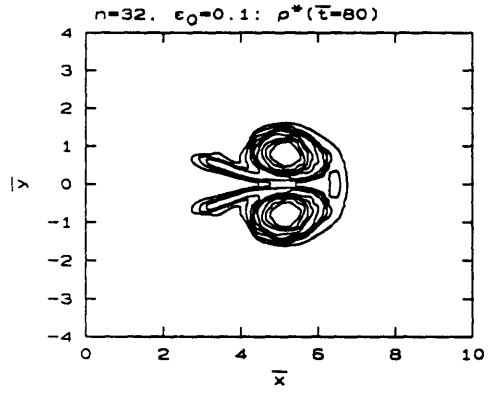
n=32. ε_0=0.1: $\rho^*(\bar{t}$=80)
$\bar{y}$
$\bar{x}$

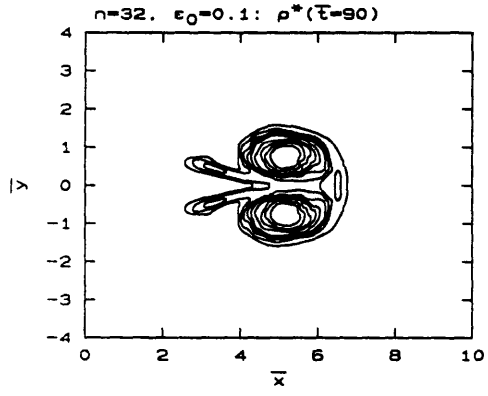
n=32. ε_0=0.1: $\rho^*(\bar{t}$=90)
$\bar{y}$
$\bar{x}$

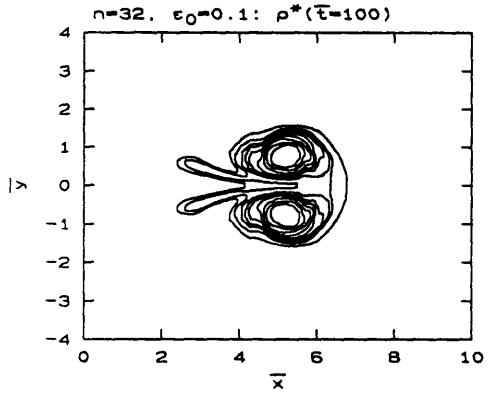
n=32. ε_0=0.1: $\rho^*(\bar{t}$=100)
$\bar{y}$
$\bar{x}$

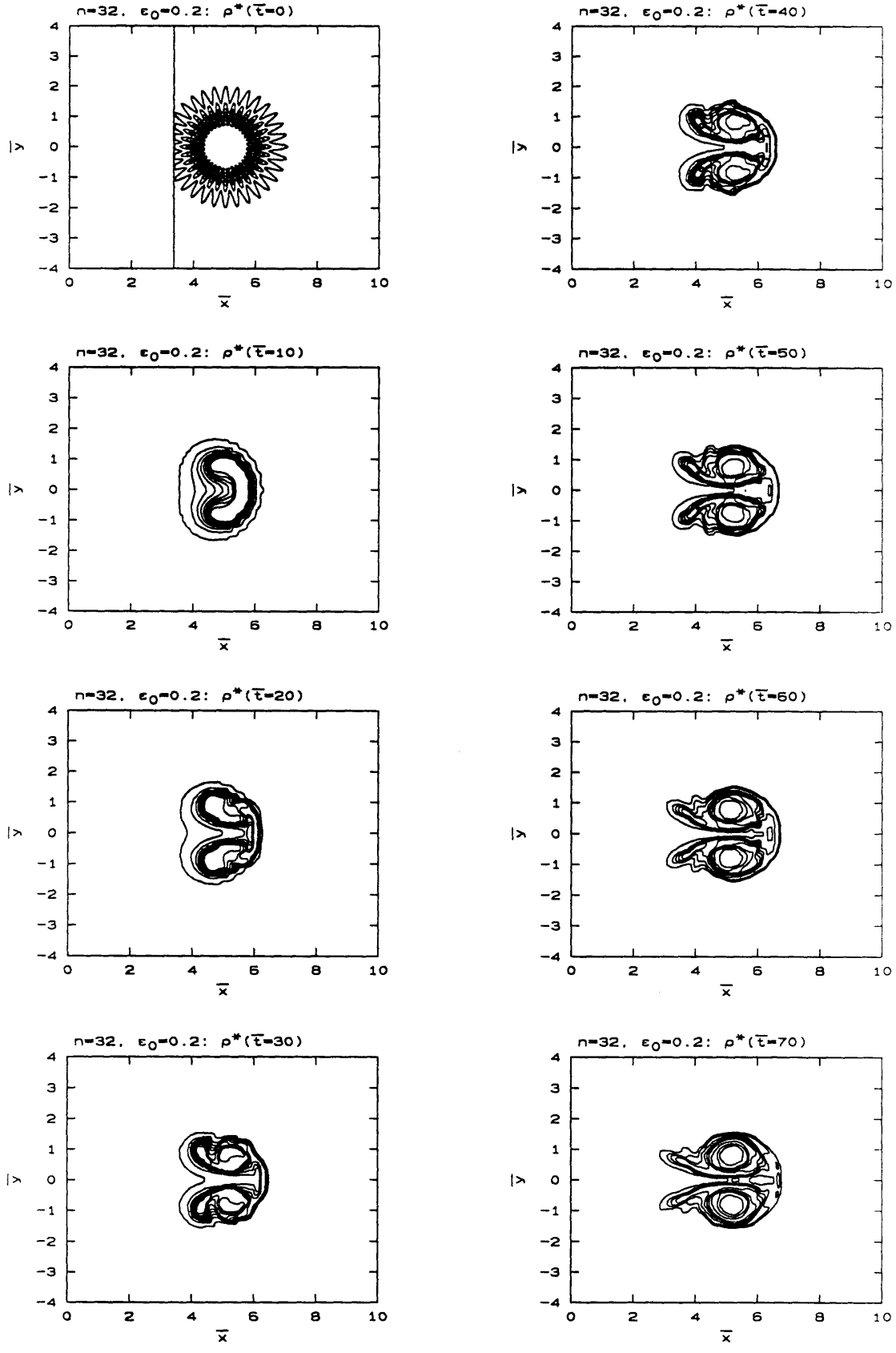

Figure 7.11 - Sinusoidal jets with M=1.1 and $\bar{\rho}_L/\bar{\rho}_H = 0.138$, n=32, ϵ_0=0.2.

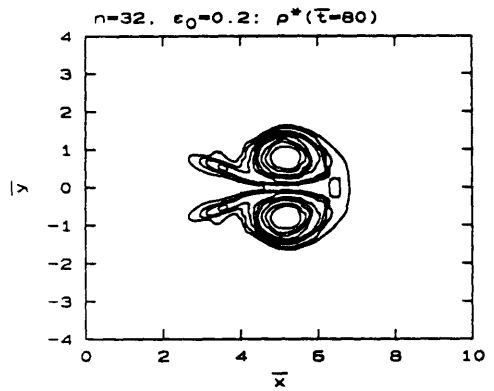
n=32, ε0=0.2: ρ*(t̄=80)
ȳ
x̄

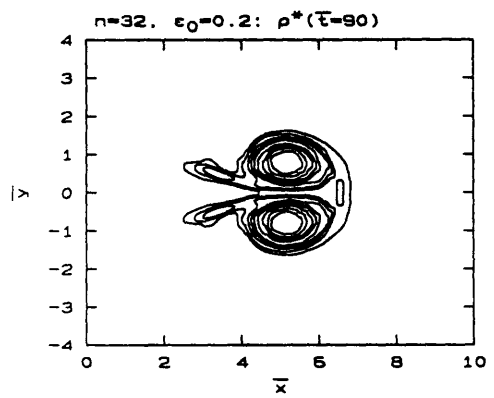
n=32, ε0=0.2: ρ*(t̄=90)
ȳ
x̄

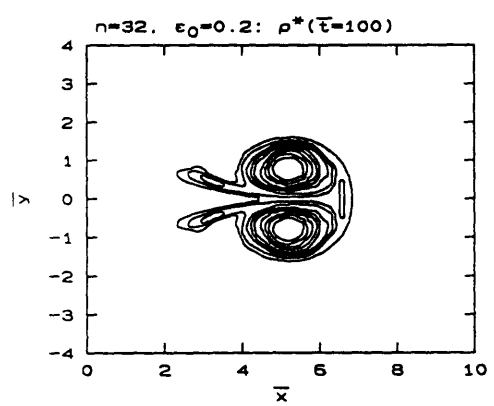
n=32, ε0=0.2: ρ*(t̄=100)
ȳ
x̄

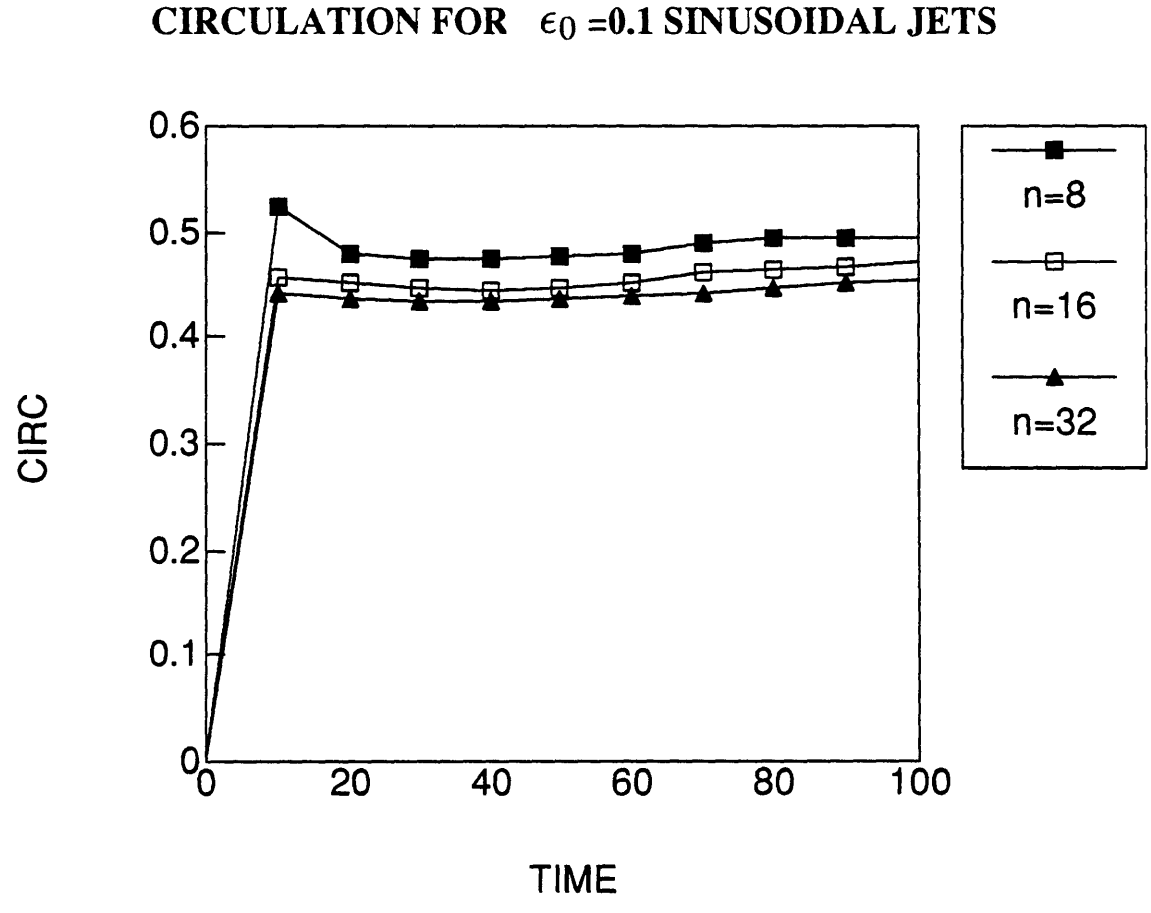

Figures 7.12 - Comparison of $\overline{\Gamma}(\bar{t})$ for the $\epsilon_0 = 0.1$ sinusoidal jets.

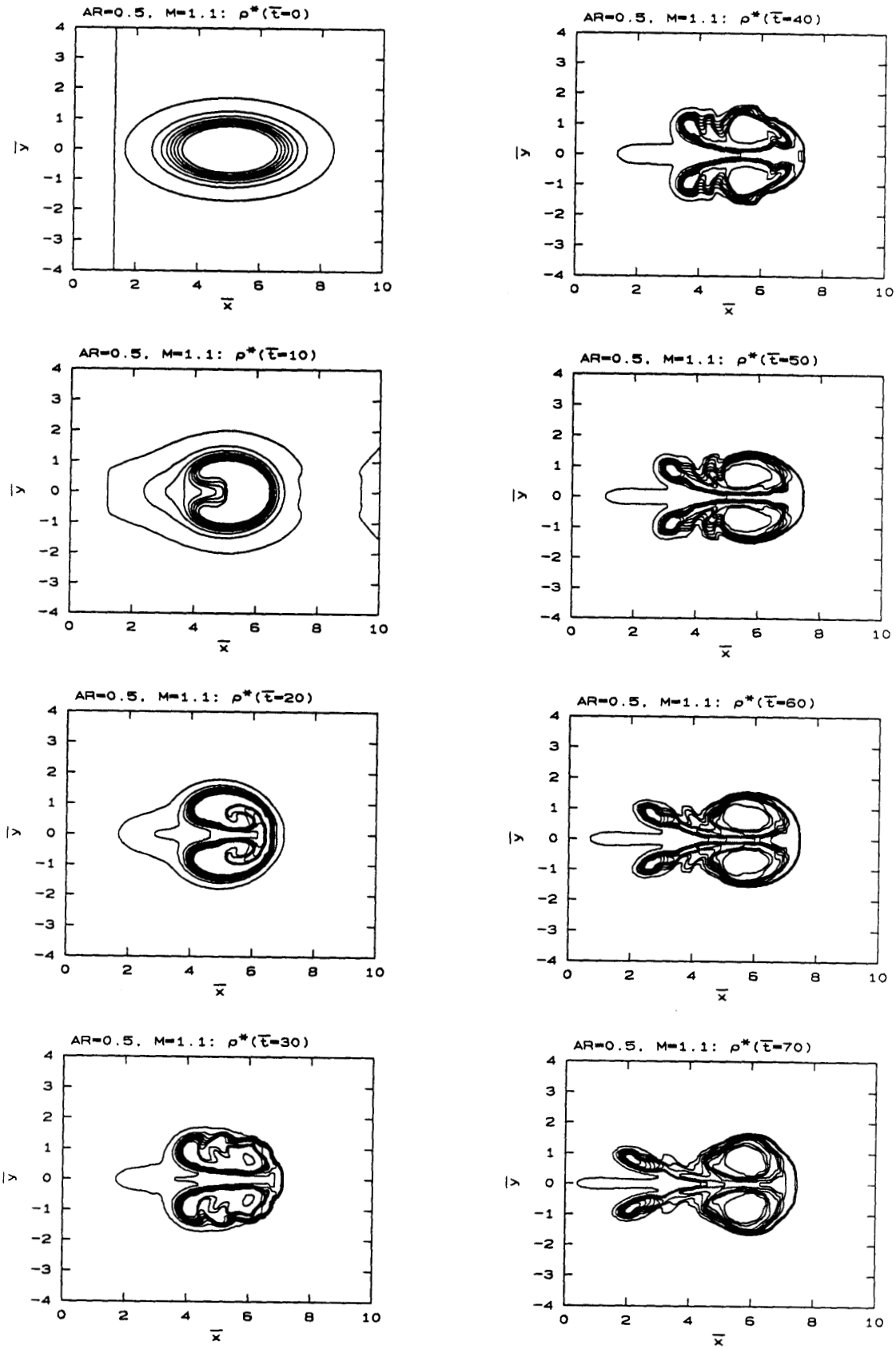

Figure 7.13 - AR = 0.5 elliptical jet with M=1.1 and $\overline{\rho}_L / \overline{\rho}_H = 0.138$.

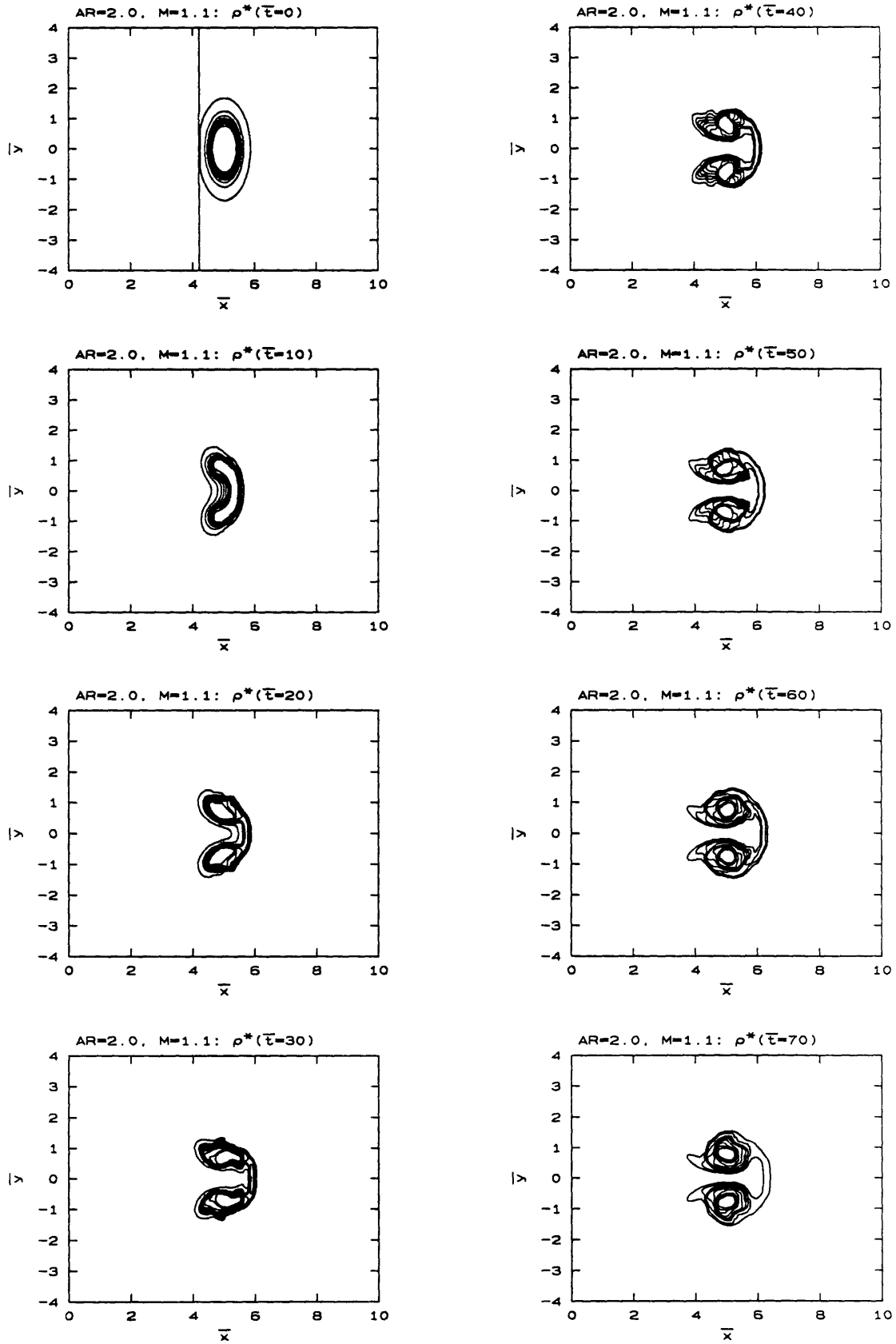

Figure 7.14 - AR = 2.0 elliptical jet with M=1.1 and $\bar{\rho}_L / \bar{\rho}_H = 0.138$.

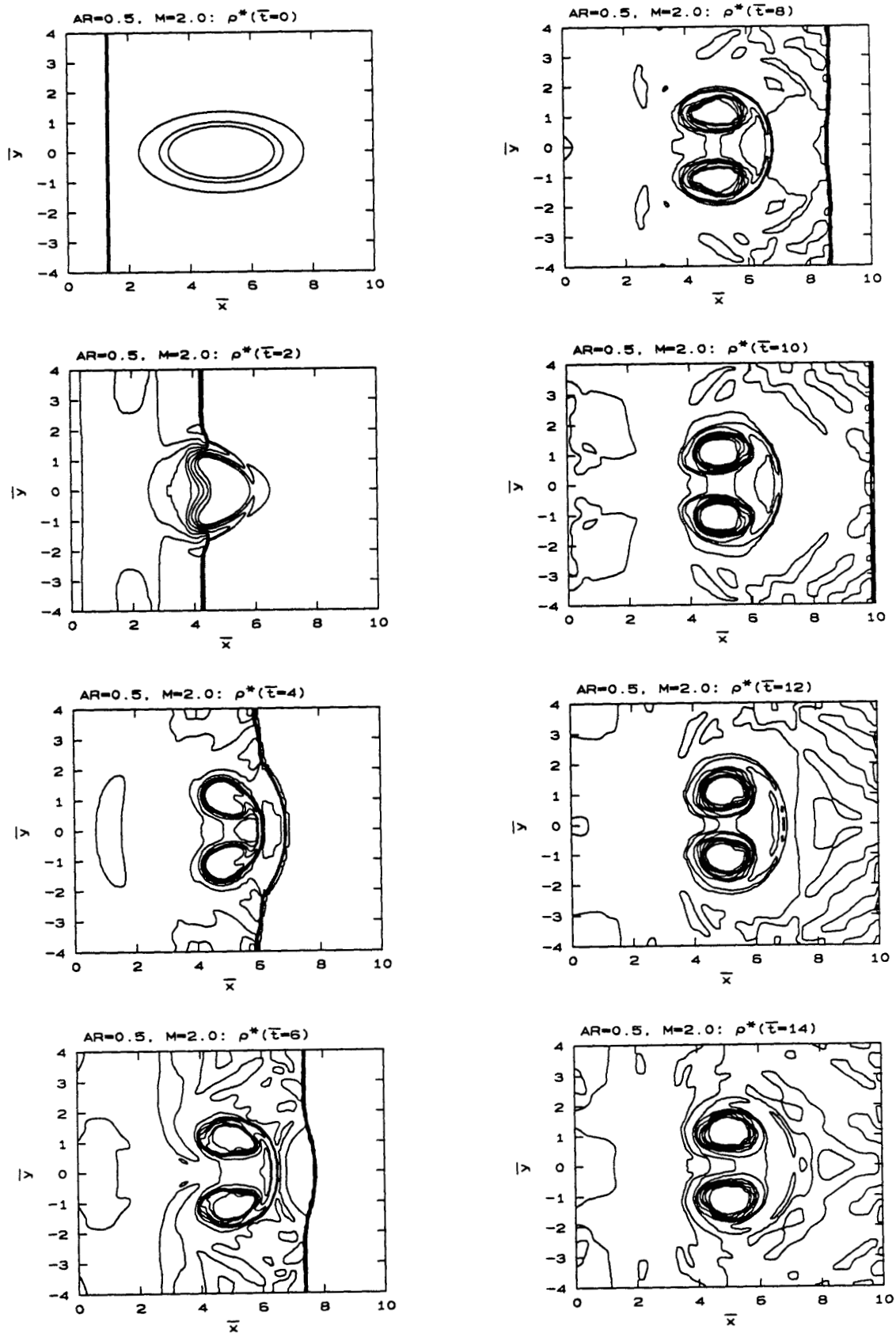

Figure 7.15 - AR = 0.5 elliptical jet with M=2.0 and $\overline{\rho}_L / \overline{\rho}_H = 0.138$.

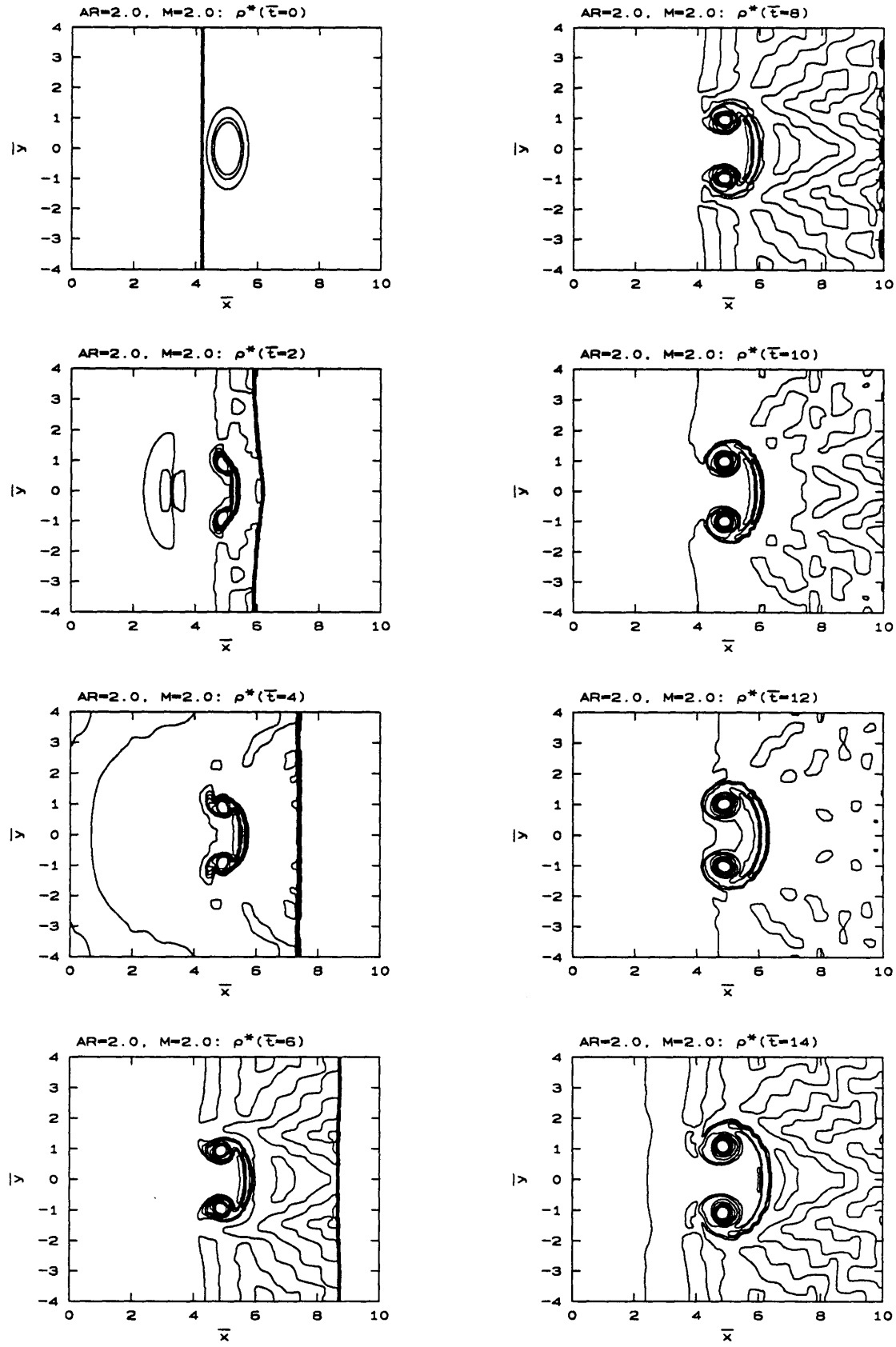

Figure 7.16 - AR = 2.0 elliptical jet with M=2.0 and $\bar{\rho}_L / \bar{\rho}_H = 0.138$.

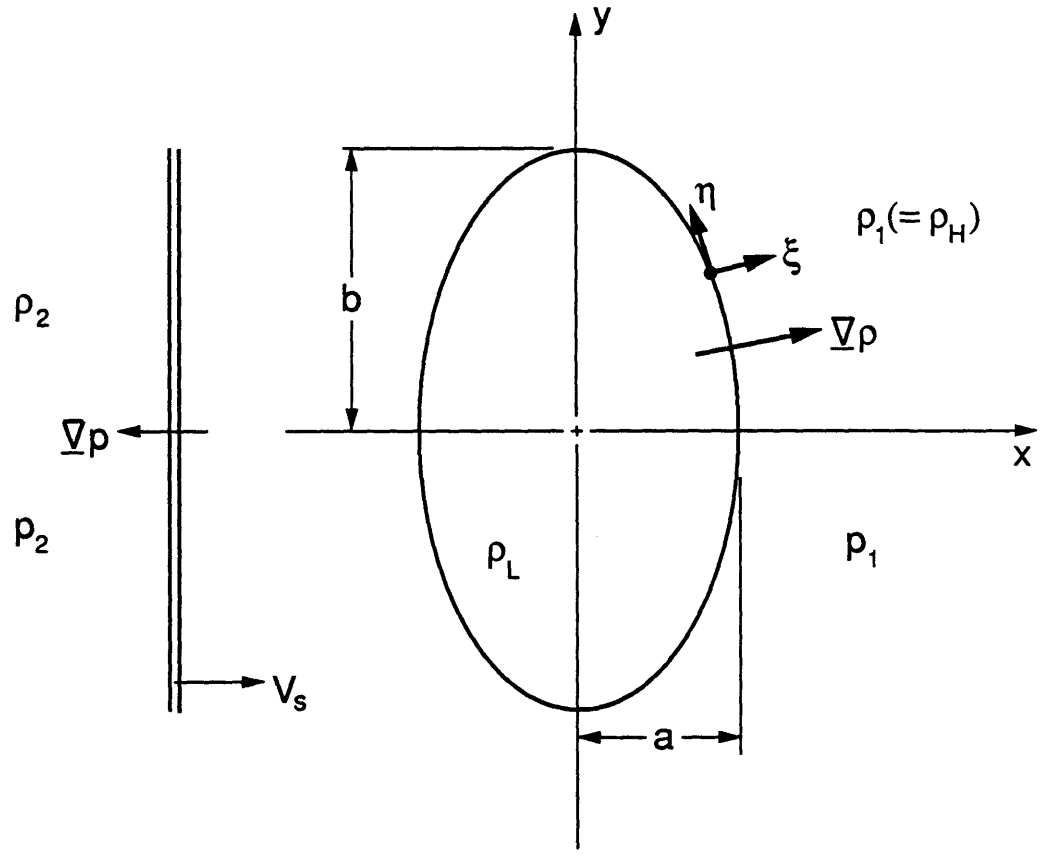

Figure 7.17 - Schematic for elliptical jet circulation and impulse models.

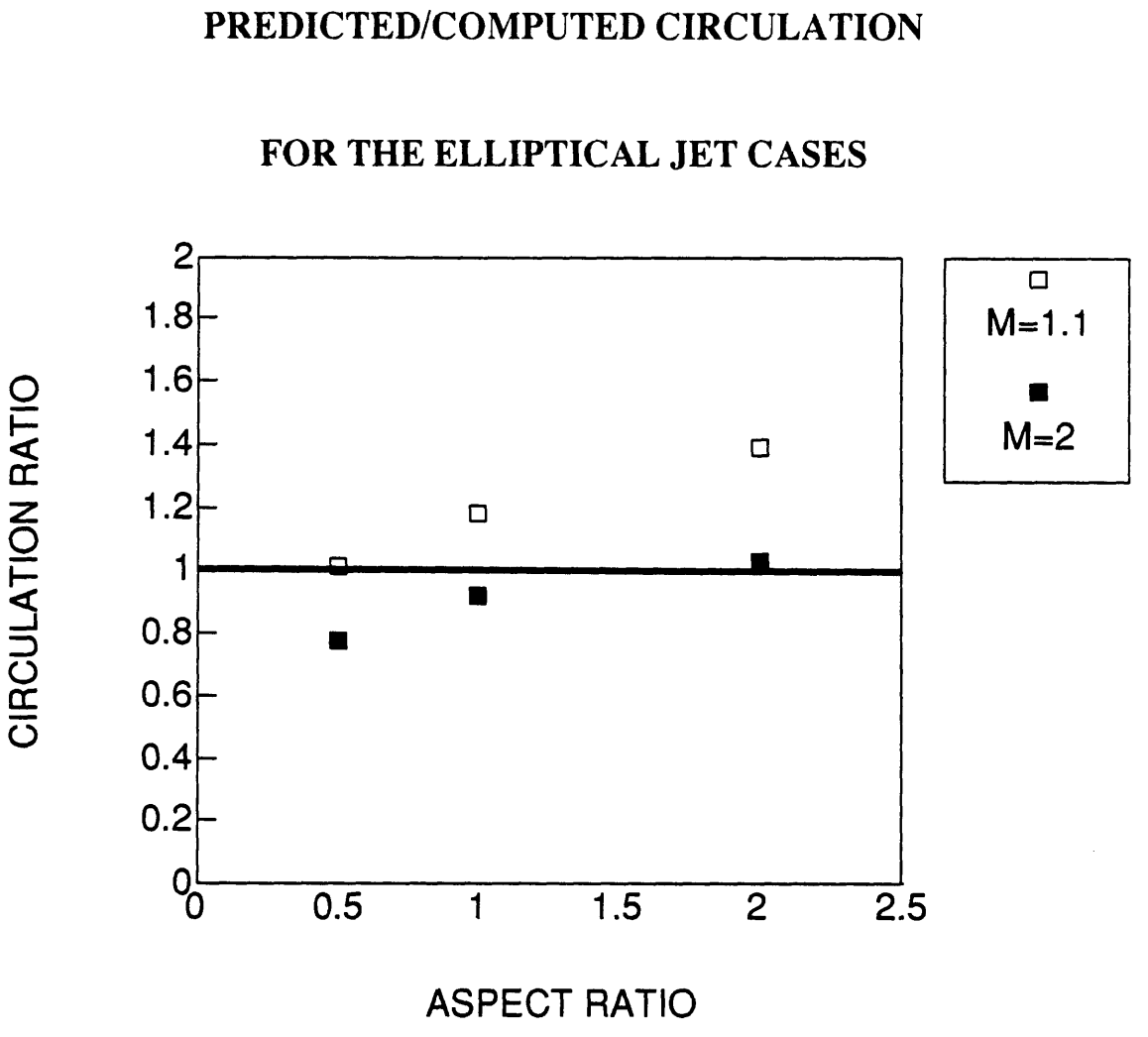

Figure 7.18 - Computed and predicted $\overline{\Gamma}(\bar{t})$ for the elliptical jet flows.

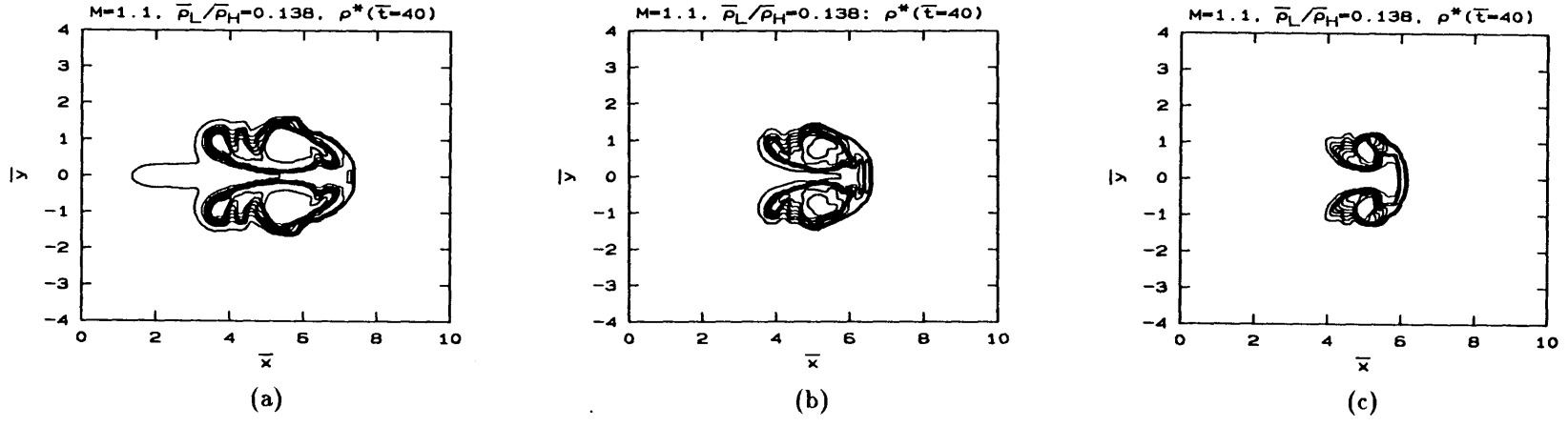

Figure 7.19 - Elliptical jet density contours for $\bar{\rho}_L/\bar{\rho}_H = 0.138$, M=1.1 at $\bar{t}$=40: (a) AR=0.5, (b) AR=1.0, (c) AR=2.0.

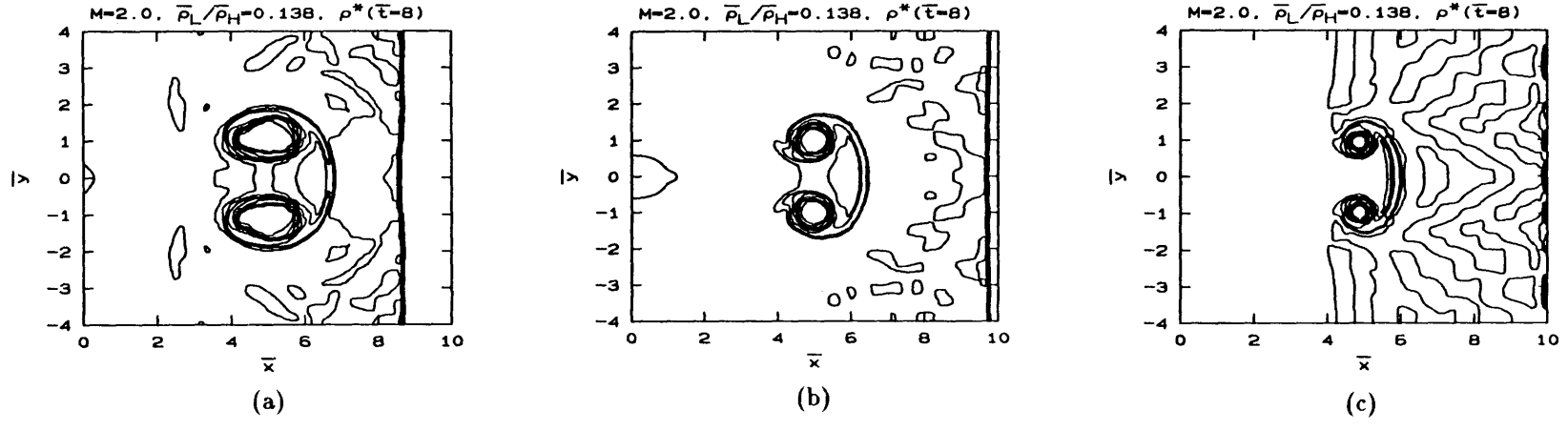

Figure 7.20 - Elliptical jet density contours for $\bar{\rho}_L/\bar{\rho}_H = 0.138$, M=2.0 at $\bar{t}$=8: (a) AR=0.5, (b) AR=1.0, (c) AR=2.0.

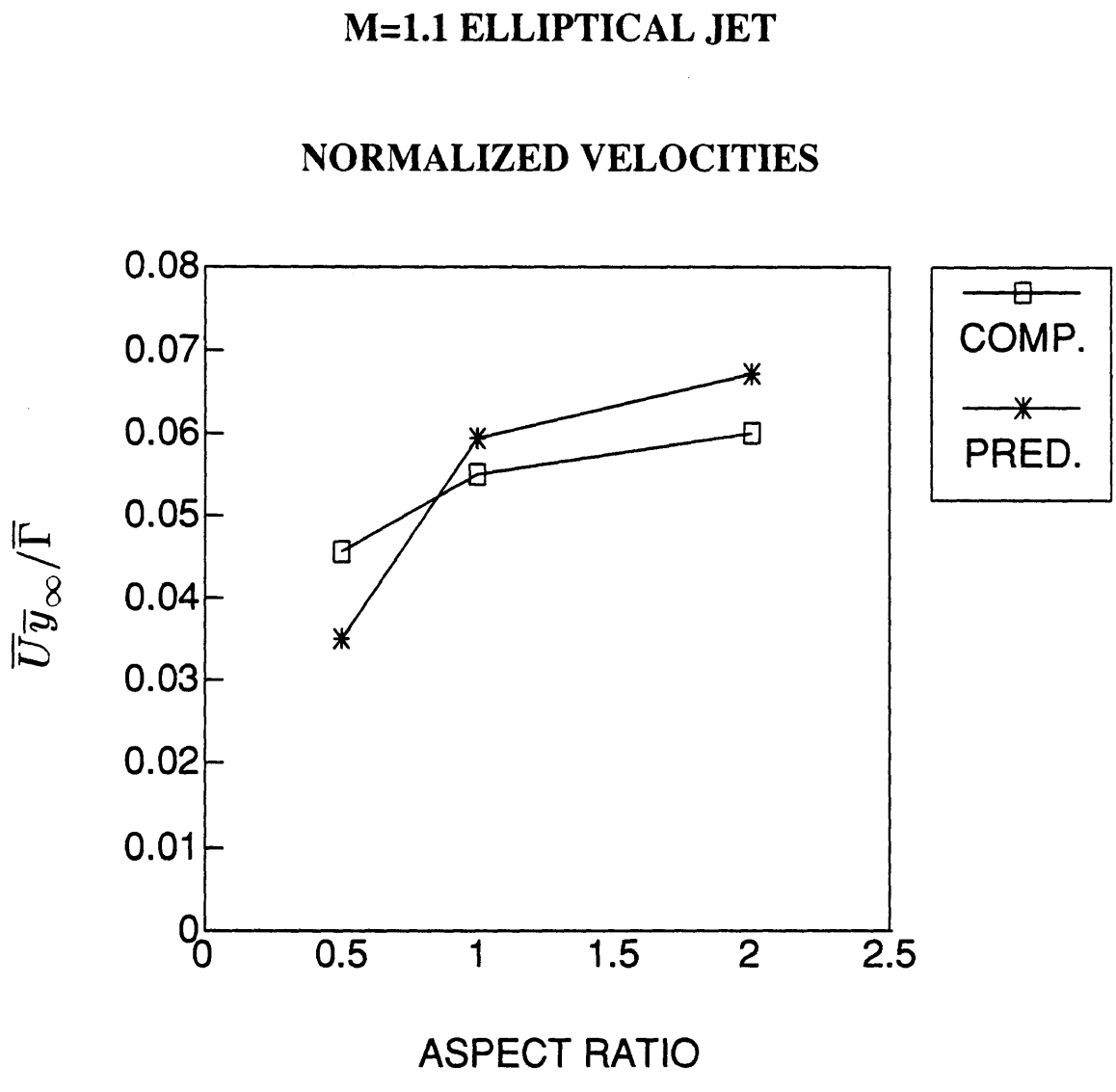

Figure 7.21 - Computed and predicted $\overline{U}\overline{y}_\infty/\overline{\Gamma}$ for the M=1.1 elliptical jet flows.

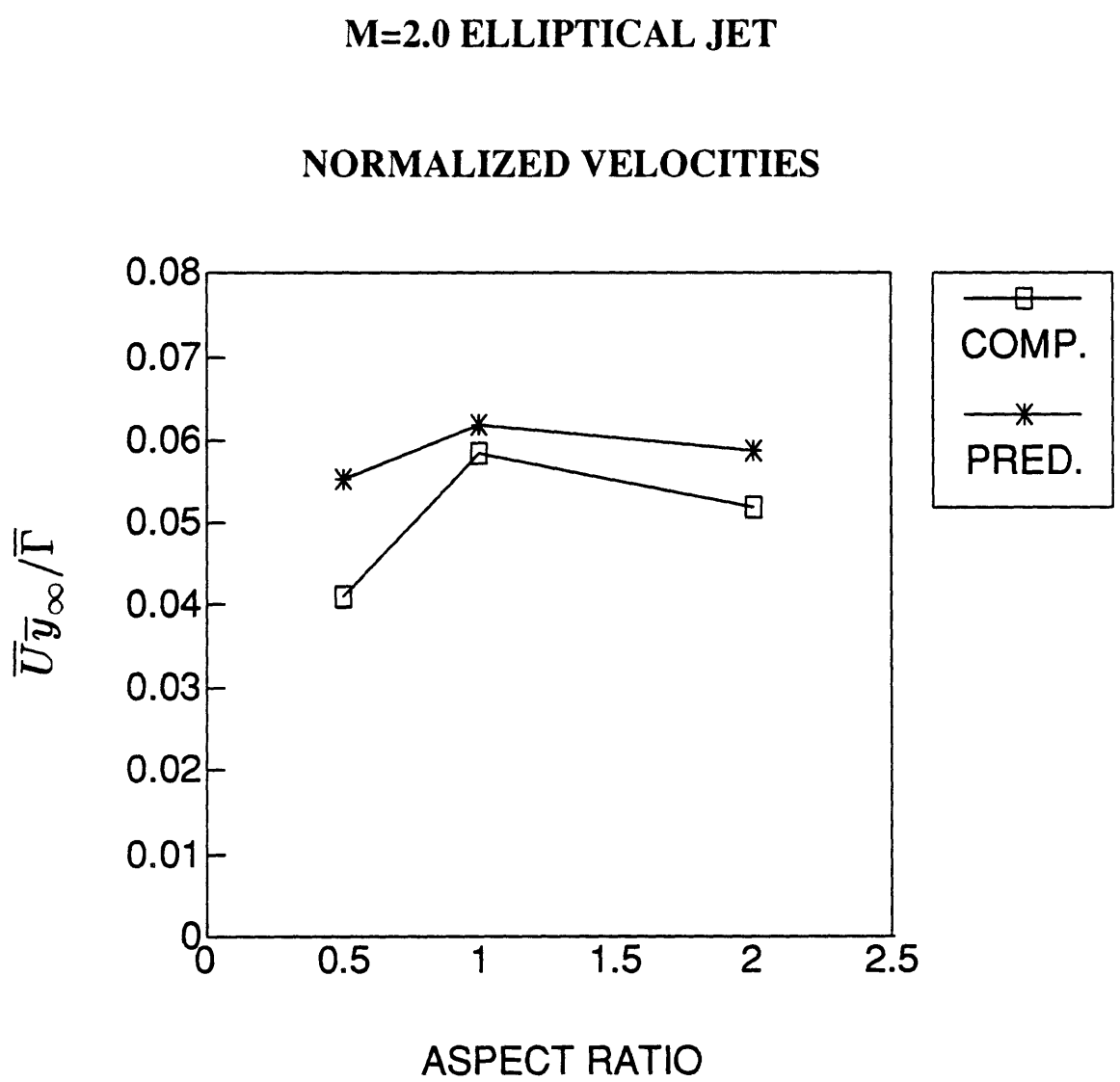

Figure 7.22 - Computed and predicted $\overline{U}\overline{y}_\infty/\overline{\Gamma}$ for the M=2.0 elliptical jet flows.

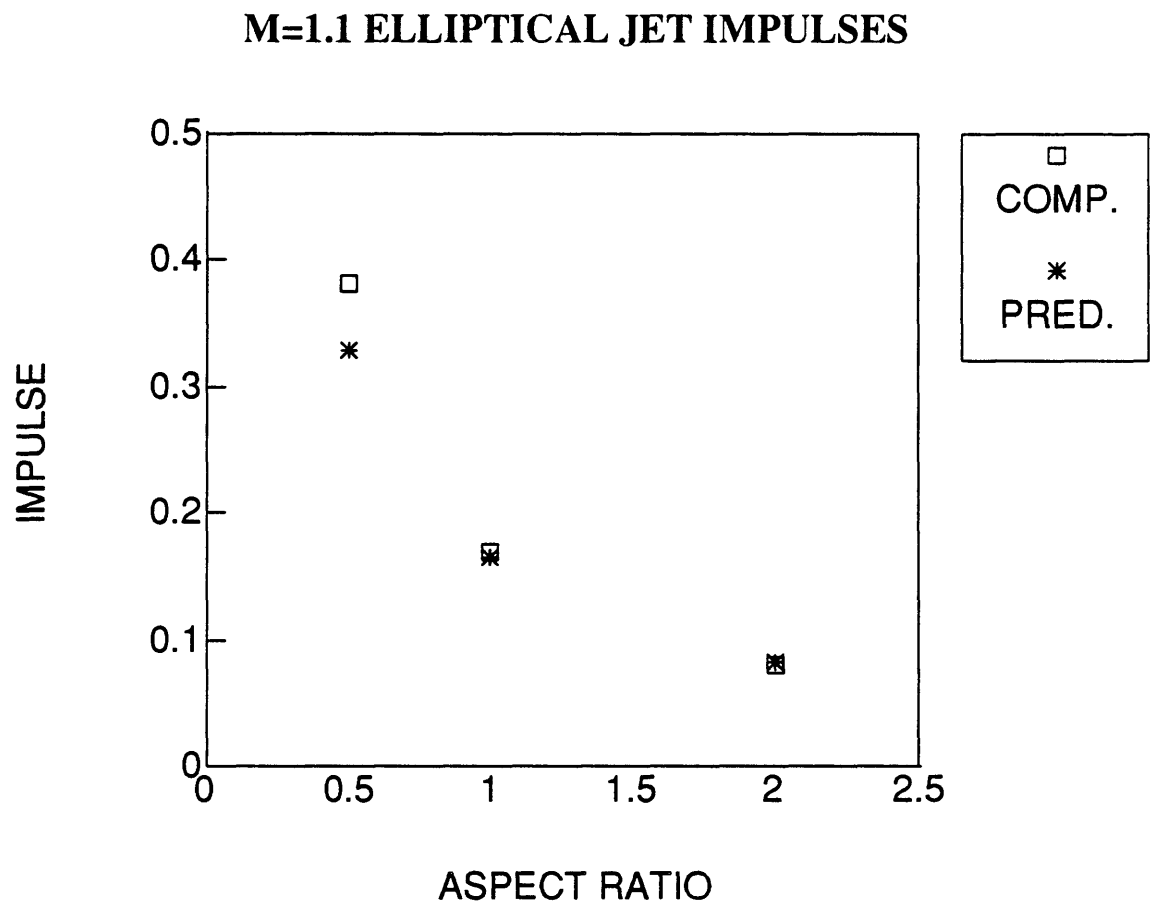

Figure 7.23 - Computed $\overline{I}_x'$ and predicted $\overline{I}_x(\overline{t} = 0^+)$ for the M=1.1 elliptical jet flows.

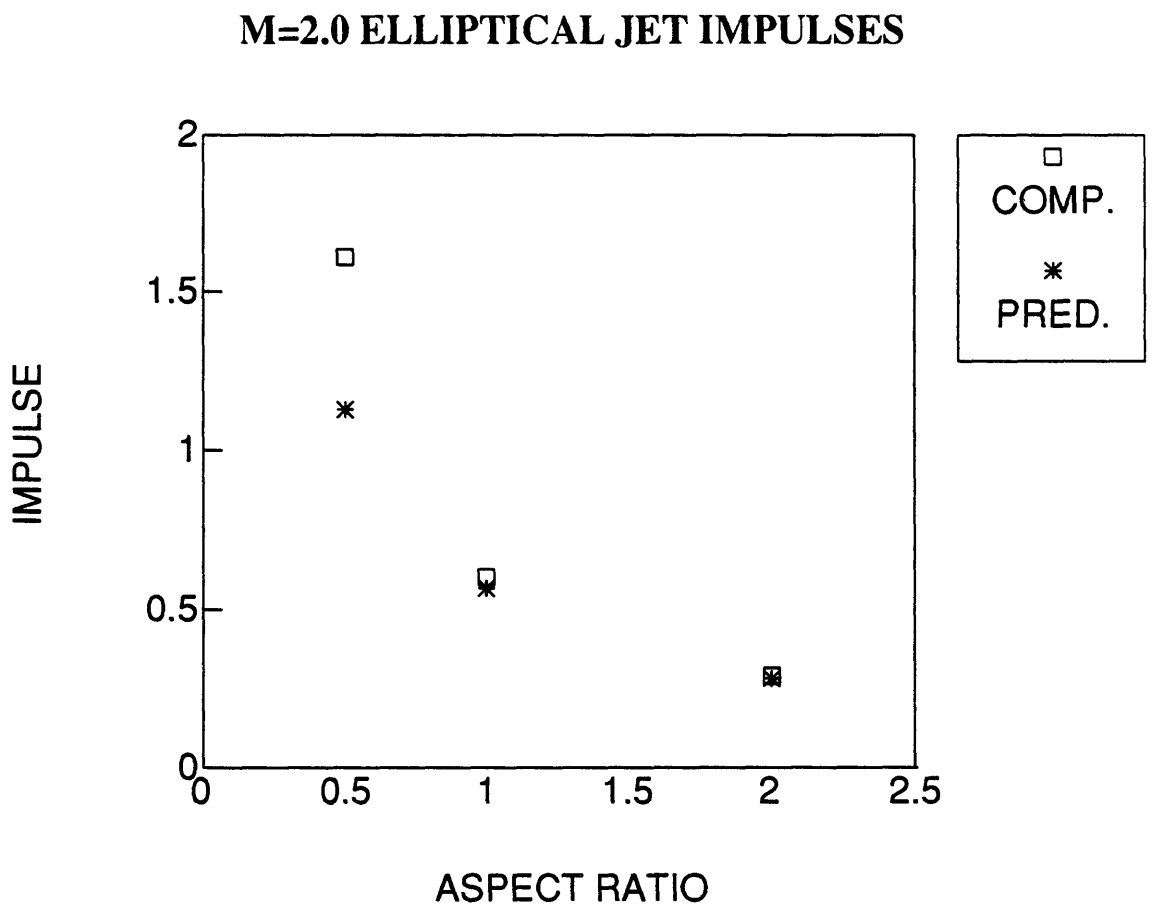

Figure 7.24 - Computed $\overline{I}_x'$ and predicted $\overline{I}_x(\bar{t} = 0^+)$ for the M=2.0 elliptical jet flows.

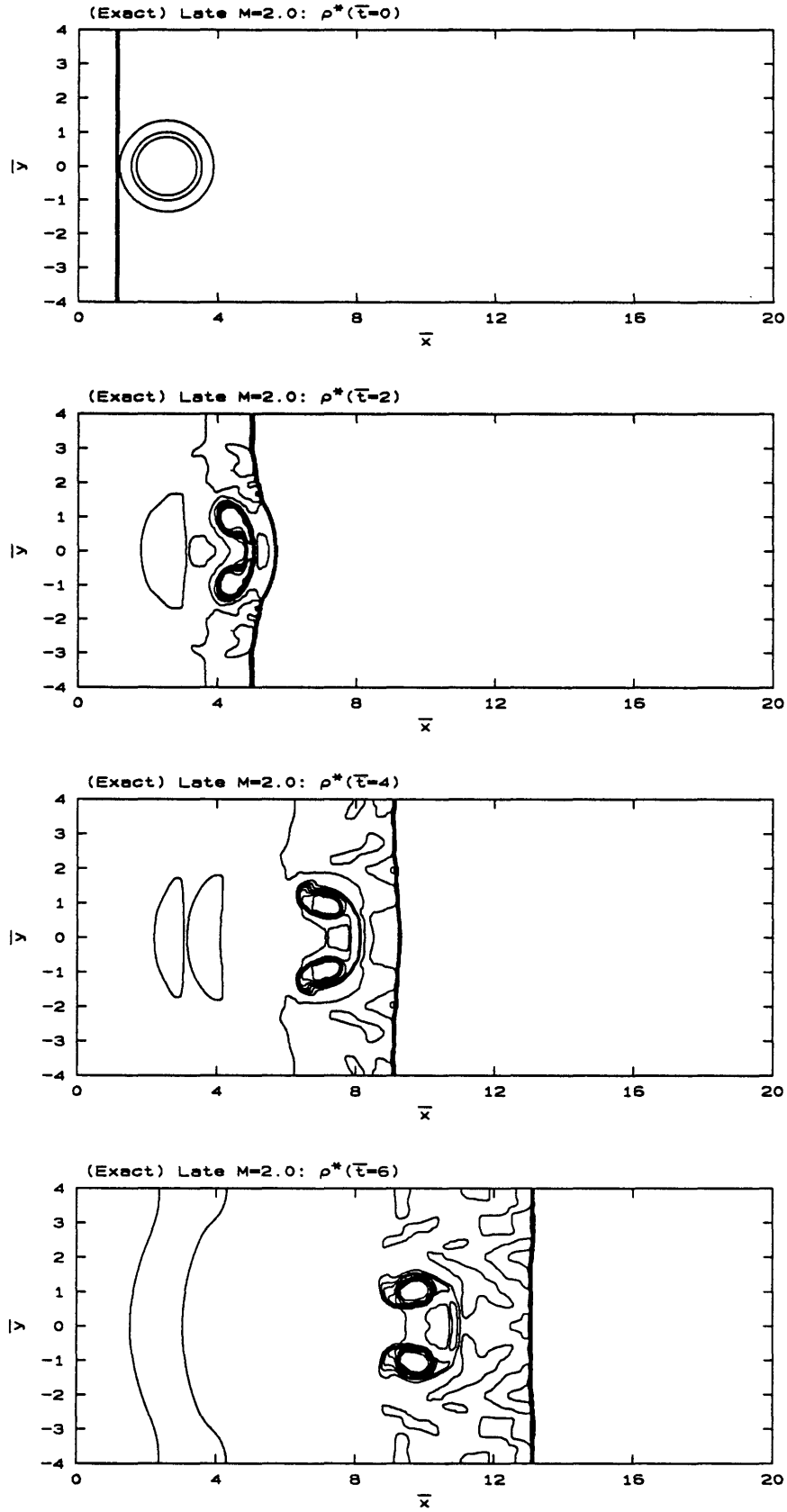

Figure 7.25 - M=2.0, $\overline{\rho}_L/\overline{\rho}_H = 0.138$, late-time exact reflected shock.

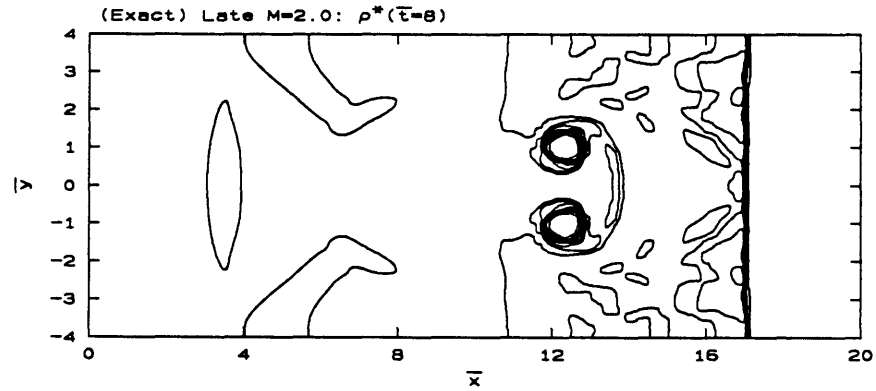
(Exact) Late M=2.0: ρ*(t̄=8)
ȳ
x̄
4
3
2
1
0
-1
-2
-3
-4
0
4
8
12
16
20

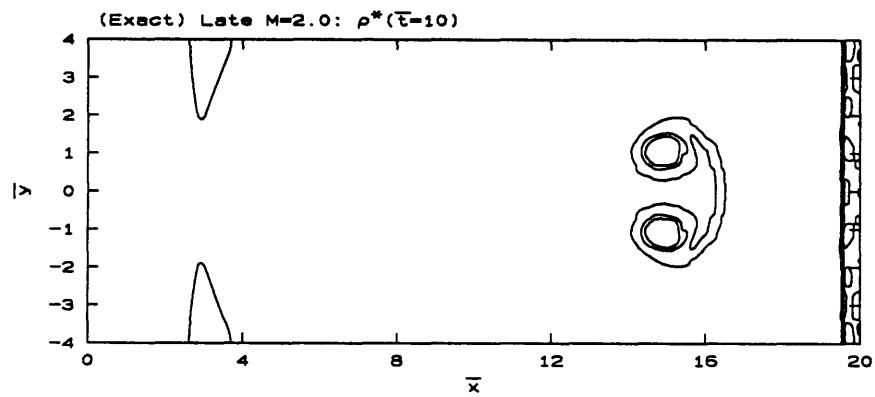
(Exact) Late M=2.0: ρ*(t̄=10)
ȳ
x̄
4
3
2
1
0
-1
-2
-3
-4
0
4
8
12
16
20

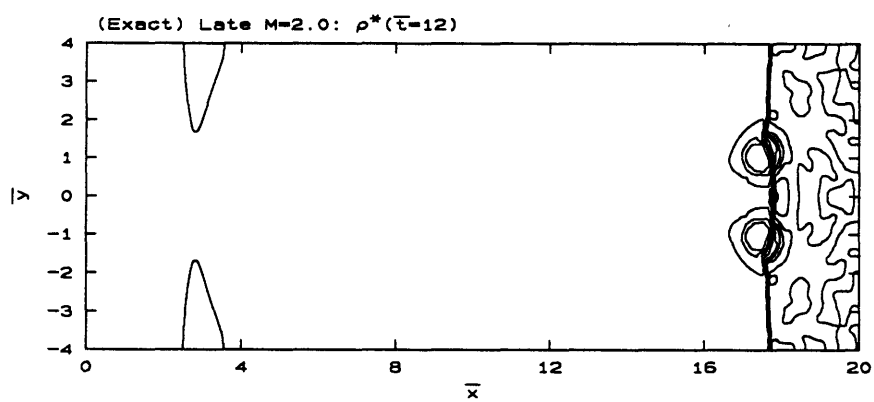
(Exact) Late M=2.0: ρ*(t̄=12)
ȳ
x̄
4
3
2
1
0
-1
-2
-3
-4
0
4
8
12
16
20

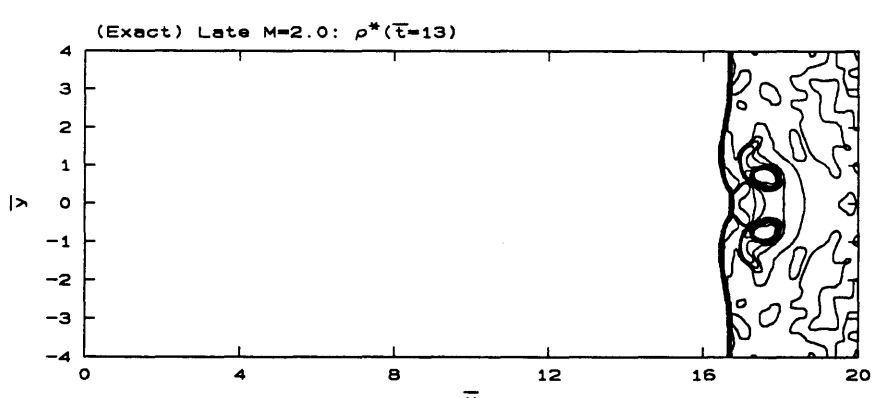
(Exact) Late M=2.0: ρ*(t̄=13)
ȳ
x̄
4
3
2
1
0
-1
-2
-3
-4
0
4
8
12
16
20

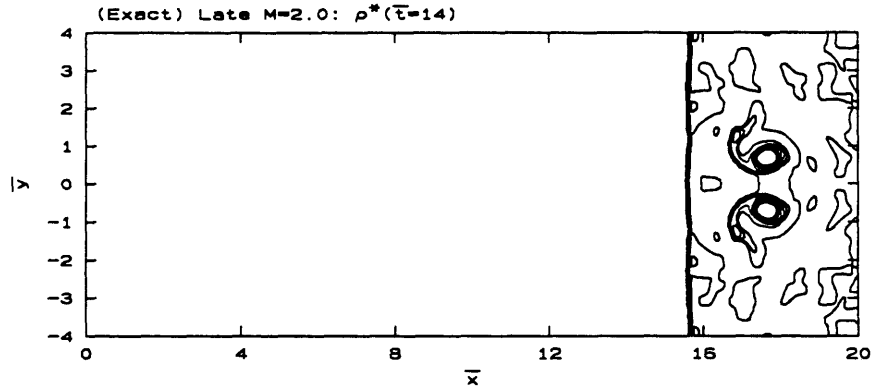
(Exact) Late M=2.0: ρ*(t̄=14)
4
3
2
1
0
-1
-2
-3
-4
ȳ
0
4
8
12
16
20
x̄

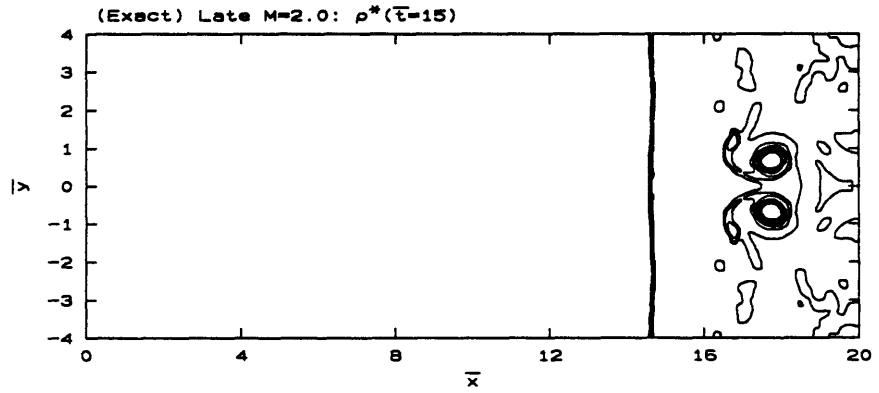
(Exact) Late M=2.0: ρ*(t̄=15)
4
3
2
1
0
-1
-2
-3
-4
ȳ
0
4
8
12
16
20
x̄

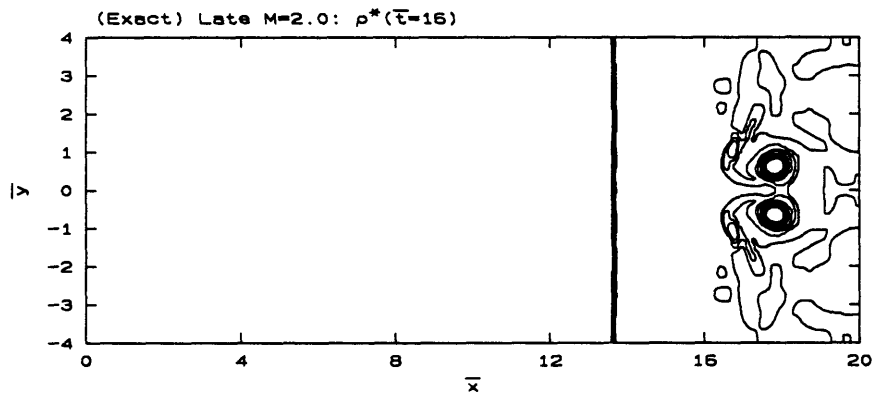
(Exact) Late M=2.0: ρ*(t̄=16)
4
3
2
1
0
-1
-2
-3
-4
ȳ
0
4
8
12
16
20
x̄

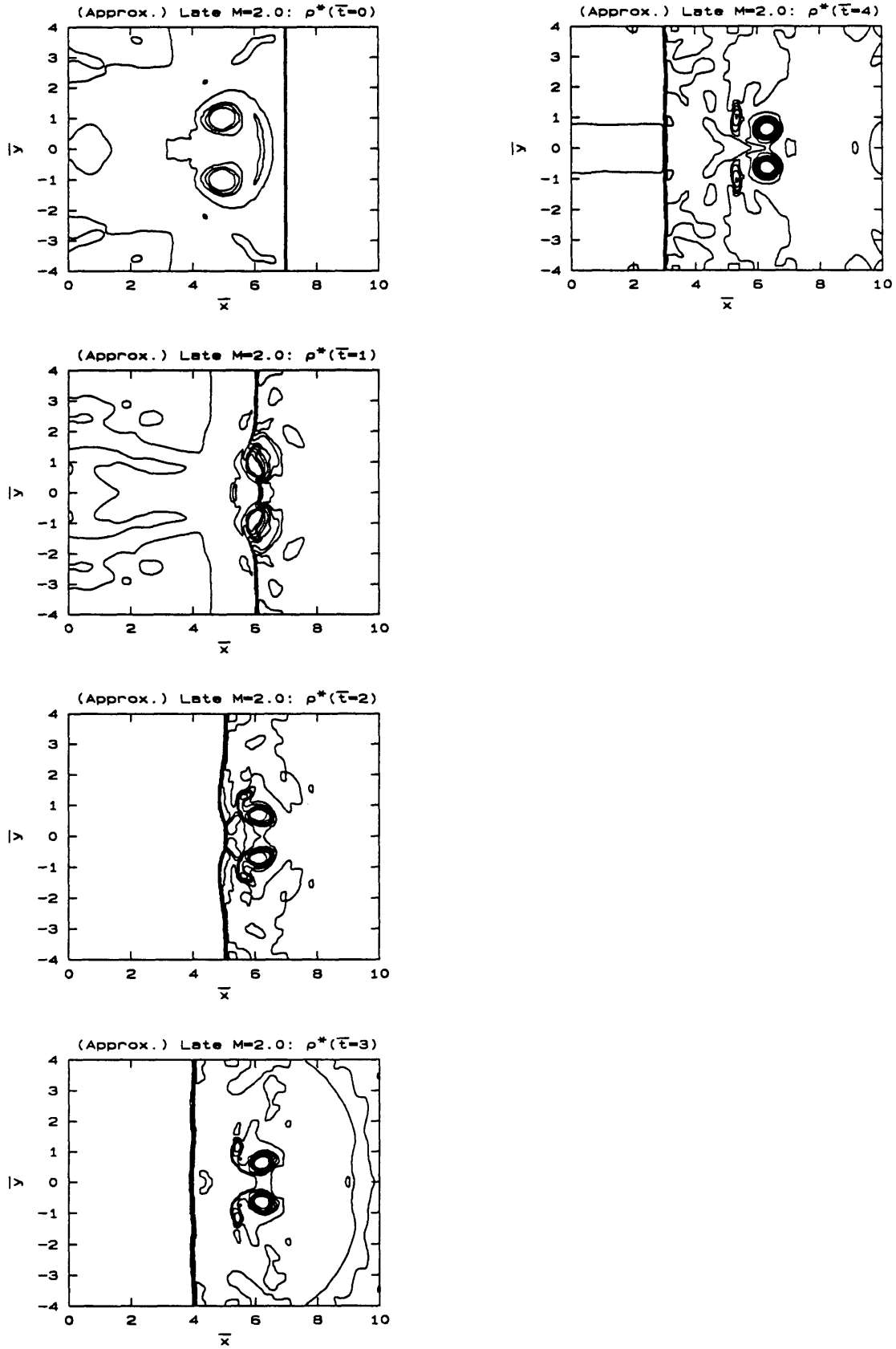

Figure 7.26 - M=2.0, $\overline{\rho}_L/\overline{\rho}_H = 0.138$, late-time approximate reflected shock.

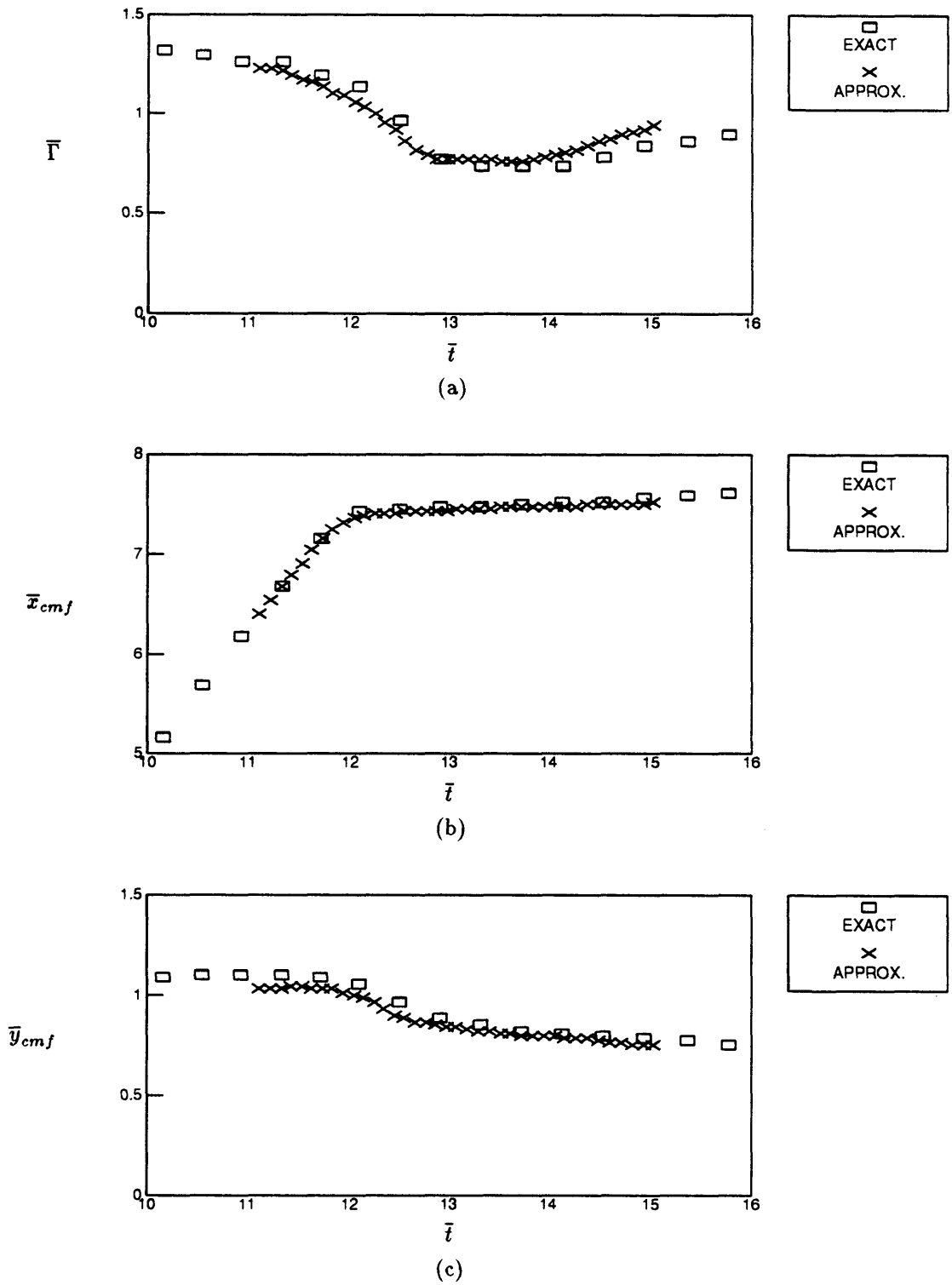

Figure 7.27 - Comparison of the exact and approximate computations: (a) $\overline{\Gamma}$(t), (b)$\overline{x}_{cmf}$(t), (c) $\overline{y}_{\infty}$(t).

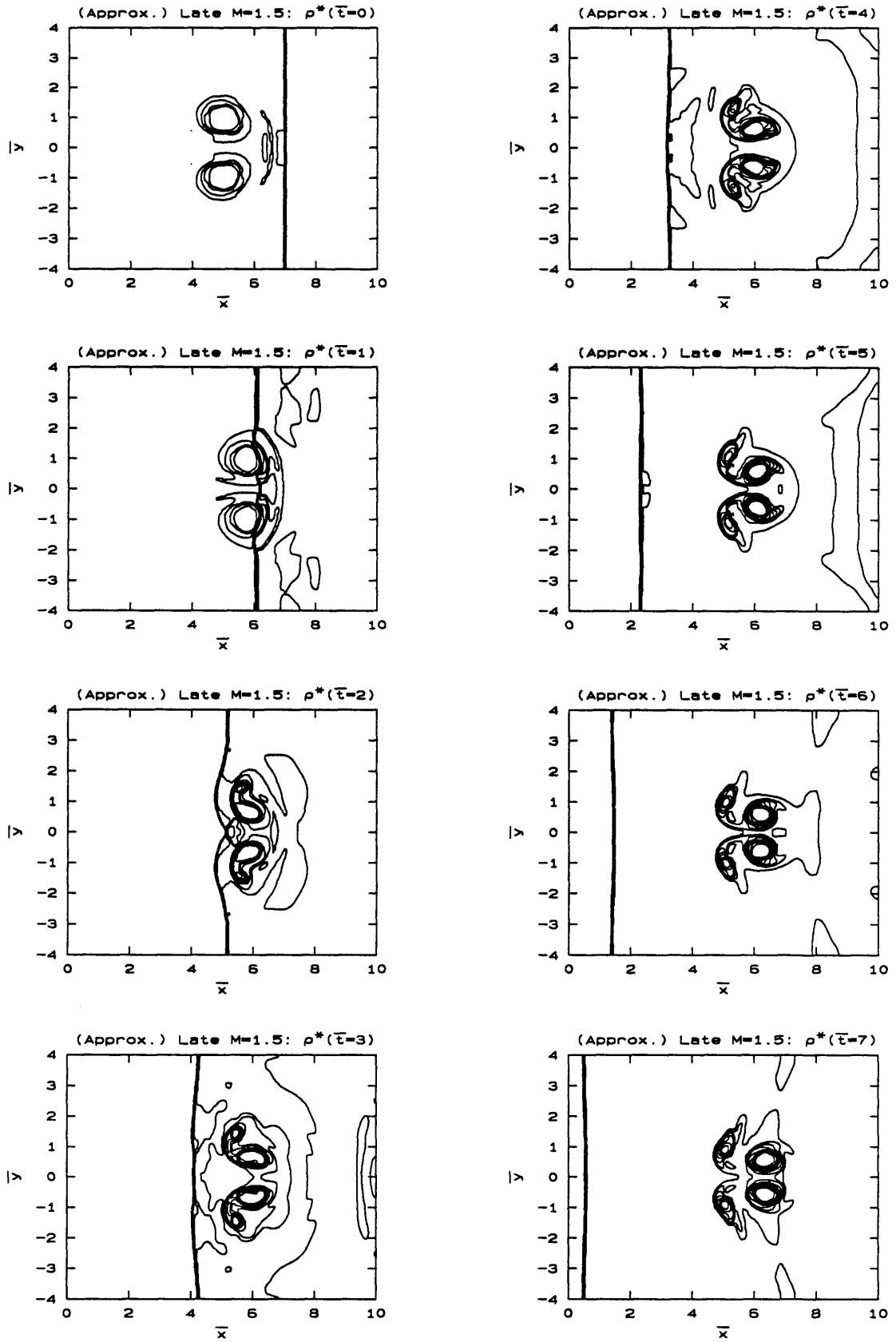

Figure 7.28 - M=1.5, $\overline{\rho}_L/\overline{\rho}_H = 0.138$, late-time approximate reflected shock.

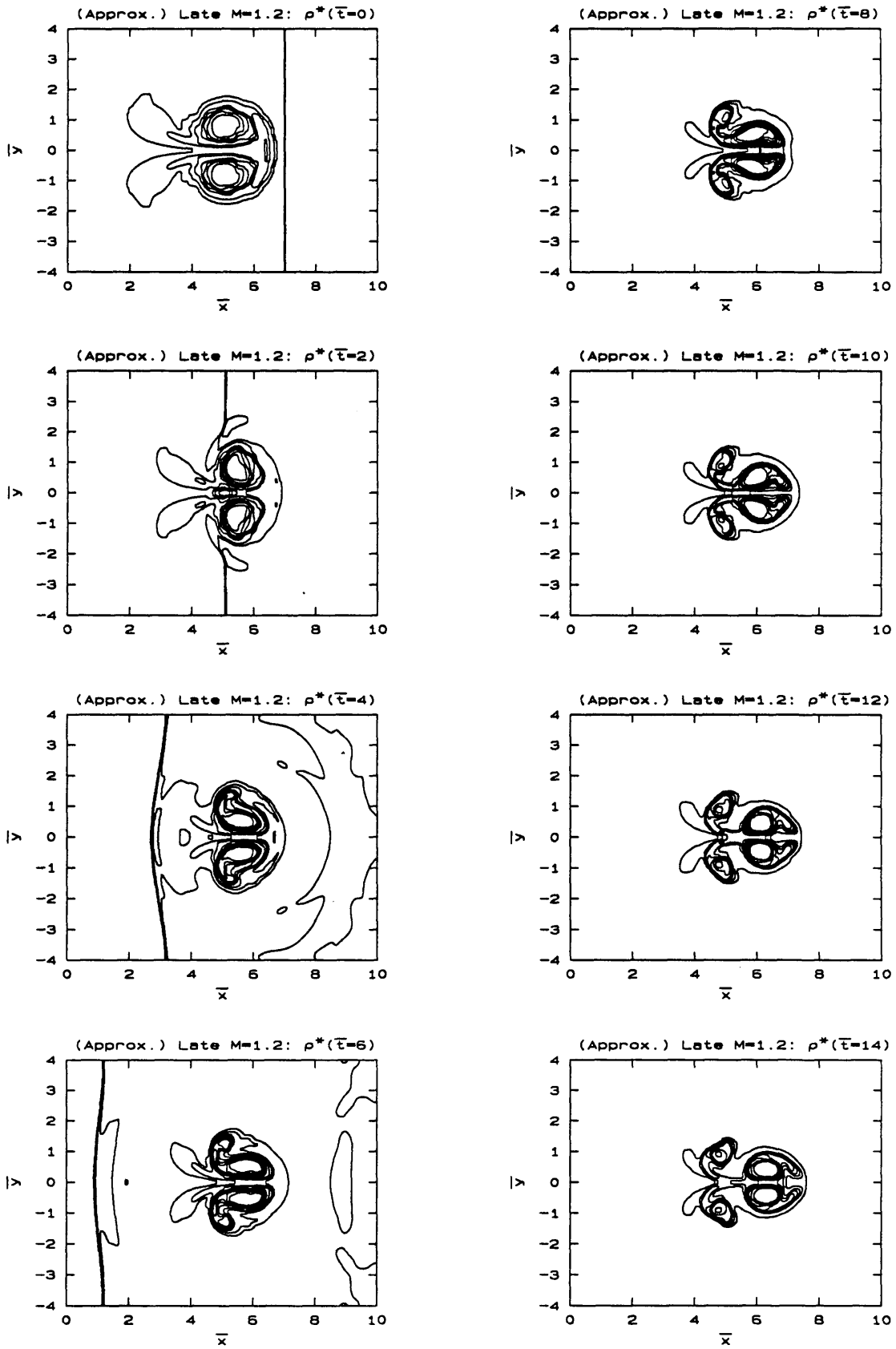

Figure 7.29 - M=1.2, $\overline{\rho}_L/\overline{\rho}_H = 0.138$, late-time approximate reflected shock.

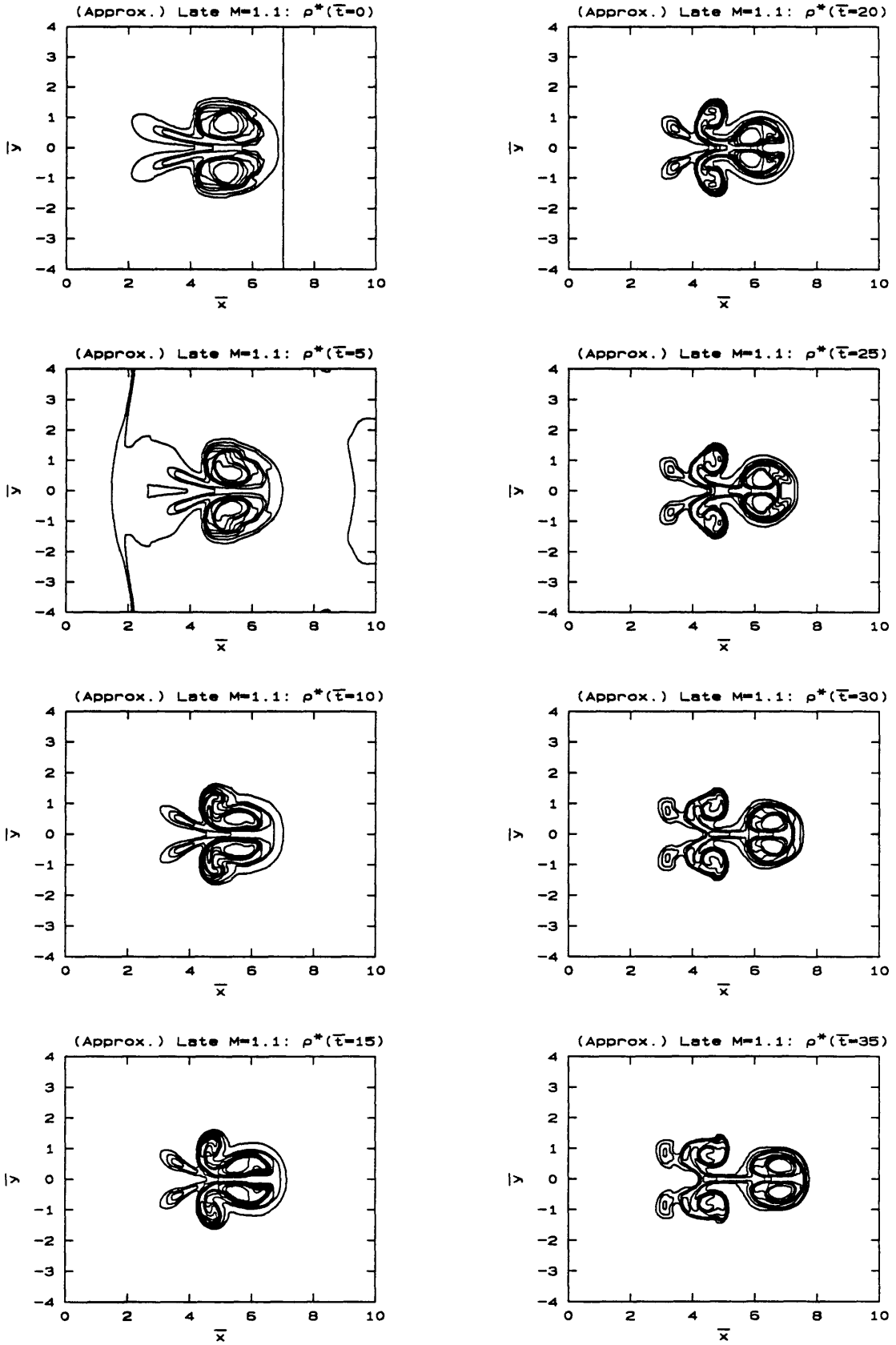

Figure 7.30 - M=1.1, $\overline{\rho}_L/\overline{\rho}_H = 0.138$, late-time approximate reflected shock.

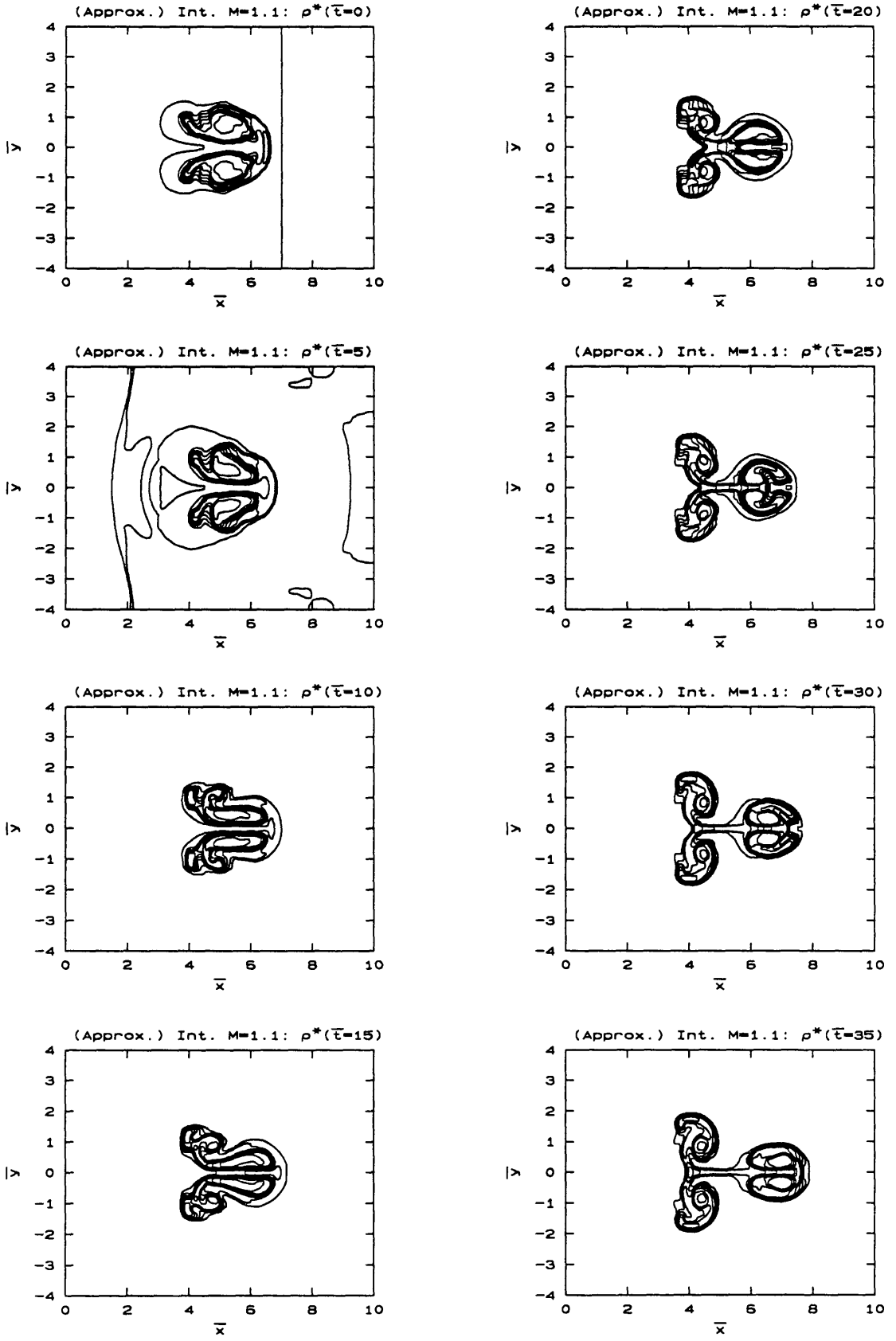

Figure 7.31 - M=1.1, $\overline{\rho}_L/\overline{\rho}_H = 0.138$, intermediate-time approximate reflected shock.

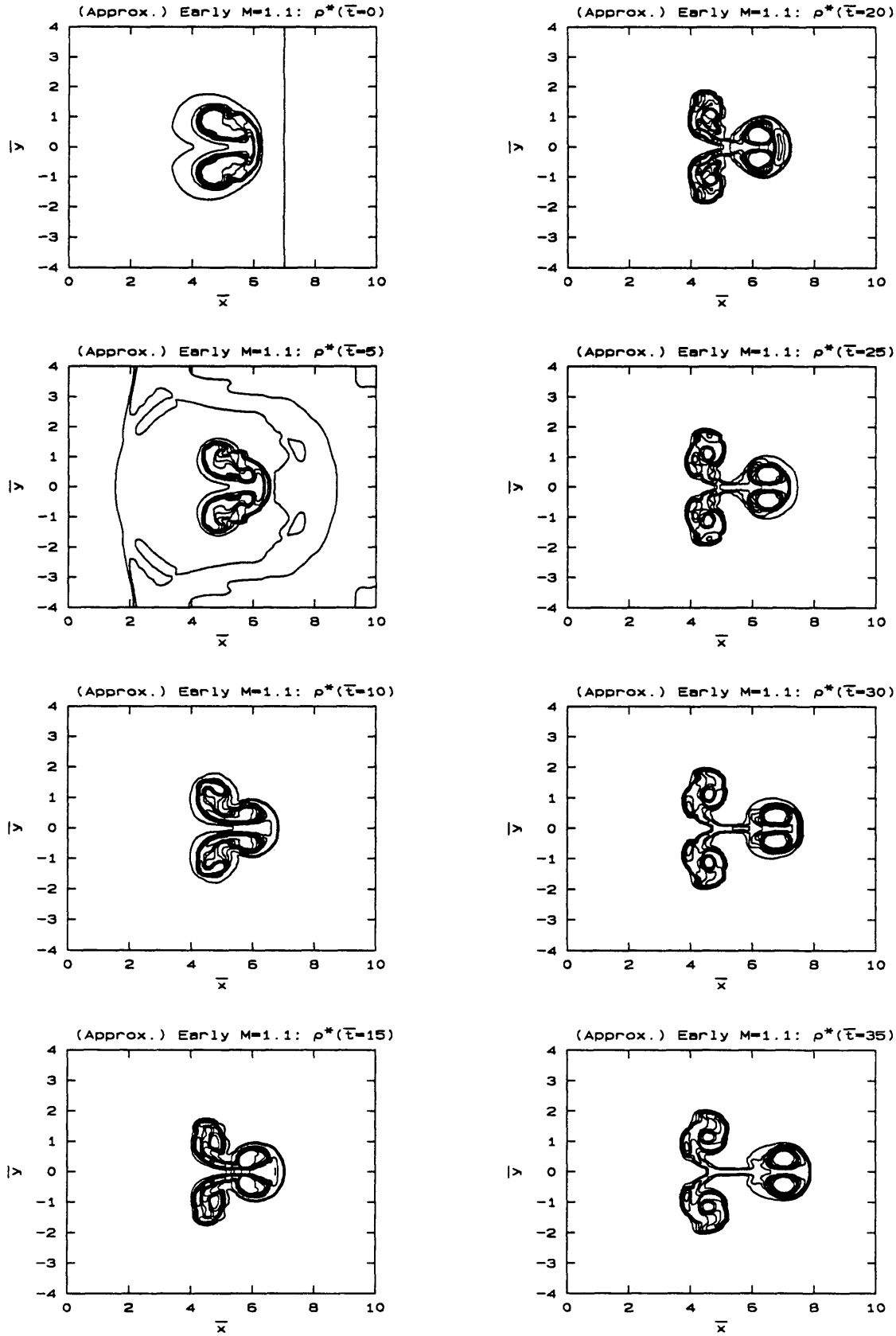

Figure 7.32 - M=1.1, $\bar{\rho}_L/\bar{\rho}_H = 0.138$, early-time approximate reflected shock.

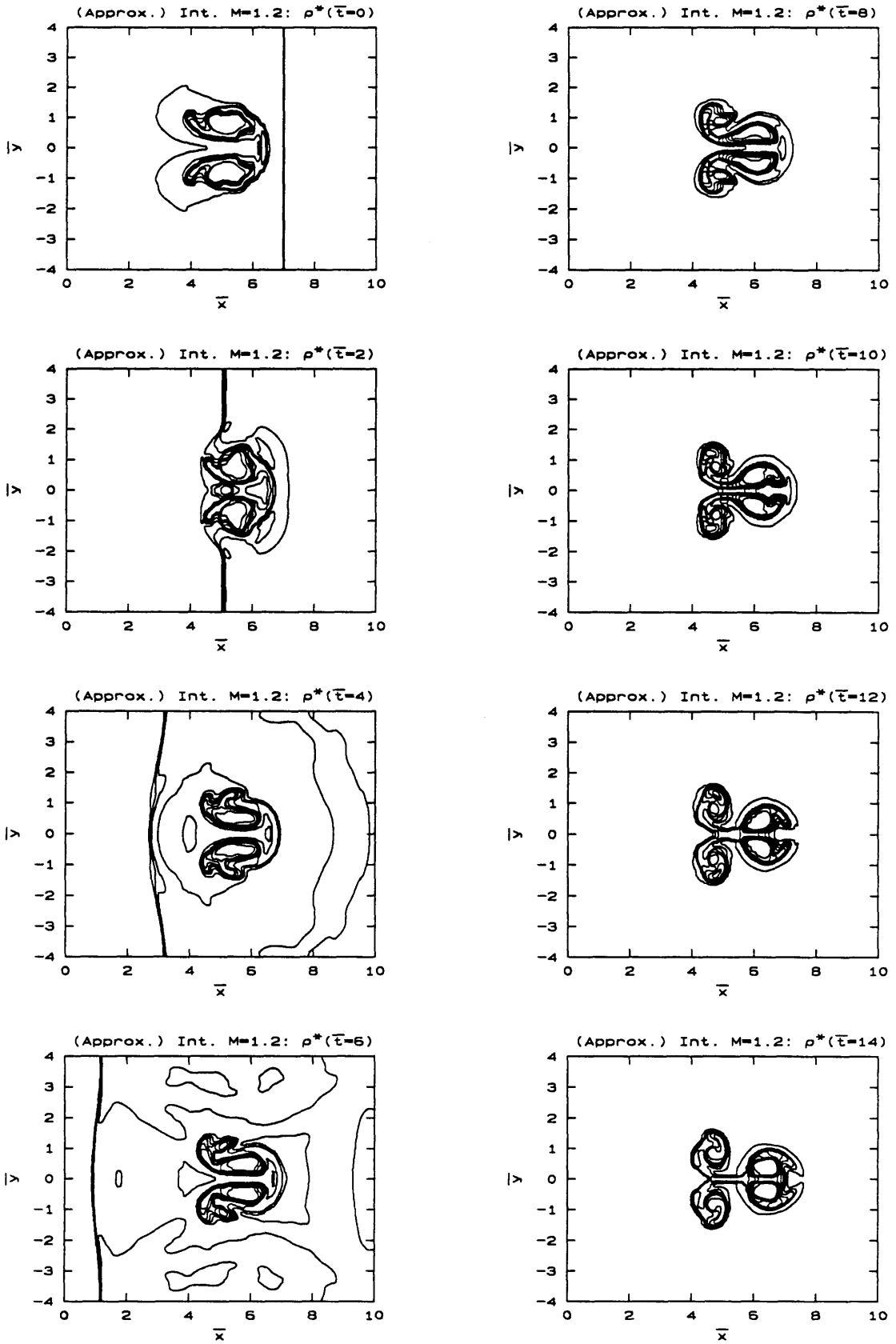

Figure 7.33 - M=1.2, $\overline{\rho}_L/\overline{\rho}_H = 0.138$, intermediate-time approximate reflected shock.

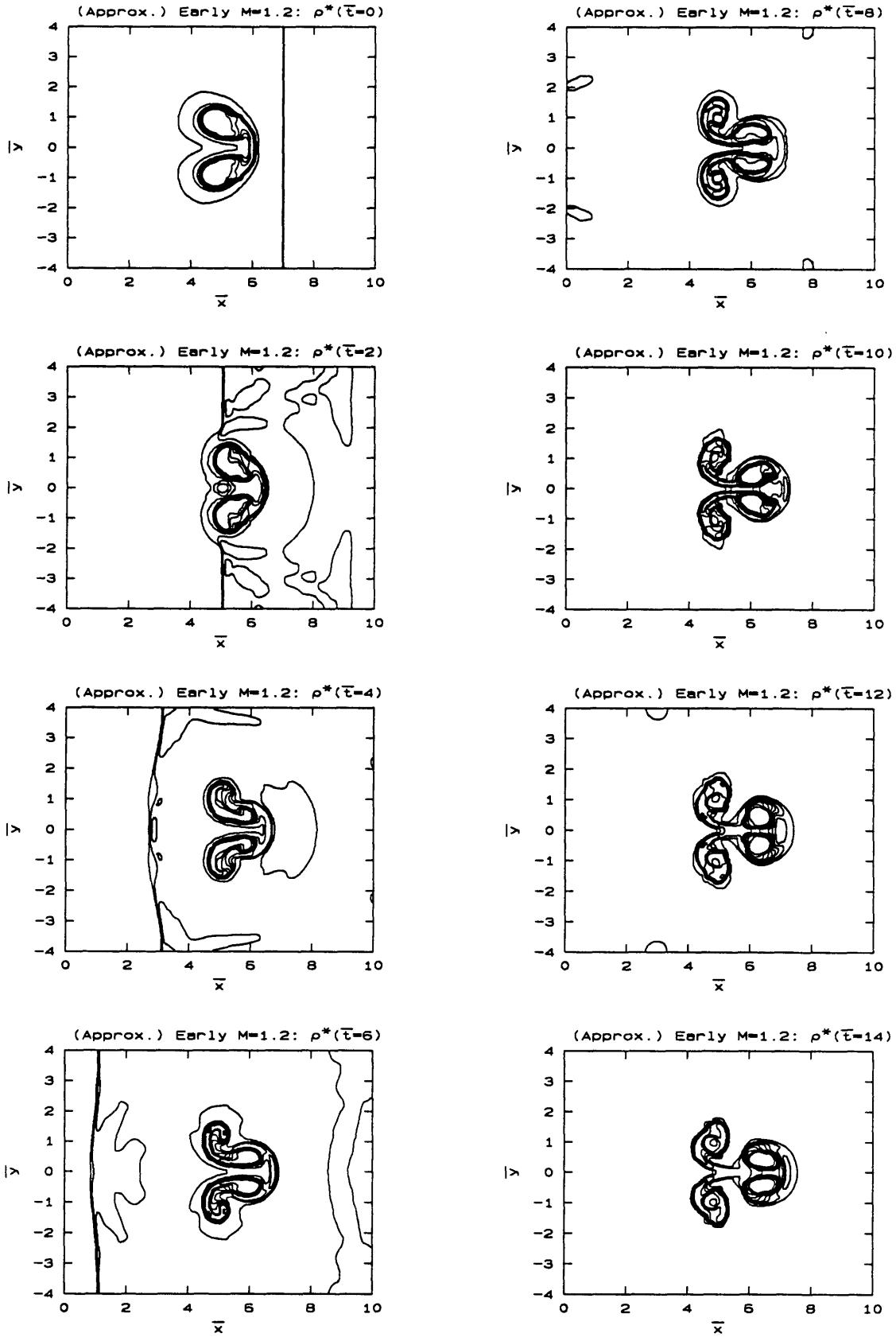

Figure 7.34 - M=1.2, $\overline{\rho}_L/\overline{\rho}_H = 0.138$, early-time approximate reflected shock.

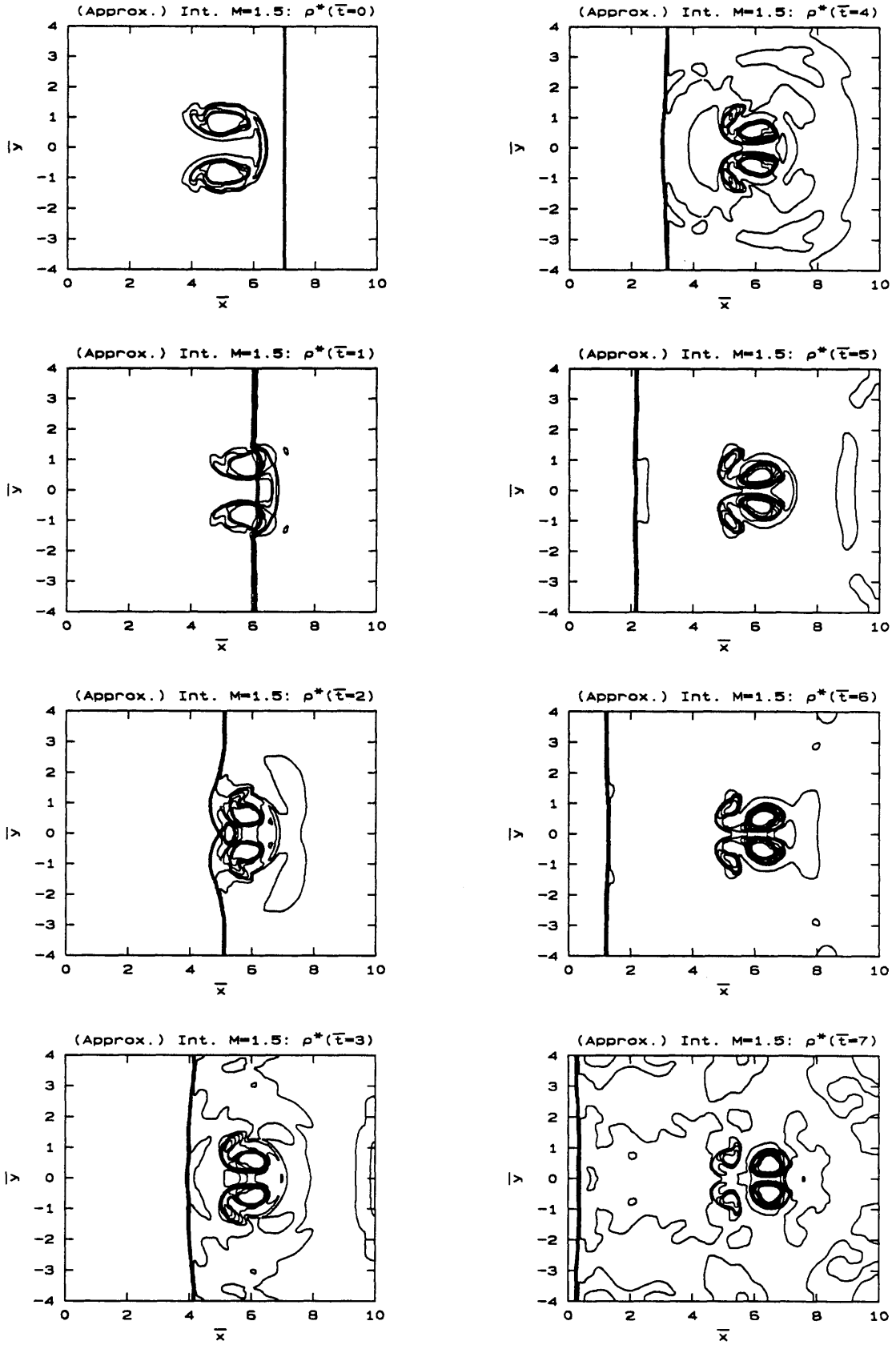

Figure 7.35 - M=1.5, $\overline{\rho}_L/\overline{\rho}_H = 0.138$, intermediate-time approximate reflected shock.

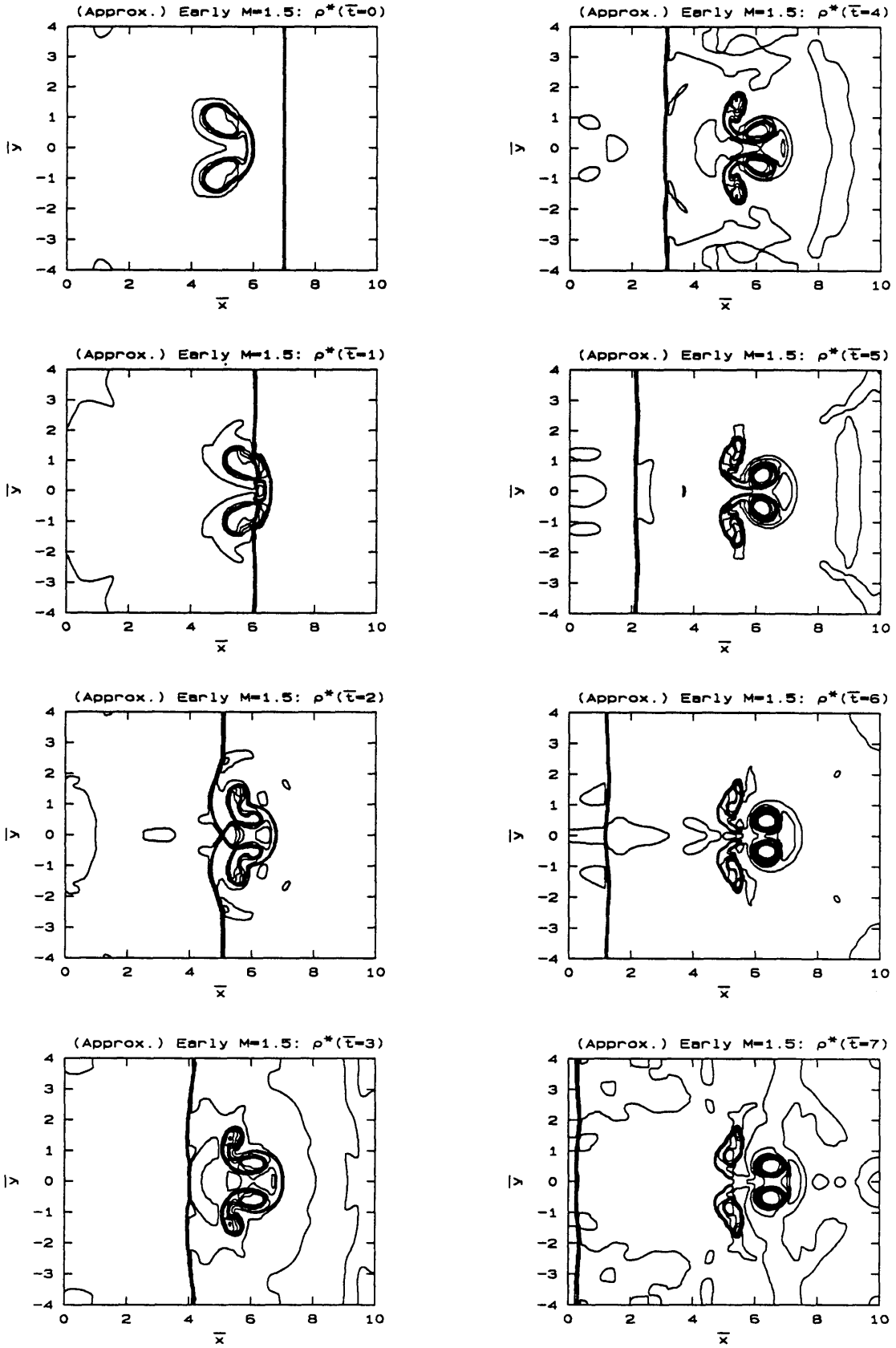

Figure 7.36 - M=1.5, $\overline{p}_L/\overline{p}_H = 0.138$, early-time approximate reflected shock.

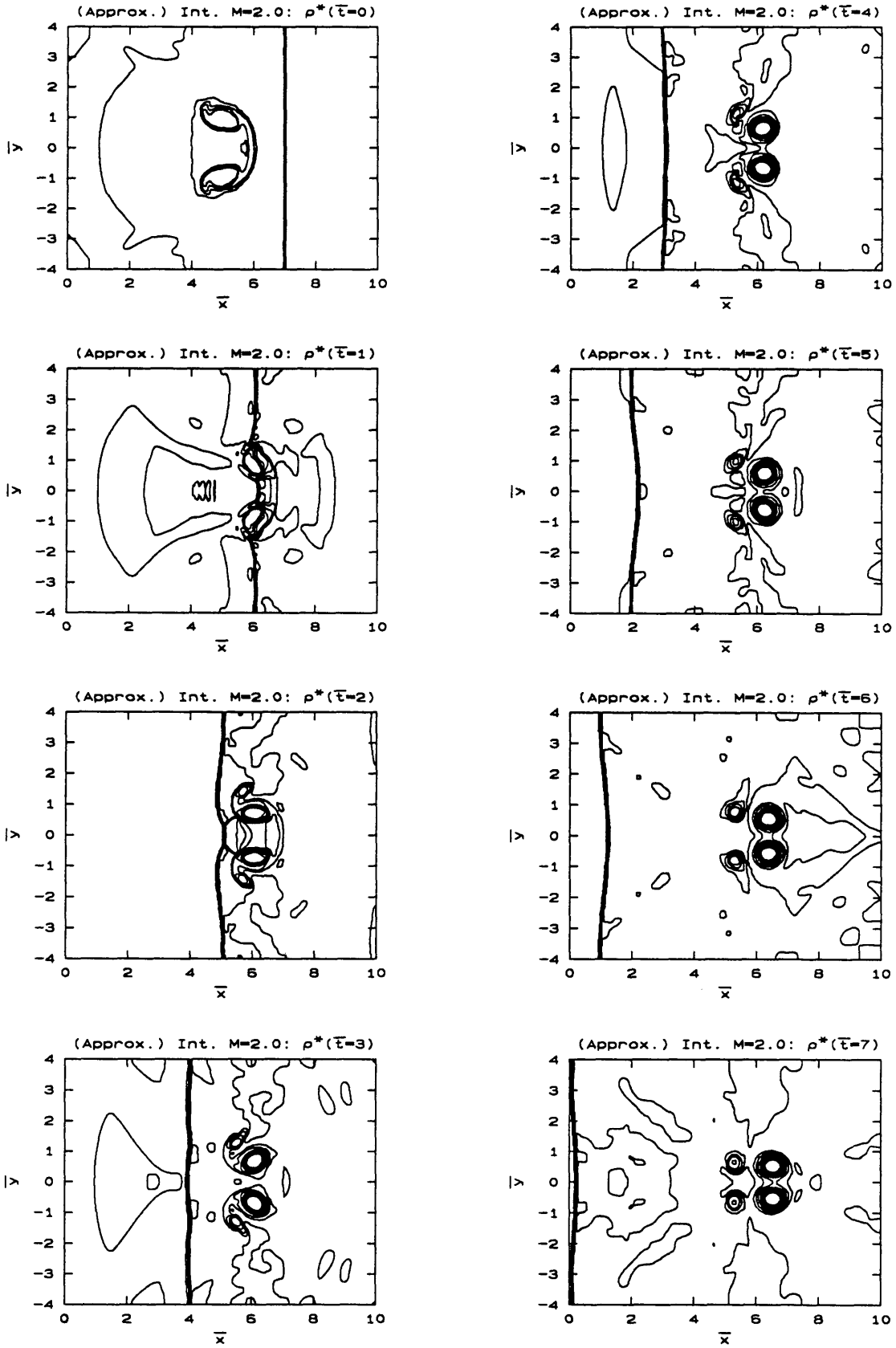

Figure 7.37 - M=2.0, $\overline{\rho}_L/\overline{\rho}_H = 0.138$, intermediate-time approximate reflected shock.

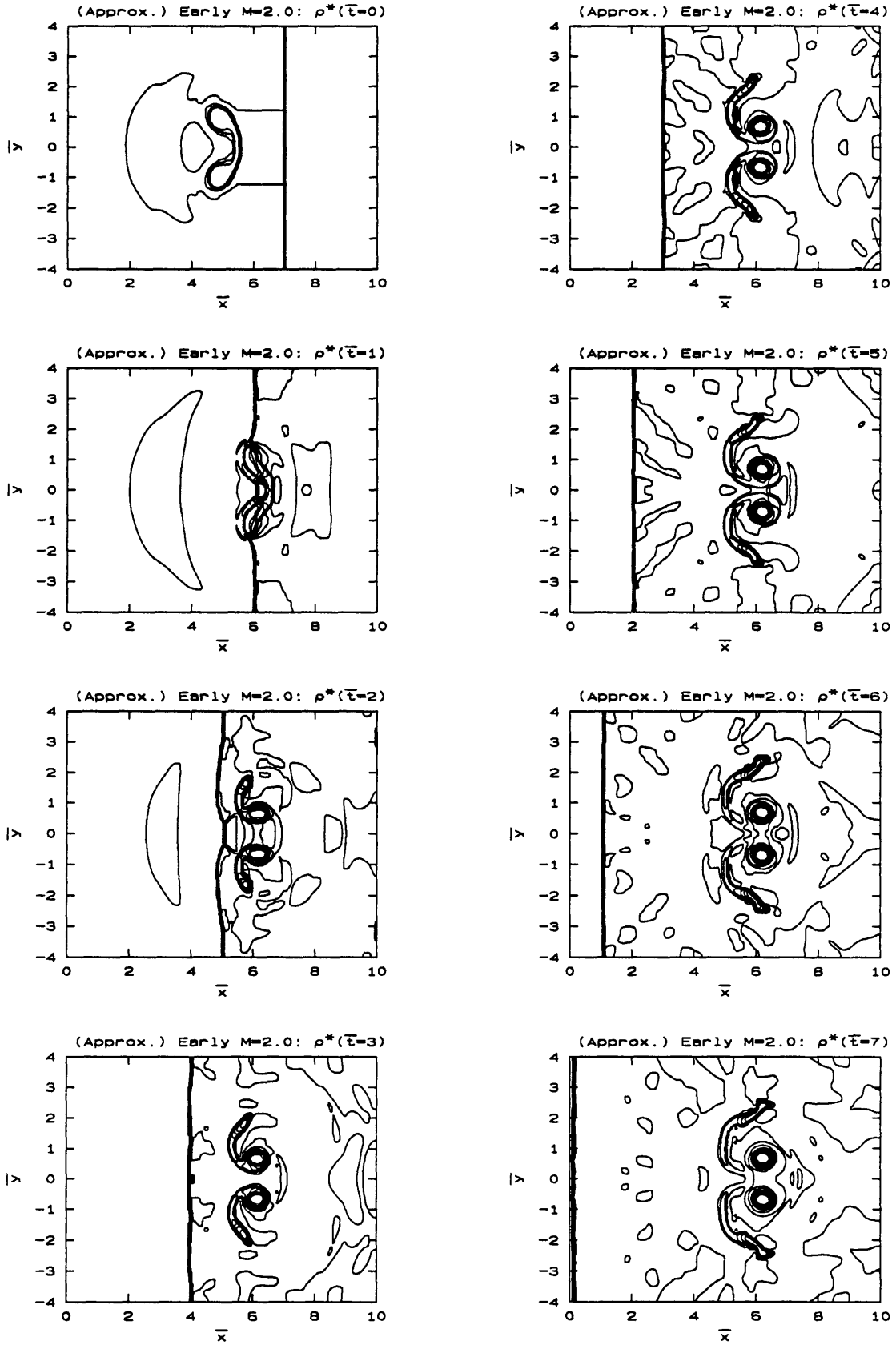

Figure 7.38 - M=2.0, $\overline{\rho}_L/\overline{\rho}_H = 0.138$, early-time approximate reflected shock.

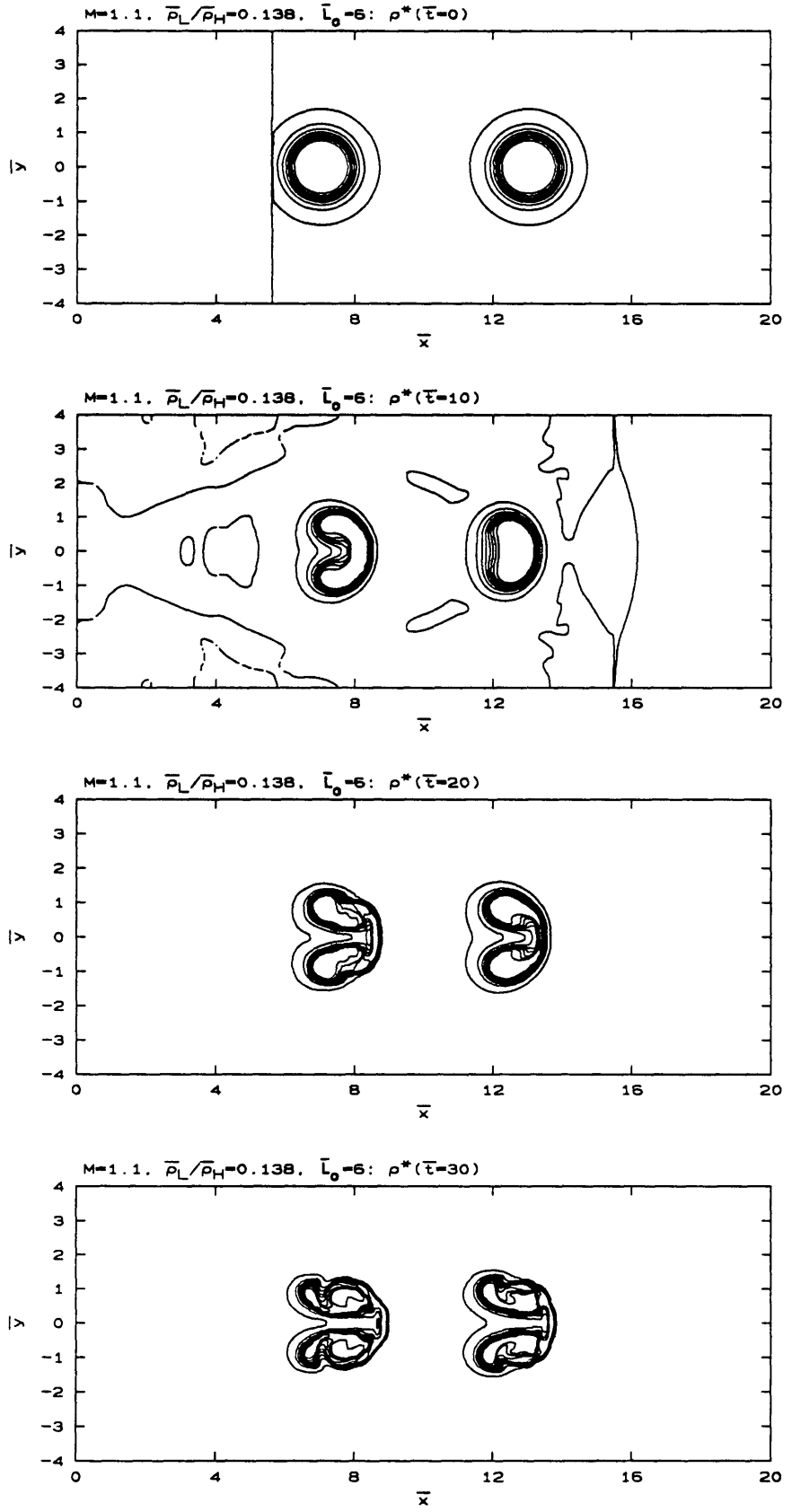

Figure 7.39 - Horizontal jet pair with M=1.1, $\bar{\rho}_L/\bar{\rho}_H = 0.138$, $\bar{L}_0 = 6$.

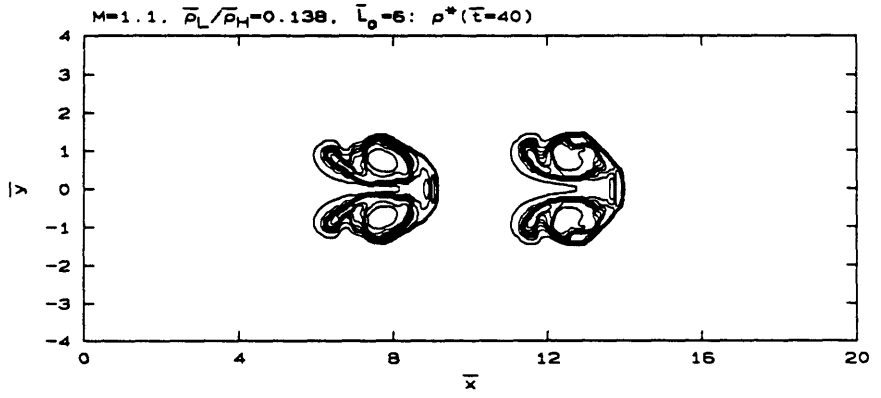
M=1.1. $\overline{\rho}_L/\overline{\rho}_H$=0.138. $\overline{l}_0$=6: $\rho^*(\overline{t}$=40)
$\overline{y}$
$\overline{x}$

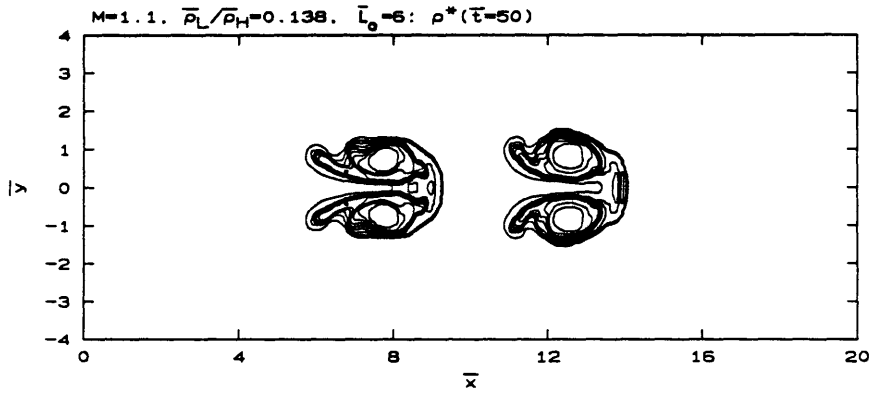
M=1.1. $\overline{\rho}_L/\overline{\rho}_H$=0.138. $\overline{l}_0$=6: $\rho^*(\overline{t}$=50)
$\overline{y}$
$\overline{x}$

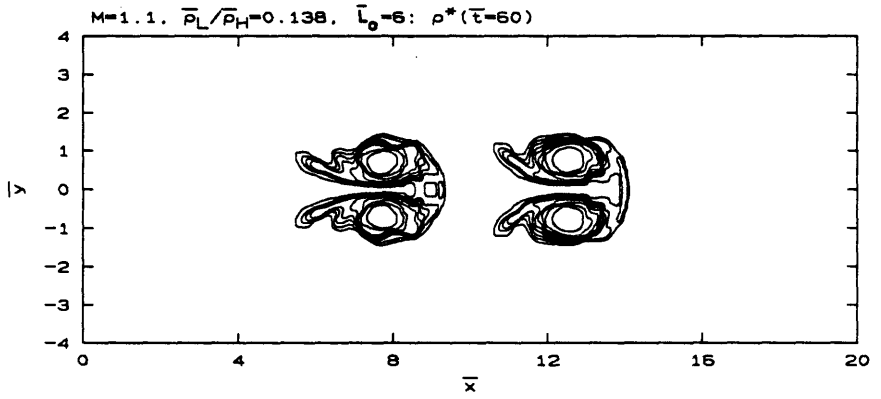
M=1.1. $\overline{\rho}_L/\overline{\rho}_H$=0.138. $\overline{l}_0$=6: $\rho^*(\overline{t}$=60)
$\overline{y}$
$\overline{x}$

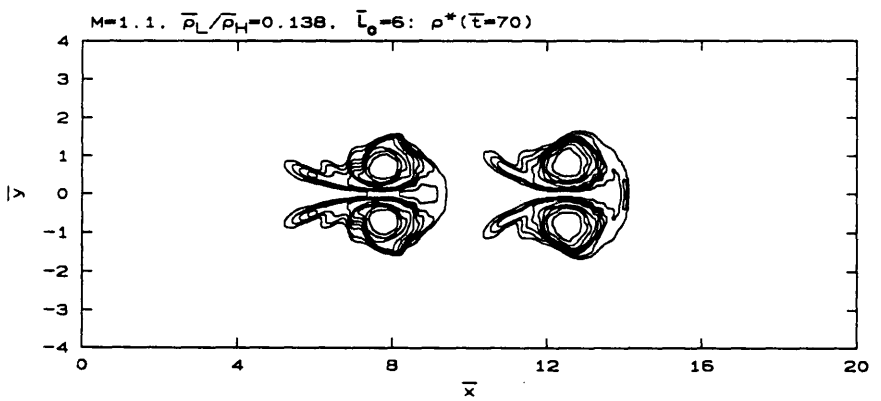
M=1.1. $\overline{\rho}_L/\overline{\rho}_H$=0.138. $\overline{l}_0$=6: $\rho^*(\overline{t}$=70)
$\overline{y}$
$\overline{x}$

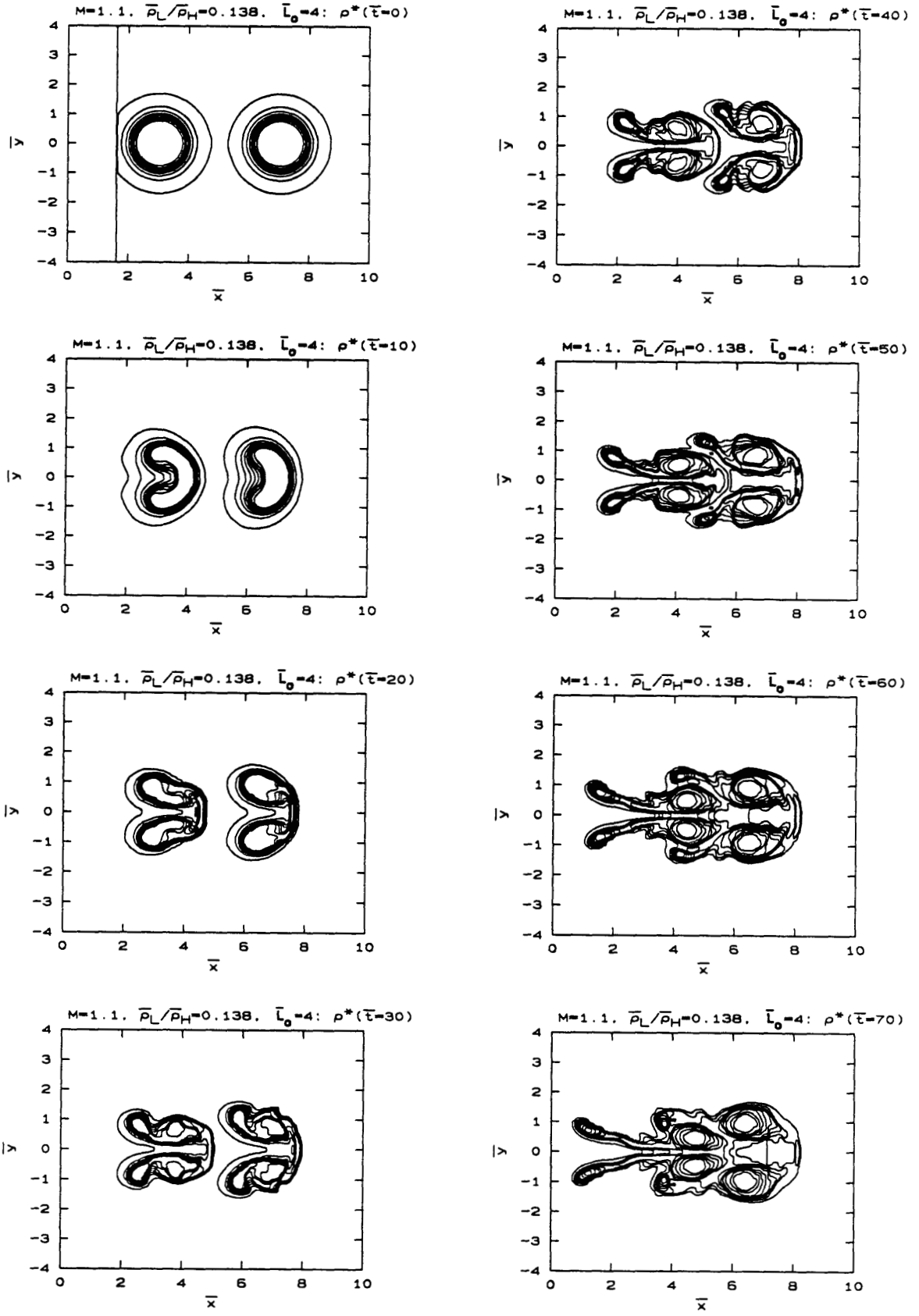

Figure 7.40 - Horizontal jet pair with M=1.1, $\overline{\rho}_L/\overline{\rho}_H = 0.138$, $\overline{L}_0 = 4$.

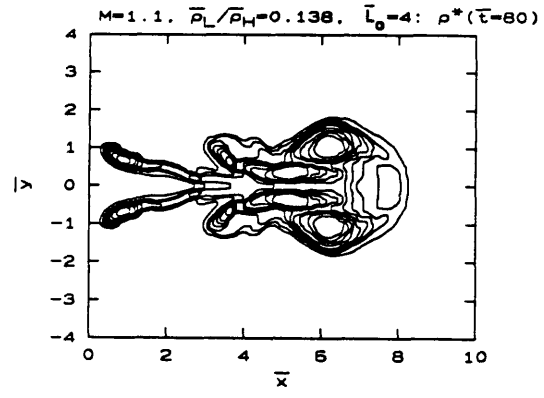
M=1.1. $\overline{\rho}_L/\overline{\rho}_H$=0.138. $\overline{L}_0$=4: $\rho^*(\overline{t}$=80)
$\overline{y}$
$\overline{x}$

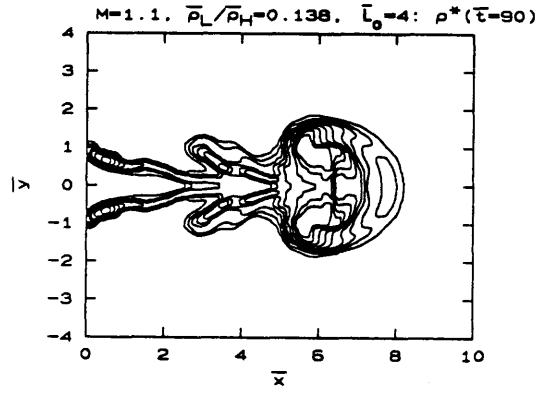
M=1.1. $\overline{\rho}_L/\overline{\rho}_H$=0.138. $\overline{L}_0$=4: $\rho^*(\overline{t}$=90)
$\overline{y}$
$\overline{x}$

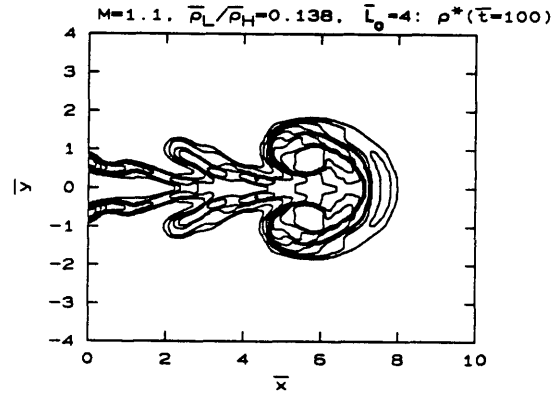
M=1.1. $\overline{\rho}_L/\overline{\rho}_H$=0.138. $\overline{L}_0$=4: $\rho^*(\overline{t}$=100)
$\overline{y}$
$\overline{x}$

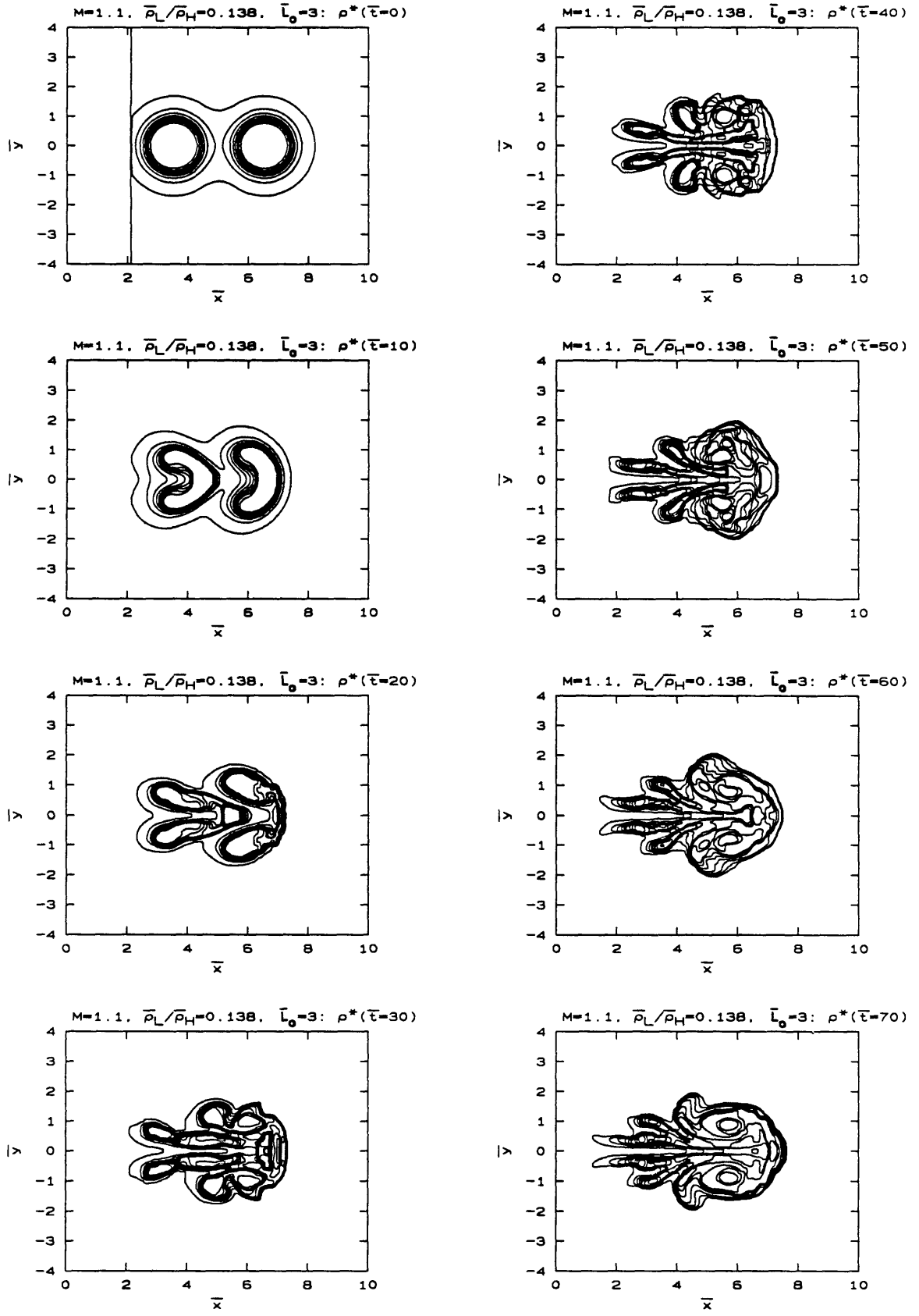

Figure 7.41 - Horizontal jet pair with M=1.1, $\overline{\rho}_L/\overline{\rho}_H = 0.138$, $\overline{L}_0 = 3$.

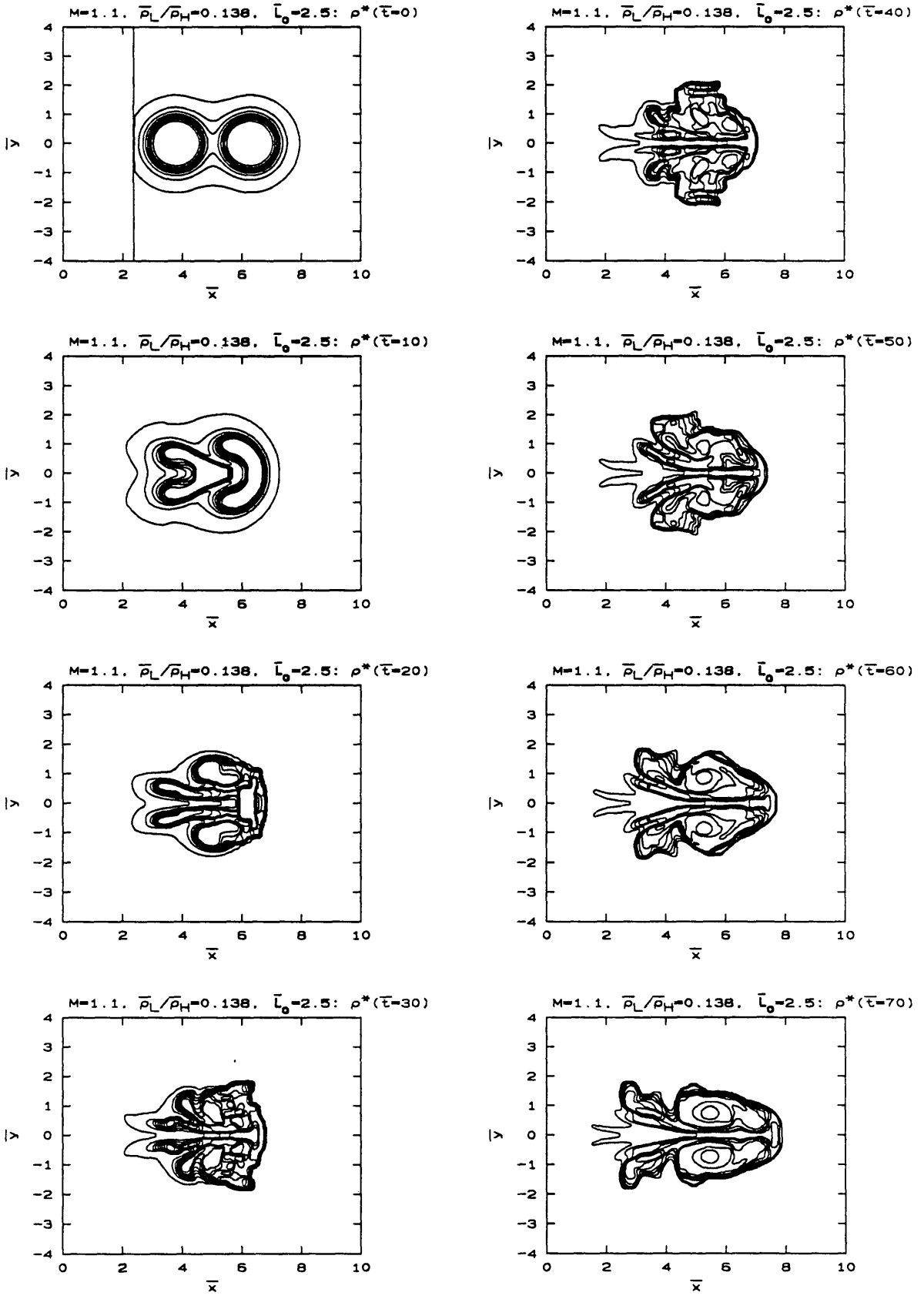

Figure 7.42 - Horizontal jet pair with M=1.1, $\overline{\rho}_L/\overline{\rho}_H = 0.138$, $\overline{L}_0 = 2.5$.

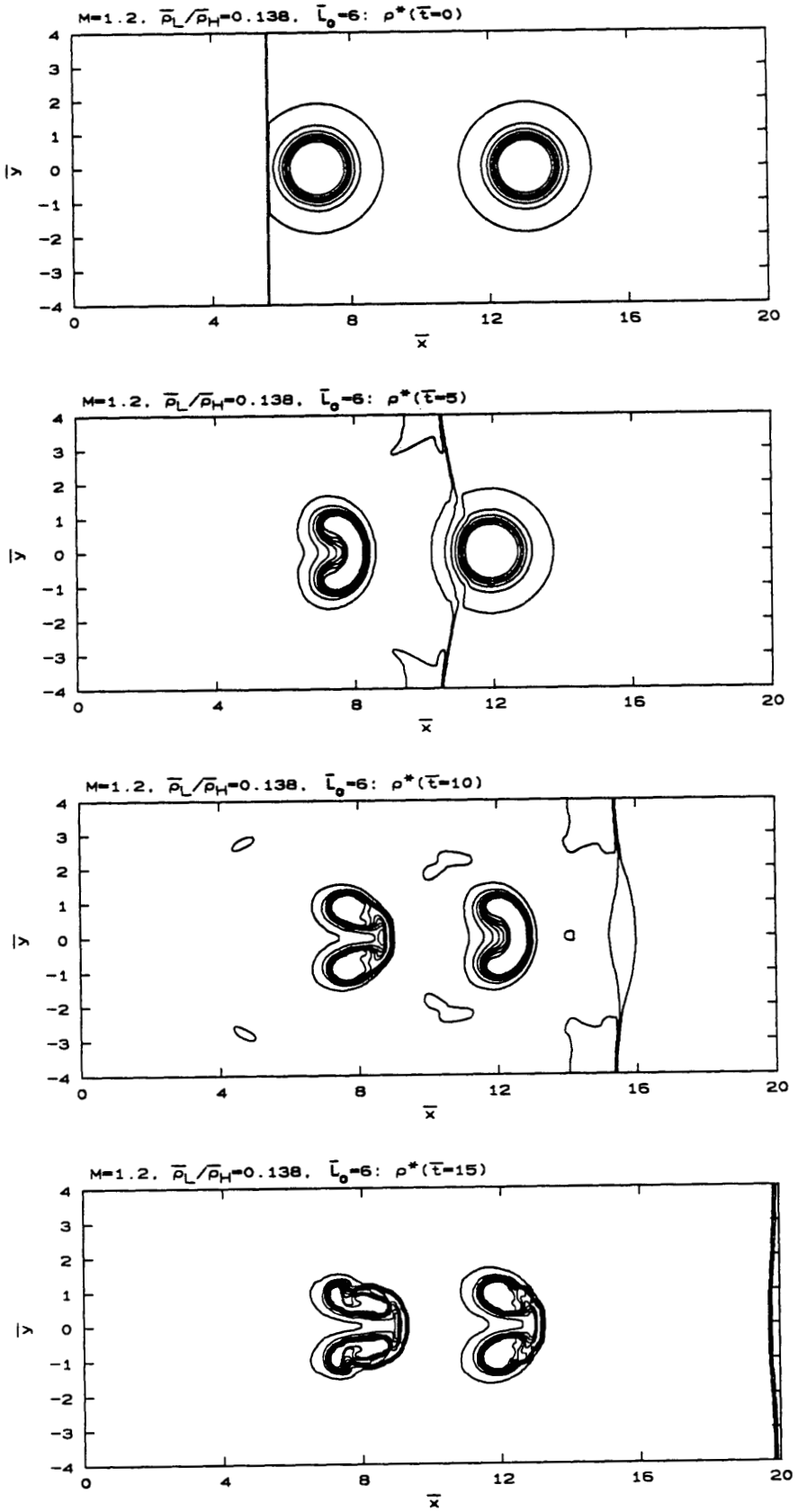

Figure 7.43 - Horizontal jet pair with M=1.2, $\overline{\rho}_L/\overline{\rho}_H = 0.138$, $\overline{L}_0 = 6$.

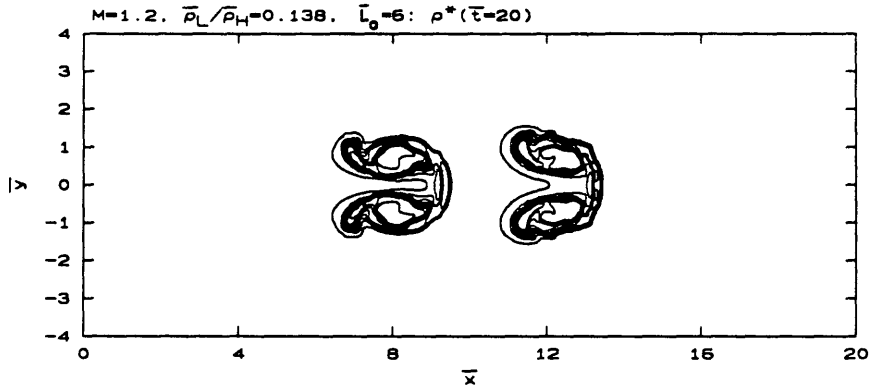
M=1.2. $\bar{\rho}_L/\bar{\rho}_H$=0.138. $\bar{l}_0$=6: $\rho^*(\bar{t}$=20)
$\bar{y}$
$\bar{x}$

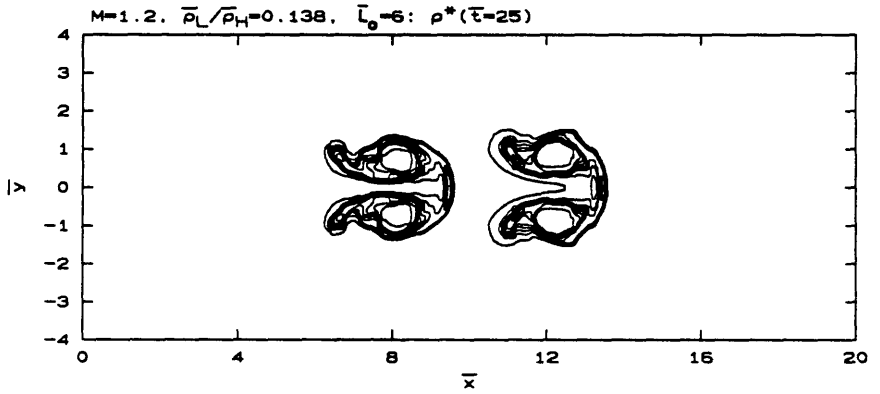
M=1.2. $\bar{\rho}_L/\bar{\rho}_H$=0.138. $\bar{l}_0$=6: $\rho^*(\bar{t}$=25)
$\bar{y}$
$\bar{x}$

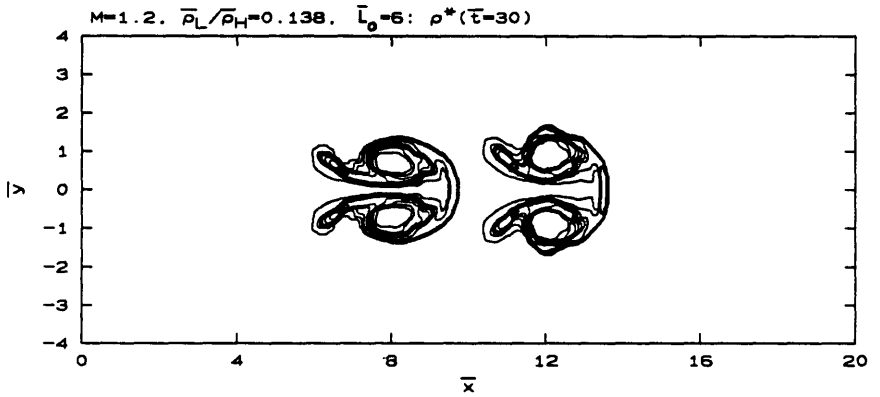
M=1.2. $\bar{\rho}_L/\bar{\rho}_H$=0.138. $\bar{l}_0$=6: $\rho^*(\bar{t}$=30)
$\bar{y}$
$\bar{x}$

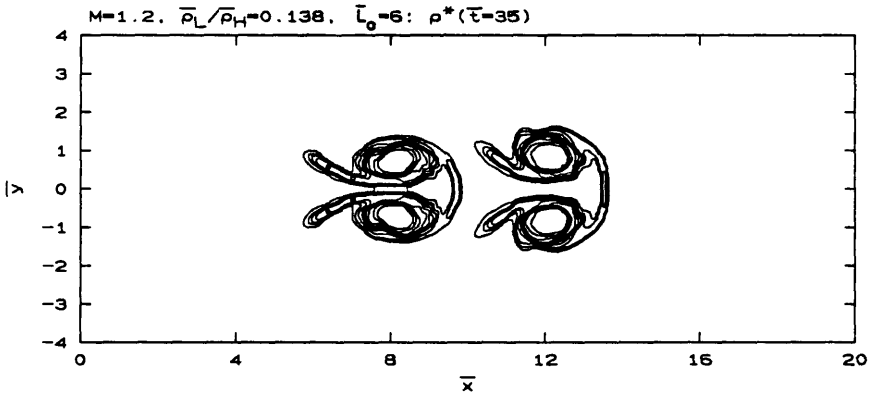
M=1.2. $\bar{\rho}_L/\bar{\rho}_H$=0.138. $\bar{l}_0$=6: $\rho^*(\bar{t}$=35)
$\bar{y}$
$\bar{x}$

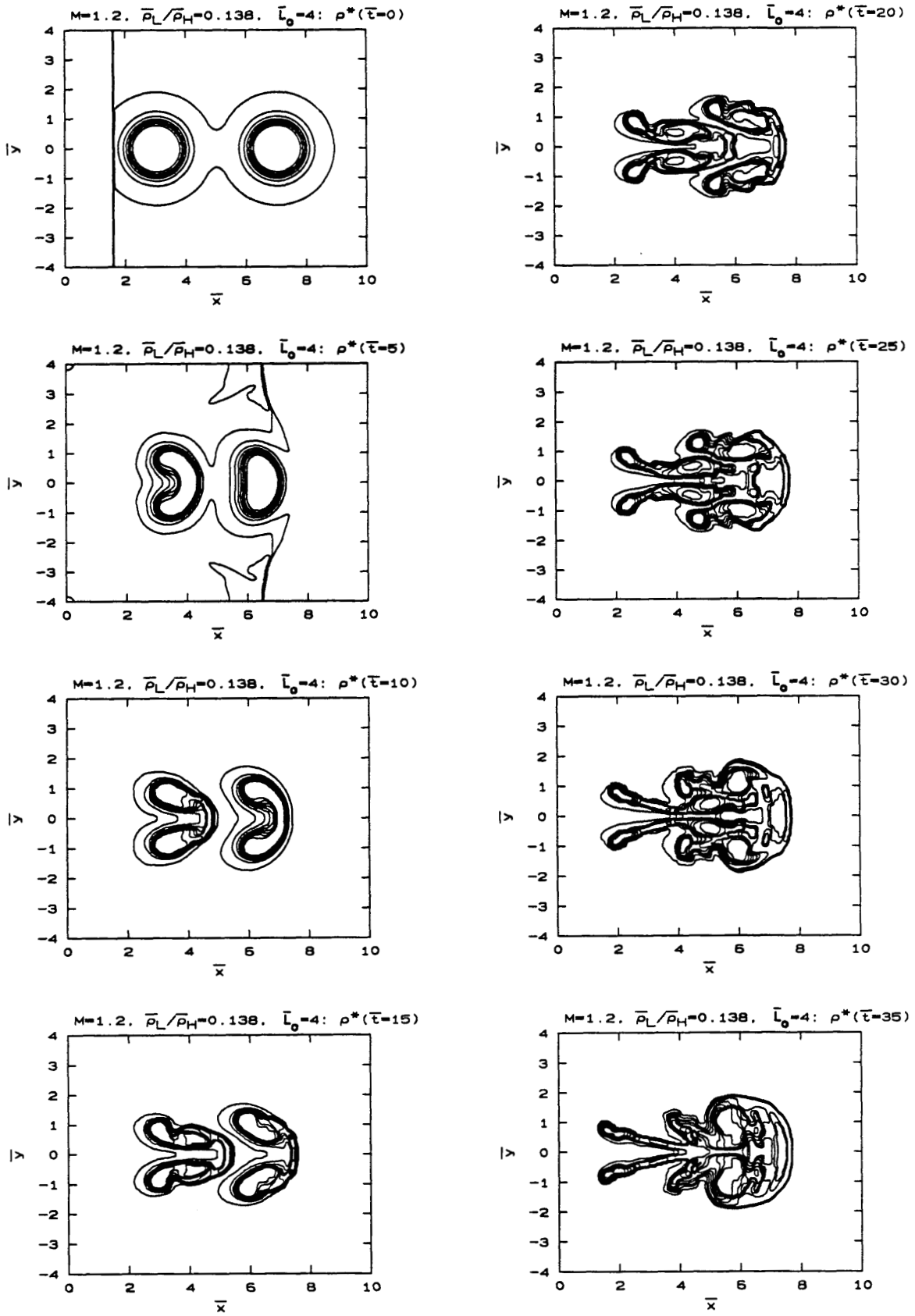

Figure 7.44 - Horizontal jet pair with M=1.2, $\overline{\rho}_L/\overline{\rho}_H = 0.138$, $\overline{L}_0 = 4$.

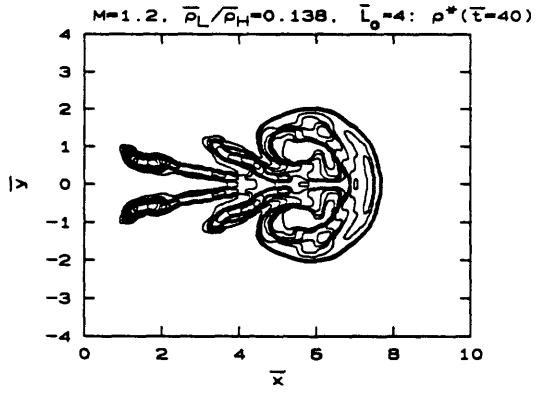
M=1.2. $\bar{\rho}_L/\bar{\rho}_H$=0.138. $\bar{l}_0$=4: $\rho^*(\bar{t}$=40)
$\bar{y}$
$\bar{x}$

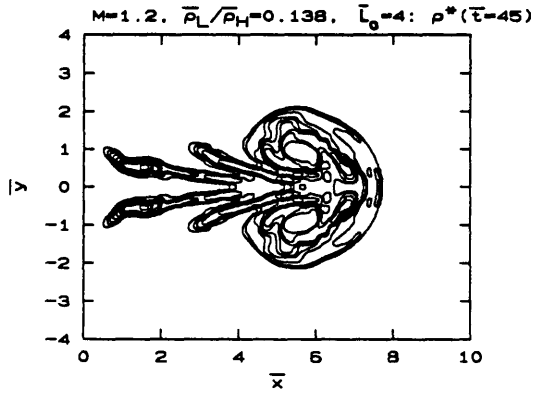
M=1.2. $\bar{\rho}_L/\bar{\rho}_H$=0.138. $\bar{l}_0$=4: $\rho^*(\bar{t}$=45)
$\bar{y}$
$\bar{x}$

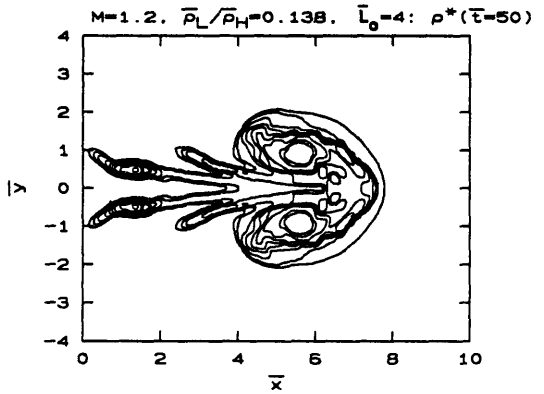
M=1.2. $\bar{\rho}_L/\bar{\rho}_H$=0.138. $\bar{l}_0$=4: $\rho^*(\bar{t}$=50)
$\bar{y}$
$\bar{x}$

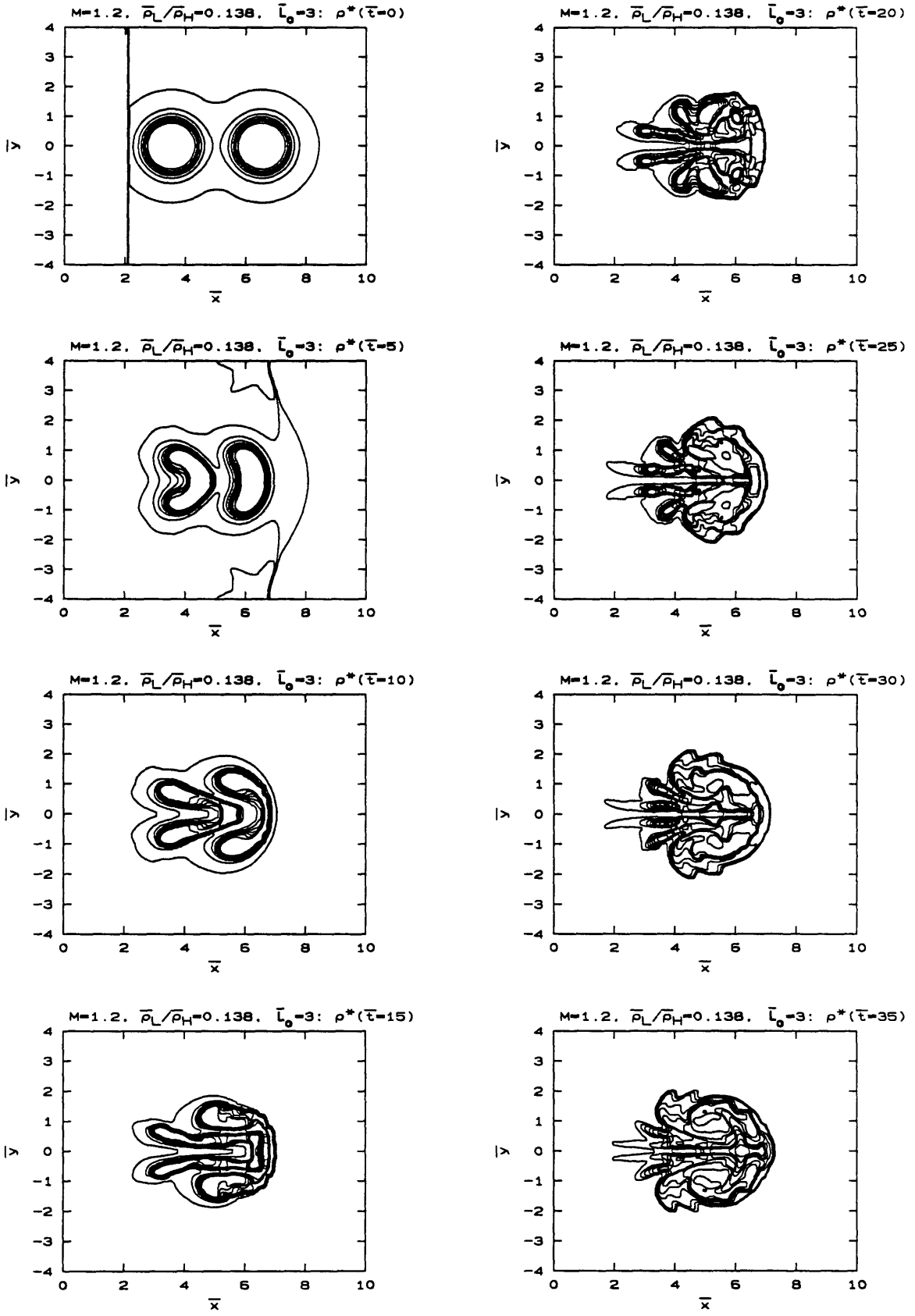

Figure 7.45 - Horizontal jet pair with M=1.2, $\overline{\rho}_L/\overline{\rho}_H = 0.138$, $\overline{L}_0 = 3$.

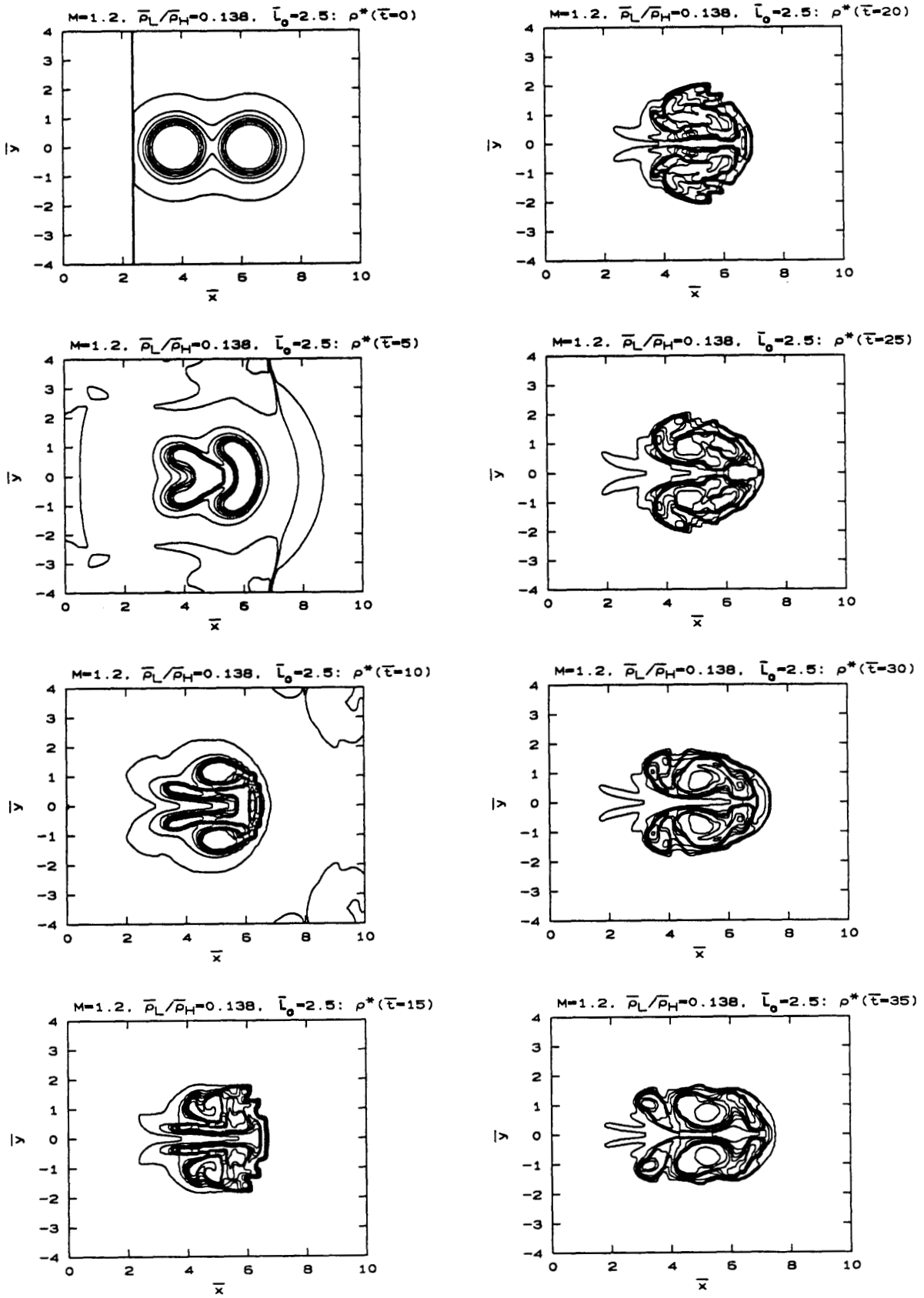

Figure 7.46 - Horizontal jet pair with M=1.2, $\overline{\rho}_L/\overline{\rho}_H = 0.138$, $\overline{L}_0 = 2.5$.

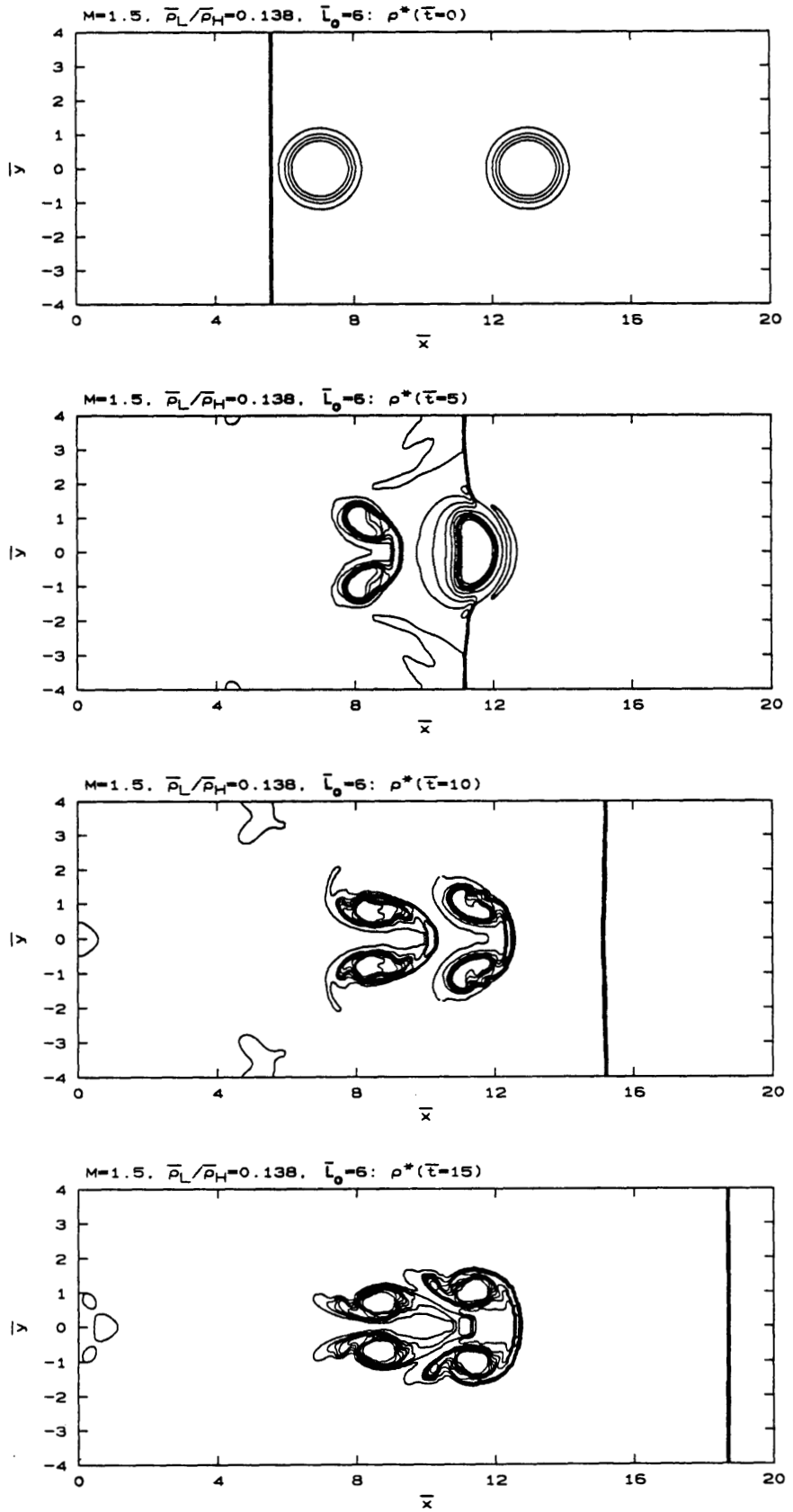

Figure 7.47 - Horizontal jet pair with M=1.5, $\overline{\rho}_L/\overline{\rho}_H = 0.138$, $\overline{L}_0 = 6$.

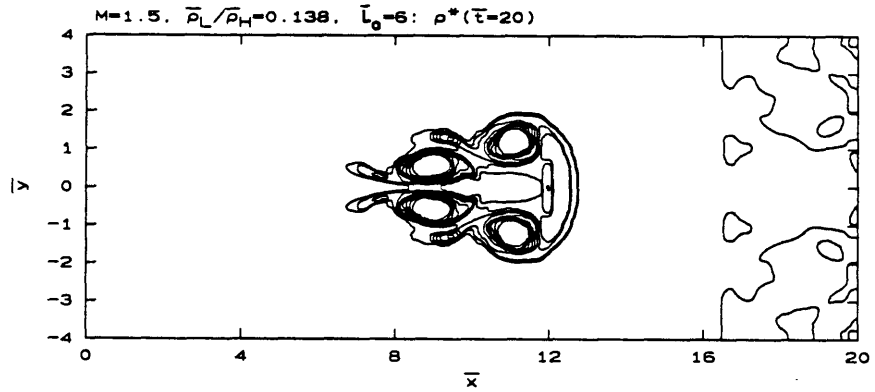
M=1.5. $\bar{\rho}_L/\bar{\rho}_H$=0.138. $\bar{L}_0$=6: $\rho^*(\bar{t}$=20)
$\bar{y}$
$\bar{x}$

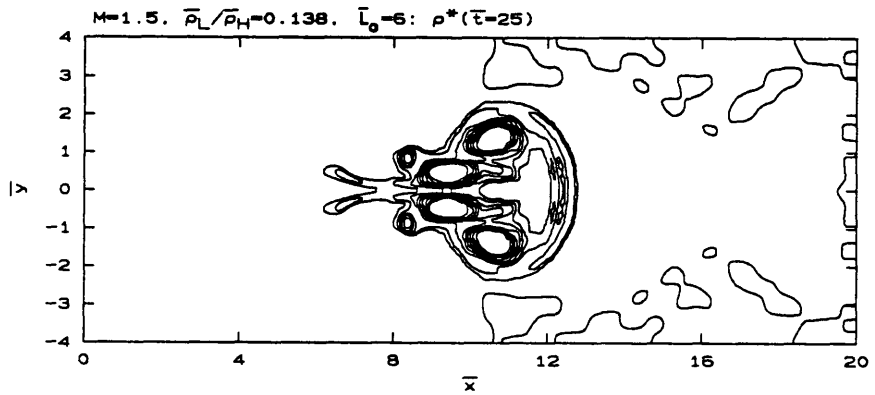
M=1.5. $\bar{\rho}_L/\bar{\rho}_H$=0.138. $\bar{L}_0$=6: $\rho^*(\bar{t}$=25)
$\bar{y}$
$\bar{x}$

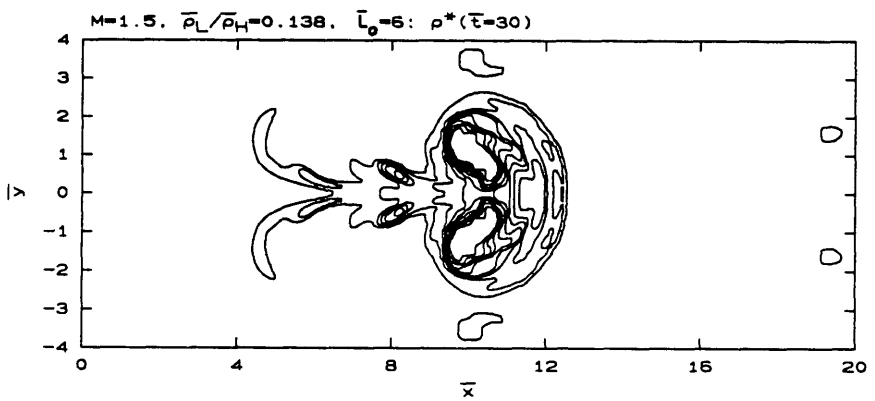
M=1.5. $\bar{\rho}_L/\bar{\rho}_H$=0.138. $\bar{L}_0$=6: $\rho^*(\bar{t}$=30)
$\bar{y}$
$\bar{x}$

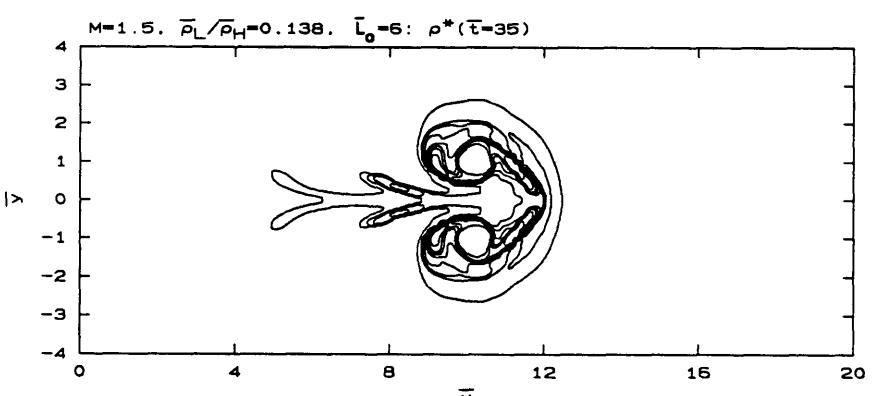
M=1.5. $\bar{\rho}_L/\bar{\rho}_H$=0.138. $\bar{L}_0$=6: $\rho^*(\bar{t}$=35)
$\bar{y}$
$\bar{x}$

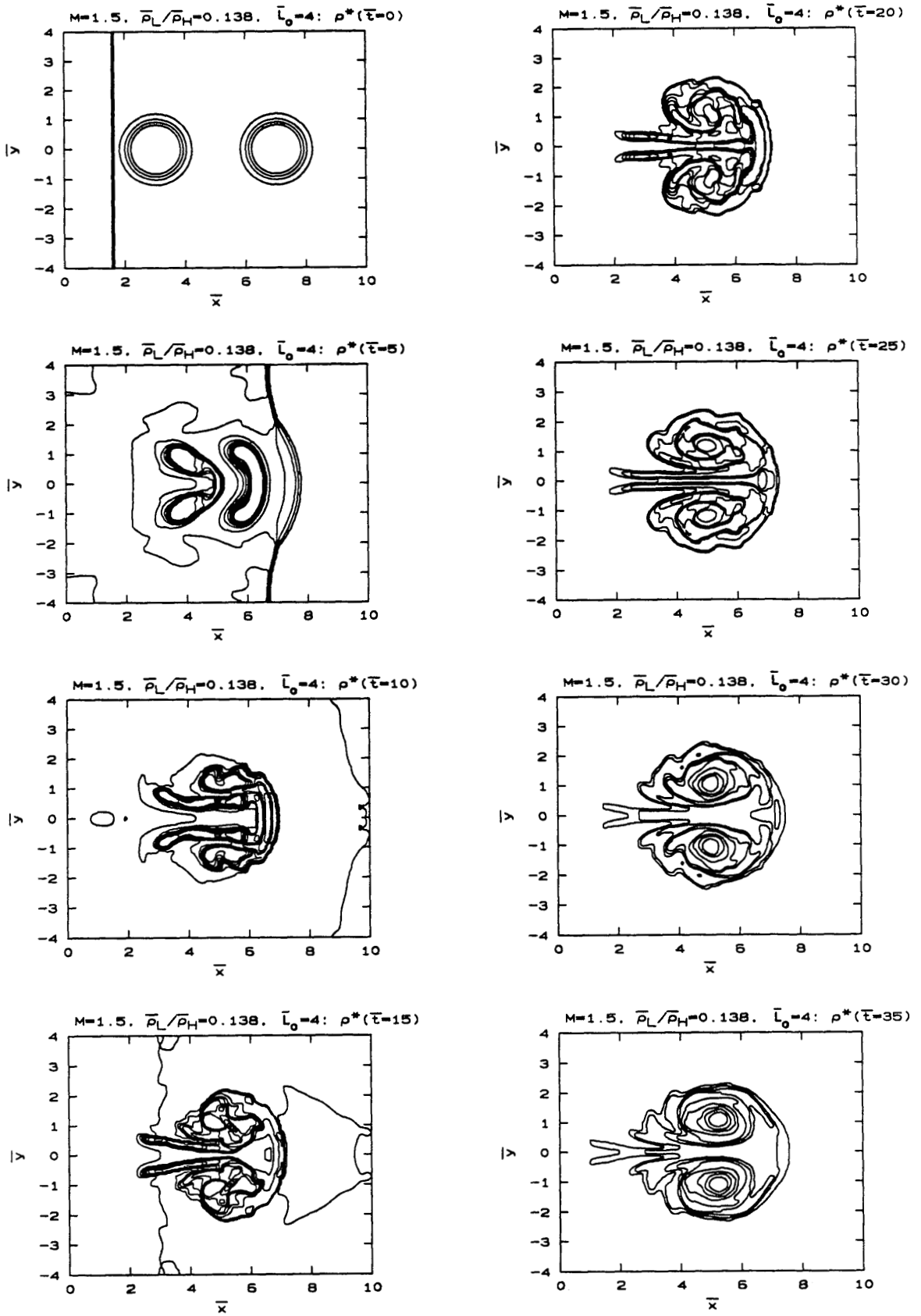

Figure 7.48 - Horizontal jet pair with M=1.5, $\overline{\rho}_L/\overline{\rho}_H = 0.138$, $\overline{L}_0 = 4$.

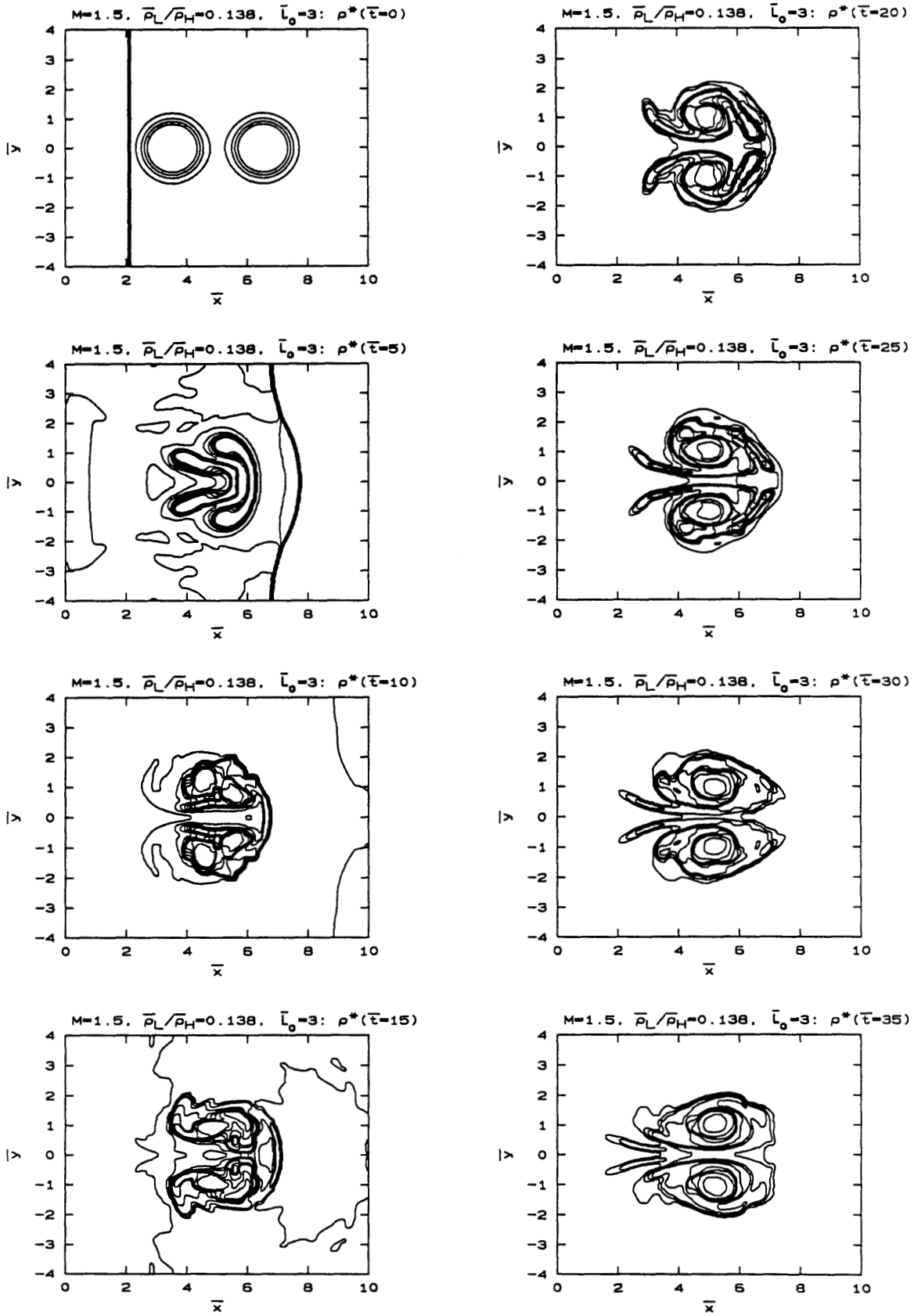

Figure 7.49 - Horizontal jet pair with M=1.5, $\overline{\rho}_L/\overline{\rho}_H = 0.138$, $\overline{L}_0 = 3$.

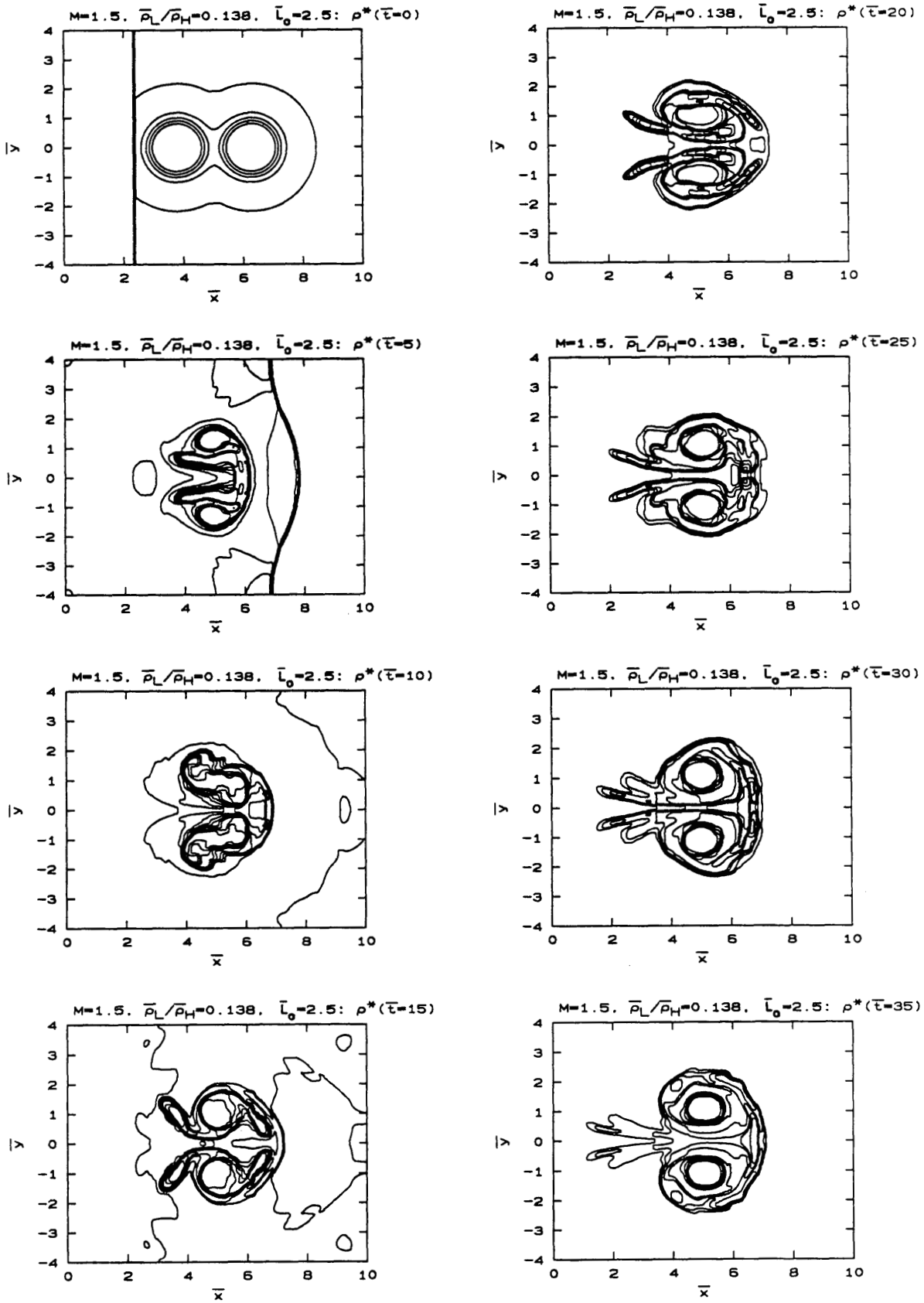

Figure 7.50 - Horizontal jet pair with M=1.5, $\overline{\rho}_L/\overline{\rho}_H = 0.138$, $\overline{L}_0 = 2.5$.

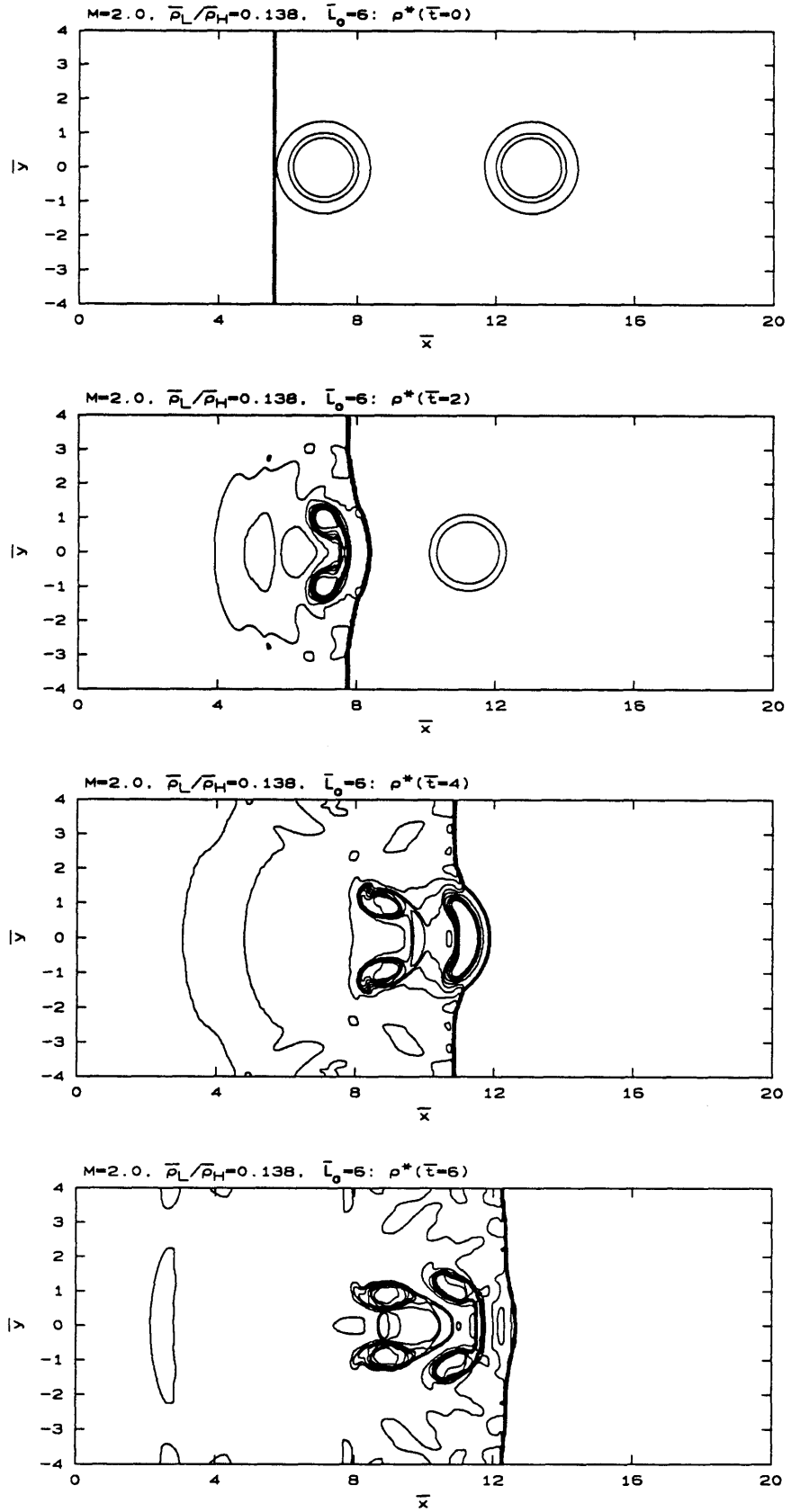

Figure 7.51 - Horizontal jet pair with M=2.0, $\overline{\rho}_L/\overline{\rho}_H = 0.138$, $\overline{L}_0 = 6$.

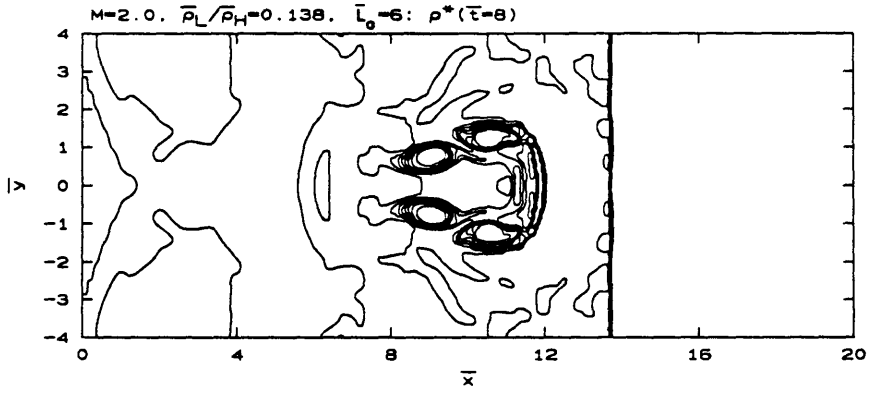
M=2.0. $\bar{\rho}_L/\bar{\rho}_H$=0.138. $\bar{l}_o$=6: $\rho^*(\bar{t}$=8)
$\bar{y}$
$\bar{x}$

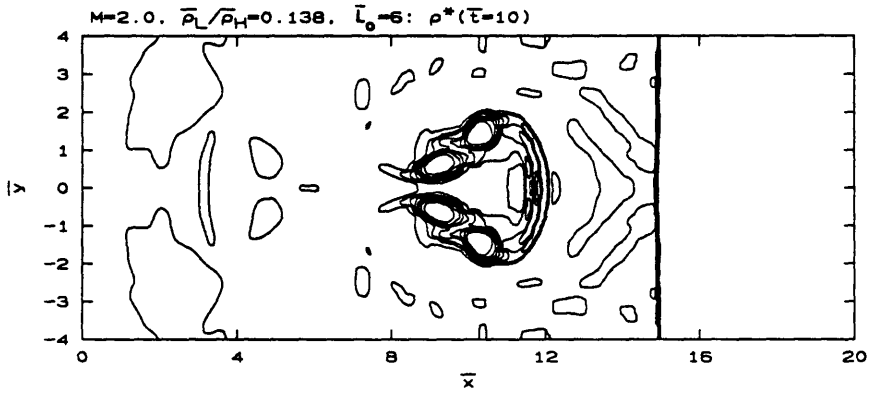
M=2.0. $\bar{\rho}_L/\bar{\rho}_H$=0.138. $\bar{l}_o$=6: $\rho^*(\bar{t}$=10)
$\bar{y}$
$\bar{x}$

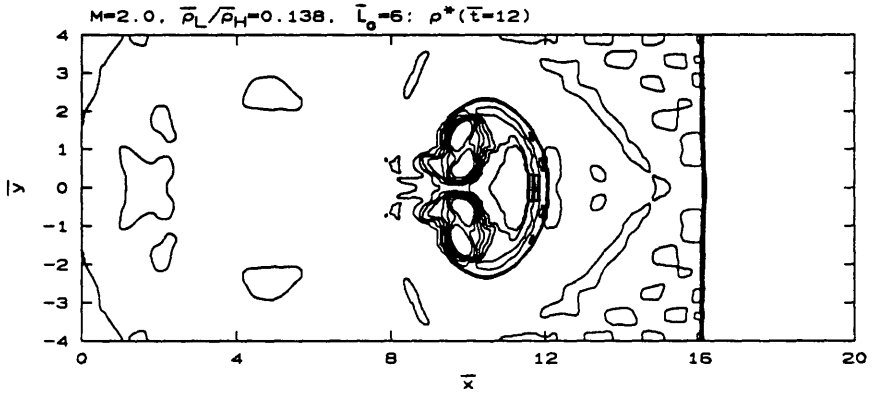
M=2.0. $\bar{\rho}_L/\bar{\rho}_H$=0.138. $\bar{l}_o$=6: $\rho^*(\bar{t}$=12)
$\bar{y}$
$\bar{x}$

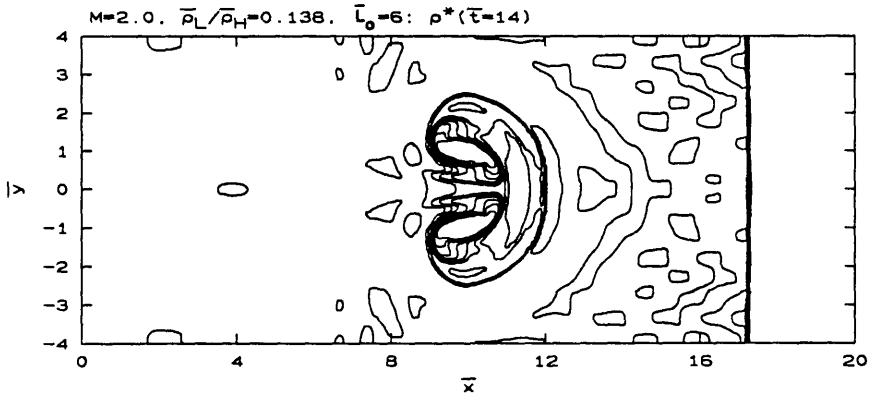
M=2.0. $\bar{\rho}_L/\bar{\rho}_H$=0.138. $\bar{l}_o$=6: $\rho^*(\bar{t}$=14)
$\bar{y}$
$\bar{x}$

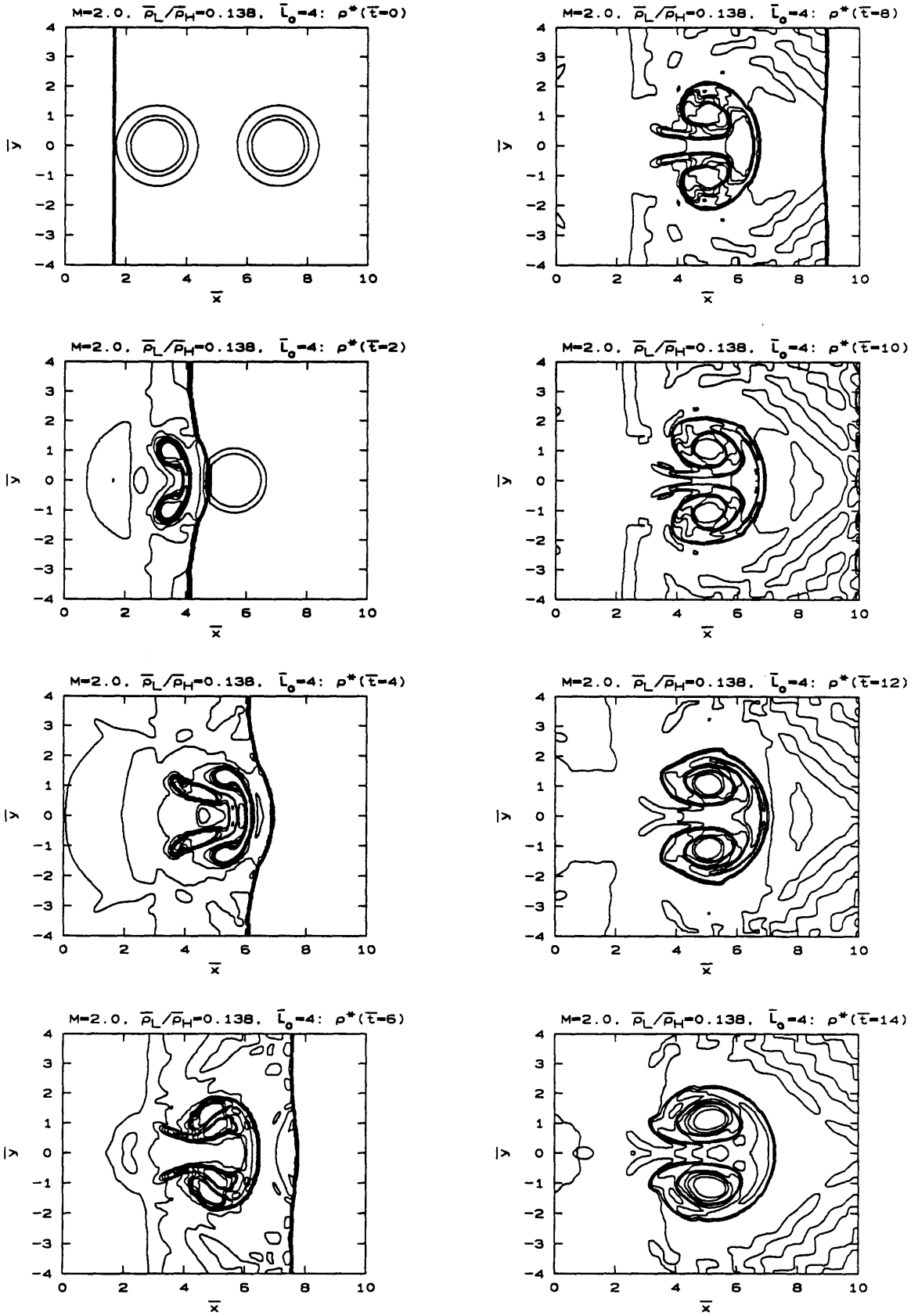

Figure 7.52 - Horizontal jet pair with M=2.0, $\overline{\rho}_L/\overline{\rho}_H = 0.138$, $\overline{L}_0 = 4$.

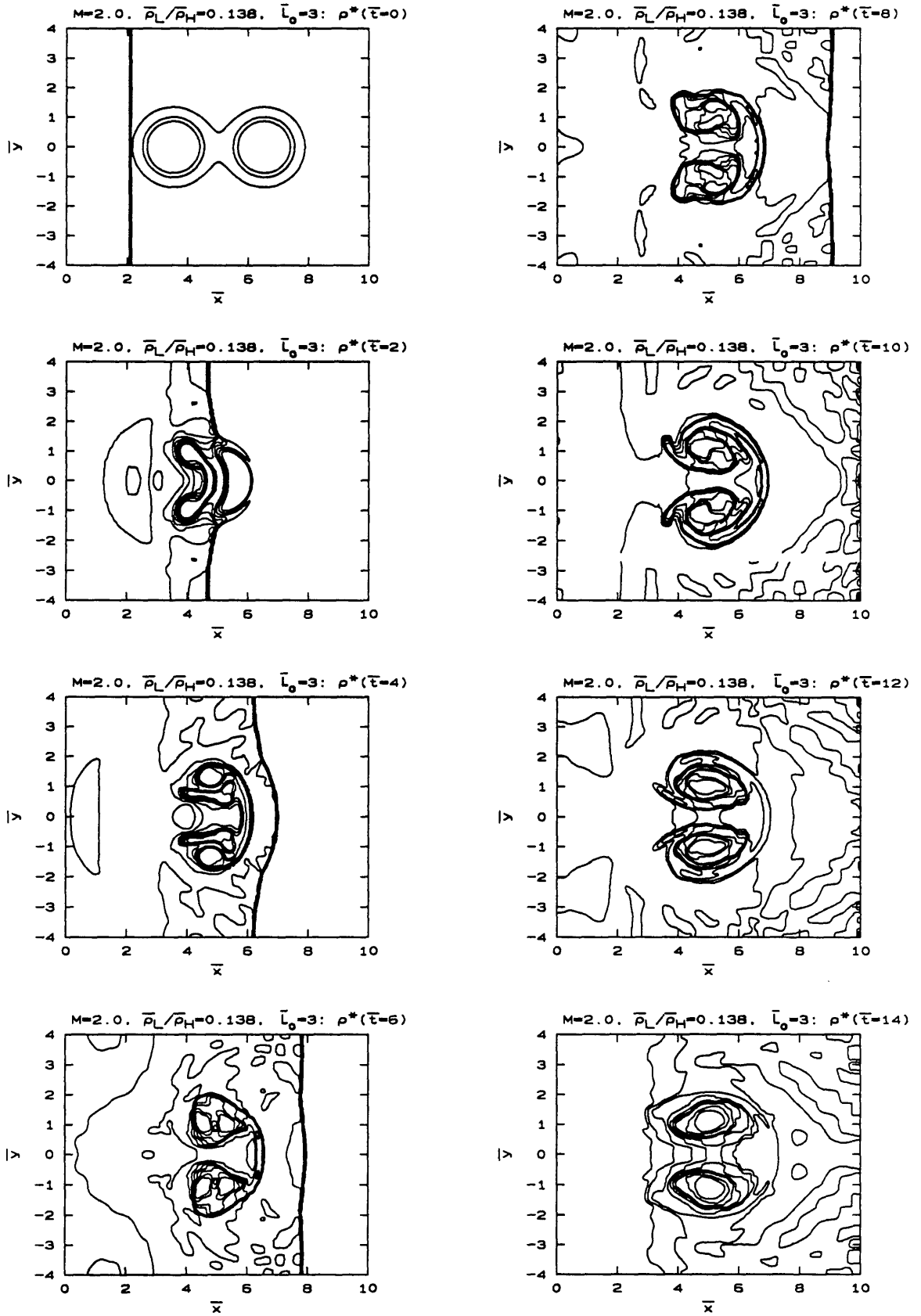

Figure 7.53 - Horizontal jet pair with M=2.0, $\overline{\rho}_L/\overline{\rho}_H = 0.138$, $\overline{L}_0 = 3$.

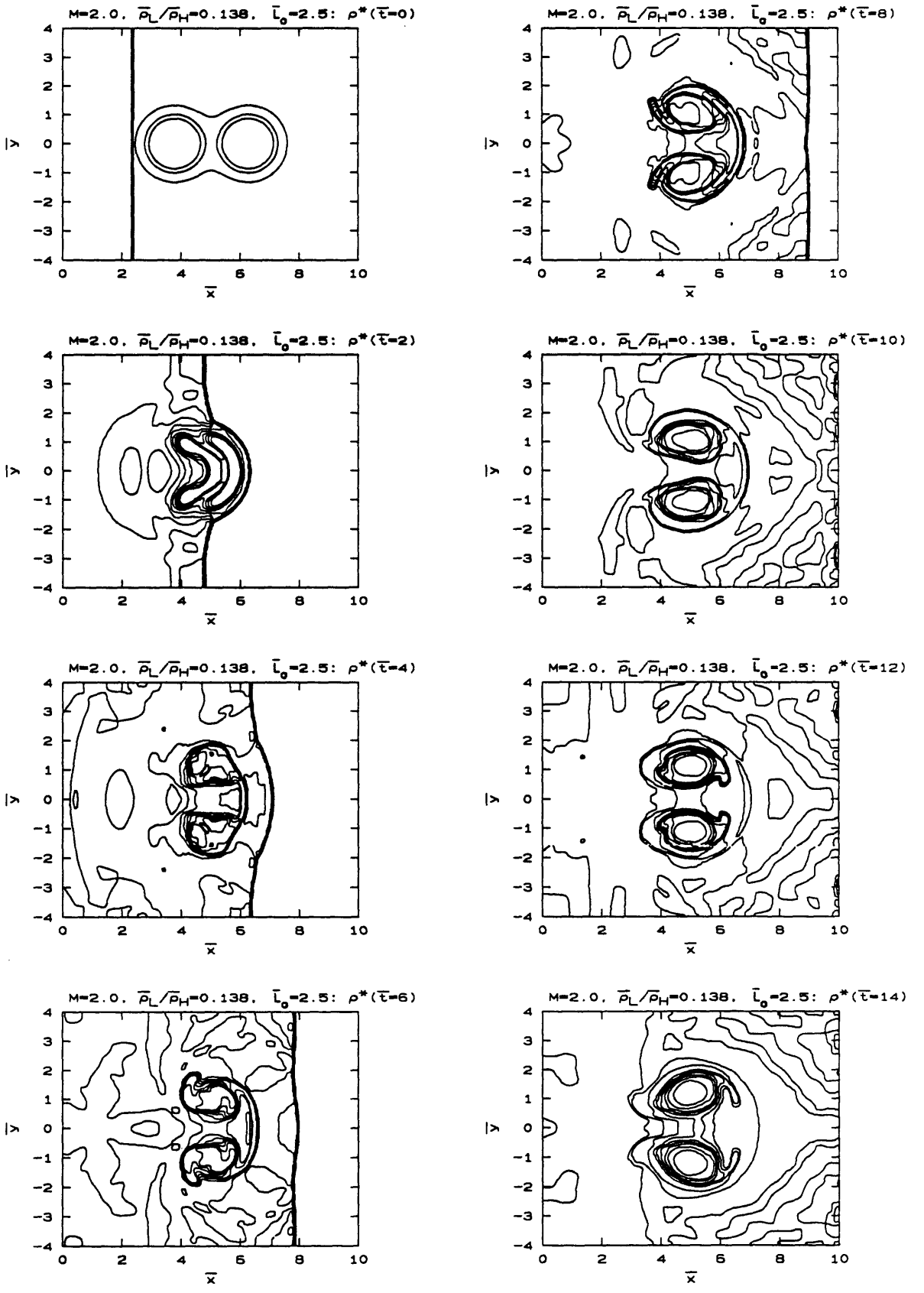

Figure 7.54 - Horizontal jet pair with M=2.0, $\overline{\rho}_L/\overline{\rho}_H = 0.138$, $\overline{L}_0 = 2.5$.

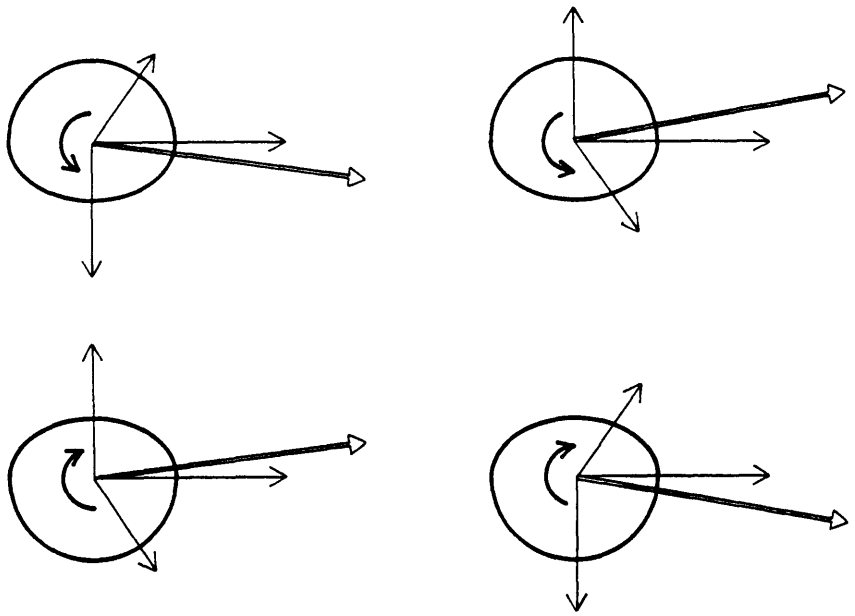

(a)

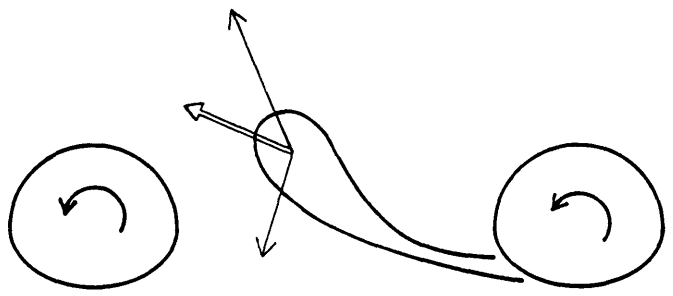

(b)

Figure 7.55 - Horizontal jet pair induced velocities: (a) Vortex core motion, (b) tail motion.

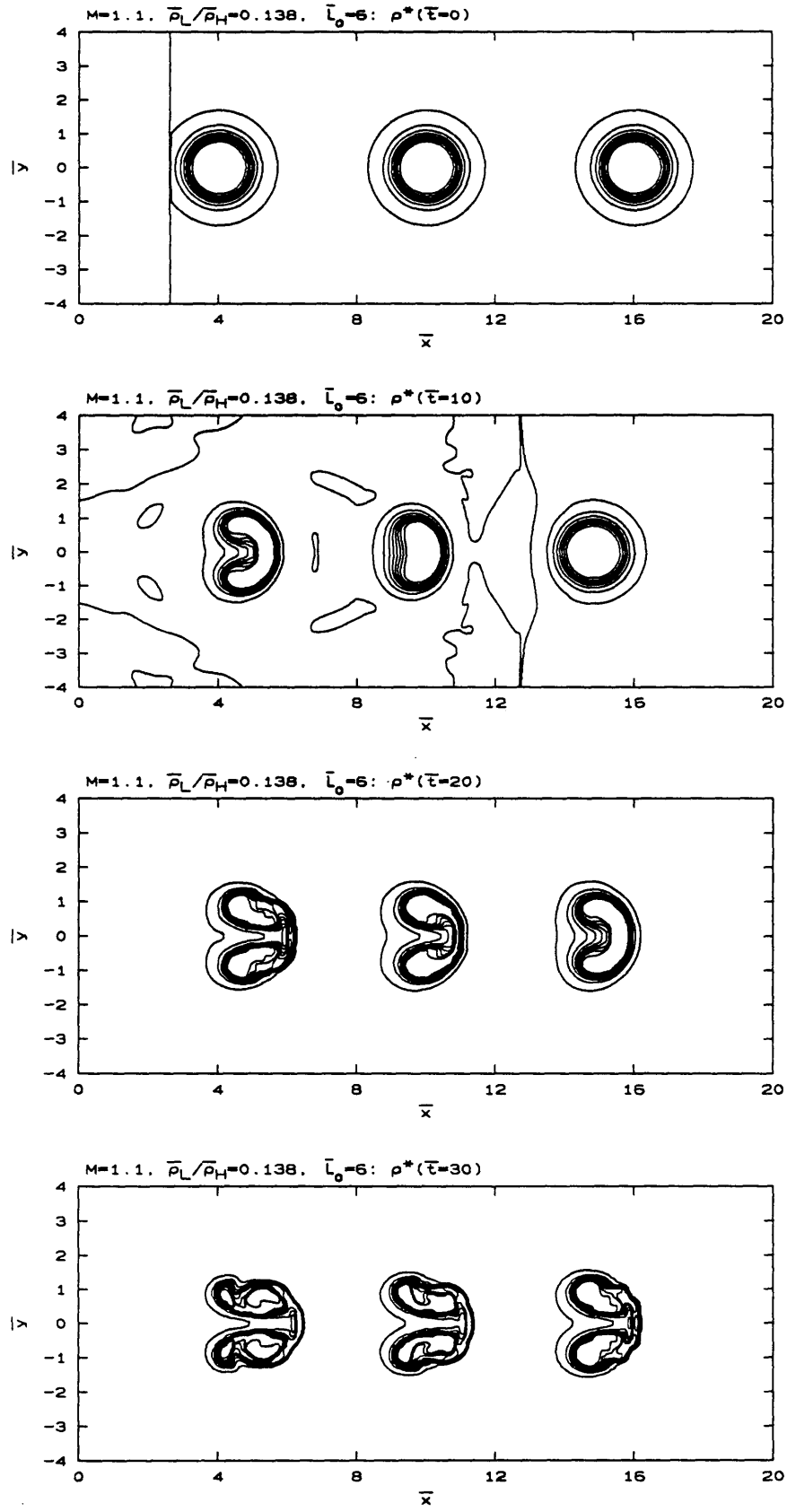

Figure 7.56 - Horizontal jet trio with M=1.1, $\overline{\rho}_L/\overline{\rho}_H = 0.138$, $\overline{L}_0 = 6$.

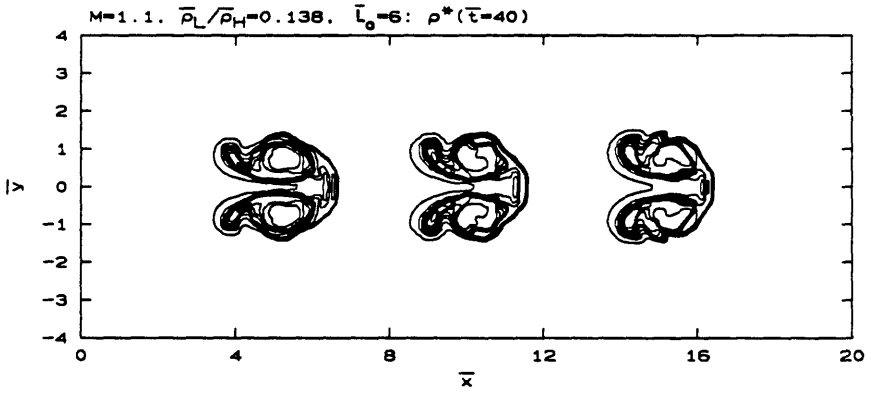
M=1.1. $\overline{\rho}_L/\overline{\rho}_H$=0.138. $\overline{l}_o$=6: $\rho^*(\overline{t}$=40)
$\overline{y}$
$\overline{x}$

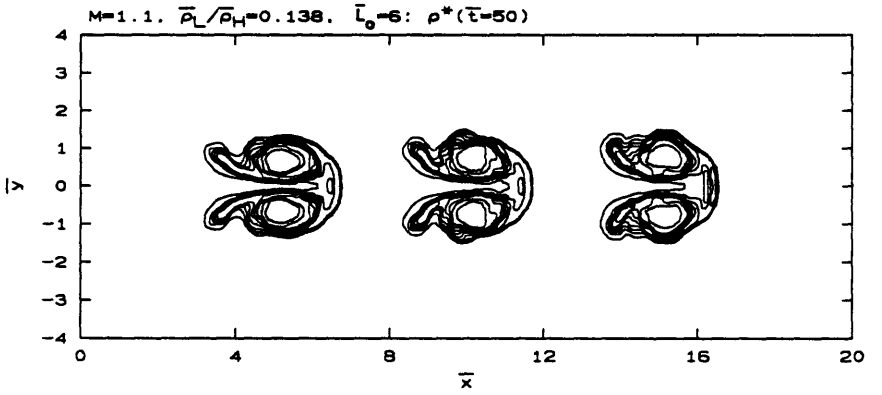
M=1.1. $\overline{\rho}_L/\overline{\rho}_H$=0.138. $\overline{l}_o$=6: $\rho^*(\overline{t}$=50)
$\overline{y}$
$\overline{x}$

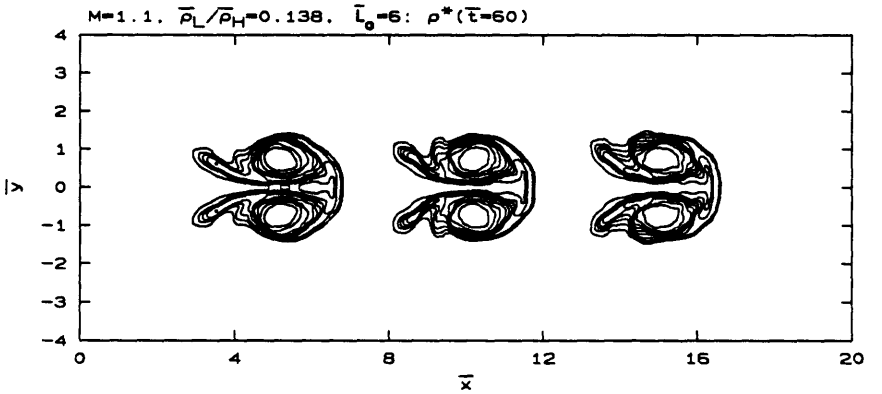
M=1.1. $\overline{\rho}_L/\overline{\rho}_H$=0.138. $\overline{l}_o$=6: $\rho^*(\overline{t}$=60)
$\overline{y}$
$\overline{x}$

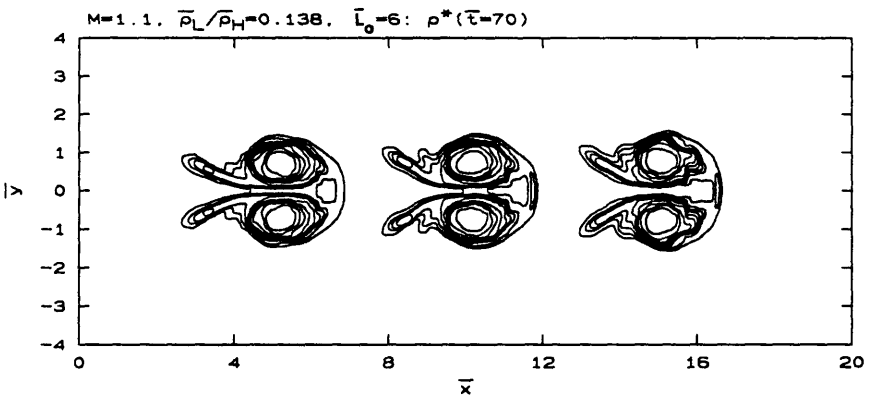
M=1.1. $\overline{\rho}_L/\overline{\rho}_H$=0.138. $\overline{l}_o$=6: $\rho^*(\overline{t}$=70)
$\overline{y}$
$\overline{x}$

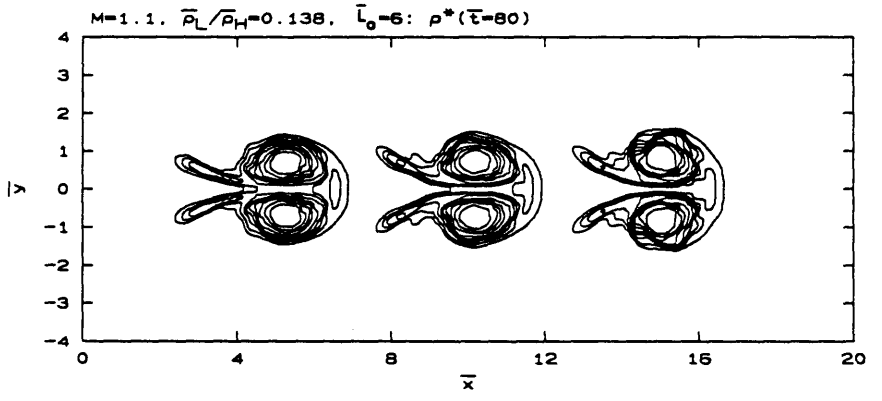
M=1.1. $\bar{\rho}_L/\bar{\rho}_H$=0.138. $\bar{L}_0$=6: $\rho^*(\bar{t}$=80)
$\bar{y}$
$\bar{x}$

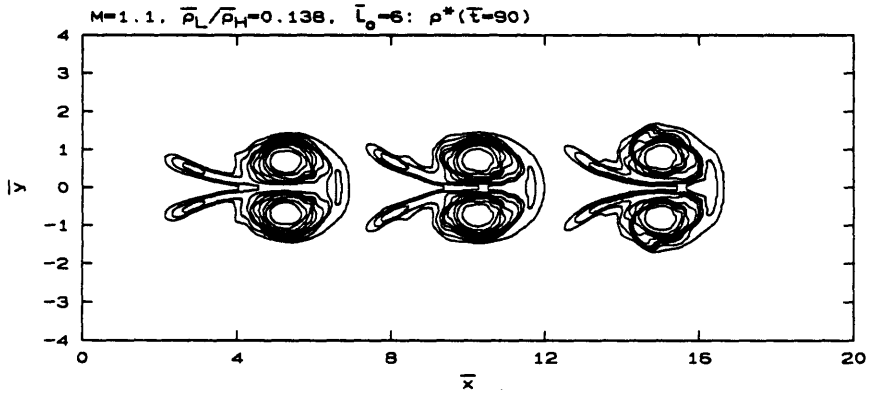
M=1.1. $\bar{\rho}_L/\bar{\rho}_H$=0.138. $\bar{L}_0$=6: $\rho^*(\bar{t}$=90)
$\bar{y}$
$\bar{x}$

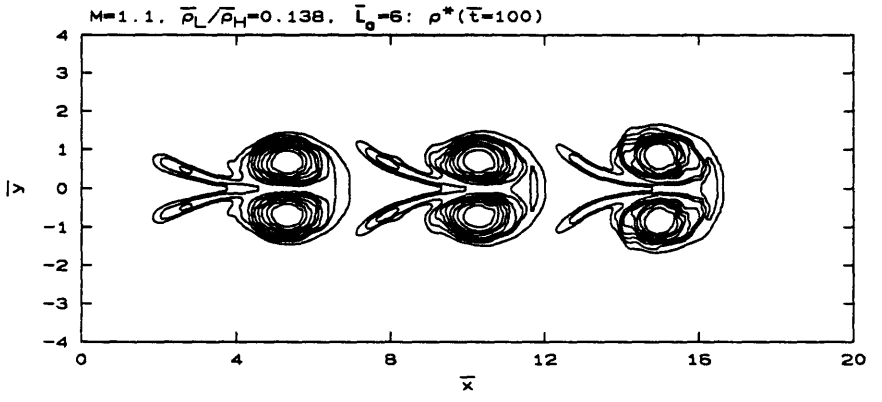
M=1.1. $\bar{\rho}_L/\bar{\rho}_H$=0.138. $\bar{L}_0$=6: $\rho^*(\bar{t}$=100)
$\bar{y}$
$\bar{x}$

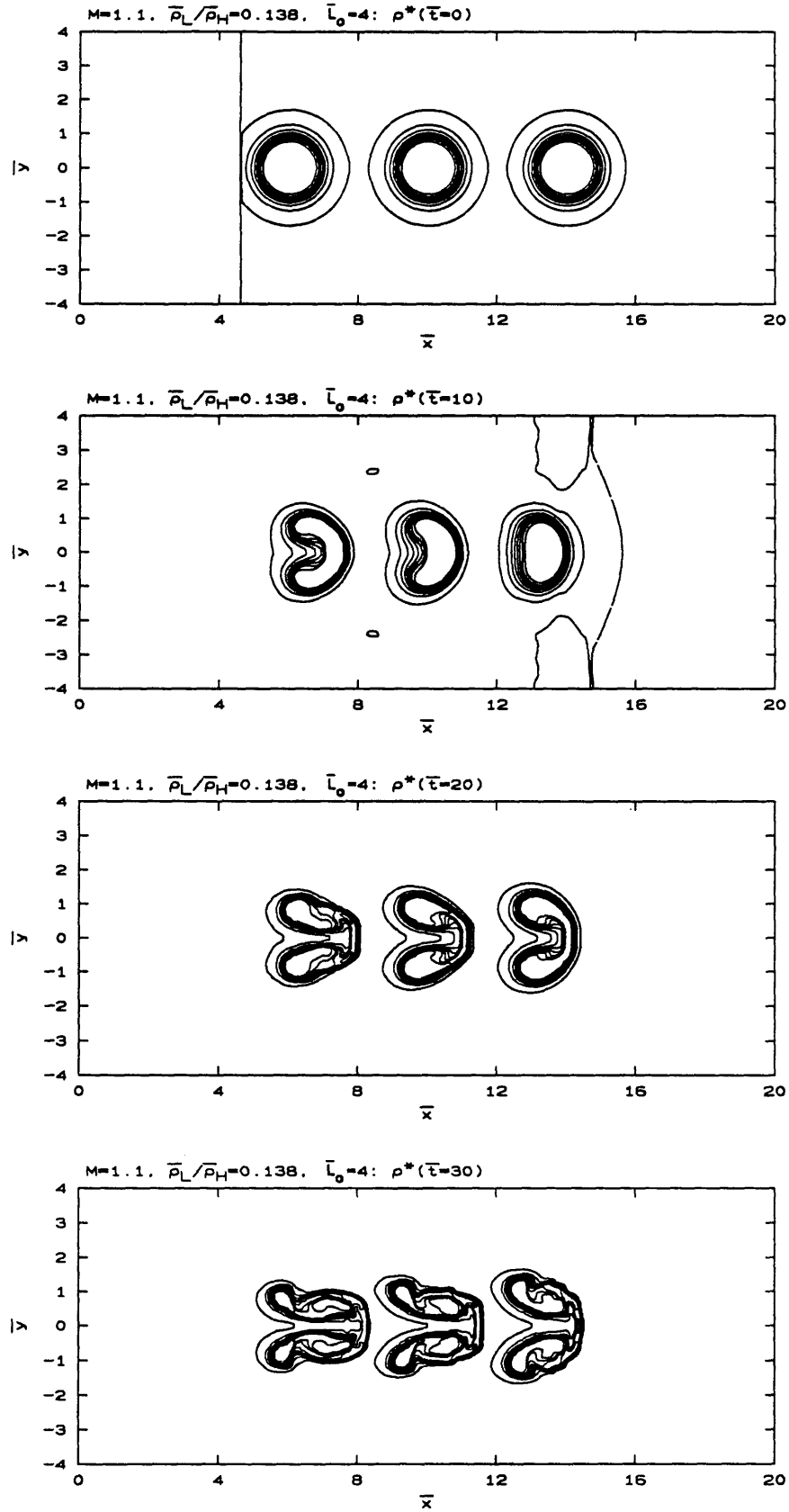

Figure 7.57 - Horizontal jet trio with M=1.1, $\overline{\rho}_L/\overline{\rho}_H = 0.138$, $\overline{L}_0 = 4$.

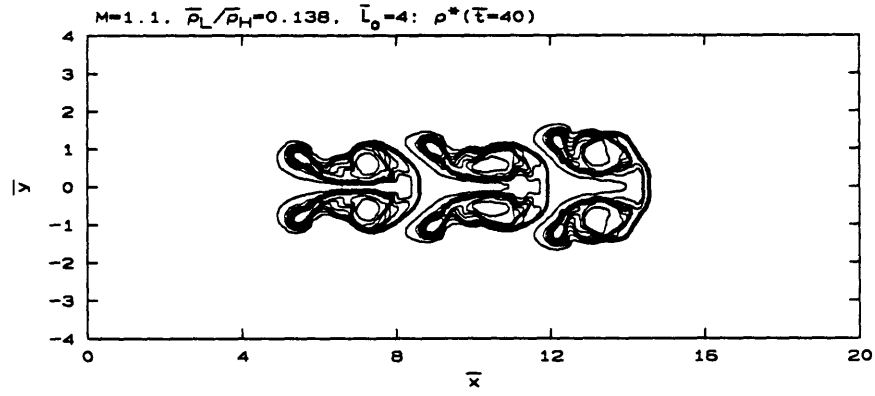
M=1.1, $\bar{\rho}_L/\bar{\rho}_H$=0.138, $\bar{l}_0$=4: $\rho^*(\bar{t}$=40)
$\bar{y}$
$\bar{x}$

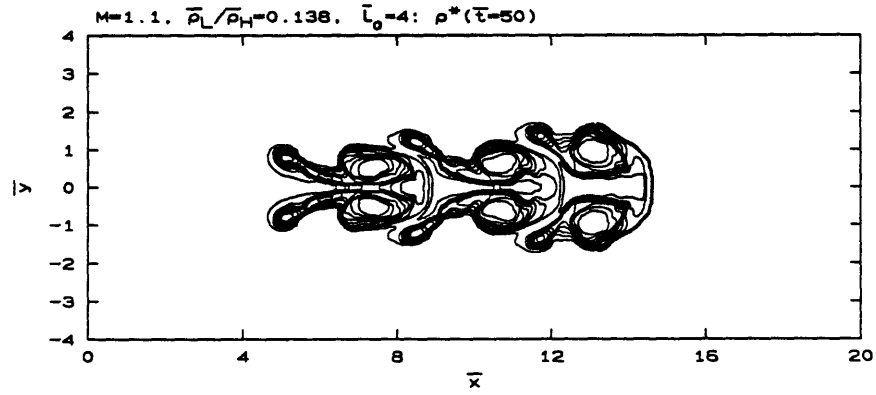
M=1.1, $\bar{\rho}_L/\bar{\rho}_H$=0.138, $\bar{l}_0$=4: $\rho^*(\bar{t}$=50)
$\bar{y}$
$\bar{x}$

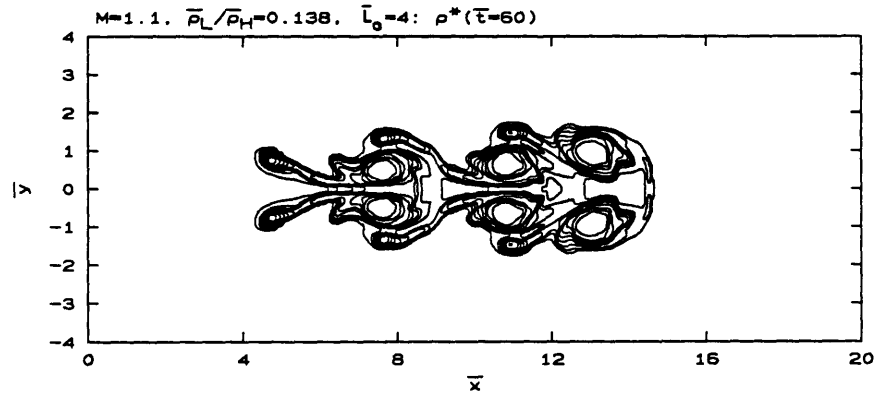
M=1.1, $\bar{\rho}_L/\bar{\rho}_H$=0.138, $\bar{l}_0$=4: $\rho^*(\bar{t}$=60)
$\bar{y}$
$\bar{x}$

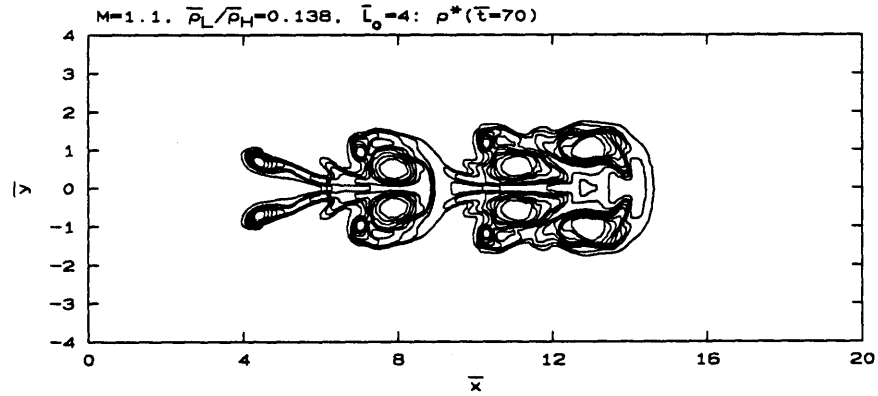
M=1.1, $\bar{\rho}_L/\bar{\rho}_H$=0.138, $\bar{l}_0$=4: $\rho^*(\bar{t}$=70)
$\bar{y}$
$\bar{x}$

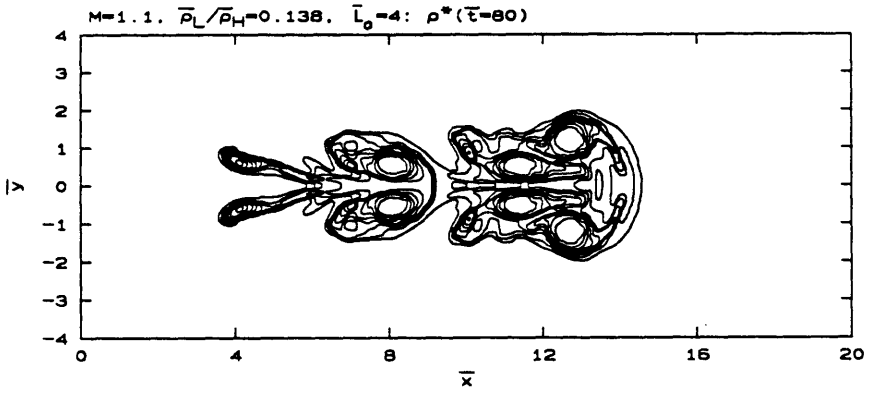
M=1.1. $\bar{\rho}_L/\bar{\rho}_H$=0.138. $\bar{l}_o$=4: $\rho^*(\bar{t}$=80)
$\bar{y}$
$\bar{x}$

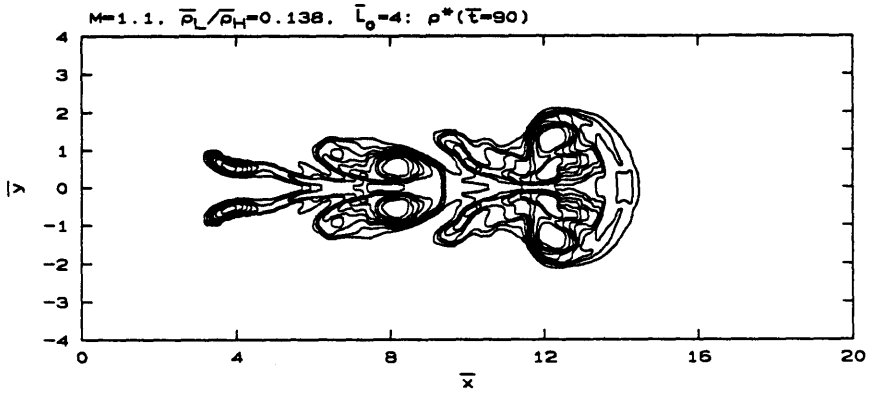
M=1.1. $\bar{\rho}_L/\bar{\rho}_H$=0.138. $\bar{l}_o$=4: $\rho^*(\bar{t}$=90)
$\bar{y}$
$\bar{x}$

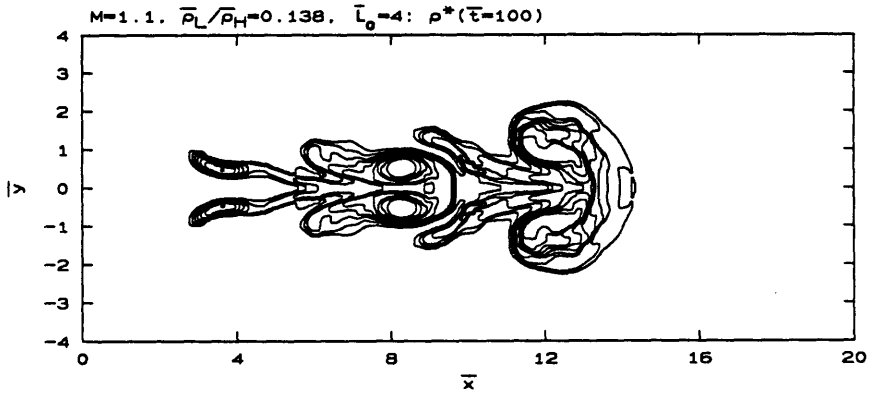
M=1.1. $\bar{\rho}_L/\bar{\rho}_H$=0.138. $\bar{l}_o$=4: $\rho^*(\bar{t}$=100)
$\bar{y}$
$\bar{x}$

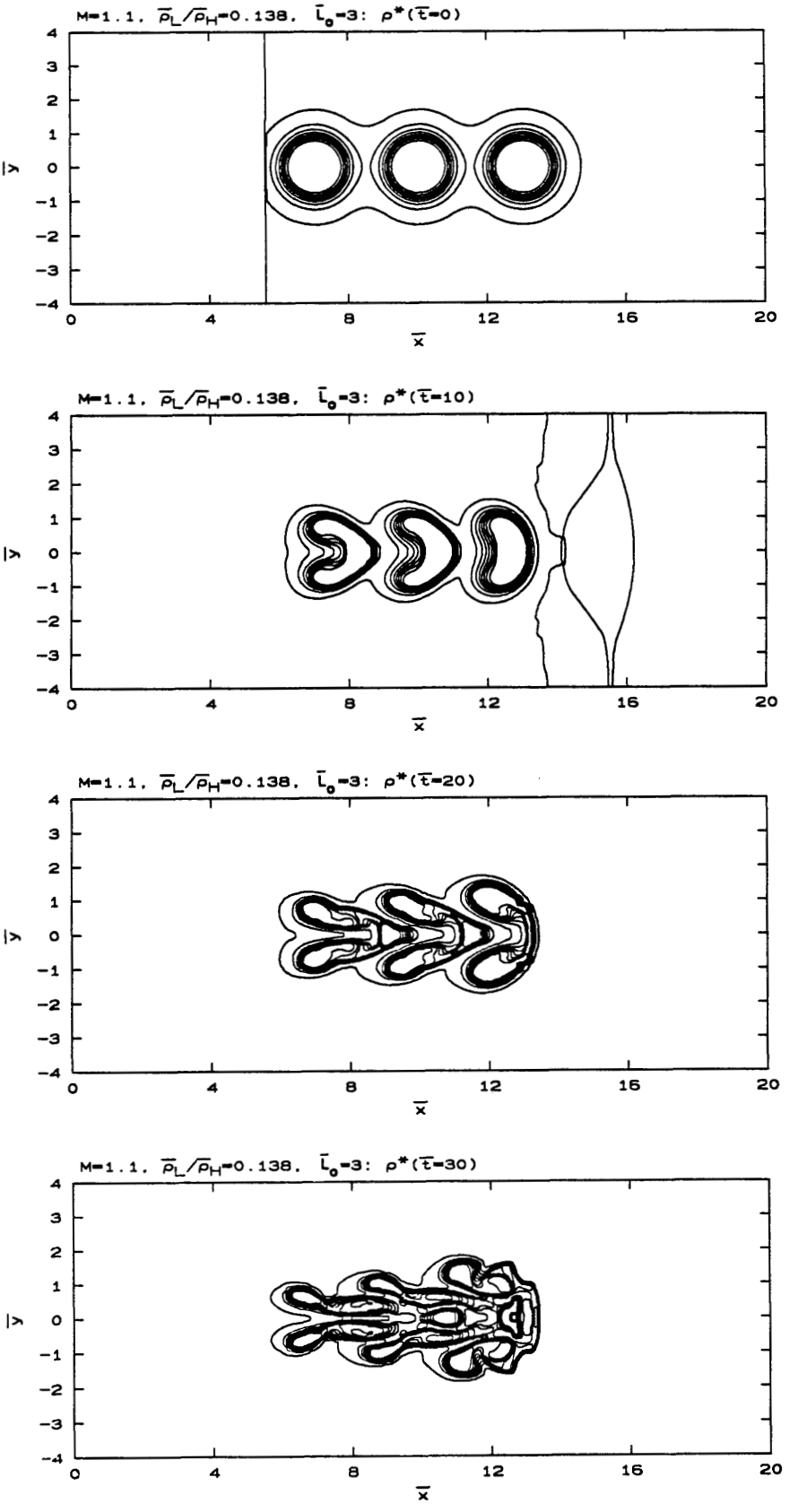

Figure 7.58 - Horizontal jet trio with M=1.1, $\overline{\rho}_L/\overline{\rho}_H = 0.138$, $\overline{L}_0 = 3$.

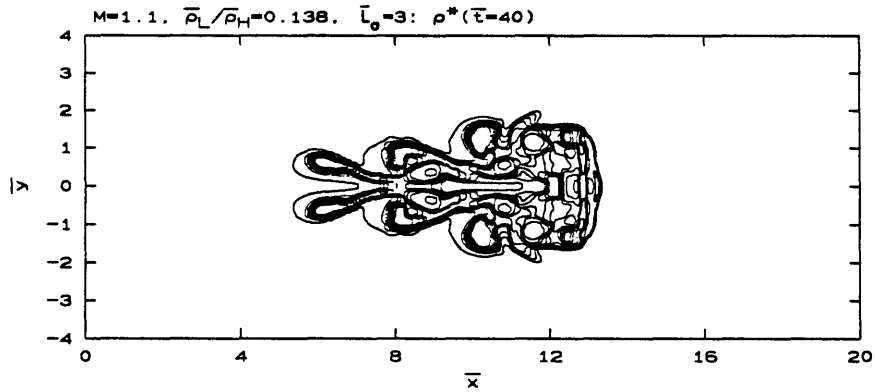
M=1.1. $\bar{\rho}_L/\bar{\rho}_H$=0.138. $\bar{l}_o$=3: $\rho^*(\bar{t}$=40)
$\bar{y}$
$\bar{x}$

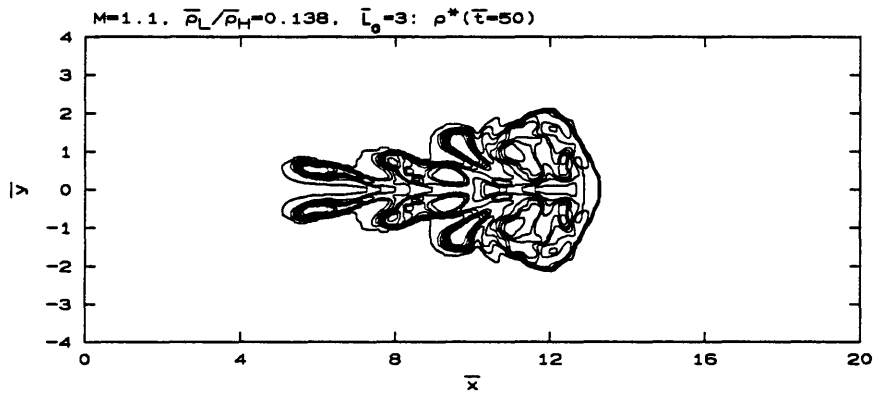
M=1.1. $\bar{\rho}_L/\bar{\rho}_H$=0.138. $\bar{l}_o$=3: $\rho^*(\bar{t}$=50)
$\bar{y}$
$\bar{x}$

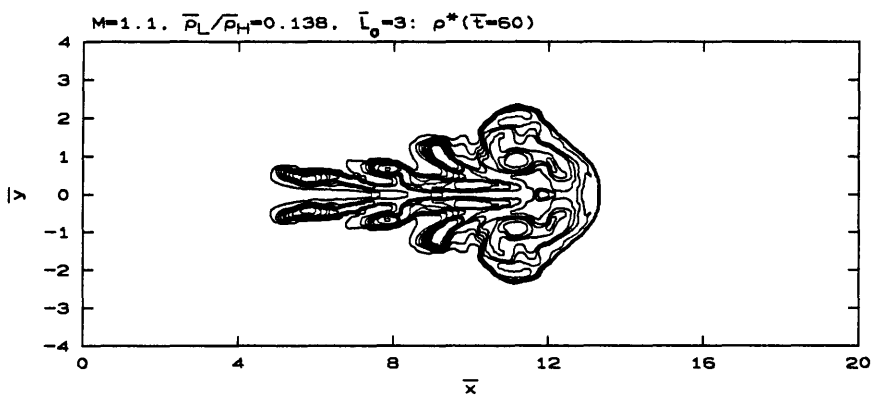
M=1.1. $\bar{\rho}_L/\bar{\rho}_H$=0.138. $\bar{l}_o$=3: $\rho^*(\bar{t}$=60)
$\bar{y}$
$\bar{x}$

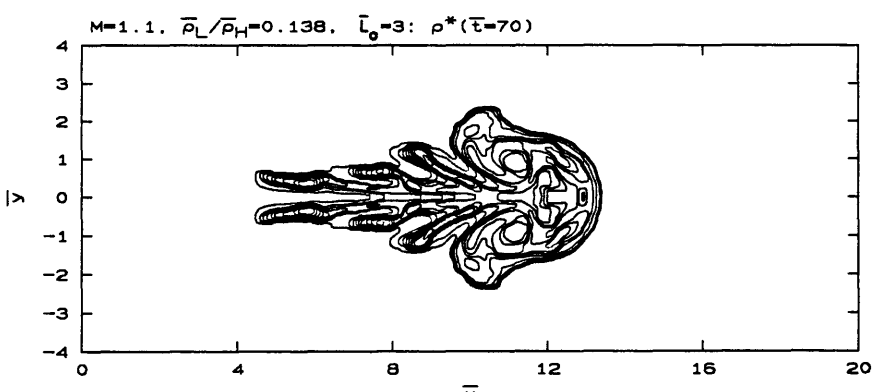
M=1.1. $\bar{\rho}_L/\bar{\rho}_H$=0.138. $\bar{l}_o$=3: $\rho^*(\bar{t}$=70)
$\bar{y}$
$\bar{x}$

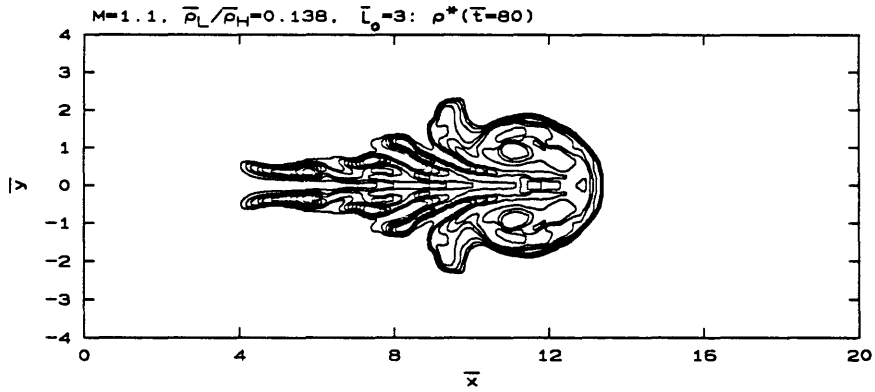
M=1.1. $\overline{\rho}_L/\overline{\rho}_H$=0.138. $\overline{l}_o$=3: $\rho^*(\overline{t}$=80)
4
3
2
1
0
−1
−2
−3
−4
$\overline{y}$
0
4
8
12
16
20
$\overline{x}$

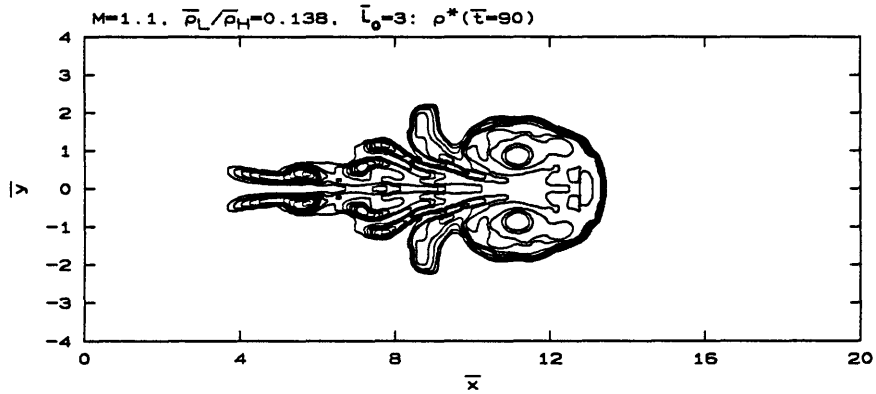
M=1.1. $\overline{\rho}_L/\overline{\rho}_H$=0.138. $\overline{l}_o$=3: $\rho^*(\overline{t}$=90)
4
3
2
1
0
−1
−2
−3
−4
$\overline{y}$
0
4
8
12
16
20
$\overline{x}$

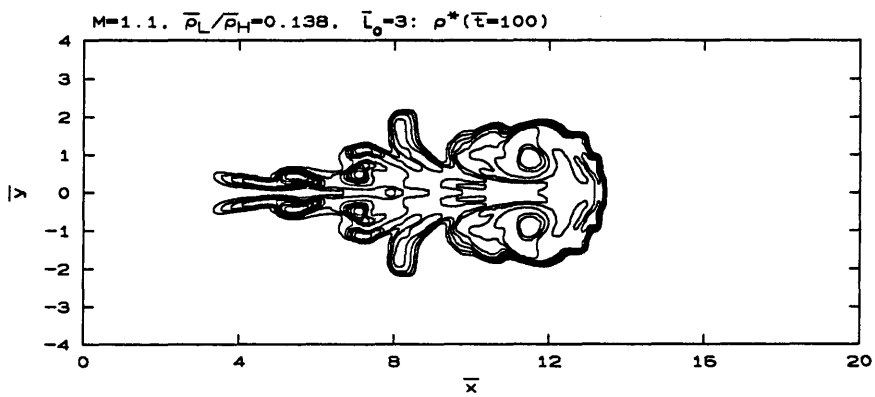
M=1.1. $\overline{\rho}_L/\overline{\rho}_H$=0.138. $\overline{l}_o$=3: $\rho^*(\overline{t}$=100)
4
3
2
1
0
−1
−2
−3
−4
$\overline{y}$
0
4
8
12
16
20
$\overline{x}$

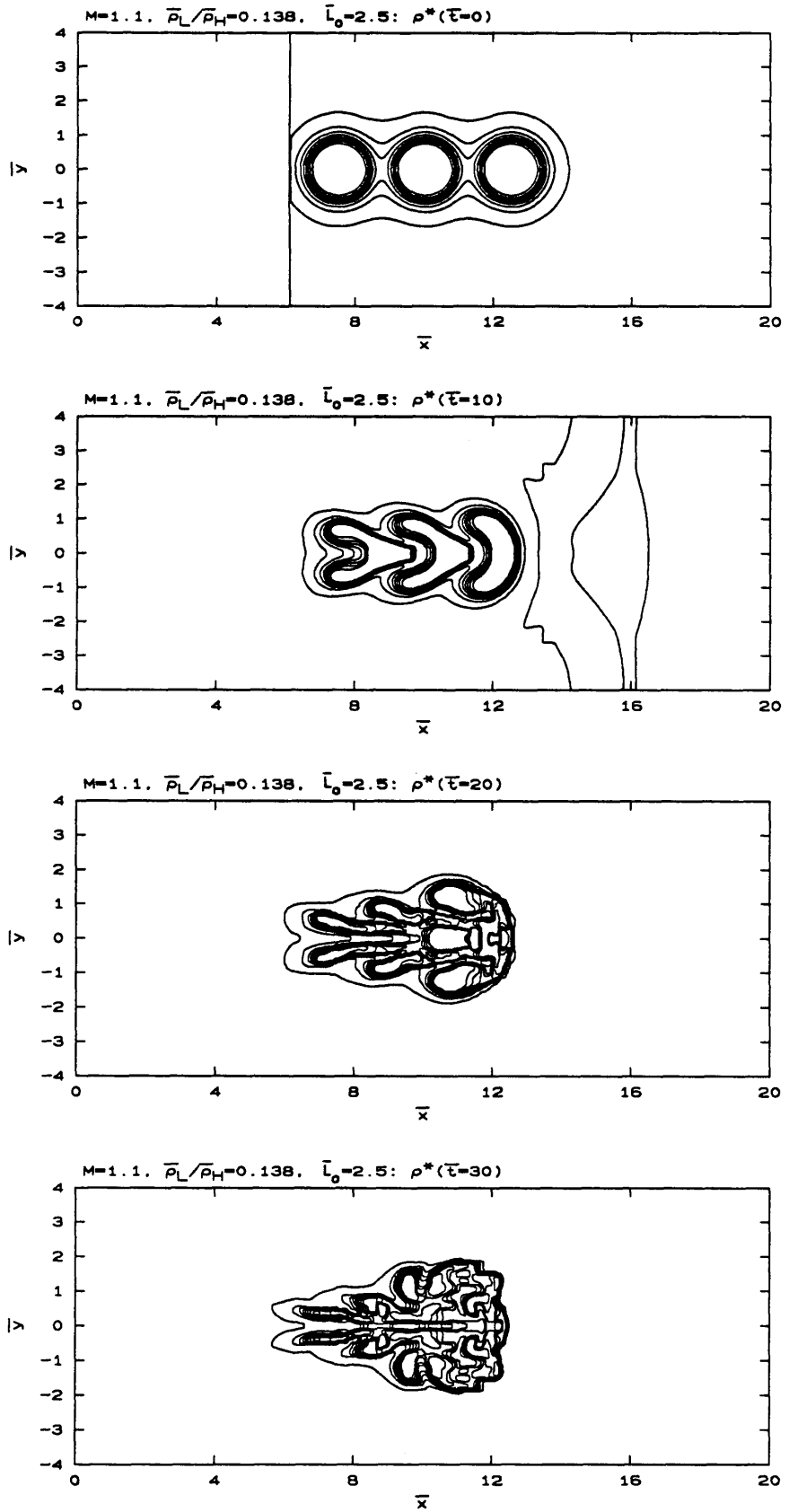

Figure 7.59 - Horizontal jet trio with M=1.1, $\overline{\rho}_L/\overline{\rho}_H = 0.138$, $\overline{L}_0 = 2.5$.

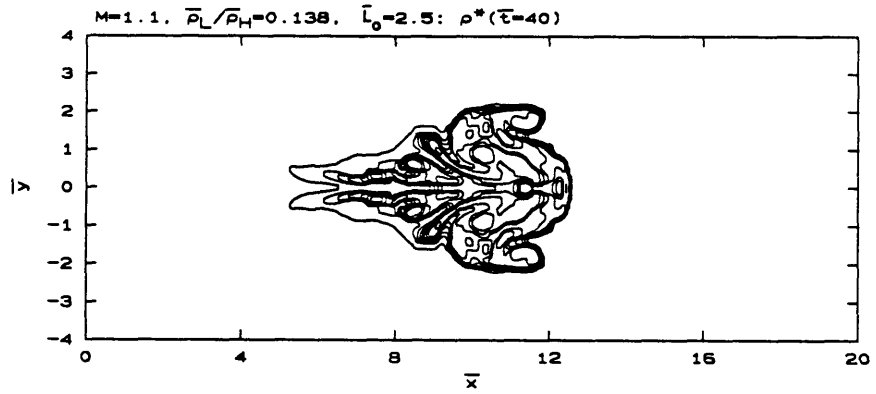
M=1.1. $\bar{\rho}_L/\bar{\rho}_H$=0.138. $\bar{L}_0$=2.5: $\rho^*(\bar{t}$=40)
$\bar{y}$
$\bar{x}$

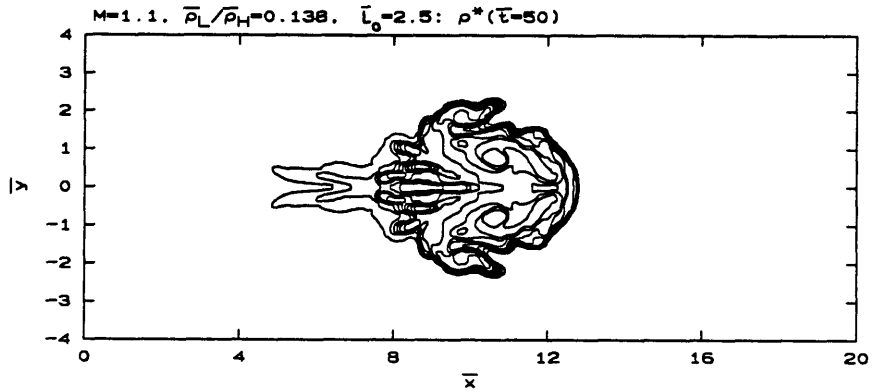
M=1.1. $\bar{\rho}_L/\bar{\rho}_H$=0.138. $\bar{L}_0$=2.5: $\rho^*(\bar{t}$=50)
$\bar{y}$
$\bar{x}$

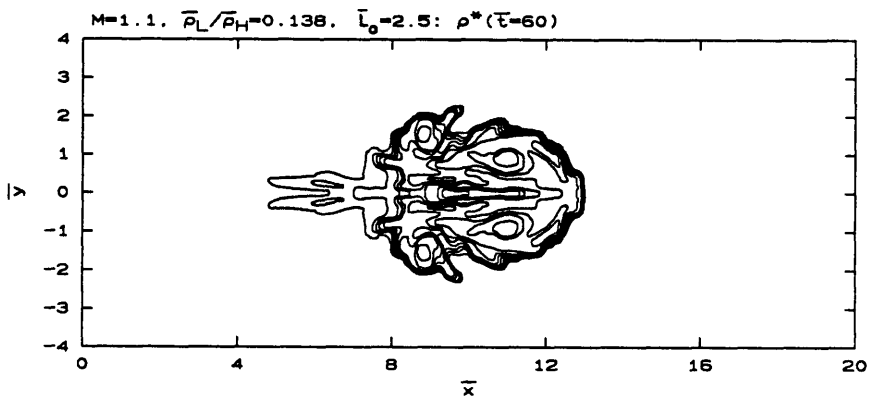
M=1.1. $\bar{\rho}_L/\bar{\rho}_H$=0.138. $\bar{L}_0$=2.5: $\rho^*(\bar{t}$=60)
$\bar{y}$
$\bar{x}$

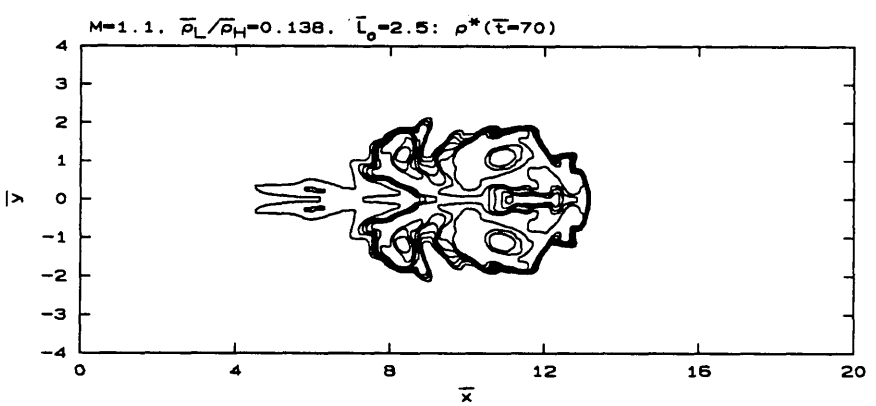
M=1.1. $\bar{\rho}_L/\bar{\rho}_H$=0.138. $\bar{L}_0$=2.5: $\rho^*(\bar{t}$=70)
$\bar{y}$
$\bar{x}$

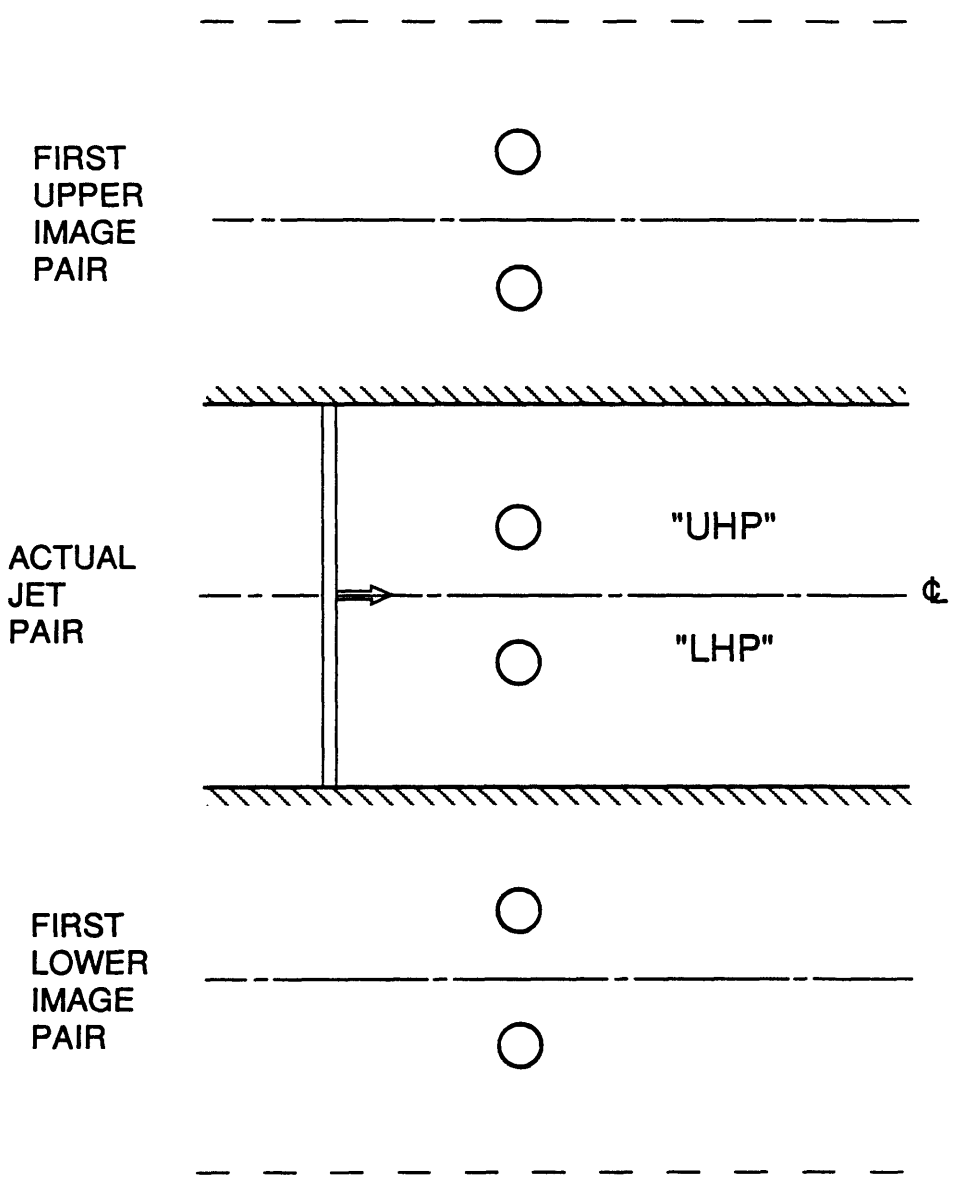

Figure 7.60 - Vertical jet pair: equivalent infinite array of jets.

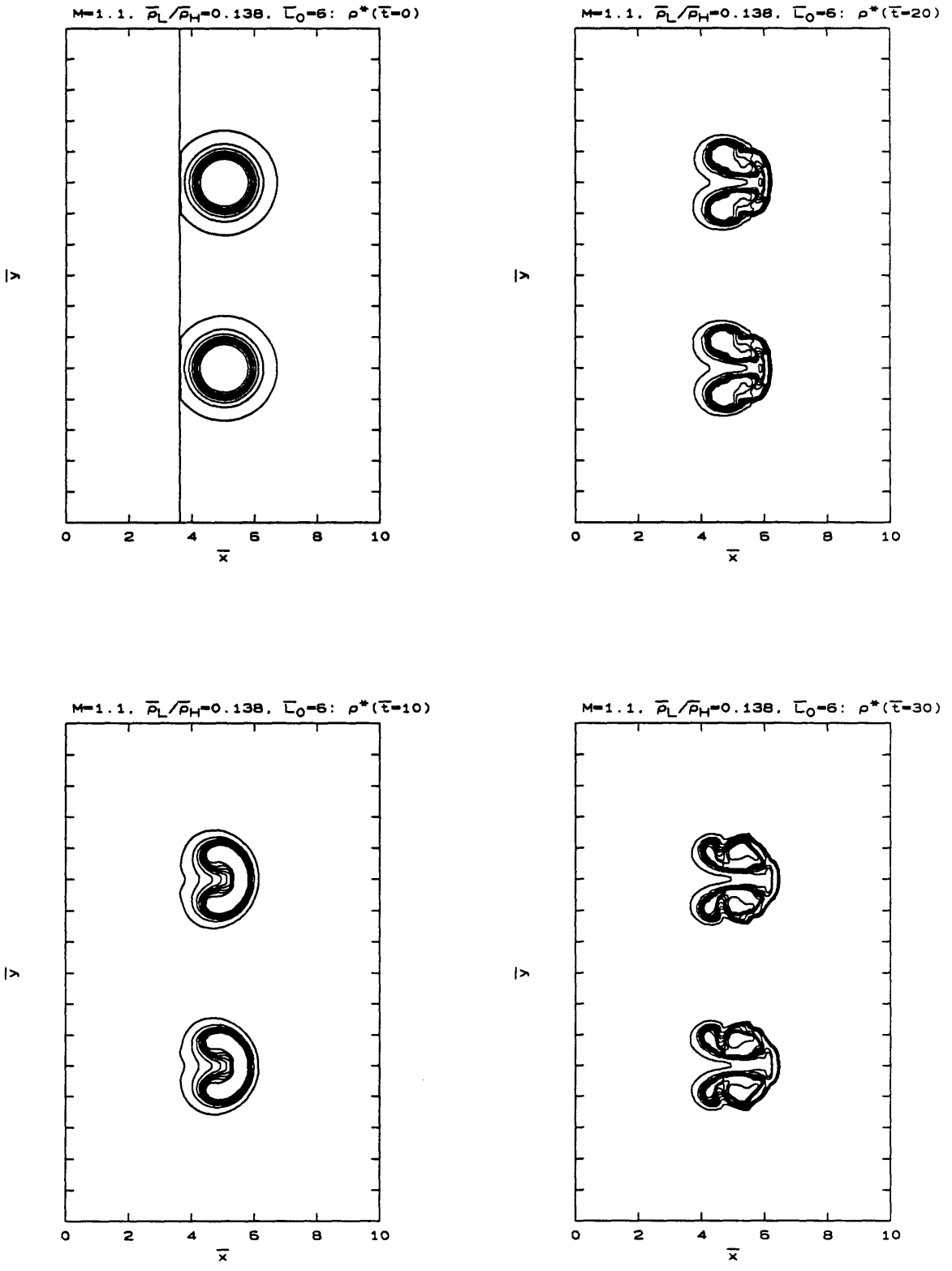

Figure 7.61 - Symmetric vertical jet pair with M=1.1, $\overline{\rho}_L/\overline{\rho}_H = 0.138$, $\overline{L}_0 = 6$.

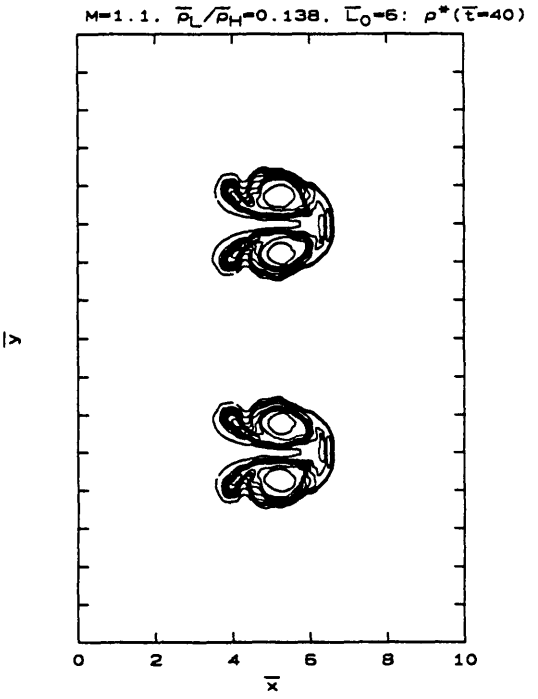
M=1.1, $\bar{\rho}_L/\bar{\rho}_H$=0.138, $\bar{L}_0$=6: $\rho^*(\bar{t}$=40)
$\bar{y}$
0
2
4
6
8
10
$\bar{x}$

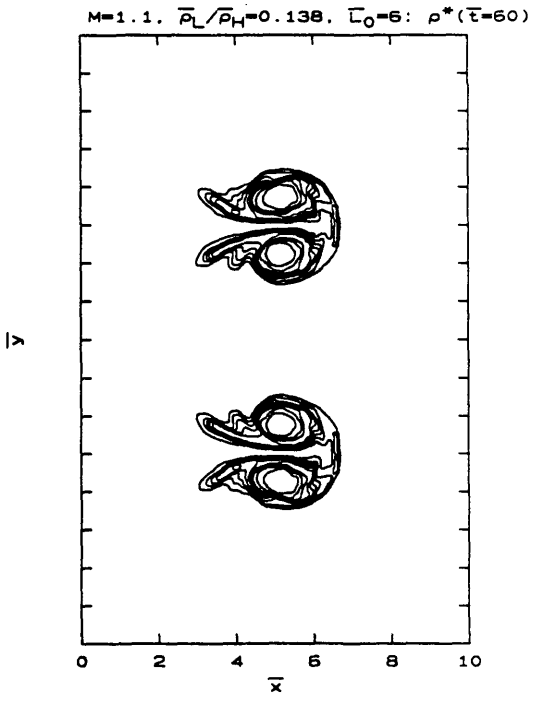
M=1.1, $\bar{\rho}_L/\bar{\rho}_H$=0.138, $\bar{L}_0$=6: $\rho^*(\bar{t}$=60)
$\bar{y}$
0
2
4
6
8
10
$\bar{x}$

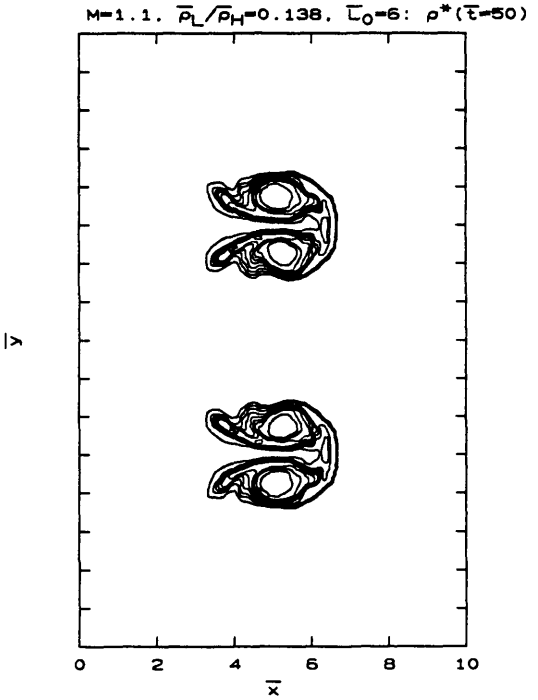
M=1.1, $\bar{\rho}_L/\bar{\rho}_H$=0.138, $\bar{L}_0$=6: $\rho^*(\bar{t}$=50)
$\bar{y}$
0
2
4
6
8
10
$\bar{x}$

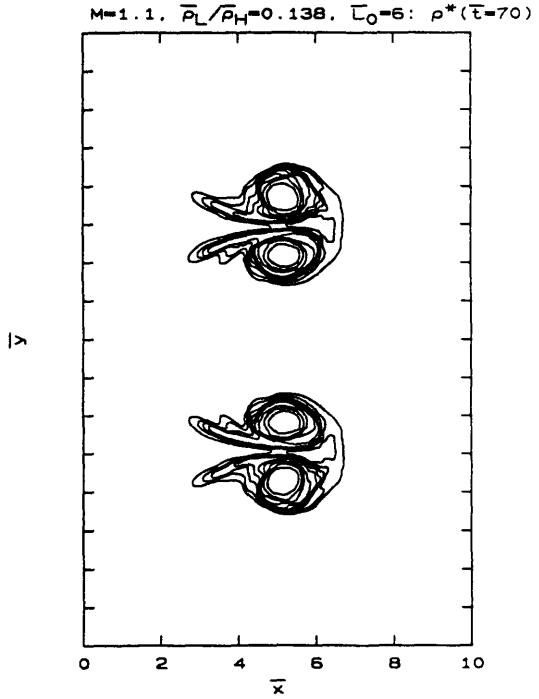
M=1.1, $\bar{\rho}_L/\bar{\rho}_H$=0.138, $\bar{L}_0$=6: $\rho^*(\bar{t}$=70)
$\bar{y}$
0
2
4
6
8
10
$\bar{x}$

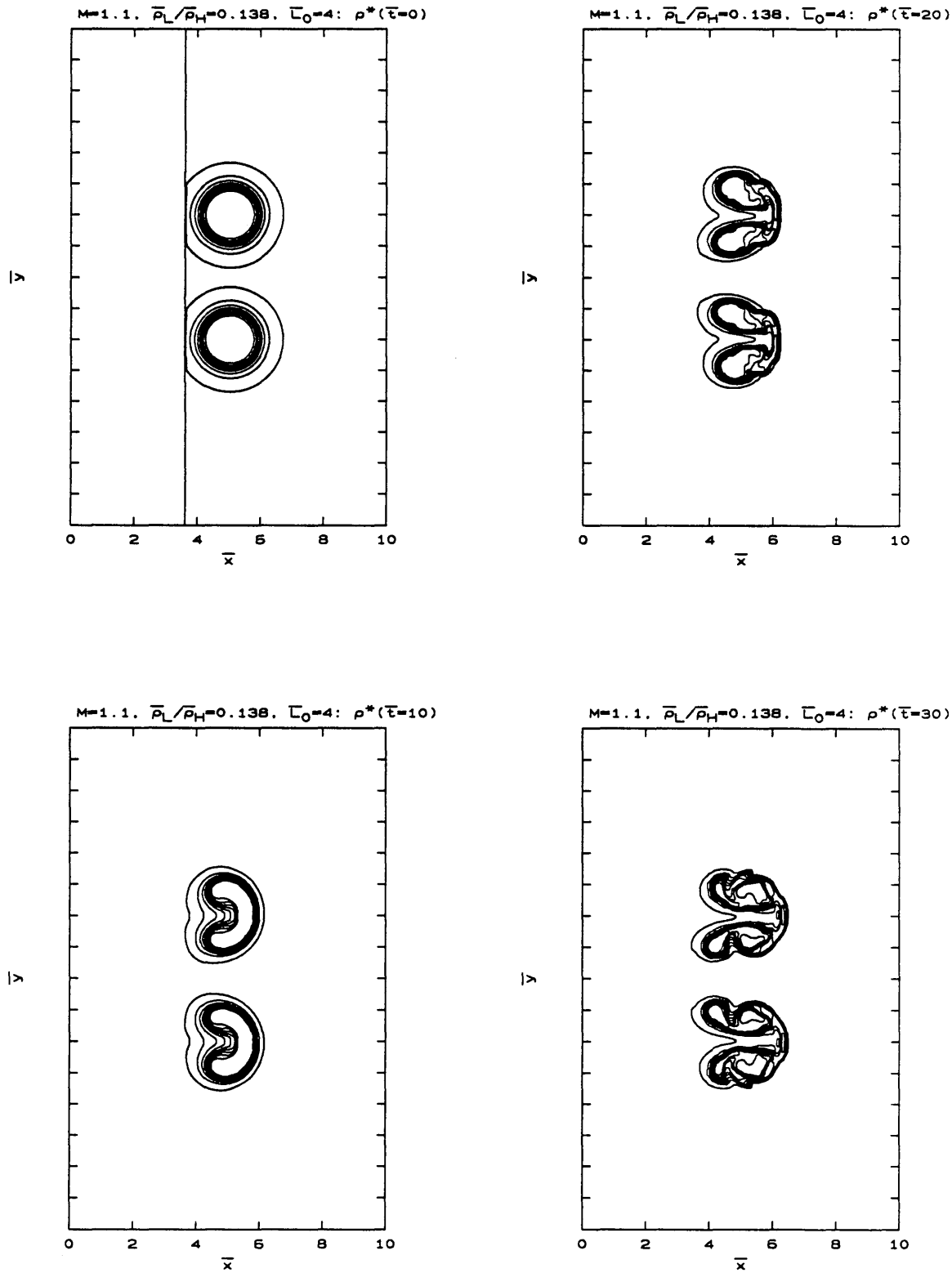

Figure 7.62 - Symmetric vertical jet pair with M=1.1, $\overline{\rho}_L/\overline{\rho}_H = 0.138$, $\overline{L}_0 = 4$.

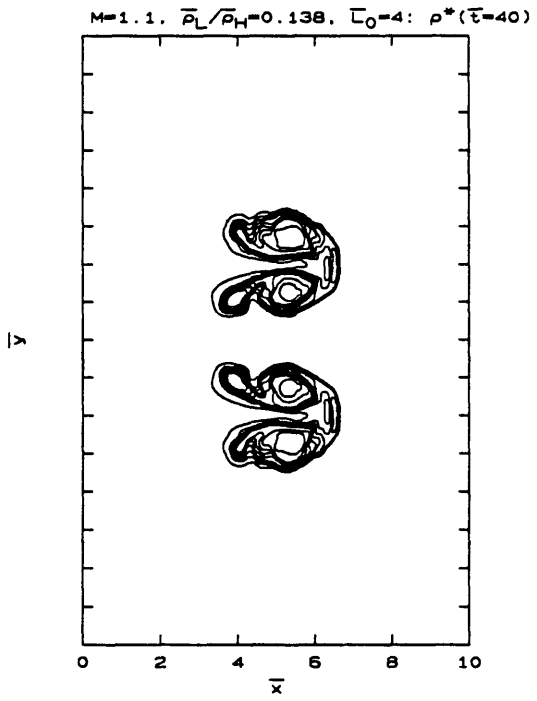
M=1.1, $\bar{\rho}_L/\bar{\rho}_H$=0.138, $\bar{L}_0$=4: $\rho^*(\bar{t}$=40)
$\bar{y}$
0
2
4
6
8
10
$\bar{x}$

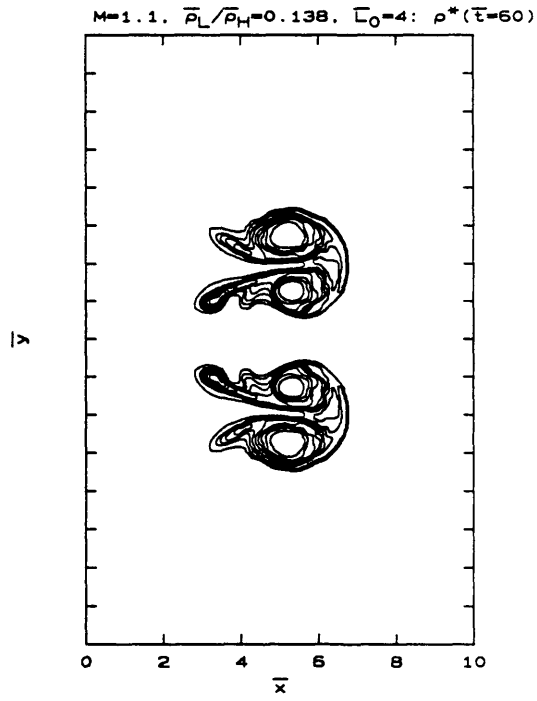
M=1.1, $\bar{\rho}_L/\bar{\rho}_H$=0.138, $\bar{L}_0$=4: $\rho^*(\bar{t}$=60)
$\bar{y}$
0
2
4
6
8
10
$\bar{x}$

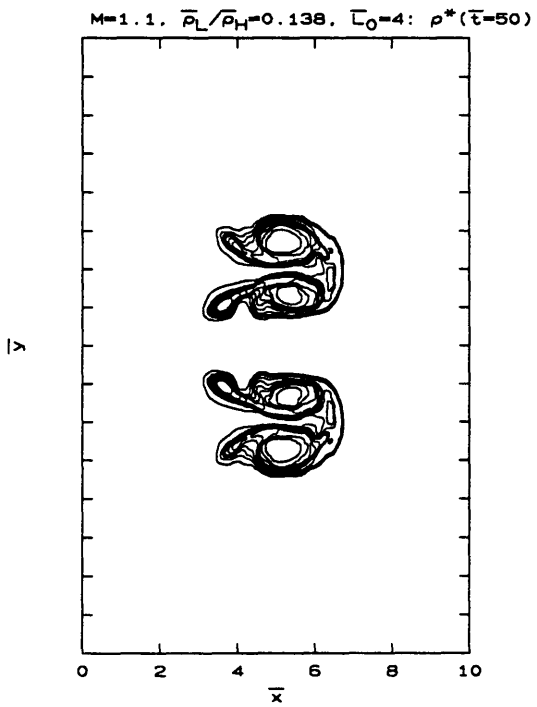
M=1.1, $\bar{\rho}_L/\bar{\rho}_H$=0.138, $\bar{L}_0$=4: $\rho^*(\bar{t}$=50)
$\bar{y}$
0
2
4
6
8
10
$\bar{x}$

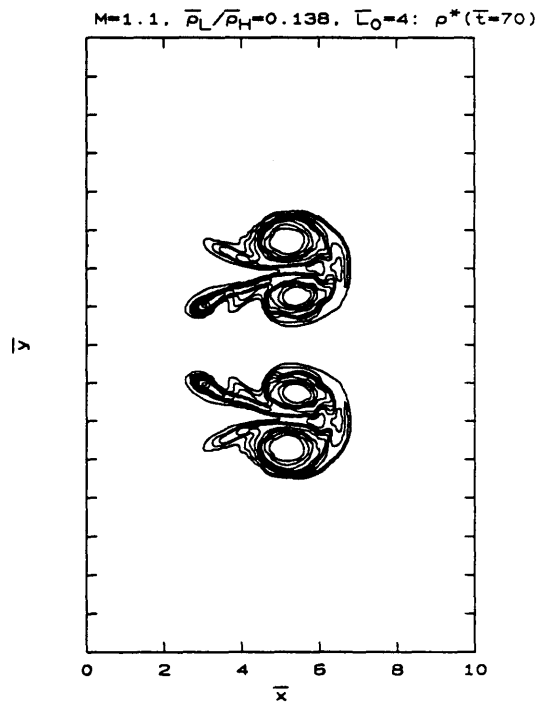
M=1.1, $\bar{\rho}_L/\bar{\rho}_H$=0.138, $\bar{L}_0$=4: $\rho^*(\bar{t}$=70)
$\bar{y}$
0
2
4
6
8
10
$\bar{x}$

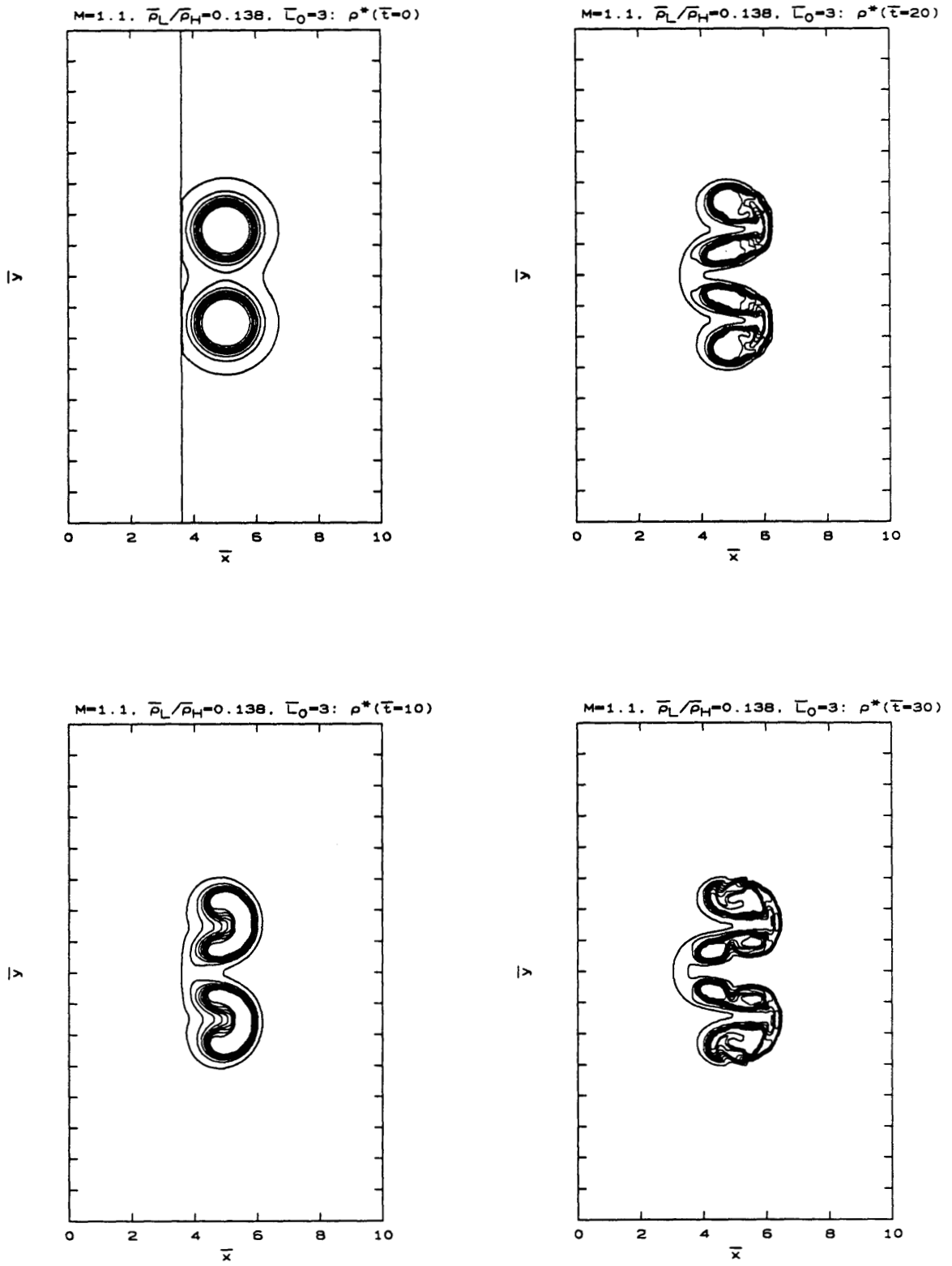

Figure 7.63 - Symmetric vertical jet pair with M=1.1, $\overline{\rho}_L/\overline{\rho}_H = 0.138$, $\overline{L}_0 = 3$.

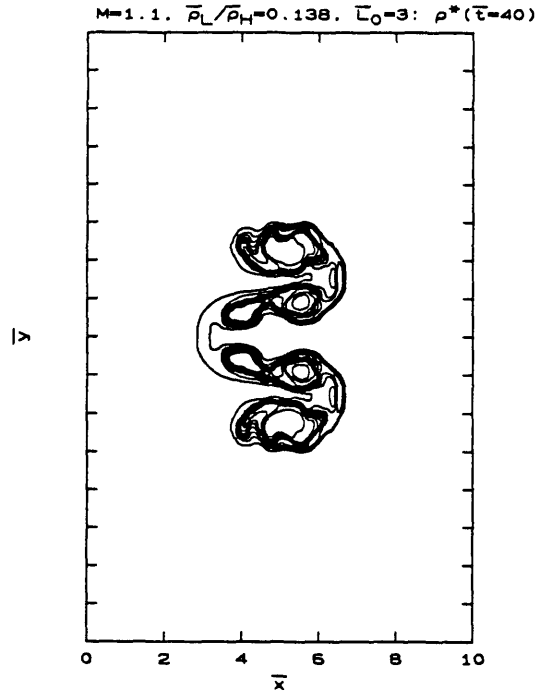
M=1.1. $\overline{\rho}_L/\overline{\rho}_H$=0.138. $\overline{L}_0$=3: $\rho^*(\overline{t}$=40)
$\overline{y}$
0
2
4
6
8
10
$\overline{x}$

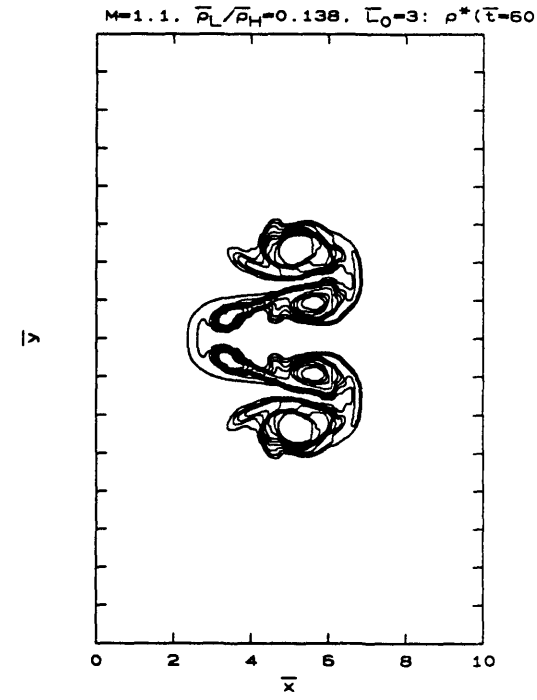
M=1.1. $\overline{\rho}_L/\overline{\rho}_H$=0.138. $\overline{L}_0$=3: $\rho^*(\overline{t}$=60)
$\overline{y}$
0
2
4
6
8
10
$\overline{x}$

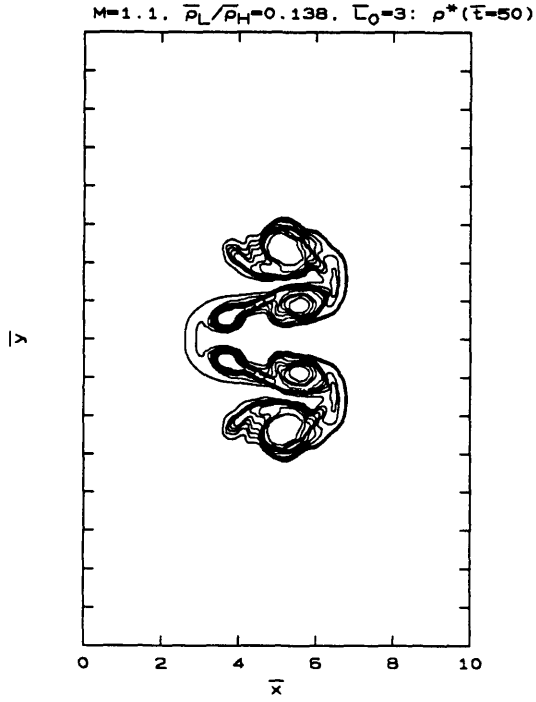
M=1.1. $\overline{\rho}_L/\overline{\rho}_H$=0.138. $\overline{L}_0$=3: $\rho^*(\overline{t}$=50)
$\overline{y}$
0
2
4
6
8
10
$\overline{x}$

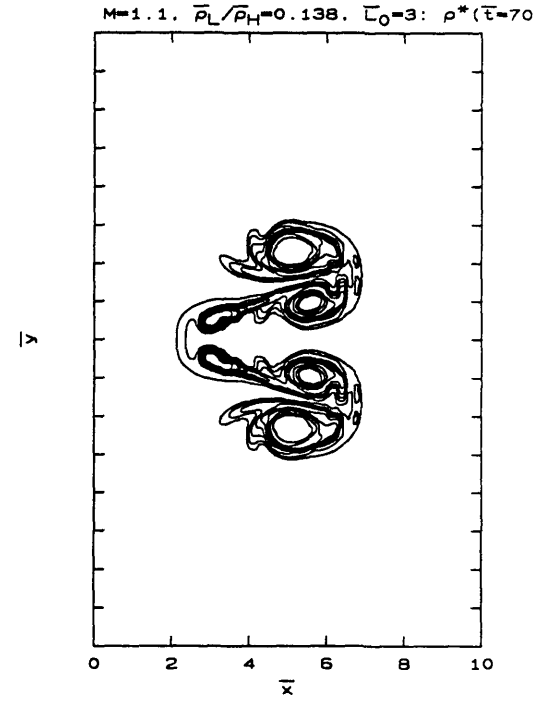
M=1.1. $\overline{\rho}_L/\overline{\rho}_H$=0.138. $\overline{L}_0$=3: $\rho^*(\overline{t}$=70)
$\overline{y}$
0
2
4
6
8
10
$\overline{x}$

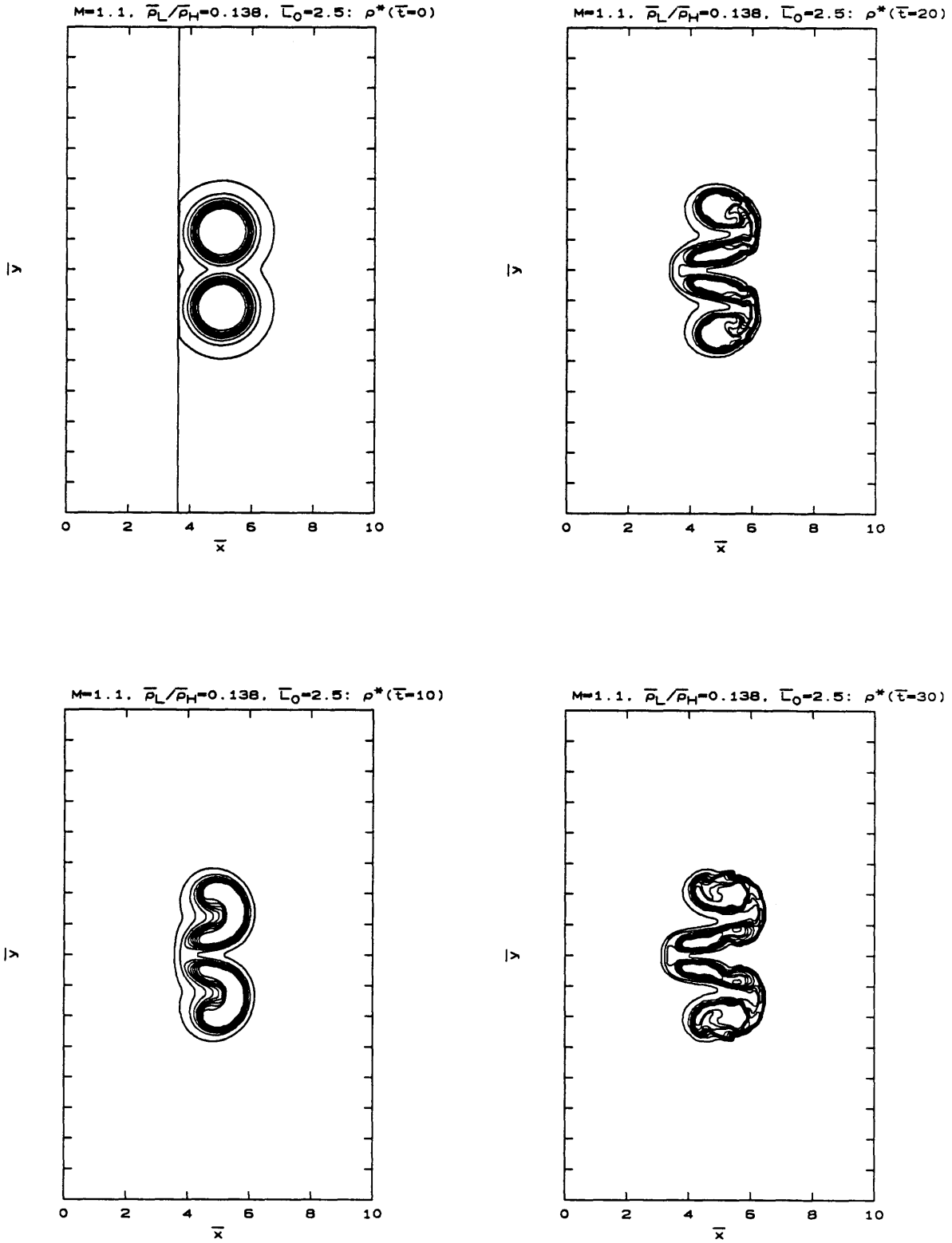

Figure 7.64 - Symmetric vertical jet pair with M=1.1, $\overline{\rho}_L/\overline{\rho}_H = 0.138$, $\overline{L}_0 = 2.5$.

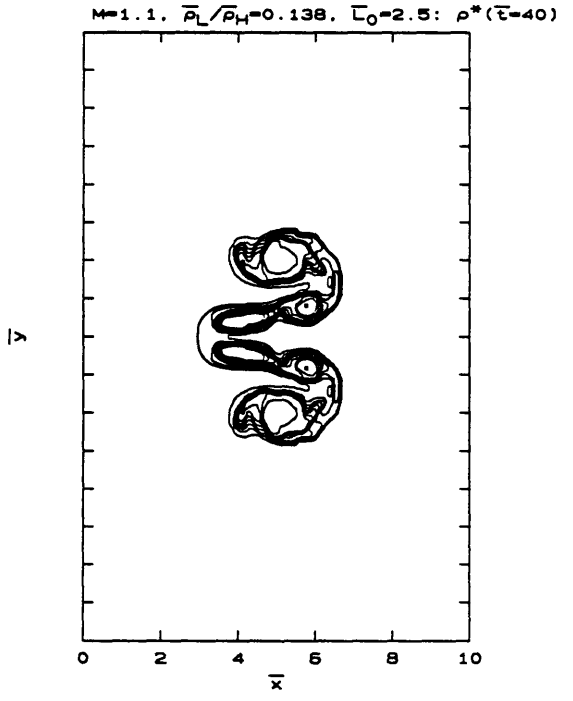
M=1.1, $\bar{\rho}_L/\bar{\rho}_H$=0.138, $\bar{L}_0$=2.5: $\rho^*(\bar{t}$=40)
$\bar{y}$
0
2
4
6
8
10
$\bar{x}$

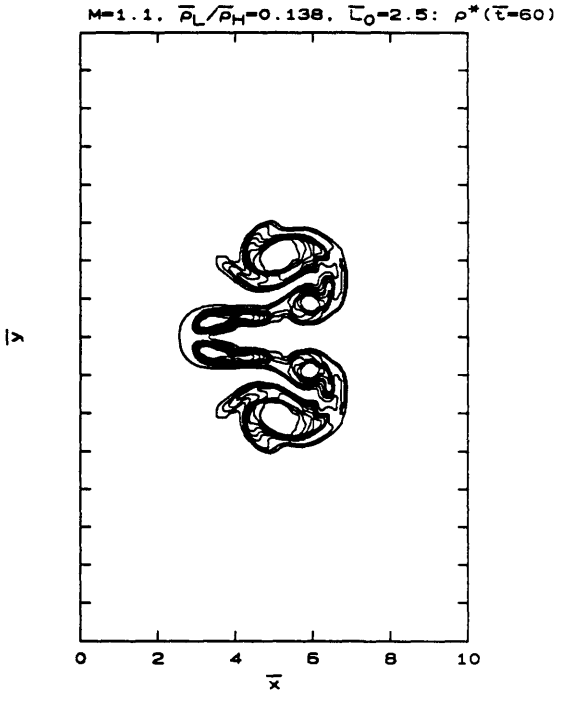
M=1.1, $\bar{\rho}_L/\bar{\rho}_H$=0.138, $\bar{L}_0$=2.5: $\rho^*(\bar{t}$=60)
$\bar{y}$
0
2
4
6
8
10
$\bar{x}$

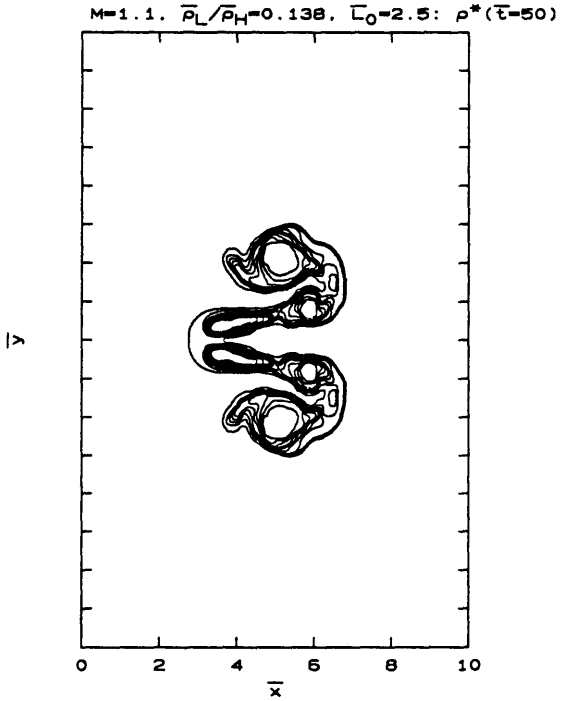
M=1.1, $\bar{\rho}_L/\bar{\rho}_H$=0.138, $\bar{L}_0$=2.5: $\rho^*(\bar{t}$=50)
$\bar{y}$
0
2
4
6
8
10
$\bar{x}$

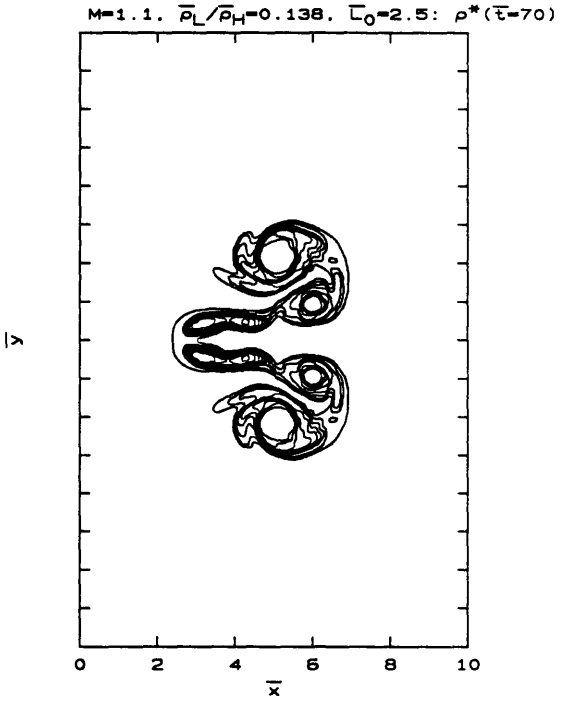
M=1.1, $\bar{\rho}_L/\bar{\rho}_H$=0.138, $\bar{L}_0$=2.5: $\rho^*(\bar{t}$=70)
$\bar{y}$
0
2
4
6
8
10
$\bar{x}$

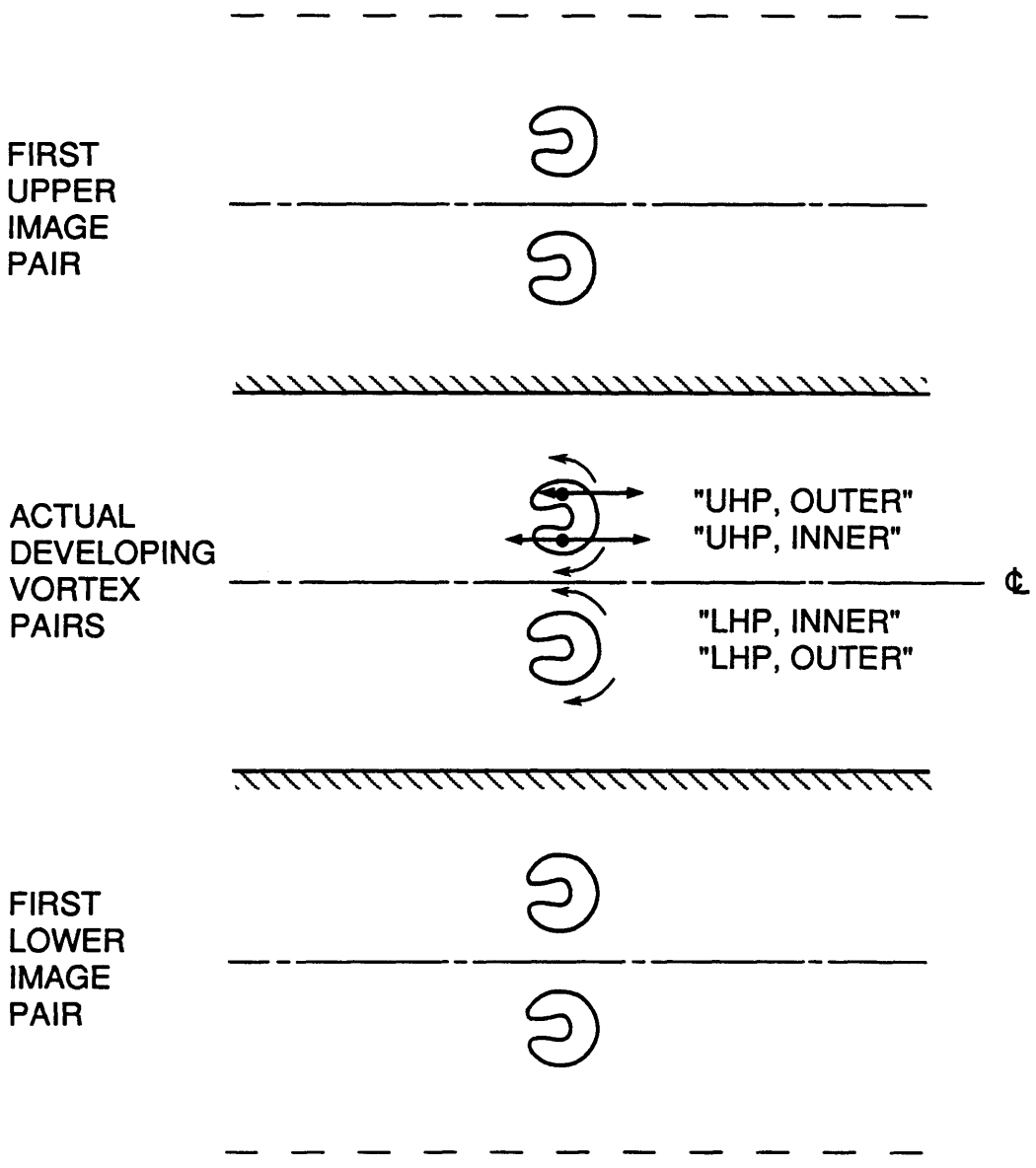

Figure 7.65 - Induced velocities for the vertical jet pair.

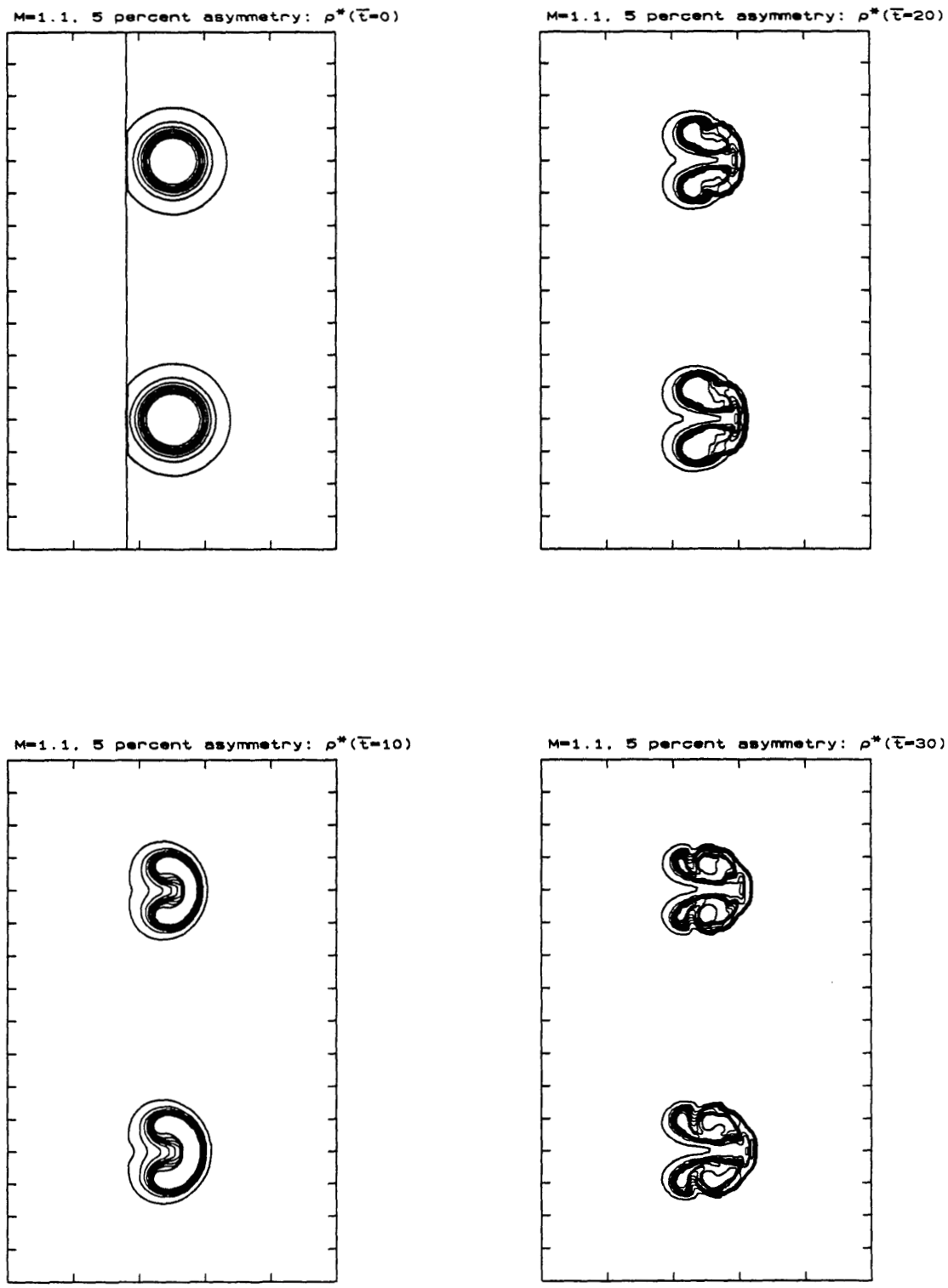

Figure 7.66 - Asymmetric vertical jet pair : weak shock and slight asymmetry.

M=1.1, 5 percent asymmetry: $\rho^*(\bar{t}=40)$

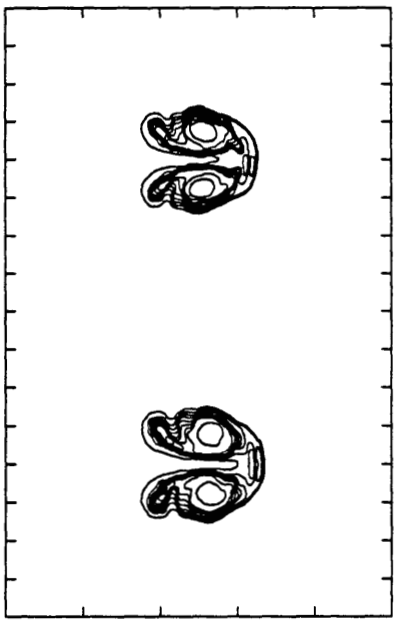

M=1.1, 5 percent asymmetry: $\rho^*(\bar{t}=50)$

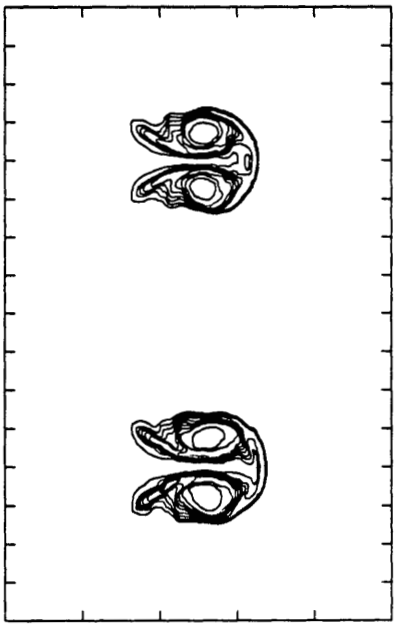

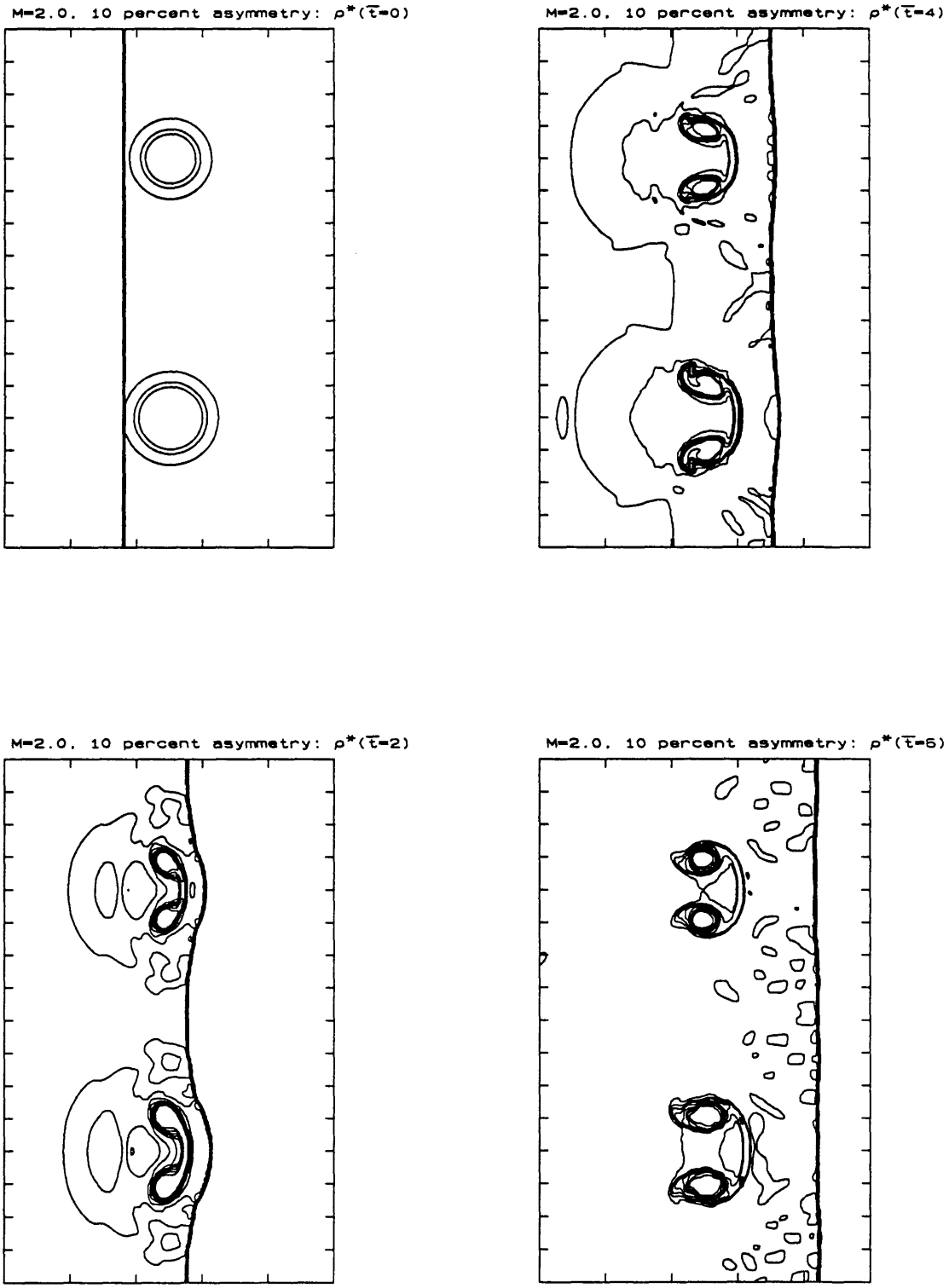

Figure 7.67 - Asymmetric vertical jet pair : strong shock and moderate asymmetry.

M=2.0, 10 percent asymmetry: $\rho^*(\bar{t}=8)$

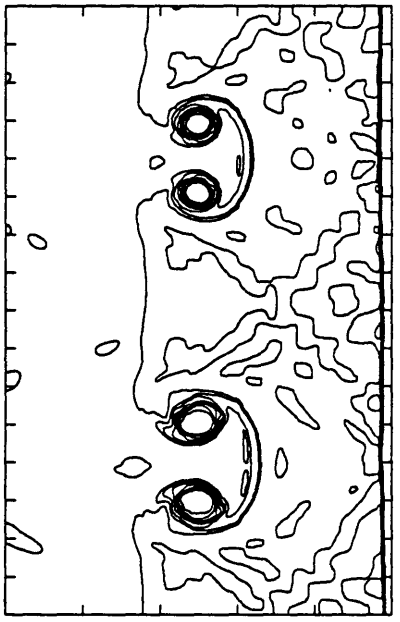

M=2.0, 10 percent asymmetry: $\rho^*(\bar{t}=12)$

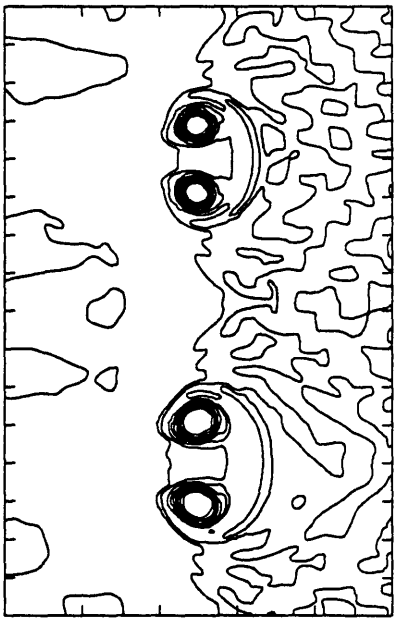

M=2.0, 10 percent asymmetry: $\rho^*(\bar{t}=10)$

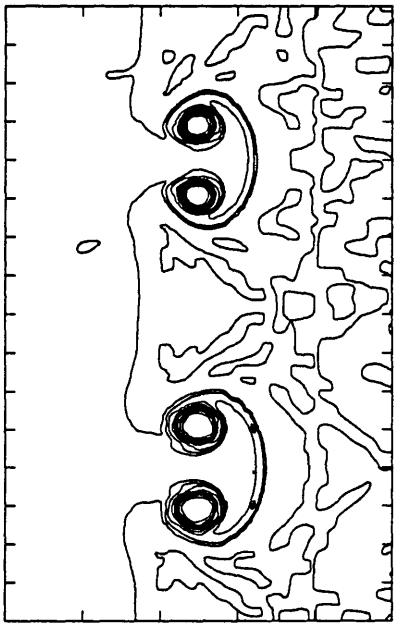

M=2.0, 10 percent asymmetry: $\rho^*(\bar{t}=14)$

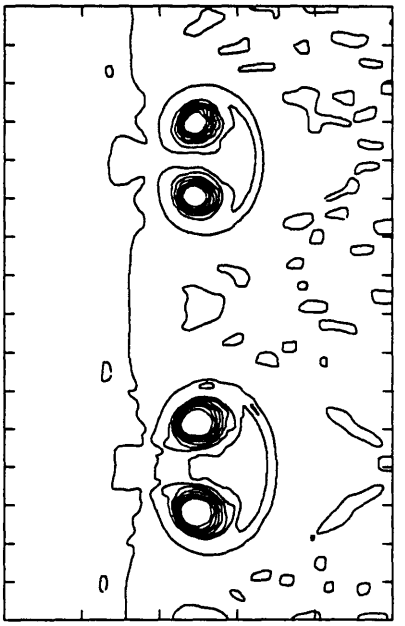

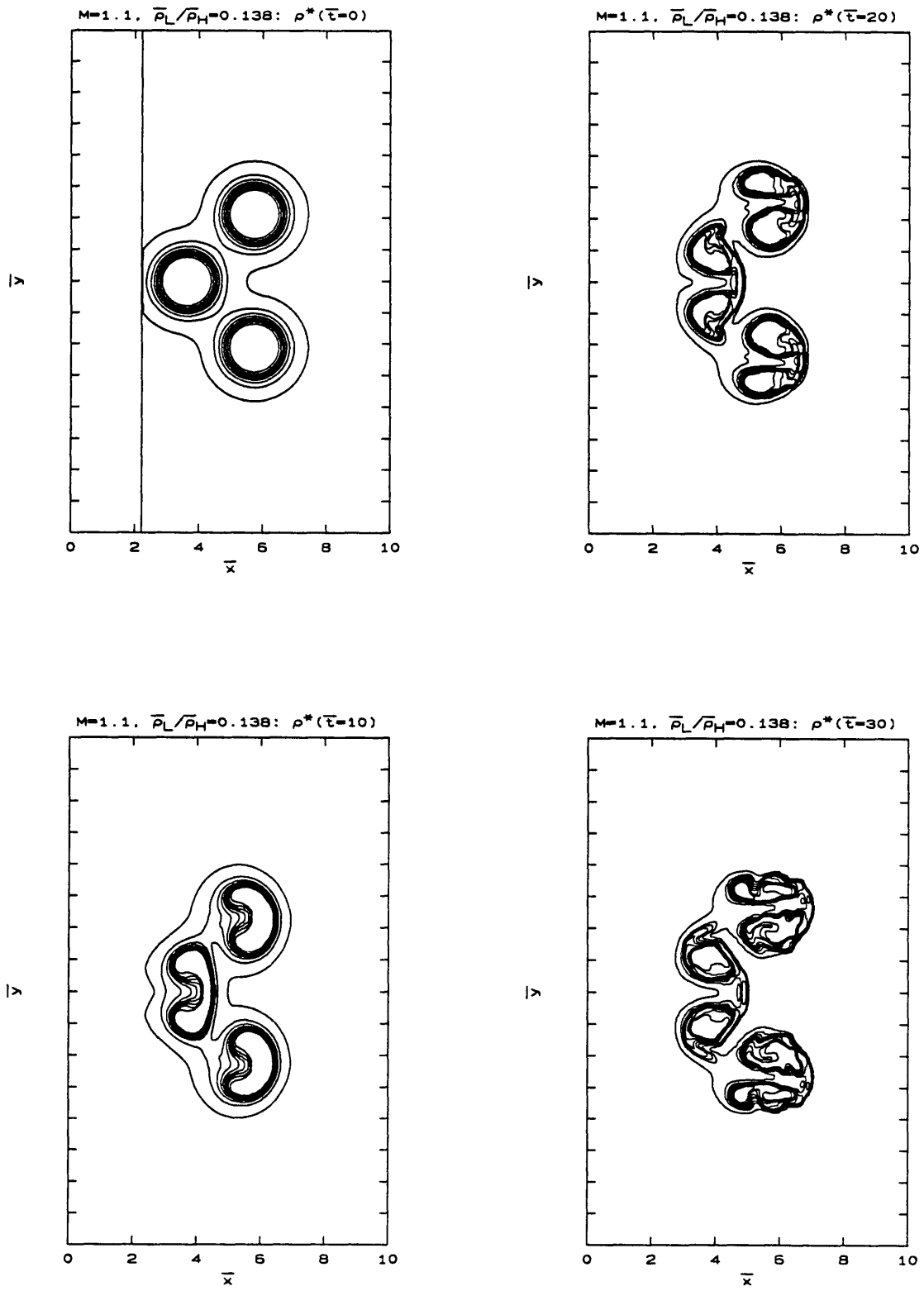

Figure 7.68 - Equilateral jet trio with M=1.1 and $\overline{\rho}_L/\overline{\rho}_H = 0.138$.

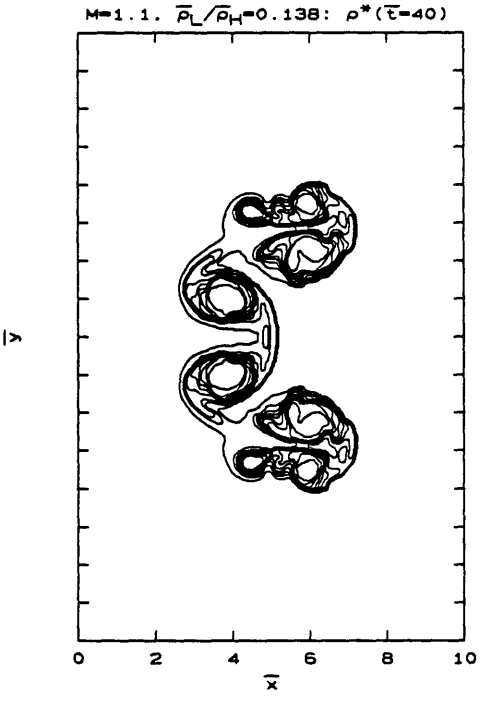
M=1.1. $\overline{\rho}_L/\overline{\rho}_H$=0.138: $\rho^*(\overline{t}$=40)
$\overline{y}$
0
2
4
6
8
10
$\overline{x}$

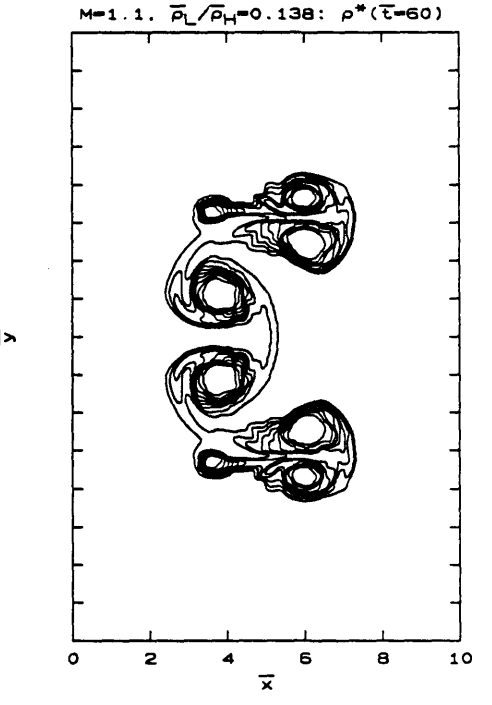
M=1.1. $\overline{\rho}_L/\overline{\rho}_H$=0.138: $\rho^*(\overline{t}$=60)
$\overline{y}$
0
2
4
6
8
10
$\overline{x}$

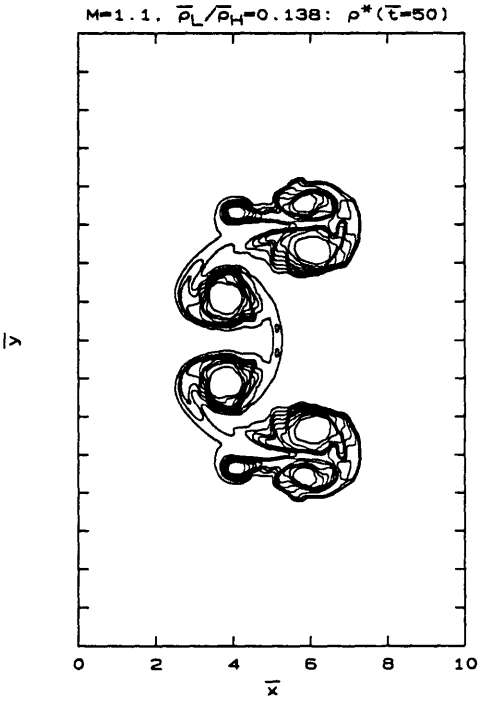
M=1.1. $\overline{\rho}_L/\overline{\rho}_H$=0.138: $\rho^*(\overline{t}$=50)
$\overline{y}$
0
2
4
6
8
10
$\overline{x}$

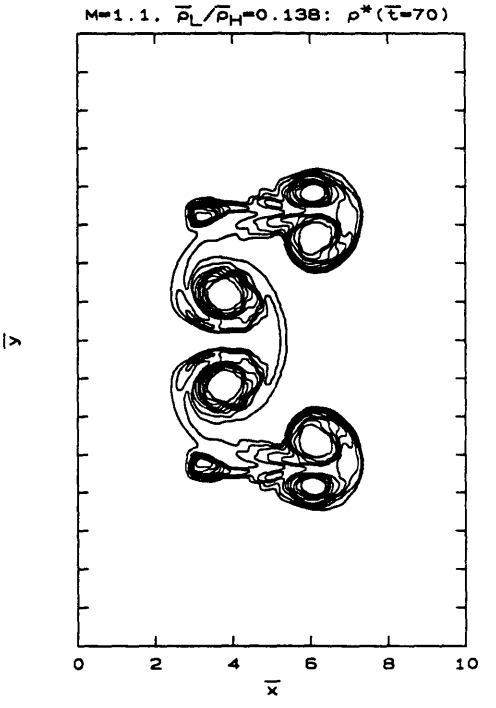
M=1.1. $\overline{\rho}_L/\overline{\rho}_H$=0.138: $\rho^*(\overline{t}$=70)
$\overline{y}$
0
2
4
6
8
10
$\overline{x}$

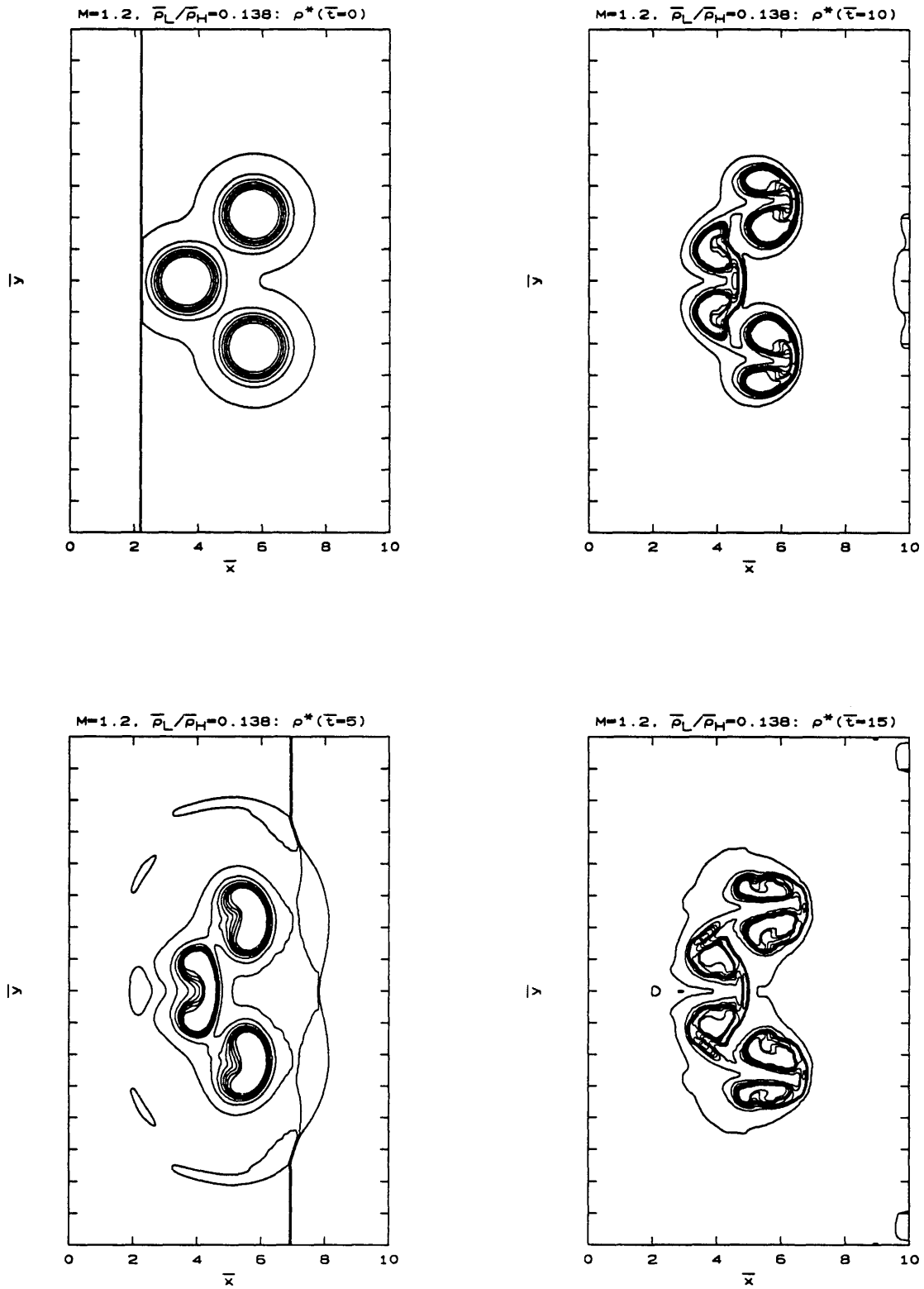

Figure 7.69 - Equilateral jet trio with M=1.2 and $\bar{\rho}_L/\bar{\rho}_H = 0.138$.

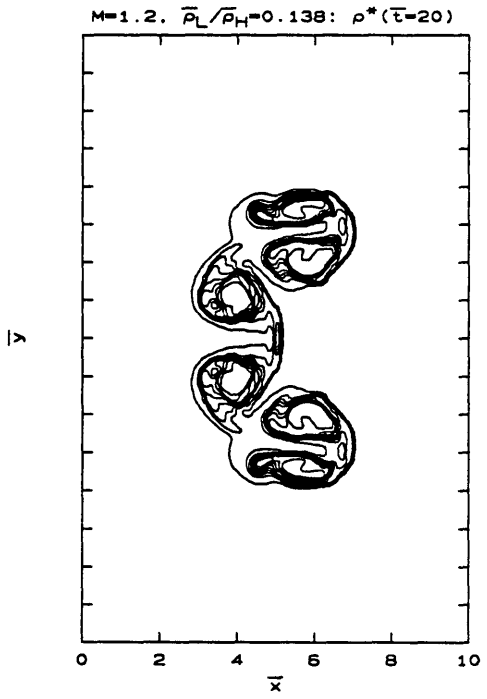
M=1.2. $\bar{\rho}_L/\bar{\rho}_H$=0.138: $\rho^*(\bar{t}$=20)
$\bar{y}$
0
2
4
6
8
10
$\bar{x}$

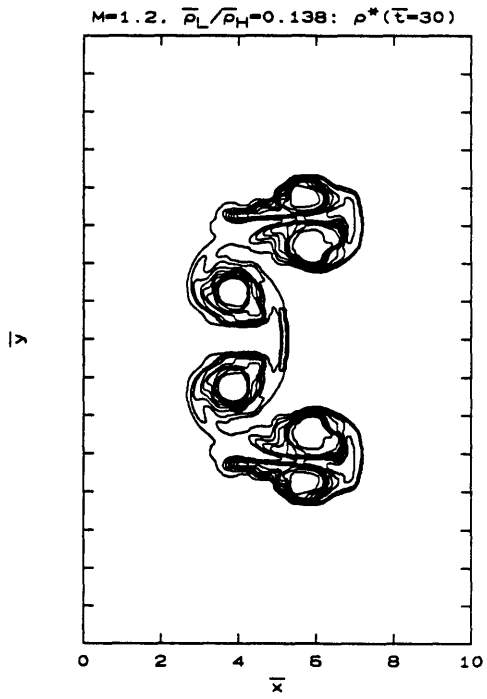
M=1.2. $\bar{\rho}_L/\bar{\rho}_H$=0.138: $\rho^*(\bar{t}$=30)
$\bar{y}$
0
2
4
6
8
10
$\bar{x}$

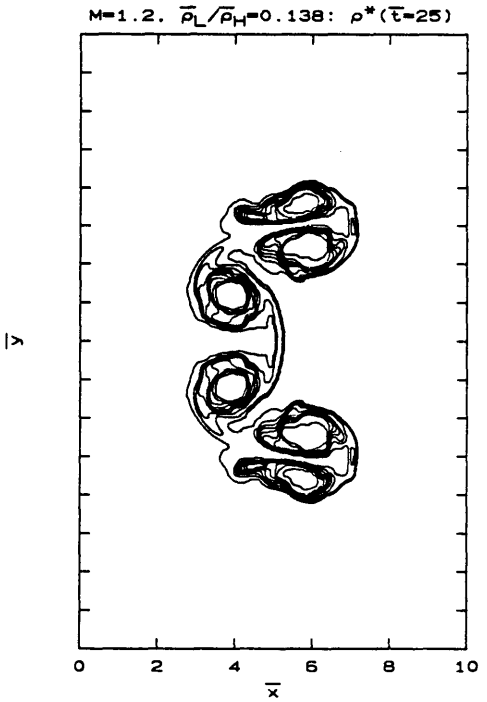
M=1.2. $\bar{\rho}_L/\bar{\rho}_H$=0.138: $\rho^*(\bar{t}$=25)
$\bar{y}$
0
2
4
6
8
10
$\bar{x}$

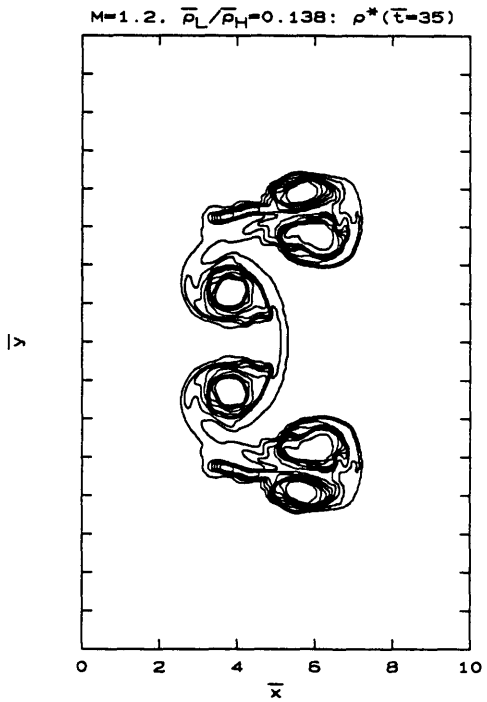
M=1.2. $\bar{\rho}_L/\bar{\rho}_H$=0.138: $\rho^*(\bar{t}$=35)
$\bar{y}$
0
2
4
6
8
10
$\bar{x}$

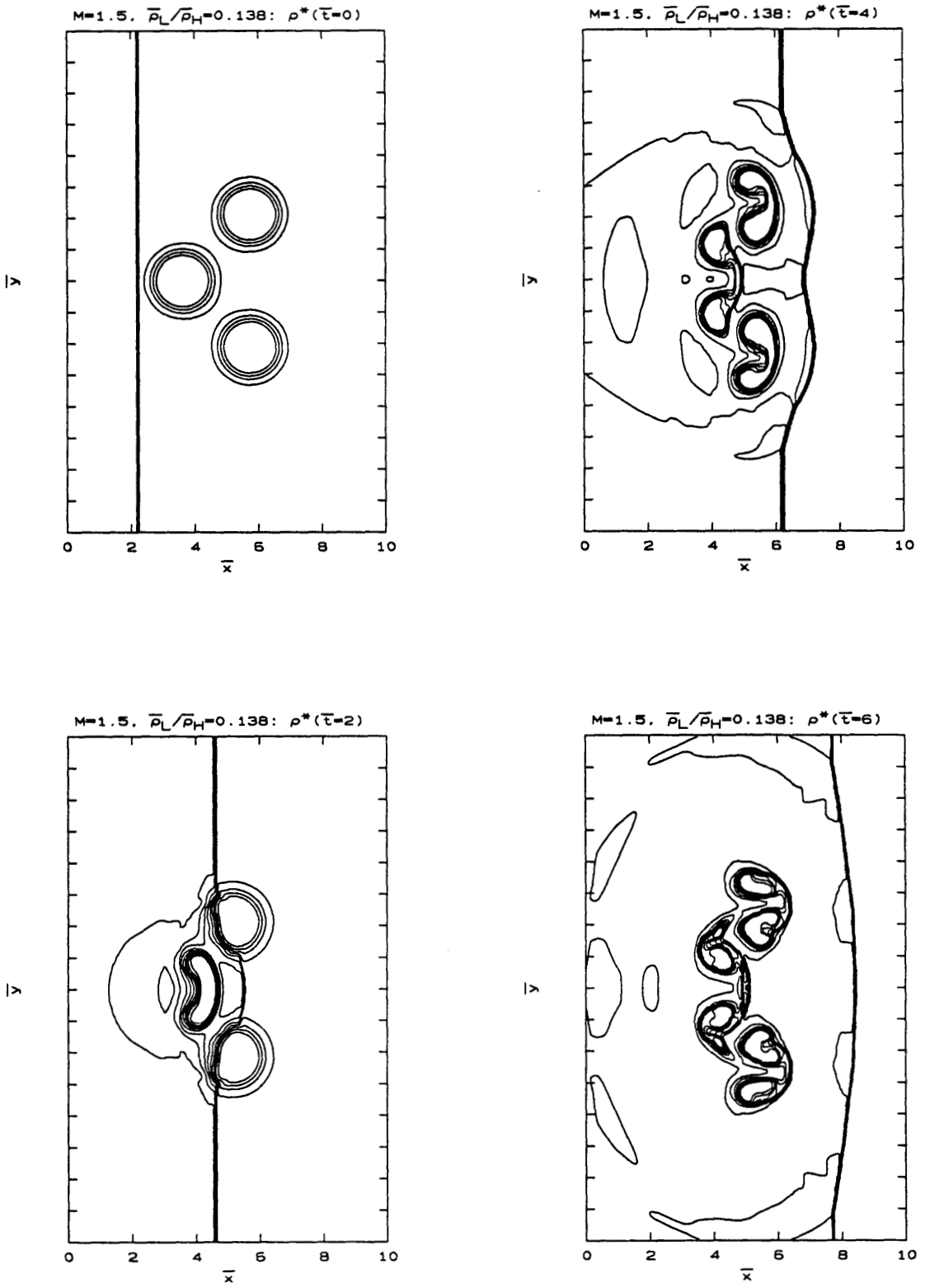

Figure 7.70 - Equilateral jet trio with M=1.5 and $\overline{\rho}_L/\overline{\rho}_H = 0.138$.

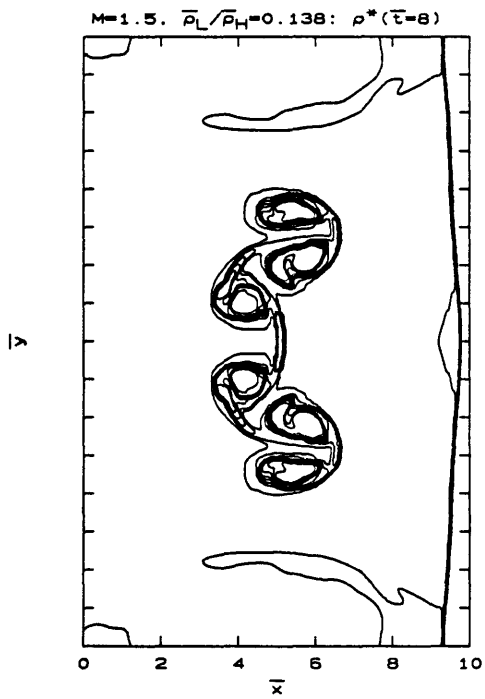
M=1.5. $\overline{\rho}_L/\overline{\rho}_H$=0.138: $\rho^*(\overline{t}$=8)
$\overline{y}$
0
2
4
6
8
10
$\overline{x}$

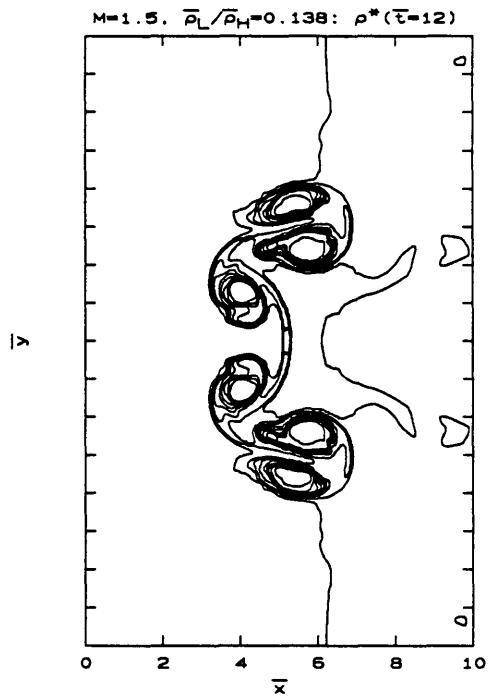
M=1.5. $\overline{\rho}_L/\overline{\rho}_H$=0.138: $\rho^*(\overline{t}$=12)
$\overline{y}$
0
2
4
6
8
10
$\overline{x}$

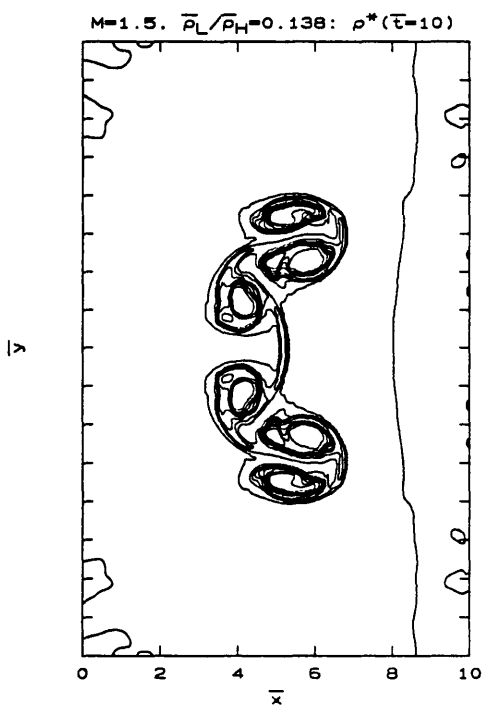
M=1.5. $\overline{\rho}_L/\overline{\rho}_H$=0.138: $\rho^*(\overline{t}$=10)
$\overline{y}$
0
2
4
6
8
10
$\overline{x}$

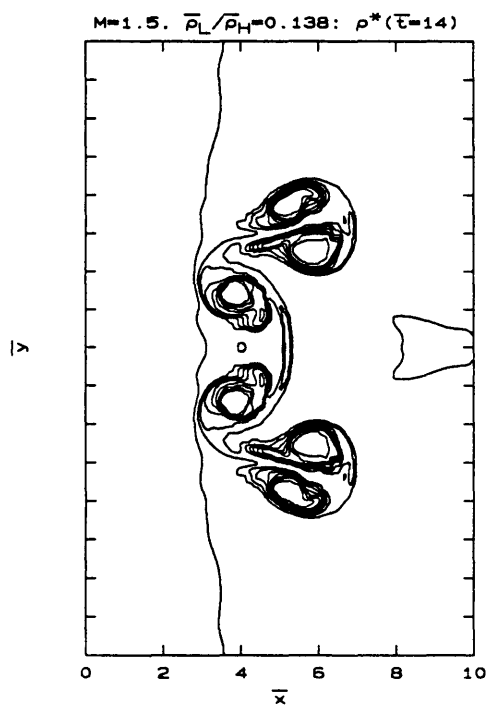
M=1.5. $\overline{\rho}_L/\overline{\rho}_H$=0.138: $\rho^*(\overline{t}$=14)
$\overline{y}$
0
2
4
6
8
10
$\overline{x}$

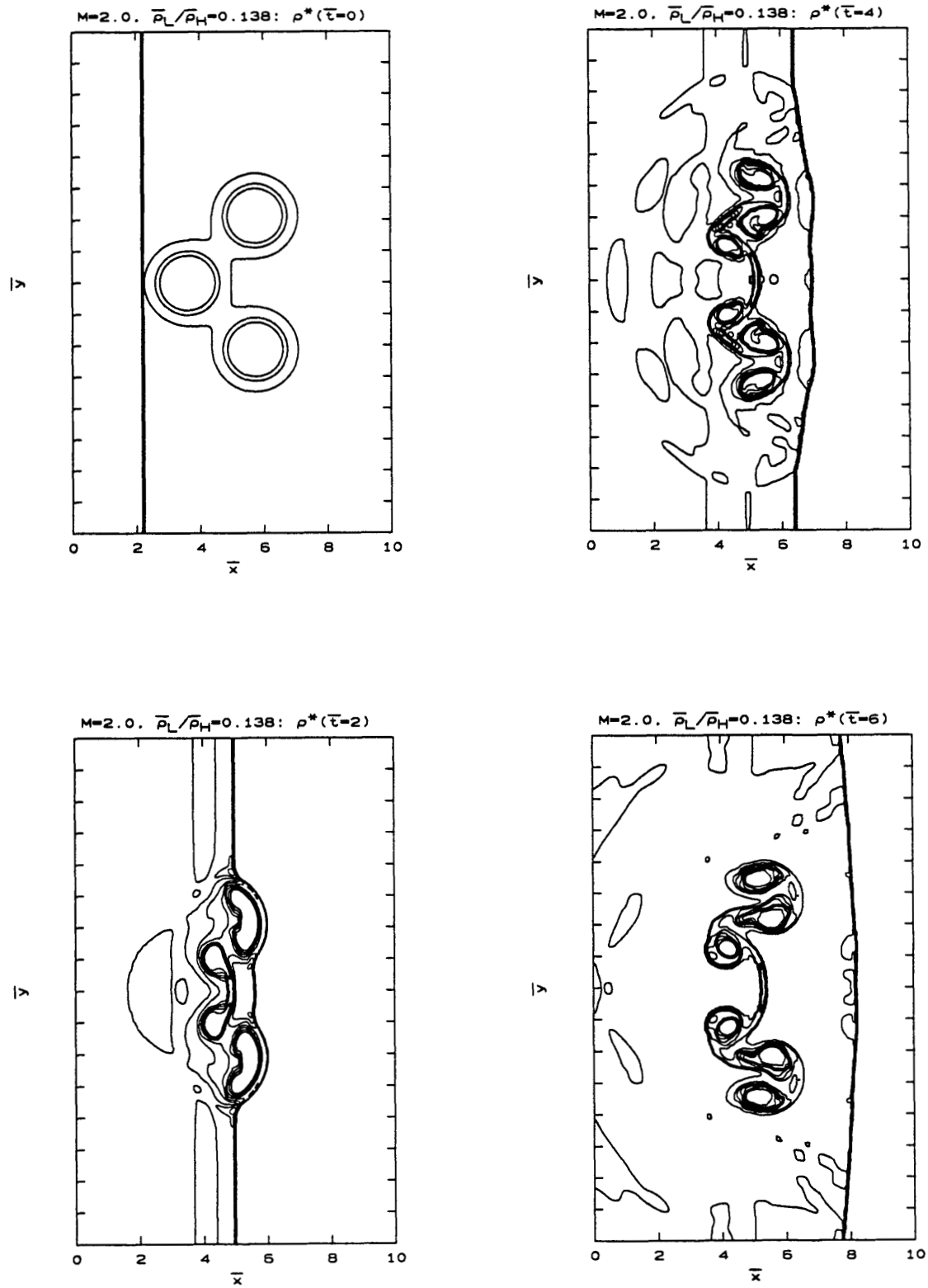

Figure 7.71 - Equilateral jet trio with M=2.0 and $\overline{\rho}_L/\overline{\rho}_H = 0.138$.

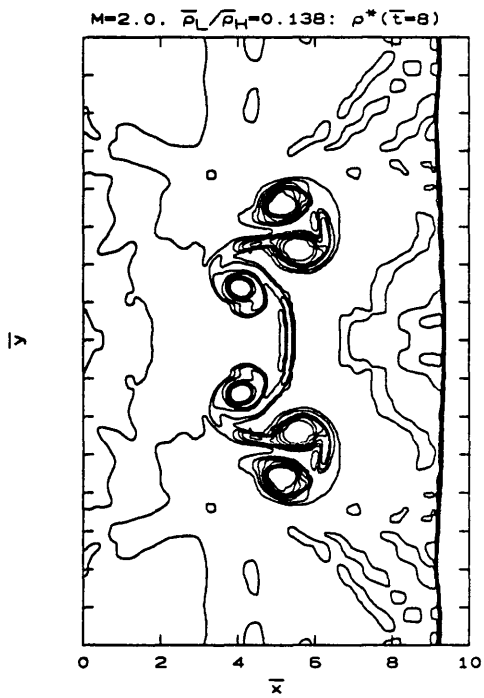
M=2.0. $\overline{\rho}_L/\overline{\rho}_H$=0.138: $\rho^*(\overline{t}$=8)
$\overline{y}$
0
2
4
6
8
10
$\overline{x}$

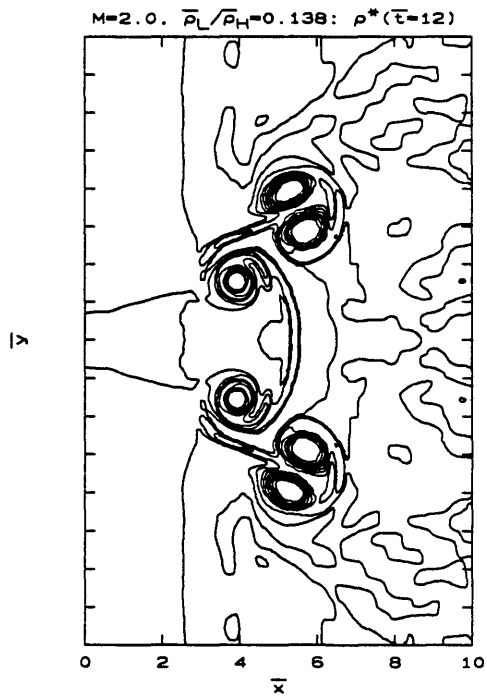
M=2.0. $\overline{\rho}_L/\overline{\rho}_H$=0.138: $\rho^*(\overline{t}$=12)
$\overline{y}$
0
2
4
6
8
10
$\overline{x}$

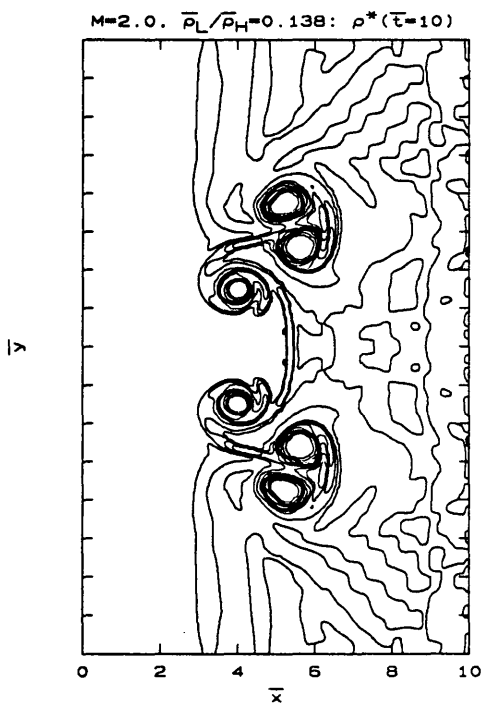
M=2.0. $\overline{\rho}_L/\overline{\rho}_H$=0.138: $\rho^*(\overline{t}$=10)
$\overline{y}$
0
2
4
6
8
10
$\overline{x}$

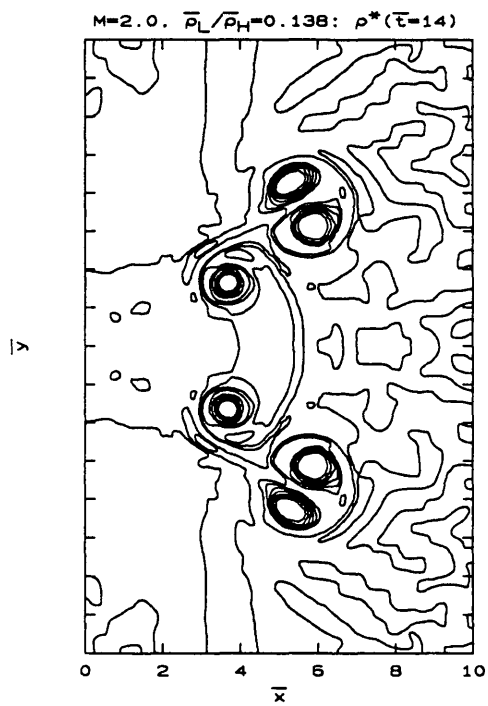
M=2.0. $\overline{\rho}_L/\overline{\rho}_H$=0.138: $\rho^*(\overline{t}$=14)
$\overline{y}$
0
2
4
6
8
10
$\overline{x}$

(a)

(b)

(c)

Figure 8.1 - Mixing: (a) Initial, (b) stretching, (c) diffusion.

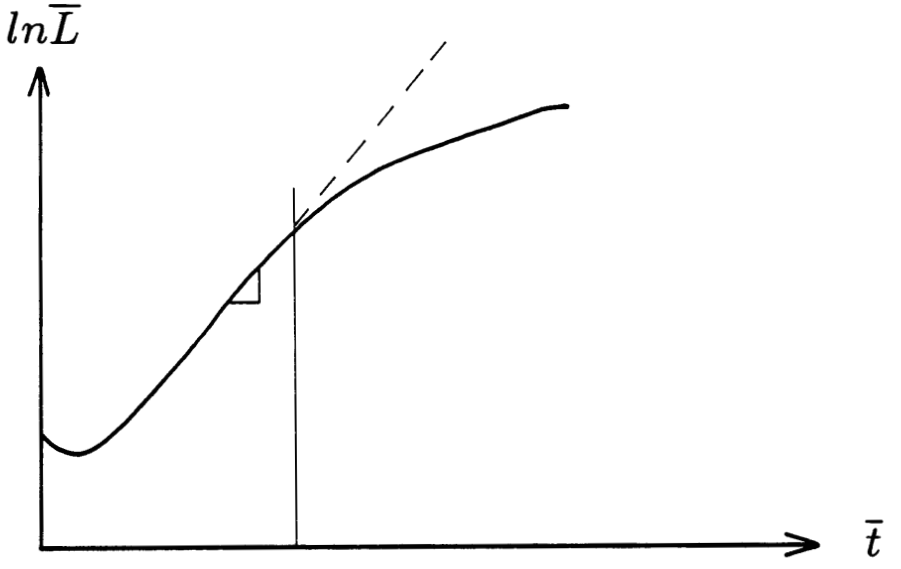

(a)

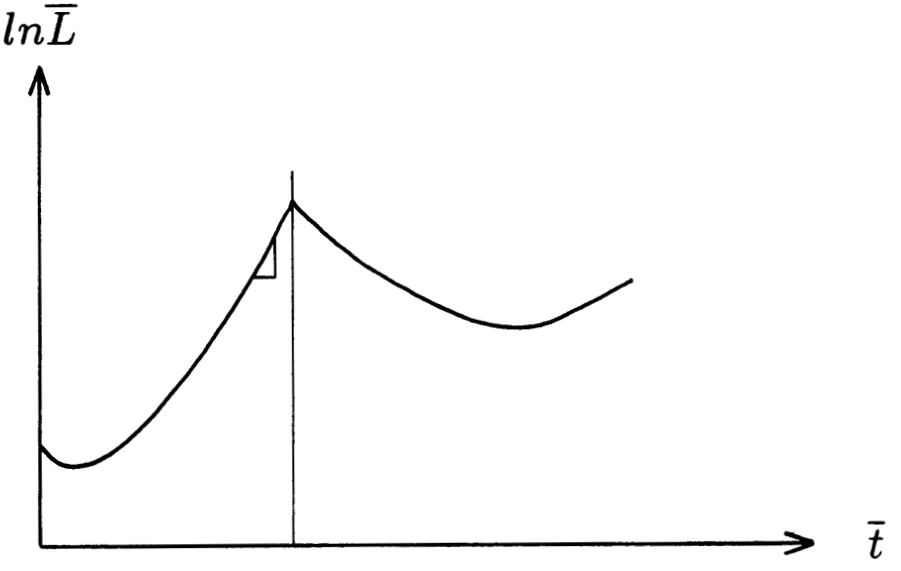

(b)

Figure 8.2 - Exponential stretching measure: (a) diffusion-limited, (b) resolution-limited.

Page 338, Figure 8.3
"EARLY" and "LATE" should be switched in the legend

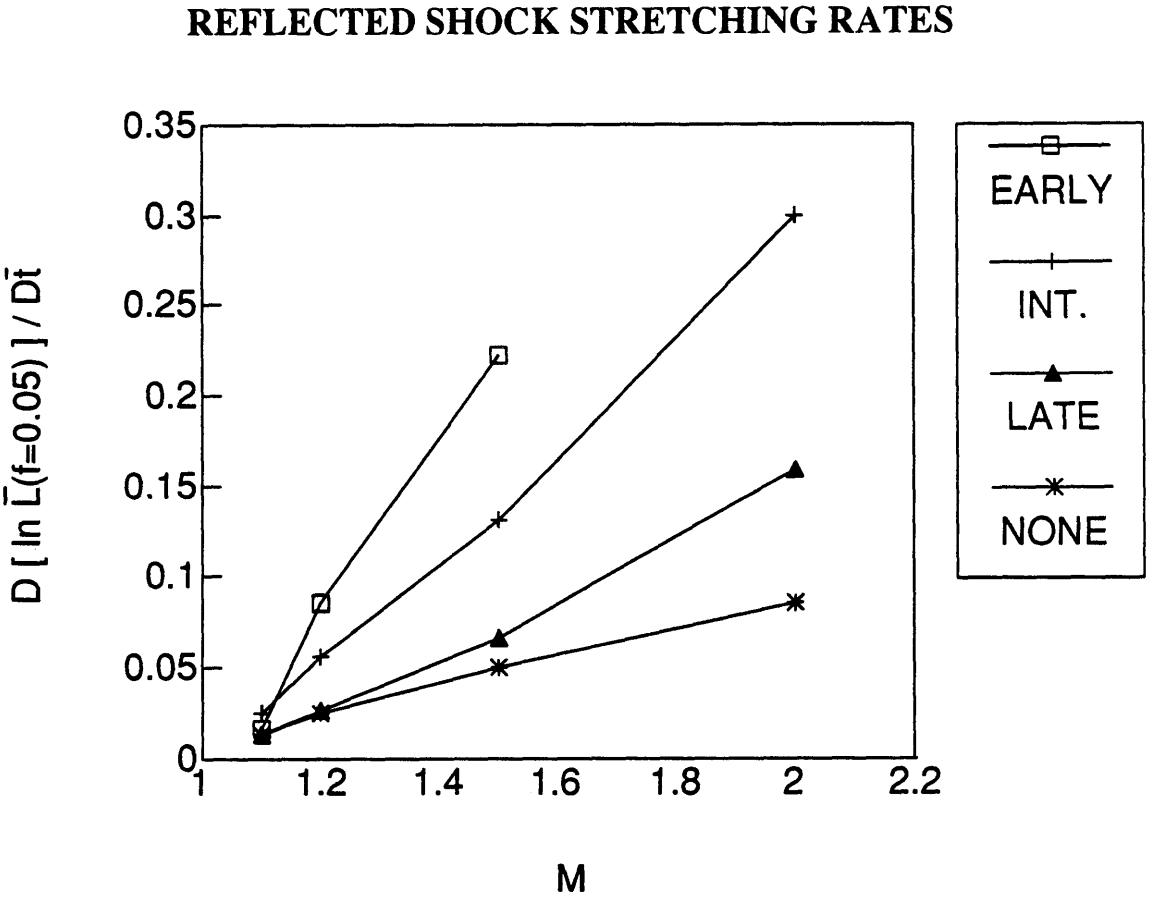

Figure 8.3 - Stretching rates for the reflected shock flows.

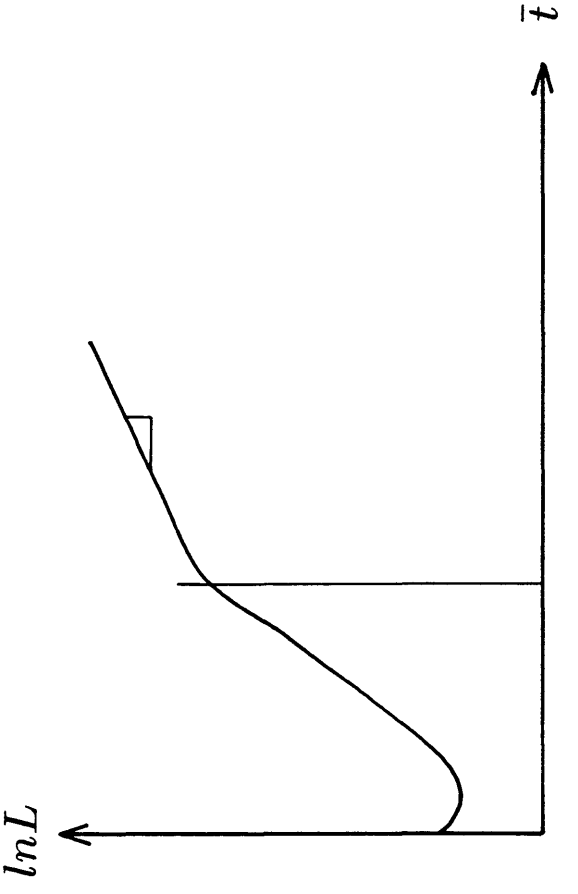

Figure 8.4 - Late-time stretching measure.

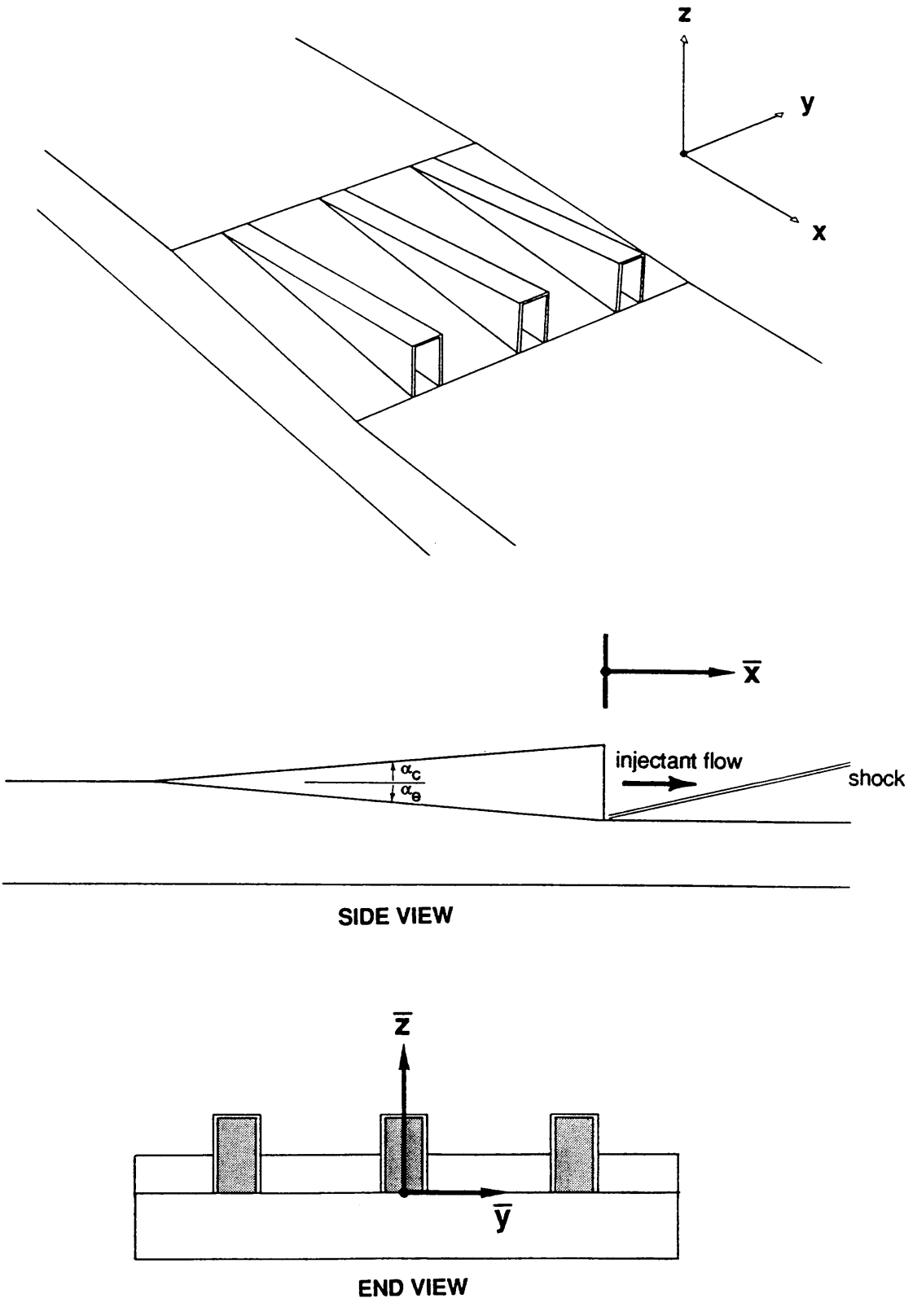

Figure 8.5 - Waitz's general injector configuration [Reproduced from Waitz (1991), p. 138].

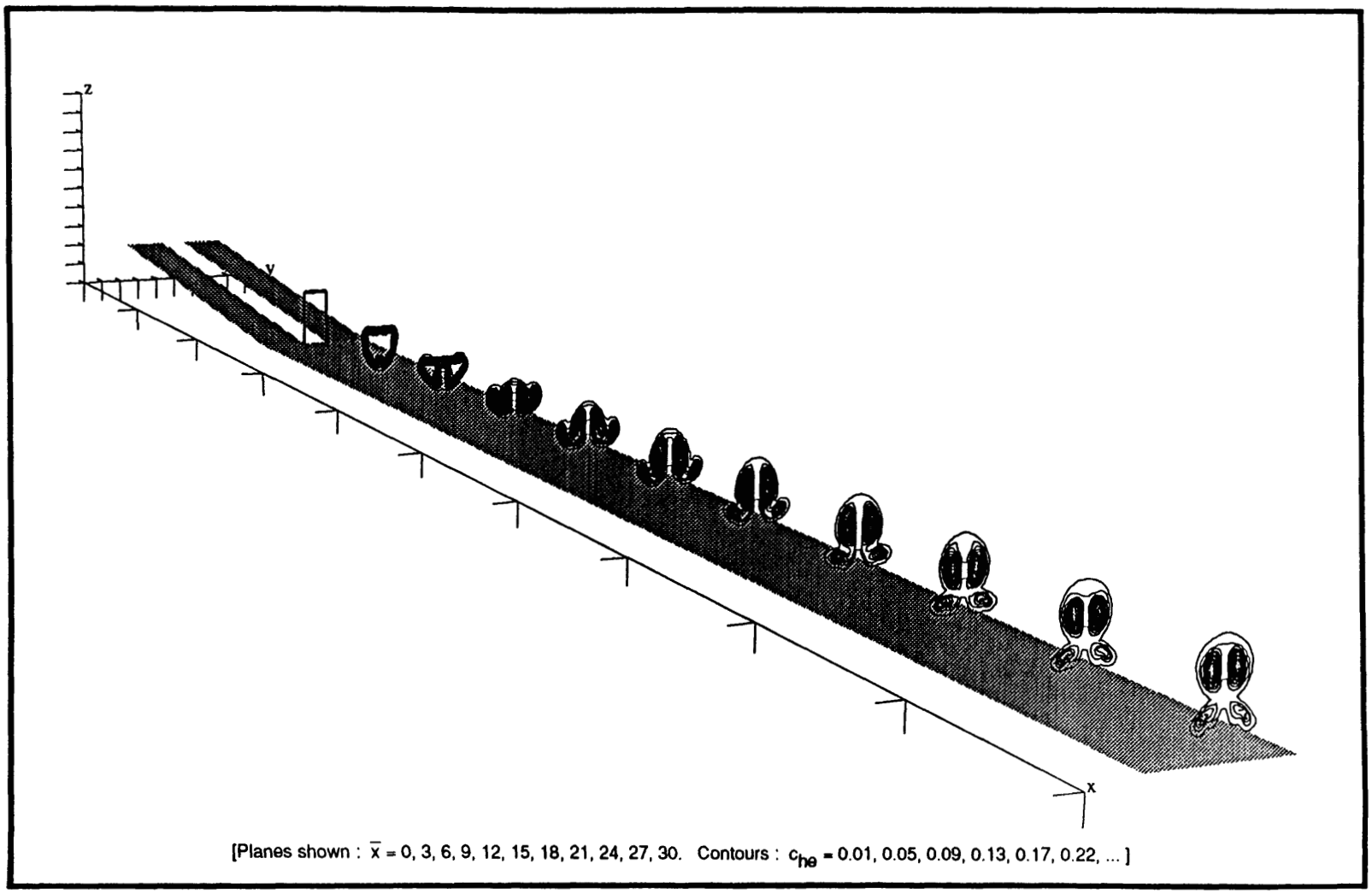

Figure 8.6 - Waitz's computations for the 'all-shock' geometry [Reproduced from Waitz (1991), p. 253].

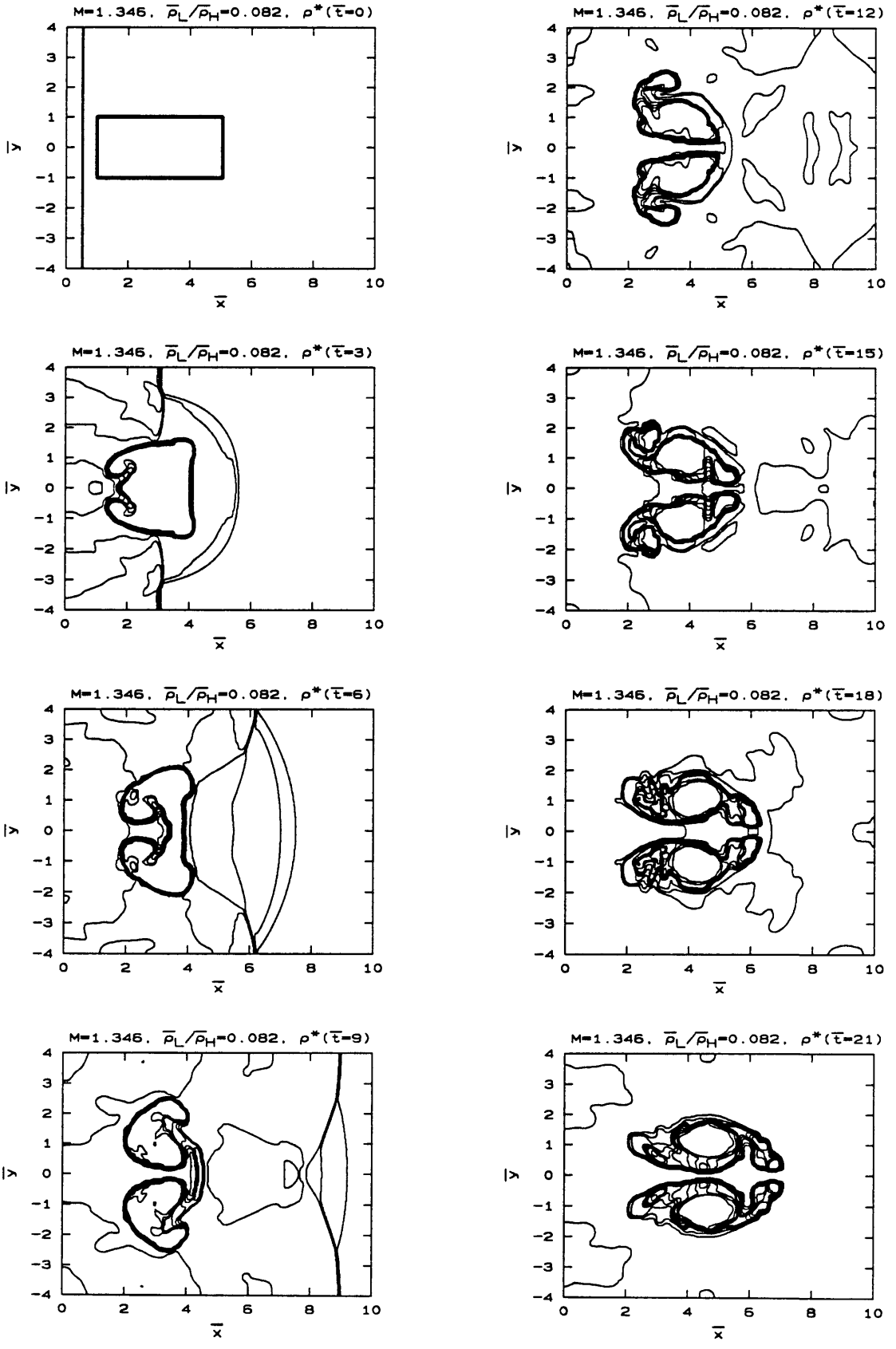

Figure 8.7 - Two-dimensional computation corresponding to Fig. 8.6.

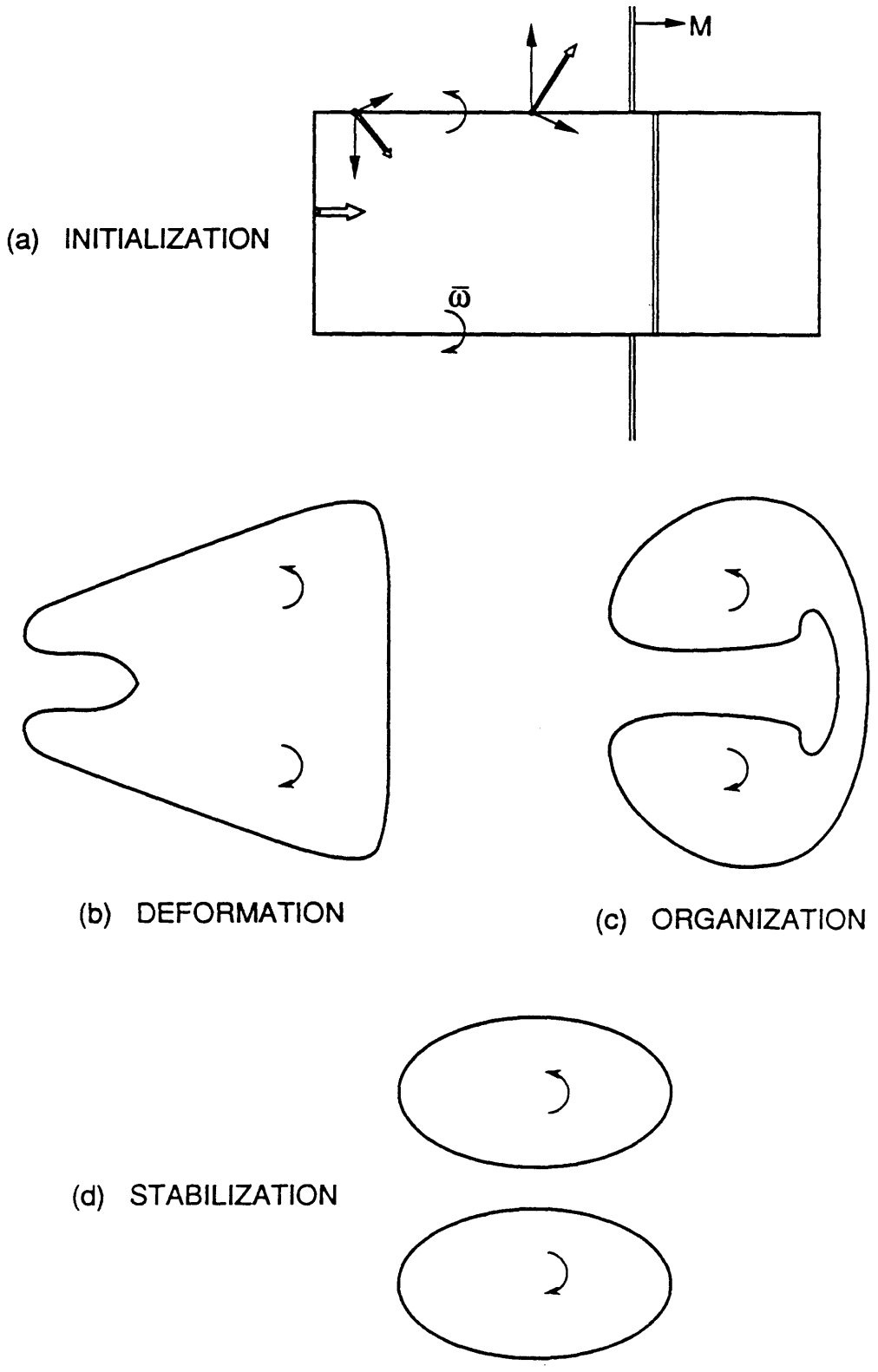

Figure 8.8 - Development of a vortex pair from a rectangular jet.

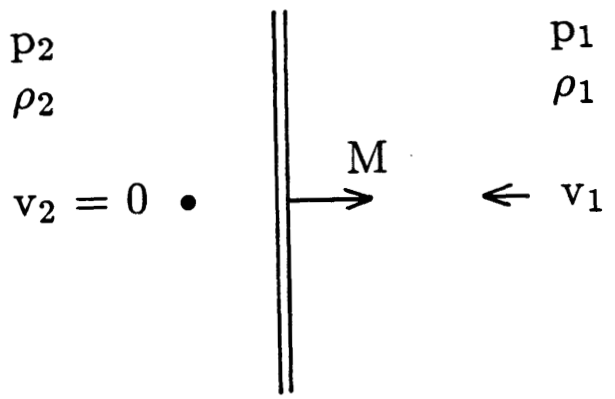

(a)

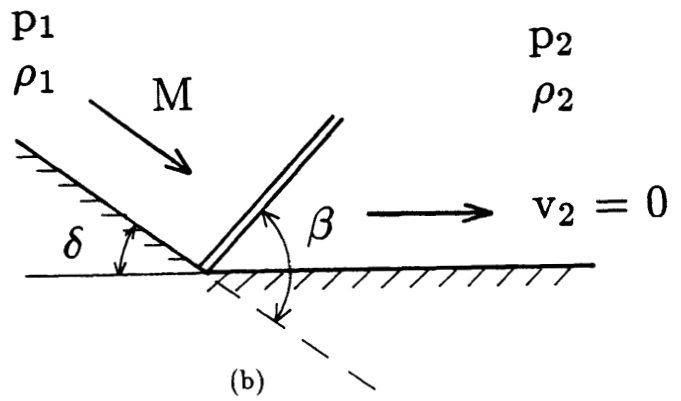

(b)

Figure 8.9 - Analogy between 2-D and 3-D flows.

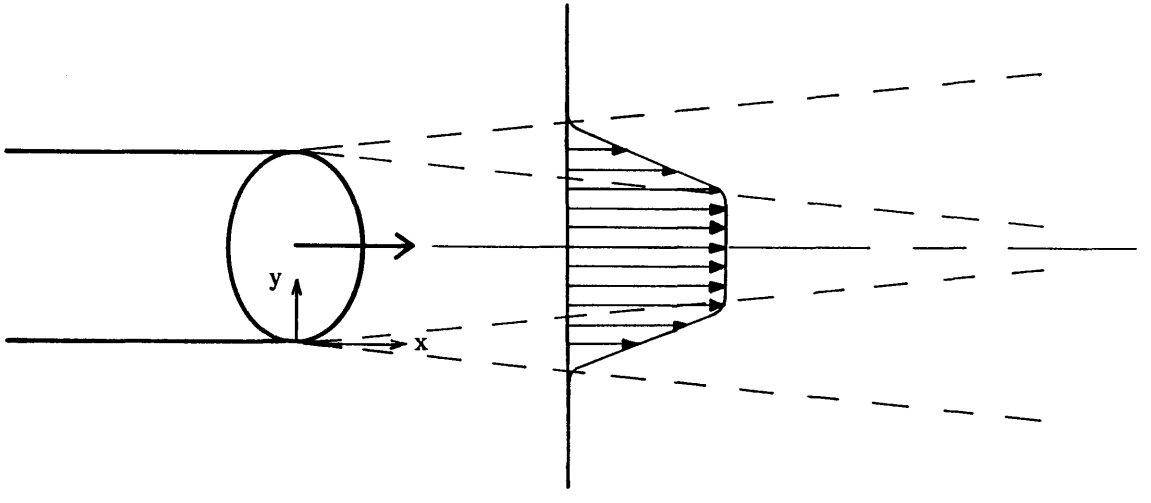

Figure A.1 - Mixing layer at the edge of an axisymmetric jet.

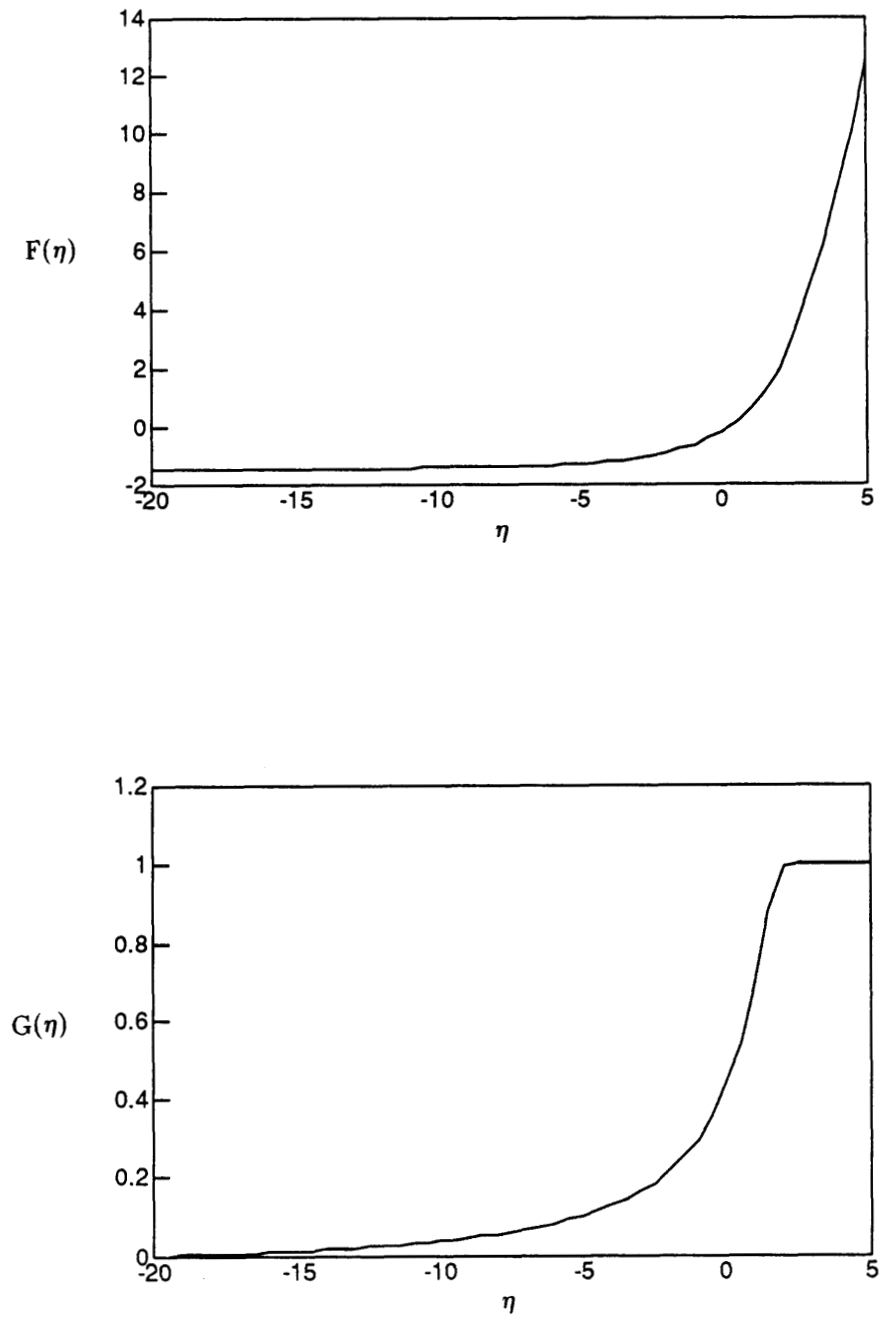

Figure A.2 - Similarity solutions for the mixing layer: (a) $F(\eta)$, (b) $G(\eta)$.

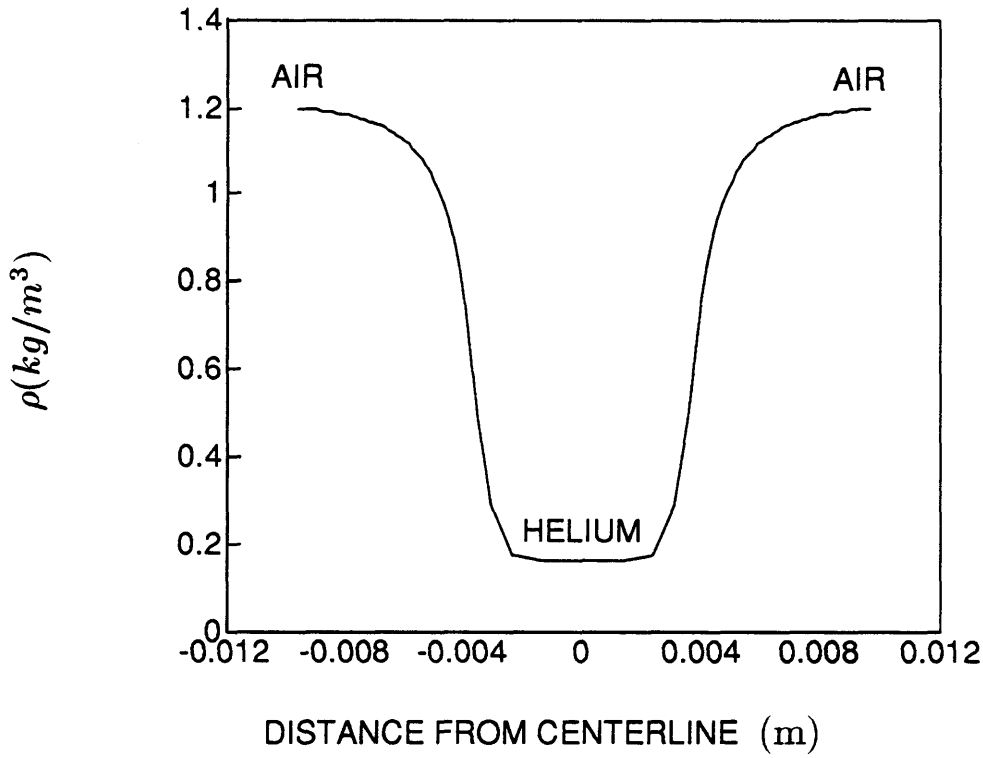

Figure A.3 - Mixing layer profile for a Helium jet corresponding to Jacobs' experimental conditions.